Université de Montréal

Liquides ioniques électroactifs dans la composition d'électrolytes avancés pour des applications en énergie

Electroactive ionic liquids in advanced electrolyte composition for energy application

Par Bruno Gélinas

Département de chimie

Faculté des Arts et des Sciences

Thèse présentée à la Faculté des études supérieures et postdoctorales en vue de l'obtention du grade de *philosophiæ doctor* (Ph.D.) en chimie

Avril 2017

Résumé

Cette thèse contribue au développement de nouveaux électrolytes pour améliorer la sécurité des batteries à ion lithium par le biais d'une étude et du développement d'électrolytes avancés à base de nouveaux liquides ioniques. En utilisant des approches synthétiques nouvellement développées, plusieurs liquides ioniques électroactifs, qui sont obtenus en modifiant le cation ou l'anion du liquide ionique, sont étudiés pour comprendre comment la structure des constituants ioniques du sel affecte ses propriétés physico-chimiques et électrochimiques. La méthodologie générale qui a guidé le travail tout au long de la thèse doit établir des comparaisons entre des liquides ioniques similaires qui présentent le groupe redox sur le cation et sur l'anion. Les progrès réalisés dans la compréhension des liquides ioniques redox dans cette thèse ont permis leur application dans plusieurs types de dispositifs de stockage d'énergie. La thèse décrira comment les électrolytes avancés basés sur ces liquides ioniques ont été appliqués pour éviter la surcharge des électrodes positives dans les batteries à ion lithium, pour améliorer la sécurité en réduisant l'inflammabilité, pour augmenter la concentration des additifs utilisant leur grande solubilité, pour augmenter la densité énergétique des supercapaciteurs et afin d'obtenir des espèces électrochromes stables avec l'air et avec l'humidité dans les dispositifs électrochromiques autoblanchiments. Cette thèse contribue au domaine du stockage d'énergie en améliorant les électrolytes et au domaine du liquide ionique en fournissant de nouvelles méthodes de synthèse, de nouvelles structures ioniques et une meilleure compréhension du fondamental des liquides ioniques électroactifs.

Mots-clés : Électrochimie, piles à ion lithium, synthèse de liquides ioniques, espèce électroactive, électrolyte concentré et navette redox.

Abstract

This thesis contribute to the development of new electrolytes to improve the safety of lithium-ion batteries through the study and development of advanced electrolytes based on novel ionic liquids. Using newly developed synthetic approaches, several electroactive ionic liquids, which are obtained by modifying either the cation or the anion of the ionic liquid, are studied to understand how the structure of the salt's ionic constituents affect its physico-chemical and electrochemical properties. The general methodology that guided the work throughout the whole thesis has to establish comparisons between similar ionic liquids that present the redox group on the cation and on the anion. The progress that has been made in understanding redox ionic liquids in this thesis allowed their application in several types of energy storage devices. The thesis will describe how advanced electrolytes based on these ionic liquids have been applied to prevent overcharging positive electrode materials in lithium-ion batteries, to improve safety by decreasing flammability, to increase the concentration of additives over their solubility, to increase energy density of supercapacitors and to achieve air- and moisture-stable electrochromic species for self-bleaching electrochromic devices. This thesis contributes to the field of energy storage by improving electrolytes and to the domain of ionic liquid by providing new synthesis methods, novel ion structures, and a better understanding of the fundamental of electroactive ionic liquids.

Keywords: Electrochemistry, lithium ion batteries, synthesis of ionic liquids, electroactive species, concentrated electrolyte and redox shuttle.

Table des matières

Liste des tableaux

Chapitre 1

Chapitre 3

CHAPITRE 4

Chapitre 5

Chapitre 6

Chapitre 7

Chapitre 8

Annexe 1

Annexe 2

Liste des figures

Chapitre 1

Chapitre 2

Chapitre 3

Chapitre 4

Chapitre 5

Chapitre 6

Chapitre 7

Chapitre 8

Annexe 1

Annexe 2

Liste des abréviations et symboles

A	Aire d'électrode (Surface)
ACN	Acétonitrile
APIL	Liquide ionique aprotique
ARIL	Liquide ionique redox dont l'anion est électroactif
B_0	Champ magnétique externe
BMIm	1-butyl-3-méthyl-imidazolium
BPyr	Butylpyridinium
C	Concentration
C/n	Vitesse de chargement
C_{dl}	Capacitance de double-couche
CE	Efficacité de coloration
CPPP	Cellule photovoltaïque à pigment photosensible
CV	Voltampérométrie cylcique
DCM	Dichlorométhane
DDB	2,5-di-tert-butyl-1,4-diméthoxybenzène
DDBF	2,5-di-tert-butyl-1,4-bis(2,2,2-trifluoroéthoxy)benzène
DDB-pNTf	3-(2,5-di-tert-butyl-4-méthoxyphenoxy)propylsulfonyl (trifluorométhylsulfonyl) imide
DEC	Carbonate de diéthylène
DMB-NTf	2,5-diméthoxyphénylsulfonyl (trifluorométhylsulfonyl) imide
DMC	Carbonate de diméthylène
DMF	N,N-Diméthylformamide
DmFc	Décaméthylferrocene
DMSO	Diméthylsulfoxide
D_O	Coéfficient de diffusion de l'espèce oxydée
DOSY	Expérience RMN 2D pour l'autodiffusion (Diffusion ordered spectroscopy)
DPSC	Chronoampérométrie à double saut de potentiel
D_R	Coefficient de diffusion de l'espèce réduite
D_S	Coefficient d'autodiffusion
DSC	Analyse calorimétrique différentielle
e	Charge élémentaire
E	Potentiel ou énergie
E'	Potential d'équilibre
E°	Potentiel standard
$E_{1/2}$	Potentiel de demi-vague
E_a	Énergie d'activation
EC	Carbonate d'éthylène
ECD	Dispositif électrochromique
ECM	Matériel électrochromique
EDLC	Capaciteurs de double couche électrique
ELi	Sel de lithium électrochromique
EMIm	1-éthyl-3-méthyl-imidazolium
E_p	Potentiel au pic

ES	Sel électroactif
ESI	Ionisation par électronébulisateur
EV	Éthylviologène
F	Constante de Faraday
Fc	Ferrocène
$FcEImC_{12}$	1-(méthylferrocènyl)-3-dodécenylimidazolium
$FcEImC_4$	1-(méthylferrocènyl)-3-butylimidazolium
$FcEImC_8$	1-(méthylferrocènyl)-3-octylimidazolium
$FcEMIm/FcEImC_1$	1-(méthylferrocènyl)-3-méthylimidazolium
FcNTf	Ferrocénylsulfonyl(trifluorométhylsulfonyl)imide
FTO	Oxyde d'étain dopé au fluorure
g	Amplitude du gradient de champ
G_4	Tétraglyme
GCD	Galvanostatique de charge–décharge
G_z	Impulsion magnétique additionelle
HR MS	Spectroscopie de masse à haute résolution
HSAB	Acides et bases; dures et molles
I	Courant
i_0	Courant d'échange
i_a	Courant anodique
i_c	Courant cathodique
I_{cc}	Courant de court-circuit
I_L	Courant limite
IL (LI)	Liquide ionique
Im	Imidazolium
I_p	Courant au pic
i_{ss}	Courant d'état stationnaire
ITO	Oxyde d'indium-étain
J	Flux des espèces
K	Constante de cellule
k	Constante de Boltzmann
k_0	Constante de vitesse de transfert électrogène hétérogène
LFP	$LiFePO_4$
Li	Ion de lithium
Li BETI	Lithium bis(perfluoroéthylsulfonyl)imide
Li BOB	Lithium bis(oxalato)borate
Li FAP	Lithium fluoroalkylphosphate
Li NTf_2 ou Li TFSI	Lithium bis(trifluorométhanesulfonyl)imide
Li OTf	Lithium triflate
LIB	Batterie à ions lithium
LTO	$Li_4Ti_5O_{12}$
LTP	$LiTi_2(PO_4)_3$
MBPip	1-butyl-1-méthylpiperidinium
MDB	2-tert-butyl-1,4-diméthoxybenzène
MDB-NTf	4-tert-butyl-2,5-diméthoxyphénylsulfonyl(trifluorométhylsulfonyl)imide
Me_3BuN	Triméthylbutylammonium

n	Nombre d'électron échangé
N_a	Nombre d'Avogado
NCS	N-chlorosuccinimide
NMP	N-méthyl-2-pyrrolidone
NMR	Résonance magnétique nucléaire
NTf_2 or TFSI	Bis(trifluorométhanesulfonyl)imide
OCP	Potentiel de circuit ouvert
OM	Orbitale moléculaire
OMe	Groupe méthoxy
P	Puissance
PC	Carbonate de propylène
PFG-STE/PFGSE	Écho stimuli par gradient de champ pulsé
P_H	Hauteur d'impulsion
PIL	Liquide ionique protique
Pt	Platine
PTFE	Polyétrafluoroéthylene (teflon)
PVDF	Polyvinylidene fluoride
P_W	Largeur d'impulsion
Q	Capacité
r	Rayon de solvatation ou rayon de la microélectrode
R	Constante universelle des gaz parfaits
R_{ct}	Résistance de transfert de charge
RDE	Voltampérométrie à électrode rotative
RESC	Supercapaciteur utilisant un electrolyte redox
RF	Radiofréquence
RIL	Liquide ionique redox
RILSC	Supercapiciteur ulisant un liquide ionique redox
R_{nc}	Résistance non-compensée
R_s	Résistance de la solution
R-S	Navette redox
RTIL	Liquide ionique à température ambiante
S	Intensité du signal spin–écho
SCE	Supercapaciteur électrochimique
SDC	Autodécharge
SEI	Électrolyte solide passif à l'interface
S_H	Hauteur des marches
SN2	Substitution nucléophile bimoléculaire de deuxième ordre
SWV	Voltammétrie impulsionnel à vagues carrées
T	Température absolue
t_1	Temps de relaxation longitudinale
t_2	Temps de relaxation transversale
TBAP	Tétrabutylammonium perchlorate
t-But	Groupe tert-butyle
T_d	Température de décomposition
TEMPO	2,2,6,6-Tétraméthyl-1-piperidinyloxy
T_g	Température de transition vitreuse

TGA	Analyse thermogravimétrique
THF	Tétrahydrofurane
t_i	Nombre de transport d'un ion
T_m	Température de fusion
TMB-NTf	2,4,5-triméthoxyphénylsulfonyl(trifluorométhylsulfonyl)imide
TSIL	Liquide ionique fonctionnel
VFT	Modèle de Vogel-Fulcher-Tamman
w	Masse d'électrodes
W_g	Énergie spécifique gravimétrique
x_i	Fraction molaire de l'ion
XRD	Diffraction X-Ray
$-Z_{im}$	Partie imaginaire du diagramme de Nyquist
Z_{re}	Partie réelle du diagramme de Nyquist
Z_w	Élément de Warburg
α	Coefficient de transfert
γ	Ratio gyromagnetique ou ratio des coefficients de diffusion
Γ_s	Taux de recouvrement de la surface
δ	Durée du gradient de champ, déplacement chimique et couche de diffusion
Δ	Temps de diffusion
ΔE_p or ΔE_{pa-pc}	Différence de potentiel entre le potentiel au pic anodique et cathodique
ΔG	Énergie libre de Gibbs
ΔH	Enthalpie
ΔI	Différence entre le courant direct et inverse
ΔOD	Densité optique
ΔQ_c	Charge transferee
ΔS	Entropie
ΔT	Transmittance du contraste
ΔW	Différence avec la ligne idéale de Walden
η	Viscosité dynamique
η_c	Surtention due à l'appauvrissement de concentration
η_{ct}	Surtension due au transfert de charge
Λ	Conductivité molaire
ν	Vitesse de balayage ou viscosité cinétique
σ	Conductivité ionique
φ	Rendement quantique
Ψ	Paramètre cinétique
ω	Vitesse de rotation de l'électrode rotative
ω_L	Fréquence de Lamor

Remerciements

J’aimerais en premier lieu remercier mon directeur de recherche Prof. Dominic Rochefort de m'avoir accueilli à bras ouverts dans son laboratoire. Je suis très reconnaissant qu’il m’ait donné ma première expérience en laboratoire et pour tous les conseils, opportunités d’apprentissage autant au niveau professionnel qu’au niveau scientifique, pour la motivation dans les moments plus difficiles et pour les mises en garde envers des projets à risque d’échec. Grâce à ce mentor, j’ai grandi comme scientifique et j’ai maintenant une formation solide pour réaliser d’ambitieux projets.

Je veux aussi remercier tous les membres du groupe Rocherfort, mais spécialement, John Forgie de m’avoir aidé et partagé son expertise. Il a été une personne importante dans mon développement et aussi, au démarrage de mon projet. De plus, j’ai eu la chance de superviser plusieurs stagiaires dont Han Jin Xie, Myriann Natali et Dyuman Das qui se sont démarquées par leur rigueur et leur excellent travail en laboratoire. De plus, Han Jin a réalisé le projet des supercapaciteurs. J’ai aussi des remerciements à faire à Thomas Bibienne qui a fait la confection de mes piles à ion lithium.

J’aimerais remercier le professeur, Mickaël Dollé qui a été un excellent collaborateur dans les études des piles à ion lithium, car cette aide a été précieuse à mes yeux. J’aimerais remercier le personnel de soutien du département de chimie de l'Université de Montréal pour les formations aux divers instruments, aux techniciennes de laboratoire pour les prêts de matériels, les analyses effectuées (spectre de masse et analyse élémentaire), l’atelier mécanique/souffleur de verre pour la réparation et la conception des pièces et du matériel. Un gros merci à Cédric Malveau qui a fait les mesures d’autodiffusion par RMN et à Sylvain Essiembre pour l’aide lors des analyses thermiques. J’aimerais remercier les fonds de recherche du conseil de recherches en sciences naturelles et en génie du Canada (NSERC) et les Fonds de recherche du Québec en nature et technologies (FQRNT) pour leur support financier à la recherche.

Finalement, j’aimerais remercier ma famille et mes amis qui ont façonné la personne que je suis. Deux vertus m’ont permis de réaliser cette thèse : la polyvalence de mon père et la persévérance de ma mère. Mon dernier remerciement est pour ma conjointe qui m’a supporté dans les réussites et dans les échecs. Merci Stéphanie, d’avoir vécu cette aventure avec moi.

Chapitre 1 : Introduction aux électrolytes avancés

1.1. Avant-propos

Jamais les dispositifs de stockage d'énergie n'ont suscité autant d'intérêt que de nos jours. Bien sûr, chacun de nous a déjà eu l'occasion de se familiariser avec ce type de dispositif tel que la batterie qui est une technologie mature et un peu plus d'un centenaire. Les supercapaciteurs qui sont une technologie plus récente souvent utilisée pour des applications demandant peu d'énergie. Ces quelques exemples de dispositifs de stockage d'énergie font partie du quotidien de chacun de nous, mais l'amélioration de ceux-ci pourrait augmenter leur importance dans le domaine de l'énergie et diminuer la dépendance de l'humanité envers l'énergie pétrolière.

Règle générale, les chimistes chercheurs oeuvrant dans le domaine de l'énergie priorisent le développement de nouveaux matériaux d'électrodes, cependant l'intérêt pour les électrolytes est très récent et grandissant. D'ailleurs, cette thèse présente des innovations au niveau de l'électrolyte pour les batteries à ion lithium, les supercapaciteurs et les dispositifs électrochromiques en utilisant des liquides ioniques fonctionnalisés par un composant intrinsèquement électroactif.

1.2. Introduction aux liquides ioniques et aux liquides ioniques fonctionnels

1.2.1. Mise en contexte des liquides ioniques et généralité

Les liquides ioniques (LIs) sont des sels fondus qui sont formés exclusivement d'ions. La première synthèse de LI qui à ce moment n'étaient pas encore connus, a été observée en 1914 lorsaue Paul Walden a décrit les propriétés du nitrate d'éthylammonium et il a donné comme définition très arbitraire que le point de fusion des LIs est sous les 100°C. Il existe deux catégories de LIs : protiques (LIP) et aprotiques (LIAP). Un LIP est produit par le transfert de proton entre une base et un acide de Brønsted ce qui n'est pas le cas pour un LIAP. Les applications de ces deux types de LIs diffèrent complètement par le biais de leurs propriétés physicochimiques propres à

chacun. Par exemple, il n'est pas possible d'utiliser les LIPs pour des applications dont le LI pourrait subir des réactions de réductions afin d'éviter le dégagement d'hydrogène (e.g. batterie à ion lithium) et cette thèse utilisera exclusivement des LIAPs qui sont mieux adaptés pour les besoins identifiés en début de projet. Les propriétés des LIAPs sont différentes selon le cation et l'anion utilisés. En général, ils ont une pression de vapeur pratiquement nulle, ils sont non inflammables, possédant une grande stabilité thermique, une large fenêtre électrochimique et une conductivité élevée. Toutefois, ils sont visqueux et hygroscopiques.[1, 2] De plus, ils sont miscibles avec la plupart des solvants organiques polaires et la dernière génération de LIs est stable avec l'air et l'humidité.

Pour définir les LIs simplement, il s'agit de sels composés de larges ions présentant une asymétrie et un système de résonance dans leur structure ce qui a pour conséquence de diminuer l'énergie réticulaire (Énergie de Lattice). En d'autres mots, il s'agit de combiner un acide mou et une base molle selon le principe de Pearson pour former un sel fondu de basse température de fusion. Par exemple, les sels halogénure de sodium illustrent bien ce qui est expliqué, car leurs points de fusion sont 1012°C pour le NaF, 801°C pour le NaCl, 747 °C pour le NaBr et 660 °C pour le NaI. Les énergies réticulaires pour ces mêmes sels alcalins sont 908, 788, 736, 686 kJ mol^{-1}, respectivement. Normalement, les sels fondus purement inorganiques ne permettent pas d'obtenir des points de fusion sous la barre fictive des 100°C, toutefois, la chimie organique donne accès à cet état de phase recherché, l'état liquide à des températures plus près de la température ambiante. La **Figure 1.1** présente quelques exemples d'anions et de cations typiquement utilisés dans une multitude d'applications telles qu'en synthèse organique et/ou solvant, pour l'extraction et séparation, en analytique, comme lubrifiant, pour les écrans à cristaux liquides et en énergie comme électrolyte. Plus précisément, les LIs possèdent d'excellentes propriétés en tant qu'électrolyte pour les systèmes de stockage ou production d'énergie tels que les batteries, les supercapaciteurs, les piles à combustible et les cellules photovoltaïques à pigment photosensible.[3] Pour la nomenclature utilisée dans cette thèse et souvent employée dans la littérature, les acronymes pour les cations est l'abréviation du nom du cation précédé par la première lettre de la(des) chaîne(s) alkyle(s) latérale(s) qui participe directement à l'atome cationique qui est souvent l'azote ou le phosphore. Le 1-**B**utyl-3-**M**éthyl-**Im**idazolium (BMIm, cation dérivé de l'imidazole), le 1-**B**utyl-1-**M**éthyl-**Pip**éridinium (BMPip, cation dérivé de la pipéridine) et 1-**B**utyl-**Pyr**idinium (BPyr, cation dérivé de la pyridine) sont des exemples de cations largement utilisés dans la structure des

LIs communs. La nomenclature pour l'anion est légèrement différente, car les anions sont beaucoup plus inorganiques que les cations et c'est typiquement l'utilisation directe de la formule chimique (e.g. tétrafluoroborate, BF_4 et hexafluorophosphate, PF_6). L'abréviation qui est important à connaître pour les anions et pour cette thèse est le trifluorométhanesulfonyle qui est donné par l'abréviation Tf correspondant à un groupe triflique. Par exemple, le bis(trifluorométhanesulfonyl)imide et le trifluorométhanesulfonate (triflate) est le NTf_2 (souvent répertorié comme TFSI dans la communauté des batteries) et le OTf, respectivement. Ces détails de nomenclature seront rappelés au fil de cette thèse et des précisions seront apportées pour une meilleure compréhension. Il existe évidemment des exceptions à cette nomenclature qui diffèrent d'un domaine à l'autre et malheureusement, IUPAC n'a pas règlementé la nomenclature pour les LIs.

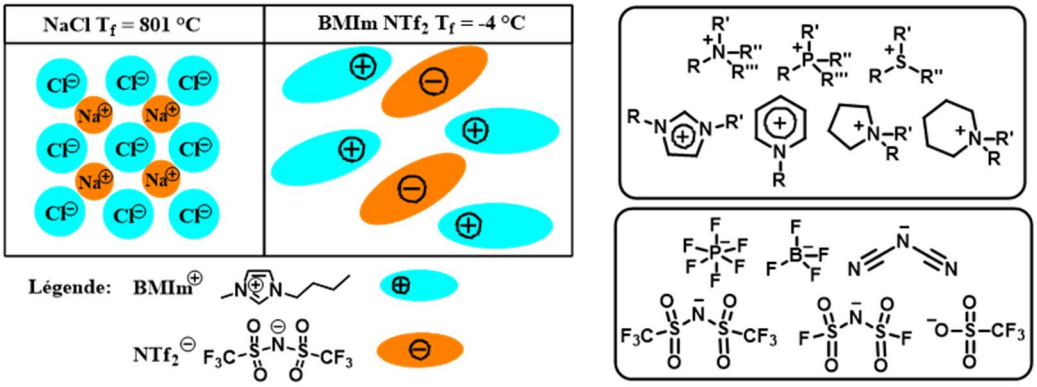

Figure 1.1. Définition des liquides ioniques et quelques exemples d'anions et de cations.

La caractérisation des propriétés physicochimiques des LIs telles que le point de fusion, la viscosité et la conductivité ionique est fondamentale. Il est primordial que ces caractérisations soient effectuées avant même d'être utilisées comme composante d'un électrolyte. Évidemment, ces caractérisations feront partie des résultats présentés dans cette thèse. La viscosité et le point de fusion sont des propriétés qui dépendent des forces de Van der Waals, des ponts hydrogènes, des forces électrostatiques et des transferts de charge. De plus, des structures asymétriques favorisent le désordre et la flexibilité des chaînes latérales aide à détruire ces interactions. La densité de la charge a aussi son effet sur les propriétés physicochimiques, car avec une sphère ionique plus grande, la densité électronique est plus petite et les forces électrostatiques sont donc diminuées. Par conséquent, l'augmentation de porteurs de charge aide à délocaliser la charge pour avoir une sphère ionique plus grande. La conductivité ionique dépend de la viscosité et de la mobilité des

ions. Cette conductivité a son importance, car il est favorable d'avoir une haute conductivité ionique pour un usage des LIs comme composante d'un électrolyte. Dans le cadre de ce projet de recherche, les LIs à base d'imidazolium et de bis(trifluoromethanesulfonyl)imide sont digne d'intérêt par le biais d'excellentes propriétés physicochimiques telles qu'une conductivité ionique d'environ 3,9 à 8,5 mS cm^{-1} et d'une viscosité de 34 à 52 cP.[4]

1.2.2. Les liquides ioniques fonctionnels

Les liquides ioniques fonctionnels (LIFs), aussi appelés liquides ioniques à tâche spécifique, sont obtenus par la modulation structurelle du cation, de l'anion ou même des deux avec l'insertion d'un groupement fonctionnel dans l'objectif d'accomplir une tâche bien précise. Les LIFs peuvent être obtenus par une voie de synthèse propre à l'ion modifiable et au groupement fonctionnel, où le groupement fonctionnel est lié d'une façon covalente à l'ion. Ensuite, il s'agit de faire une réaction de métathèse d'ions pour l'obtention d'un LI. Dans la plupart des cas, les propriétés physicochimiques du LIFs sont souvent significativement chamboulées en comparaison avec le LI non-modifié analogue.

Le concept derrière les LIFs à la base est de contourner la dissolution de l'espèce fonctionnelle dans le solvant choisi et du même coup d'éviter les problèmes de solubilité. En d'autres mots, le LIF a deux fonctions soit la fonction spécifique à l'application voulue et celle d'être un solvant. De plus, le LIF bénéficie des propriétés des LIs mentionnées dans la **Section 1.2.1** et par conséquent, le LIF est réutilisable pour accomplir plusieurs fois sa tâche par le biais de la faible volatilité de celui-ci qui minimise les pertes par évaporation suivant les traitements de purification. Cependant, dépendamment de la fonction ajoutée, il est possible que les propriétés physicochimiques ne soient pas adéquates pour l'application à l'état pur et il est nécessaire d'utiliser des solutions LIF-LI ou LIF-solvant. Les LIFs ont été développés pour plusieurs applications telles que l'extraction de métaux lourds,[5] la synthèse organique,[6] la capture de CO_2 (séparation),[7] l'extraction/lavage,[8] la catalyse de métal de transition,[9] la synthèse de nanoparticule,[10] la formation de monocouche auto-assemblé[11] et en électrochimie.[12, 13] Voici la **Figure 1.2** qui illustre quelques exemples de LIFs.[14]

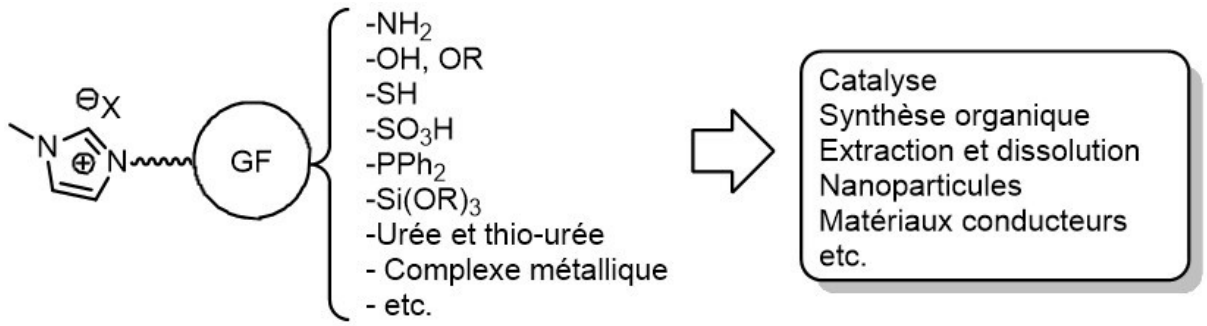

Figure 1.2. Exemples de liquides ioniques fonctionnels (LIFs) utilisant plusieurs groupements fonctionnels (GF).

1.2.3. Les liquides ioniques électroactifs et leurs applications

Un exemple pertinent de LIFs dans le domaine de l'électrochimie est la modification d'un imidazolium avec un groupement ferrocénylméthyle, ce qui résulte à l'obtention d'un LI intrinsèquement électroactif. Ces liquides ioniques électroactifs aussi nommés liquides ioniques redox (LIRs) ont été développés ces dernières années pour étudier le transfert d'électrons dans des solutions très concentrées en espèces électroactives qui ouvrent la porte à un nouveau domaine d'électrochimie.[15, 16] Le comportement électrochimique à haute concentration est complètement différent qu'en solutions très diluées. Les connaissances sur ce type d'électrochimie dans la littérature ne sont pas complètement comprises encore aujourd'hui. Cette thèse présentera plusieurs résultats pionniers dans ces champs d'intérêt qui seront importants pour établir la base de cette électrochimie inexplorée. La caractérisation de LIR à différents niveaux de concentration sera au cœur de cette thèse.

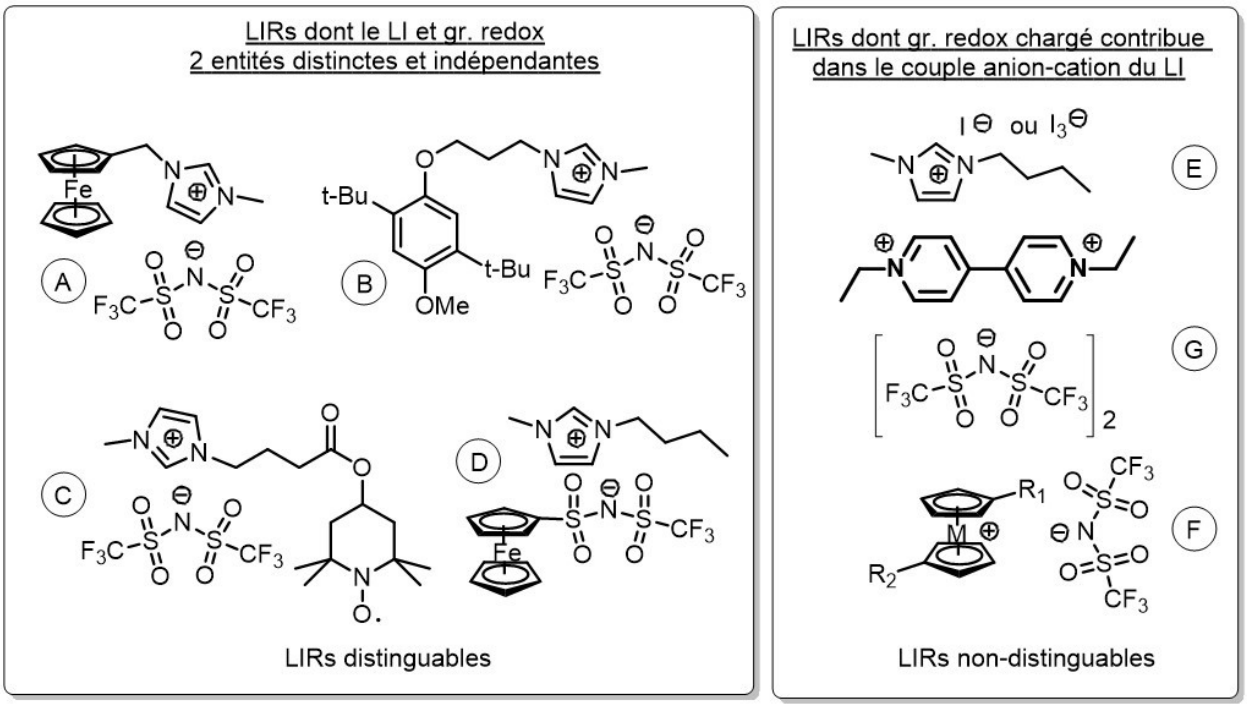

Figure 1.3. Exemples de liquides ioniques électroactifs qui sont classés comme suit : LIRs distinguables et non-distinguables.

Il est possible de classer les LIRs dans deux groupes propres à leur structure. La première classe, les LIRs distinguables, consiste en des liquides ioniques électroactifs dont le couple anion-cation du LI est indépendant à la partie électroactive (2 entités différentes). Évidemment, la seconde classe est les LIRs non-distinguables dont la partie redox participe au couple anion-cation du LI. De plus, la présente librairie chimique sur les LIRs contenant le ferrocène est presque exclusivement sur la modification de l'imidazolium (**Figure 1.3**, LIR-A),[17-20] avec quelques exceptions telles qu'un ferrocène fonctionnalisé par un LI phosphonium[13, 21] et un LI métallocénium (**Figure 1.3**, LIR-F où M = Fe, Co).[22, 23] Le choix du groupement électroactif et l'ion fonctionnalisé peuvent varier selon les propriétés recherchées du LIR pour l'application voulue. Notre groupe a rapporté les premiers rapports du développement des LIRs basés sur le ferrocène et le DDB (**Figure 1.3**, LIR-A et LIR-B) comme navette redox (N-R) dans la composition d'un électrolyte pour contrer la surcharge de la BIL ce qui est un sujet crucial de cette thèse.[24-26] De plus, certains chercheurs ont aussi utilisé des LIRs à base d'iodure (**Figure 1.3**, LIR-E)[27] et de TEMPO fonctionnalisé avec un LI (**Figure 1.3**, LIR-C) comme médiateur dans la composition d'un électrolyte pour les cellules photovoltaïques à pigment photosensible (CPPPs).[28] Comme il

a été rapporté dans la littérature, il est aussi possible d'utiliser les LIRs comme le viologène dans des dispositifs électrochromiques (**Figure 1.3**, LIR-G).[29-31] Dans le cadre de cette thèse, 1-butyl-3-méthyl-imidazolium ferrocénylsulfonyl (trifluoromethylsulfonyl) imide (BMIm FcNTf, **Figure 1.3**, LIR-D) sera en premier plan et il sera question des propriétés propres à ce LIR qui se distingue par la modification d'un anion et qui est peu connu dans la littérature. D'ailleurs, Fontaine et al. ont récenmment présenté des ioniques ioniques birédox dont l'anion et le cation sont électroactifs.[32, 33] Aussi, les applications possibles seront discutées dans les prochains chapitres.

1.3. Mise en contexte des batteries à ion lithium et les surtensions

1.3.1. Les batteries à ion lithium

L'intérêt pour l'exploitation des sources d'énergie renouvelable est en ascension dans la dernière décennie. D'ailleurs, la préservation de l'environnement est au cœur des discussions politiques et un sujet environnemental de notre époque est les émissions de gaz à effet de serre (GES) qui pourrait être responsable du réchauffement climatique selon plusieurs experts. Les centrales thermiques classiques (i.e une production d'électricité issue d'une combustion de combustible) sont en partie responsable de l'émission de GES. Dans le contexte de diminuer les GESs qui est vraisemblement l'incitatif de développer de nouvelles sources d'énergie alternative, les énergies renouvelables sont un choix de prédilection qui s'explique par le fait qu'elles ne dégagent aucun GES. À titre d'exemple, les énergies renouvelables typiques sont l'énergie solaire, l'énergie éolienne, l'énergie géothermique et l'hydroélectricité. Cependant, la plupart de ces sources d'énergie ont un point en commun : le contrôle de la production d'énergie est difficile ou même imprévisible et la production d'énergie fluctue beaucoup (i.e. Source d'énergie intermittente). En effet, l'ensoleillement et la vitesse du vent sont hors contrôle de l'Homme tandis que la quantité de combustible est brulée selon le besoin énergétique. Prenant en compte cette réalité, l'importance du stockage d'énergie dans le domaine de l'énergie prend tout son sens. De plus, les véhicules de transport utilisant le moteur à combustion sont aussi bien connus pour être un acteur important dans l'émission de GES et le stockage d'énergie est crucial pour une voiture électrique autonome. De plus, les pertes énergétiques sont moins importantes pour le moteur électrique que pour le moteur à essence (i.e. cycle de Carnot) qui est une force motrice pour mettre en place la voiture électrique dans un monde où l'énergie est précieuse. En ce moment, la

technologie qui répond le mieux au besoin du marché est la batterie à ion lithium (BIL). Le principe de fonctionnement de la BIL repose sur l'insertion, la désinsertion dans le matériel d'électrode et le transport de masse des ions de lithium entre l'électrode négative et positive. Les termes d'électrodes positives et négatives seront préférés pour éliminer les confusions comme il y a inversion d'appellation entre la charge et la décharge utilisant la nomenclature de cathode et d'anode. D'une façon plus détaillée, la **Figure 1.4** illustre bien le principe de la BIL. Lors de la décharge, il y a désinsertion de l'ion de lithium à l'électrode négative (i.e. anode), ensuite il y a transport de masse d'ion de lithium vers l'électrode positive (i.e. cathode) et il y a l'insertion d'un ion de lithium dans le matériel d'électrode positive. Évidemment, l'insertion et la désinsertion se font d'une façon simultanée, car l'électrolyte est riche en ion de lithium. Pour la charge, c'est tout simplement le contraire et donc, il y a l'insertion à l'électrode négative et la désinsertion à l'électrode positive. De plus, les électrons se déplacent pour conserver une électroneutralité lors de la charge et la décharge.

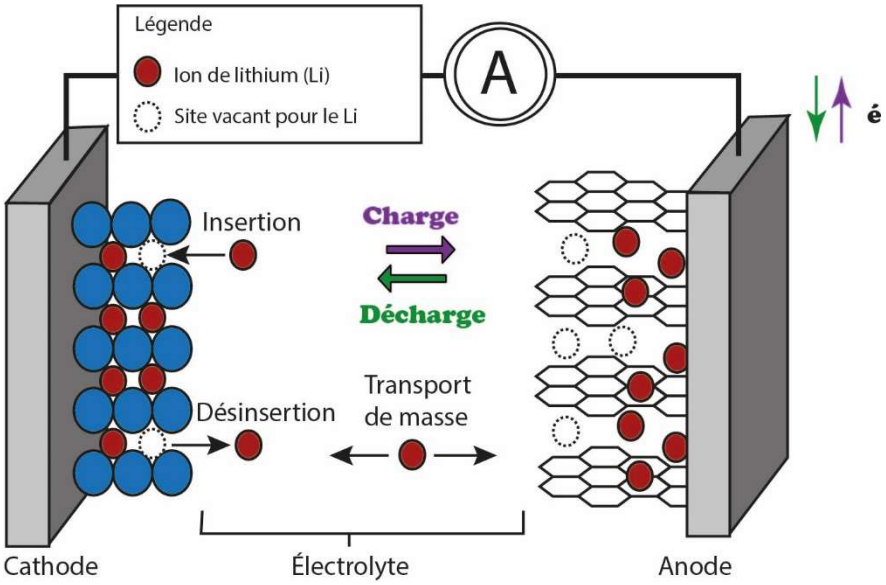

Figure 1.4. Principe de la batterie à ion lithium.

L'utilisation des BILs sur le marché commercial fait une montée fulgurante. Il s'agit d'un choix populaire pour les dispositifs électroniques tels que les portables et les cellulaires, car ils ont une excellente durée de vie et une haute énergie spécifique.[34, 35] Sur la **Figure 1.5**, il est possible de constater la courbe de Ragone qui montre une excellente densité d'énergie pour les BILs. Les investigations qui ont pour but d'améliorer la BIL sont faites à plusieurs niveaux et avec différentes

approches telles que les aspects suivants : la densité d'énergie, la vitesse de charge, la durée de vie, l'autodécharge, l'impact sur l'environnement, le domaine de température d'opération et la plus importante de toute, dans le cadre de cette thèse, la sécurité d'utilisation.

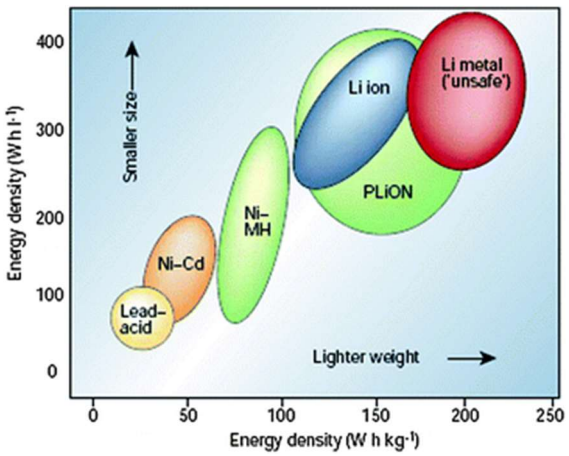

Figure 1.5. Densité d'énergie gravimétrique et volumétrique des différentes technologies des batteries. (Tirée de Armand & Tarascon (2001). Nature, Ref. 35)

1.3.2. Problématique des piles à ion lithium

Comme mentionné dans la section précédente, les BILs sont en ce moment le choix le plus prometteur pour les véhicules électriques.[36] Les recherches pour la voiture électrique ont notamment pour but d'assurer la sécurité, car la BIL actuelle présente des risques lors de son utilisation qui limite cette dernière à des applications de faible demande énergétique. Par exemple, la Tesla roadster contient un peu plus de 6000 piles dans 11 modules qui sont connectés en série. Après la sortie de la manufacture, la capacité de chaque module est théoriquement exactement la même. Cependant pour certaines raisons variables, si un des modules a une capacité inférieure aux autres, il y a un vieillissement prématuré qui peut engendrer des surtensions et l'état de charge (en anglais, state of charge) diminue. En d'autres mots et comme illustré sur la **Figure 1.6**, lors de la recharge de la batterie, le module qui possède une faible capacité est complètement chargé avant l'ensemble des modules, donc c'est exactement à ce moment que la surcharge survient et augmente les risques d'avoir des événements malheureux. Le changement de modules accentue leur débalancement, donc la seule solution efficace pour le moment est de changer la batterie complètement ce qui n'est pas favorable du point de vue économique et environnemental. De plus,

l'utilisation de solvants avec de hautes pressions de vapeur augmente les probabilités d'explosion via des réactions exothermiques qui s'emballent rapidement.[37-39]

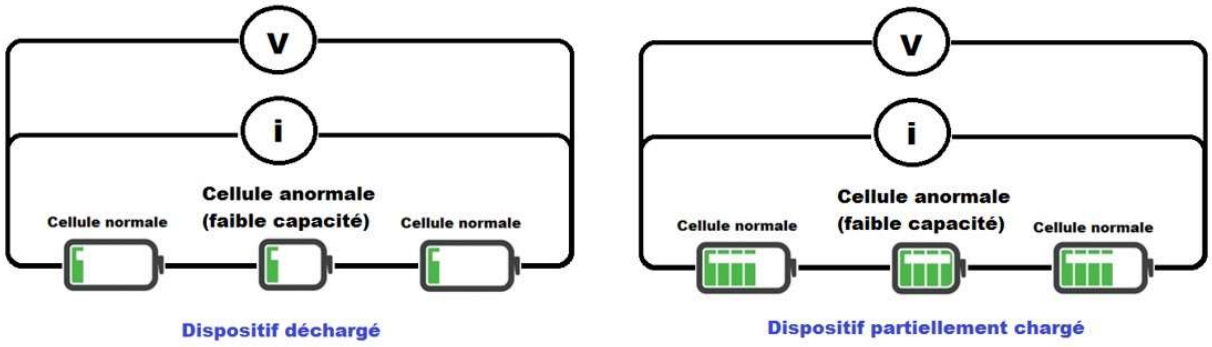

Figure 1.6. Schématisation d'une batterie complètement déchargée (A) et partiellement chargée (B) avec un module avec une faible capacité qui est complètement chargée. (Adaptée de Chen, Z., Y. Qin, et al. (2009). Electrochim. Acta, Ref. 37)

Les électrolytes couramment utilisés commercialement sont un mélange carbonate de propylène (PC), d'éthylène (EC), de diéthyle (DEC) et de diméthyle (DMC) pour n'en nommer que quelques-uns, avec un sel de lithium soluble tel que le hexafluorophosphate (PF_6) de lithium qui est abondamment utilisé et qui sera davantage traité dans la **Section 1.4**. Il y a aussi divers additifs qui peuvent être ajoutés pour améliorer la cyclabilité et la sécurité. Bien que les solvants possèdent une constante diélectrique et une viscosité requises pour dissoudre de façon appréciable une quantité adéquate de sel de lithium et pour assurer un transport de masse rapide du lithium afin de conserver l'efficacité de la pile, ils restent inflammables, volatils et sujets à l'oxydation à de haut potentiels. Le problème majeur des BILs est la difficulté de prévenir d'une façon interne lors des situations d'abus. En effet, pour le moment, afin de remédier à cette problématique, un dispositif externe qui assure le contrôle des modules est utilisé. Cependant, ces dispositifs sont très coûteux. Par exemple, une situation de surcharge peut dégrader le matériel d'électrode et l'électrolyte qui mène à une génération de chaleur et augmente la température interne de la cellule.[40] Les BILs sont très sensibles aux surtensions et aux conditions thermiquement extrêmes comme illustrées à la **Figure 1.7**.[40]

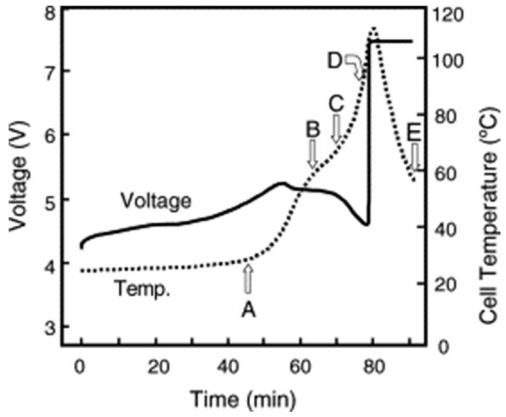

Figure 1.7. Corrélation entre le potentiel et la température d'une cellule à ion lithium prismatique avec une surcharge à une vitesse de charge de 1 C. (Tirée de Satoh et al., (2005), J. Power Sources, Ref. 40)

Les oxydes d'un métal de transition comme matériel d'électrode positive sont souvent utilisés dus au fait qu'ils sont très oxydants. Par conséquent, il en résulte une très grande différence de potentiel avec les électrodes négatives à base de lithium métallique. Cependant, à des potentiels très oxydants, il se produit des réactions parasites irréversibles telles que la suroxydation de l'électrode positive produisant la décomposition du matériel d'électrode qui occasionne souvent le dégagement d'oxygène et la décomposition de l'électrolyte. Ces réactions exothermiques sont exothermiques et il y a augmentation de la température interne qui présentent un réel danger. Ceci est illustré sur la **Figure 1.8** pour l'oxyde de cobalt ($LiCoO_2$) qui est couramment utilisé et il a été démontré que ce matériau d'électrode positive démontre des lacunes au point de vue de la sécurité.[41] Pour une meilleure compréhension de la **Figure 1.8**, une bande de valence (i.e. bande remplie d'électron) est un continuum énergétique, car les niveaux d'énergie des orbitales moléculaires sont très voisins l'un de l'autre dans un solide créant une bande.

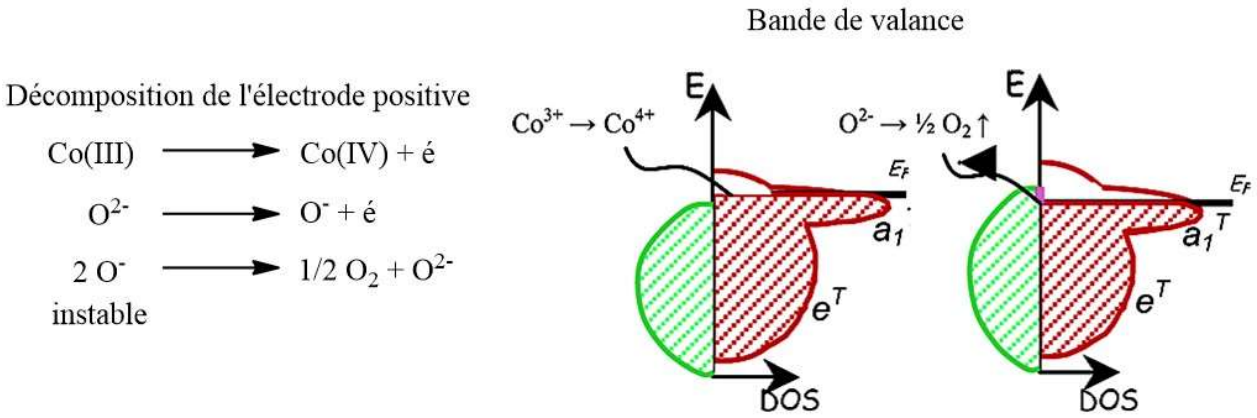

Figure 1.8. Réactions exothermiques de la décomposition du $LiCoO_2$ comme matériel d'électrode positive (À gauche) et le diagramme à bande correspondant qui représente l'appauvrissement en électron à l'électrode positive lors d'une surcharge. (À droite)

Les électrolytes couramment utilisés qui seront approfondis dans la prochaine section ne peuvent prévenir ces réactions et même, ils peuvent aggraver la situation en raison de leur inflammabilité et de leur haute pression de vapeur. Il existe de nombreux mécanismes de sécurité disponibles pour éviter les situations d'abus telles que la navette redox qui est le plus simple de tous pour empêcher les surcharges et le mécanisme est illustré sur la **Figure 1.9.**[42-44]

1.3.3. Mécanismes de protection des surtensions de l'électrode positive

Dans cette section, il s'agit de présenter les différents mécanismes de protection pour les BILs dans le but de les comparer et d'évaluer les forces et les faiblesses de chacun (**Tableau 1.1**). La caractéristique commune à ces différents mécanismes est la consommation du courant d'excès produit par les surtensions et grâce à ce mécanisme, il est possible de charger complètement la BIL.[37-39] Par conséquent, ces mécanismes sont le régulateur de la tension externe, les agents désactivants et les navettes redox (N-R).

Tableau 1.1. Avantages et désavantages des différentes méthodes pour contrôler les surcharges.

Mécanismes	Avantages	Désavantages
Régulateur de surtension externe	Universel Réversible Gestion de la chaleur	Coût Complexité Poids et volume
Agent désactivant	Coût Complexité Poids et volume	Irréversible Chaleur provenant de réactions chimiques Dégagement gazeux Bloque graduellement l'insertion du lithium
Navette redox	Réversible Gestion de la chaleur Coût Complexité Poids et volume	Non universel Limité par la diffusion

La technologie la plus utilisée comme protection des BILs est un régulateur électronique qui contrôle le voltage sur chaque cellule avec un circuit externe. Le courant d'excès engendré par les situations d'abus passe dans le circuit externe et maintient le bon fonctionnement dans la BIL. Un des avantages de taille est la polyvalence de ce mécanisme dû au fait qu'il est accommodable pour la plupart des BILs. De plus, il y a une bonne gestion de la température interne de la BIL qui est primordiale. Cependant, le grand problème est qu'il s'agit d'un dispositif volumineux et coûteux qui limite les applications.

La seconde technique pour la protection de la BIL est d'ajouter un additif pour désactiver la surtension en consommant le courant d'excès. Quelques exemples de désactivant sont le 3-thiophénylpropane, le biphényle, le 3-chlorothiophène et le furane pour n'en nommer que quelques-uns.[37] Le mécanisme se caractérise par l'irréversibilité de celui-ci. En effet, il s'agit d'une polymérisation de l'additif et/ou il en résulte un dégagement gazeux lors de la désactivation. Le résultat représente un réel désavantage, car le polymère produit nuit à l'insertion du lithium, diminue le transport de masse et la pression interne de la cellule augmente. L'efficacité de la BIL diminue progressivement. Après un certain temps, le courant ne pourra plus passer ce qui ouvrira le circuit électrique. De plus, lors de la polymérisation, il y a dégagement de chaleur dû à la réaction

chimique. Toutefois, c'est peu coûteux, il s'agit d'un contrôle interne et par conséquent, ce n'est pas volumineux comme le précédent mécanisme. Dans le domaine, les chercheurs ont abandonné cette option.

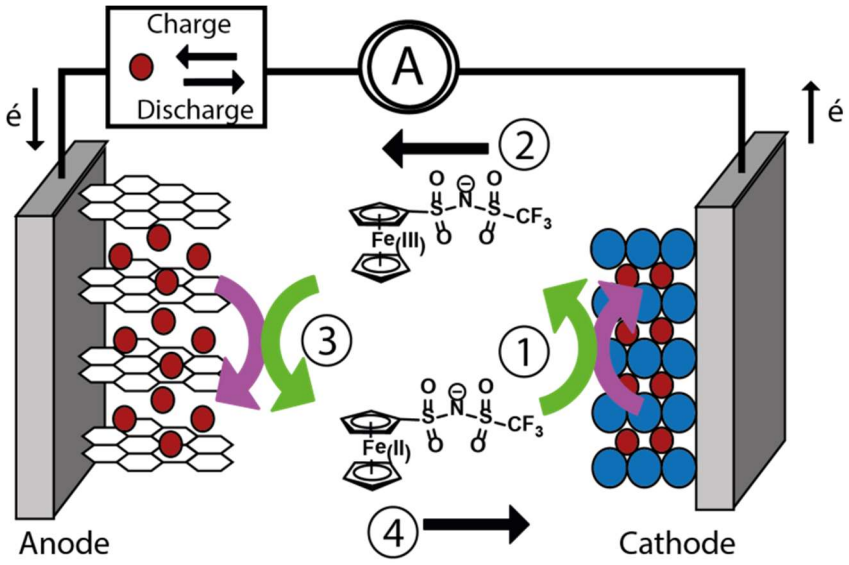

Figure 1.9. Mécanisme de la navette redox (N-R, Redox Shuttle).

La troisième technique est la navette redox qui possède quelques similitudes avec le mécanisme précédent. Par conséquent, il s'agit aussi d'un contrôle interne par une espèce électroactive, ce qui n'ajoute pas de volume au système et peut s'avérer peu coûteux. Cependant, l'immense avantage qui le différencie du désactivateur est la cyclabilité de l'espèce électroactive. Comme illustré sur la **Figure 1.9** qui montre le principe d'opération de la N-R, lors de la surtension, le courant d'excès est consommé par l'oxydation de l'espèce réduite (#1) et l'espèce oxydée diffuse lentement (#2) selon la deuxième loi de Fick pour la réduction de celle-ci (#3) pour obtenir la forme réduite qui est maintenant disponible pour la prochaine surtension (#4). En d'autres mots, la N-R éloigne la surcharge de l'électrode positive pour protéger celle-ci. Les limites pour l'instant de ce mécanisme sont la concentration possible et suffisante pour consommer la totalité du courant engendré par la surtension et la perte d'efficacité de la BIL par cet ajout qui engendre une diminution de la conductivité ionique ainsi que la diminution du transport de masse de l'ion de lithium. De plus, la navette redox n'est pas universelle et une règle de base est que l'espèce électroactive doit avoir une différence de potentiel d'au moins 300 mV plus oxydant que le matériel d'électrode positive d'intérêt pour éviter l'autodécharge durant les situations normales de

chargement. En adaptant l'équation de Bulter-Volmer à ce système (cette équation sera détaillée dans le **Chapitre 2**), le courant de fuite dû à la N-R est décrit par l'équation suivante (**Équation 1.1**) où i est le courant de fuite, i_0 est le courant d'échange de la N-R, ε est le potentiel d'opération à l'électrode de travail et E' est le potentiel d'équilibre de la N-R. Par conséquent, l'autodécharge et le courant de fuite sont minimisés quand |ε-E'| ≈ 300 à 400 mV selon cette équation. C'est-à-dire, à des potentiels d'opération normaux, l'oxydation de la N-R n'a pratiquement pas lieu et l'autodécharge est négligeable.

$$i = i_0 \exp\left(\frac{\varepsilon - E'}{RT}\right) \quad \textbf{Équation 1.1}$$

1.3.4. Navette redox pour la protection des surtensions

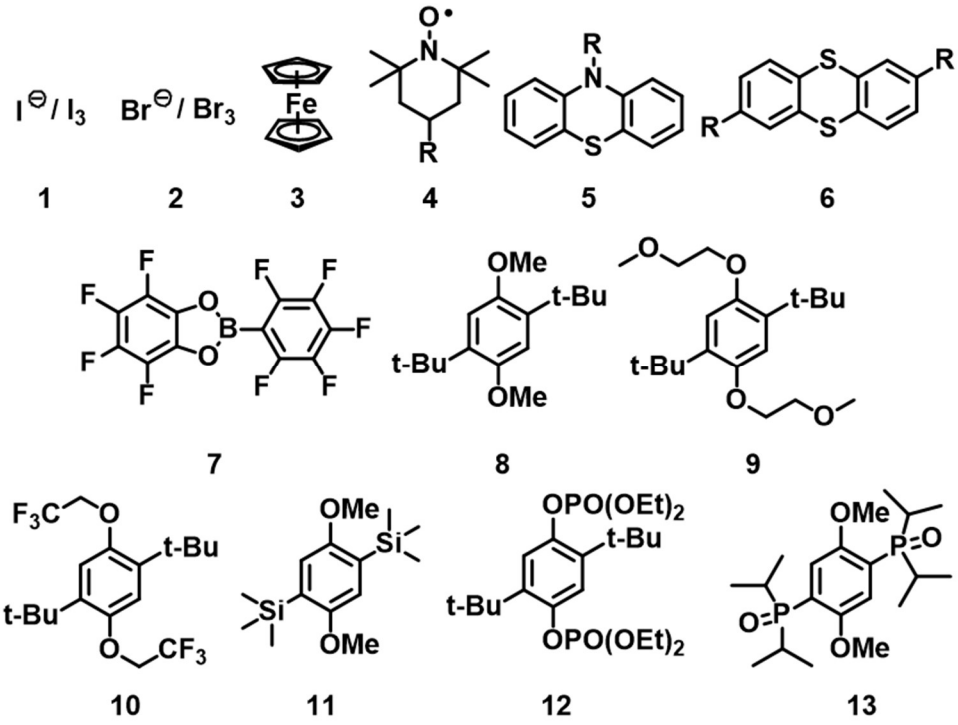

Figure 1.10. Aperçu de quelques navettes redox (N-Rs) de la littérature pour les BILs.

Tableau 1.2. Potentiel d'équilibre de quelques N-Rs utilisées pour la protection des BILs

# N-R	Nom de la N-R et les dérivés	Potentiel vs. Li/Li^+	Auteur
N-R.1	I^-/I_3^-	3,0	Behl et al.
N-R.2	Br^-/Br_3-	3,5	Behl et al.
N-R.3	Ferrocene	3,0-3,6	Abraham et al.
N-R.4	TEMPO	3,5-3,6	Dahn et al.
N-R.5	Phénothiazine	3,5-3,8	Dahn et al.
N-R.6	Thiantrène	4,0-4,4	Lee et al.
N-R.7	PFPTFBB	4,4	Amine et al.
N-R.8	DDB	3,9	Dahn et al.
N-R.9	DBBB	3,9	Amine et al.
N-R.10	DDFB	4,3	Dahn et al.
N-R.11	BTMSDB	4,1	Zang et al.
N-R.12	TEDBPDP	4,8	Amine et al.
N-R.13	BPDB	4,5	Amine et al.
N-R.14	$Li_2B_{12}H_{12-x}F_x$	4,4	Amine et al.

Avant de présenter les navettes redox (N-R; **Figure 1.10**; **Tableau 1.2**) apparues dans la littérature, il y a quelques propriétés importantes pour obtenir une navette redox idéale telles que le potentiel d'équilibre adéquat comme mentionné auparavant (**Section 1.3.3**), une électrochimie réversible de la N-R (aussi stable sous la forme oxydée que réduite), une solubilité requise de la N-R dans l'électrolyte choisi, le transport de masse doit être relativement rapide et la N-R n'affecte pas les performances de la BIL. L'objectif principal de ce domaine de recherche est de développer des espèces électroactives avec un potentiel de plus en plus oxydant en gardant une stabilité électrochimique pour être en mesure de protéger des électrodes positives de plus haut potentiel sur plusieurs cycles. À la fin des années 1980, la toute première navette redox retracée dans la littérature est le couple I^-/I_3^-.[45, 46] Il y a aussi le couple Br^-/Br_3^- qui a été évalué et possède une oxydation supérieure à l'iode.[47] Comme l'iodure et le bromure n'ont aucune modulation possible, les chercheurs ont décidé d'investiguer les dérivés de ferrocène et ils ont réussi à obtenir une gamme de potentiel qui dépend de la substitution du ferrocène (N-R.3) allant de 3,0 à 3,6 V vs. Li/Li^+.[42, 48] Ensuite, il y a eu l'apparition de plusieurs centres électroactifs organiques à base de dérivés de (2,2,6,6-tétraméthylpipéridin-1-yl)oxy (TEMPO, N-R.4, [49]), de dérivés de phénothiazine (N-R.5, [50, 51]), de dérivés de thiantrène (N-R.6, [52]), de 2-(pentafluorophényl)-tétrafluoro-1,3,2-benzodioxaborole (PFPTFBB, N-R.7, [53]), et de 2,5-di-tert-butyl-1,4-

diméthoxybenzène (DDB, N-R.8, [54, 55]) ont été investigués comme N-R dans les deux dernières décennies. Plusieurs dérivés de diméthoxybenzène ont été rapportés et le DDB n'a aucun égal en ce moment dans la littérature au point de vue de la performance d'opération de la N-R.[52, 56, 57] D'ailleurs, les dérivées de diméthoxybenzènes en comparaison avec les autres centres électroactives purement organiques sont les plus prometteurs pour atteindre une N-R réversible à haut potentiel. Le **Tableau 1.2** donne le potentiel d'équilibre des différentes N-Rs (i.e espèces électroactives) qui est une propriété primordiale dans le développement de N-R.

Depuis, plusieurs recherches ont été faites pour comprendre cette augmentation de cyclabilité en comparant avec d'autres dérivés de diméthoxybenzène. La première conclusion de ces recherches est que l'encombrement stérique des tert-butyles en position 2,5 empêche la réaction radicalaire qui peut polymériser l'espèce oxydée formée avec l'espèce réduite (Dimérisation avec une élimination du proton). Le second constat est que le diméthoxybenzène en position 1,2 présente une décomposition intramoléculaire avec le pont hydrogène possible entre les deux méthoxyles et donc, le diméthoxybenzène en position 1,4 est à prescrire.[58-60] Comme la solubilité est un facteur limitant pour le DDB, Amine et al. ont développé une N-R (DBBB, N-R.9; [61]) qui tire avantage des propriétés physiques des groupes oligo(éthylène glycol) pour remplacer les groupes méthoxyles avec l'objectif d'augmenter la solubilité de la N-R dans des électrolytes utilisant les carbonates sans sacrifier les performances de la N-R (0,4 mol dm^{-3} avec les oligo(éthylène glycol) et 0,1 mol dm^{-3} pour le DDB). Il a aussi été démontré qui est possible de moduler le potentiel du DDB en ajoutant des groupes de 2,2,2-trifluoroéthoxyle pour obtenir le 1,4-di-t-butyl-2,5-bis(2,2,2-trifluoroéthoxy)benzène (DDFB, N-R.10) qui présente un potentiel de 4,25 V vs. Li/Li^+.[62] Dictés par la compréhension de la nécessité de l'encombrement stérique sur le centre aromatique, Zang et al. ont étudié la modification du DDB en remplaçant les tert-butyles par des triméthylsilyles (BTMSDB, N-R.11; [63]) pour augmenter le potentiel d'oxydation et ils ont effectivement constaté un plus haut potentiel, mais les performances d'opération de la N-R ont drastiquement chuté (81 vs. > 300 cycles pour le DDB). Cette étude suggère que cette diminution vient du fait qu'il est davantage favorable d'éliminer un triméthylsilyles comme réaction de décomposition qu'un tert-butyle. Le domaine de recherche a crucialement besoin d'une navette redox qui a un potentiel au-delà de 4,5 V vs. Li/Li^+ et à ce jour, il y a le tétraéthyl-2,5-di-tert-butyl-1,4-phénylène diphosphate (TEDBPDP, N-R.12) qui répond à ces attentes avec un potentiel de 4,8 V vs. Li/Li^+,[64] mais la réversibilité n'est pas adéquate à cause des excellents groupes partants

qui favorisent la décomposition. Toujours dans cette optique, un dérivé de diméthoxybenzène utilisant des oxydes phosphine comme encombrement stérique (BPDB, N-R.13, [65]) a été mis au point et les auteurs expliquent le dilemme qui existe entre avoir un haut potentiel d'oxydation (4,5 V vs. Li/Li^+) et la stabilité électrochimique. L'avancé considérable de cette étude est l'amélioration de la cyclabilité de leur N-R instable lors de la réaction de réduction à l'interface de l'électrode négative de lithium métallique│électrolyte suivant la protection de l'électrode positive par oxydation. En d'autres mots, l'espèce oxydée est instable avec le lithium métallique. Ils démontrent une augmentation de cyclabilité avec l'ajout du bis(oxalato)borate de lithium (Li BOB) (25 et 95 cycles; sans et avec le sel Li BOB, respectivement). Li BOB est déjà considéré comme un additif et/ou électrolyte de support qui forme un électrolyte solide passif à l'interface de l'électrode négative │électrolyte qui sera nommé SEI tout au long de cette thèse.[66-68] Par conséquent, cette robuste SEI aide à supprimer la décomposition de leur N-R.[65] Il existe de rares exemples de sels de lithium électroactifs et un exemple pertinent est un sel de lithium utilisant un anion basé sur un agrégat de borate (N-R.14, [69]) présentant un potentiel de 4,4 V vs. Li/Li^+.

Maintenant, le défi de ces recherches est encore d'augmenter la solubilité de ces navettes redox et d'augmenter le potentiel en conservant une bonne stabilité électrochimique. De plus, les N-Rs actuelles en général n'apportent aucune amélioration du point de vue de la stabilité thermique et l'inflammabilité de l'électrolyte. Dans les présentes recherches, la solubilité, le potentiel d'équilibre et la stabilité électrochimique des N-Rs développées seront au cœur de cette thèse en tenant compte des connaissances établies dans la littérature. Pour faire cette étude, nous avons choisi les LIs comme plateforme puisqu'ils sont miscibles avec les carbonates et ils améliorent l'inflammabilité de l'électrolyte. La pertinence d'introduire les liquides ioniques redox (LIRs) comme N-R contre les surcharges est facilement défendable suivant les propriétés requises pour les N-R et des électrolytes destinés au BIL. Finalement, la synthèse organique de LIR donne infiniment de possibilités.

1.4. Électrolytes utilisés dans les batteries à ion lithium

1.4.1. Les électrolytes utilisés pour les batteries à ion lithium

Longtemps, les batteries au plomb et alcalines ont monopolisé le marché du stockage d'énergie, car ils utilisent des électrolytes aqueux dont la conductivité ionique n'a pas d'égale, même encore aujourd'hui (Voir **Tableau 1.3** [4]). Cette conductivité ionique exceptionnelle est due à l'excellente constante diélectrique de l'eau et aussi au mécanisme de Grotthuss par lequel un proton se transfert à travers les ponts hydrogène des molécules d'eau, ce qui augmente significativement la mobilité des protons. Le transport des charges ne s'effectue pas uniquement par le déplacement physique des ions comme dans la plupart des électrolytes. La question qui est concevable de se poser: quel est l'intérêt d'utiliser des solvants organiques ou non-aqueux s'il n'est pas possible d'atteindre cet ordre de grandeur de conductivité ionique? La réponse est que la fenêtre électrochimique est limitée par l'hydrolyse de l'eau et par conséquent, la fenêtre électrochimique maximale est de 1,23 V ce qui limite beaucoup les matériaux d'électrode possibles. D'ailleurs, il ne faut pas oublier que l'énergie stockée dépend de la différence de potentiel des électrodes utilisées. Très récemment, la BILs a fait son apparition sur le marché commercial en utilisant un solvant organique tel que le sel hexafluorophosphate de lithium dans un mélange de carbonate cyclique et linéaire.

Tableau 1.3. Différentes conductivités ioniques selon l'électrolyte avec l'application correspondante à 25 °C**.**

Électrolytes	Solvants	σ / mS cm^{-1}	Applications
H_2SO_4 (30 wt. %)	H_2O	730	Batterie au plomb
KOH (29,4 wt. %)	H_2O	540	Pile alcaline
EMIm BF_4 (Liquide ionique; 2 mol dm^{-3})	CH_3CN	47	Supercapaciteur
Li NTf_2 (1 mol dm^{-3})	EC:DME (1:1)	13,3	BIL
Li PF_6 (1 mol dm^{-3})	EC:DME (1:1)	16,6	BIL

Les électrolytes jouent un rôle de premier plan dans la confection de la BIL à plusieurs niveaux tels que la fenêtre électrochimique, la stabilité thermique et le transport des ions. Il y a plusieurs électrolytes qui ont été développés pour améliorer ces propriétés telles que l'utilisation

de liquides ioniques, de polymères ou même des matériaux inorganiques (électrolyte de verre-céramique) comme il est résumé dans le **Tableau 1.4**.[70] Bien sûr, les mélanges de ceux-ci ont aussi été évalués afin de combiner les bienfaits de chacun dans l'obtention d'un électrolyte hybride qui sera approfondi pour le mélange entre les solvants organiques et les liquides ioniques dans cette section. Le développement d'électrolytes essaie de rencontrer la plupart des propriétés dans l'objectif d'avoir une BIL performante à faible coût qui ne présente aucun risque pour l'environnement et lors de son utilisation.

Tableau 1.4. Électrolytes non-aqueux classiques pour la BILs

Électrolytes	Exemples	Conductivité Ionique à 25°C / mS cm^{-1}	Limite électrochimique pour réduction et oxydation / V vs Li/Li^+		Inflammable
Liquide organique	1 mol dm^{-3} Li PF_6 EC-DEC (1:1 v/v)	7	1,3	4,5	oui
Liquide ionique	1 mol dm^{-3} Li BF_4 EMIm BF_4 1 mol dm^{-3} Li NTf_2 EMIm NTf_2	8 2	0,9 1,0	5,3	non
Polymère	Li NTf_2-P(EO/MEEGE)	0,1	< 0	4,7	oui
Solide inorganique	0,05Li_4SiO_4 + 0,57Li_2S 0,38 SiS_2	1	< 0	8,0	non

En général, les carbonates sont largement utilisés, car ils sont de bons solvants pour dissoudre les sels de lithium. Pour expliquer cette solubilité, les carbonates présentent d'assez hauts nombres de Gultmann qui mesurent la force du solvant suivant la basicité de Lewis (Environ de 15 kcal mol^{-1}). Traditionnellement, prenant en compte la viscosité, la conductivité ionique et la concentration du sel de lithium, la concentration typique est entre 1 à 1,5 mol dm^{-3} de sel de lithium dans l'électrolyte.[71] Ce genre de compromis teintera l'ensemble des recherches qui sont répertoriées dans les prochains chapitres de cette thèse. Cependant, les électrolytes basés sur les carbonates sont hautement inflammables avec un point éclair sous les 30°C.[72] De plus, le sel de lithium le plus commercial, Li PF_6, peut subir une réaction de décomposition autocatalytique qui forme du LiF et PF_5, car le 6^e fluor est très labile et il y a aussi formation d'acide fluorhydrique en présence d'eau

dans l'électrolyte (Réaction irréversible : $PF_5 + H_2O = PF_3O + 2HF$) au-dessus de 60°C en utilisant les carbonates.[73] Malgré l'existence d'additifs pour empêcher la décomposition thermique du Li PF_6,[74] ce sel ne sera pas utilisé dans les études présentées et il sera remplacé par le Li NTf_2, un des sels de lithium qui présente une des plus basses énergies réticulaires (Lattice). Ce sel présente d'autres défis qui seront davantage exposés en détail prochainement. La littérature présente aussi d'autres candidates comme sel de lithium dans la technologie de BIL tel que le tétrafluoroborate de lithium (Li BF_4), perchlorate de lithium (Li ClO_4), hexafluoroarsenate de lithium (Li AsF_6), bis(oxalato)borate de lithium (Li BOB), fluoroalkylphosphate (Li FAP), bis(perfluoroéthylsulfonyl)imide de lithium (Li BETI) et triflate de lithium (Li OTf) pour n'en énumérer que quelques-uns.[75] Cependant, en utilisant des électrodes positives toujours plus oxydantes, les matériaux d'électrodes et spécialement les électrolytes ne sont pas nécessairement stables sur une plage de températures nécessaires et de potentiels voulus. Donc, il y a dégradation de ceux-ci quand ils excèdent ces limites. La recherche axée sur l'amélioration de la stabilité électrochimique de l'électrolyte sur une grande plage de potentiel est utile dans le but d'avoir une grande différence de potentiel en les électrodes.

1.4.2. Fenêtre électrochimique des électrolytes et les matériaux d'électrode positive

Une course démesurée pour développer de nouveaux matériaux d'électrodes est lancée pour avoir la plus grande différence de potentiel avec le lithium. Cependant, la chimie de l'électrolyte n'avance pas au même rythme et les électrolytes actuels basés sur les solvants de carbonates présentent un début de décomposition à 4,5-5,0 V vs. Li/Li^+.[76] Il y a déjà plusieurs électrodes positives à haut-voltage pour lesquelles la capacité spécifique est limitée par la plage de potentiel de l'électrolyte tel que le $LiNiPO_4$ de type olivine (5,2 V vs. Li/Li^+, Allen et al. [77]), le $LiCoPO_4$ de type olivine (4,8 V vs. Li/Li^+, Yoshino et al. [78]), le $LiNi_{0,5}Mn_{1,5}O_4$ de type spinelle normal (4,1 et 4,7 V vs. Li/Li^+, Dahn et al. [79]) et le $LiCoMnO_4$ (3,9 et 5,0 V vs. Li/Li^+, Westa et al.) pour n'en nommer que quelques-uns. Voici la **Figure 1.11** qui présente le potentiel de différents matériaux d'électrodes.[80]

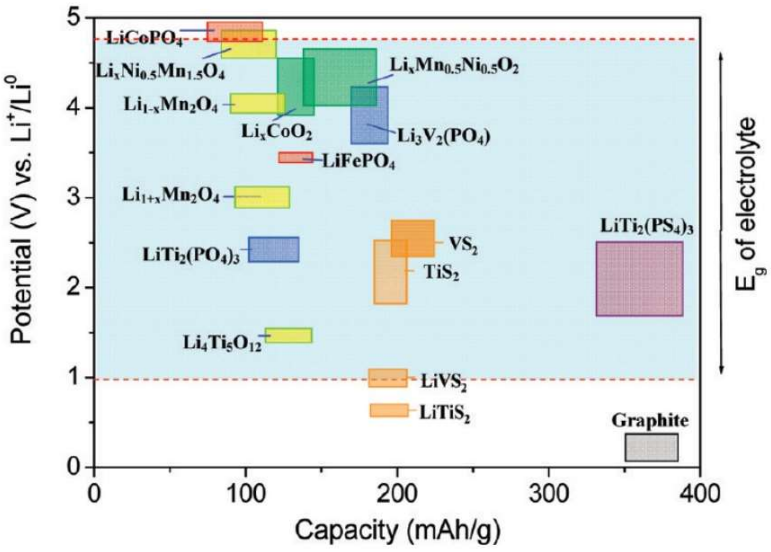

Figure 1.11. Voltage selon la capacité pour différents matériaux d'électrode relatifs à une fenêtre électrochimique (E_g de l'électrolyte montré sur la figure) utilisant un électrolyte de 1 mol dm^{-3} de Li PF_6 dans EC-DEC (1:1 v/v). (Tirée de Goodenough et al., (2010), Chem. Mater., Ref. 80)

Par conséquent, il y a eu plusieurs approches pour élargir la fenêtre électrochimique d'une façon anodique pour couvrir la région de 5 V tels que l'utilisation de sulfones,[81] de dinitriles,[82] l'utilisation d'additif pour l'électrolyte[83] ou l'utilisation des liquides ioniques[84] dans la composition de l'électrolyte. Toutefois, ces électrolytes précédents ne forment pas d'électrolyte solide passif à l'interface de l'électrode négative (SEI) | électrolyte et d'ailleurs, ils sont beaucoup plus visqueux. Par conséquent, des chercheurs se sont intéressés au solvant de carbonate fluoré qui augmente aussi la limite anodique en conservant la formation de la SEI.[76] Il est toujours possible d'ajouter le carbonate de vinylène et le carbonate d'éthylène aux électrolytes afin d'augmenter la formation de SEI qui ne se fait pas d'une façon intrinsèque.[85-87] La couche SEI prévient la co-intercalation de solvant et l'exfoliation du graphite qui est utilisé comme électrode négative.[88, 89]

1.4.3. Les liquides ioniques sans solvant comme électrolyte dans les batteries à ion lithium

Les raisons préalablement énumérées telles que l'ininflammabilité, la haute limite oxydative (~5,3 V vs. Li/Li^+) et la bonne stabilité thermique et électrochimique des liquides ioniques (LIs) à température ambiante ont convaincu les chercheurs de considérer les LIs comme potentiel candidat comme composante d'électrolyte.[90-94] Malheureusement, malgré que les LIs sont très attrayants

pour améliorer la sécurité, les électrolytes composés de LIs et d'un sel de lithium sans solvant organique sont visqueux et la limitation majeure est le faible nombre de transport du lithium (Concept détaillé pour plus de clarté dans le **Chapitre 2**). Ce faible nombre de transport dû à la présence du cation du LI ($t_{Li}+ \approx 0,1$; valeur typique pour cet électrolyte;[95] $t_{Li}+ \approx 0,3$ pour un électrolyte traditionnel[96]) mène à une polarisation de concentration en ion de lithium à l'interface des électrodes | électrolyte, une diminution de la vitesse de charge/décharge et une diminution de la puissance de la BIL.[97] En d'autres mots, en se penchant sur le mécanisme de la BIL, la conductivité ionique d'un électrolyte idéal est en majeure partie faite par la mobilité de l'ion de lithium. De fil en aiguille, les chercheurs convergent vers une conclusion et celle-ci est que pour obtenir un $t_{Li}+$ élevé utilisant les LIs, il faut employer un LI basé sur le lithium cationique ou dans un mélange avec une très haute concentration en lithium. Cependant, il ne s'agit pas d'une mince tâche, car les sels de lithium présentent de hauts points de fusion. D'ailleurs, le Li NTf_2 présente une transition solide-solide à 152°C et un point de fusion à 234°C.[98] Pour les électrolytes où le sel de lithium est en plus grande quantité que le LI (LI-dans-Sel de lithium condition), le point de fusion de ce mélange est aux alentours de 75°C et les BILs qui emploient ce type d'électrolyte sont viables seulement pour des applications à haute température.[98]

1.4.4. Les électrolytes concentrés et les liquides ioniques solvatés comme électrolyte

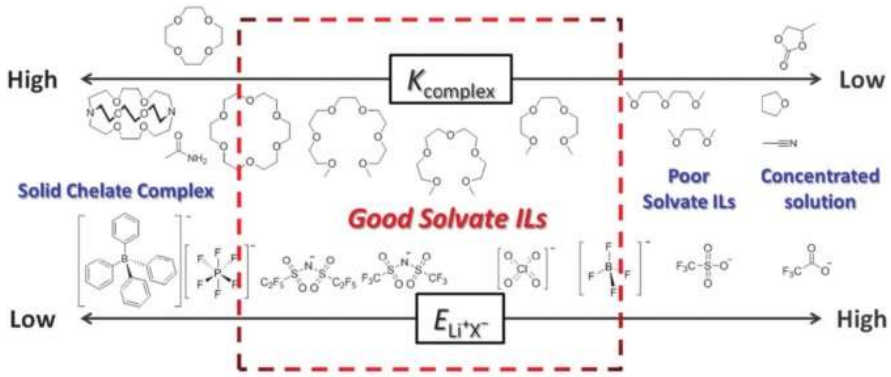

Figure 1.12. Schéma qui différencie les électrolytes concentrés et les liquides ioniques solvatés où $K_{complex}$ est la contante d'équilibre pour le complexe et (Tirée de Watanabe et al., (2010), PCCP, Ref. 100)

Les électrolytes fortement concentrés en sel de lithium (i.e. au-delà de 2,0 M de sel) augmentent en intérêt récemment, car les propriétés diffèrent en comparaison avec les électrolytes classiques

et commerciaux qui contient de 1,0 à 1,5 M de sel. Malgré que cet électrolyte est dispendieux et que sa conductivité ionique est plus basse due à l'augmentation de sa viscosité, ce type d'électrolyte démontre une meilleure stabilité en augmentant la fenêtre électrochimique, l'électrolyte est moins volatile (i.e. les molécules de solvant sont pour la plupart coordonnées au lithium) et grâce à la haute concentration, les réactions d'insertion aux électrodes se font rapidement.[99] En augmentant l'effet chélate entre la molécule de solvant et l'ion de lithium, il n'est plus question d'électrolyte concentré, mais il s'agit bien d'un électrolyte basé sur un liquide ionique solvaté comme illustré sur la **Figure 1.12** où $K_{complex}$ est le constante d'équilibre et E_{Li+X-} est l'énergie d'interaction entre la pair anion-ion de lithium.[100] Angell et al. proposent cette nouvelle classe de LIs et dans ce LI solvaté, le solvant coordonnant est fortement coordonné sur un centre métallique (e.g. Li^+) créant un complexe cationique. La conséquence de la formation de ce complexe est de diminuer les interactions électrostatiques entre l'anion et le complexe cationique.[101] L'énergie réticulaire diminue drastiquement et il y a formation d'un LI pour ces raisons. Watanabe et al. ont repris l'idée et ils ont tiré avantage de ce concept en l'appliquant dans le cadre d'un nouveau type d'électrolyte pour les BILs.[102] Ils ont démontré un nouveau LI qui est composé d'un robuste complexe cationique dont un tétraglyme(G_4) chélate un ion de lithium (Oligoéther de $CH_3(CH_2CH_2O)CH_3$-$Li)^+$ et ce cation est pairé avec le NTf_2 comme anion. L'idée est d'avoir un LI contenant intrinsèquement un ion de lithium dans la structure même du LI ce qui résulte à un haut nombre de transport (t_{Li+}: 0.52) et qui montre une amélioration significative en comparaison avec les LIs à base d'imidazolium.[103] Par exemple, le $Li(G4)_1$ NTf_2 (2,75 mol dm^{-3} de lithium) qui est un LI solvaté présentant à ce jour les meilleures propriétés physicochimiques (i.e. conductivité ionique, viscosité et point de fusion) montre une viscosité de 95 cP et un coefficient de diffusion pour le lithium de 1,3 x10^{-7} cm^2 s^{-1} ce qui peut être mis en comparaison avec une solution de perchlorate de lithium (1 mol dm^{-3}) dans le carbonate de propylène offrant 6,8 cP et 10,3 x10^{-7} cm^2 s^{-1}, respectivement. De plus, voici la **Figure 1.13** qui montre les performances d'une BIL utilisant ce type d'électrolyte et il est facile d'observer que pour une densité de courant sous 1 mA cm^{-2}, la capacité spécifique de la décharge atteint pratiquement la capacité théorique pour le $LiCoO_2$ employant ces deux électrolytes, mais au-delà de cette valeur, la diminution de la capacité est beaucoup plus significative pour le $Li(G4)_1$ NTf_2 que pour un électrolyte basé sur un carbonate.[104] (Le **Chapitre 2** présentera les détails d'interprétation d'une courbe charge-décharge, mais pour le besoin ici, la capacité spécifique se lit quand le potentiel d'opération chute

en potentiel.) Toutefois, cet électrolyte est très bien adapté pour les batteries au lithium-souffre, car l'effet de navette des polysulfures qui cause l'autodécharge est atténué par la faible solubilité des polysulfures dans ce type d'électrolyte.[105]

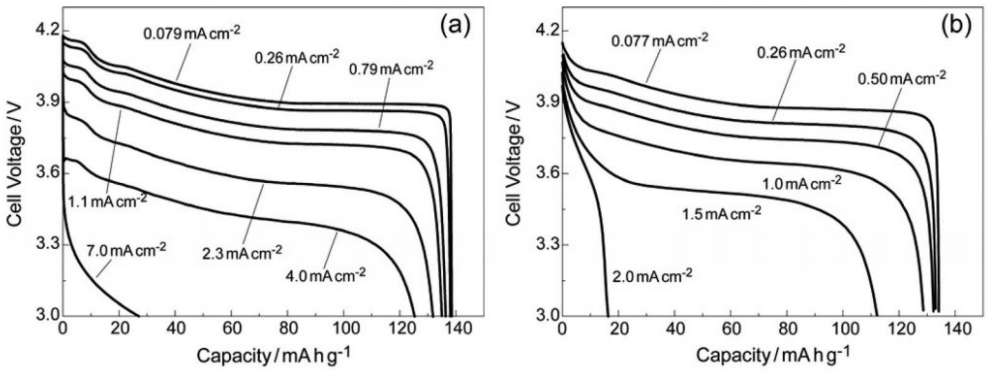

Figure 1.13. Profile de charge-décharge en fonction de différentes densités de courant pour une cellule de $Li/LiCoO_2$ utilisant l'électrolyte a) le perchlorate de lithium (1 mol dm^{-3}) dans le carbonate de propylène et le $Li(G4)_1$ NTf_2 (2,75 mol dm^{-3} de lithium). (Tirée de Watanabe et al., (2012), J. Electrochem. Soc., Ref. 104)

1.4.5. Mélange de carbonates et de liquides ioniques comme électrolyte

Récemment, les mélanges de LIs et de solvants ont gagné en intérêt comme électrolyte pour la BIL.[106-109] Le mélange de LIs avec les solvants organiques a été proposé pour diminuer l'impact négatif des LIs sur le nombre de transport du lithium en conservant ses excellentes propriétés. Dû à la miscibilité des LIs avec les solvants de carbonates, il est possible d'atteindre une haute concentration en LI toujours en présence de sel de lithium. Pour ce type d'électrolyte, lorsque la totalité des sels (sel de lithium + LI) en rapport massique avec le solvant organique de l'électrolyte augmente au-dessus de 1, il s'agit d'une situation de "solvant-dans-sel". Par opposition, avec des valeurs inférieures à 1, il s'agit de "sel-dans-solvant" pour des conditions habituellement rencontrées pour les électrolytes.[71] Ce nouveau type d'électrolyte présente quelques avantages de taille tels qu'un haut nombre de transport pour le lithium (en comparaison avec le LI sans solvant),[110] un électrolyte ininflammable (nécessite une importante proportion en LI),[111] une amélioration de la cyclabilité/performance et de la sécurité de la BIL.[71, 100, 109, 111-113] De plus, Kühnel et al. ont rapporté que l'incorporation de LIs dans la composition de l'électrolyte utilisant le sel de lithium, Li NTf_2, peut supprimer la corrosion du collecteur de courant, car le

$Al(NTf_2)_3$ est peu soluble dans les LIs.[114-116] La différence entre la pile à ion lithium et la pile au lithium réside sur l'électrode négative employée. L'électrode négative de la BIL consiste en une électrode de graphite avec du lithium pratiquement métallique intercalé entre des feuillets, tandis que pour la batterie au lithium, il s'agit d'une électrode négative sous l'état métallique (solide mou). La BIL est considérée comme une batterie secondaire, c'est-à-dire qu'elle peut être rechargeable. De plus, la batterie au lithium présente une plus haute densité d'énergie, mais la formation de dendrites suivant la réduction du lithium lors de la déposition/plaquage de l'ion de lithium en lithium à l'état zéro empêche ce type de batteries d'être cyclé en toute sécurité sans court-circuit utilisant un électrolyte liquide.[66] En améliorant le contrôle de la déposition du lithium métallique, la batterie du même nom est très attrayante du point de vue de sa très haute capacité. Notamment, l'utilisation d'électrolyte de polymère solide et inorganique solide (céramique) sont d'excellents candidats pour la suppression de dendrites. Cependant, les électrolytes solides sont problématiques au niveau des propriétés cinétiques limitées dues à leur faible conductivité ionique et à la haute résistance interfaciale (i.e. Matériel d'électrode │électrolyte solide).[117-120] Les électrolytes de type ''solvant-dans-sel'' ont suscité de l'intérêt pour prévenir d'une façon efficace la formation de dendrites lors de la réduction du lithium pendant la charge sans les résistances interfaciales des électrolytes solides. De plus, le mélange entre des polymères et des LIs ont été sujets d'études pour améliorer le contact entre les électrodes et l'électrolyte dans l'optique de diminuer la résistance interfaciale. Toutefois, cette thèse ne montre aucun résultat utilisant des polymères comme composante d'électrolyte.[121] Conséquemment, il y aura une attention particulière sur les propriétés de solvatation et de transport de l'ion de lithium au cours de ces études ce qui est d'une importance capitale pour une excellente compréhension d'un électrolyte avancé dédié au BIL.

1.5. Les supercaciteurs et leur électrolytes électroactifs

1.5.1. Comparaison entre les supercapaciteurs et les batteries à ion lithium.

Les deux dispositifs de stockage d'énergie les plus étudiés sont les batteries, qui ont été abondamment traitées dans les sections antérieures et les supercapaciteurs électrochimiques (SCEs). Selon le diagramme de Ragone (**Figure 1.14**),[122] la différence intrinsèque de ces deux dispositifs est au niveau de la densité d'énergie spécifique et de la puissance spécifique qui s'explique par la façon dont ces dispositifs emmagasinent l'énergie. Pour ces mêmes raisons, à

première vue, ces deux dispositifs semblent concurrentiels, mais ils présentent davantage une complémentarité, car les champs d'applications sont propres à chacun. Dans les batteries, l'énergie est emmagasinée via des réactions électrochimiques ayant lieu au cœur des électrodes et cet échange électron produit un courant faradique à l'interface électrode|électrolyte. Toutefois, pour les SCEs, l'énergie est stockée par le biais d'un balancement électrostatique entre les ions de l'électrolyte et la grande surface de l'électrode carbonée. Le courant produit par ce type de dispositif est capacitif contrairement aux batteries. Résultant de leur mécanisme d'entreposage d'énergie respectif, la batterie en général peut emmagasiner davantage d'énergie que les SCEs, toutefois les SCEs délivrent/emmagasinent l'énergie beaucoup plus rapidement que la batterie, c'est-à-dire qu'il est possible de charger ou décharger un SCE avec un temps de l'ordre de grandeur de la seconde plutôt que quelques heures pour la batterie. Donc, les applications des SCEs sont dédiées à des applications de faible demande énergétique qui peuvent demander une haute puissance. En général, la cyclabilité des SCEs est largement supérieure en comparaison avec la batterie, car l'utilisation de matériaux beaucoup plus inerte et la mécanique des matériaux utilisés est beaucoup moins mise à l'épreuve.

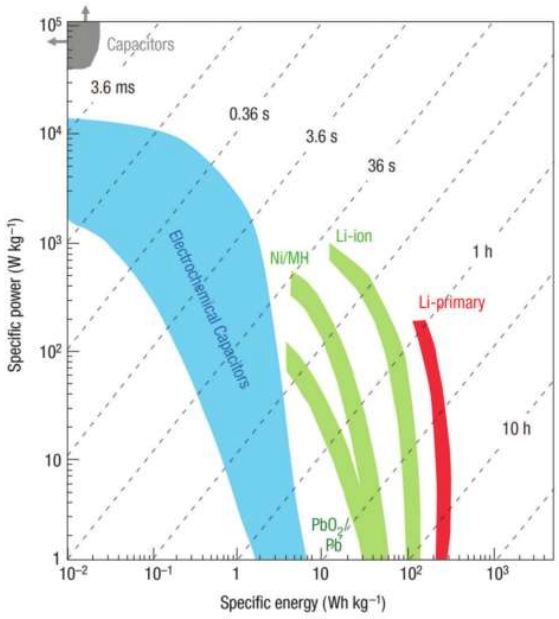

Figure 1.14. Diagramme de Ragone représentant la densité d'énergie spécifique et la puissance spécifique des batteries, dont la BIL et des supercapaciteurs électrochimiques. (Tirée de Banks (2011). RSC Adv., Ref. 125)

Les SCEs sont séparés en trois classes: les capaciteurs de double couche électrique (CDCE), les pseudocapaciteurs et les capaciteurs hybrides. L'objectif de ce domaine est évidemment d'emmagasiner toujours plus d'énergie afin d'augmenter la capacitance et la différence de potentiel ($E= 0,5\ CV^2$ où E est l'énergie, C est la capacitance et V est le potentiel). Par conséquent, il est très avantageux d'augmenter la fenêtre électrochimique via la puissance carrée attribuée au potentiel. Les CDCEs accumulent l'énergie en utilisant la double couche électrique qui découle du courant capacitif et par conséquent, la capacitance est intimement et fondamentalement reliée à la superficie des électrodes telle qu'un matériau poreux. L'ordre de grandeur de la densité d'énergie de ce type de dispositif est d'environ 10 W h kg^{-1}, mais l'intérêt de ces dispositifs se manifeste par leur puissance qui se chiffre de 1 à 100 kW kg^{-1}.[123] Malgré la popularité des CDCEs, ils présentent une faible densité d'énergie et il est difficile de l'améliorer. Afin de niveler la densité d'énergie, les pseudocapaciteurs sont une alternative intéressante. Pour ce type de dispositif, il y a des réactions faradiques de surface très rapides qui s'apparentent beaucoup aux batteries[124] via les composantes électroactives telles que des oxydes métalliques (Ex. MnO_2),[125] ou des polymères conducteurs (Ex. polyanilline).[126] La densité d'énergie des pseudocapaciteurs atteint maintenant l'ordre de 50 W h kg^{-1} et des puissances spécifiques de 1 kW kg^{-1}.[127, 128] Évidemment, les dispositifs hybrides sont la combinaison des deux classes antérieures qui propose d'emmagasiner de l'énergie par l'entremise de la double couche électrique et des réactions électrochimiques ultrarapides à l'interface de l'électrolyte et de l'électrode.

1.5.2. Électrolyte des supercapaciteurs et électrolyte électroactive.

Largement discuté dans ce chapitre d'introduction, l'électrolyte joue un rôle considérable dans les dispositifs électrochimiques et les SCEs ne font pas exception. Par conséquent, deux chapitres en annexe sont ajoutés à cette thèse et des efforts ont été déployés pour développer d'innovants électrolytes consacrés aux SCEs. Durant l'investigation des dispositifs électrochimiques discutés préalablement, les connaissances acquises sur les liquides ioniques électroactifs comme composante d'électrolyte ont mené à concevoir un électrolyte pour les SCEs. L'utilisation des LIs en tant qu'électrolyte pour les SCEs est tout indiquée via les excellentes propriétés des LIs telles que la large fenêtre électrochimique et l'utilisation d'un liquide constitué uniquement d'ions démontrant que les LIs sont parfaitement adaptés pour cette application. De plus, la faible pression de vapeur des LIs, la bonne stabilité thermique et électrochimique et le

voltage au-delà de 3 V présentent des avantages à examiner. Il est facile de faire le parallèle avec les électrolytes organiques volatiles et les électrolytes aqueux ayant une petite fenêtre électrochimique due à l'hydrolyse de l'eau. Toutefois, la forte viscosité augmente significativement la résistance du dispositif et la capacité est influencée par cette viscosité. Une approche scientifique similaire aux BILs en utilisant des mélanges de solvant et de LIs est apparue dans la littérature parallèlement aux études des BILs et ces investigations démontrent un impact positif sur la capacitance et la fenêtre électrochimique du même coup.[129-131]

Il est possible d'ajouter des espèces électroactives à l'électrolyte comme additif dans le but d'augmenter la capacitance. Cette approche est très apparentée aux batteries redox à flux, aussi appelé pile d'oxydoréduction (Redox flow battery en anglais) qui se définit par la charge ou décharge d'une solution électroactive au lieu d'un matériau d'électrode habituellement constatée dans la littérature. Les électrolytes électroactifs parus dans la littérature ont été incorporés dans des électrolytes aqueux, organiques et/ou utilisant les LIs.[132-136] Les espèces électroactives rapportées sont par exemple l'hydroquinone,[134, 137, 138] le phénylènediamine,[139-141] l'iodure de potassium,[142] le ferricyanure de potassium ($K_3Fe(CN)_6$)[143] et le sulfate de Cu(II)/Fe(II)[144] pour n'en nommer que quelques-uns. La plupart de ces exemples utilisent des milieux aqueux, toutefois, la pauvre littérature montre également des électrolytes électroactifs à base de LI utilisant l'iodure de 1-éthyl-3-méthyl-imidazolium[145] ou l'incorporation de Cu(II) dans un LI.[146] Le problème majeur est l'autodécharge par l'effet de navette redox des additifs électroactifs par le même principe que les navettes redox contre les surtensions dans les BILs. Cette problématique se retrouve aussi par l'autodécharge des disulfures dans les batteries au soufre.[147] Lors de l'autodécharge, la réaction électrochimique se fait entre l'espèce électroactive et l'électrode, ensuite l'espèce électroactive produite diffuse vers l'électrode opposée et réagit à l'interface de celle-ci pour produire l'espèce électroactive initiale. Comme il n'existe pas de différence de potentiel entre l'espèce oxydée et réduite, la décharge se fait aisément et ce mécanisme est néfaste énergétiquement parlant. Donc, l'approche scientifique pour empêcher la perte d'énergie par transport de masse de l'espèce électroactive se divise en deux stratégies : 1) utiliser une membrane sélective qui isole les deux électrodes et 2) produire une espèce électroactive insoluble, donc il y a électrodéposition sur la surface de l'électrode lors de la réaction électrochimique.[147] Dernièrement, une méthode très embryonnaire qui exploite le changement

de conformation en solution est dictée par la chimie supramoléculaire pour diminuer d'une façon significative le transport de masse entre les électrodes.[148]

1.6. Description de la thèse et objectifs

L'approche scientifique s'est faite à deux niveaux pour bien cerner le développement d'innovantes navettes redox et d'électrolytes avancés. Dans un premier lieu, il s'agit de faire des études fondamentales pour améliorer la compréhension de la relation entre la structure chimique des LIRs étudiés et ces propriétés propres à son électrochimie et ses propriétés de transport. Aussi, des études fondamentales pour évaluer les propriétés de transport de l'ensemble des composantes d'un électrolyte avancé seront présentées. Dans un deuxième temps, il s'agira de fabriquer des dispositifs pour établir des preuves de concept pour démontrer ces possibles applications et toujours s'appuyer sur les études fondamentales préalablement effectuées. À la lumière de cette thèse, l'objectif principal était d'établir les premiers pas dans la conception de nouveaux LIRs résultant d'une modification d'anion, qui est peu investiguée à ce jour, et d'introduire ces LIRs comme composante dans des électrolytes pour les applications décrites dans le **Chapitre 1** : Introduction.

Le **Chapitre 2** présente l'ensemble des techniques utilisées et des détails théoriques cruciaux pour une bonne compréhension des prochains chapitres. Le **Chapitre 3** présente des structures de 1-(méthylferrocényl)-3-alkyl-imidazolium dont la chaîne latérale a été modifiée et les propriétés électrochimiques seront discutées. Le **Chapitre 4** démontre la différence entre le ferrocène, un LI commun en comparaison avec l'innovant LIR utilisant le ferrocénylsulfonyl(trifluorométhylsulfonyl)imide (FcNTf) comme anion. Le **Chapitre 5** montre les propriétés de transport du lithium et du FcNTf dans un mélange de LI avec un solvant de carbonate. Le **Chapitre 6** est l'étude des performances des BILs utilisant le FcNTf comme N-R. Le **Chapitre 7** est la présentation de navette strictement organique dans l'optique d'obtenir une espèce électroactive avec un haut potentiel d'oxydation. Le **Chapitre 8** est une investigation sur un dispositif électrochromique utilisant le FcNTf et le viologène. Le **Chapitre 9** est une discussion sur les grandes conclusions de cette thèse et les perspectives. De plus, les **Annexes 1** et **2** montrent les propriétés d'électrodéposition et d'innovants supercapaciteurs utilisant le FcNTf.

1.7. Références

[1] L.P.N. Rebelo, J.N. Canongia Lopes, J.M.S.S. Esperança, E. Filipe, On the critical temperature, normal boiling point, and vapor pressure of ionic liquids, J. Phys. Chem. B, 109 (2005) 6040-6043.
[2] P. Bonhôte, A.-P. Dias, N. Papageorgiou, K. Kalyanasundaram, M. Grätzel, Hydrophobic, highly conductive ambient-temperature molten salts, Inorg. Chem., 35 (1996) 1168-1178.
[3] M. Armand, F. Endres, D.R. MacFarlane, H. Ohno, B. Scrosati, Ionic-liquid materials for the electrochemical challenges of the future, Nat. Mater., 8 (2009) 621-629.
[4] M. Galiński, A. Lewandowski, I. Stępniak, Ionic liquids as electrolytes, Electrochim. Acta, 51 (2006) 5567-5580.
[5] A.E. Visser, R.P. Swatloski, W.M. Reichert, R. Mayton, S. Sheff, A. Wierzbicki, J.H. Davis, R.D. Rogers, Task-specific ionic liquids for the extraction of metal ions from aqueous solutions, Chem. Comm., (2001) 135-136.
[6] J. Fraga-Dubreuil, M.-H. Famelart, J.P. Bazureau, Ecofriendly fast synthesis of hydrophilic poly(ethyleneglycol)-ionic liquid matrices for liquid-phase organic synthesis, Org. Process Res. Dev., 6 (2002) 374-378.
[7] E.D. Bates, R.D. Mayton, I. Ntai, J.H. Davis, CO2 capture by a task-specific ionic liquid, J. Am. Chem. Soc., 124 (2002) 926-927.
[8] A.E. Visser, R.P. Swatloski, W.M. Reichert, R. Mayton, S. Sheff, A. Wierzbicki, J.J.H. Davis, R.D. Rogers, Task-specific ionic liquids for the extraction of metal ions from aqueous solutions, Chem. Comm., (2001) 135-136.
[9] H. Olivier-Bourbigou, L. Magna, D. Morvan, Ionic liquids and catalysis: Recent progress from knowledge to applications, Appl. Catal., A, 373 (2010) 1-56.
[10] K.-S. Kim, D. Demberelnyamba, H. Lee, Size-selective synthesis of gold and platinum nanoparticles using novel thiol-functionalized ionic liquids, Langmuir, 20 (2003) 556-560.
[11] B.S. Lee, Y.S. Chi, J.K. Lee, I.S. Choi, C.E. Song, S.K. Namgoong, S.-g. Lee, Imidazolium ion-terminated self-assembled monolayers on Au: Effects of counteranions on surface wettability, J. Am. Chem. Soc., 126 (2003) 480-481.
[12] O. Fontaine, C. Lagrost, J. Ghilane, P. Martin, G. Trippé, C. Fave, J.C. Lacroix, P. Hapiot, H.N. Randriamahazaka, Mass transport and heterogeneous electron transfer of a ferrocene derivative in a room-temperature ionic liquid, J. Electroanal. Chem., 632 (2009) 88-96.
[13] J.E.F. Weaver, D. Breadner, F.G. Deng, B. Ramjee, P.J. Ragogna, R.W. Murray, Electrochemistry of ferrocene-functionalized phosphonium ionic liquids, J. Phys. Chem. C, 115 (2011) 19379-19385.
[14] S.-g. Lee, Functionalized imidazolium salts for task-specific ionic liquids and their applications, Chem. Comm., (2006) 1049-1063.
[15] J.-L. Thomas, Howarth J, K.A. M., Electrochemical anion recognition by novel ferrocenyl imidazole systems, Molecules, 7 (2002) 861-866.
[16] B.T. Ye Gao, and Jeanne M. Shreeve, The first (ferrocenylmethyl)imidazolium and (ferrocenylmethyl)triazolium room temperature ionic liquids, Inorg. Chem., 43 (2004) 3406-3412.
[17] V.O. Nyamori, M. Gumede, M.D. Bala, Synthesis, characterisation and properties of ferrocenylalkylimidazolium salts, J. Organomet. Chem., 695 (2010) 1126-1132.
[18] R. Balasubramanian, W. Wang, R.W. Murray, Redox ionic liquid phases: Ferrocenated imidazoliums, J. Am. Chem. Soc., 128 (2006) 9994-9995.

[19] W. Wang, R. Balasubramanian, R.W. Murray, Electron transport and counterion relaxation dynamics in neat ferrocenated imidazolium ionic liquids, J. Phys. Chem. C, 112 (2008) 18207-18216.
[20] B.n.d. Chamiot, C.c. Rizzi, L. Gaillon, J. Sirieix-Plénet, J.l. Lelièvre, Redox-switched amphiphilic ionic liquid behavior in aqueous solution, Langmuir, 25 (2009) 1311-1315.
[21] P. Kubler, J. Sundermeyer, Ferrocenyl-phosphonium ionic liquids - synthesis, characterisation and electrochemistry, Dalton Trans., 43 (2014) 3750-3766.
[22] T. Inagaki, T. Mochida, Metallocenium ionic liquids, Chem. Lett., 39 (2010) 572-573.
[23] T. Inagaki, T. Mochida, M. Takahashi, C. Kanadani, T. Saito, D. Kuwahara, Ionic liquids of cationic sandwich complexes, Chem. Eur. J., 18 (2012) 6795-6804.
[24] J.C. Forgie, S. El Khakani, D.D. MacNeil, D. Rochefort, Electrochemical characterisation of a lithium-ion battery electrolyte based on mixtures of carbonates with a ferrocene-functionalised imidazolium electroactive ionic liquid, Phys. Chem. Chem. Phys., 15 (2013) 7713-7721.
[25] J.C. Forgie, D. Rochefort, Electroactive imidazolium salts based on 1,4-dimethoxybenzene redox groups: synthesis and electrochemical characterisation, RSC Adv., 3 (2013) 12035-12038.
[26] S.E. Khakani, J.C. Forgie, D.D. MacNeil, D. Rochefort, Redox shuttles for lithium-ion batteries at concentrations up to 1 M using an electroactive ionic liquid based on 2,5-di-tert-butyl-1,4-dimethoxybenzene, J. Electrochem. Soc., 162 (2015) A1432-A1438.
[27] Z. Fei, D. Kuang, D. Zhao, C. Klein, W.H. Ang, S.M. Zakeeruddin, M. Grätzel, P.J. Dyson, A supercooled imidazolium iodide ionic liquid as a low-viscosity electrolyte for dye-sensitized solar cells, Inorg. Chem., 45 (2006) 10407-10409.
[28] X. Chen, D. Xu, L. Qiu, S. Li, W. Zhang, F. Yan, Imidazolium functionalized TEMPO/iodide hybrid redox couple for highly efficient dye-sensitized solar cells, J. Mater. Chem. A, 1 (2013) 8759-8765.
[29] K. Tanabe, T. Yasuda, M. Yoshio, T. Kato, Viologen-based redox-active ionic liquid crystals forming columnar phases, Org. Lett., 9 (2007) 4271-4274.
[30] H. Tahara, Y. Furue, C. Suenaga, T. Sagara, A dialkyl viologen ionic liquid: X-ray crystal structure analysis of bis(trifluoromethanesulfonyl)imide salts, Cryst. Growth Des., 15 (2015) 4735-4740.
[31] N. Jordão, L. Cabrita, F. Pina, L.C. Branco, Novel bipyridinium ionic liquids as liquid electrochromic devices, Chem. Eur. J., 20 (2014) 3982-3988.
[32] E. Mourad, L. Coustan, S.A. Freunberger, A. Mehdi, A. Vioux, F. Favier, O. Fontaine, Biredox ionic liquids: electrochemical investigation and impact of ion size on electron transfer, Electrochim. Acta, 206 (2016) 513-523.
[33] E. Mourad, L. Coustan, P. Lannelongue, D. Zigah, A. Mehdi, A. Vioux, S.A. Freunberger, F. Favier, O. Fontaine, Biredox ionic liquids with solid-like redox density in the liquid state for high-energy supercapacitors, Nat. Mater., 16 (2017) 446-453.
[34] M. Armand, J.M. Tarascon, Building better batteries, Nature, 451 (2008) 652-657.
[35] J.M. Tarascon, M. Armand, Issues and challenges facing rechargeable lithium batteries, Nature, 414 (2001) 359-367.
[36] K. Kang, Y.S. Meng, J. Bréger, C.P. Grey, G. Ceder, Electrodes with high power and high capacity for rechargeable lithium batteries, Science, 311 (2006) 977-980.
[37] Z. Chen, Y. Qin, K. Amine, Redox shuttles for safer lithium-ion batteries, Electrochim. Acta, 54 (2009) 5605-5613.
[38] P.G. Balakrishnan, R. Ramesh, T.P. Kumar, Safety mechanisms in lithium-ion batteries, J. Power Sources, 155 (2006) 401-414.

[39] S.S. Zhang, A review on electrolyte additives for lithium-ion batteries, J. Power Sources, 162 (2006) 1379-1394.
[40] T. Ohsaki, T. Kishi, T. Kuboki, N. Takami, N. Shimura, Y. Sato, M. Sekino, A. Satoh, Overcharge reaction of lithium-ion batteries, J. Power Sources, 146 (2005) 97-100.
[41] M. Banobre-Lopez, F. Rivadulla, R. Caudillo, M.A. Lopez-Quintela, J. Rivas, J.B. Goodenough, Role of doping and dimensionality in the superconductivity of NaxCoO2, Chem. Mater., 17 (2005) 1965-1968.
[42] K.M. Abraham, D.M. Pasquariello, E.B. Willstaedt, Normal-butylferrocene for overcharge protection of secondary lithium batteries, J. Electrochem. Soc., 137 (1990) 1856-1857.
[43] M. Jonsson, J. Lind, T. Reitberger, T.E. Eriksen, G. Merenyi, Redox chemistry of substituted benzene - the one-electron reduction potentials of methoxy-substituted benzene radical cations, J. Phys. Chem., 97 (1993) 11278-11282.
[44] M.N. Golovin, D.P. Wilkinson, J.T. Dudley, D. Holonko, S. Woo, Application of metallocenes in rechargeable lithium batteries for overcharge protection, J. Electrochem. Soc., 139 (1992) 5-10.
[45] W.K. Behl, D.T. Chin, Electrochemical overcharge protection of rechargeable lithium batteries. 1. Kinetics of iodide tri-iodide iodine redox reactions on platinum in LiAsF6 tetrahydrofuran solution, J. Electrochem. Soc., 135 (1988) 16-21.
[46] W.K. Behl, D.T. Chin, Electrochemical overcharge protection of rechargeable lithium batteries. 2. Effect of lithium iodide-iodine additives on the behavior of lithium electrode in LiASF6-tetrahydrofuran solutions, J. Electrochem. Soc., 135 (1988) 21-25.
[47] W.K. Behl, Anodic oxidation of lithium bromide in tetrahydrofuran solutions, J. Electrochem. Soc., 136 (1989) 2305-2310.
[48] M.N. Ates, C.J. Allen, S. Mukerjee, K.M. Abraham, Electronic effects of substituents on redox shuttles for overcharge protection of Li-ion batteries, J. Electrochem. Soc., 159 (2012) A1057-A1064.
[49] C. Buhrmester, L.M. Moshurchak, R.L. Wang, J.R. Dahn, The use of 2,2,6,6-tetramethylpiperinyl-oxides and derivatives for redox shuttle additives in Li-ion cells, J. Electrochem. Soc., 153 (2006) A1800-A1804.
[50] C. Buhrmester, L. Moshurchak, R.L. Wang, J.R. Dahn, Phenothiazine molecules: Possible redox shuttle additives for chemical overcharge and overdischarge protection for Lithium-ion batteries, J. Electrochem. Soc., 153 (2006) A288-A294.
[51] A.P. Kaur, C.F. Elliott, S. Ergun, S.A. Odom, Overcharge performance of 3,7-bis(trifluoromethyl)-N-ethylphenothiazine at high concentration in Lithium-ion batteries, J. Electrochem. Soc., 163 (2016) A1-A7.
[52] D.-Y. Lee, H.-S. Lee, H.-S. Kim, H.-Y. Sun, D.-Y. Seung, Redox shuttle additives for chemical overcharge protection in lithium ion batteries, Korean J. Chem. Eng., 19 (2002) 645-652.
[53] Z. Chen, K. Amine, Bifunctional electrolyte additive for lithium-ion batteries, Electrochem. Comm., 9 (2007) 703-707.
[54] C. Buhrmester, J. Chen, L. Moshurchak, J.W. Jiang, R.L. Wang, J.R. Dahn, Studies of aromatic redox shuttle additives for LiFePO4-based Li-ion cells, J. Electrochem. Soc., 152 (2005) A2390-A2399.
[55] J. Chen, C. Buhrmester, J.R. Dahn, Chemical overcharge and overdischarge protection for lithium-ion batteries, Electrochem. Solid-State Lett., 8 (2005) A59-A62.
[56] F. Tran-Van, M. Provencher, Y. Choquette, D. Delabouglise, Dihydrophenazine derivatives for overcharge protection of rechargeable lithium batteries, Electrochim. Acta, 44 (1999) 2789-2792.

[57] M. Adachi, K. Tanaka, K. Sekai, Aromatic compounds as redox shuttle additives for 4 V class secondary lithium batteries, J. Electrochem. Soc., 146 (1999) 1256-1261.
[58] J.-H. Chen, L.-M. He, R.L. Wang, The stability of redox shuttles for overcharge protection in Lithium-ion cells: Studied by a computational model and molecular orbital analysis, J. Electrochem. Soc., 160 (2013) A155-A159.
[59] Z. Zhang, L. Zhang, J.A. Schlueter, P.C. Redfern, L. Curtiss, K. Amine, Understanding the redox shuttle stability of 3,5-di-tert-butyl-1,2-dimethoxybenzene for overcharge protection of lithium-ion batteries, J. Power Sources, 195 (2010) 4957-4962.
[60] T. Li, L. Xing, W. Li, B. Peng, M. Xu, F. Gu, S. Hu, Theoretic calculation for understanding the oxidation process of 1,4-dimethoxybenzene-based compounds as redox shuttles for overcharge protection of lithium ion batteries, J. Phys. Chem. A, 115 (2011) 4988-4994.
[61] L. Zhang, Z. Zhang, P.C. Redfern, L.A. Curtiss, K. Amine, Molecular engineering towards safer lithium-ion batteries: a highly stable and compatible redox shuttle for overcharge protection, Energy Environ. Sci., 5 (2012) 8204-8207.
[62] L.M. Moshurchak, W.M. Lamanna, M. Bulinski, R.L. Wang, R.R. Garsuch, J. Jiang, D. Magnuson, M. Triemert, J.R. Dahn, High-potential redox shuttle for use in lithium-ion batteries, J. Electrochem. Soc., 156 (2009) A309-A312.
[63] J. Huang, I.A. Shkrob, P. Wang, L. Cheng, B. Pan, M. He, C. Liao, Z. Zhang, L.A. Curtiss, L. Zhang, 1,4-Bis(trimethylsilyl)-2,5-dimethoxybenzene: a novel redox shuttle additive for overcharge protection in lithium-ion batteries that doubles as a mechanistic chemical probe, J. Mater. Chem. A, 3 (2015) 7332-7337.
[64] L. Zhang, Z.C. Zhang, H.M. Wu, K. Amine, Novel redox shuttle additive for high-voltage cathode materials, Energy Environ. Sci., 4 (2011) 2858-2862.
[65] J. Huang, N. Azimi, L. Cheng, I.A. Shkrob, Z. Xue, J. Zhang, N.L. Dietz Rago, L.A. Curtiss, K. Amine, Z. Zhang, L. Zhang, An organophosphine oxide redox shuttle additive that delivers long-term overcharge protection for 4 V lithium-ion batteries, J. Mater. Chem. A, 3 (2015) 10710-10714.
[66] K. Xu, Nonaqueous liquid electrolytes for lithium-based rechargeable batteries, Chem. Rev., 104 (2004) 4303-4418.
[67] L. Zhang, J. Huang, K. Youssef, P.C. Redfern, L.A. Curtiss, K. Amine, Z. Zhang, Molecular engineering toward stabilized interface: An electrolyte additive for high-performance Li-ion battery, J. Electrochem. Soc., 161 (2014) A2262-A2267.
[68] I.A. Shkrob, Y. Zhu, T.W. Marin, D.P. Abraham, Mechanistic insight into the protective action of bis(oxalato)borate and difluoro(oxalate)borate anions in Li-ion batteries, J. Phys. Chem. C, 117 (2013) 23750-23756.
[69] Z. Chen, Y. Ren, A.N. Jansen, C.-k. Lin, W. Weng, K. Amine, New class of nonaqueous electrolytes for long-life and safe lithium-ion batteries, Nat. Commun., 4 (2013) 1513.
[70] J.B. Goodenough, Y. Kim, Challenges for rechargeable Li batteries, Chem. Mater., 22 (2009) 587-603.
[71] S. Liumin, H. Yong-Sheng, L. Hong, A. Michel, C. Liquan, A new class of Solvent-in-Salt electrolyte for high-energy rechargeable metallic lithium batteries, Nat. Commun., 4 (2013) 1481-1481.
[72] L. Vogdanis, B. Martens, H. Uchtmann, F. Hensel, W. Heitz, Synthetic and thermodynamic investigations in the polymerization of ethylene carbonate, Die Makromolekulare Chemie, 191 (1990) 465-472.

[73] S.E. Sloop, J.K. Pugh, S. Wang, J.B. Kerr, K. Kinoshita, Chemical reactivity of PF 5 and LiPF6 in ethylene carbonate/dimethyl carbonate solutions, Electrochem. Solid-State Lett., 4 (2001) A42-A44.
[74] W. Li, C. Campion, B.L. Lucht, B. Ravdel, J. DiCarlo, K.M. Abraham, Additives for stabilizing LiPF6-based electrolytes against thermal decomposition, J. Electrochem. Soc., 152 (2005) A1361-A1365.
[75] V. Aravindan, J. Gnanaraj, S. Madhavi, H.-K. Liu, Lithium-ion conducting electrolyte salts for lithium batteries, Chem. Eur. J., 17 (2011) 14326-14346.
[76] Z. Zhang, L. Hu, H. Wu, W. Weng, M. Koh, P.C. Redfern, L.A. Curtiss, K. Amine, Fluorinated electrolytes for 5 V lithium-ion battery chemistry, Energy Environ. Sci., 6 (2013) 1806-1810.
[77] J. Wolfenstine, J. Allen, Ni3+/Ni2+ redox potential in LiNiPO4, J. Power Sources, 142 (2005) 389-390.
[78] S. Okada, S. Sawa, M. Egashira, J.-i. Yamaki, M. Tabuchi, H. Kageyama, T. Konishi, A. Yoshino, Cathode properties of phospho-olivine LiMPO4 for lithium secondary batteries, J. Power Sources, 97–98 (2001) 430-432.
[79] Q. Zhong, A. Bonakdarpour, M. Zhang, Y. Gao, J.R. Dahn, Synthesis and electrochemistry of LiNi x Mn2 − x O 4, J. Electrochem. Soc., 144 (1997) 205-213.
[80] J.B. Goodenough, Y. Kim, Challenges for rechargeable Li batteries, Chem. Mater., 22 (2010) 587-603.
[81] K. Xu, C.A. Angell, High anodic stability of a new electrolyte solvent: Unsymmetric noncyclic aliphatic sulfone, J. Electrochem. Soc., 145 (1998) L70-L72.
[82] M. Nagahama, N. Hasegawa, S. Okada, High Voltage performances of Li2NiPO4F cathode with dinitrile-based electrolytes, J. Electrochem. Soc., 157 (2010) A748-A752.
[83] L. Yang, T. Markmaitree, B.L. Lucht, Inorganic additives for passivation of high voltage cathode materials, J. Power Sources, 196 (2011) 2251-2254.
[84] V. Borgel, E. Markevich, D. Aurbach, G. Semrau, M. Schmidt, On the application of ionic liquids for rechargeable Li batteries: High voltage systems, J. Power Sources, 189 (2009) 331-336.
[85] M. Nie, J. Demeaux, B.T. Young, D.R. Heskett, Y. Chen, A. Bose, J.C. Woicik, B.L. Lucht, Effect of vinylene carbonate and fluoroethylene carbonate on SEI formation on graphitic anodes in Li-ion batteries, J. Electrochem. Soc., 162 (2015) A7008-A7014.
[86] R. Fong, U. von Sacken, J.R. Dahn, Studies of lithium intercalation into carbons using nonaqueous electrochemical cells, J. Electrochem. Soc., 137 (1990) 2009-2013.
[87] R. Yazami, Surface chemistry and lithium storage capability of the graphite–lithium electrode, Electrochim. Acta, 45 (1999) 87-97.
[88] J.O. Besenhard, M. Winter, J. Yang, W. Biberacher, Filming mechanism of lithium-carbon anodes in organic and inorganic electrolytes, J. Power Sources, 54 (1995) 228-231.
[89] P. Verma, P. Maire, P. Novák, A review of the features and analyses of the solid electrolyte interphase in Li-ion batteries, Electrochim. Acta, 55 (2010) 6332-6341.
[90] B. Garcia, S. Lavallée, G. Perron, C. Michot, M. Armand, Room temperature molten salts as lithium battery electrolyte, Electrochim. Acta, 49 (2004) 4583-4588.
[91] E. Markevich, V. Baranchugov, D. Aurbach, On the possibility of using ionic liquids as electrolyte solutions for rechargeable 5 V Li ion batteries, Electrochem. Comm., 8 (2006) 1331-1334.
[92] Y. Wang, K. Zaghib, A. Guerfi, F.F.C. Bazito, R.M. Torresi, J.R. Dahn, Accelerating rate calorimetry studies of the reactions between ionic liquids and charged lithium ion battery electrode materials, Electrochim. Acta, 52 (2007) 6346-6352.

[93] H. Sakaebe, H. Matsumoto, N-Methyl-N-propylpiperidinium bis(trifluoromethanesulfonyl)imide (PP13–TFSI) – novel electrolyte base for Li battery, Electrochem. Comm., 5 (2003) 594-598.
[94] S. Seki, Y. Kobayashi, H. Miyashiro, Y. Ohno, A. Usami, Y. Mita, N. Kihira, M. Watanabe, N. Terada, Lithium secondary batteries using modified-imidazolium room-temperature ionic liquid, J. Phys. Chem. B, 110 (2006) 10228-10230.
[95] T. Frömling, M. Kunze, M. Schönhoff, J. Sundermeyer, B. Roling, Enhanced lithium transference numbers in ionic liquid electrolytes, J. Phys. Chem. B, 112 (2008) 12985-12990.
[96] M. Ue, S. Mori, Mobility and ionic association of lithium salts in a propylene carbonate-ethyl methyl carbonate mixed solvent, J. Electrochem. Soc., 142 (1995) 2577-2581.
[97] A. Fernicola, F. Croce, B. Scrosati, T. Watanabe, H. Ohno, LiTFSI-BEPyTFSI as an improved ionic liquid electrolyte for rechargeable lithium batteries, J. Power Sources, 174 (2007) 342-348.
[98] M.J. Marczewski, B. Stanje, I. Hanzu, M. Wilkening, P. Johansson, "Ionic liquids-in-salt" - a promising electrolyte concept for high-temperature lithium batteries?, Phys. Chem. Chem. Phys., 16 (2014) 12341-12349.
[99] Y. Yamada, A. Yamada, Review—superconcentrated electrolytes for lithium batteries, J. Electrochem. Soc., 162 (2015) A2406-A2423.
[100] T. Mandai, K. Yoshida, K. Ueno, K. Dokko, M. Watanabe, Criteria for solvate ionic liquids, Phys. Chem. Chem. Phys., 16 (2014) 8761-8772.
[101] C.A. Angell, A new class of molten salt mixtures the hydrated dipositive ion as an independent cation species, J. Electrochem. Soc., 112 (1965) 1224-1227.
[102] C. Austen Angell, Y. Ansari, Z. Zhao, Ionic liquids: Past, present and future, Faraday Discuss., 154 (2012) 9.
[103] K. Ueno, K. Yoshida, M. Tsuchiya, N. Tachikawa, K. Dokko, M. Watanabe, Glyme–lithium salt equimolar molten mixtures: Concentrated solutions or solvate ionic liquids?, J. Phys. Chem. B, 116 (2012) 11323-11331.
[104] K. Yoshida, M. Tsuchiya, N. Tachikawa, K. Dokko, M. Watanabe, Correlation between battery performance and lithium ion diffusion in glyme–lithium bis(trifluoromethanesulfonyl)amide equimolar complexes, J. Electrochem. Soc., 159 (2012) A1005-A1012.
[105] K. Dokko, N. Tachikawa, K. Yamauchi, M. Tsuchiya, A. Yamazaki, E. Takashima, J.-W. Park, K. Ueno, S. Seki, N. Serizawa, M. Watanabe, Solvate ionic liquid electrolyte for Li–S batteries, J. Electrochem. Soc., 160 (2013) A1304-A1310.
[106] S. Theivaprakasam, D.R. MacFarlane, S. Mitra, Electrochemical studies of N-Methyl N-Propyl Pyrrolidinium bis(trifluoromethanesulfonyl) imide ionic liquid mixtures with conventional electrolytes in LiFePO4/Li cells, Electrochim. Acta, 180 (2015) 737-745.
[107] S. Fang, L. Qu, D. Luo, S. Shen, L. Yang, S.-i. Hirano, Novel mixtures of ether-functionalized ionic liquids and non-flammable methylperfluorobutylether as safe electrolytes for lithium metal batteries, RSC Adv., 5 (2015) 33897-33904.
[108] A. Hofmann, M. Schulz, S. Indris, R. Heinzmann, T. Hanemann, Mixtures of ionic liquid and sulfolane as electrolytes for Li-ion batteries, Electrochim. Acta, 147 (2014) 704-711.
[109] L. Lombardo, S. Brutti, M.A. Navarra, S. Panero, P. Reale, Mixtures of ionic liquid – Alkylcarbonates as electrolytes for safe lithium-ion batteries, J. Power Sources, 227 (2013) 8-14.
[110] P.M. Bayley, G.H. Lane, N.M. Rocher, B.R. Clare, A.S. Best, D.R. MacFarlane, M. Forsyth, Transport properties of ionic liquid electrolytes with organic diluents, Phys. Chem. Chem. Phys., 11 (2009) 7202-7208.

[111] A. Guerfi, M. Dontigny, P. Charest, M. Petitclerc, M. Lagacé, A. Vijh, K. Zaghib, Improved electrolytes for Li-ion batteries: Mixtures of ionic liquid and organic electrolyte with enhanced safety and electrochemical performance, J. Power Sources, 195 (2010) 845-852.
[112] R.S. Kühnel, N. Böckenfeld, S. Passerini, M. Winter, A. Balducci, Mixtures of ionic liquid and organic carbonate as electrolyte with improved safety and performance for rechargeable lithium batteries, Electrochim. Acta, 56 (2011) 4092-4099.
[113] S. Menne, R.S. Kühnel, A. Balducci, The influence of the electrochemical and thermal stability of mixtures of ionic liquid and organic carbonate on the performance of high power lithium-ion batteries, Electrochim. Acta, 90 (2013) 641-648.
[114] R.-S. Kühnel, M. Lübke, M. Winter, S. Passerini, A. Balducci, Suppression of aluminum current collector corrosion in ionic liquid containing electrolytes, J. Power Sources, 214 (2012) 178-184.
[115] T. Evans, J. Olson, V. Bhat, S.-H. Lee, Effect of organic solvent addition to PYR13FSI + LiFSI electrolytes on aluminum oxidation and rate performance of Li(Ni1/3Mn1/3Co1/3)O2 cathodes, J. Power Sources, 265 (2014) 132-139.
[116] A. Hofmann, L. Merklein, M. Schulz, T. Hanemann, Anodic aluminum dissolution of LiTFSA containing electrolytes for Li-ion-batteries, Electrochim. Acta, 116 (2014) 388-395.
[117] F. Croce, G.B. Appetecchi, L. Persi, B. Scrosati, Nanocomposite polymer electrolytes for lithium batteries, Nature, 394 (1998) 456-458.
[118] Z. Gadjourova, Y.G. Andreev, D.P. Tunstall, P.G. Bruce, Ionic conductivity in crystalline polymer electrolytes, Nature, 412 (2001) 520-523.
[119] A.D. Robertson, A.R. West, A.G. Ritchie, Review of crystalline lithium-ion conductors suitable for high temperature battery applications, Solid State Ionics, 104 (1997) 1-11.
[120] S. Kondo, K. Takada, Y. Yamamura, New lithium ion conductors based on Li2S-SiS2 system, Solid State Ionics, 53–56, Part 2 (1992) 1183-1186.
[121] A. Swiderska-Mocek, Application of quaternary polymer electrolyte based on ionic liquid in LiFePO4/Li, Li4Ti5O12/Li and LiFePO4/Li4Ti5O12 batteries, Electrochim. Acta, 139 (2014) 337-344.
[122] P. Simon, Y. Gogotsi, Materials for electrochemical capacitors, Nat. Mater., 7 (2008) 845-854.
[123] M.S. Whittingham, History, Evolution, and future status of energy storage, Proc. IEEE, 100 (2012) 1518-1534.
[124] V. Augustyn, J. Come, M.A. Lowe, J.W. Kim, P.-L. Taberna, S.H. Tolbert, H.D. Abruña, P. Simon, B. Dunn, High-rate electrochemical energy storage through Li+ intercalation pseudocapacitance, Nat. Mater., 12 (2013) 518-522.
[125] W. Deng, X. Ji, Q. Chen, C.E. Banks, Electrochemical capacitors utilising transition metal oxides: an update of recent developments, RSC Adv., 1 (2011) 1171-1178.
[126] G.A. Snook, P. Kao, A.S. Best, Conducting-polymer-based supercapacitor devices and electrodes, J. Power Sources, 196 (2011) 1-12.
[127] H. Wang, H.S. Casalongue, Y. Liang, H. Dai, Ni(OH)2 nanoplates grown on graphene as advanced electrochemical pseudocapacitor materials, J. Am. Chem. Soc., 132 (2010) 7472-7477.
[128] Y. Wang, X. Yang, L. Qiu, D. Li, Revisiting the capacitance of polyaniline by using graphene hydrogel films as a substrate: the importance of nano-architecturing, Energy Environ. Sci., 6 (2013) 477-481.
[129] A.B. McEwen, S.F. McDevitt, V.R. Koch, Nonaqueous electrolytes for electrochemical capacitors: imidazolium cations and inorganic fluorides with organic carbonates, J. Electrochem. Soc., 144 (1997) L84-L86.

[130] X. Zhang, D. Zhao, Y. Zhao, P. Tang, Y. Shen, C. Xu, H. Li, Y. Xiao, High performance asymmetric supercapacitor based on MnO2 electrode in ionic liquid electrolyte, J. Mater. Chem. A, 1 (2013) 3706-3712.
[131] V. Ruiz, T. Huynh, S.R. Sivakkumar, A.G. Pandolfo, Ionic liquid-solvent mixtures as supercapacitor electrolytes for extreme temperature operation, RSC Adv., 2 (2012) 5591-5598.
[132] S.-E. Chun, B. Evanko, X. Wang, D. Vonlanthen, X. Ji, G.D. Stucky, S.W. Boettcher, Design of aqueous redox-enhanced electrochemical capacitors with high specific energies and slow self-discharge, Nat. Commun., 6 (2015).
[133] S.T. Senthilkumar, R.K. Selvan, J.S. Melo, Redox additive/active electrolytes: a novel approach to enhance the performance of supercapacitors, J. Mater. Chem. A, 1 (2013) 12386-12394.
[134] S. Roldán, C. Blanco, M. Granda, R. Menéndez, R. Santamaría, Towards a further generation of high-energy carbon-based capacitors by using redox-active electrolytes, Angew. Chem. Int. Ed., 50 (2011) 1699-1701.
[135] E. Frackowiak, K. Fic, M. Meller, G. Lota, Electrochemistry serving people and nature: High-energy ecocapacitors based on redox-active electrolytes, ChemSuschem, 5 (2012) 1181-1185.
[136] L.-Q. Mai, A. Minhas-Khan, X. Tian, K.M. Hercule, Y.-L. Zhao, X. Lin, X. Xu, Synergistic interaction between redox-active electrolyte and binder-free functionalized carbon for ultrahigh supercapacitor performance, Nat. Commun., 4 (2013).
[137] W. Chen, R.B. Rakhi, H.N. Alshareef, Capacitance enhancement of polyaniline coated curved-graphene supercapacitors in a redox-active electrolyte, Nanoscale, 5 (2013) 4134-4138.
[138] S. Roldán, M. Granda, R. Menéndez, R. Santamaría, C. Blanco, Mechanisms of energy storage in carbon-based supercapacitors modified with a quinoid redox-active electrolyte, J. Phys. Chem. C, 115 (2011) 17606-17611.
[139] J. Wu, H. Yu, L. Fan, G. Luo, J. Lin, M. Huang, A simple and high-effective electrolyte mediated with p-phenylenediamine for supercapacitor, J. Mater. Chem., 22 (2012) 19025-19030.
[140] H. Yu, J. Wu, J. Lin, L. Fan, M. Huang, Y. Lin, Y. Li, F. Yu, Z. Qiu, A reversible redox strategy for SWCNT-based supercapacitors using a high-performance electrolyte, ChemPhysChem, 14 (2013) 394-399.
[141] H. Yu, L. Fan, J. Wu, Y. Lin, M. Huang, J. Lin, Z. Lan, Redox-active alkaline electrolyte for carbon-based supercapacitor with pseudocapacitive performance and excellent cyclability, RSC Adv., 2 (2012) 6736-6740.
[142] S.T. Senthilkumar, R.K. Selvan, Y.S. Lee, J.S. Melo, Electric double layer capacitor and its improved specific capacitance using redox additive electrolyte, J. Mater. Chem. A, 1 (2013) 1086-1095.
[143] L.-H. Su, X.-G. Zhang, C.-H. Mi, B. Gao, Y. Liu, Improvement of the capacitive performances for Co-Al layered double hydroxide by adding hexacyanoferrate into the electrolyte, Phys. Chem. Chem. Phys., 11 (2009) 2195-2202.
[144] Q. Li, K. Li, C. Sun, Y. Li, An investigation of Cu2+ and Fe2+ ions as active materials for electrochemical redox supercapacitors, J. Electroanal. Chem., 611 (2007) 43-50.
[145] T. Tooming, T. Thomberg, L. Siinor, K. Tõnurist, A. Jänes, E. Lust, A type high capacitance supercapacitor based on mixed room temperature ionic liquids containing specifically adsorbed iodide anions, J. Electrochem. Soc., 161 (2014) A222-A227.
[146] G. Sun, K. Li, C. Sun, Electrochemical performance of electrochemical capacitors using Cu(II)-containing ionic liquid as the electrolyte, Microporous Mesoporous Mater., 128 (2010) 56-61.

[147] L. Chen, H. Bai, Z. Huang, L. Li, Mechanism investigation and suppression of self-discharge in active electrolyte enhanced supercapacitors, Energy Environ. Sci., 7 (2014) 1750-1759.
[148] K. Sato, T. Yamasaki, T. Mizuma, K. Oyaizu, H. Nishide, Dynamic switching of ionic conductivity by cooperative interaction of polyviologen and liquid crystals for efficient charge storage, J. Mater. Chem. A, 4 (2016) 3249-3252.

Chapitre 2 : Théorie et techniques expérimentales

2.1. Avant-propos et mise en contexte

Ce chapitre a pour but la présentation des principes des méthodes utilisées tout au long de cette thèse et d'assurer au lecteur une base nécessaire pour une bonne compréhension des prochains chapitres. La synthèse de liquides ioniques fonctionnalisés, des analyses physicochimiques des LIs à l'état pur et une caractérisation électrochimique des électrolytes seront approfondies dans les prochaines sections. La configuration des montages et cellules sera aussi expliquée. La théorie est décrite au besoin et cette thèse donne une importance capitale à l'électrochimie qui sera au cœur des études menées dans les divers projets. Pour éviter la dilution de cette thèse, le choix des techniques et des principes décrits s'explique par l'importance, la nécessité de plus ample information et la complexité de ceux-ci. La synthèse des LIs avancés qui constitue la pierre angulaire de ces travaux sera décrite en détail, car elle represente de nombreuses innovation par rapport au articles existants et les détails ont été conservés au minimum dans les articles publiés

2.2. Synthèse de liquides ioniques avancés

2.2.1. Synthèse des liquides ioniques fonctionnalisés.

Le développement des méthodes de synthèse de LIs s'est fait en plusieurs générations distinctes dans le but d'obtenir des LIs avec des propriétés qui répondent à leur besoin. L'engouement des chercheurs s'explique par le fait que les propriétés peuvent être complètement différentes d'un LI à l'autre dépendamment de la structure du LI. En 1996, l'une des avancées significatives a été faite par Bonhôte qui a présenté pour la première fois des LIs utilisant l'imidazolium et bis(trifluorométhylsulfonyl)imide (NTf_2) qui se distinguent par sa stabilité avec un air sec ou humide.[1] En faisant la rétrosynthèse de la plupart des LIs, la dernière étape pour simplement produire un LI est la métathèse d'ions et la force motrice de cette réaction est dictée par le principe de Pearson (Théorie HSAB). Par conséquent, il est avantageux d'utiliser des sels précurseurs dont l'anion est mou et le cation est dur ou vice-versa pour évidemment favoriser la

force motrice de la réaction. Donc, la combinaison entre l'anion et le cation mous est favorisée et mène au LI voulu. Dans le cadre de cette thèse, il s'agit de fonctionnaliser un LI en modifiant le cation ou l'anion. Pour synthétiser le cation, nous avons eu recours le plus souvent recours à une N-alkylation d'un alkylimidazole avec un halogénure d'alkyle où le groupement fonctionnel peut se retrouver sur l'alkylimidazole ou sur l'halogénure d'alkyle (i.e. Réaction de Menshutkin). Cette voie de synthèse est la plus populaire dans la littérature dans l'obtention d'un LI fonctionnalisé utilisant le couple imidazolium/NTf_2. En générale, ce couple anion-cation se distingue par la formation d'un LI moins visqueux, stable avec l'air, miscible avec les solvants. De plus, nous avons mis l'emphase sur le développement de nouveaux LIs dont l'anion est modifié afin de le comparer avec le cation modifié et d'étudier ces propriétés propres à ces LIs.

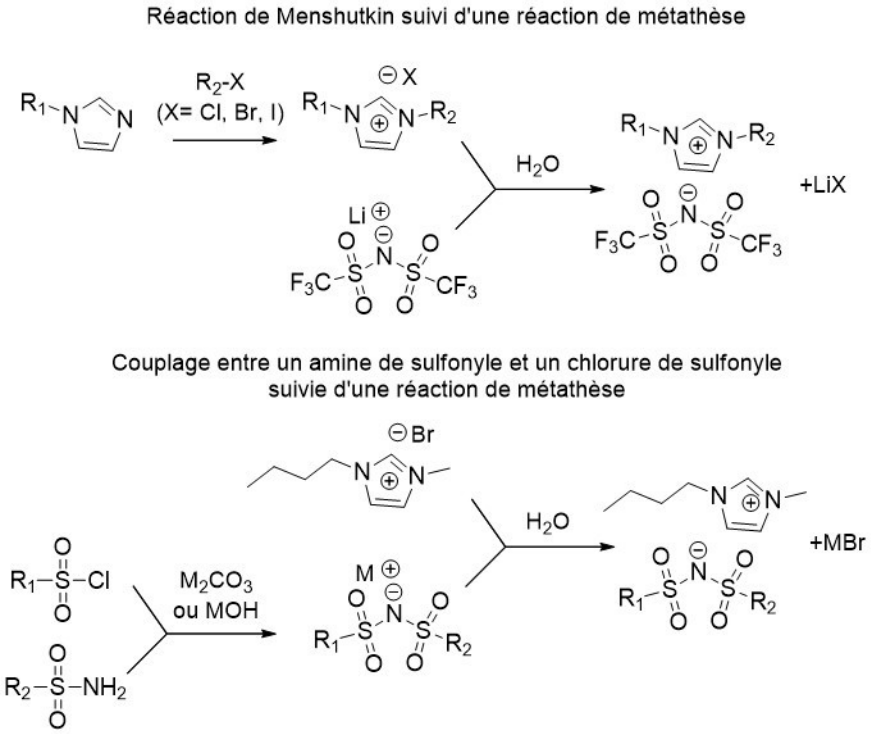

Figure 2.1. Schéma illustrant la différence entre la fonctionnalisation d'un anion ou d'un cation reposant sur le couple imidazolium et bis(sulfonyl)imide.

2.2.2. Synthèse de l'anion bis(trifluorométhylsulfonyl)imide.

Les triflamides sont rarement fonctionnalisés et cette thèse présente un effort soutenu pour développer une voie de synthèse pour fonctionnaliser l'anion qui est beaucoup moins documenté dans la littérature. Desmarteau a beaucoup contribué à améliorer la synthèse des

bis(perfluoroalkyl)sulfonyl)imides et en fait, il est le premier à avoir isolé l'anion NTf_2.[2, 3] La réaction (**Figure 2.2**-méthode A) est basée sur le couplage d'un fluorure de trifluorométhanesulfonyle (**Figure 2.2**-1) avec un sel de N-trimétylsilyl-trifluorométhanesulfonyl imide (**Figure 2.2**-3).[2, 3] La limite et la problématique de cette voie de synthèse proviennent du fait que le fluorure de trifluorométhanesulfonyle se retrouve sous forme gazeuse à la température ambiante et les réactifs de ce type de réaction sont très sensibles à l'humidité. Toujours en traitant avec de l'ammoniac gazeux, l'anhydride triflique est une solution pour contourner cette problématique (**Figure 2.2**-méthode B)[4] et le trifluorométhanesulfonamide est un réactif clé dans l'objectif d'obtenir des bis(perfluoroalkyl)sulfonyl)imide asymétrique. La méthode B est le couplage entre un chlorure de sulfonyle (Bon nucléophile) et le trifluorométhanesulfonamide (Bon électrophile) utilisant une base qui se prête bien à l'ajout d'un groupement fonctionnel. L'un des premiers exemples de la littérature est la réaction entre un chlorure d'arènesulfonyle et le triflamide (i.e. trifluorométhanesulfonamide).[5-9] Récemment, Arvai et al. présentent une méthode (**Figure 2.2**-méthode C) utilisant des réactifs plus doux utilisant un groupe benzyle comme groupe protecteur. La force motrice de la déprotection est en partie causée par l'effet électroattracteur des chaînes fluorées favorisant la libération de l'anion NTf_2 ou des dérivées de celui-ci (groupe nucléofuge) par une substitution nucléophile.[10, 11]

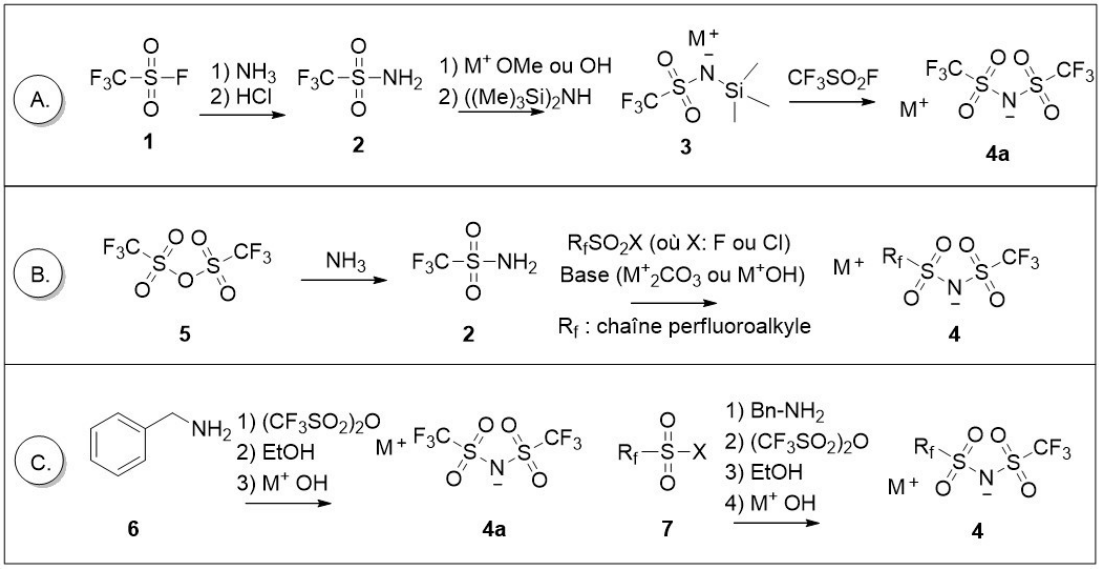

Figure 2.2. Schéma illustrant la synthèse d'anion basé sur le bis(perfluoroalkyl)sulfonyl) imide

2.2.3. Synthèse de chlorure de sulfonyle.

En continuant la rétrosynthèse, outre l'importance du trifluorométhanesulfonamide pour une voie de synthèse d'anion de di(sulfonyl)imide asymétrique (**Figure 2.2**-méthode B), la synthèse de chlorure de sulfonyle est tout aussi indispensable. Selon la **Figure 2.3**, il existe deux méthodes typiques pour obtenir les chlorures de sulfonyle via une chlorosulfonation ou par une chloration oxydative d'un composé sulfoné. En général, les chlorures de sulfonyle qui découlent de la chlorosulfonation sont préparés par le traitement d'un acide sulfonique ou d'un sulfonate avec des agents chlorants tels que le chlorure de thionyle,[12] pentachlorure de phosphore,[13] trichlorure de phosphoryle,[14] triphosgène,[15] et chlorure cyanurique[16] pour n'en nommer que quelques-uns. Préalablement, la sulfonation aliphatique ou aromatique peut se faire de plusieurs façons comme par le biais de l'acide chlorosulfurique (i.e. source de trioxyde de souffre et de l'acide chlorhydrique), par l'ouverture d'une sultone suite à une N-alkylation ou une O-alkylation et enfin, par l'utilisation de sulfite de sodium (i.e. alkylation de Strecker) réagissant avec un composé comportant un groupement nucléofuge. La sulfonation aromatique par substitution électrophile respecte la règle d'Holleman suivant les groupements activants (i.e. électrodonneur) et désactivants (i.e. électroattracteur) qui dicteront la position substituée. Les réactifs utilisés pour la préparation de chlorure de sulfonyle à partir de composés sulfonés tels que les thiols, les disulfides, les thioacétates, les thiocarbamates et les sels d'isothiouronium sont faits à l'aide d'une solution aqueuse ou organique avec du dichlore, du chlorure cyanurique, du peroxyde d'hydrogène en présence d'une source de chlore, de l'hypochlorite de sodium, du N-chlorosuccinimide (NCS) et, etc. En d'autres mots, il s'agit de traiter le composé sulfoné en présente de réactifs oxydants et chlorants.

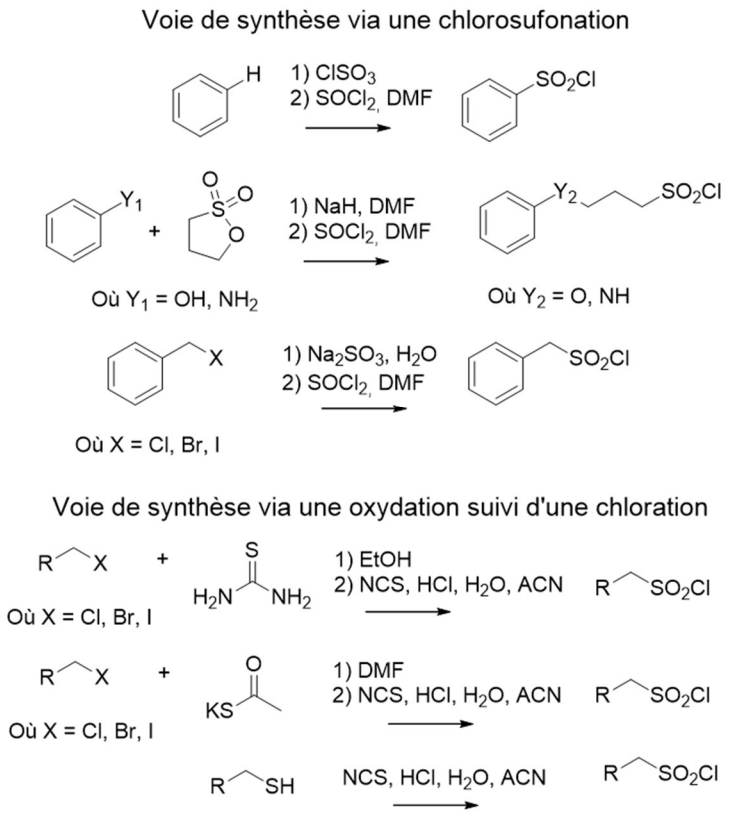

Figure 2.3. Schéma illustranst la synthèse de chlorure de sulfonyle.

2.3. Analyses physicochimiques

2.3.1. Analyses thermiques

Les analyses thermiques ont pour but de l'étude des transitions de phase, les variations de masse ou d'énergie en fonction de la température qui sont dictées par le changement des propriétés chimiques et physiques de la matière investiguée. Les analyses thermiques présentées dans cette section sont l'analyse thermogravimétrique (ATG, en anglais TGA) et l'analyse calorimétrique différentielle (ACD, en anglais DSC) dont les schémas instrumentales sont présentés sur la **Figure 2.4**. L'ATG est une expérience dans laquelle on mesure les variations de masse d'un échantillon selon la température appliquée ou le temps avec une température constante. L'ACD est une expérience dans laquelle on étudie l'énergie absorbée par l'échantillon en fonction de la température qui est comparé à une référence.

L'instrument pour effectuer l'ATG est constitué d'une microbalance reliée à une nacelle contenant l'échantillon qui est placée dans un four sous une atmosphère contrôlée (**Figure 2.4A**). D'ailleurs, la température est programmée utilisant une rampe de température linéaire et préalable déterminée et nous avons choisi 10 °C min^{-1} comme vitesse de chauffe, car elle ne doit pas être trop rapide afin d'avoir une température de décomposition précise et suffisamment rapide pour observer des réactions endothermiques. La masse ou le pourcentage de masse en fonction de la température correspond à la courbe thermogravimétrique. Dépendamment des caractérisations voulues, le point d'inflexion de la courbe ou une perte massique peuvent être observés. L'atmosphère est modulable via l'utilisation d'un gaz inerte comme l'azote ou l'helium et l'air peut être employé pour étudier la décomposition en présence d'oxygène et d'eau.

L'appareil pour l'ACD est tout indiqué pour mesurer les températures de transition et l'enthalpie de réaction. D'ailleurs, le sens de l'échange de chaleur indique s'il s'agit d'une réaction endothermique ou exothermique. Par exemple, la fusion d'un solide va absorber plus de chaleur que la référence qui montrera la température de fusion. Cette quantité de chaleur est mesurable et correspond à l'enthalpie obtenue par l'aire de la courbe du thermogramme. Il existe deux techniques pour l'ACD qui est à compensation de puissance et à flux de chaleur (**Figure 2.4B et 4C**). La différence entre ces méthodes réside dans le type d'instrumentation par le biais de fours (compensation de puissance) et par porte-échantillons (flux de chaleur) pour la référence et pour l'échantillon qui sont séparés l'un de l'autre pour les deux méthodes. L'ACD à compensation de puissance repose sur deux sources de chaleur distinctes pour maintenir la température des deux fours à la même température (**Figure 2.4B)**. En d'autres mots, une source augmente linéairement et la seconde source compense dans l'objectif d'obtenir une température uniforme entre les deux fours. L'instrument utilisé dans le cadre de cette thèse est un ACD à flux de chaleur. Le principe est basé sur une coupelle d'aluminium contenant l'échantillon qui est posé sur un disque thermoélectrique en alliage constantan (i.e. alliage métallique constitué de cuivre et de nickel) et lorsque la chaleur est transférée, la différence du flux thermique est mesurée par un thermocouple utilisant des fils de chromel (**Figure 2.4C**). Les coupelles se retrouvent dans une chambre délimitée par un bloc chauffant et remplie d'un gaz inerte. La référence est normalement une coupelle d'aluminium vide. La vitesse de chauffe peut être modulée (i.e. modulation sinusoïdale) qui est une technique nommée ACD modulée et ce profil de chauffage est avantageux du point de vue de la résolution, de la sensibilité et de la distinction des transitions non-réversibles et réversibles.

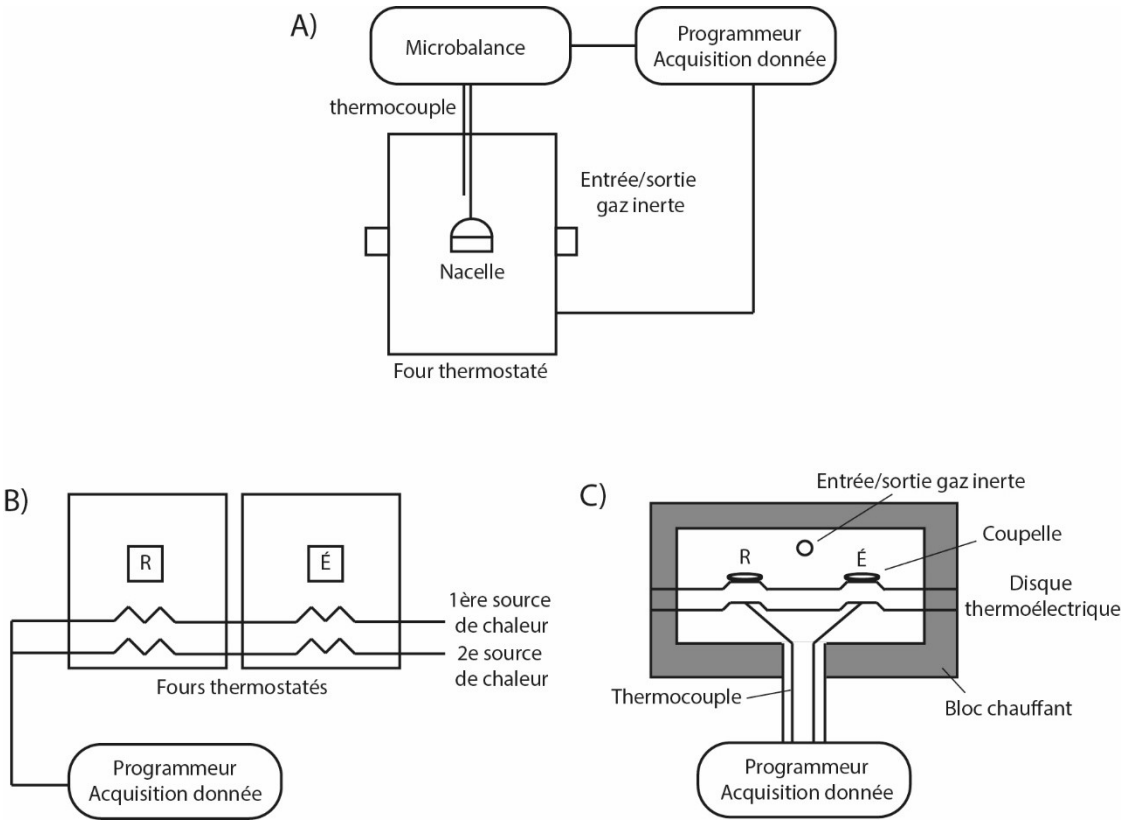

Figure 2.4. A) L'analyse thermogravimétrique (ATG) et l'analyse calorimétrique différentielle (ACD) B) à compensation de puissance et C) à flux de chaleur.

Typiquement, l'ATG des LIs montre une perte massique au-delà de 75 °C correspondant à l'évaporation d'eau par le biais de l'hygroscopicité des ILs et la température de décomposition identifiable par la perte de 5 à 10% sur la courbe thermogravimétrique est en général d'environ 300 à 450 °C pour une analyse à court terme (i.e. 10 ou 20 °C min^{-1}).[17] Cependant, il y a été aussi montré une dégradation à plus basse température, mais cinétiquement plus lente et par exemple, le BMIm NTf_2 commence à se dégrader à 150 °C.[18] La majorité des dégradations des LIs basés sur l'Im et le NTf_2 se fait par la réaction inverse de Menshutkin et par dégagement de dioxyde de soufre.[17] Les températures de transitions de phase des LIs sont gouvernées par les forces de Van der Waals et les forces électrostatiques. Par conséquent, la structure du LI a un effet significatif sur ces propriétés thermiques. Les LIs présentent des plages liquides de plus de 300 °C, car les LIs ne présentent pas de températures d'évaporation via la faible pression de vapeur des LIs. Par exemple, le BMIm NTf_2 possède une température de transition vitreuse, de fusion et de congélation de -87, -3 et -16 °C, respectivement.[19, 20] En théorie, le point de congélation se produit à la même

température que le point de fusion, cependant certains LIs affichent un état de surfusion et/ou une recristallisation lente.[20]

2.3.2. Viscosité dynamique

La viscosité dynamique d'un fluide est la propriété rhéologique qui se définit par sa résistance à l'écoulement de la matière et les unités de mesure habituellement rencontrées sont le centipoise (cP) ou le millipascal seconde (mPa s). La viscosité de l'eau est d'environ de 1 cP à 20°C. Il existe plusieurs méthodes pour obtenir la viscosité dont celles basés sur un viscosimètre à piston oscillant et un viscosimètre à bille qui ont été utilisées dans le cadre de cette thèse (**Figure 2.5**). Normalement, ce type d'instrument donne la viscosité dynamique qui est dictée par la contrainte de cisaillement (résistance de frottement entre les plans de cisaillement) selon le gradient de vitesse d'écoulement. Les fluides newtoniens ont une viscosité dynamique indépendante du gradient de vitesse et par conséquent, le fluide s'écoule indépendamment des forces extérieures. La viscosité de fluides newtoniens ne dépend que de la température et de la pression. Par exemple, les solutions aqueuses, la plupart des solvants, l'air et plusieurs gaz sont des fluides newtoniens. De plus, la viscosité cinétique est le quotient de la viscosité dynamique par la densité (i.e. la masse volumique) du fluide.

Par conséquent, les viscosimètres à piston oscillant reposent sur le déplacement d'un piston émergé à travers d'un fluide (**Figure 2.5A**). Pendant l'expérimentation, le piston oscille et induit un champ électromagnétique mesurable. Donc, le temps de déplacement du piston dépend de la contrainte de cisaillement préalablement discutée et la viscosité est déterminée. Dans le même ordre d'idée, le principe de fonctionnement du viscosimètre à bille repose sur le roulement d'une bille, habituellement en acier inoxydable ou en or, à travers du fluide d'intérêt (**Figure 2.5B)**. Le tube contenant la bille et le fluide s'incline à plusieurs angles et le temps de déplacement de la bille perçue par un senseur est intimement relié à la viscosité.

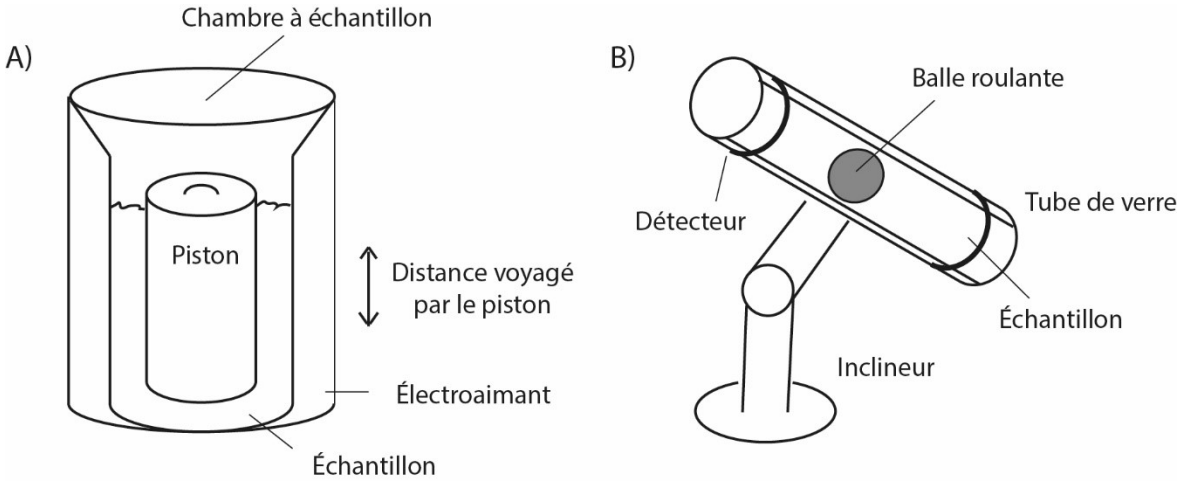

Figure 2.5. A) viscosimètre à piston oscillant et B) viscosimètre à bille.

En général, les LIs sont beaucoup plus visqueux que les solvants conventionnels, la différence de viscosité est de 2 à 3 ordres de grandeur entre ces fluides. Par exemple, la viscosité à température ambiante du toluène, 1-hexyl-3-méthylimidazolium bis(trifluorométhylsulfonyl)imide et de l'acétate de bis(hydroxyéthyl)ammonium est de 0,6 cP, 70 cP,[21] 5647 cP,[22] respectivement. Cette propriété physicochimique dépendant de la structure et de la présence d'interactions telles que les interactions électrostatiques, les interactions de Van Der Waals et les ponts hydrogènes. De plus, des structures asymétriques favorisent le désordre et la flexibilité des chaînes aident à détruire ces interactions tout dépendamment de la longueur de la chaîne aliphatique. La densité de la charge a aussi son effet sur la viscosité, car avec une sphère ionique plus grande, la densité de charge est plus petite et les forces électrostatiques sont donc diminuées. L'augmentation de porteurs de charge aide à délocaliser la charge pour obtenir une sphère anionique ou cationique plus grande.

2.3.3. Présence d'eau par titrage coulométrique de Karl-Fisher

La présence d'eau ou le taux d'humidité est incontournable quand il y a manipulation de LIs hygroscopiques et le titrage coulométrique de Karl-Fisher est un outil indispensable pour doser l'eau au niveau de la partie par million (ppm). Un LI qui a été manipulé avec précaution sous atmosphère inerte a normalement 50 à 200 ppm d'eau; un LI qui a été exposé à une atmosphère normalement humide a environ 200 à 1000 ppm d'eau et un LI qui a été utilisé pour l'extraction d'une phase aqueuse a plus de 10 000 ppm d'eau. L'eau considérée comme une impureté a un impact significatif sur les propriétés physicochimiques et électrochimiques et peut être seulement

minimisée par une manipulation adéquate. D'ailleurs, la présence d'eau est aussi problématique pour les électrolytes de BIL par le biais d'utilisation de lithium métallique comme électrode négative.

La réaction mise en jeu dans le titrage Karl-Fisher est donnée par l'**Équation 2.1**. En présence d'eau, le diiode réagit avec le dioxyde de soufre qui résulte de la réaction d'oxydoréduction suivante et par conséquent, il y a consommation de l'eau de l'échantillon.

$$I_2 + SO_2 + 2\,H_2O \rightarrow H_2SO_4 + 2\,HI \qquad \textbf{Équation 2.1}$$

De plus, l'utilisation d'une base est prescrite pour neutraliser les acides formés et cette neutralisation déplace l'équilibre par le principe du Chatelier. Le diiode et le dioxyde de soufre dans les conditions ambiantes sont à l'état solide et à l'état gazeux, respectivement, et la dissolution de ces réactifs est faite dans des solvants polaires tels que le méthanol qui est généralement utilisé. Dans ces conditions bien précises, il y a formation de l'hydrogénosulfite par le biais de la réaction entre le méthanol et le dioxyde de souffre comme montré par l'**Équation 2.2**

$$I_2 + CH_3OSO_2H + H_2O \rightarrow CH_3OSO_3H + 2\,HI \qquad \textbf{Équation 2.2}$$

Contrairement à la première réaction mise en jeu, la stœchiométrie de cette réaction d'oxydoréduction est maintenant qu'une seule molécule d'eau réagit avec le diiode, car l'hydrogénosulfite est oxydé en hydrogénosulfate. Il est possible de réécrire l'équation sous condition basique (**Équation 2.3**). Préalablement, la base utilisée était la pyridine, mais maintenant les bases typiquement utilisées sont l'imidazole et la diéthanolamine.

$$I_2 + CH_3OSO_2{}^-RNH^+ + H_2O \rightarrow CH_3OSO_3{}^-RNH^+ + 2\,I^-RNH^+ \qquad \textbf{Équation 2.3}$$

Ce titrage coulométrique s'appuie sur le couple redox I^-/I_2 pour doser l'eau dans l'échantillon. Dans le montage d'un instrument Karl-Fisher, il s'agit de deux paires d'électrodes dont l'une des paires génère par oxydation le diiode à partir de l'iodure et la seconde paire mesure la différence de potentiel dans le système (**Figure 2.6**). Suite à l'injection de l'échantillon, il y a consommation totale de l'eau au point d'équivalence par le diiode généré. La variation du potentiel permet la mesure du point d'équivalence entre le diiode et l'eau. La détection du point de fin de titrage se fait d'une façon biampérométrique et statique. En présence d'eau et en absence de diiode, le mélange réactionnel correspond à une certaine différence de potentiel et il y a une chute de

potentiel quand le diiode devient présent dans le système pour maintenir un courant constant. Un milligramme d'eau est équivalent à 10,71 coulombs.

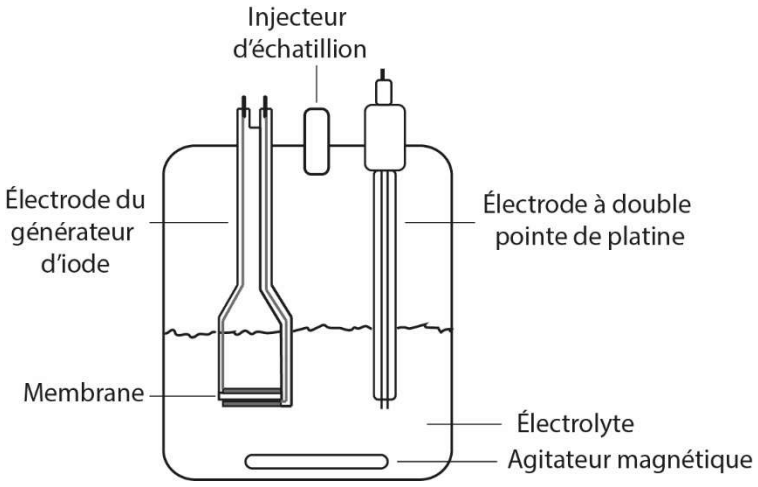

Figure 2.6. Cellule du coulomètre Karl Fisher.

2.3.4. L'autodiffusion par résonance magnétique nucléaire

Généralité de la résonance magnétique nucléaire

La résonance magnétique nucléaire (RMN) est un outil puissant pour les chimistes dans la caractérisation de composés organiques. Cette technique est adéquate pour étudier des nucléides actifs en RMN dont le nombre de spin est non-nul tel que le ^{1}H, ^{7}Li, ^{19}F et ^{13}C pour en nommer quelques-uns. L'abondance isotopique et la constante gyromagnétique ont un impact significatif sur les nucléides étudiables. L'information tirée par RMN résulte de l'absorption des radiofréquences (RFs) par certains nucléides qui sont émises par une source électromagnétique (i.e. domaine des RFs : 4 à 750 MHz). En absence de champ magnétique externe, il y a une dégénérescence pour les différents états de spin nucléaire résultant à une distribution aléatoire de l'orientation des spins. Toutefois, avec l'application d'un champ magnétique externe (B_0), il y a formation de plusieurs niveaux correspondant à l'orientation et à la grandeur du nombre de spin (Effet Zeeman) et les moments magnétiques adoptent une orientation alignée ou opposée au champ magnétique externe appliqué (B_0). La différence d'énergie de ces niveaux est proportionnelle au champ magnétique appliqué et la distribution de population de ces états d'énergie est donnée par l'équation de Boltzmann. Normalement, à la température ambiante, l'état d'énergie où le spin est

aligné avec le champ magnétique est légèrement plus peuplé que l'état d'énergie avec le spin opposé. Pour l'obtention du spectre RMN, il y a une RF émise par impulsion, appelée la fréquence (ω_L) et la précession de Larmor (par définition, une précession est un mouvement de rotation, autour d'un axe parallèle au champ magnétique) provoquant la condition de résonance et selon la règle de Lorentz, l'impulsion bascule le système de spin de 90°. La relation de Larmor est donnée par **l'Équation 2.4** et γ est la constante gyromagnétique.

$$\omega_L = \gamma\, B_0 \qquad \textbf{Équation 2.4}$$

Suivant l'impulsion d'excitation pour retrouver l'état d'équilibre thermodynamiquement favorisé, il existe deux processus de relaxation (**Figure 2.7A**) tels que la relaxation spin-réseau (i.e. temps de relaxation longitudinale, t_1) et la relaxation spin-spin (i.e. temps de relaxation transverse, t_2). Pendant le retour à l'équilibre et étant irradié sur une plage de RFs d'une façon simultanée, la décroissance libre de l'induction correspond à un signal complexe résultant aux différents mécanismes de relaxation des noyaux en résonance qui décroit d'une façon exponentielle. Le signal enregistré utilisant un interférogramme est traduit par la Transformé de Fourier pour distinguer les différents signaux d'induction libre. Le spectre RMN est alors obtenu et l'effet d'écrantage magnétique fait par le diamagnétisme électronique, aussi appelé blindage peut être complètement différent pour des noyaux de même nature se trouvant dans différents environnements chimiques et physiques. Le déplacement chimique (δ) qui tient compte du champ magnétique local et induit par les électrons de liaison est donné par l'**Équation 2.5.** Le produit de référence est souvent le tetraméthylsilane.

$$\delta = \frac{\upsilon_i - \upsilon_{réf}}{\upsilon_{réf}}\, 10^6 \qquad \textbf{Équation 2.5}$$

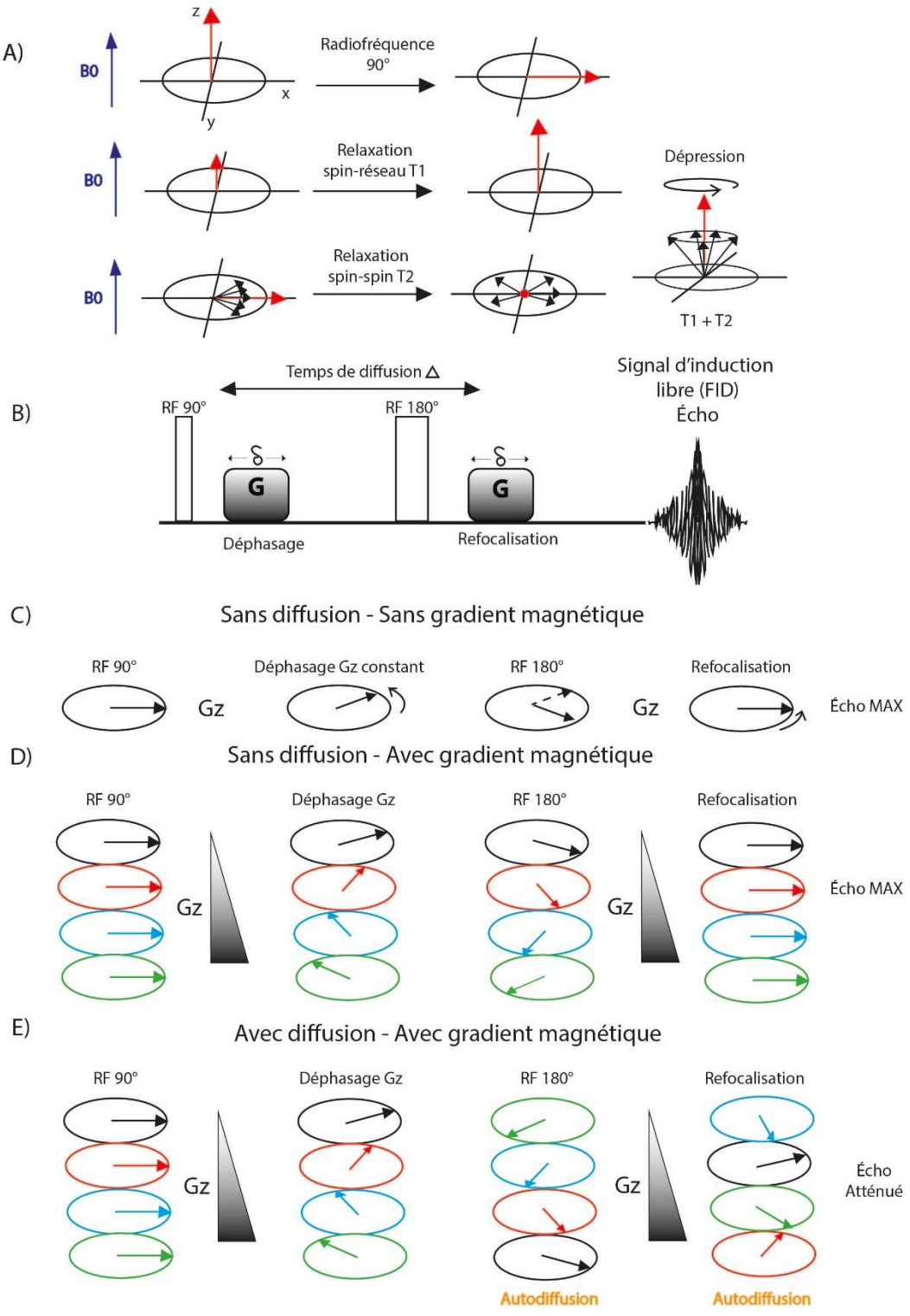

Figure 2.7. A) Processus de relaxation T_1 et T_2 B) Séquence à gradient pulsé. La séquence est appliquée pour un système C) sans diffusion/sans gradient, D) sans diffusion/avec gradient et E) avec diffusion/avec gradient.

La résonance magnétique nucléaire à gradient pulsé

La spectroscopie RMN à gradients pulsés est une méthode utilisée pour mesurer le coefficient d'autodiffusion de différentes molécules marquées d'un noyau actif en RMN. Cette méthode correspond à une méthode directe avec un temps d'acquisition de 10^{-3} à quelques secondes, toutefois il existe aussi une méthode indirecte à partir des temps de relaxation (temps d'analyse : 10^{-9} à 10^{-6} s). Cette technique à gradient pulsé est bien adaptée pour les solutions isotropes telles que les ions et le solvant qui constituent l'électrolyte. La technique consiste à relier le déplacement moyen des spins d'un noyau actif en RMN au coefficient d'autodiffusion de l'espèce diffusionnelle. La position spatiale de l'espèce étudiée est donc localisée et encodée à l'aide d'impulsions de gradients de champ magnétique en fonction du temps. Dans une solution isotrope, l'autodiffusion se définit par le mouvement brownien et aléatoire qui n'est pas soumis à un gradient thermique ou de concentration. Selon la relation de Stokes-Einstein, la diffusion (D) dépend de la viscosité dynamique (η), de la taille solvatée de l'espèce diffusionnelle (Rayon de la sphère de solvatation, r) et de la température (**Équation 2.6**). Dans une solution homogène isotropique, la probabilité de trouver une espèce diffusionnelle au-delà de la position initiale selon le temps est une distribution radiale et gaussienne.

$$D = \frac{k_B T}{6\pi\eta r} \quad \textbf{Équation 2.6}$$

Les toutes premières expériences RMN réalisées par Hahn ont traité un signal RMN en fonction du temps et il a démontré une corrélation entre la diffusion et l'amplitude du signal RMN sous un gradient magnétique.[23] De plus, Stejskal et Tanner ont fait la preuve qui est possible d'utiliser l'atténuation de l'écho pour déterminer l'autodiffusion en connaissant l'amplitude et la durée du gradient. Ils ont développé la séquence d'écho de spin à gradients de champs pulsés (en anglais, Pulse Field Gradient Spin Echo PFG-SE, **Figure 2.7B**) et ici, cette séquence sera nommée la spin-écho.[24]

La RMN à gradients pulsés fait appel à des gradients d'impulsion magnétique linéaire à travers un échantillon afin d'avoir une dépendance entre le champ magnétique effectif ressenti par les noyaux et leur position dans l'échantillon. L'origine d'un champ magnétique non-homogène s'explique par la durée de l'impulsion de l'ordre de la milliseconde. En appliquant une impulsion

magnétique additionnelle (G_z) et parallèle au champ magnétique externe (B_0), l'**Équation 2.6** doit être réécrite de la façon suivante pour déterminer la fréquence de Larmor engendrée par une impulsion magnétique sur le long de l'axe des z (**Équation 7**).

$$\omega_L(z) = \gamma\ (B_0 + \ G_z z) \qquad \textbf{Équation 2.7}$$

Afin d'atteindre les conditions de résonnance du spin, une impulsion d'excitation de 90° est donc utilisée et un gradient de champ pulsé d'une certaine amplitude (G_z) et d'une certaine durée (δ) est alors appliqué pour introduire un déphasage de l'aimantation globale des spins par un processus de relaxation transversale T_2 (i.e. dans le plan xy) (**Figure 2.7B**). Pour une plus grande clarté, le gradient de champ magnétique et le phénomène d'autodiffusion seront traités à tour de rôle.

S'il n'a pas de gradient de champ magnétique, le déphasage se fait de la même façon pour chaque noyau indépendamment sa position (**Figure 2.7C**). Toutefois, l'impulsion de gradient de champ magnétique (**Figure 2.7D** et **E**) provoque un déphasage différent pour les magnétisations des spins qui sont dépendants de leur position dans l'échantillon. C'est précisément le point de départ pour encoder le déplacement des spins qui sera exploité dans cette technique. Ensuite, il y a une RF pour basculer la magnétisation du spin de 180° qui a pour effet de renverser le sens de la précession. Le second gradient de champ pulsé ressenti par les différents noyaux est identique au premier s'il n'a pas eu d'autodiffusion, mais dans le sens inverse pour refocaliser les spins (**Figure 2.7D**). C'est-à-dire que les spins qui ont présenté un fort déphasage seront fortement refocalisés et évidemment, les spins faiblement déphasés seront faiblement refocalisés. Il est possible de constater que l'écho est à son maximum et le gradient de champ magnétique n'atténue pas son signal. Comme les espèces sont fixées, la refocalisation et le déphasage sont équivalents, mais opposés.

Dans le même ordre d'idée pour les systèmes réels où les espèces sont libres d'autodiffuser (**Figure 2.7E**), les périodes de déphasage et refocalisation ne sont pas identiques, car les noyaux n'ont pas ressenti la même impulsion magnétique lors de ces périodes par le biais de l'autodiffusion entre ces deux périodes durant le temps de diffusion (Δ). Par conséquent, la refocalisation est donc incomplète et l'atténuation du signal écho est fonction du coefficient d'autodiffusion qui décode le déplacement fait préalablement encoder. En d'autres mots, s'il y a une forte atténuation du signal

spin-écho, ce phénomène correspond à une diffusion rapide. Le coefficient d'autodiffusion peut être calculé par l'équation de Stejskal-Tanner nommé en tant qu'**Équation 2.8** et la mobilité obtenue est une valeur moyenne.

$$Ln(S/S_0) = -\gamma^2 g^2 D_s \delta^2 (\Delta - \delta/3) \qquad \textbf{Équation 2.8}$$

Où S est l'intensité du signal spin-écho, δ est la durée de l'impulsion du champ magnétique avec une amplitude g, γ est constante gyromagnétique et Δ est le temps de diffusion.

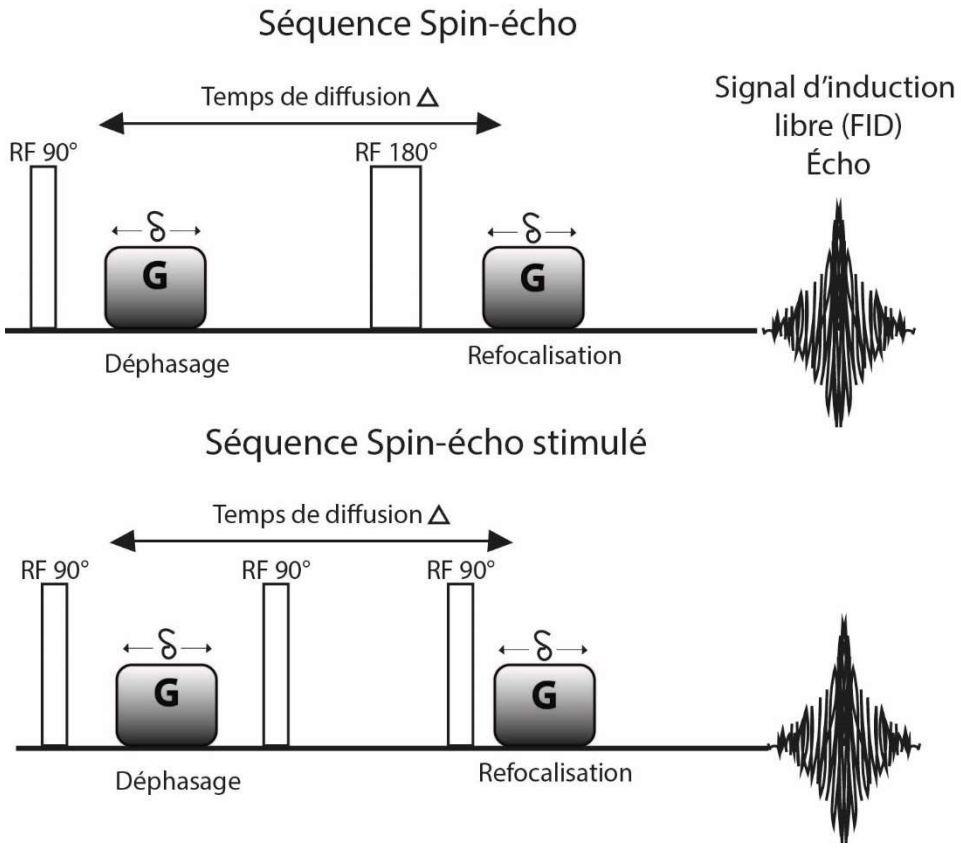

Figure 2.8. Séquences spin-écho versus spin-écho stimulé.

Toutefois, il existe une multitude de séquence pour magnétiser le spin du noyau à sa guise et la séquence simple et classique de spin-écho ne convient pas parfaitement aux LIs causant des erreurs d'environ de 20 % qui est sûrement expliqué par la haute viscosité des LIs.[25] Pour nos électrolytes, le choix de la séquence de spin-écho stimulé a été fait, car elle utilise des temps d'analyse relativement plus longs en termes d'échelle de temps pour la mesure de coefficients d'autodiffusion lents. Dans la séquence de spin-écho stimulé, au lieu d'avoir une seconde RF de

180° comme dans la spin-écho, elle utilise une deuxième et une troisième RF de 90° qui sont séparés par un temps donné (**Figure 2.8**) et suite à la deuxième RF, il s'agit de l'état d'entreposage de spin à l'opposé du champ magnétique externe qui aura comme effet de diminuer la relaxation transversale (T_2). C'est-à-dire, l'impact direct est que l'atténuation dépendant de la relaxation longitudinale (T_1) au lieu de T_2 pour cette séquence, car il y a la possibilité d'utiliser des temps de diffusion plus grands. Cette séquence doit être utilisée quand $T_1 >> T_2$, car la moitié de l'intensité est perdue avec l'utilisation de cette méthode. La spectroscopie RMN 2D est aussi utile avec cette technique qui est communément appelée DOSY (en anglais, diffusion ordered spectroscopy), car c'est un outil puissant qui relie le déplacement chimique avec le coefficient d'autodiffusion pour les solutions isotropiques contenant multi-espèces diffusionnelles.

Utilisation de la résonnance magnétique nucléaire pour les électrolytes

Le transport de masse des ions est essentiel pour développer des électrolytes possédant une haute conductivité ionique. De plus, la puissance de la BIL est un facteur considérable pour lequel les propriétés de l'électrolyte jouent un rôle clé. Alors que le nombre de transport de l'ion de lithium doit être aussi élevé (plus proche de l'unité) que possible, il se trouve généralement plus près de 0,4 à 0,5 dans les électrolytes communs (sel de lithium dans un solvant de carbonate) et même en dessous de 0,1 dans les LIs. Les nombres de transport d'ions (t_i) sont obtenus à partir des coefficients d'autodiffusion (spin-écho) de tous les ions présents dans l'électrolyte, conformément à l'équation suivante (**Équation 2.9**).

$$t_i = \frac{x_i D_i}{\sum_i x_i D_i} \qquad \textbf{Équation 2.9}$$

où x_i et D_i sont la fraction molaire et le coefficient d'autodiffusion des ions contenus dans l'électrolyte, respectivement. Dans le même ordre d'idée, la conductivité ionique de l'électrolyte issue de la RMN dépend des coefficients d'autodiffusion et elle est donnée par la relation de Nernst-Einstein (**Équation 2.10**), comme suit,

$$\sigma_{RMN} = \frac{N_A e^2}{kT} \sum_i c_i D_i \qquad \textbf{Équation 2.10}$$

où σ_{RMN} est la conductivité ionique donnée par RMN, e est la charge élémentaire, k est la constante de Boltzmann, T est la température absolue, N_A est le nombre d'Avogadro, c est la concentration d'ions et D est le coefficient d'autodiffusion mesuré par spin-écho. Il est important de savoir que cette technique ne différentie aucunement les ions pairés et les agrégats contrairement à la conductivité ionique obtenue par la spectroscopie impédance à courant alternatif. Il est aussi possible de suivre les molécules de solvants contenus dans l'électrolyte qui peut être très intéressant dans des mélanges de solvants.

2.4. Analyses électrochimiques

2.4.1. Spectroscopie d'impédance et conductivité ionique

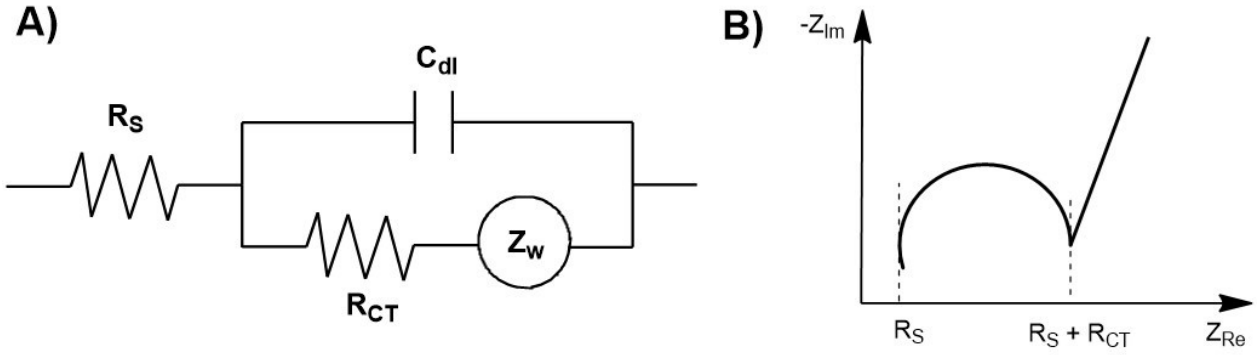

Figure 2.9. A) Circuit équivalent de Randle et B) diagramme de Nyquist typique.

Généralement, la prise de mesures de la conductivité ionique est faite à l'aide d'une cellule thermostatée munie de deux électrodes de platine qui sont à une certaine distance et avec une certaine surface. Il est intéressant que cette cellule soit d'un volume en dessous d'un millilitre afin d'observer une homogénéité de la température. Le principe de la conductimétrie est de mesurer la résistance du système, ici Pt|électrolyte|Pt, afin d'obtenir la conductance. Pour obtenir la conductivité ionique, il s'agit de préalablement mesurer la constante de la cellule qui dépend de la surface et de la distance des électrodes en utilisant une solution standard dont la conductivité est connue à une température donnée. Ensuite, avec cette constante de la cellule et la résistance du système, il est un jeu d'enfant de calculer la conductivité ionique ($\sigma = k/R$).

La spectroscopie d'impédance est une méthode largement utilisée pour mesurer la conductivité ionique par l'entremise de la résistance de la solution et pour la caractérisation de

plusieurs paramètres électrochimiques. Grâce à la modélisation du circuit électrique équivalent au système électrochimique étudié (Le circuit de Randle, **Figure 2.9A**), il est possible de déterminer les résistances, les capacitances et certains processus cinétiques. Donc, l'impédance est l'application d'une perturbation de tension alternative faible et localisée qui résulte ainsi à un courant alternatif d'où vient le nom de la méthode (Impédance à courant alternatif). Il est préférable que l'oscillation de surtension soit de faible intensité pour conserver un régime linéaire pour la relation courant-tension qui facilite la compréhension des résultats et de plus, la loi d'Ohm est toujours valide en impédance. Les choix des fréquences de perturbation, l'amplitude des fréquences et du potentiel appliqué ont une importance capitale dépendamment de la caractérisation voulue.

Lors de l'acquisition des données à différentes fréquences, il est possible de tracer la partie imaginaire ($-Z_{Im}$) selon la partie réelle (Z_{Re}) donnant le diagramme de Nyquist (**Figure 2.9B**). Pour simplifier les explications et omettre les mathématiques derrière l'impédance, les résistances du système sont indépendantes de la fréquence de perturbation, car les résistances n'apportent pas de déphasage entre la tension et le courant alternatifs. Par conséquent, la résistance est une grandeur réelle, contrairement à la capacitance qui a une contribution imaginaire via son déphasage. L'introduction des nombres complexes n'est qu'un moyen pratique pour le traitement de composantes vectorielles, tous deux ont une existence physique et mesurable. Il y a une multitude de circuits équivalents et le plus fréquent est celui de Randle pour un système électrochimique qui prend en considération la résistance de la solution (R_S), la capacitance de double-couche (C_{dl}), la résistance au transfert de charge (R_{CT}) et l'élément de Warburg (Z_w) attribué à la diffusion. La portion du demi-cercle (observé à plus haute fréquence) correspond à la limitation du transfert électronique et tandis que la droite pseudo-linéaire représente la limitation du transport de masse (observé à plus basse fréquence). Les électrodes de platine de la cellule de conductivité sont d'excellents catalyseurs de réactions électrochimiques et l'utilisation d'un métal noble comme le platine est nécessaire pour éviter les réactions parasites telles que l'oxydation du métal et la dissolution de celui-ci qui affectera considérablement les données recueillies. Par conséquent, la résistance au transfert de charge est donc diminuée et la résistance de la solution est mesurable en utilisant l'abscisse à l'origine du diagramme de Nyquist en extrapolant. Avec cette résistance, il est donc possible d'obtenir la conductivité ionique comme mentionnée préalablement.

2.4.2. Méthodes voltampérométriques et ampérométriques

Réaction électrochimique via un processus faradique

Avant de discuter des méthodes voltampérométriques et ampérométriques, il est primordial de définir quelques concepts en électrochimie. Les notions d'oxydant et de réducteur lors d'une réaction d'oxydoréduction sont définies à un échange d'électron(s) entre un accepteur et un donneur. Par définition, il est appelé oxydant l'accepteur d'électron, et réducteur le donneur d'électron. Par conséquent, l'oxydation est une perte d'électron subie par le réducteur, alors que la réduction est un gain d'électron subi par l'oxydant tout en conservant l'électronégativité. Toutefois, une réaction électrochimique se produit à l'interface d'une électrode polarisée qui peut être classée comme étant une réaction hétérogène (Électrolyte|Électrode) tandis que la réaction d'oxydoréduction est une réaction homogène (i.e. oxydant et réducteur en solution). Cette réaction électrochimique, aussi appelée électrolyse, est un processus faradique, car il y a échange d'électron(s) entre l'analyte en solution et l'électrode. L'électrode joue le rôle de catalyseur des réactions électrochimiques qui dépend du potentiel appliqué. Les processus faradiques sont gouvernés par la loi de Faraday, d'où vient le nom, et ces processus peuvent se produire s'ils sont favorables thermodynamiquement et cinétiquement parlant. Dans un système électrochimique, il y a plusieurs facteurs qui peuvent affecter le courant engendré et la vitesse de réaction comme le transport de masse, le transfert électronique, des réactions homogènes à proximité de l'interface (e.g. protonation ou dimérisation) ou des réactions hétérogènes à l'interface (adsorption, désorption, électrodéposition et décomposition catalytique)(Voir, **Figure 2.10**). Toutefois, il existe aussi des processus non-faradiques, aussi appelés capacitifs, qui sont dus au balancement des interfaces électrode|électrolyte (i.e. condensateur) par l'adsorption et la désorption des ions en solution. En s'appuyant sur le modèle de Helmholtz et sur les modèles plus récents, ce balancement crée une double couche électrique. L'électrolyte de support est essentiel pour assurer le flux de courant dans la solution. Il est important de clarifier que ces charges ne sont pas injectées dans le matériau d'électrode, contrairement à la réaction faradique. Le courant non-faradique dépend de la composition de l'électrolyte, de l'aire de l'électrode (porosité) et du potentiel appliqué.

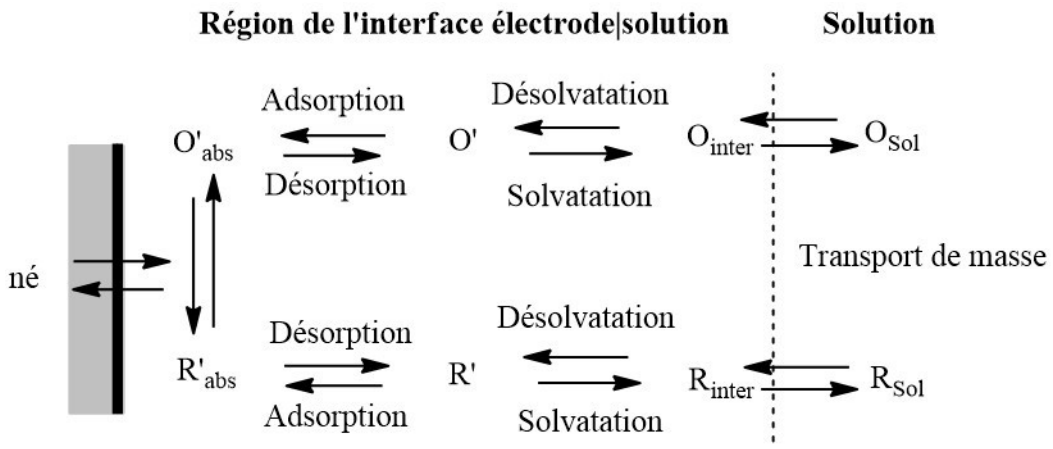

Figure 2.10. Route typique pour une espèce électroactive lors d'une réaction électrochimique. Illustration reproduite de la Ref.[26].

Réaction électrochimique contrôlée par transport de masse

Le transport de masse se produit par trois différents phénomènes physiques pendant une réaction électrochimique. La migration est un mouvement spontané de particule chargée négative ou positive pour équilibrer les charges en solution ou à l'interface de la solution sous l'influence du champ électrique. L'électromigration de l'espèce électroactive peut être supprimée en ajoutant une grande concentration de sel inerte d'environ cent fois plus concentrée que l'analyte. La convection est un mouvement mécanique de la solution au niveau macromoléculaire. La force motrice de celle-ci est l'agitation de la solution utilisant un barreau aimanté, une électrode tournante et/ou des vibrations qui perturbent la solution. Il existe aussi une convection naturelle qui est un mouvement normal à 25°C, par exemple. La diffusion est un mouvement spontané sous l'influence d'un gradient de concentration de l'espèce chimique diffusionnelle pour maintenir une concentration uniforme en respectant le deuxième principe de la thermodynamique. Ici, il est présenté les deux équations de Fick dont le flux des espèces en fonction du gradient de la concentration (1ère loi de Fick; **Équation 2.11**) et la variation de la concentration avec le temps pour un système à une dimension (2e loi de Fick; **Équation 2.12**.

$$J = -D\frac{\partial C}{\partial x} \qquad \textbf{Équation 2.11}$$

$$\frac{\partial C}{\partial t} = -D\frac{\partial^2 C}{\partial x^2} \qquad \textbf{Équation 2.12}$$

Ces trois phénomènes sont modélisés par une équation différentielle de Nernst-Planck qui dépend du temps (t) et de la position (x), qui donne le flux des espèces (J) selon les processus de transport présent dans le système à l'étude.

$$J(x,t) = -D\frac{\delta C(x,t)}{\delta x} - \frac{zFDC}{RT}\cdot\frac{\partial\phi(x,t)}{\delta x} + C(x,t)V(x,t) \quad \textbf{Équation 2.13}$$

Où C est la concentration de l'espèce électroactive, R est la constante universelle des gaz, T la température, z la valence de l'espèce ionique, F la constante de Faraday, D est le coefficient de diffusion et V est attribué à la convection. En absence de migration et de convection, les équations de Fick décrivent adéquatement les expériences en électroanalyse et ils sont les points de départ de plusieurs équations en électrochimie.

Expérience électrochimique utilisant une variation de potentiel

L'objectif principal des expériences contrôlant le potentiel appliqué est d'obtenir une réponse par l'entremise du courant généré correspond à l'espèce électroactive à l'interface électrode|solution. Comme mentionné auparavant, en modifiant le potentiel, des réactions faradiques seront favorisées et catalysées à des potentiels bien précis. Pour des systèmes dictés par la thermodynamique, le potentiel des électrodes peut être intimement corrélé avec la concentration des espèces électroactives avec l'équation bien connue de Nernst (**Équation 2.14**). Les potentiels standards, E° sont tabulés dans plusieurs ouvrages de référence.

$$E' = E° + \frac{2{,}3R}{nF}\log\frac{C_{Ox}}{C_{Red}} \qquad \textbf{Équation 2.14}$$

Où E' est le potentiel d'équilibre, E° est le potentiel standart, C est la concentration de l'espèce oxydante ou réducteur, R est la constante universelle des gaz, T la température, n le nombre d'électron(s) échangé(s) et F la constante de Faraday. Comme illustrée sur la **Figure 2.11**, les processus d'oxydation et de réduction d'une espèce électroactive peuvent être décrits en comparant les niveaux d'énergie des orbitales moléculaires (OM) occupées ou vacantes avec le

niveau d'énergie de l'électrode (i.e. potentiel). Dans une réaction d'oxydation, l'électrode se polarise de plus en plus positivement permettant à l'électron de l'analyte dont l'électron est le plus susceptible d'être donné et injecté dans le matériau d'électrode. C'est-à-dire, la force motrice est que les électrons soient au plus bas niveau d'énergie. Pour une réduction et avec le même raisonnement, l'électrode est polarisée négativement qui permet l'ajout d'un électron dans une OM vacante de l'espèce électroactive.

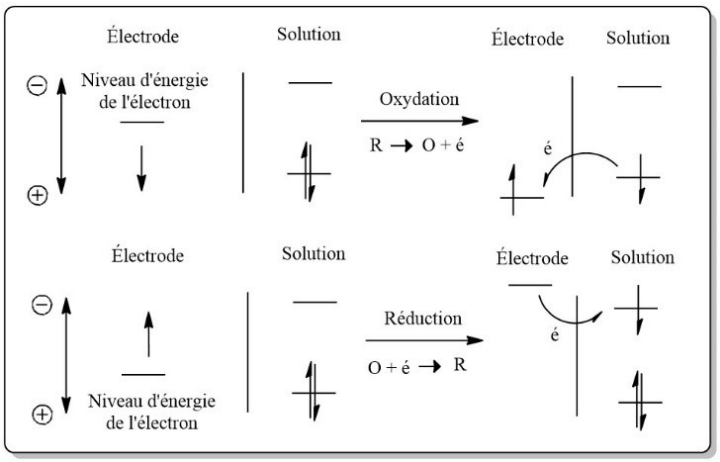

Figure 2.11. Illustration de l'oxydation et de la réduction des espèces électroactives.

L'équation de Butler-Volmer (dérivée de l'équation d'Arrhenius adapté au transfert électronique, **Équation 2.15**) décrit la relation entre le courant et le potentiel appliqué pour les réactions qui sont contrôlées par le transfert de charge. C'est-à-dire, une réaction électrochimique qui utilise des conditions expérimentales où le potentiel appliqué est au voisinage du potentiel d'équilibre de l'espèce électroactive. Ces conditions ont comme impact que les courants anodique et cathodique co-existent et le courant net est la sommation de ces courants. Avec une grande surtension anodique ou cathodique (E-E',η) selon le potentiel d'équilibre, un des deux courants est dominant et l'autre est négligeable. Dans cette situation, le transfert de charge n'est pas limitant et c'est plutôt le transport de masse qui est le facteur limitant comme discuté dans la section précédente. Bien sûr, le courant mesuré dépend de la constante de vitesse hétérogène (k°), mais aussi du coefficient de transfert (α) qui indique que l'accélération et la décélération du courant anodique et cathodique peuvent être asymétriques. Si les espèces oxydée et réduite sont aussi stables l'une comme l'autre, le coefficient de transfert est égal à 0,5. En utilisant les courbes de

Tafel, il est possible d'extrapoler dans le but d'obtenir le courant d'échange (i_0) qui correspond à la situation où E=E' et $i_{net} = i_c + i_a = 0$.

$$i = nFAk^{\circ}\left[C_{ox}(0,t)\exp\left(\frac{-\alpha nF(E-E')}{RT}\right) - C_{Red}(0,t)\exp\left(\frac{(1-\alpha)nF(E-E')}{RT}\right)\right] \quad \textbf{Équation 2.15}$$

$$i = i_0\left[\exp\left(\frac{-\alpha nF}{RT}\right) - \exp\left(\frac{(1-\alpha)nF\eta}{RT}\right)\right] \quad \textbf{Équation 2.16}$$

Voltampérométrie cyclique et voltampérométrie hydrodynamique

À l'inverse de la potentiométrie qui se fait sans électrolyse, plusieurs types de voltammétrie utilisent un balayage de potentiel à l'aide d'un potentiostat pour produire des réactions non-spontanée aux électrodes. La plus populaire de toutes est la voltampérométrie cyclique (VC) qui utilise une rampe de balayage linéaire dans un sens et ensuite, dans le sens contraire (i.e. rampe de forme triangulaire, **Figure 2.12A**). L'électrolyte contenant l'espèce électroactive est placé dans une cellule électrochimique (e.g. cellule en cœur favorisant la proximité des électrodes, **Figure 2.13A**) et trois électrodes sont ajoutées dont l'électrode de travail, l'électrode auxiliaire et l'électrode de référence. Le rôle de l'électrode de travail est de catalyser les réactions électrochimiques et les matériaux communs et inertes de cette électrode sont le carbone vitreux, l'or, l'argent et le platine dont la forme peut être un disque, un pique ou un cylindre. L'électrode auxiliaire, un fil en spiral ou un grillage, ferme le circuit électrique et afin d'éviter des réactions parasites, la surface de cette électrode est largement supérieure à celle de l'électrode de travail. L'électrode de référence a un potentiel constant lors de l'expérimentation. Il existe deux types d'électrode de référence telle que 1) une référence considérée comme constant (e.g. l'électrode de calomel saturée, la Ag/AgCl) ou 2) une pseudo référence (e.g. le fil d'argent ou de platine) et la différence de potentiel est appliquée entre l'électrode de travail et l'électrode de référence (**Figure 2.13B**). Il est important de noter que le potentiel de l'électrode de référence dépend de l'équilibre entre le métal solide et l'ion métallique constituant de la référence, mais aussi, des autres cations présentent dans l'électrolyte. Dans certaines situations, il est nécessaire de calibrer le potentiel appliqué avec une référence interne tel que le ferrocène recommandé par l'IUPAC, mais il est important que la référence interne soit dans un système électrochimique équivalent. L'avantage du système électrochimique à trois électrodes est que le potentiel appliqué est indépendant du courant

mesuré. Dans les systèmes électrochimiques dont la résistivité de la solution est significative, la distance entre l'électrode de travail et l'électrode de référence doit être minimisée pour améliorer la qualité des résultats. Les choix des électrodes, de l'électrolyte de support et du solvant sont uniques à l'expérimentation voulue, toutefois, il faut considérer la plage électrochimique de ceux-ci et surtout, du potentiel de l'espèce électroactive pour bien cadrer la plage de potentiel nécessaire. De plus, il est incontournable de faire barboter la solution électrolytique avec un gaz inerte tel que l'azote ou l'argon pour purger le système de toutes traces d'oxygène dissous, car celle-ci est électroactive et le courant faradique attribué à l'oxygène est donc mesurable. La qualité des VCs dépend grandement de la qualité du polissage de l'électrode de travail préalablement fait à l'aide d'alumine. La détermination de l'aire effective de l'électrode de travail se fait à l'aide d'une espèce électroactive dont le coefficient de diffusion est bien connu (e.g. Ferricyanure ou Ferrocène), car l'aire effective est plus grande que l'aire géométrique via la rugosité de celle-ci.

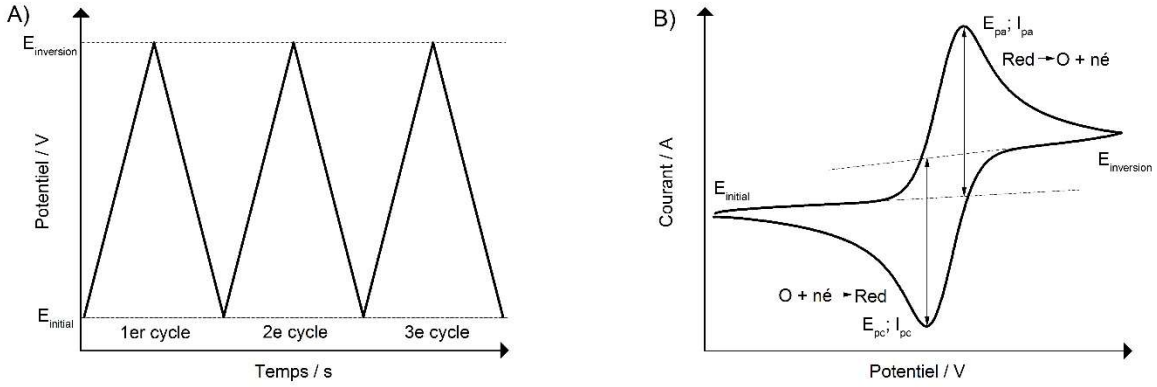

Figure 2.12. A) Rampe de balayage linéaire pour la voltampérométrie cyclique et B) un voltampérogramme cyclique typique pour une espèce électroactive réversible.

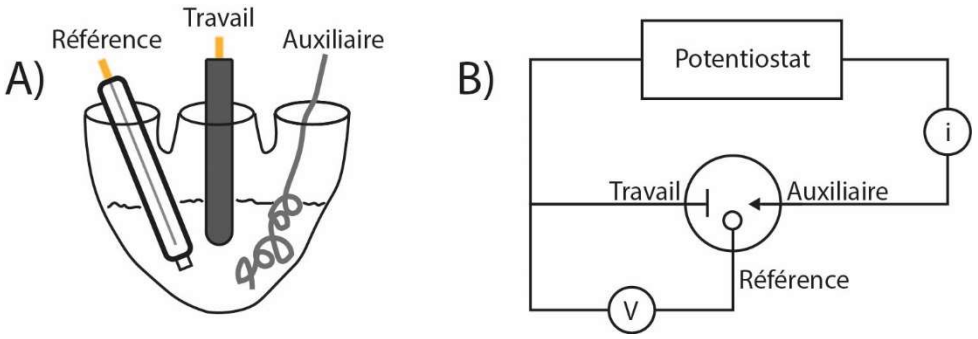

Figure 2.13. A) Montage expérimental d'une cellule à trois électrodes en voltampérométrie cyclique et B) branchement d'une cellule à trois électrodes avec un potentiostat.

La **Figure 2.12B** montre une allure typique d'une réaction électrochimique réversible où l'espèce électroactive est en solution et échange un électron à l'interface de l'électrode. Une construction géométrique est aussi faite pour minimiser le courant capacitif dans le traitement de mesure. Les données brutes exploitables sont le courant au pic (I_p) pour le courant anodique et cathodique. De plus, il y a aussi le potentiel au pic (E_p) pour le potentiel anodique et cathodique qu'il est aussi possible de noter. Le courant au pic dépend du coefficient de diffusion (D), de la concentration (C) et du nombre d'électron(s) échangé(s) (n) de l'espèce électroactive, de l'aire effective de l'électrode (A) et de la vitesse de balayage (υ). Pour un système réversible, l'équation de Randles-Sevcik est utilisée pour calculer une de ces variables lorsque les autres sont connues (**Équation 2.17**).

$$I_p = 0.4463nFAC\left(\frac{nF}{RT}\right)^{1/2} v^{1/2}D^{1/2} \quad \textbf{Équation 2.17}$$

Évidemment pour vérifier la réversibilité du système, un des critères est que la concentration et la racine carrée de la vitesse de balayage soient directement proportionnelles avec le courant au pic. De plus, le ratio entre les courants au pic anodique et cathodique doit être le plus près de l'unité que possible. Pour la position des potentiels au pic, il est possible de calculer le potentiel d'équilibre avec ceux-ci. Donc, le potentiel d'équilibre se calcule en effectuant une moyenne des potentiels au pic utilisant l'équation suivante (**Équation 2.18**).

$$E' = \frac{E_{p,a}+E_{p,c}}{2} \quad \textbf{Équation 2.18}$$

La séparation entre les potentiels au pic (ΔE_p) donne de l'information au sujet du nombre d'électron(s) échangé(s) et de la réversibilité du système. Cette égalité de l'**équation 2.19** est seulement vraie pour un système réversible (0,059 V par électron échangé).

$$\Delta E_p = E_{p,a} - E_{p,c} = \frac{0{,}059\,V}{n} \quad \textbf{Équation 2.19}$$

Dans un système réversible, le ΔE_p ne varie pas en fonction de la vitesse de balayage. Le ΔE_p peut être légèrement plus élevé en comparant avec la théorie où la résistance de la solution n'est pas compensée. La méthode de Nicholson est couramment utilisée pour estimer la constante de vitesse de transfert d'électrons hétérogène à l'aide de l'**Équation 2.20** qui varie selon le paramètre cinétique Ψ (Équation empirique entre Ψ en fonction de ΔE_p) et le coefficient de transfert α. Il est important pour cette méthode de compenser la résistance de la solution.

$$k_0 = \Psi \left(\frac{D_R}{D_O}\right)^{\frac{\alpha}{2}} \left(\frac{\pi F D_O \upsilon}{RT}\right)^{\frac{1}{2}} \quad \textbf{Équation 2.20}$$

Où C est la concentration de l'espèce oxydante ou réductrice, R est la constante universelle des gaz, T la température, n le nombre d'électron(s) échangé(s), F la constante de Faraday et D le coefficient de diffusion et υ est la vitesse de balayage. Pour finir, à des potentiels au-delà du potentiel au pic, le courant décroit inversement proportionnel avec la racine carrée du temps. En d'autres mots, l'équation de Cottrell est vérifiable pour une espèce électroactive réversible et non-adsorbée (Plus de détails dans la section de la chronoampérométrie, **Équation 2.21**).

$$I(t) = \frac{nFAD^{1/2}C}{(\pi t)^{1/2}} \quad \textbf{Équation 2.21}$$

De plus, cette équation montre aussi la grandeur de la couche de diffusion (Définition de couche de diffusion : la région voisinant une électrode où la concentration de l'espèce électroactive est différente de la concentration en solution) qui augmente avec le temps ($\delta(x,t) = (2Dt)^{1/2}$, une dimension). En résumé, l'interface électrode|solution est composée d'une double couche électrique et d'une couche de diffusion lorsque le potentiel appliqué produit une réaction électrochimique. Par conséquent, il est facile d'observer sur un voltampérogramme une décroissance de courant au-

delà du potentiel au pic et malgré un potentiel adéquat pour engendrer la réaction électrochimique (favorable thermodynamiquement), cette réaction est limitée par la diffusion (restriction cinétique).

Plusieurs facteurs peuvent expliquer l'irréversibilité d'un système électrochimique tel que l'instabilité de l'espèce électroactive produite par le biais d'une décomposition, d'une isomérisation, d'une dimérisation et d'une réaction avec un réactif présent dans l'électrolyte (Mécanisme EC, réaction électrochimique suivi d'une réaction chimique irréversible ou réversible). D'ailleurs, le mécanisme EC peut présenter un voltampérogramme cyclique irréversible ou quasi-réversible dépendamment de la constante de vitesse de la réaction chimique subséquente. Donc, la vitesse de balayage a un impact significatif sur l'allure du voltampérogramme cyclique et le rapport $I_{p,a}/I_{p,c}$ différencie un système irréversible et quasiréversible (i.e. un système irréversible ne présente pas de pic de retour). De plus, l'électrodéposition présente un profil quasi-réversible malgré le transfert d'électron réversible, car les constantes de vitesse pour l'électrodéposition et la redissolution ne sont pas dans le même ordre de grandeur. Pour un système réversible où l'espèce électroactive est adsorbée sur la surface de l'électrode, l'équation de Nernst prévoit un ΔE_p égal à zéro pour un système idéal où le transfert électronique est ultrarapide et aucune diffusion de l'espèce électroactive n'est nécessaire. L'équation de Randles-Sevcik (**Équation 2.17)** n'est pas valide dans cette situation bien précise, car l'espèce électroactive n'est pas en solution. Pour ce système avec une espèce électroactive adsorbée, le courant au pic est directement proportionnel à la vitesse de balayage et au taux de recouvrement de la surface (Γ_s) donné par l'**Équation 2.22**.

$$I_p = \frac{n^2 F^2 A \Gamma_s}{4RT} \mathrm{V} \qquad \textbf{Équation 2.22}$$

Comme la diffusion est lente et limitante, l'apport d'espèces électroactives à la surface de l'électrode peut être augmenté en mode hydrodynamique utilisant une électrode tournante (e.g. 500 à 5000 rotations par minute). La voltampérométrie à électrode rotative permet d'obtenir un flux d'analytes suffisamment important pour réussir à mesurer de petites concentrations et d'analyser des espèces électroactives dont le coefficient de diffusion est lent. Malgré la convection faite par l'électrode tournante, à proximité de l'électrode, il existe une couche de diffusion de Nernst où le transport de masse se fait seulement par la diffusion. La rampe de balayage de cette voltampérométrie est une rampe linéaire sans retour contrairement en VC et l'allure de la courbe

est sigmoïdale utilisant des vitesses de rotation angulaires de l'électrode pour avoir un transport de masse non-limitant (**Figure 2.14**).

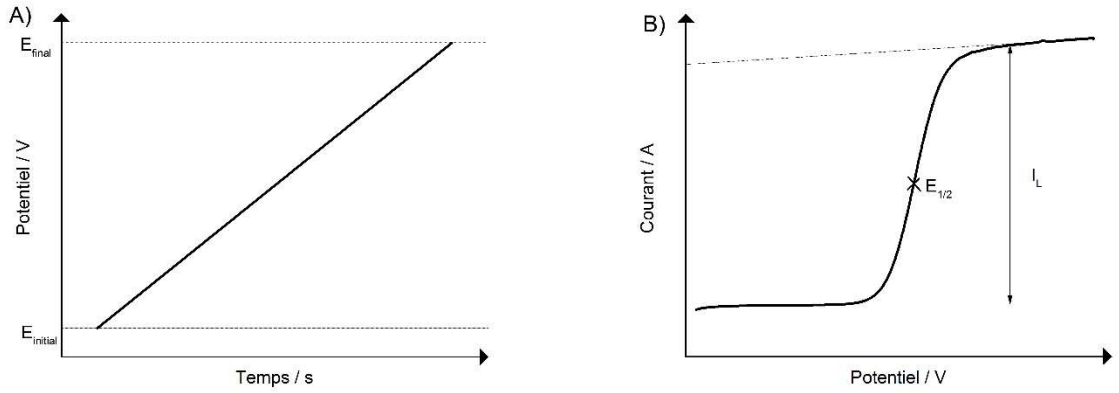

Figure 2.14. A) Rampe de balayage linéaire pour la voltampérométrie à électrode rotative et B) un voltampérogramme à électrode rotative typique pour une espèce électroactive réversible.

Comme présenté sur la **Figure 2.14B**, l'état stationnaire du courant correspond au courant limite et le point d'inflexion de la courbe indique le potentiel de demi-vague ($E_{1/2}$). Évidemment, l'équation de Randles-Sevcik ne s'applique pas en voltampérométrie à électrode rotative. L'équation de Levich stipule que le courant limite dépend de l'aire de l'électrode (A), du coefficient de diffusion (D), de la concentration (C), de la viscosité cinématique de l'électrolyte (υ) et de la vitesse de rotation angulaire (ω) (**Équation 2.23**). La couche de diffusion (δ) est donnée par l'**Équation 2.24** et elle varie en fonction de l'inverse de la racine carrée de la vitesse de rotation angulaire. Par conséquent, la couche de diffusion diminuera s'il y a augmentation de la vitesse de rotation angulaire.

$$I_L = 0.620nFACD^{\frac{2}{3}}\omega^{\frac{1}{2}}v^{\frac{-1}{6}} \qquad \textbf{Équation 2.23}$$

$$\delta = 1{,}61D^{\frac{1}{3}}\omega^{-\frac{1}{2}}v^{\frac{1}{6}} \qquad \textbf{Équation 2.24}$$

Chronoampérométrie et microélectrode

Dans les expériences électrochimiques, il est possible de faire varier et de mesurer ces trois paramètres, dont le potentiel, le courant, et le temps qui sont intimement liés. La réponse du système dépend de ces paramètres pour la plupart des techniques électrochimiques. Par exemple, la voltampérométrie cyclique est une courbe courant-potentiel, mais l'impact du temps se fait sentir au niveau du choix de la vitesse de balayage (Rappel : 1 A = 1 C s^{-1}). Contrairement à la voltampérométrie cyclique, la chronoampérométrie (CA) utilise des potentiels constants et en définition, il s'agit de la réponse du courant à ce potentiel en fonction du temps. Le transport de masse se fait uniquement par diffusion et la courbe courant-temps reflète le gradient de concentration formé. Donc, la couche de diffusion s'élargit graduellement avec le temps qui a comme conséquence directe d'épuiser l'espèce électroactive à l'interface solution|électrode. Ce phénomène explique la décroissance de courant et pour une macroélectrode planaire, l'équation de Cottrell relie le courant selon le temps pour une espèce électroactive réversible et diffusionnelle (**Équation 2.21**). La technique chronoampérométrique la plus utilisée est la CA à double sauts de potentiel qui est montré à la **Figure 2.15A**. Cette technique consiste à utiliser un potentiel où aucune réaction électrochimique n'est engendrée pour équilibrer le système et ensuite, il s'agit d'appliquer deux sauts de potentiel successifs pour produire une réaction faradique dont le deuxième saut de potentiel est la réaction de retour. Le choix de potentiel est très important et le potentiel ne doit pas être un facteur limitant en utilisant un potentiel largement supérieur au potentiel d'équilibre (e.g. au-delà du $E_{p,a}$ pour une oxydation). La **Figure 2.15B** montre une courbe typique pour cette méthode et les données exploitables dictées par la diffusion sont les valeurs correspondant à au-delà de 0,2 s, car dans le régime de courte durée de temps, l'impact du courant capacitif est significatif. De plus, le courant capacitif décroit beaucoup rapidement et la relation suivante décrit la décroissance du courant capacitif en fonction du temps (**Équation 2.25**). À des régimes de temps de longue durée (100 s), il est possible de constater des déviations correspondant à la convection naturelle.

$$I_{dl}(t) = \frac{\Delta E}{R_s}\exp\left(\frac{-t}{R_s C_{dl}}\right) \qquad \textbf{Équation 2.25}$$

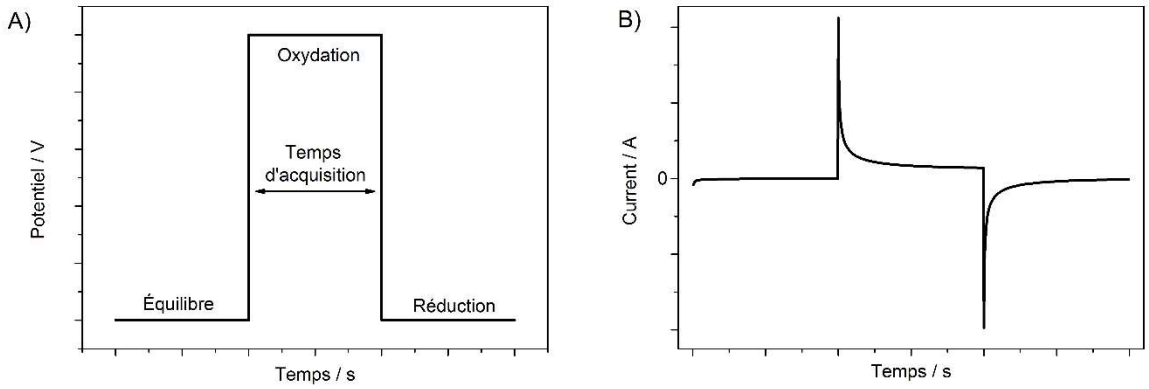

Figure 2.15. A) Programmation d'une expérience de chronoampérométrie lors d'une oxydation suivie d'une réduction utilisant préalablement un temps d'équilibre. Le potentiel appliqué est constant. B) Courbe ampérométrique pour une espèce électroactive réversible et diffusionnelle.

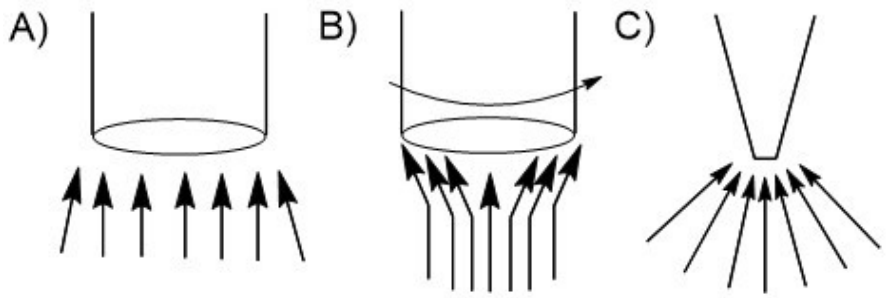

Figure 2.16. Illustration du transport de masse A) pour une macroélectrode via une diffusion planaire, B) pour une macroélectrode via une convection et C) pour une microélectrode via une diffusion radiale.

Les techniques électrochimiques discutées jusqu'à présent utilisent une diffusion qui se fait d'une façon planaire à une macroélectrode (**Figure 2.16A**). Il a été aussi question dans la section précédente que le flux d'espèce électroactive puisse être augmenté en créant un vortex lors de la rotation d'une électrode (**Figure 2.16B)**. Le transport de masse des espèces électroactive peut être augmenté par l'utilisation de microélectrodes dont le microdisque est de l'ordre de 0,1 à 100 μm, car le champ diffusionnel est planaire et surtout, radial (**Figure 2.16C**). Par conséquent, les avantages d'utiliser des microélectrodes sont que les densités de courant sont plus élevées que les macroélectrodes via le flux plus élevé d'espèce électroactive (i (densité de courant) = I/A) et aussi, la chute ohmique due à la résistance de la solution est atténuée par la mesure de courant de plus

faible intensité (Rappel : Loi d'ohm E=RI). La résistance non-compensée (R_{nc}) occasionne une distorsion de la réponse en voltampérométrie et cette résistance est inversement proportionnelle au rayon de l'électrode et la conductivité ionique ($R_{nc} = (4\sigma r)^{-1}$). Pour une microélectrode, la chute de iR_{nc} est de 0,09 mV au lieu de 5 à 10 mV pour une macroélectrode utilisant une solution de ferrocène dissous dans l'acétonitrile.[27] Sachant que nous allons utiliser des électrolytes résistives utilisant les LIs, cette méthode est un outil indispensable pour mesurer des coefficients de diffusion dans des électrolytes non-aqueux.

L'une des microélectrodes les plus communes utilise un disque comme géométrie d'électrode, mais il existe aussi des microélectrodes hémisphériques et cylindriques. Pour la continuité, il s'agit d'une démonstration utilisant une microélectrode à disque, mais un raisonnement équivalent peut être fait pour les autres géométries. L'équation suivante (**Équation 2.26**) est une adaptation de la deuxième loi de Fick (**Équation 2.12**) spécialement pour une microélectrode à disque et la résolution de cette équation différentielle partielle est faite par une transformation de Laplace qui donne accès à l'**Équation 2.27**.

$$\frac{\partial C\,(r,z,t)}{\partial t} = D\left[\frac{\partial^2 C\,(r,z,t)}{\partial r^2} + \frac{1}{r}\cdot\frac{\partial C\,(r,z,t)}{\partial r} + \frac{\partial^2 C\,(r,z,t)}{\partial z^2}\right] \quad \textbf{Équation 2.26}$$

$$i_{total} = i_{planaire} + i_{radial} = \frac{nFAD^{\frac{1}{2}}C}{(\pi t)^{\frac{1}{2}}} + 4nFDCr_{disque} \quad \textbf{Équation 2.27}$$

À la lumière de l'**Équation 2.27**, le courant total est la sommation des courants planaire et radial et ce courant total est fonction du temps. En fait, il s'agit d'une modification de l'équation de Cottrell qui tient maintenant compte du courant radial. Par conséquent, il est nécessaire d'atteindre un état où le transport de masse est régulier et non-limitant. D'ailleurs, cette condition expérimentale donnera l'opportunité d'obtenir une relation entre le courant et le rayon indépendamment du temps. En utilisant les bonnes conditions expérimentales, il est possible de rendre l'un de ces types de diffusion négligeable l'un par rapport à l'autre. À l'aide d'une microélectrode, le choix d'une vitesse de balayage relativement basse (environ sous 20 mV s^{-1}) est nécessaire pour atteindre un état stationnaire, car l'épaisseur de la couche de diffusion est plus grande à haute vitesse de balayage. Le courant à l'état stationnaire est dicté par la diffusion radiale. À haute vitesse de balayage, les allures des voltampérogrammes utilisant une macroélectrode ou

une microélectrode sont très similaires outre l'ordre de grandeur de courant mesuré, car la diffusion planaire est dominante. Donc, le courant de l'état stationnaire (voltampérogramme sigmoïdal) est dépendant du coefficient de diffusion, la concentration et le rayon de la microélectrode (**Équation 2.28**).

$$i_s = nF(\pi {r_{disque}}^2)DC \cdot \frac{4}{\pi r_{disque}} = 4nFDCr_{disque} \quad \textbf{Équation 2.28}$$

Pour analyser les courbes ampérométriques qui ont été mesurées à l'aide d'une microélectrode dans l'objectif de mesurer le coefficient de diffusion d'une façon précise, l'équation empirique de Shoup et Szabo est adéquate pour des régimes de court et de long terme (**Équation 2.29**). Cette technique est bien adaptée pour les électrolytes organiques où la résistance de solution est plus élevée qu'en solution aqueuse. Il est fortement conseillé d'utiliser une cage de Faraday pour empêcher les ondes électromagnétiques nuisibles et extérieures, car les courants normalement mesurés sont de l'ordre du nanoampère. Toutefois, pour la courbe de retour (2^{e} saut), il est nécessaire de faire une simulation à l'aide de cette équation empirique. Il existe aussi la méthode de Stojek pour corréler ces courbes courant-temps qui s'adaptent bien pour les deux sauts de potentiel.

$$i = 4nFDCr\, f(\tau) \qquad \textbf{Équation 2.29}$$

$$f(\tau) = 0{,}7854 + 0{,}8862 \left(\frac{Dt}{r^2}\right)^{-\frac{1}{2}} + 0{,}2146 \exp\left(-0{,}7823 \left(\frac{Dt}{r^2}\right)^{-\frac{1}{2}}\right)$$

Voltampérométrie impulsionnelle

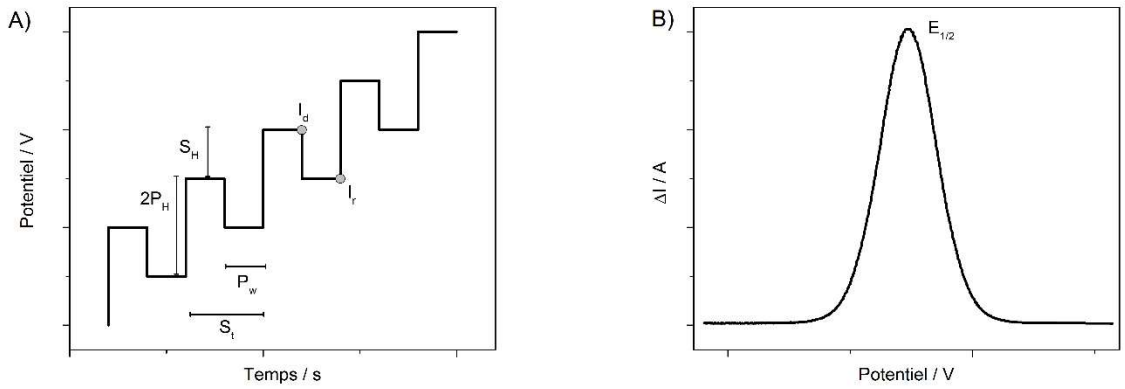

Figure 2.17. A) Rampe de balayage impulsionnelle pour la voltammétrie impulsionnelle à vagues carrées et B) un voltampérogramme impulsionnel à vagues carrées typique pour une espèce électroactive réversible. L'exemple présente une réaction d'oxydation.

La voltampérométrie impulsionnelle, introduite par Barker et Jenkin, a été développée pour diminuer la limite de détection des méthodes d'électroanalyse. Par exemple, la voltampérométrie cyclique présente une limite de détection de 10^{-5} M et la voltampérométrie impulsionnelle, aussi dictée par la diffusion, réussit à diminuer cette limite à 10^{-8} M. La raison qui explique cette diminution est attribuée à l'atténuation de l'importance du courant non-faradique en comparaison avec le courant faradique grâce à la rampe de balayage impulsionnelle. Par conséquent, le rapport courant faradique et non-faradique est donc maximisé qui a comme conséquence d'augmenter la sensibilité de la méthode. La plupart des techniques impulsionnelles est le mariage entre la voltampérométrie et la chronoampérométrie. Au lieu de balayer le potentiel et de mesurer directement le courant (e.g. voltampérométrie linéaire), un saut de potentiel est appliqué en maintenant ce potentiel un certain temps avant de mesurer le courant (e.g. voltampérométrie impulsionnelle). En résumé, le courant capacitif est éliminé, car ce courant décroit plus rapidement que le courant faradique qui est dicté par l'équation de Cottrell comme mentionné dans la section antérieure. En d'autres mots, il y a une discrimination de courant lors des expérimentations impulsionnelles. Il existe plusieurs rampes de balayage impulsionnelles telles que la

voltampérométrie impulsionnelle normale, impulsionnelle différentielle et impulsionnelle à vagues carrées.

La voltampérométrie impulsionnelle à vagues carrées est la technique préconisée dans cette thèse. Cette voltampérométrie impulsionnelle consiste en une succession d'ondes de forme carrée et d'amplitude constante superposées en forme d'escalier (**Figure 2.17A**). Le courant est mesuré à deux reprises lors de chaque cycle (ou vague), une fois pour l'impulsion directe et une fois pour l'impulsion inverse. L'amplitude des vagues carrées est assez large et les deux sauts de potentiel (direct et inverse) engendrent le courant direct et inverse dont la différence de ces courants est utilisée pour tracer un voltampérogramme impulsionnel à vagues carrées (ΔI en fonction du potentiel, **Figure 2.17B**). Pour une réaction électrochimique réversible, l'allure de courbe d'un voltampérogramme impulsionnel à vagues carrées est un pic symétrique où le potentiel au pic représente le potentiel de demi-vague. De plus, la réponse de la voltampérométrie impulsionnelle à vagues carrées est quatre fois plus haute que la voltampérométrie impulsionnelle différentielle qui explique le choix de la méthode. Un des avantages de taille est la résolution de la voltampérométrie impulsionnelle à vagues carrées pour des dérivées d'espèces électroactives dont le potentiel est près l'un de l'autre. L'incrément de potentiel, le temps et l'amplitude d'impulsion sont évidemment modifiables pour l'expérience voulue. Ces paramètres ont un impact direct sur la vitesse de balayage, le nombre de points mesurés, la différence de courant mesuré et la forme du pic.

2.4.3. Analyse de charge/décharge galvanostatique en pile bouton

Assemblage et confection de piles boutons

Par définition, la batterie est un dispositif qui convertit de l'énergie chimique contenue dans les matériaux actifs des électrodes en énergie électrique via des réactions d'oxydoréduction. La batterie a une plus haute efficacité de conversion que le moteur thermique qui est limité par le cycle de Carnot dicté par la deuxième loi de la thermodynamique. D'ailleurs, l'appellation de batteries et de piles sont souvent confondus et pour une meilleure clarté, une batterie consiste d'une ou plusieurs piles connectées en série ou en parallèle. Dans le contexte de cette thèse, il s'agit de pile bouton ou encore d'une seule cellule qui ont été testée. Les composantes majeures de la pile bouton de type CR2032 sont les électrodes (négative + positive) et l'électrolyte (**Figure 2.18**). Les

électrodes, aussi bien l'électrode positive que négative, peuvent être des électrodes dites composites et elles sont constituées d'une matière carbonée, d'un polymère liant et du matériel actif parfois enrobé d'une couche conductrice carbonée (**Figure 2.18A)**. Cette composition permet de s'assurer une bonne propriété mécanique, un bon transport ionique, une bonne conductivité électronique afin d'acheminer les électrons dans le circuit électrique externe et de favoriser un bon contact électrique avec le collecteur de courant d'aluminium. Il est important que l'électrode composite soit uniforme pour que l'ensemble du matériel actif soit accessible lors de la charge et de la décharge afin d'éviter une résistance due au contact électrique entre le collecteur de courant et l'électrode composite. Dans le cadre de cette thèse, les électrodes négatives utilisées seront le lithium métallique (électrode non-composite) et une électrode composite à base de $Li_4Ti_5O_{12}$ (LTO; 1,55 V vs Li/Li^+). De plus, les électrodes positives présentées seront basées sur le $LiTi_2(PO_4)_3$ (LTP; 2,4 V vs Li/Li^+) et le $LiFePO_4$ (LFP; 3,40 V vs Li/Li^+) étant les matériaux actifs.[28] Il est inutile de préciser que la formulation de la composition de l'électrode a un impact direct sur la performance de la pile. Normalement, la matière carbonée utilisée est le noir d'acétylène et le polymère liant souvent favorisé est le polyfluorure de vinylidène. Donc, le noir d'acétylène, le polymère liant et le matériel actif broyé préalablement dont son pourcentage massique est vivement avantagé (i.e. au-delà de 70 %) sont mélangés dans une petite quantité de solvant. Cette mixture similaire à une encre est ensuite étalée sur un feuillet d'aluminium avec un revêtement carboné qui joue comme rôle de collecteur de courant. Pour la confection des piles boutons, des disques seront découpés dans ces feuillets et l'électrode composite (i.e. LTO, LTP et LFP) est maintenant prête après une période de séchage pour être utilisés lors de l'ensemble. Pour l'électrode de lithium métallique, les disques sont directement découpés dans une feuille de lithium métallique.

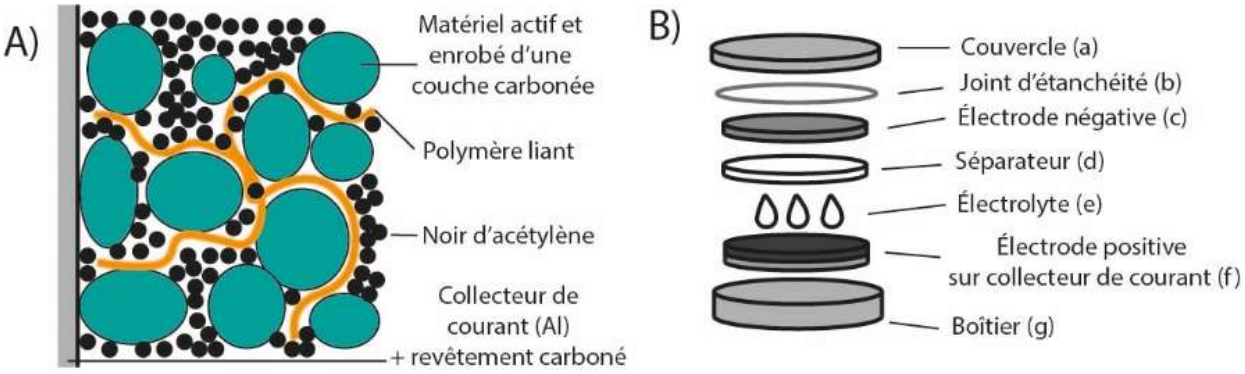

Figure 2.18. A) composition d'une électrode composite et B) Composante d'une pile bouton.

Pour l'ensemblage, l'électrode positive (f) est placée à l'intérieur d'un boîtier en acier inoxydable ouvert (g). Par la suite, l'électrode positive est mouillée par l'ajout de l'électrolyte (e) à l'étude. En résumé, les électrolytes qui seront présentés dans les prochains chapitres sont un mélange d'un sel de lithium dans un solvant de carbonate en présence d'un liquide ionique électroactif. Après, il y a l'ajout d'un séparateur (d, film microporeux, Celgard) de polypropylène sous forme de disque aussi afin d'éviter le contact entre les électrodes et dans la même optique, d'empêcher le court-circuit interne. Normalement, il doit se mouiller avec l'électrolyte (e) déjà ajouté dans l'étape précédente, car il est perméable à l'électrolyte. Si ce n'est pas le cas, les raisons qui pourraient expliquer cette imperméabilité sont que l'électrolyte n'est pas compatible avec le séparateur ou que l'électrolyte pourrait présenter une teneur en eau trop importante, car le film microporeux utilisé comme séparateur est hydrophobe. Pour finir, un joint de plastique (b) est utilisé pour assurer une bonne étanchéité de la pile et l'électrode négative (c) est placée avant de fermer utilisant le couvercle (a) du boitier à l'aide d'une presse prévue à cet effet. Cette fermeture est permanente et elle évite la fuite de l'électrolyte et le contact avec l'extérieur. Évidemment, l'assemblage et la confection de la pile bouton se réalisent en boîte à gant afin d'éviter la contamination de l'oxygène et de l'humidité de l'air, car il ne faut pas oublier qu'il y a manipulation de lithium métallique.

Principe et généralité de la batterie

La plus avantageuse combinaison de matériaux d'électrodes positive et négative est des matériaux légers avec une grande différence de potentiel de cellule et une haute capacité spécifique. C'est pour cette raison que le lithium métallique est aussi étudié, car il est un des métaux les plus légers qui présente un potentiel d'oxydoréduction très négatif. Le stockage d'énergie et les caractéristiques de puissance des batteries suivent exactement les lois de la thermodynamique et les principes de la cinétique pour des réactions chimiques adaptées en électrochimie. Donc, l'équation de base en thermodynamique est applicable dans le domaine du stockage d'énergie (**Équation 2.30**).

$$\Delta G^\circ = \Delta H^\circ - T\Delta S^\circ = -nFE^\circ \qquad \textbf{Équation 2.30}$$

Évidemment, l'énergie libre de Gibbs est de l'énergie disponible issue d'une réaction chimique pour effectuer un travail. Pour une réaction spontanée, l'énergie libre de Gibbs est négative comme lorsque la batterie se décharge et elle libère de l'énergie disponible sous forme d'énergie électrique dans le contexte de la batterie. Bien sûr, la charge produit la réaction inverse qui n'est pas spontanée et cette énergie chimique emmagasinée dans la batterie est une énergie potentielle d'être utilisé au moment propice. Évidemment, la quantité d'énergie délivrée dépend des réactions d'oxydoréduction mise en jeu et de l'équation de Nernst vue dans la section antérieure. Le potentiel de cellule théorique est donné par la différence entre l'électrode positive et négative et typiquement, il correspond au potentiel de circuit ouvert. Cependant, l'énergie disponible est moindre que l'énergie chimique entreposée, car il y a des pertes énergétiques par le biais des surtensions et de la résistance interne de la batterie. D'ailleurs, il y a des surtensions lors de la charge et de la décharge. Les trois types de polarisations engendrant des pertes énergétiques sont la polarisation d'activation (η_{ct}; transfert de charge entre les électrodes et les réactifs, Équation Bulter-Volmer), la polarisation ohmique (résistance de la solution et interne de la cellule) et la polarisation de concentration (η_c; appauvrissement des réactifs à la surface de l'électrode via le transport de masse lent). Ici, la **Figure 2.19** présente l'influence des types de polarisation sur le potentiel d'opération utilisant une batterie qui décharge au fil du temps et l'équation d'Ohm (**Équation 2.31**) adapté pour un système de stockage d'énergie montre la variation du potentiel d'opération selon les surtensions présentes dans le système.

$$E = E_{co} - [(\eta_{ct})_a + (\eta_c)_a] - [(\eta_{ct})_c + (\eta_c)_c] - iR_s = iR \qquad \textbf{Équation 2.31}$$

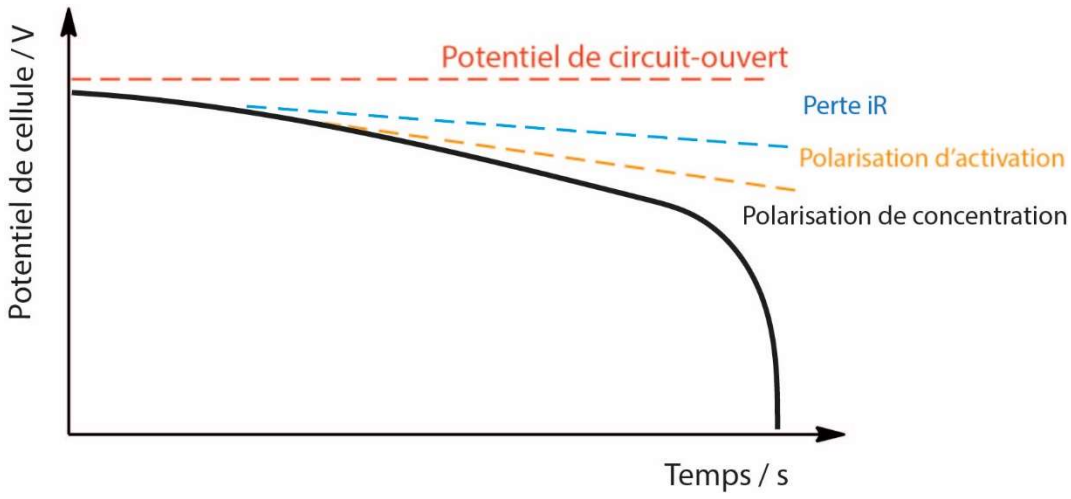

Figure 2.19. Polarisation de cellule pour la décharge.

Terminologie dans le domaine des batteries

Plusieurs termes spécifiques au domaine des batteries seront utilisés au cours de cette thèse et la liste qui suit donne une définition claire de chacun.

- Potentiel de circuit ouvert – Ce potentiel est mesuré sans l'application de chargement, c'est-à-dire qu'aucun courant ne passe d'une électrode à l'autre utilisant une très haute résistance de l'ordre 10^{12} Ω et ce potentiel est normalement près du potentiel théorique.
- Potentiel de circuit fermé – Ce potentiel est mesuré avec l'application de chargement et il est aussi appelé le potentiel d'opération. Ce potentiel est habituellement mesuré en cyclage galvanostatique.
- Potentiel théorique – Ce potentiel est fonction de la différence de l'électrode positive et négative utilisant les réactions d'oxydoréduction mise en jeu et ce potentiel théorique est la différence de potentiel maximal pour une paire d'électrodes données.
- Potentiel nominal – Ce potentiel est le potentiel typique pour une paire d'électrodes données acceptant les pertes de surtension. Ce potentiel est similaire au potentiel moyen.
- Potentiel de fin et d'arrêt – Ce potentiel est le potentiel qui correspond à la fin de la charge ou de la décharge. Souvent, le chargement est inversé ou arrêté lorsqu'il est atteint.
- Potentiel médian – Le potentiel qui correspond à 50 % de charge.
- Capacité spécifique théorique – La capacité spécifique théorique est définie comme la quantité de courant engendrée par la matière active suivant la réaction d'oxydoréduction pour une période de temps donnée. La capacité spécifique dépend du nombre d'électron(s) échangé(s), de la masse molaire qui est dictée par la loi de Faraday (**Équation 2.32**). Il est possible d'utiliser une constante d'unité de conversion (γ) de 3,6 si la masse molaire est en g mol^{-1} dans l'objectif d'obtenir la capacité spécifique en mAh g^{-1}.

$$Q_{théorique} = \frac{n \cdot F}{\gamma \cdot Mw_{active}} \qquad \textbf{Équation 2.32}$$

- Capacité spécifique pratique – La capacité spécifique pratique est la capacité expérimentale d'une batterie réelle. La capacité spécifique est habituellement mesurée en cyclage galvanostatique où le potentiel de fin et d'arrêt est atteint à un temps donné (**Équation 2.33**). La densité de courant est choisie selon la vitesse C voulue.

$$Q_{pratique} = \frac{i \cdot A \cdot t_{fin}}{\gamma \cdot m_{active}} \qquad \textbf{Équation 2.33}$$

- Capacité nominale – La capacité nominale en mAh est la quantité d'électricité engendrée selon la masse de matière active contenue dans une électrode qui dépend aussi de la capacité spécifique théorique selon l'**Équation 2.34**. Une capacité nominale pratique peut être aussi calculée de la même façon.

$$Q_{nominale} = Q_{théorique} \cdot m_{active} \qquad \textbf{Équation 2.34}$$

- Énergie spécifique théorique – L'énergie spécifique, aussi appelée densité d'énergie gravimétrique, est utilisée pour définir la quantité d'énergie qu'une batterie peut stocker ou délivrer par unité de masse. Elle est souvent exprimée en Wh kg^{-1} et le calcul nécessite la capacité spécifique théorique comme il s'agit de l'énergie spécifique théorique (**Équation 2.35**). Pour augmenter l'énergie de la batterie, il y a deux options, dont l'augmentation de la capacité spécifique ou l'augmentation du potentiel de cellule. Évidemment, l'énergie spécifique théorique est l'énergie maximum pour une paire d'électrodes. Il est possible de différencier deux types d'énergie spécifique théorique; la première qui assume seulement la matière active ou la seconde qui tient compte de toutes les masses des composantes utilisées pour la confection d'une batterie, dont l'électrolyte et les composés non-réactifs (**Équation 2.36**).

$$E_{spécifique,théorique} = \frac{n \cdot F}{\gamma \cdot Mw_{active}} \cdot E_{cell} = Q_{théorique} \cdot E_{cell} \qquad \textbf{Équation 2.35}$$

$$E_{spécifique,théorique}(\text{Batterie réelle}) = \frac{Q_{nominale} \cdot E_{cell}}{\sum m_{composante}} \qquad \textbf{Équation 2.36}$$

- Énergie spécifique pratique – L'énergie spécifique pratique est utilisée pour définir la quantité d'énergie réelle qu'une batterie peut stocker ou délivrer par unité de masse. L'énergie spécifique pratique est habituellement mesurée en cyclage galvanostatique où l'aire sous la courbe de la courbe galvanostatique (Le potentiel en fonction du temps) est nécessaire pour le calcul de l'énergie (**Équation 2.36**). L'approximation possible de faire est de multiplier la capacité spécifique pratique avec le potentiel nominal.

$$E_{spécifique,pratique} = \frac{\int_0^{t_{fin}} V(t) \cdot i \cdot A \cdot dt}{\gamma \cdot m_{active}} \qquad \textbf{Équation 2.37}$$

- Puissance spécifique pratique moyenne – La puissance spécifique en W kg^{-1} est l'énergie disponible sur une période de temps par unité de masse. Pour une courbe galvanostatique comme le courant est constant, la puissance spécifique moyenne est donnée par l'énergie spécifique divisée par le temps de décharge ou de charge (**Équation 2.38**). La **Figure 2.20** illustre bien la différence entre l'énergie et la puissance. Les batteries sont reconnues pour entreposer beaucoup d'énergie, mais elles délivrent l'énergie lentement (faible puissance). Au contraire des supercapaciteurs, ils démontrent une très haute puissance, mais typiquement, l'énergie emmagasinée est très limitée par la surface.

$$P_{spécifique,pratique} = \frac{\int_0^{t_{fin}} V(t) \cdot i \cdot A \cdot dt}{\gamma \cdot m_{active} \cdot t_{fin}} = \frac{E_{spécifique,pratique}}{t_{fin}} \qquad \textbf{Équation 2.38}$$

- Densité d'énergie – La densité d'énergie est utilisée pour définir la quantité d'énergie qu'une batterie peut stocker ou délivrer par unité de volume.
- Densité de puissance – La densité de puissance pratique est utilisée pour définir la quantité d'énergie réelle qu'une batterie peut stocker ou délivrer par unité de volume.
- Vitesse de C – Les courants de chargement (charge et décharge) sont souvent exprimés comme étant des vitesses de C dans l'objectif de normaliser à l'aide de la capacité nominale des électrodes utilisées. Donc, la méthode galvanostatique utilise des courants constants et les vitesses C aident à comparer des systèmes complètement différents. Une vitesse de C est un paramètre expérimental utilisant un courant appliqué au borne à laquelle une batterie est déchargée ou chargée par rapport à sa capacité nominale. Une vitesse de 1 C signifie que la batterie se décharge ou se charge en 1 heure avec le courant utilisé correspondant selon la capacité nominale. Avec un courant deux fois plus grand pour une même batterie, il s'agit d'une vitesse de 2 C (30 minutes de décharge) et avec un courant deux fois plus petit, la vitesse de C sera donc de 0,5 C (2 heures de décharge). La relation suivante donne la vitesse de C en fonction du courant constant utilisé en galvanostatique et de la capacité nominale de la batterie (**Équation 2.39**)

$$Vitesse\ de\ C = \frac{I}{Q_{nominale}} \qquad \textbf{Équation 2.39}$$

- État de charge – Cette expression est souvent exprimée en pourcentage qui caractérise la capacité disponible et restante pour la batterie en question. L'état de charge est affecté par les conditions d'opération telles que le courant de chargement (charge et décharge) et de la

température. L'état de charge est donné par l'**Équation 2.40** où une batterie à 0 % est une batterie complètement déchargée.

$$État\ de\ charge\ (\%) = \frac{Q_{restante}}{Q_{nominale}} \times 100 \qquad \textbf{Équation 2.40}$$

- Cycle de vie – Le nombre de cycles charge-décharge que peut subir une batterie avant que la batterie ne parvienne plus à atteindre les critères de performance. Dans le contexte d'une batterie surchargé, nous visons 80 % de la charge initiale. La durée de vie de la batterie est affectée par la fréquence, l'amplitude des cycles, la température et l'humidité et la qualité des matériaux.
- L'efficacité coulombique – Il s'agit de la caractérisation de la réversibilité des réactions d'oxydoréduction pour la charge et la décharge pour un même cycle. L'efficacité coulombique est définie comme étant le ratio entre la capacité spécifique de la décharge ($Q_{décharge}$) et la capacité spécifique de la charge (Q_{charge}). Ces capacités spécifiques pratiques sont mesurées en galvanostatique comme mentionnées auparavant. Ce rapport est souvent exprimé en pourcentage (**Équation 2.41**). Pour un système parfaitement réversible, le ratio attendu est de 100%.

$$Efficacité\ coulombique\ (\%) = \frac{Q_{décharg}}{Q_{charg}} \times 100 \qquad \textbf{Équation 2.41}$$

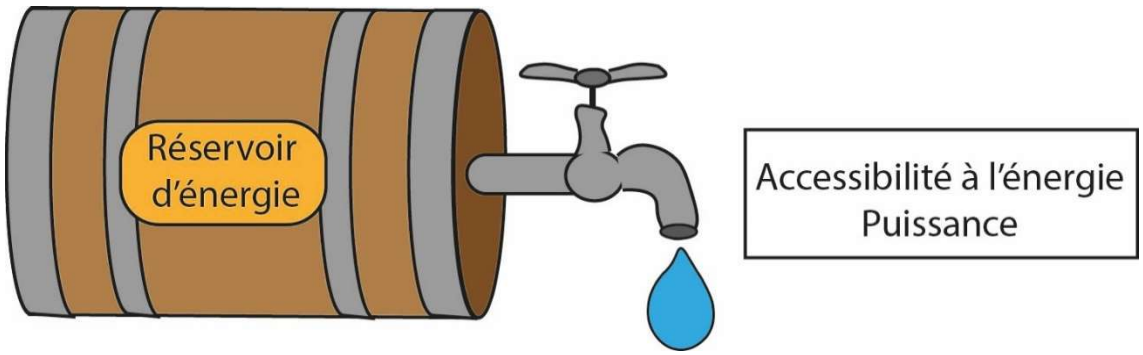

Figure 2.20. Illustration qui montre la différence entre l'énergie et la puissance.

Analyse galvanostatique utilisant des navettes redox

Les méthodes de chronopotentiométrie à courant constant sont largement utilisées en électrochimie et le cyclage des batteries en mode galvanostatique demeure très utilisé en industrie

pour évaluer les performances des batteries telles que la cyclabilité, la capacité spécifique, l'impact de l'électrolyte et le comportement du potentiel d'opération en fonction du temps. Le cyclage galvanostatique consiste à appliquer un courant dit positif, car ce courant charge la batterie engendrant des réactions d'oxydoréductions non-spontanées aux électrodes et évidemment, en inversant le signe du courant constant, la décharge est observable selon le temps en libérant l'énergie emmagasinée. Par conséquent, cette méthode est toute indiquée pour caractériser les réactions d'oxydoréduction impliquées dans les batteries telles que l'intercalation du lithium et du plaquage du lithium pour les piles au lithium pour en nommer quelques-uns. La **Figure 2.21A** montre une courbe de type galvanostatique et sur cette même figure, il est possible de voir la charge (courbe orange) suivie subséquemment par la décharge (courbe bleue) et la courbe charge-décharge forme un cycle. D'ailleurs, il est possible d'évaluer la cyclabilité en effectuant plusieurs charges-décharges. Expérimentalement, le potentiel d'opération est largement affecté par le régime de charge-décharge, défini par la notation de la vitesse de C/n, dépendamment du courant imposé aux bornes de la batterie. La capacité spécifique peut être considérable réduite entre un régime rapide (10 C; 6 minutes de décharge) et un régime lent (C/10, 10 heures de décharge), car les processus électrochimiques tels que le transport de masse et l'organisation des produits impliqués dans la réaction d'oxydoréduction sont lents qui expliquent aussi la faible puissance des batteries en général. Le calcul du courant imposé selon le régime de vitesse C se retrouve dans la section antérieure. Comme le courant est calculé selon la capacité spécifique théorique, il est important d'établir des balises en programmant préalablement des potentiels de fin et d'arrêt pour éviter des surtensions où des réactions parasites peuvent se produire. La **Figure 2.21A** montre des plateaux plats aussi bien pour la charge que pour la décharge et ces allures de courbes sous forme de plateau indiquent une bonne mobilité du lithium (pour les BILs) et une conductivité ionique suffisante. De plus, il y a une différence de potentiel entre le plateau de charge et de décharge qui est cohérente avec les différentes polarisations et résistances internes mentionnées dans la section de terminologie.

Dans le chapitre précédent, il a été question de navette redox jouant de rôle de protecteur de surtension lors de la charge d'une batterie. La technique galvanostatique est une méthode idéale pour caractériser l'implication des navettes redox dans les BILs. Comme la galvanostatique classique, il s'agit d'imposer un courant de charge et de décharge égale en valeur absolue, mais le cyclage charge-surcharge-décharge consiste à appliquer ce courant positif deux fois plus longtemps

pour avoir une durée de plateau égale entre la charge et la surcharge et par rapport au courant de décharge. La surcharge, présentée sur la **Figure 2.21B** (courbe rouge), est une manière fictive de surcharger la batterie, car réellement, la surcharge est consommée par la navette redox et éloignée de l'électrode positive afin d'éviter l'augmentation du potentiel. En d'autres mots, la navette redox a un potentiel légèrement supérieur à l'électrode positive (i.e. idéalement 300 mV) et au lieu que le potentiel soit interrompu par l'instrument au potentiel de fin et d'arrêt, il s'agit d'une interruption de l'élévation du potentiel par le mécanisme de la navette redox d'une façon interne et autonome. Une allure de courbe de plateau pour la surcharge indique que la navette redox est efficace. De plus, il est possible d'appliquer un courant positif pour engendrer la charge et la surcharge avec un temps infini pour évaluer l'efficacité, la cyclabilité et la durée de vie de la navette redox et à la mort de la navette redox, le potentiel est arrêté par l'instrument comme la méthode typique. Ce type d'étude est pour recueillir de l'information sur le vieillissement prématuré à potentiel flottant dicté par le potentiel de la navette redox.

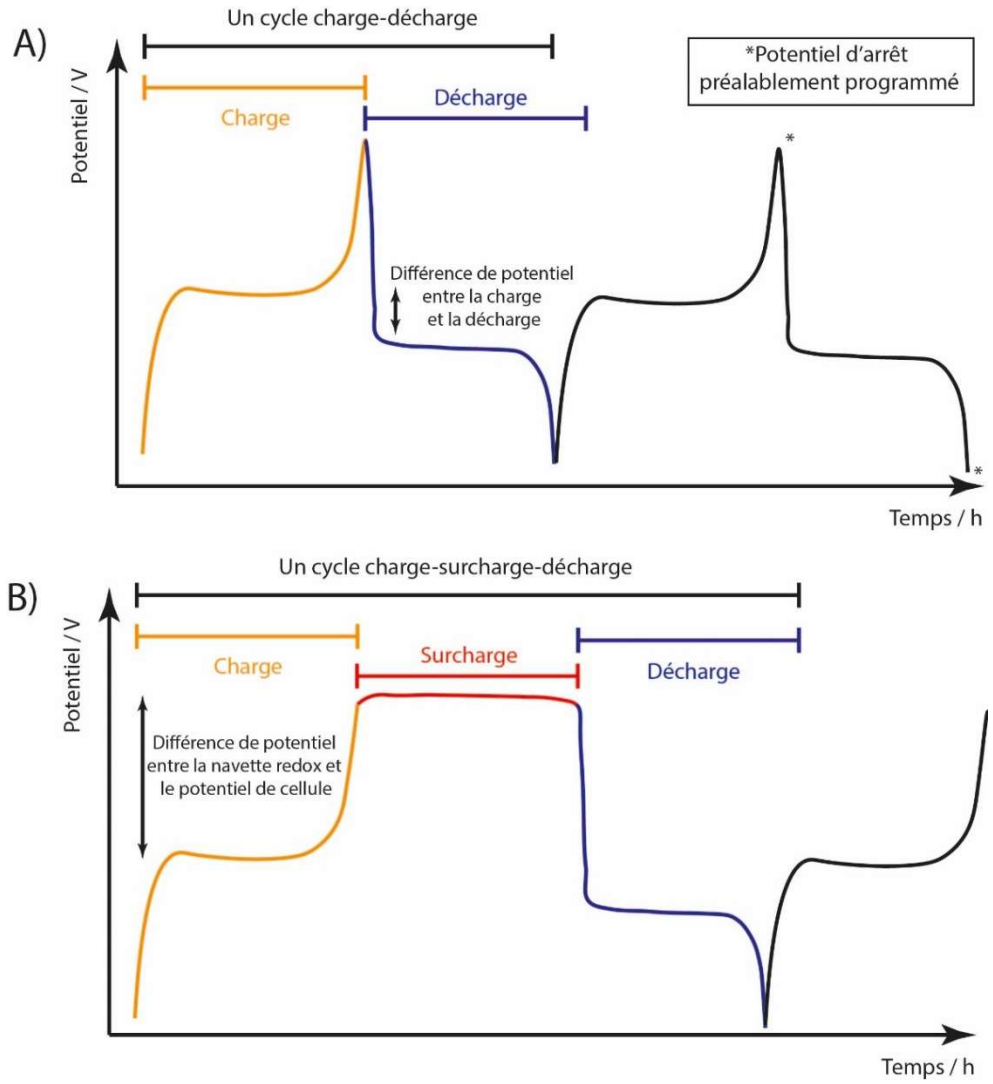

Figure 2.21. Des courbes galvanostatiques montrant A) une courbe charge-décharge sans navette redox et B) une courbe charge-surcharge-décharge utilisant une navette redox présent dans l'électrolyte.

2.5. Références

[1] P. Bonhôte, A.-P. Dias, N. Papageorgiou, K. Kalyanasundaram, M. Grätzel, Hydrophobic, highly conductive ambient-temperature molten salts, Inorg. Chem., 35 (1996) 1168-1178.
[2] J. Foropoulos, D.D. DesMarteau, Synthesis, properties, and reactions of bis((trifluoromethyl)sulfonyl) imide, (CF3SO2)2NH, Inorg. Chem., 23 (1984) 3720-3723.
[3] D.D. Desmarteau, M. Witz, N-fluoro-bis(trifluoromethanesulfonyl) imide. An improved synthesis, J. Fluorine Chem., 52 (1991) 7-12.
[4] B.H. Thomas, G. Shafer, J.J. Ma, M.-H. Tu, D.D. DesMarteau, Synthesis of 3,6-dioxa-Δ7-4-trifluoromethyl perfluorooctyl trifluoromethyl sulfonimide: bis[(perfluoroalkyl)sulfonyl] superacid monomer and polymer, J. Fluorine Chem., 125 (2004) 1231-1240.
[5] L. Yagupol'skii, Yagupol'skii, [(Trifluoromethyl)sulfonyl]imino and bis[[(trifluoromethyl)sulfonyl]imino] derivatives of arenesulfonic acids, Zhurnal organicheskoĭ khimii, 31 (1995) 747-752.
[6] B.A. Shainyan, L.L. Tolstikova, Trifluoromethanesulfonamides and related compounds, Chem. Rev., 113 (2013) 699-733.
[7] M.B. Herath, S.E. Creager, R.V. Rajagopal, O.E. Geiculescu, D.D. DesMarteau, Ionic conduction in polyether-based lithium arylfluorosulfonimide ionic melt electrolytes, Electrochim. Acta, 54 (2009) 5877-5883.
[8] S. Ladouceur, S. Paillet, A. Vijh, A. Guerfi, M. Dontigny, K. Zaghib, Synthesis and characterization of a new family of aryl-trifluoromethanesulfonylimide Li-salts for Li-ion batteries and beyond, J. Power Sources, 293 (2015) 78-88.
[9] V. Morizur, S. Olivero, J.R. Desmurs, P. Knauth, E. Dunach, Novel lithium and sodium salts of sulfonamides and bis(sulfonyl)imides: synthesis and electrical conductivity, New J. Chem., 38 (2014) 6193-6197.
[10] E. Paillard, F. Toulgoat, R. Arvai, C. Iojoiu, L. Cointeaux, M. Medebielle, F. Alloin, B. Langlois, J.Y. Sanchez, Syntheses of a wide family of new aryl based perfluorosulfonimide lithium salts. Electrochemical performances of the related polymer electrolytes, J. Fluorine Chem., 132 (2011) 1213-1218.
[11] R. Arvai, F. Toulgoat, B.R. Langlois, J.-Y. Sanchez, M. Médebielle, A simple access to metallic or onium bistrifluoromethanesulfonimide salts, Tetrahedron, 65 (2009) 5361-5368.
[12] H.H. Bosshard, R. Mory, M. Schmid, H. Zollinger, Eine methode zur katalysierten herstellung von carbonsäure- und sulfosäure-chloriden mit thionylchlorid, Helv. Chim. Acta, 42 (1959) 1653-1658.
[13] A. Barco, S. Benetti, G.P. Pollini, R. Taddia, A new preparation of sulfonyl chlorides via pyridinium sulfonates, Synthesis, 1974 (1974) 877-878.
[14] S. Fujita, A convenient preparation of arenesulfonyl chlorides from the sodium sulfonates and phosphoryl chloride/ sulfolane, Synthesis, 1982 (1982) 423-424.
[15] R.C. Reynolds, P.A. Crooks, J.A. Maddry, M.S. Akhtar, J.A. Montgomery, J.A. Secrist, Synthesis of thymidine dimers containing internucleoside sulfonate and sulfonamide linkages, J. Org. Chem., 57 (1992) 2983-2985.
[16] G. Blotny, A new, mild preparation of sulfonyl chlorides, Tetrahedron Lett., 44 (2003) 1499-1501.
[17] C. Maton, N. De Vos, C.V. Stevens, Ionic liquid thermal stabilities: decomposition mechanisms and analysis tools, Chem. Soc. Rev., 42 (2013) 5963-5977.

[18] R.E. Del Sesto, T.M. McCleskey, C. Macomber, K.C. Ott, A.T. Koppisch, G.A. Baker, A.K. Burrell, Limited thermal stability of imidazolium and pyrrolidinium ionic liquids, Thermochim. Acta, 491 (2009) 118-120.
[19] H. Tokuda, S. Tsuzuki, M.A.B.H. Susan, K. Hayamizu, M. Watanabe, How ionic are room-temperature ionic liquids? An indicator of the physicochemical properties, J. Phys. Chem. B, 110 (2006) 19593-19600.
[20] S. Zhang, N. Sun, X. He, X. Lu, X. Zhang, Physical properties of ionic liquids: Database and evaluation, J. Phys. Chem. Ref. Data, 35 (2006) 1475-1517.
[21] J.A. Widegren, J.W. Magee, Density, Viscosity, Speed of sound, and electrolytic conductivity for the ionic liquid 1-hexyl-3-methylimidazolium bis(trifluoromethylsulfonyl)imide and its mixtures with water, J. Chem. Eng. Data, 52 (2007) 2331-2338.
[22] G.L. Burrell, I.M. Burgar, F. Separovic, N.F. Dunlop, Preparation of protic ionic liquids with minimal water content and 15N NMR study of proton transfer, Phys. Chem. Chem. Phys., 12 (2010) 1571-1577.
[23] E.L. Hahn, Spin echoes, Phys. Rev., 80 (1950) 580-594.
[24] E.O. Stejskal, J.E. Tanner, Spin diffusion measurements: Spin echoes in the presence of a time-dependent field gradient, J. Chem. Phys., 42 (1965) 288-+.
[25] G. Annat, D.R. MacFarlane, M. Forsyth, Transport properties in ionic liquids and ionic liquid mixtures: The challenges of NMR pulsed field gradient diffusion measurements, J. Phys. Chem. B, 111 (2007) 9018-9024.
[26] A.J. Bard, L.R. Faulkner, J. Leddy, C.G. Zoski, Electrochemical methods: fundamentals and applications, Wiley New York, 1980.
[27] R.J. Forster, D.A. Walsh, Voltammetry | Overview, in: W. Editors-in-Chief: Paul, T. Alan, P. Colin (Eds.) Encyclopedia of Analytical Science (Second Edition), Elsevier, Oxford, 2005, pp. 181-188.
[28] N. Nitta, F. Wu, J.T. Lee, G. Yushin, Li-ion battery materials: present and future, Mater. Today, 18 (2015) 252-264.

Chapitre 3 : L'effet des chaînes latérales d'un imidazolium à base de ferrocényle

3.1. Avant-propos et mise en contexte

Ce chapitre a été rédigé sous forme d'un article qui a été soumis au *Journal of The Electrochemical Society*. Au moment de l'expérimentation, les liquides ioniques électroactifs étaient peu étudiés et l'impact des variations structurelles comme la variation de la chaîne latérale sur les propriétés électrochimiques l'était encore moins. Il y avait, au moment de publier, des recherches existantes concernant l'électrochimie des liquides ioniques électroactifs basé sur le 1-ferrocenylméthyl-3-alkyl-imidazolium à l'état pure et à différentes températures. La contribution de cette publication est l'électrochimie de ces liquides ioniques électroactifs sous forme diluée dans les carbonates. Ce type de résultat a montré sans aucun doute que l'impact de la modification structurelle diminue significativement dans un mélange carbonate et liquide ionique électroactif en présence d'un sel de lithium. À la lumière de ces résultats, nous étions confiants que nous pouvions faire des modifications structurelles plus significatives dans l'objectif de mieux comprendre les liquides ioniques électroactifs.

3.2. Article: Conductivity and Electrochemistry of Ferrocenyl-Imidazolium Redox Ionic Liquids with Different Alkyl Chain Lengths

Bruno Gélinas[a], John C. Forgie[a], and Dominic Rochefort[a],

[a]Département de Chimie, Université de Montréal, Montréal, Québec H3C 3J7, Canada

Journal of The Electrochemical Society, 161 (4) H161-H165 (2014)

Manuscript submitted November 25, 2013; revised manuscript received January 17, 2014. Published January 24, 2014. This was Paper 2604 from the San Francisco, California, Meeting of the Society, October 27–November 1, 2013. [DOI: 10.1149/2.017404jes]

3.2.1. Abstract

Electroactive ionic liquids obtained by modifying imidazolium with ferrocenyl moiety and alkyl chains of different lengths (n = 1, 4, 8 and 12) were studied in their pure form and dissolved in ethylene/diethylene carbonates (EC/DEC) solvent. Bis(trifluoromethanesulfonyl)imide (TFSI) was used as the anion. The conductivity of the pure ionic liquids (0.1 to 0.04 $mS \cdot cm^{-1}$) was found to decrease with the increase in alkyl chain length as expected from larger van der Waals interactions. The conductivities of carbonate solutions of redox ionic liquid (50% vol.) were less affected by the chain length but were strongly dependent on the presence of Li ions due to their coordination with TFSI, providing viscous solutions (86–111 cP) which decreased the self-diffusion of the redox imidazolium by a factor of 6. The equilibrium potential of the RIL dissolved in the carbonate solvent was not affected by the alkyl chain length, but mass transport by migration caused a distortion in cyclic voltammograms for highly concentrated solutions.

3.2.2. Introduction

The interest in imidazolium-based ionic liquids is driven in part by their potential application in various fields and by their excellent stability in the presence of air and moisture, especially when used with the BF_4^- and $TFSI^-$ anions.[1, 2] Depending on the anion, imidazolium ionic liquids possess a high conductivity,[3] a low vapor pressure,[4] a high thermal stability and a large electrochemical window of stability. Another explanation for their popularity lies in the well-known and versatile chemistry of imidazole, allowing the modification of imidazolium to develop functionalized (task-specific) ionic liquids. The electrochemistry of redox-active ionic liquids (RIL) obtained by the modification of alkylimidazolium cations with a ferrocenyl group was firstly studied by Murray et al.,[5, 6] showing electron hopping between the ferrocenyl moieties present at high concentration in the pure ionic liquid phase. Other studies focused on the properties of these intrinsically electroactive phases with different cation structures.[7-10] While there are currently very few examples of the application of redox ionic liquids, the combination of the stability of ionic liquids with the high concentration of redox centers offers unique properties for the development of electrolytes in energy storage devices. We reported recently on a potential application of redox ionic liquids as a redox shuttle in lithium-ion batteries to prevent cathode overcharge and increase their safety.[11] We found that, although the melting point of ferrocenylimidazolium TFSI (47°C) prevented its use in pure form, highly concentrated solutions of the RIL in carbonates with LiTFSI salt could be applied as the electrolyte to prevent cathode over-oxidation. In order to develop improved electrolytes based on redox ionic liquids, it will be important to determine how the properties of the pure RIL will be reflected in solutions. Results obtained so far show that the addition of an electron-rich moiety such as ferrocene increases the viscosity of pure ionic liquids by increasing π-π intermolecular interactions but no data on the properties of solutions of these RIL are found.

In this contribution we prepared four RILs based on 1-(methylferrocenyl)-3-methylimidazolium TFSI ($FcEImC_1$), 1-(methylferrocenyl)-3-butylimidazolium TFSI ($FcEImC_4$), 1-(methylferrocenyl)-3-octylimidazolium TFSI ($FcEImC_8$) and 1-(methylferrocenyl)-3-dodecenylimidazolium TFSI ($FcEImC_{12}$) and studied the conductivity in undiluted state. We also evaluated the conductivity, viscosity and electrochemical properties of mixtures of these ionic liquids with a solvent based on ethylene carbonate and diethyl carbonate (EC/DEC). A volume

ratio of 1:2 for the carbonate mixture was selected for its good electrolyte properties in Li-ion batteries using a cathode of $LiFePO_4$, which is used as the reference system to develop and test redox shuttles in our research group. The common structure of these RILs is presented in **Figure 3.1**. The conductivity of the 1-methylferrocenyl 3-alkylimidazolium salts was measured on the pure phases and as mixtures at various ratios (50, 10, 1 v/v%) with EC/DEC 1:2 (ethylene carbonate/diethylene carbonate) solutions containing lithium bis(trifluoromethanesulfonyl)imide (LiTFSI) as the supporting electrolyte. Due to the high viscosity of the ionic liquids, their electrochemical characterization was carried out in mixtures only.

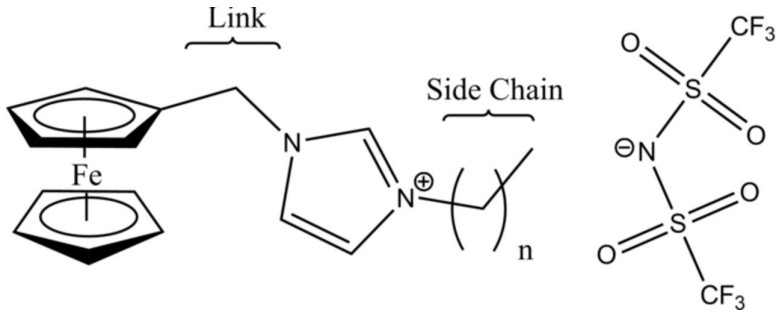

Figure 3.1. Structure of redox ionic liquids (RILs) used given with their corresponding abbreviation (n=0: $FcEImC_1$; n=3: $FcEImC_4$; n=7: $FcEImC_8$; n=11: $FcEImC_{12}$)

3.2.3. Experimental

All reagents and precursor chemicals were obtained from Sigma-Aldrich unless stated otherwise and solvents were obtained from Fisher. These were used as received. All synthesized compound were characterized by ^1H and ^{13}C NMR on a Bruker AMX 300 MHz spectrometer at room temperature and by electrospray ionization mass spectrometry. The accurate mass values were obtained on an Agilent LC-MSD TOF.

The synthetic steps to the ferrocene-modified alkylimidazoliums are presented in **Figure 3.2**. In short, the procedure is based on the quaternization of dimethylaminomethylferrocene with iodomethane to give dimethylaminomethylferrocene methiodide in 86% yield. This was followed by an S_N2 displacement of the trimethylamine iodide with a primary alcohol to give hydroxymethylferrocene in 57% yield. This product was reacted with N,N'-carbonyldiimidazole to give the desired (ferrocenylmethyl) imidazole in 56% yield. $FcEImC_1$ iodide was obtained in a manner according to literature procedure.[5, 11] $FcEImC_4$,

$FcEImC_8$ and $FcEImC_{12}$ bromides were made using the appropriate bromoalkanes. Finally, to produce the desired ionic liquids, metathesis reactions with an aqueous solution of LiTFSI were performed with each of the halide salts. The detailed procedure with ^1H NMR and mass spectrometry analysis can be found as Supplementary Material. No halides were detected during the analysis of the ionic liquids or appeared on the cyclic voltammograms. Therefore if residual halides remain from the cleaning procedures, they are present in trace amounts.

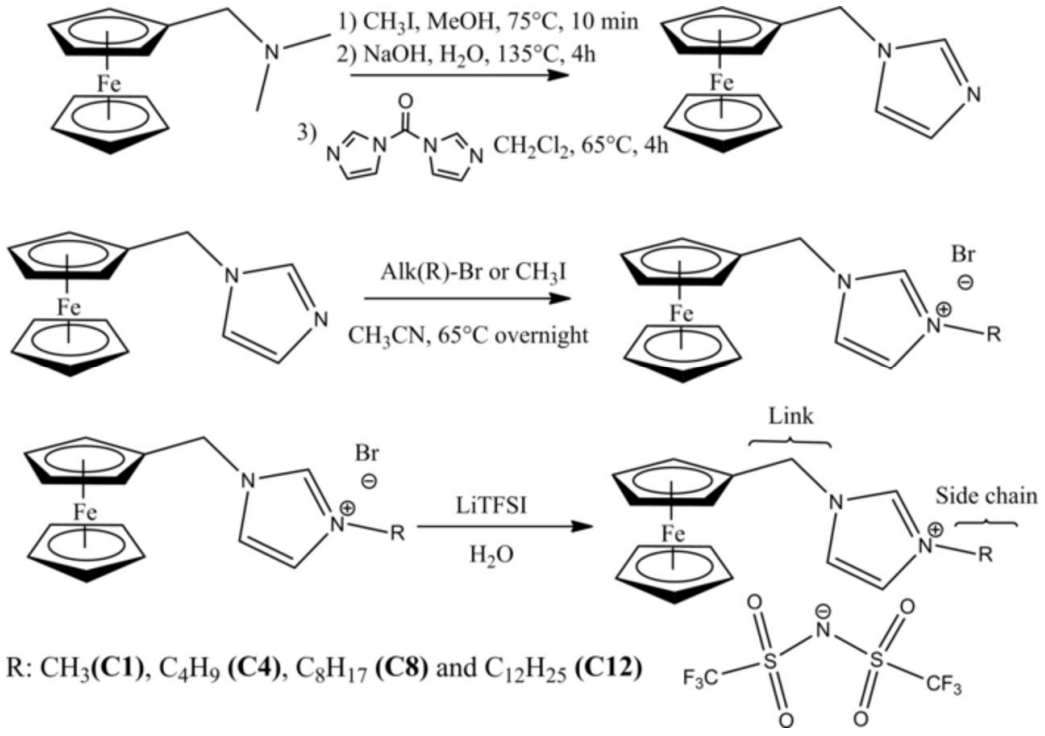

Figure 3.2. Synthetic steps of the ferrocenyl-imidazolium redox ionic liquids (RILs).

The ionic conductivities of the RIL (neat form and in mixtures with carbonates) were measured by AC impedance technique using a Parstat 2273 potentiostat from Princeton Applied Research. The measurements were carried out from 1 MHz to 1 Hz and at temperatures ranging from 25°C to 75°C with an interval of 5°C for each measurement to determine the activation energy from Arrhenius plots. The temperature was controlled with a thermostated bath and was monitored using a thermocouple placed in contact with the solution. The flow conductivity cell was an Orion (018012) composed of two platinum electrodes. The cell was calibrated daily using a standard 0.117 M KCl (0,015 S cm^{-1}) solution. The solution resistance was measured at the intercept of the curve of the Nyquist plot on the real impedance axis. The viscosity of all samples was measured

on a Cambridge Applied Systems viscometer (model VL-4100) using pistons with range 0.5 to 10 cP and 10 to 200 cP at 25°C.

The electrochemical measurements in EC:DEC 1:2 were performed using a standard three-electrode cell, consisting of a silver wire pseudo-reference electrode, a platinum wire counter electrode and platinum working electrode with 0.0201 cm^2 of area, with a Parstat 2273 potentiostat. A ferrocene solution was measured to calibrate the quasi-reference electrode and all values presented here are reported to the half-wave potential of this redox couple (Fc^+/Fc). The diffusion coefficient was measured using a series of scan rates and calculated from the Randle-Sevcik equation.

The stimulated echo pulse sequence developed by Tanner (STE: 90-t1-90-t2-90-t1-echo) was used to measure the self-diffusion coefficients (D_s). Measurements were performed at room temperature on a Bruker AV500 NMR spectrometer operating at a frequency of 500 MHz for protons. The measurements of the diffusion coefficients for the cation, the anion, and the lithium ion were made by ^1H, ^{19}F, and ^7Li NMR, respectively. The self-diffusion coefficients (D_s) were obtained from Stejskal-Tanner equation.[12]

3.2.4. Results and Discussion

Conductivity

Conductivity is key factor to consider when developing electrolytes for electrochemical energy storage devices, and the different intermolecular interactions in complex solutions can affect the transport properties by the components of the ionic liquids. To evaluate the effect of the side chain length, the conductivity of the pure RIL phases was firstly measured. The conductivity and molar conductivity results, presented in **Table 3.1**, show that the $FcEImC_8$ and the $FcEImC_{12}$ have the lowest conductivity of all samples because of the increased interactions between the longer side chains. The impact of these weak interactions is lesser for the shorter chains explaining the similar results obtained for $FcEImC_4$ and $FcEImC_1$. The ionic conductivities for $FcEImC_1$ and $FcEImC_{12}$ are 0.10 mS cm^{-1} and 0.04 mS cm^{-1} at 25°C, respectively. In comparison, the unmodified imidazolium equivalents C_2C_1Im TFSI and C_8C_1Im TFSI have a ionic conductivity of 9.1 mS cm^{-1} and 1.3 mS cm^{-1} at 25°C, respectively.[13] The lower conductivity of the ferrocenyl-

modified imidazoliums can be explained by a higher viscosity due to the significant increase in the size of the cation and the increased interactions between ferrocenyl groups. **Figure 3.3A** shows the effect of temperature on the conductivity of the pure RIL which is well described by the VFT (Vogel-Fulcher-Tamman) model, as it is the case in general for ionic liquids, functionalized or not.[14] The curves of **Figure 3.3A** were fitted using equation 1, and the fitting parameters are listed in **Table 3.1**. The curves in **Figure 3.3A** show very similar temperature dependence (curvature) on the ionic conductivity for the RIL with C_4 chain length and above. The tendency is very different for the methyl side chain substituent, which presents a more pronounced curvature, especially at lower temperatures. The effect of alkyl chain length on the physicochemical parameters of imidazolium TFSI ionic liquids was studied by Watanabe and co-workers.[15] They showed a dissimilar curvature of the conductivity vs. temperature plots between the $C_{1\text{-}2}$ and $C_{4\text{–}8}$ alkyl chains of imidazolium TFSI, attributed to the lower impact of the van der Waals interactions between very short chains. The B parameters of VFT function (related to activation energy) in Watanabe's paper were very similar for the shorter chains and increased with the chain length above C_4. In the present case, this parameter increases with all chain lengths, suggesting the presence of different interactions. It is therefore possible, for the redox ionic liquids under study here, that when van der Walls interactions are minimized by very short chains, π-π interactions between ferrocene units become predominant. Shorter chains would also allow this short-range interaction to take place efficiently. The increased curvature of the VFT curve at low temperatures for the C_1 chain could also be an effect of the higher melting point of this RIL, explaining the lower molar conductivity of the C_1 RIL compared to that of the C_4 at 25°C (**Table 3.1**). At 75°C, the trend in molar conductivity (σ) is to increase from C_1 to C_{12}.

$$\sigma = \sigma_0 exp^{\left(\frac{-B}{T-T_0}\right)} \qquad (1)$$

Table 3.1. Ionic conductivities and molar ionic conductivities of the pure RILs and VFT fitting parameters.

RILs	σ, 25°C / S cm^{-1}	Λ, 25°C / S cm^2 mol^{-1}	σ, 75°C / S cm^{-1}	Λ, 75°C / S cm^2 mol^{-1}	σ_0 / S cm^{-1}	B / K	T_0 / K
$FcEImC_1$	1.0×10^{-4}	3.4×10^{-2}	2.2×10^{-3}	7.4×10^{-1}	0.04	271	255
$FcEImC_4$	9.9×10^{-5}	3.7×10^{-2}	1.6×10^{-3}	5.9×10^{-1}	0.10	502	227
$FcEImC_8$	6.6×10^{-5}	2.6×10^{-2}	1.1×10^{-3}	4.4×10^{-1}	0.39	899	195
$FcEImC_{12}$	4.3×10^{-5}	1.7×10^{-2}	7.9×10^{-4}	3.1×10^{-1}	0.44	996	190

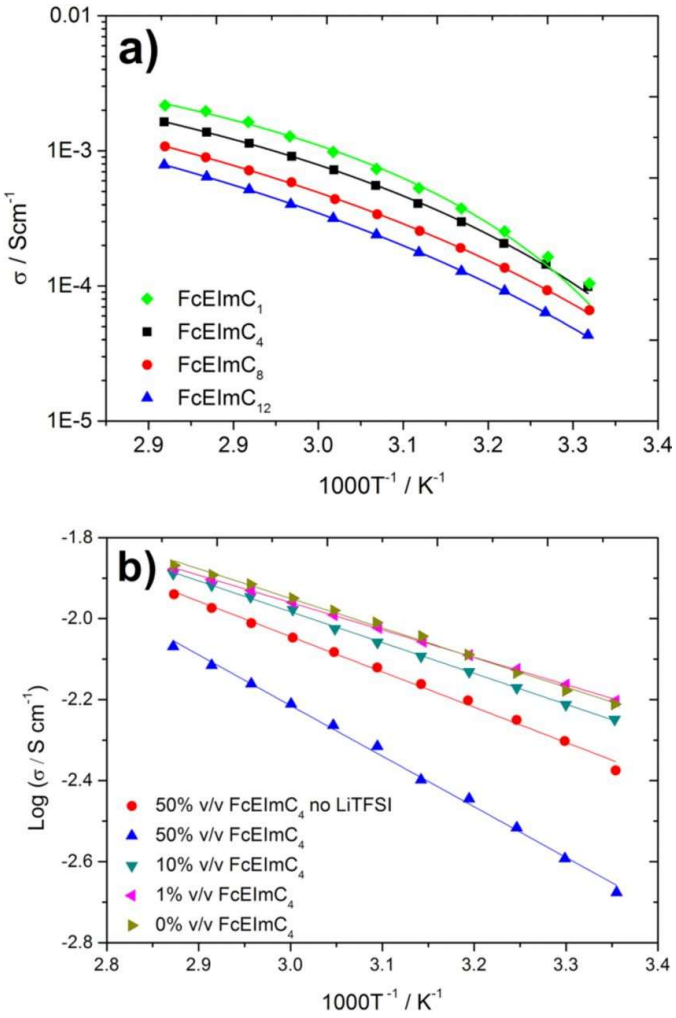

Figure 3.3. a) Temperature dependence on the ionic conductivity of pure redox ionic liquids b) Arrhenius plots for the $FcEImC_4$ in EC/DEC 1:2 with or without of LiTFSI. Measurements were done at 5 °C intervals between 25 and 75 °C.

The RILs in very dilute solutions in carbonates (10% v/v and below) follow the Arrhenius law, as exemplified by the linearity of the curves in **Figure 3.3B**. For clarity purposes, only the solutionsof $FcEImC_4$ are presented in **Figure 3.3B**, but solutions of the other cations presented the same behavior. **Table 3.2** presents the conductivity of dilute solutions of the RILs at different concentrations in the mixture of carbonates, with and without LiTFSI. At very low concentrations (1 and 10 vol%) of ionic liquid the transport of Li^+ and $TFSI^-$ ions have a higher impact on the conductivity of the solution than the other components of the solution. At these concentrations, the

ionic liquids have only a slight effect on the viscosity. Expectedly, the ferrocenylimidazolium alkyl chain length does not affect the conductivity significantly at these low concentrations. With an increase of the RIL concentration, the impact of side chain length on conductivity becomes significant and the trend observed is the same as for the pure ionic liquids (see above). Since the foreseen applications of redox ionic liquids will involve adding high concentrations of RIL in solvents (if a use in pure form is not possible), the impact of the size of the cation has an influence on the transport properties of the resulting electrolyte. The effect of alkyl chain length is however less drastic than in their pure form. **Table 3.2** also shows the detrimental effect of Li^+ on the viscosity and conductivity of concentrated ionic liquid solutions (50% vol.). As is it now well established,[16] TFSI coordinates with lithium ions, resulting in the formation of a solvated species as $[Li(TFSI)_2]^-$. The additional amount of TFSI brought by the ionic liquid in high concentrations favors the formation of the complex and decreases the conductivity. The effect of Li coordination by TFSI on the solution can be further studied by self-diffusion measurements.

Table 3.2. Ionic conductivities and viscosities of RIL solutions in EC/DEC 1:2 (v/v) at 25°C

RIL ratio v/v (%)	[LiTFSI] / M	σ $FcEImC_1$ / mS cm^{-1}	σ $FcEImC_4$ / mS cm^{-1}	σ $FcEImC_8$ / mS cm^{-1}	σ $FcEImC_{12}$ / mS cm^{-1}	Activation Energy / kJ mol^{-1}	Viscosity / cP
50	0	4.0 (2.7[a])	4.2 (3.1[a])	3.0 (2.4[a])	2.2 (1.8[a])	13-16	10-14
50	1.5	1.5	2.1	0.9	0.8	~25	86-111
10	1.5	5.5	5.6	5.0	4.4	13-16	7-11
1	1.5	6.2	6.3	6.1	5.8	13-16	5-8

[a] (Molar conductivity of 50% without 1.5 M LiTFSI / S cm^2 mol^{-1})

Self-diffusion

Pulsed field gradient stimulated echo (PFG-STE) NMR was used to compare the self-diffusion of individual constituents of the carbonate solutions of the redox ionic liquid $FcEImC_4$-TFSI. **Table 3.3** presents the self-diffusion coefficients of these constituents with various

concentrations of redox ionic liquid as well as for the pure carbonate solvent. The coefficients for the $FcEImC_4$ and the TFSI in solution at 50% vol. are different, suggesting that they are not strongly associated even at high concentrations. In comparison, self-diffusion coefficients for pure imidazolium-TFSI ionic liquids show very similar values.[15] Addition of 1.5 M of LiTFSI to the 50% vol. solution caused a significant decrease in the mobility of all constituents, including solvent, due to the higher viscosity (see **Table 3.2**). When the concentration in $FcEImC_4$-TFSI was decreased to 1% vol., both Li^+ and $TFSI^-$ ions had the same diffusivity they had without any $FcEImC_4$-TFSI. As discussed above, they are at this low concentration in RIL the constituents with the major impact on conductivity, explaining why the effect of the alkyl chain length is not seen at 1% vol.

The self-diffusion coefficient of both $FcEImC_4^+$ and $TFSI^-$ in the 50% vol. solution can used to calculate the equivalent molar conductivity (NMR) using Equation 2, where D_X is the self-diffusion coefficient of the ionic specie X, and F, R and T are the Faraday constant, ideal gas constant and temperature, respectively.

$$\Lambda_{NMR} = F^2\left(D_{FcEImC_4^+} + D_{TFSI^-}\right)/RT \qquad (2)$$

The Λ_{NMR} obtained is 4.4 $S \cdot cm^2 \cdot mol^{-1}$, while Λ_{cond} (calculated from conductivity measurements, **Table 3.2**) is 3.1 $S \cdot cm^2 \cdot mol^{-1}$. The $\Lambda_{cond}/\Lambda_{NMR}$ ratio of 0.70 shows a significant degree of association between the cations and anions even solution (50% vol.) since a ratio of 1 would mean that the actual diffusion of the molecules (NMR) occurs at the same rate as the transport of charges (conductivity). The association of ions, responsible for the lower molar conductivity, in the pure melt is likely more pronounced than in unmodified imidazolium counterparts explaining the low conductivity of the ionic liquid.

Table 3.3. Self-diffusion coefficient of $FcEImC_4$-TFSI at different concentrations in EC:DEC (1:2) solvent.

RIL Ratio	[LiTFSI]	Self-diffusion coefficients / $cm^2\ s^{-1}$				
v/v / %	/ M	Li^+	EC	DEC	$FcEImC_4^+$	$TFSI^-$
50	0	x	1.3×10^{-6}	1.6×10^{-6}	4.8×10^{-7}	7.0×10^{-7}
50	1.5	9.4×10^{-8}	1.3×10^{-7}	1.7×10^{-7}	7.5×10^{-8}	1.0×10^{-7}
10	1.5	7.6×10^{-7}	1.5×10^{-6}	1.5×10^{-6}	6.7×10^{-7}	8.9×10^{-7}
1	1.5	1.1×10^{-6}	2.2×10^{-6}	2.2×10^{-6}	9.7×10^{-7}	1.3×10^{-6}
0	1.5	1.1×10^{-6}	2.3×10^{-6}	2.4×10^{-6}	x	1.6×10^{-6}
0	0	x	9.7×10^{-6}	9.2×10^{-6}	x	x

Electrochemistry

While the alkyl chain length significantly affects the transport properties of the redox ionic liquid at high concentrations, its effect on the redox potential should be minimal due the lack of a strong electron withdrawing or donating effect of alkyl groups. Cyclic voltammograms were recorded for all four RIL dissolved at 10% vol. in EC:DEC (1:2) solutions with 1.5 M LiTFSI as supporting electrolyte. The curves, presented in **Figure 3.4A** show very similar equilibrium potentials for all compounds, at a value of ca. 180 mV more positive of the ferrocene/ferrocenium couple under the same conditions. This displacement of the potential toward higher values is due to withdrawing effect of the imidazolium ring. The oxidation peak also appears to be slightly affected by the chain length with the values of $E_{p,a}$ increasing by ca. 50 mV between the C_{12} and the C_1 and C_4. This could be due to a migrational component to the overall mass transport. A 10% vol. solution, the concentration used in **Figure 3.4A**, represents a concentration in $FcEImC_n$ of ca. 0.1–0.13 M, only 10 times the concentration of the supporting electrolyte. The electrochemical response of $FcEImC_4$-TFSI at various concentrations was studied further to evaluate the effect of the solution composition. **Figure 3.4B** shows the cyclic voltammograms of these solutions recorded at

100 mV s^{-1}. The shape of the oxidation peak on the cyclic voltammograms at 50% vol. is clearly distorted, the peak being at a higher potential value than expected for a purely diffusional regime. This displacement of the oxidation peak toward positive values causes the shift in the redox potentials listed in **Table 3.4** for the higher concentrations. At low concentration (i.e. 1% vol.) all solutions showed the same redox potential of 160 mV vs. Fc^{+}/Fc. A significant peak potential splitting is noticed and increases with the concentration in RIL and is attributed to the iR drop. **Table 3.4** also shows a higher oxidation limit (at which the current increases by 10% from the background value) for the solutions with a larger proportion of the ionic liquid due to its better electrochemical stability. The solutions with low concentrations of RIL were limited by the oxidation of the carbonate mixture.

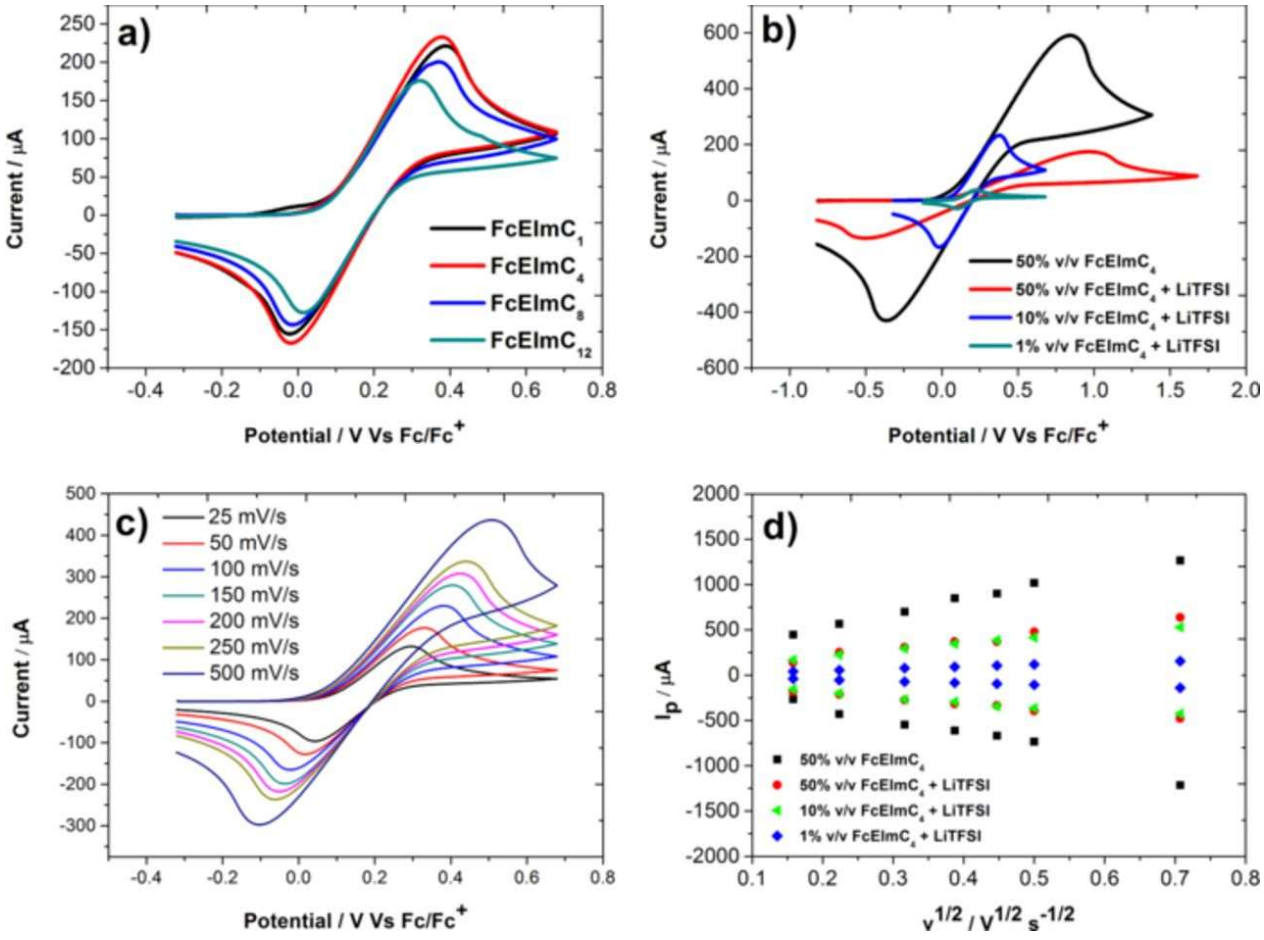

Figure 3.4. Cyclic voltammograms (scan rate of 100 mV s^{-1}) for a) a 10% solution of RILs in EC/DEC 1:2 with 1.5 M LiTFSI and b) different concentrations of $FcEImC_4$ (1, 10 and 50%) in EC/DEC 1:2 with and without 1.5 M LiTFSI. c) CVs of 10% $FcEImC_4$ in EC/DEC 1:2 (v/v) with 1.5 M LiTFSI at scan rates ranging from 25–500 mV s^{-1}; d) Randles Sevcik Plot of I_p vs $v^{1/2}$.

Table 3.4. Equilibrium potentials for $FcEImC_n$-TFSI and the oxidation limit of the RIL in solution. Data was obtained from CV recorded at 100 mV $\cdot s^{-1}$ and all potentials are given vs. the Fc^+/Fc couple (+0.55 V vs. NHE).

RILs	RIL ratio / %	[LiTFSI] / M	E' / V	ΔE_{pa-pc} / V	Ox limit / V
$FcEImC_1$	50	0	0.23	1.12	2.84
	50	1.5	0.23	1.29	2.16
	10	1.5	0.19	0.41	1.78
	1	1.5	0.16	0.11	1.62
$FcEImC_4$	50	0	0.24	1.21	2.61
	50	1.5	0.23	1.47	2.38
	10	1.5	0.18	0.40	1.99
	1	1.5	0.16	0.11	2.08
$FcEImC_8$	50	0	0.27	1.14	2.69
	50	1.5	0.27	1.24	2.37
	10	1.5	0.18	0.39	1.61
	1	1.5	0.16	0.11	1.59
$FcEImC_{12}$	50	0	0.23	1.09	2.74
	50	1.5	0.21	1.25	2.67
	10	1.5	0.17	0.31	2.56
	1	1.5	0.16	0.11	1.58

Table 3.5. Diffusion coefficients for oxidation of RIL ($FcEImC_1$, $FcEImC_4$, $FcEImC_8$ and $FcEImC_{12}$)

RIL	[LiTFSI]	D_R / $cm^2\ s^{-1}$			
Ratio v/v /%	/ M	$FcEImC_1$	$FcEImC_4$	$FcEImC_8$	$FcEImC_{12}$
50	0	2.9×10^{-8}	4.3×10^{-8}	1.4×10^{-8}	1.5×10^{-8}
50	1.5	2.1×10^{-9}	1.4×10^{-8}	5.1×10^{-9}	1.6×10^{-9}
10	1.5	2.9×10^{-8}	2.0×10^{-7}	2.2×10^{-7}	8.7×10^{-8}
1	1.5	2.8×10^{-7}	2.1×10^{-6}	2.4×10^{-6}	4.8×10^{-7}

Figure 3.4C shows the cyclic voltammograms of a 10% vol. solution of $FcEImC_4$-TFSI recorded at various scan rates. The effect of scan rate on peak current for all concentrations of $FcEImC_4$-TFSI is shown in **Figure 3.4D** and the diffusion coefficients (all four ionic liquids) of **Table 3.5** were calculated from the Randles-Sevcik equation (Equation 3);

$$i_p = 0.4463\, nFAC \left(\frac{nF\nu D}{RT}\right)^{\frac{1}{2}} \qquad (3)$$

where ip is the peak current (A), n the equivalent number of electrons exchanged during the reaction, A the surface area of the electrode (cm^2), C the concentration (mol/cm^3), D the diffusion coefficient (cm^2/s), T the temperature (K) ν the potential scan rate (V/s), F and R are the Faraday (C/mol) and ideal gas ($J/mol \cdot K$) constants, respectively. As expected from the conductivity measurements, the addition of Li salt to highly concentrated solutions decreased the diffusion of the electroactive species because of an increase in viscosity (see above). The diffusion coefficient of $FcEImC_4$-TFSI and $FcEImC_8$- TFSI are very similar in solutions at 10% vol. and below. These values concur with the conductivities of the solutions (Table 3.2). While the radius of the molecule is expected to increase between a butyl and an octyl side chain, the latter has also more flexibility to rearrange and to fold. This conformation of the side chain could provide an effective radius similar to the C_4 chain.

3.2.5. Conclusions

We studied the conductivity and electrochemistry of a series of ferrocene-modified imidazolium redox ionic liquids to evaluate the effect of the alkyl side chain length on the properties of the pure phase and on their solutions. With an increase in the length of the side chain, the ionic conductivities of neat RILs decrease, a trend which is also found in similar but unmodified imidazolium ionic liquids. The impact of the increase in side chain length for RIL is less pronounced than in common ILs, because the degree of freedom is limited by the ionic mobility of the large cation. The mass transport of RIL is affected by the side chain, but the equilibrium potential is not affected because the modification is done in opposite side on the structure of the imidazolium cation. Further investigation on the nature of the interactions between ferrocenyl and imidazolium in these redox ionic liquids will be necessary to develop RIL with lower viscosity.

3.2.6. Acknowledgments

The authors acknowledge the financial support from Fonds de recherche du Quebec en nature et technologies (FQRNT) under their ´ program for the reduction of greenhouse gases.

3.2.7. References

[1] J.S. Wilkes, M.J. Zaworotko, Air and water stable 1-ethyl-3-methylimidazolium based ionic liquids, J. Chem. Soc., Chem. Commun., (1992) 965-967.
[2] B.D. Fitchett, T.N. Knepp, J.C. Conboy, 1-Alkyl-3-methylimidazolium bis(perfluoroalkylsulfonyl)imide water-immiscible ionic liquids - The effect of water on electrochemical and physical properties, J. Electrochem. Soc., 151 (2004) E219-E225.
[3] P. Bonhote, A.P. Dias, N. Papageorgiou, K. Kalyanasundaram, M. Gratzel, Hydrophobic, highly conductive ambient-temperature molten salts, Inorg. Chem., 35 (1996) 1168-1178.
[4] L.P.N. Rebelo, J.N.C. Lopes, J. Esperanca, E. Filipe, On the critical temperature, normal boiling point, and vapor pressure of ionic liquids, J. Phys. Chem. B, 109 (2005) 6040-6043.
[5] W. Wang, R. Balasubramanian, R.W. Murray, Electron transport and counterion relaxation dynamics in neat ferrocenated imidazolium ionic liquids, J. Phys. Chem. C, 112 (2008) 18207-18216.
[6] R. Balasubramanian, W. Wang, R.W. Murray, Redox ionic liquid phases: Ferrocenated imidazoliums, J. Am. Chem. Soc., 128 (2006) 9994-9995.
[7] O. Fontaine, C. Lagrost, J. Ghilane, P. Martin, G. Trippé, C. Fave, J.C. Lacroix, P. Hapiot, H.N. Randriamahazaka, Mass transport and heterogeneous electron transfer of a ferrocene derivative in a room-temperature ionic liquid, J. Electroanal. Chem., 632 (2009) 88-96.
[8] J.E.F. Weaver, D. Breadner, F. Deng, B. Ramjee, P.J. Ragogna, R.W. Murray, Electrochemistry of ferrocene-functionalized phosphonium ionic liquids, J. Phys. Chem. C, 115 (2011) 19379-19385.
[9] T. Inagaki, T. Mochida, Metallocenium ionic liquids, Chem. Lett., 39 (2010) 572-573.
[10] V.O. Nyamori, M. Gumede, M.D. Bala, Synthesis, characterisation and properties of ferrocenylalkylimidazolium salts, J. Organomet. Chem., 695 (2010) 1126-1132.
[11] J.C. Forgie, S. El Khakani, D.D. MacNeil, D. Rochefort, Electrochemical characterisation of a lithium-ion battery electrolyte based on mixtures of carbonates with a ferrocene-functionalised imidazolium electroactive ionic liquid, Phys. Chem. Chem. Phys., 15 (2013) 7713-7721.
[12] E.O. Stejskal, J.E. Tanner, Spin diffusion measurements: Spin echoes in the presence of a time-dependent field gradient, J. Chem. Phys., 42 (1965) 288-+.
[13] H. Tokuda, S. Tsuzuki, M.A.B.H. Susan, K. Hayamizu, M. Watanabe, How ionic are room-temperature ionic liquids? An indicator of the physicochemical properties, J. Phys. Chem. B, 110 (2006) 19593-19600.
[14] W. Xu, E.I. Cooper, C.A. Angell, Ionic liquids: Ion mobilities, glass temperatures, and fragilities, J. Phys. Chem. B, 107 (2003) 6170-6178.
[15] H. Tokuda, K. Hayamizu, K. Ishii, M. Susan, M. Watanabe, Physicochemical properties and structures of room temperature ionic liquids. 2. Variation of alkyl chain length in imidazolium cation, J. Phys. Chem. B, 109 (2005) 6103-6110.
[16] A. Andriola, K. Singh, J. Lewis, L. Yu, Conductivity, viscosity, and dissolution enthalpy of LiNTF2 in ionic liquid BMINTF2, J. Phys. Chem. B, 114 (2010) 11709-11714.

3.3. Supplementary Material

3.3.1. Synthesis

Preparation of N,N-dimethylaminomethylferrocene methiodide [1]. To a cooled solution of 6.00 g (23.24 mMol) of N,N-dimethylaminomethylferrocene in 1.54 ml (51 mMol) of absolute methanol was added dropwise a solution of 1.54 ml (24.74 mMol) methyl iodide. The solution was heated to 75°C for 10 minutes. The brown solid obtained was crushed and then washed on filter paper with ether until the washings were colorless. The resulting precipitate was dried under vacuum to obtain 8.01 g of the product (yield: 86%). ^{1}H NMR (300 MHz, $CDCl_3$) δ (ppm): 4.89 (s, 2H); 4.56 (s, 2H); 4.33 (s, 2H); 4.29 (s, 5H); 3.30 (s, 9H).

Preparation of hydroxymethylferrocene [1]. To a solution of 1.71 g (1.07 M) of sodium hydroxide in 40 ml of distilled water was dissolved 4.01 g (10.39 mMol) of N,N-Dimethylaminomethylferrocene methiodide. The mixture was heated to and held at 135°C for 3 hours. After cooling down to room temperature, the compound was extracted from the aqueous phase with 4 volumes of 100 ml of ether which were combined afterwards and washed with several volumes of distilled water. The organic solution was dried over magnesium sulfate and after filtering, the solvent was removed under vacuum to provide a yellow powder. Using this procedure, 1.28 g of compound was obtained, corresponding to yield of 57%. ^{1}H NMR (300 MHz, $CDCl_3$) δ (ppm): 4.22-4.10 (m, 11H); 1.50 (s, 1H).

Preparation of N-(Ferrocenylmethyl)imidazole [2]. In 13 ml of dichloromethane, 2.48 g (11.48 mMol) of hydroxymethylferrocene and 1.94 g (11.96 mMol) of 1,1'-carbonyldiimidazole, corresponding to equal molar equivalents, were dissolved. The mixture was heated at 65°C for 3 hours. After cooling to room temperature, 100 ml of ether was added to the mixture and the solution was washed with 4 volumes of 100 ml of 20% phosphoric acid aqueous solution. 2 M aqueous solution of sodium hydroxide was added to the solution until it reached a pH of 5. The solution was extracted with dichloromethane until the aqueous layer became colorless. The solution was concentrated under vacuum and the concentrated solution was dried over sodium sulfate. After filtering, the solvent was removed to obtain 1.73 g (yield: 56%) of product. ^{1}H NMR (300 MHz, $CDCl_3$) δ (ppm): 7.55 (s, 1H); 7.12 (s, 2H); 4.84 (s, 2H); 416-4.14 (m, 9H).

Preparation of 1-(Ferrocenylmethyl)-3-alkylimidazolilium halide [3]. In 10 ml of acetonitrile, 1.00 g (3.744 mMol) of N-(Ferrocenylmethyl)imidazole was dissolved and an equal molar equivalent of 1-halide-alkane (Iodomethane, 1-bromobutane, 1-bromooctane 1-bromododecyl) was added. The solution was heated to 50°C for 15 hours. The solvent was removed and washed several times with ether. The brown oil was recrystallized with dichloromethane/hexane**.** **[FcEImC$_1$ I]** ^{1}H NMR (300 MHz, DMSO-d$_6$) δ (ppm) : 9.08 (s, 1H); 7.75 (t, 1H); 7.66 (t, 1H); 5.17 (s, 2H); 4.44 (t, 2H); 4.24 (m, 7H); 3.82 (s, 3H). **[FcEImC$_4$ Br]** ^{1}H NMR (300 MHz, CDCl$_3$) δ (ppm) : 10.40 (s, 1H); 7.25 (s, 2H); 5.40 (s, 2H); 4.40 (s, 2H); 4.35-4.15 (m, 9H); 1.90 (q, 2H); 1.3(q, 2H); 0.9 (t, 3H). **[FcEImC$_8$ Br]** ^{1}H NMR (300MHz, DMSO-d$_6$) δ (ppm): 9.24 (s, 1H); 7.77 (s, 2H); 5.15 (s, 2H); 4.41 (s, 2H); 4.22-4.21 (m, 9H); 1.74 (q, 2H); 1.21 (s, 10H); 0.83 (t, 3H). **[FcEImC$_{12}$ Br]** ^{1}H NMR (300 MHz, DMSO-d$_6$) δ (ppm): 9.24 (s, 1H); 7.77 (s, 2H); 5.15 (s, 2H); 4.44 (s, 2H); 4.22-4.21 (m, 9H); 1.74 (q, 2H); 1.21 (s, 18H); 0.83 (t, 3H).

Preparation of 1-(Ferrocenylmethyl)-3-alkylimidazolilium bis(trifluoromethane-sulfonyl)imide [4]. The 1-(Ferrocenylmethyl)-3-alkylimidazolium bromide or iodide obtained in the prior step was dissolved in a minimum volume of water. In some case, the solution had to be heated to 90°C to achieve complete dissolution. The imidazolium aqueous solution was added dropwise to a solution of 1.2 molar equivalents of lithium bis(trifluoromethanesulfonyl)imide that was dissolved in a minimum amount of water. For 2 hours, the combined solution was mixed in an ultrasound bath and afterwards allowed to settle for 12 hours. The water excess was carefully removed and the resulting ionic liquid phase was dissolved in dichloromethane. The brown solution was washed 3 times with water. The solution was dried with magnesium sulfate and after filtering, the solvent was removed. All the 1-(Ferrocenylmethyl)-3-alkylimidazolium ionic liquids obtained through this synthetic method are highly viscous dark-brown liquids. **[FcEImC$_1$ TFSI]** ^{1}H NMR (300 MHz, DMSO-d$_6$) δ (ppm) : 9.06 (s, 1H); 7.73 (t, 1H); 7.64 (t, 1H); 5.16 (s, 2H); 4.43 (t, 2H); 4.24 (m, 7H); 3.82 (s, 3H). ^{13}C NMR (125 MHz, DMSO-d$_6$) δ (ppm) : 135.85; 123.58; 121.99; 120.74; 80.89; 68.91; 68.85; 68.69; 48.28; 35.75. (ESI) m/z: [M*$^+$](C$_{15}$H$_{17}$FeN$_2$): 281.07444 and [M*$^-$](C$_2$F$_6$NO$_4$S$_2$): 279.9178 **[FcEImC$_4$ TFSI]** ^{1}H NMR (300 MHz, DMSO-d$_6$) δ (ppm): 9.24 (s, 1H); 7.77 (s, 2H); 5.147 (s, 2H); 4.41 (s, 2H); 4.22-4.21 (m, 9H); 1.74 (q, 2H); 1.21 (q, 2H); 0.83 (t, 3H). ^{13}C NMR (125 MHz, DMSO-d$_6$) δ (ppm) : 135.97; 122.76; 121.26; 118.7 ; 81.48; 69.20; 49.11; 48.85; 31.75; 19.27; 13.68. (ESI) m/z: [M*$^+$](C$_{18}$H$_{23}$FeN$_2$): 323,1215 and [M*$^-$](C$_2$F$_6$NO$_4$S$_2$): 279.9178. **[FcEImC$_8$ TFSI]** ^{1}H NMR (300 MHz, DMSO-d$_6$) δ (ppm): 9.24 (s, 1H);

7.77 (s, 2H); 5.15 (s, 2H); 4.41 (s, 2H); 4.22-4.21 (m, 9H); 1.74 (q, 2H); 1.21 (s, 10H); 0.83 (t, 3H). ^{13}C NMR (125 MHz, DMSO-d_6) δ (ppm): 135.81; 122.82; 121.24; 118.66; 81.34; 69.32; 49.34; 48.84; 31.51; 29.68; 28.93; 28.78; 28.68; 25.94; 22.51; 14.28. (ESI) m/z: [M*$^+$]($C_{22}H_{31}FeN_2$): 377.1887 and [M*$^-$]($C_2F_6NO_4S_2$): 279.9180. **[FcEImC$_{12}$ TFSI]** ^{1}H NMR (300 MHz, DMSO-d_6) δ (ppm): 9.24 (s, 1H); 7.77 (s, 2H); 5.15 (s, 2H); 4.41 (s, 2H); 4.22-4.21 (m, 9H); 1.74 (q, 2H); 1.21 (s, 18H); 0.83 (t, 3H). ^{13}C NMR (125 MHz, DMSO-d_6) δ (ppm): 135.88; 122.92; 121.26; 118.70; 81.48; 69.16; 49.11; 48.85; 31.76; 29.45; 29.35; 29.27; 29.18; 28.78; 25.96; 22.55; 22.55; 14.37. (ESI) m/z: [M*$^+$]($C_{26}H_{39}FeN_2$): 433.2516 and [M*$^-$]($C_2F_6NO_4S_2$): 279.9176.

3.3.2. References

[1] J.K. Lindsay, C.R. Hauser, Aminomethylation of ferrocene to form N,N-dimethylaminomethylferrocene and its conversion to the corresponding alcohol and aldehyde1, J. Org. Chem., 22 (1957) 355-358.

[2] A.A. Simenel, E.A. Morozova, Y.V. Kuzmenko, L.V. Snegur, Simple route to ferrocenyl(alkyl)imidazoles, J. Organomet. Chem., 665 (2003) 13-14.

[3] V.O. Nyamori, M. Gumede, M.D. Bala, Synthesis, characterisation and properties of ferrocenylalkylimidazolium salts, J. Organomet. Chem., 695 (2010) 1126-1132.

[4] P. Bonhôte, A.-P. Dias, N. Papageorgiou, K. Kalyanasundaram, M. Grätzel, Hydrophobic, highly conductive ambient-temperature molten salts, Inorg. Chem., 35 (1996) 1168-1178.

Chapitre 4: Synthèse et caractérisation d'un liquide ionique utilisant un anion électroactif

4.1. Avant-propos et mise en contexte

Ce chapitre a été rédigé sous forme d'un article qui a été soumis à *Electrochimica Acta*. Outre les liquides ioniques basés sur les iodures et bromures comme anion électroactifs, la littérature est pratiquement inexistante sur les liquides ioniques fonctionnalisés utilisant un anion redox. Donc, cette investigation a une contribution considérable pour établir les bases pour cette nouvelle classe de liquide ionique électroactif. Nous avons choisi de se baser sur l'anion bis(trifluorométhanesulfonyl)imide, car l'introduction de celui-ci dans les piles au lithium-ion est très bien documenté dans la littérature et le plus important, la voie de synthèse d'anion de di(sulfonyl)imide asymétrique est connu dans la littérature. En résumé, l'article présente une comparaison entre ce nouveau liquide ionique électroactif avec le ferrocène et le liquide ionique non-électroactif.

4.2. Article: Synthesis and characterization of an electroactive ionic liquid based on the ferrocenylsulfonyl(trifluoromethylsulfonyl)imide anion

Bruno Gélinas[a] and Dominic Rochefort[a],

[a]Département de Chimie, Université de Montréal, Montréal, Québec H3C 3J7, Canada

Electrochimica Acta 162 (2015) 36–44

Article history: Received 17 July 2014, Received in revised form 24 November 2014, Accepted 25 November 2014, Available online 26 November 2014. http://dx.doi.org/10.1016/j.electacta.2014.11.154 0013-4686/

4.2.1. Highlights

- A new redox ionic liquid is obtained by the modification of the NTf_2 anion.
- The equilibrium potential of BMIm FcNTf was found at +224 mV vs. Fc/Fc^+.
- Steric effect of anion decreased the transport and charge transfer rate of FcNTf.
- Electrochemistry of self-supported BMIm FcNTf solutions showed film formation.

4.2.2. Abstract

This work is a report on the synthesis and characterization of a new electroactive redox ionic liquid employing a redox anion. The physicochemical and electrochemical properties of 1-butyl-3-methylimidazolium ferrocenylsulfonyl-(trifluoromethylsulfonyl)-imide (BMIm FcNTf) were investigated in its neat form, as dissolved in electrolytes and compared to 1-butyl-3-methylimidazolium bis (trifluoromethylsulfonyl) imide (BMIm NTf_2) and ferrocene (Fc). The thermal properties of pure BMIm FcNTf were determined by thermogravimetric analysis (TGA) and modulated DSC which showed that the grafting of Fc on the ionic liquid results in a higher melting point and lower decomposition temperature. Ionic conductivity and viscosity were, like unmodified ionic liquids, well-described with the VolgelTammann-Fulcher (VTF) function, but the BMIm FcNTf showed a higher viscosity and lower conductivity due to the additional

intermolecular interactions resulting from the ferrocene moiety on the anion. Diffusion, redox potential and heterogeneous rate constants were then evaluated in diluted solutions of BMIm FcNTf in acetonitrile with a supporting electrolyte using cyclic voltammetry (CV), rotating disk electrode voltammetry (RDE) and double potential step chronoamperometry (DPSC) to study the impact of grafting a trifluoromethylsulfonylimide group on ferrocene. Square wave voltammetry (SWV) was employed to evaluate the supporting electrolyte's effect on the equilibrium potential of BMIm FcNTf.

Graphical abstract

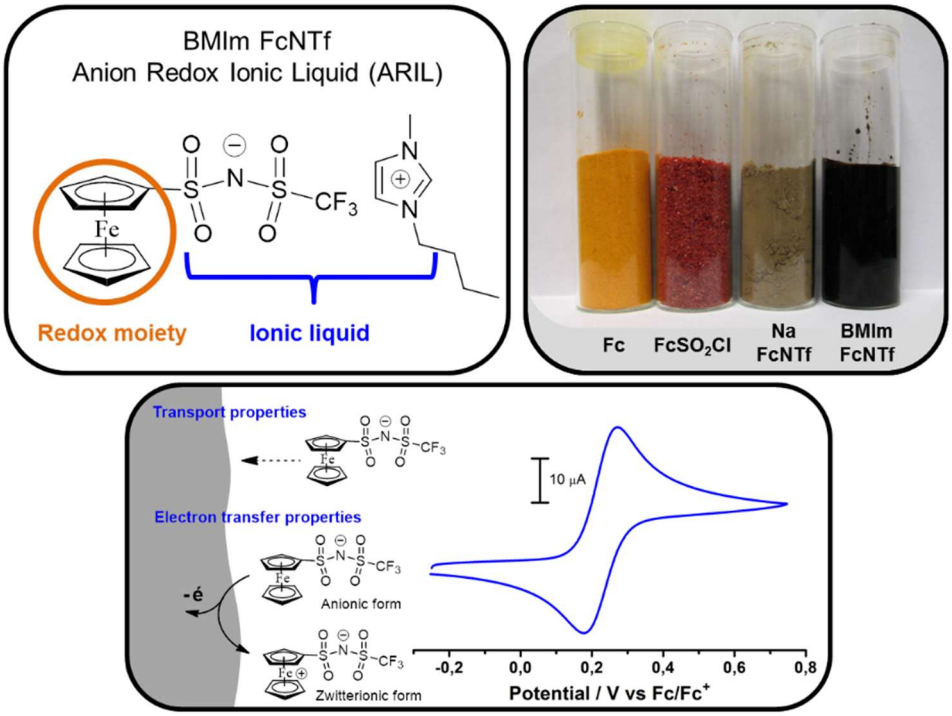

Keywords: redox ionic liquid, functional ionic liquid, solvation, ionic conductivity, heterogeneous electron transfer rate

4.2.3. Introduction

Ionic liquids (ILs), defined as salts having a melting point below 100°C, are very attractive media in electrochemistry due to their intrinsic conductivity, low vapor pressure, high thermal stability and large window of electrochemical stability.[1-5] They have been suggested as an alternative to molecular solvents for countless applications and in various systems and devices. Research on ILs is motivated in large part by the many possible chemical modifications that can be made to one of their components to impart a specific functionality to the melt. These so-called functionalized or task-specific ILs (TSILs) have been developed for many applications such as metal ion extraction,[6] organic synthesis,[7] CO_2 capture (separation),[8] extraction,[9] transition metal catalysis,[10] nanoparticle synthesis,[11] self-assembled monolayer formation[12] and electrochemistry.[13, 14] A clear example of TSILs relevant to the field of electrochemistry is found through the modification of alkylimidazoliums with a ferrocenyl redox moiety, resulting in an intrinsically electroactive liquid. Such redox-active ionic liquids (RIL) have been developed in the recent years to study electron transfer in highly concentrated solutions.[15, 16]

As the work of Murray and collaborators on ferrocene-modified IL demonstrated,[14, 17] the investigation of such RILs can lead to new knowledge on electron transfer in liquid phases due to the intimate proximity of redox centers that cannot be achieved in solute-solvent systems. However, there are very few reports on electroactive ILs and there is a very narrow array of available structures and given that the design of a new RIL is hindered by a lack of knowledge of their structure-properties relationships.[18-24] In addition, the current library of RILs almost exclusively contains structures based on the modification of alkylimidazoliums, with some exceptions from reports on ferrocene-functionalized phosphonium IL[14, 25] and metallocenium ILs.[26, 27] Our group reported on the development of RIL as redox additive in electrolytes for lithium-ion batteries to protect the cathode against overcharging.[28, 29] Cathode overcharging can lead to electrode and electrolyte degradation and thermal runaway which is aggravated by the use of solvents with a high vapor pressure.[30-32] This situation can be avoided through the use of an electroactive species added to the electrolyte that prevents overcharging by shuttling the excess current away from the cathode in the so-called redox shuttle mechanism.[33] The strategy employed combined the excellent thermal properties of ILs with a redox-active group available for use in LIBs.

A new type of RIL was reported in which the anion was modified with an electroactive moiety instead of the cation. This RIL was obtained by modifying bis(trifluoromethylsulfonyl) imide (NTf_2) anion with ferrocenyl, which was used with a common imidazolium cation to yield 1-butyl-3-methylimidazolium ferrocenylsulfonyl (trifluoromethylsulfonyl) imide (BMIm FcNTf, **Figure 4.1**). The goal of this study was to establish the impact of the physicochemical and electrochemical properties of intrinsically electroactive IL phases to RIL based on ferrocene tethered to NTf moiety and compare with the unmodified IL,1-butyl-3-methylimidazolium bis (trifluoromethylsulfonyl) Imide (BMIm NTf_2, **Figure 4.1**) and the electrochemical properties of ferrocene (Fc).

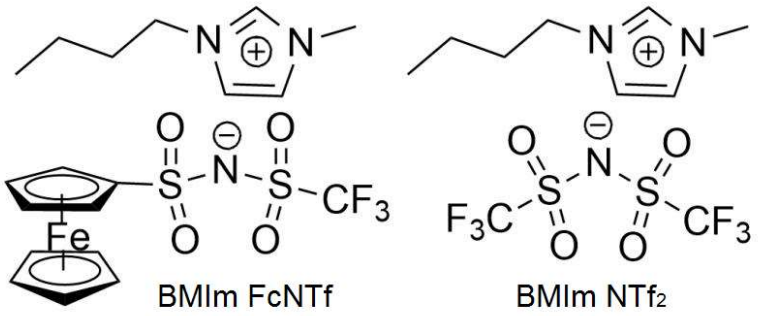

Figure 4.1. Chemical structure of 1-butyl-3-methylimidazolium ferrocenylsulfonyl (trifluoromethylsulfonyl)imide (BMIm FcNTf) and 1-butyl-3-methylimidazolium bis(trifluoromethylsulfonyl)imide (BMIm NTf_2).

4.2.4. Experimental

Chemicals

The reagents used were ferrocene, chlorosulfonic acid, phosphorus trichloride, anhydrous sodium carbonate, 1-methylimidazole and 1-bromobutane which were obtained from Sigma-Aldrich (unless stated otherwise). Trifluoromethanesulfonamide was purchased from Synquest Laboratories and solvents were obtained from Fisher. These were used as received. All synthesized compounds were characterized by ^{1}H and ^{13}C NMR on a Bruker AMX 300 MHz spectrometer at room temperature using DMSO-d_6 and by electrospray ionization mass spectrometry. Accurate mass values were obtained by Agilent LC-MSD TOF. Elemental analysis of the BMIm FcNTf was

performed on an EAS 1108 apparatus from a Fisons Instruments SPA. The water used in the procedures was purified with a Milli-Q system to a resistivity of 18.2 MΩ cm (25°C).

Synthesis

The synthetic steps of BMIm FcNTf are summarized in **Figure 4.2** and detailed below. This synthetic pathway was followed to obtain an asymmetric version of NTf_2 which can be adapted to modify the anion with other functional groups. The overall yield obtained for the BMIM FcNTf following the synthetic pathway (**Figure 4.2**) was 31%. The ^{1}H, ^{13}C and ^{19}F NMR for the BMIm FcNTf are provided in **Figure S4.5 to S4.7** and the details of the ^{1}H NMR of each intermediate are provided in the Supporting Information.

Preparation of ferrocenesulfonyl chloride (2): Ferrocenesulfonyl chloride was synthesized according to a process given in the literature [34]: Yield: 56% and red crystal. ^{1}H NMR (DMSO-d_6, 300 MHz): d (ppm) = 4.99 (s, 2H), 4.81 (s, 2H), 4.46 (s, 5H). m.p. 99°C.

Preparation of sodium ferrocenylsulfonyl(trifluoromethylsulfonyl) imide (3): trifluoromethanesulfonamide was dissolved in a flask in acetonitrile and anhydrous sodium carbonate was added. The solution was stirred for 10 minutes at room temperature. A slow addition of ferrocenesulfonyl chloride was then made. The resulting solution was stirred and heated at reflux temperature (90 °C) for 24 hours. The brown solution was filtered and the precipitate was washed with acetone to achieve a white precipitate. Removal of the solvent under reduced pressure produced a brown product. A mixture of THF/Hexane was used for the recrystallization, obtaining a light brown powder. A better purification was done in the following step to remove sodium ((trifluoromethyl) sulfonyl) amide. Yield: 67%. ^{1}H NMR (DMSO-d_6, 300 MHz): d (ppm) = 4.53 (t, 2H), 4.28 (s, 7H). ^{19}F NMR (DMSO-d_6, 282 MHz): d (ppm) = -77.62. ^{13}C NMR (DMSO-d_6, 125 MHz): d (ppm) = 121.90; 119.32; 94.61; 70.44; 69.19; 68.61. (ESI) m/z: [M^{*-}] (calcd for $C11H9F3FeNO4S2^{-}$): 395.928 Found: 395.926.

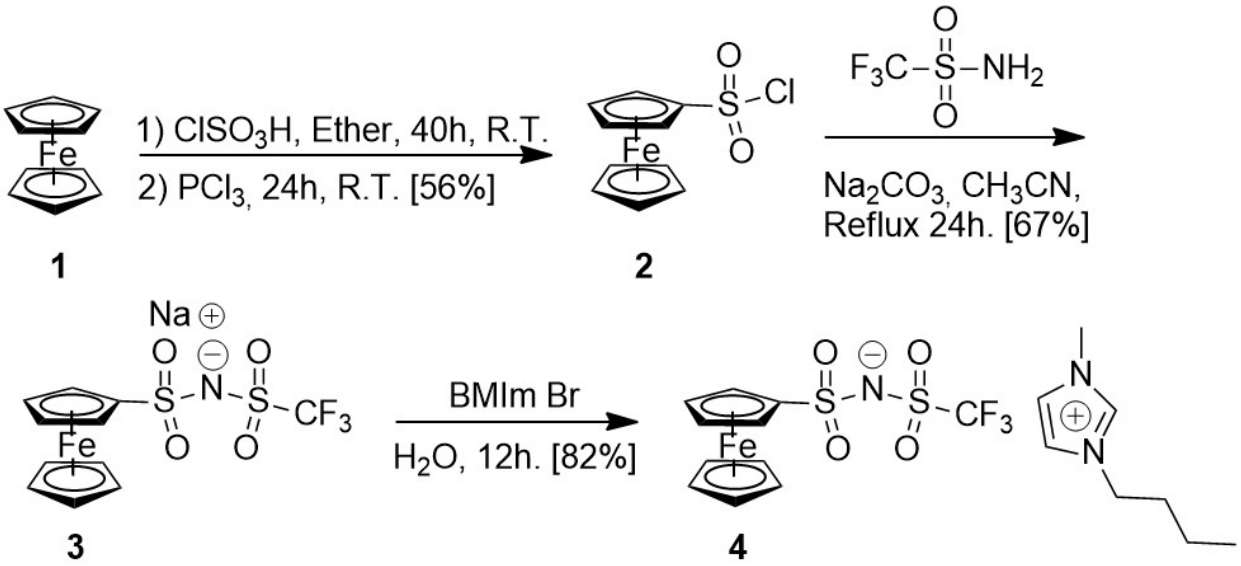

Figure 4.2. Synthetic pathway of BMIm FcNTf.

Thermal analysis

Thermogravimetric analysis (TGA) was performed using a TGA 2950, TA Instruments, and measurements were performed under nitrogen ranging from room temperature to 600 °C with a ramp of 10 °C per minute. Weight loss by decomposition was corrected to remove artifacts such the presence of water and temperature decomposition was determined to be 5% weight loss. Modulated differential scanning calorimetry (DSC) was performed on DSC TA Q2000 using universal analysis software. The measurements were taken between -50 to 65 °C during 2 cycles with a ramp of 1 °C per minute and with an isothermal of 5 minutes between the cooling and heating. The modulation parameter was ±0.11 °C every 40 seconds.

Conductivity and viscosity measurements

The ionic conductivities of the neat RIL were performed following the AC impedance technique using a Parstat 2273 potentiostat from Princeton Applied Research. The measurements were carried out from 1 MHz to 1 Hz and at temperatures ranging from 80 °C to 32 °C with an interval of 4 °C and the temperature was controlled with a thermostated bath and monitored using a thermocouple placed in contact with the RIL. The flow conductivity cell was an Orion (18012)

composed of two platinum electrodes. The cell was calibrated daily using a standard 0.117 M KCl (15 mS cm^{-1}) solution. The solution resistance was measured at the intercept of the Nyquist plot curve on the real impedance axis. The viscosity of the BMIm FcNTf was measured on a Cambridge Applied Systems viscometer (model VL-4100) using pistons with range 200–1000 cP at 80 to 56 °C.

Electrochemistry

To determine the mass transport values, electrochemical measurements in acetonitrile with tetrabutylammonium perchlorate (TBAP) as supporting electrolyte were performed using a standard three-electrode cell, consisting of a silver wire pseudoreference electrode, a platinum wire counter electrode and platinum working electrode with a BioLogic SP-50 potentiostat. The electrochemical surface area of the steady electrode (CV) and rotating disk electrode (RDE) were determined using 1 mM potassium ferricyanide in aqueous solution (1 M KCl) to find 0.022 cm^2 and 0.157 cm^2 respectively (using Randles-Sevcik and Levich equations). The solutions were degassed with a flow of argon for 15 minutes prior to the measurements, which was left over the surface of the solution during the measurements. All potentials were reported to the mid-point potential of the ferrocene/ferrocenium (Fc/Fc^+) redox couple which was determined in the particular electrolyte. The diffusion coefficients were measured from three different experiments and compared. The values from CV were obtained from the Randles-Sevcik equation:

$$i_p = 0.4463nFAC\left(\frac{nF}{RT}\right)^{1/2} v^{1/2}D^{1/2} \qquad (1)$$

The diffusion coefficients were also calculated using RDE voltammetry measurements from the gradient of limiting current against the square root of the angular velocity of the RDE using the Levich equation:

$$i_L = 0.620nFACD^{\frac{2}{3}}\omega^{\frac{1}{2}}v^{\frac{-1}{6}} \qquad (2)$$

The diffusion coefficients were measured with a platinum microdisk electrode (100mm diameter) using double potential step chronoamperometry (DPSC) and the data analysis proposed by Compton et al. and Stojek et al.[35, 36] The microelectrode radius was determined from steady

state voltammetry measurements on ferrocene solutions at different concentrations (0.5, 1.0 and 2.0 mM) in CH_3CN containing 0.1 M TBAP (**Figure S4.13**). Following Eq. (3), the microelectrode radius (54 ± 1mm) was calculated using diffusion coefficient from the literature (2.3 x 10^{-9} m^2 s^{-1}).[35, 37]

$$i_{ss} = 4nFrDC \qquad (3)$$

Chronoamperometric experiments were performed inside a Faraday cage. The potential, after equilibration at the initial value, was stepped up from -0.38V to 0.42 V for Fc or from -0.18 V to 0.62 V for FcNTf and back to the initial potential. The current decay was measured for 5 s and the data points were recorded at every 10 ms or 10 nA. The time-dependent current response obtained on the forward step was analyzed by the Shoup and Szabo equation. The response for both forward and backward steps was analyzed by Stojek's method to determine the diffusion coefficients of the reduced and oxidized form.

The heterogeneous rate transfer constant (k_0) was established using the potential difference between the anodic peak and the cathodic peak (ΔE_{pa-pc}) using Nicholson's method, by determination of the kinetic parameter Ψ from the ΔE_{pa-pc} values. To minimize the ohmic resistance of solution, the distance between the silver wire reference electrode and the platinum working microelectrode was kept as short as possible. The tip of the silver wire was protruding from the end of a glass capillary tube. The ΔE_{pa-pc} values were manually corrected from measurements at three concentrations of electroactive species (Fc or FcNTf: 0.5, 1.0 and 2.0 mM) after evaluation of the uncompensated resistance (Ohm's law). The transfer rate for one-electron exchange was calculated from Equation (4), where a parameter was fixed to 0.5 (independent for reversible electrochemical reaction):

$$k_s = \Psi \left(\frac{D_R}{D_O}\right)^{\frac{\alpha}{2}} \left(\frac{\pi F D_O v}{RT}\right)^{\frac{1}{2}} \qquad (4)$$

The equilibrium potential of $[Fc(II)NTf]^-/[Fc(III)NTf]^0$ was measured using a non-aqueous Ag/Ag^+ electrode with a glass tube with a porous vycor tip, using an internal solution of acetonitrile saturated with silver nitrate and 1.0 M TBAP. To establish the impact of the supporting electrolyte on the equilibrium potential, both cyclic voltammetry (CV) and square wave voltammetry (SWV) were used on a mixture of 10 mM of Fc and 10 mM of BMIm FcNTf in acetonitrile using different

salts as supporting electrolyte. The following SWV parameters were used: pulse width (P_w) = 10 ms, pulse height (P_H) = 50 mV and step height (S_H) = 1 mV.

4.2.5. Results and discussion

Physicochemical properties of BMIm FcNTf

The properties of BMIm FcNTf IL were determined in the pure form and the values we obtained are given in **Table 4.1** where they can be easily compared to those of the well-known IL, BMIm NTf_2. The temperatures for each phase transition observed for BMIm FcNTf were determined through differential scanning calorimetry (**Figure S4.11**). DSC scans recorded at low heating and cooling rates of 1 °C min^{-1} showed very broad melting due to the very slow dynamics of phase transitions for the IL. The first cycle showed melting at 55 °C however the second cycle showed no melting because of kinetics slower than the heating and cooling scan rate. The process was kinetically sluggish due to the asymmetrical anion and the high viscosity. Consequently, the IL remained in a liquid, yet highly viscous supercooled state for several days at room temperature before reaching complete crystallization. The thermal stability of BMIm FcNTf was evaluated using TGA which revealed a decomposition temperature of 291 °C measured at a 5% weight loss (**Figure S4.10**), while the unmodified BMIm NTf_2 was found to be stable up to 423 °C.[38] The lower decomposition at lower temperatures occurs from the breaking of the SC bond linking cyclopentadienyl to the trifluoromethylsulfonylimide moiety, Fc decomposing at T > 400 °C.[39] The volatilization of ferrocene from ionic liquids can even occur at room temperature,[40] however our TGA results showed no weight loss from the evaporation of Fc, demonstrating the absence of unbound ferrocene in the ionic liquid.

Table 4.1. Physicochemical properties of neat BMIm NTf_2 and BMIm FcNTf

Properties	BMIm NTf_2	BMIm FcNTf
$T_{decomp.}$ / °C	439[b]	291
T_g / °C	-87[c]	-36
T_m / °C	-4[a]	55
Viscosity / cP (Temp. /°C)	69 (25)[b]	1144 (56)
		260 (80)
Conductivity / mS cm^{-1} (Temp. /°C)	3.9 (20)[a]	4.3 $x10^{-2}$ (32)
		9.0 $x10^{-1}$ (80)

Ref. a) [1] b) [54] c) [41]

The temperature dependency of ionic conductivity for the pure BMIM FcNTf is given in **Figure 4.3A**. The thermal activation for ionic conduction in ILs is often best described using Vogel-Tammann-Fulcher (VTF) because the resulting fragile behavior results in a deviation from linearity in the Arrhenius plots.[41] Parameter B obtained from the fitting is 915 K for the BMIM FcNTf a value higher than the 565 K reported for the unmodified IL as expected because of a lower ionic mobility.

$$\sigma = \sigma_0 exp\left(\frac{-B}{T-T_0}\right) \quad (4)$$

The addition of Fc on the anion also caused a significant increase in the viscosity of the IL (**Table 4.1**). The viscosity obtained with the FcNTf anion is 1140 cP at the melting point (56 °C). In comparison, BMIm NTf_2 had a viscosity of 63 and 15 cP at 25 and 55 °C, respectively.[42] An analysis of the temperature dependence of viscosity (**Figure 4.3B**) showed a very different slope for the BMIM FcNTf. Previous studies by Watanabe and co-workers reported that changing the imidazolium alkyl chain length or even the nature of the cation do not affect the temperature dependence of viscosity significantly.[38, 43] They also reported almost identical Arrhenius curves of viscosity for ILs composed of BF_4^- and NTf_2^- anions with 1-ethyl-3-methylimidazolium, with only a slight effect from the anion on h. However, when comparing NTf_2 and FcNTf, a significant effect from the anion on the viscosity was noted. NTf_2 and other related anions are designed to minimize intermolecular interactions through an efficient electronic density distribution and the

presence of fluorinated groups. The high viscosity of FcNTf-based ionic liquids may be explained by the π-π interactions between the anions contributing to stronger intermolecular interactions. Ionic liquids based on aromatic anions such as benzimidazolate reported in the literature (with alkylphosphonium cations) also demonstrated very high viscosities.[44]

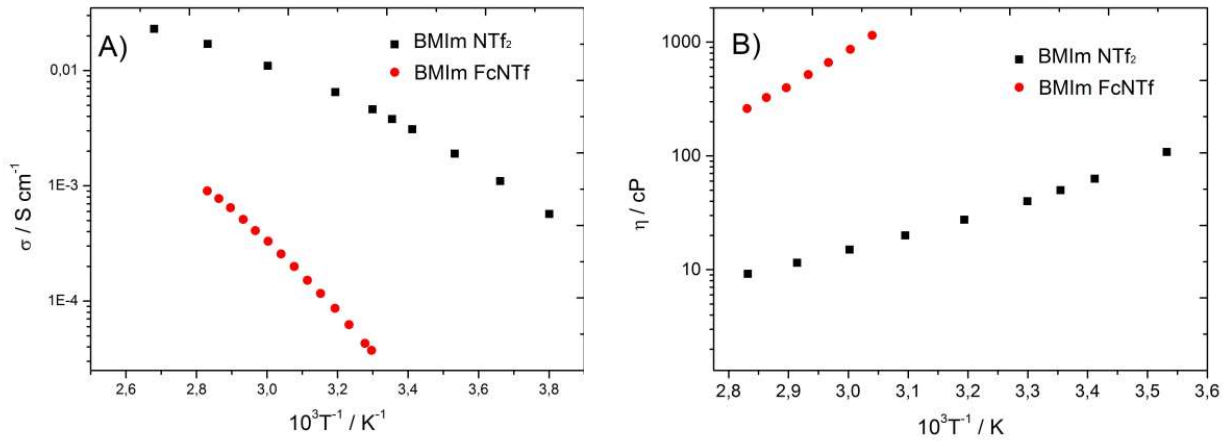

Figure 4.3. A) Temperature dependence on the ionic conductivity of neat BMIm NTf_2 (■) and BMIm FcNTf (●). Measurements were done at an interval of 4 °C from 80 to 32 °C. B) Arrhenius plot for the viscosity of neat BMIm NTf_2 (■) and BMIm FcNTf (●). Measurements were done at an interval of 4 °C from 80 to 56 °C. Data of BMIm NTf_2 from Watanabe and co-workers.[42]

A better understanding of the properties of this new RIL can be gathered from analysis of the Walden plots, which are often used to evaluate the quality and ionicity of an IL.[45, 46] The Walden plots, which were used to establish the relationship between molar conductivity and fluidity,[41] are presented in **Figure 4.4** for the neat BMIm FcNTf between 56 and 80 °C, and for the unmodified BMIm NTf_2 (data reported are from ref. [42]). The data points for the RIL BMIm FcNTf were very close to the ideal line (diluted KCl) and the vertical distance between the BMIm FcNTf data and the ideal Walden line (ΔW) was very small, 0.029 (at 68 °C), compared to its unmodified counterpart (ΔW = 0.52). The water content determined by Karl-Fischer titration was found between 140 and 170 ppm for both ionic liquids (both handled in glove box) showing that the ferrocene does not significantly affect water uptake. Using the Walden rule ($\Lambda\eta$ = constant) means that the BMIm FcNTf has an ionicity of 94% which suggests that a large fraction of the ions

were not significantly shielded by the surrounding counter ions. In comparison, the BMIm NTf_2 presented 30% of the ideal behavior. While this high ionicity for BMIm FcNTf suggests weaker an interaction between cations and anions, the viscosity suggests the opposite. It is possible that the size of anion is responsible for the high viscosity and that these anions are more closely associated than in BMIm NTf_2 due to the strong interaction of the anion-anion associations described above.

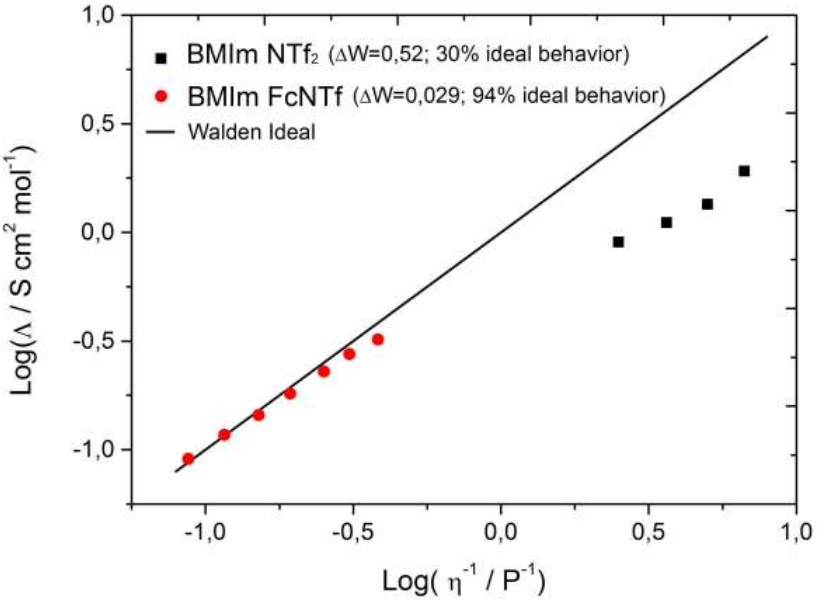

Figure 4.4. Walden plot with an increase of temperature of neat BMIm NTf_2 (■) and BMIm FcNTf (●). Measurements were done at an interval of 4 °C from 80 to 56 °C. Data of BMIm NTf_2 from Watanabe and co-workers.[42]

Electrochemistry of BMIm FcNTf in solutions at low concentrations

The electrochemistry of BMIm FcNTf was studied with RIL diluted in CH_3CN with 0.1 M of tetrabutylammonium hexafluorophosphate (TBAP) to the evaluate diffusion coefficients and heterogeneous rate constant (all data in **Table 4.2**). CVs obtained with a 1 mM solution of the RIL are given in

Figure 4.5A. The BMIm FcNTf showed reversible oxidation through a ratio of I_{pa}/I_{pc} which is around 1 and follows the Randles-Sevcik equation. The diffusion coefficients of the reduced form

in the given electrolyte was 8.4 x 10^{-6} cm^2 s^{-1} and was obtained from the peak current measurements at various scan rates (Randles-Sevcik curves in

Figure 4.5B). The diffusion coefficient is a key factor used to evaluate the maximum current that the redox shuttle in LIB can carry.[47] These values represent a diffusion rate which is roughly 50% of Fc, which is due to the larger radius of the FcNTf. Another way to calculate the diffusion coefficient is by using RDE voltammetry (**Figure 4.6A**) and the Levich curve (**Figure 4.6B**) which was obtained from the limiting current measurements at various rotating rates (100–2500 RPM). This second method yielded a diffusion coefficient of 8.9 x 10^{-6} cm^2 s^{-1}, which is similar to the diffusion value obtained by CV. To ascertain an accurate value for the diffusion coefficients of both reduced and oxidized forms, double potential step chronoamperometry (DPSC) was used with the disk microelectrode (**Figure 4.7A**). The experimental data and best-fit curves of the chronoamperometric transient (positive potential step) are given in **Figure S4.13** and the diffusion coefficients obtained were 1.98 and 1.06 x 10^{-5} cm^2 s^{-1} for the reduced forms of Fc and BMIm FcNTf, respectively. The time-dependent current responses of the positive and negative potential steps were analyzed (Stojek equation) to obtain the diffusion coefficient of both oxidized and reduced form (**Figure 4.7B** and **7C**). The diffusion coefficient found using Stojek's method reported 1.99 and 1.03 x 10^{-5} cm^2 s^{-1} for Fc and BMIm FcNTf, respectively, in close agreement with the coefficient obtained by the **Figure S4.14** fitting (Compton) and with data reported in the literature for Fc (D_{Fc} = 2.11 x 10^{-5} cm^2 s^{-1} [36]). The slower diffusion of FcNTf in diluted solutions compared to that of Fc is explained by the larger radius of the anion. The γ parameter ($\gamma = D_O/D_R$) was 1.21 for FcNTf, showing a larger diffusion coefficient for the oxidized form, which is opposite to the observations reported for the Fc/Fc^+ couple under the same conditions (γ_{Fc} = 0.95) by us

(**Table 4.2**) and others.[36] This suggests a faster diffusion of the zwitterion ($Fc^{+}NTf^{-}$) and a smaller solvation sphere due to the overall neutral charge of the oxidized form.

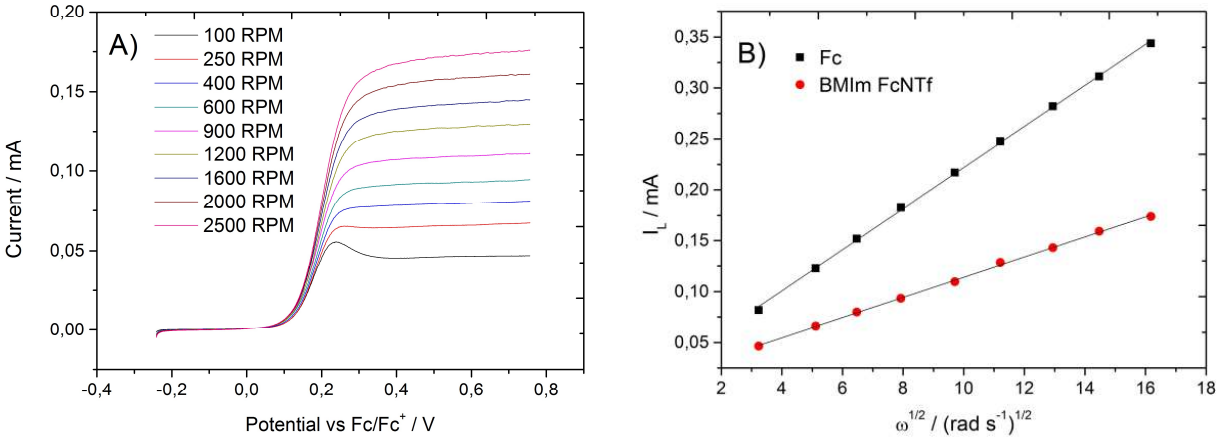

Figure 4.5. A) CVs of 1 mM BMIm FcNTf in CH_3CN with 0.1 M TBAP at various scan rates. B) Randles-Sevcik plot of 1 mM Fc (■) and BMIm FcNTf (●) in CH_3CN with 0.1 M TBAP. The scan rates used were 25 to 1000 mV s^{-1}.

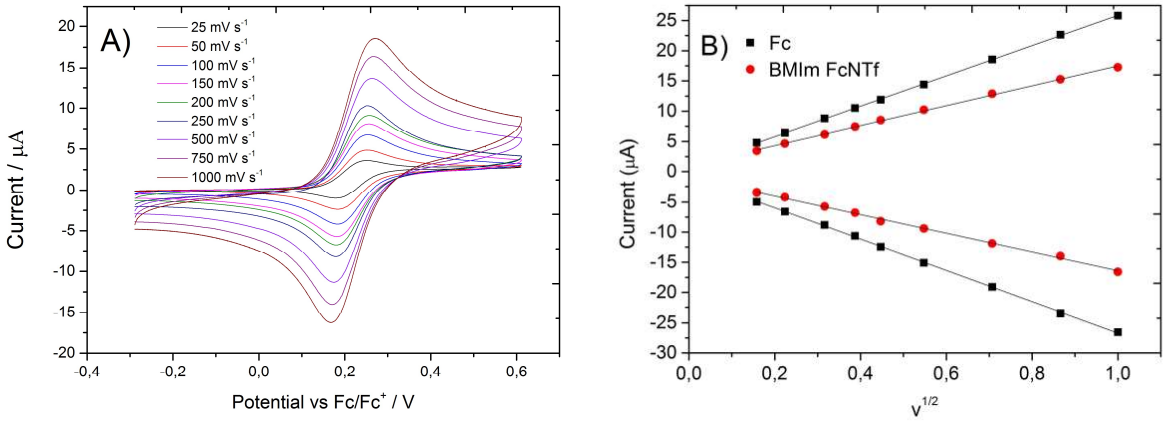

Figure 4.6. A) RDE voltammetry at 100 mV s^{-1} of 1 mM BMIm FcNTf in CH_3CN with 0.1 M TBAP at various rotating rates. B) Levich plot of 1 mM Fc (■) and BMIm FcNTf (●) in CH_3CN with 0.1 M TBAP. The rotating rates used were 100 to 2500 RPM.

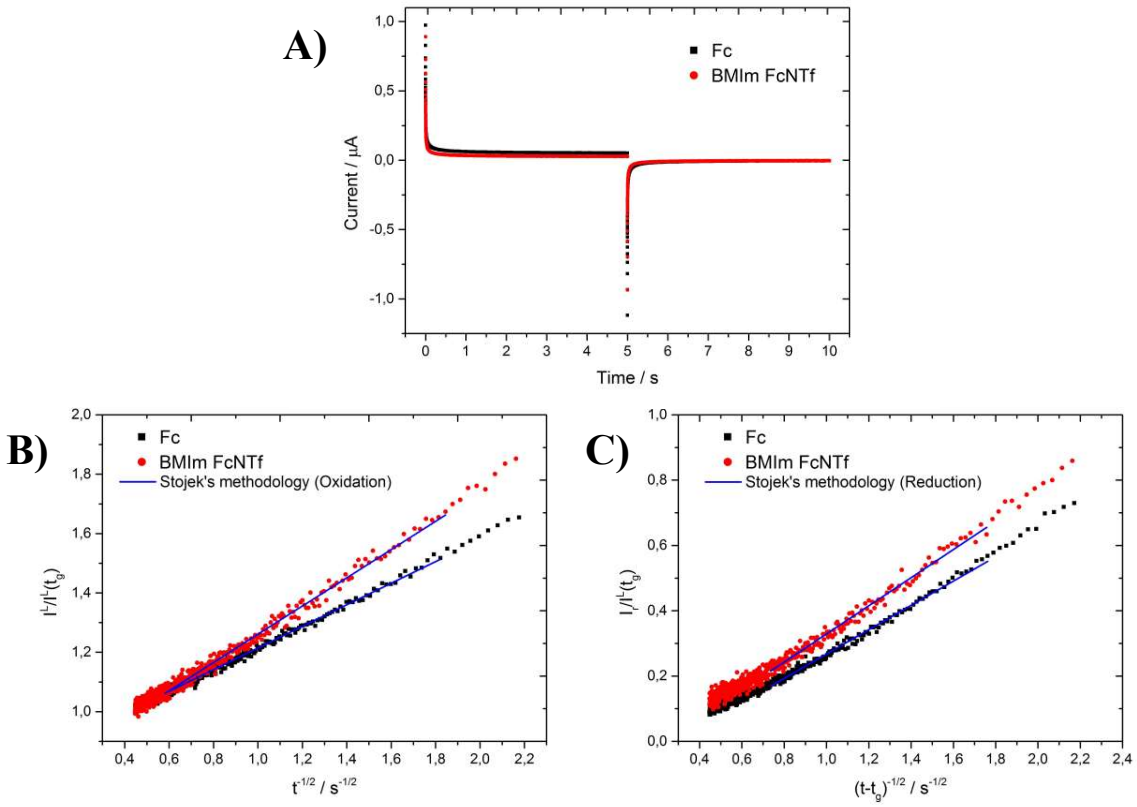

Figure 4.7. DPSC using a microelectrode of 1 mM of Fc (■) and BMIm FcNTf (●) in CH_3CN with 0.1 M TBAP. The duration τ was used 5 s. The initial and final potentials were -0.38 V [Fc] and -0.18 V [FcNTf]. The step potentials were 0.42 V [Fc] and 0.62 V [FcNTf]. (Potential vs. Fc/Fc^+) Stojek plot for the oxidation (B) and reduction (C).

Heterogeneous rate constants were obtained using Nicholson's method based on CVs recorded at various scan rates. In these experiments, the uncompensated resistance was obtained by recording the CV of three solutions at different concentrations of Fc or FcNTf and by manually correcting the resistance. The response at scan rates below 1 V s^{-1} was limited by diffusion and the electron transfer was under Nernstian control. The peak separation at scan rates higher than 1 V s^{-1} was controlled by the kinetics of electron transfer and used for the measurements. The increase in peak potential splitting (ΔE_{pa-pc}) was calculated for potential scan rates of 35 to 75 V s^{-1} and was corrected to remove the influence of uncompensated resistance. At these scan rates, a linear relationship was obtained between the kinetic parameter Ψ and the reciprocal of the square root of the scan rate (**Figure 4.8**). The k_0 values calculated are given in **Table S4.1**. The k_0 for Fc in acetonitrile (with 1.0 M TBAP) was 1.4 ± 0.4 cm s^{-1}, in agreement with the results obtained by Compton et al. (0.99 ± 0.22 cm s^{-1}).[48] The heterogeneous rate constant for FcNTf measured under the same conditions is 4.4 times lower that what was obtained for Fc. Several factors, such as the size, diffusion and asymmetry of the FcNTf can play a role in lowering the rate constant. The formation of a zwitterion upon oxidation of FcNTf can also decrease the rate constant because of an energetic cost due to an intern reorganization following the Marcus model framework. A reduction in the k_0 was also reported for a Fc unit linked on one of the alkyl chain of the methylimidazolium cation.[13, 28]

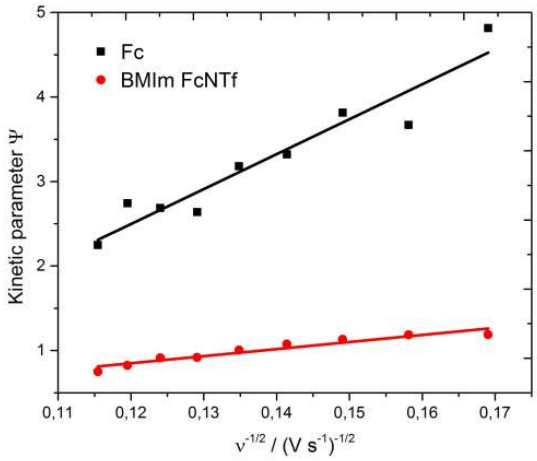

Figure 4.8. Nicholson plot of 2 mM of Fc (■) and BMIm FcNTf (●) in CH_3CN with 0.1 M TBAP. The scan rates used were 35 to 75 V s^{-1}.

Table 4.2. Electrochemical parameters using CV, RDE voltammetry and DPSC of 1 mM Fc or BMIm FcNTf in CH_3CN with 0.1 M TBAP.

Electroactive species	D_R (CV) /10^{-5} cm^2 s^{-1}	D_R (RDE) /10^{-5} cm^2 s^{-1}	D_R (DPSC) /10^{-5} cm^2 s^{-1}	D_O (DPSC) /10^{-5} cm^2 s^{-1}	γ D_O / D_R	k_0 / cm s^{-1}
Fc	1.8	2.6	1.99±0.08	1.90±0.08	0.95	1.2±0.2
BMIm FcNTf	0.8	0.9	1.03±0.05	1.25±0.05	1.21	0.27±0.01
Difference / %	53	66	50	32	-	78

Effect of cations and anions on the redox potential

The effect of various cations and anions entering the composition of battery electrolytes on the electrochemical potential of the FcNTf moiety was then studied in diluted solutions to evaluate the solvation effects of those ions. The effect of Li^+ as well as the anions NTf_2, BF_4 and PF_6 was studied by adding either $LiNTf_2$ salt or the BMIm ionic liquid with the specific anion to solutions containing BMIm FcNTf. The difference in potential between FcNTf and Fc, was noted $\Delta E_{FcNTf\text{-}Fc} = E_{FcNTf} – E_{Fc}$ and measured from the CV (mid-point E) and SWV (peak E) experiments. **Figure 4.9** displays the CV (A) and SWV (B) of 10 mM solution of Fc and BMIm FcNTf containing 0.75 M of BMIm NTf_2 or Li NTf_2. As expected from the electronegativity of the NTf moiety, the equilibrium potential of FcNTf (**Table 4.3**) was found to be 224 mV more positive than that of the Fc/Fc^+ couple measured under the same conditions. **Figure 4.9C** shows that with an increase in the concentration of BMIm NTf_2, the $\Delta E_{FcNTf\text{-}Fc}$ also increases. The CV and SWV curves used to evaluate this effect are presented in the supporting information (**Figure S4.16-S4.18**). These curves showed an increase in the equilibrium potential of the anionic FcNTf which is attributed to its interaction with the cation BMIm which screens the charge on the electroactive anion. The decrease in current also observed with the increase in BMIm concentration (**Figure S4.16**) is due to the lower diffusion of the anion in the more viscous solutions. **Figure 4.9** also shows an important effect of the Li^+ cation on the potential of FcNTf. The complexation of Li^+ by the NTf_2 anion is a well-known phenomenon in solutions and in NTf_2-based ILs which is responsible for a strong decrease in the mobility of Li^+.[49-51] The Li-FcNTf complexation increases the equilibrium potential by 45 mV (at $[Li^+] = 0.75$ M, **Figure 4.7A**) and this increase in potential is concentration-

dependent (**Figure 4.9C**). The association of Li^+ with NTf moiety causes a displacement of its electronic density towards Li^+, affecting the potential. In addition to this shift in potential, a decrease in the current was also noted in the presence of lithium which is due to the slower diffusion of the FcNTf complex with Li^+. The presence of lithium did not affect the potential of Fc or decamethylferrocene (DmFc) dissolved in 1-methyl-1-butylpyrrolidinium NTf_2[52] showing that this effect is linked to the NTf moiety.

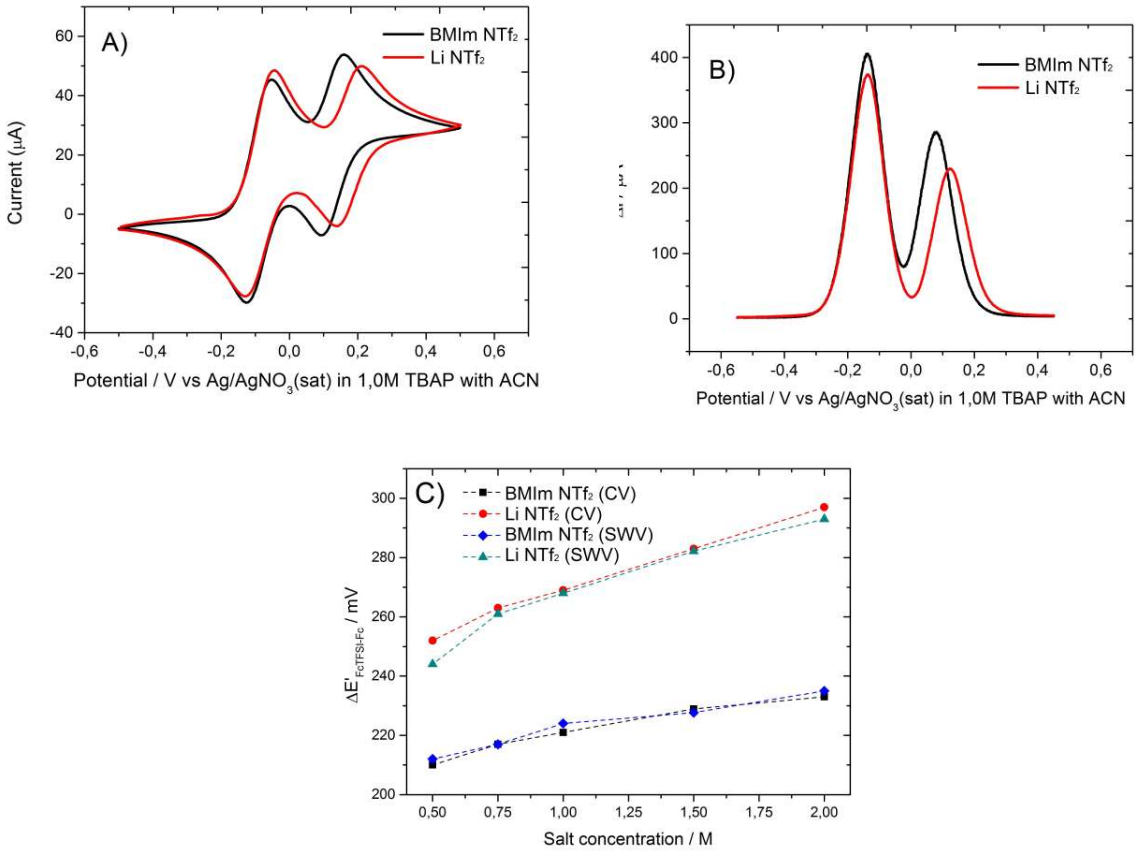

Figure 4.9. CVs (A) at 50 mV s^{-1} and SWV (B) using P_W: 10 ms, P_H: 50 mV and S_H: 1 mV. Electroactive species were 10 mM of Fc and 10 mM of BMIm FcNTf in CH_3CN and supporting electrolytes were 0.75M of BMIm NTF_2 (Black line) or Li NTf_2 (Red line). C) Difference of equilibrium potential between Fc and FcNTf dependence on supporting electrolyte concentration. (■: CV using BMIm NTf_2; ●: CV using Li NTf_2; ♦: SWV using BMIm NTf_2; ▲: SWV using Li NTf_2)

The anions in the ionic liquid can also have an influence on the redox potential of Fc.[52, 53] Torriero et al. reported mid-point potential differences between DmFc and Fc of 0.478 and 0.513 V in BMIm BF_4 and BMIm NTF_2 respectively, showing the effect of the anion in DCM. In contrast, our results with BMIm NTf_2, BMIm BF_4 and BMIm PF_6 (in ACN a better polar solvent) demonstrated no effect from the anion on the potential and a slight effect on the currents, likely due to different diffusion coefficients (**Figure S4.17**). The anionic charge on the FcNTf appears to prevent the interaction of the Fc moiety with the other anions found in solution, explaining this discrepancy between our observation and those of Torriero.

Electrochemistry of BMIm FcNTf in solutions at high concentrations

While the large iR drop prevented electrochemical measurements being taken on the neat BMIM FcNTf, CV could be carried out on a 50% v/v solution in CH_3CN, in the presence and absence of TBAP as supporting electrolyte. **Figure 4.10** reveals that for the FcNTf oxidation a higher current in the absence of a supporting electrolyte and an oxidation peak shape is indicative of processes that are not under purely diffusional control. The increased oxidation of the peak current can be explained by the migration contributing to the mass transport of the anionic FcNTf towards the positive electrode, in addition to diffusion. As expected, adding 1M of TBAP supporting electrolyte negated the migrational component of mass transport. For the self-supported system (no TBAP), the current suddenly dropped to zero upon oxidation of the species in the diffusional layer, and no current was recorded thereafter. In contrast, in the presence of a supporting electrolyte, the oxidation current curve after the peak followed the typical shape for a diffusion-limited process. The oxidation shape of the CV using 50% vol. RIL solution was clearly distorted which explains the higher equilibrium potential of FcNTf in comparison with the low concentration RIL solution using the same electrolyte condition (**Table 4.3**). The CV curve in **Figure 4.10A** shows that the sudden drop in current and the following "zero-current" line can be observed over several hundreds of mV after the drop is obtained. A diffusional current peak of very similar shape to those obtained under supported conditions was recorded during the backward scan. A blue film could be seen on the Pt working electrode after only doing a linear scan of positive potentials resulting from the deposition of insoluble Fc^+NTf species on the surface of the electrode. It is worth noting that such deposition was not observed for ionic liquids using a redox cation,[17] suggesting

that the behavior is linked to the negative charge on the FcNTf. The oxidation of the anionic FcNTf resulted in a zwitterion bearing one positive charge on the Fe center and one negative charge delocalized on the NTf moiety. This overall neutral species forms a stable film on the electrode, thereby preventing further diffusion to the electrode, as suggested in **Figure 4.10B**, until the ferrocenium gets reduced during the reverse scan. This behavior, attributed to the structure of the FcNTf anion, is currently under study with other IL cations in the pure, undiluted form.

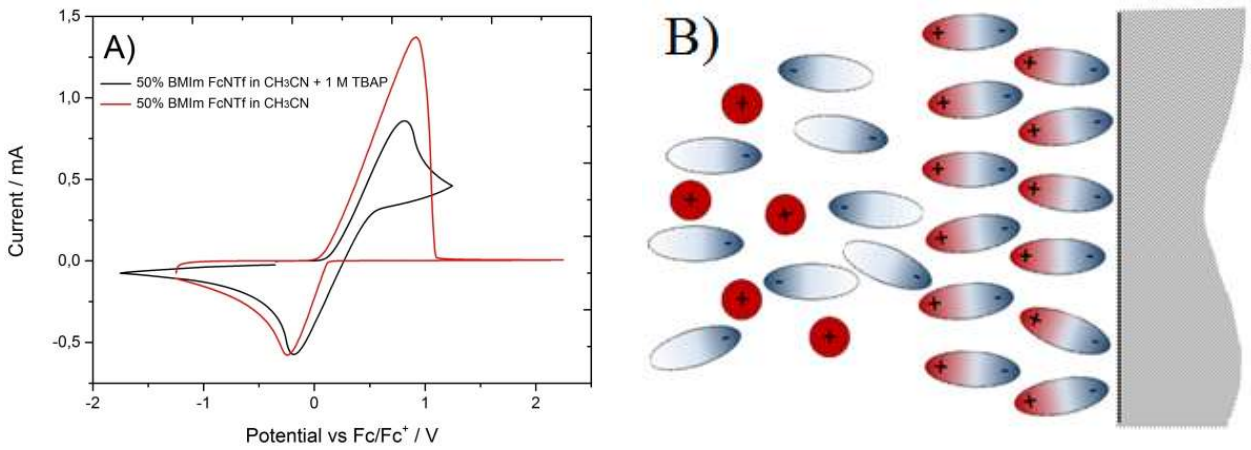

Figure 4.10. A) CVs of 50% (v/v) of BMIm FcNTf in CH_3CN with 1.0 M TBAP (Black line) and 50% (v/v) BMIm FcNTf in CH_3CN without supporting electrolyte (Red line). Scan rate used was 100 mV s^{-1}. B) Representation of the film formed on the electrode following the oxidation of the FcNTf anion at high concentrations and in the absence of supporting electrolyte. Solvent (CH_3CN) was omitted for clarity.

Table 4.3. Potential parameters obtained from cyclic voltammograms of 10 mM and 1.4 M solutions of BMIm FcNTf in CH_3CN with 1.0 M TBAP at 100 mV s^{-1}. The potentials are given vs. the Fc/Fc^+ couple.

[RIL] / M	E_{pc} / V	E_{pa} / V	E' / V	E_{pa-pc} / V	Reduction limit / V	Oxidation limit / V
0.01	0.178	0.270	0.224	0.092	-1.39	1.53
1.40[a]	-0.147	0.764	0.309	0.911	-2.23	2.32

[a] The 1.4 M solution corresponds to 50% v/v.

4.2.6. Conclusions

A new type of electroactive IL where the anion bears the redox moiety has been synthesized and characterized and its electrochemistry has been studied to determine the solvation effect of different ions. A ferrocenylsulfonyl(trifluoromethylsulfonyl) imide (FcNTf) was used with 1-butyl-3-methylimidazolium and the electroactive IL appeared to be highly viscous due to the significant interactions established between the ferrocenyl moieties on the anion. The electrochemistry of FcNTf, studied in diluted solutions in acetonitrile, showed a redox potential shifted by 224 mV more positive of the Fc under the same conditions, an effect related to the electronegativity of the NTf moiety. The redox potential of FcNTf was dependent on the concentration of the BMIm cation (added as BMIm NTf_2 in the solution) as well as on the presence of Li^+ which is known to form a complex with NTf_2 in solvents and in ILs. However, there was no significant impact of the type of anion on the redox potential of FcNTf, showing a preferential interaction of the anionic redox center with the cations in solution. The electrochemistry of self-supported, concentrated solutions of BMIm FcNTf showed the deposition of an insoluble film on the electrode which contained the oxidized, zwitterionic Fc^+NTf species. The film could be removed by reducing Fc^+NTf^- back to FcNTf. This type of electroactive IL may be of interest in the study of electron transfer processes in liquid phases in highly concentrated redox centers.

4.2.7. Acknowledgments

The authors acknowledge the financial support from Fonds de recherche du Québec en nature et technologies under their program for the reduction of greenhouse gases, and the Natural Sciences and Engineering Research Council of Canada (NSERC).

4.2.8. Appendix A. Supplementary data

Supplementary data associated with this article can be found, in the online version, at http://dx.doi.org/10.1016/j. electacta.2014.11.154.

4.2.9. References

[1] P. Bonhôte, A.-P. Dias, N. Papageorgiou, K. Kalyanasundaram, M. Grätzel, Hydrophobic, highly conductive ambient-temperature molten salts, Inorg. Chem., 35 (1996) 1168-1178.
[2] L.P.N. Rebelo, J.N. Canongia Lopes, J.M.S.S. Esperança, E. Filipe, On the critical temperature, normal boiling point, and vapor pressure of ionic liquids, J. Phys. Chem. B, 109 (2005) 6040-6043.
[3] J.J. H. Davis, Task-specific ionic liquids, Chem. Lett., 33 (2004) 1072-1077.
[4] M. Galiński, A. Lewandowski, I. Stępniak, Ionic liquids as electrolytes, Electrochim. Acta, 51 (2006) 5567-5580.
[5] C. Austen Angell, Y. Ansari, Z. Zhao, Ionic Liquids: Past, present and future, Faraday Discuss., 154 (2012) 9.
[6] A.E. Visser, R.P. Swatloski, W.M. Reichert, R. Mayton, S. Sheff, A. Wierzbicki, J.J.H. Davis, R.D. Rogers, Task-specific ionic liquids for the extraction of metal ions from aqueous solutions, Chem. Comm., (2001) 135-136.
[7] J. Fraga-Dubreuil, M.-H. Famelart, J.P. Bazureau, Ecofriendly fast synthesis of hydrophilic poly(ethyleneglycol)-ionic liquid matrices for liquid-phase organic synthesis, Org. Process Res. Dev., 6 (2002) 374-378.
[8] E.D. Bates, R.D. Mayton, I. Ntai, J.H. Davis, CO2 capture by a task-specific ionic liquid, J. Am. Chem. Soc., 124 (2002) 926-927.
[9] A.E. Visser, R.P. Swatloski, W.M. Reichert, R. Mayton, S. Sheff, A. Wierzbicki, J.H. Davis, R.D. Rogers, Task-specific ionic liquids for the extraction of metal ions from aqueous solutions, Chem. Comm., (2001) 135-136.
[10] H. Olivier-Bourbigou, L. Magna, D. Morvan, Ionic liquids and catalysis: Recent progress from knowledge to applications, Appl. Catal. A., 373 (2010) 1-56.
[11] K.-S. Kim, D. Demberelnyamba, H. Lee, Size-selective synthesis of gold and platinum nanoparticles using novel thiol-functionalized ionic liquids, Langmuir, 20 (2003) 556-560.
[12] B.S. Lee, Y.S. Chi, J.K. Lee, I.S. Choi, C.E. Song, S.K. Namgoong, S.-g. Lee, Imidazolium ion-terminated self-assembled monolayers on Au: Effects of counteranions on surface wettability, J. Am. Chem. Soc., 126 (2003) 480-481.
[13] O. Fontaine, C. Lagrost, J. Ghilane, P. Martin, G. Trippé, C. Fave, J.C. Lacroix, P. Hapiot, H.N. Randriamahazaka, Mass transport and heterogeneous electron transfer of a ferrocene derivative in a room-temperature ionic liquid, J. Electroanal. Chem., 632 (2009) 88-96.
[14] J.E.F. Weaver, D. Breadner, F.G. Deng, B. Ramjee, P.J. Ragogna, R.W. Murray, Electrochemistry of ferrocene-functionalized phosphonium ionic liquids, J. Phys. Chem. C, 115 (2011) 19379-19385.
[15] J.-L. Thomas, J. Howarth, A. Kennedy, Electrochemical anion recognition by novel ferrocenyl imidazole systems, Molecules, 7 (2002) 861-866.
[16] B.T. Ye Gao, and Jeanne M. Shreeve, The first (ferrocenylmethyl)imidazolium and (ferrocenylmethyl)triazolium room temperature ionic liquids, Inorg. Chem., 43 (2004) 3406-3412.
[17] W. Wang, R. Balasubramanian, R.W. Murray, Electron transport and counterion relaxation dynamics in neat ferrocenated imidazolium ionic liquids, J. Phys. Chem. C, 112 (2008) 18207-18216.
[18] V.O. Nyamori, M. Gumede, M.D. Bala, Synthesis, characterisation and properties of ferrocenylalkylimidazolium salts, J. Organomet. Chem., 695 (2010) 1126-1132.
[19] R. Balasubramanian, W. Wang, R.W. Murray, Redox ionic liquid phases: Ferrocenated imidazoliums, J. Am. Chem. Soc., 128 (2006) 9994-9995.

[20] W. Wang, R. Balasubramanian, R.W. Murray, Electron transport and counterion relaxation dynamics in neat ferrocenated imidazolium ionic liquids, J. Phys. Chem. C, 112 (2008) 18207-18216.
[21] B.n.d. Chamiot, C.c. Rizzi, L. Gaillon, J. Sirieix-Plénet, J.l. Lelièvre, Redox-switched amphiphilic ionic liquid behavior in aqueous solution, Langmuir, 25 (2009) 1311-1315.
[22] Y. Miura, F. Shimizu, T. Mochida, Preparation, properties, and crystal structures of organometallic ionic liquids comprising 1-ferrocenyl-3-alkylimidazolium-based salts of bis(trifluoromethanesulfonyl)amide and hexafluorophosphate, Inorg. Chem., 49 (2010) 10032-10040.
[23] B. Gelinas, J.C. Forgie, D. Rochefort, Conductivity and electrochemistry of ferrocenyl-imidazolium redox ionic liquids with different alkyl chain lengths, J. Electrochem. Soc., 161 (2014) H161-H165.
[24] A.W. Taylor, P. Licence, X-ray photoelectron spectroscopy of ferrocenyl- and ferrocenium-based ionic liquids, ChemPhysChem, 13 (2012) 1917-1926.
[25] P. Kubler, J. Sundermeyer, Ferrocenyl-phosphonium ionic liquids - synthesis, characterisation and electrochemistry, Dalton Trans., 43 (2014) 3750-3766.
[26] T. Inagaki, T. Mochida, Metallocenium ionic liquids, Chem. Lett., 39 (2010) 572-573.
[27] T. Inagaki, T. Mochida, M. Takahashi, C. Kanadani, T. Saito, D. Kuwahara, Ionic liquids of cationic sandwich complexes, Chem. Eur. J., 18 (2012) 6795-6804.
[28] J.C. Forgie, S. El Khakani, D.D. MacNeil, D. Rochefort, Electrochemical characterisation of a lithium-ion battery electrolyte based on mixtures of carbonates with a ferrocene-functionalised imidazolium electroactive ionic liquid, Phys. Chem. Chem. Phys., 15 (2013) 7713-7721.
[29] J.C. Forgie, D. Rochefort, Electroactive imidazolium salts based on 1,4-dimethoxybenzene redox groups: synthesis and electrochemical characterisation, RSC Adv., 3 (2013) 12035-12038.
[30] T. Ohsaki, T. Kishi, T. Kuboki, N. Takami, N. Shimura, Y. Sato, M. Sekino, A. Satoh, Overcharge reaction of lithium-ion batteries, J. Power Sources, 146 (2005) 97-100.
[31] R.A. Leising, M.J. Palazzo, E.S. Takeuchi, K.J. Takeuchi, Abuse testing of lithium-ion batteries: Characterization of the overcharge reaction of LiCoO2/Graphite Cells, J. Electrochem. Soc., 148 (2001) A838-A844.
[32] R.A. Leising, M.J. Palazzo, E.S. Takeuchi, K.J. Takeuchi, A study of the overcharge reaction of lithium-ion batteries, J. Power Sources, 97–98 (2001) 681-683.
[33] Z. Chen, Y. Qin, K. Amine, Redox shuttles for safer lithium-ion batteries, Electrochim. Acta, 54 (2009) 5605-5613.
[34] J. Zhang, B. Yang, Y. Yang, B. Zhang, Synthesis, characterization and crystal structure of 1-ferrocenesulfonyl-2-long carbon chain alkyl benzimidazole, Front. Chem. China, 4 (2009) 52-57.
[35] Y. Wang, E.I. Rogers, R.G. Compton, The measurement of the diffusion coefficients of ferrocene and ferrocenium and their temperature dependence in acetonitrile using double potential step microdisk electrode chronoamperometry, J. Electroanal. Chem., 648 (2010) 15-19.
[36] W. Hyk, A. Nowicka, Z. Stojek, Direct determination of diffusion coefficients of substrate and product by chronoamperometric techniques at microelectrodes for any level of ionic support, Anal. Chem., 74 (2001) 149-157.
[37] L. Xiong, A.M. Fletcher, S.G. Davies, S.E. Norman, C. Hardacre, R.G. Compton, Tuning solute redox potentials by varying the anion component of room temperature ionic liquids, Chem. Comm., 48 (2012) 5784.
[38] H. Tokuda, K. Ishii, M. Susan, S. Tsuzuki, K. Hayamizu, M. Watanabe, Physicochemical properties and structures of room-temperature ionic liquids. 3. Variation of cationic structures, J. Phys. Chem. B, 110 (2006) 2833-2839.

[39] A. Barreiro, S. Hampel, M.H. Rümmeli, C. Kramberger, A. Grüneis, K. Biedermann, A. Leonhardt, T. Gemming, B. Büchner, A. Bachtold, T. Pichler, Thermal decomposition of ferrocene as a method for production of single-walled carbon nanotubes without additional carbon sources, J. Phys. Chem. B, 110 (2006) 20973-20977.
[40] C. Fu, L. Aldous, E.J.F. Dickinson, N.S.A. Manan, R.G. Compton, Volatilisation of ferrocene from ionic liquids: kinetics and mechanism, Chem. Comm., 47 (2011) 7083-7085.
[41] W. Xu, E.I. Cooper, C.A. Angell, Ionic liquids: Ion mobilities, glass temperatures, and fragilities, J. Phys. Chem. B, 107 (2003) 6170-6178.
[42] H. Tokuda, S. Tsuzuki, M.A.B.H. Susan, K. Hayamizu, M. Watanabe, How ionic are room-temperature ionic liquids? An indicator of the physicochemical properties, J. Phys. Chem. B, 110 (2006) 19593-19600.
[43] H. Tokuda, K. Hayamizu, K. Ishii, M.A.B.H. Susan, M. Watanabe, Physicochemical properties and structures of room temperature ionic liquids. 2. Variation of alkyl chain length in imidazolium cation, J. Phys. Chem. B, 109 (2005) 6103-6110.
[44] Y. Tsuji, H. Ohno, Facile synthesis of thermally stable benzimidazolate-type ionic liquids, Chem. Lett., 42 (2013) 527-529.
[45] D.R. MacFarlane, M. Forsyth, E.I. Izgorodina, A.P. Abbott, G. Annat, K. Fraser, On the concept of ionicity in ionic liquids, Phys. Chem. Chem. Phys., 11 (2009) 4962-4967.
[46] K. Ueno, H. Tokuda, M. Watanabe, Ionicity in ionic liquids: correlation with ionic structure and physicochemical properties, Phys. Chem. Chem. Phys., 12 (2010) 1649-1658.
[47] S.R. Narayanan, S. Surampudi, A.I. Attia, C.P. Bankston, Analysis of redox additive-based overcharge protection for rechargeable lithium batteries, J. Electrochem. Soc., 138 (1991) 2224-2229.
[48] A.D. Clegg, N.V. Rees, O.V. Klymenko, B.A. Coles, R.G. Compton, Marcus theory of outer-sphere heterogeneous electron transfer reactions: High precision steady-state measurements of the standard electrochemical rate constant for ferrocene derivatives in alkyl cyanide solvents, J. Electroanal. Chem., 580 (2005) 78-86.
[49] O. Borodin, G.D. Smith, W. Henderson, Li+ cation environment, transport, and mechanical properties of the LiTFSI doped N-methyl-N-alkylpyrrolidinium+TFSI- ionic liquids, J. Phys. Chem. B, 110 (2006) 16879-16886.
[50] J.-C. Lassègues, J. Grondin, C. Aupetit, P. Johansson, Spectroscopic identification of the lithium ion transporting species in LiTFSI-doped ionic liquids, J. Phys. Chem. A, 113 (2008) 305-314.
[51] A. Andriola, K. Singh, J. Lewis, L. Yu, Conductivity, viscosity, and dissolution enthalpy of LiNTF2 in ionic liquid BMINTF2, J. Phys. Chem. B, 114 (2010) 11709-11714.
[52] A.A.J. Torriero, P.C. Howlett, Ionic liquid effects on the redox potential of ferrocene, Electrochem. Comm., 16 (2012) 84-87.
[53] A.A.J. Torriero, J. Sunarso, P.C. Howlett, Critical evaluation of reference systems for voltammetric measurements in ionic liquids, Electrochim. Acta, 82 (2012) 60-68.
[54] J.G. Huddleston, A.E. Visser, W.M. Reichert, H.D. Willauer, G.A. Broker, R.D. Rogers, Characterization and comparison of hydrophilic and hydrophobic room temperature ionic liquids incorporating the imidazolium cation, Green Chem., 3 (2001) 156-164.

4.3. Supporting Information

4.3.1. Synthesis

Preparation of 1-butyl-3-methylimidazolium bromide: Under inert conditions, 1-methyl-imidazole (1 eq) was added to neat 1-bromobutane (2 eq) at 0°C. The mixture was stirred during 12 hours under 40°C. The resulting salt was dried to give yellow oil and a white solid was obtained by several wash with diethyl ether. The final product was dried during 12 hours at room temperature. Yield: 82%. ^{1}H NMR (DMSO-d_6, 300 MHz): δ (ppm) = 9.24 (s,1H,Im^+), 7.77 (d,2H,Im^+), 4.17 (t,2H,-CH_2Im^+), 3.86 (s,3H, CH_3Im^+), 1.76 (m,2H,-CH_2-) 1.25 (m,2H,-CH_2-), 0.89 (t,3H,-CH_3). ^{13}C NMR (DMSO-d_6, 125 MHz): δ (ppm) = 136.99(Im^+); 124.05(Im^+); 122.72(Im^+); 48.91(CH_3Im^+); 36.23(-CH_2Im^+); 31.82(-CH_2-); 19.22(-CH_2-); 13.74(-CH_3). HR MS (ESI) m/z: [M*$^+$](calcd for $C_8H_{15}N_2^+$): 139.123 found: 139.124. Elemental analysis: Calcd for $C_8H_{15}BrN_2$: N 12.78; C 43.85; H 6.90. Found: N 12.73; C 43.91; H 7.02.

4.3.2. NMR analysis

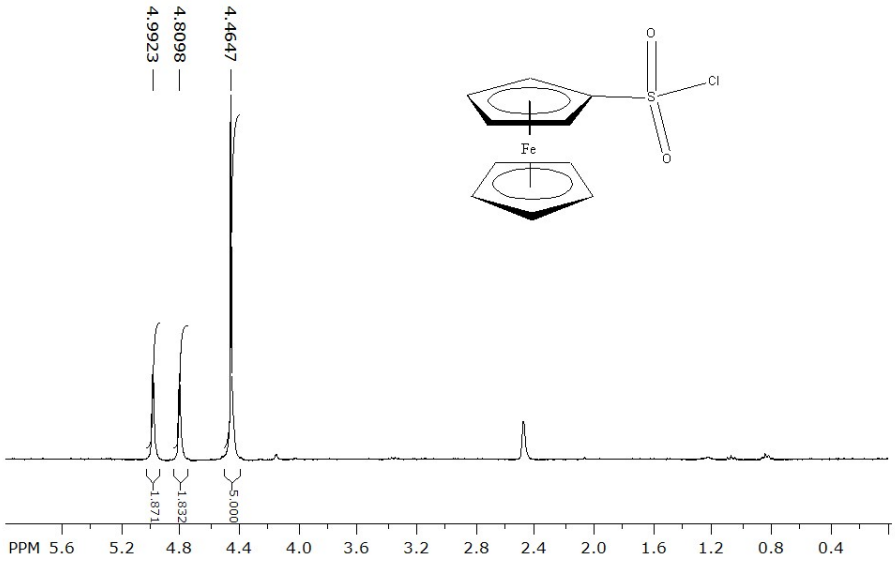

Figure S4.1. ^{1}H NMR (DMSO-d_6, 300 MHz): δ (ppm) = 4.99 (s, 2H, Cp-SO_2Cl), 4.81 (s, 2H, Cp-SO_2Cl), 4.46 (s, 5H, Cp). ($FcSO_2Cl$)

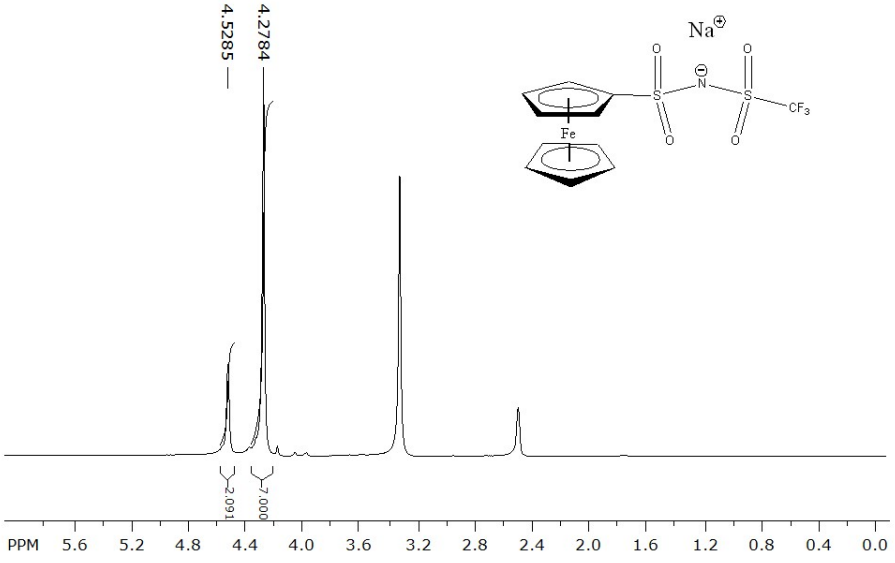

Figure S4.2. ^{1}H NMR (DMSO-d_6, 300 MHz): δ (ppm) = 4.53 (s, 2H, Cp-SO_2Cl), 4.28 (s, 7H, Cp-SO_2Cl + Cp). (Na FcNTf)

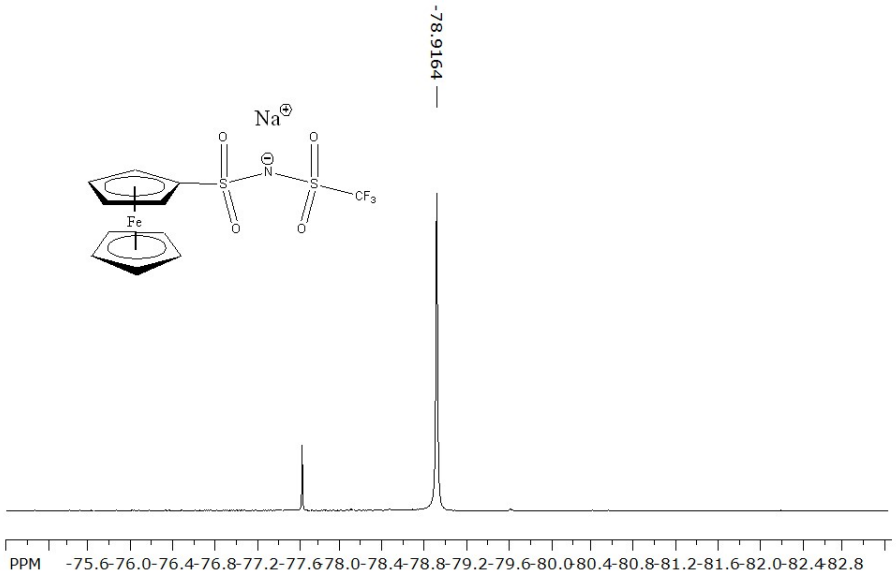

Figure S4.3. ^{19}F NMR (DMSO-d_6, 282 MHz): δ (ppm) = -77.62(-CF_3). (Na FcNTf)

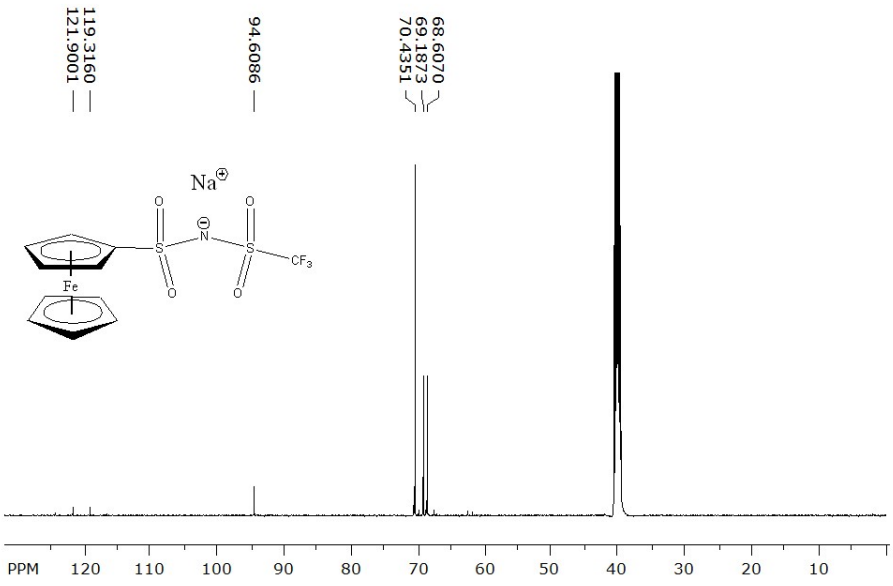

Figure S4.4. ^{13}C NMR (DMSO-d_6, 125 MHz): δ (ppm) = 121.90(-CF_3); 119.32(-CF_3); 94.61(Cp-SO_2Cl); 70.44(Cp); 69.19(Cp); 68.61(Cp). (Na FcNTf)

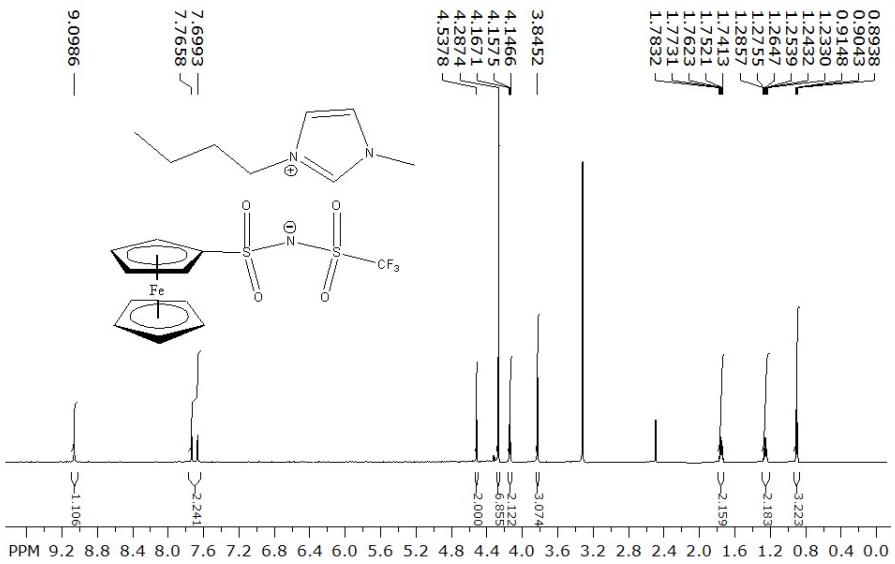

Figure S4.5. ^{1}H NMR (DMSO-d_6, 300 MHz): δ (ppm) = 9.10 (s,1H,Im^+), 7.73 (d,2H,Im^+), 4.54 (t,2H,Cp-SO_2Cl), 4.29 (s,7H, Cp-SO_2Cl+Cp), 4.16 (t,2H,-CH_2Im^+), 3.85 (s,3H, CH_3Im^+), 1.76 (m,2H,-CH_2-) 1.26 (m,2H,-CH_2-), 0.90 (t,3H,-CH_3). (BMIm FcNTf)

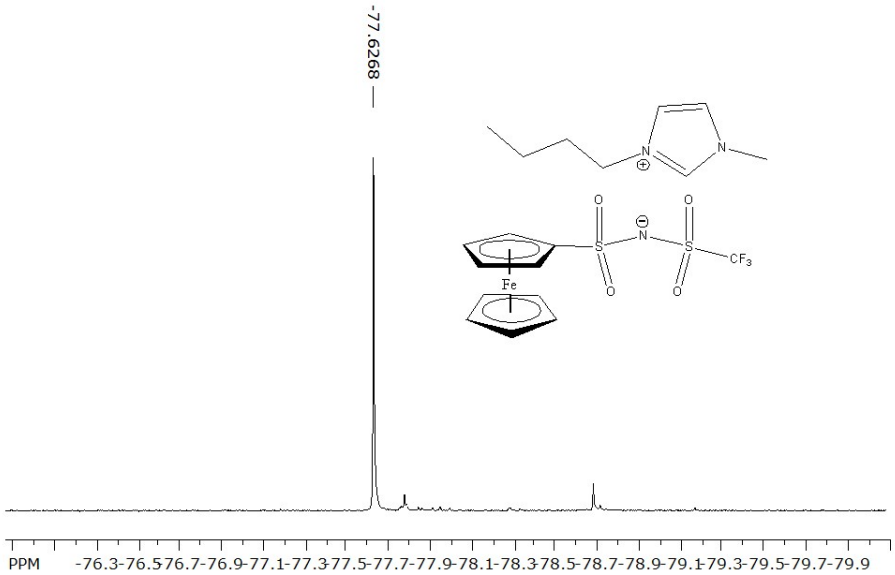

Figure S4.6. ^{19}F NMR (DMSO-d_6, 282 MHz): δ (ppm) = -77.63(-CF_3). (BMIm FcNTf)

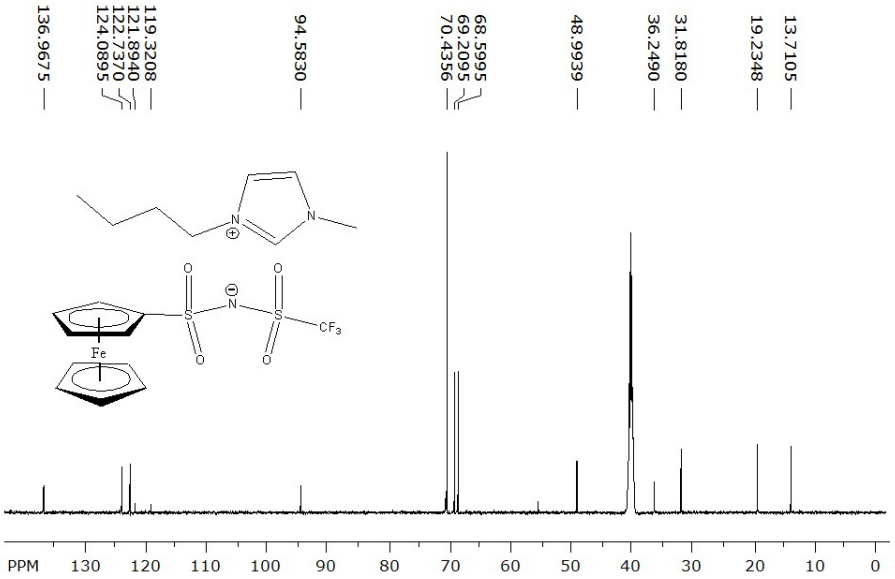

Figure S4.7. ^{13}C NMR (DMSO-d_6, 125 MHz): δ (ppm) = 136.97(Im^+); 124.09(Im^+); 122.74(Im^+); 121.89(-CF_3); 119.32(-CF_3); 94.58(Cp-SO_2Cl); 70.44(Cp); 60.21(Cp); 68.60(Cp); 48.99(CH_3Im^+); 36.25(-CH_2Im^+); 31.82(-CH_2-); 19.23(-CH_2-); 13.71(-CH_3). (BMIm FcNTf)

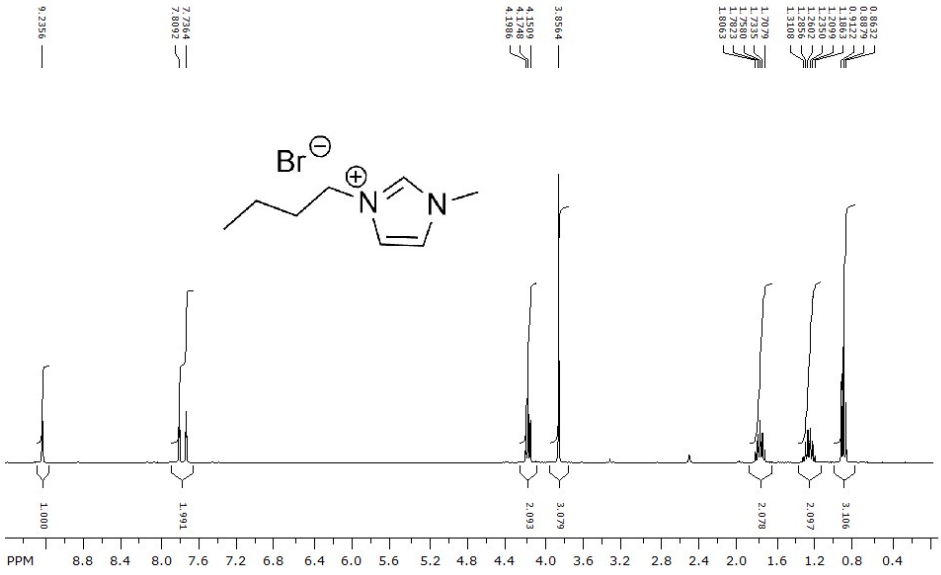

Figure S4.8. ^{1}H NMR (DMSO-d_6, 300 MHz): δ (ppm) = 9.24 (s,1H,Im^+), 7.77 (d,2H,Im^+), 4.17 (t,2H,-CH_2Im^+), 3.86 (s,3H, CH_3Im^+), 1.76 (m,2H,-CH_2-) 1.25 (m,2H,-CH_2-), 0.89 (t,3H,-CH_3). (BMIm Br)

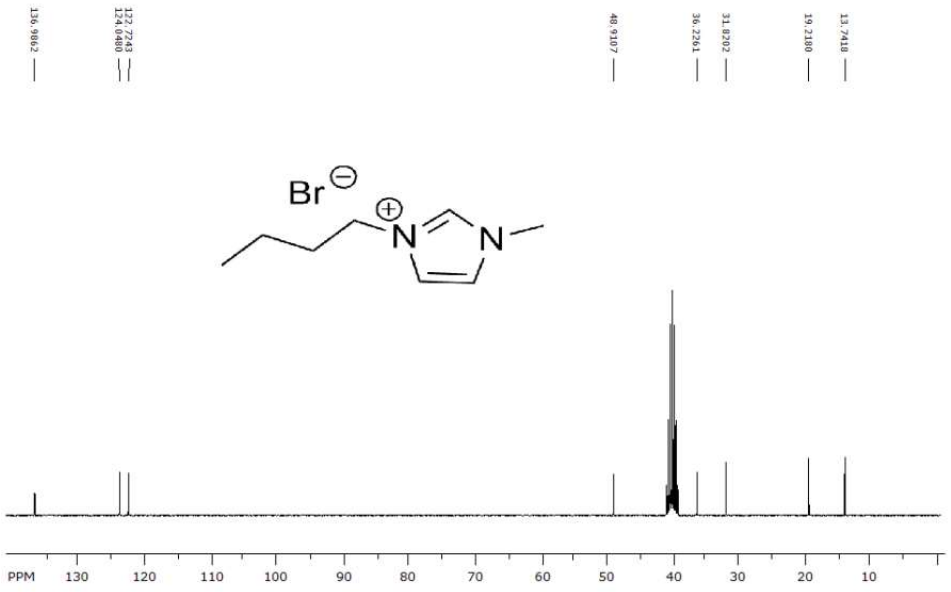

Figure S4.9. ^{13}C NMR (DMSO-d_6, 125 MHz): δ (ppm) = 136.99(Im^+); 124.05(Im^+); 122.72(Im^+); 48.91(CH_3Im^+); 36.23(-CH_2Im^+); 31.82(-CH_2-); 19.22(-CH_2-); 13.74(-CH_3). (BMIm Br)

4.3.3. Thermal analysis

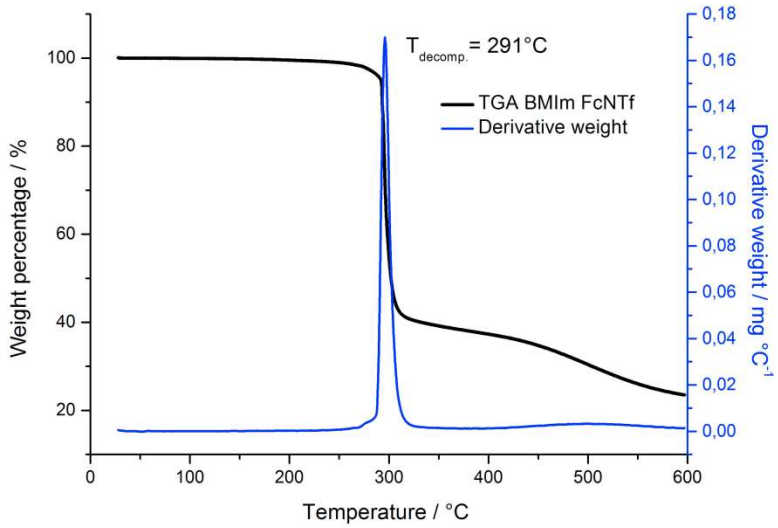

Figure S4.10. TGA of neat BMIm FcNTf with a ramp of 10°C per minute.

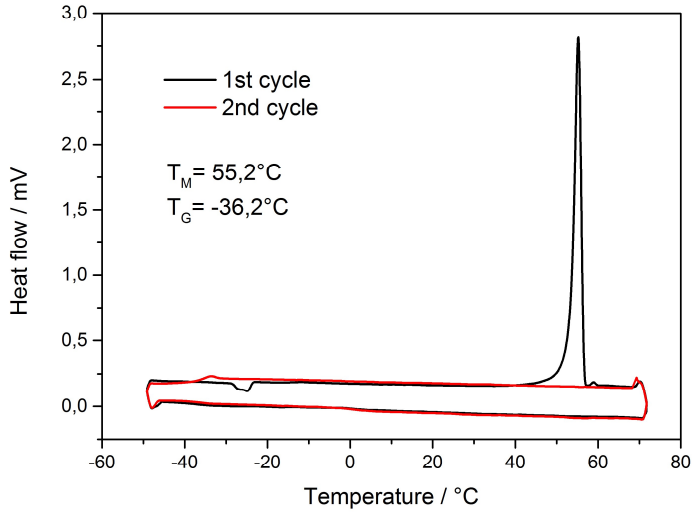

Figure S4.11. Modulated DSC of neat BMIm FcNTf. The measurements were done between -50 to 65°C during 2 cycles with a ramp of 1 °C per minute and with isothermal of 5 minutes between the cooling and heating. The parameter of modulation was ±0.11°C every 40 seconds. First cycle (black line) and second cycle (red line).

4.3.4. Electrochemical analysis

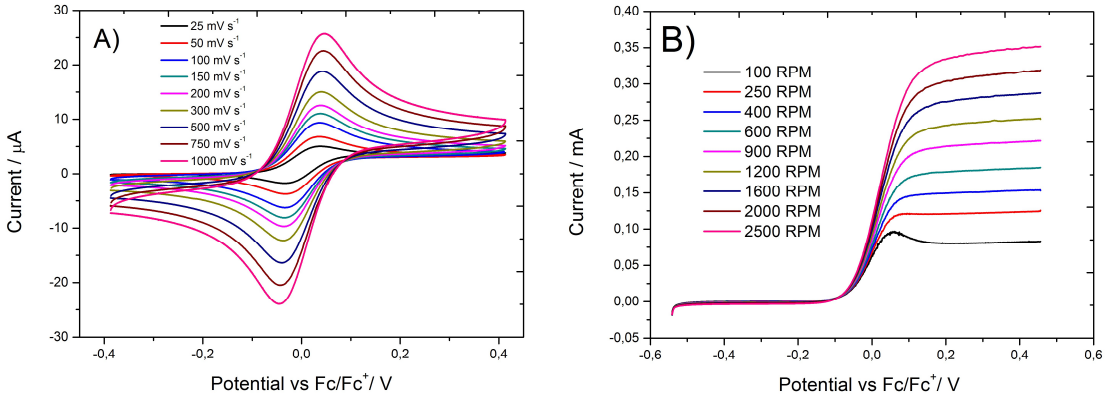

Figure S4.12. A) CVs of 1 mM of Fc in CH_3CN with 0.1 M TBAP at various scan rates. The scan rates used were 25 to 1000 mV s^{-1}. B) RDE voltammetry at 100 mV s^{-1} of 1 mM of Fc in CH_3CN with 0.1 M TBAP at various rotating rates. The rotating rates used were 100 to 2500 RPM.

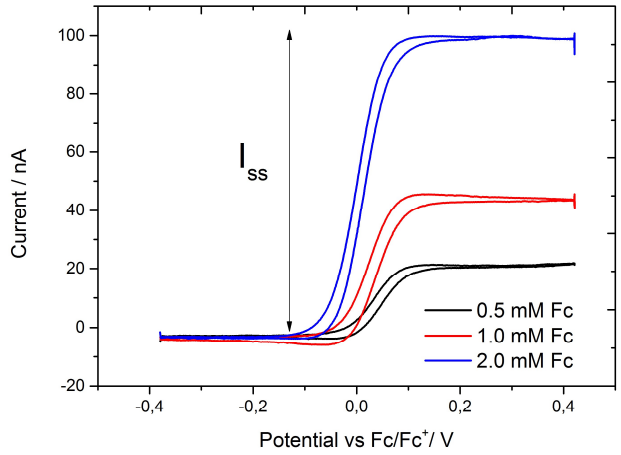

Figure S4.13. A) CVs using a microelectrode of (0.5, 1.0 and 2.0) mM of Fc in CH_3CN with 0.1 M TBAP at 10 mV s^{-1}.

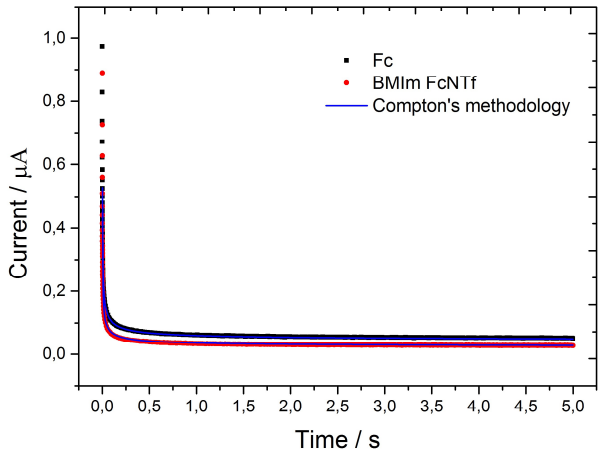

Figure S4.14. DPSC using a microelectrode of 1 mM of Fc (■) and BMIm FcNTf (●) in CH_3CN with 0.1 M TBAP. The duration τ was used 5 s. The initial potentials were -0.38 V [Fc] and -0.18 V [FcNTf]. The step potentials were 0.42 V [Fc] and 0.62 V [FcNTf] (Potential vs. Fc/Fc^+). The Compton's methodology and Shoup and Szabo fitting were used.

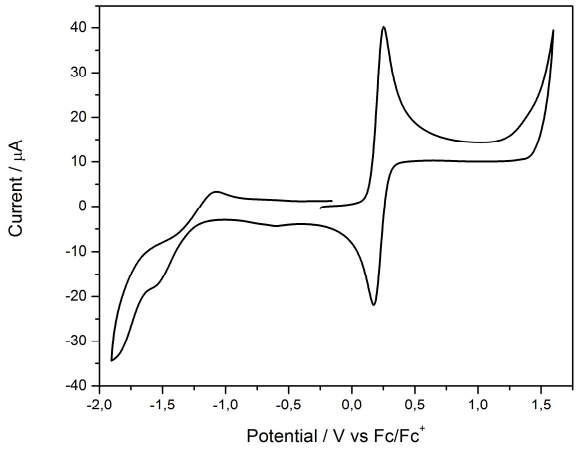

Figure S4.15. CV of 10 mM of BMIm FcNTf in CH_3CN with 1.0 M TBAP at 100 mV s^{-1} shows electrochemical potential window.

Table S4.1. Data obtained from CV analysis for the calculation of rate constants for the oxidation of Fc or BMIM FcNTf (2 mM) in CH_3CN with 0.1 M TBAP as supporting electrolyte.

Electroactive species	Scan rates / V s^{-1}	ΔE_{pa-pc} (Uncorr.) / mV	ΔE_{pa-pc} (Corr.) / mV	Ψ	k_0 / cm s^{-1}
Fc	30	86	63.7	6.16	1.66
	40	92	66.8	3.67	1.14
	50	95	67.4	3.32	1.15
	60	99	69.1	2.64	1.00
	70	101	68.8	2.74	1.13
					1.2±0.3
BMIm FcNTf	30	96	79.7	1.18	0.242
	40	98	79.5	1.19	0.281
	50	102	81.8	1.08	0.285
	60	108	86.1	0.92	0.267
	70	113	89.5	0.82	0.259
					0.27±0.01

Table S4.2. Rate constants for the oxidation of Fc or BMIM FcNTf in CH_3CN with 0.1 M TBAP as supporting electrolyte.

Electroactive species	Concentration / mM	k_0 / cm s^{-1}
Fc	0.5	1.7±0.4
	1.0	1.4±0.4
	2.0	1.3±0.3
BMIm FcNTf	0.5	0.23±0.01
	1.0	0.20±0.01
	2.0	0.27±0.01

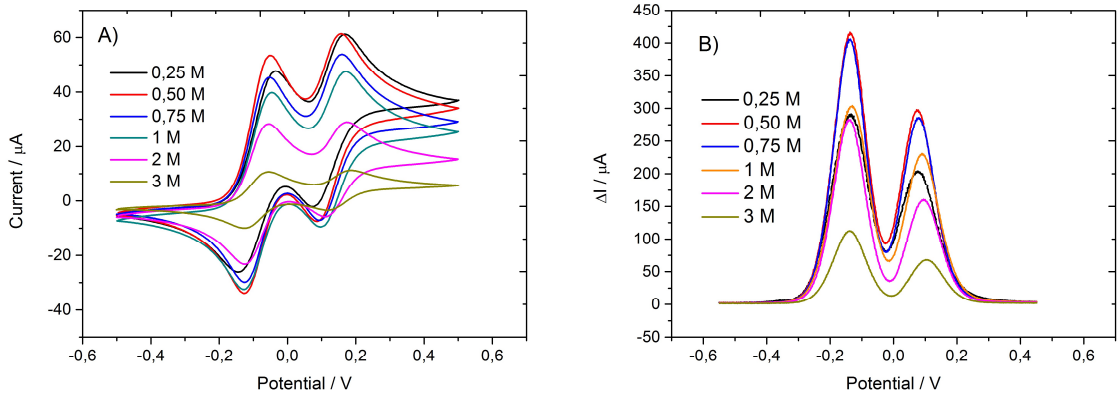

Figure S4.16. CVs (A) at 50 mV s^{-1} and SWV (B) using P_W: 10 ms, P_H: 50 mV and S_H: 1 mV. Electroactive species were 10 mM of Fc and 10 mM of BMIm FcNTf in CH_3CN with various concentrations of BMIm NTf_2. Reference electrode: $Ag/AgNO_3$(sat.) in 0.1 M TBAP with CH_3CN.

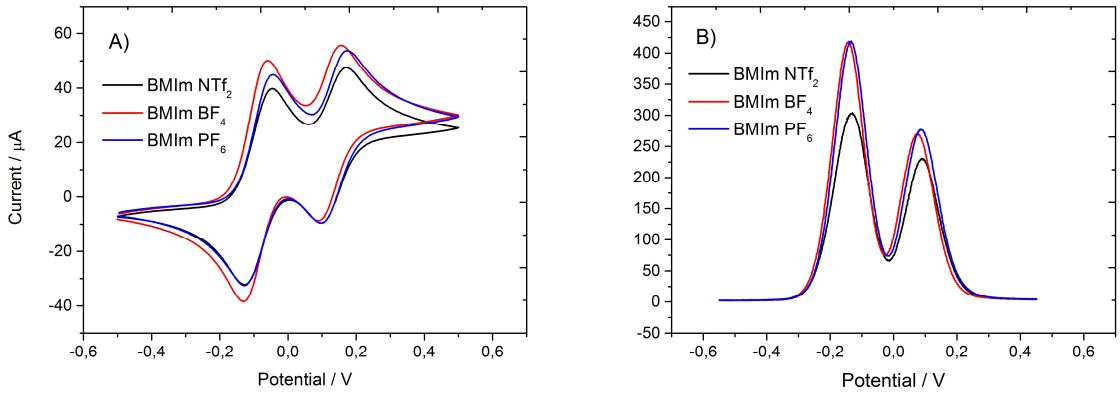

Figure S4.17. CVs (A) at 50 mV s-1 and SWV (B) using Pw: 10 ms, PH: 50 mV and SH: 1 mV. Electroactive species were 10 mM of Fc and 10 mM of BMIm FcNTf in CH_3CN with 1.0 M of IL of different anions such as BMIm NTf_2 (black line), BMIm BF_4 (red line) and BMIm PF_6 (blue line). Reference electrode: $Ag/AgNO_3$(sat.) in 0.1 M TBAP with CH_3CN.

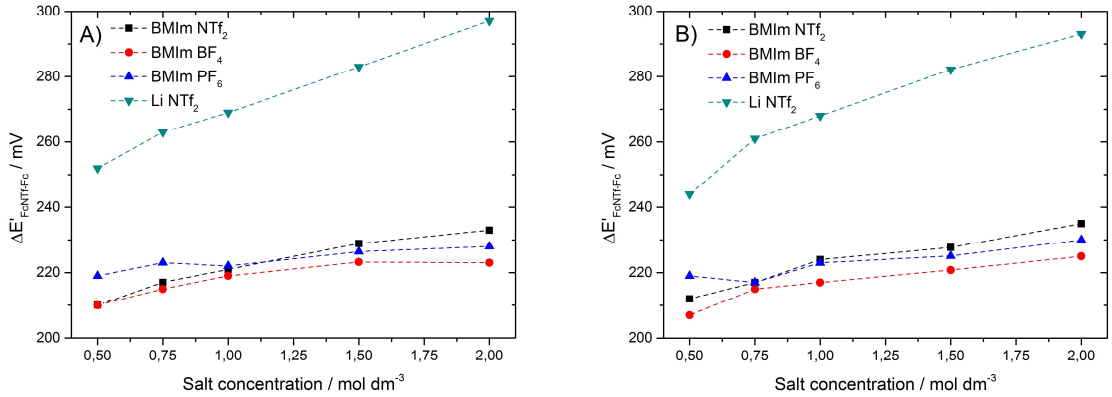

Figure S4.18. Difference of mid-point potential between Fc and BMIm FcNTf using CVs (A) and SWV (B) in CH_3CN with different electrolyte concentrations.

Chapitre 5 : Propriétés de transport et électrochimiques d'un liquide ionique électroactif et de l'ion de lithium

5.1. Avant-propos et mise en contexte

Ce chapitre a été rédigé sous forme d'un article qui a été soumis au *The journal of physical chemistry C.* À la lumière de la littérature, pour certains chercheurs, l'utilisation des liquides ioniques semble impossible d'être un bon électrolyte pour les batteries à lithium-ion. Cependant, dans les dernières années, l'engouement d'utiliser les liquides ioniques a repris de l'ampleur, car le mélange des liquides ioniques avec les solvants de carbonates donne accès à des propriétés exceptionnelles. Par conséquent, la raison et l'implication de cette article va de pair avec les récents avancées. Donc, le mélange entre un liquide ionique électroactif et le propylène carbonate en présence d'un sel de lithium pour établir les propriétés de transport et électrochimiques pour ce type d'électrolyte. Il y a aussi une importante contribution au niveau des sels de lithium électroactifs.

5.2. Article: Electrochemical and transport properties of ions in mixtures of electroactive ionic liquid and propylene carbonate with a lithium salt for lithium-ion batteries

Bruno Gélinas,[a] Myriann Natali,[a] Thomas Bibienne,[a] Qin Ping Li,[a] Mickaël Dollé[a] and Dominic Rochefort [a]

[a]Département de Chimie, Université de Montréal, Montréal, Québec H3C 3J7, Canada

J. Phys. Chem. C, 2016, 120 (10), pp 5315–5325

Received: December 5, 2015 Revised: February 15, 2016 Published: March 3, 2016, DOI: 10.1021/acs.jpcc.5b11911, Publication Date (Web): March 03, 2016,

5.2.1. Abstract

Here, we report on the electrochemistry and transport of ions in mixtures of carbonates and an electroactive ionic liquid, in which lithium bis(trifluoromethylsulfonyl)imide ($Li[NTf_2]$) is dissolved. The electroactive ionic liquid was obtained by linking a ferrocene moiety to the $[NTf_2]^-$, resulting in a redox anion (ferrocenylsulfonyl (trifluoromethylsulfonyl)imide, $[FcNTf]^-$) that can be used as a redox shuttle additive in Li-ion battery electrolytes. Electrochemical and transport properties of the $[FcNTf]^-$ electroactive anion and of Li^+ are investigated by ionic conductivity, cyclic voltammetry and self-diffusion PFGSE NMR measurements. The study of the transport properties demonstrates the formation of solvated species and ion aggregation which affects the electrochemical behavior of the $[FcNTf]^-$ anion. This study highlights that the fractional lithium ion and total ionic conductivity were significantly decreased with a high concentration of ionic liquid and lithium salt. Finally, the electroactive ionic liquid was applied in lithium-ion cells as a proof of concept of their use as redox shuttles.

Graphical abstract

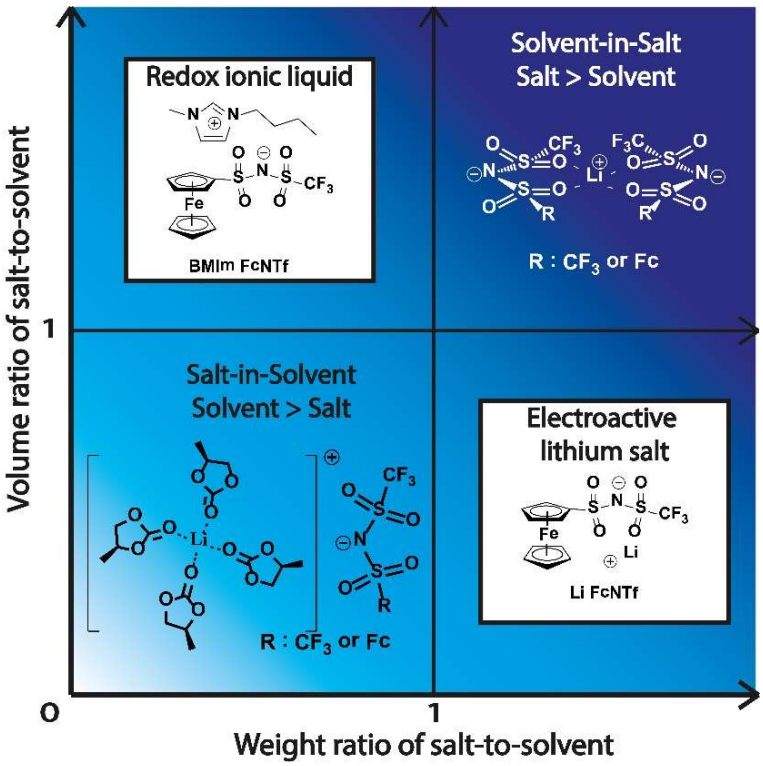

5.2.2. Introduction

Recently, mixtures of ionic liquids and solvent have been gaining interest as electrolytes for lithium-ion batteries.[1-4] On their own, ionic liquids (ILs) have a low volatility, a high electrochemical and thermal stability, a good ionic conductivity, and a high solubility in carbonate solvents, which explain their interest for use as electrolytes in energy storage devices.[5] Research on ILs shows the possibility to create well-adapted electrolytes for batteries,[6, 7] supercapacitors,[8-10] fuel cells,[11, 12] actuators,[13-15] dye-sensitized solar cells,[16, 17] and thermoelectrochemical cells,[18] by taking advantage of IL intrinsic properties but also by modifying their structure with functional groups. These possibilities are increased further by considering mixtures of two different ILs or of an IL with conventional solvents.

Mixing ILs with conventional organic solvents has been proposed to mitigate the negative impact of IL on t_{Li^+} while maintaining the desirable features of the IL in the electrolyte. Due to

their high miscibility with carbonate solvents, ILs (composed of a cation M_{IL}^+ and an anion X_{IL}^-) can be dissolved in high concentrations even in the presence of a lithium salt (Li^+X^-). In such mixtures, when the total salt (i.e., $Li^+ + X^- + M_{IL}^+ + X_{IL}^-$) weight ratio of the electrolyte increases above 1, a "solvent-in-salt" situation is reached (as opposed to the "salt-in-solvent" conditions usually encountered for electrolytes).[19] This new class of electrolyte presents some advantages such as a high t_{Li}^+,[20] a nonflammable electrolyte,[21] preventing the formation of lithium dendrites and aluminum corrosion,[22-24] and improving cyclic and safety performance of lithium-ion batteries (LIBs).[4, 19, 21, 25-27] Organic additives demonstrated two improvements to be useful in the electrolyte: helping to form a solid electrolyte interphase (SEI)[28, 29] and improving the transport properties by a decrease in viscosity. Electrolytes based on ILs are also appealing candidates to allow the application of high-voltage cathode materials.[30-32]

LIBs are widely applied in portable electronic devices and are currently the energy storage devices of choice for an application in electric vehicles.[33] With the scaling up of LIBs arises safety concerns due to the possible cathode overcharge which can lead to electrodes and electrolyte degradation and thermal runaway.[34] Conventional electrolytes such as $LiPF_6$ in carbonate-based solvents will aggravate the outcomes because of their high volatility and flammability.[35] While the use of ILs in high-energy electrochemical devices such as LIBs is very attractive to improve their safety,[6, 36, 37] they present low lithium ion transference numbers ($t_{Li}^+ \approx 0.1$)[38] which lead to concentration polarization and a decrease in rate capability of LIBs.[39] In addition to these desired characteristics, ILs functionalized with an electroactive group can also prevent cathode overcharging using the well-known redox shuttle principle.[40] Our group proposed several new electroactive ILs that could be used as a redox shuttle within LIB electrolytes.[41-43] These redox-active ionic liquids (RILs) also have the advantage of being highly miscible with carbonate electrolyte solvents, thereby increasing the maximum concentration in redox species by a factor of 10. However, very little is known on the impact of these new RILs on electrochemical and transport properties of electrolytes for LIBs, properties that can be strongly affected by the addition of ILs and at high electroactive species concentration. For instance, while Li^+ is known to complex $[NTf_2]^-$ in several electrolytes, including ionic liquids, its interaction with an electroactive anion which has a structure similar to $[NTf_2]^-$ is unknown.[44]

The aim of this research is therefore to evaluate the interaction of the electroactive IL 1-butyl-3-methylimidazolium ferrocenylsulfonyl (trifluoromethylsulfonyl) imide ([BMIm][FcNTf], **Figure 5.1**) on lithium ion transport in a LIB electrolyte. This study focuses on determining how the interactions between Li^+ and $[FcNTf]^-$ will affect the redox properties of the electroactive moiety and, of high importance, the transport of Li^+. To do so, we examined mixtures of the [BMIm][FcNTf] presented in our previous study[45] with an unmodified IL ([BMIm][NTf_2]) and propylene carbonate (PC) containing lithium salt at various concentrations. The effect of each constituent of the electrolyte on ionic conductivity, electrochemical, and self-diffusion properties was studied to have a better understanding of this type of electrolyte. The transport properties of the electroactive anion ($[FcNTf]^-$) within the electrolyte were determined by electrochemical analysis, and the transport properties of each constituent of the electrolyte were investigated by self-diffusion using pulsed field gradient (PFG) NMR spectroscopy using NMR active nuclei (^1H,^{19}F, and ^7Li). These experiments will help determine if the anion of the redox ionic liquid ([BMIm][FcNTf]) has an effect comparable to $[NTf_2]^-$-unmodified IL on lithium transport properties and to improve the electrochemistry of highly concentrated solution of electroactive RIL. Electrolytes were prepared using these electroactive ionic liquids and the lithium salt of the Fc-based anion (Li[FcNTf], **Figure 5.1**) and applied in LIB using coin cells to demonstrate the feasibility of their application as redox shuttles.

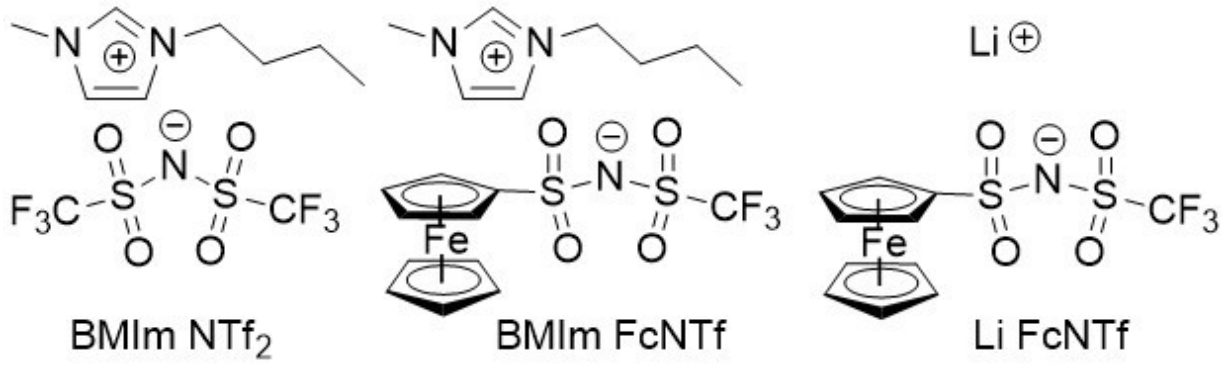

Figure 5.1. Chemical structure of 1-butyl-3-methylimidazolium bis(trifluoromethylsulfonyl)imide ([BMIm] [NTf_2]), 1-butyl-3-methylimidazolium ferrocenylsulfonyl(trifluoromethylsulfonyl)imide ([BMIm] [FcNTf]) and lithium ferrocenylsulfonyl(trifluoromethylsulfonyl)imide (Li [FcNTf]).

5.2.3. Experimental Section

Reagents and Electrolyte Preparation

The electroactive ionic liquid [BMIm][FcNTf] shown in **Figure 5.1** was prepared and purified as reported previously.[45] The synthetic steps to Li[FcNTf] are shown in **Figure S5.1**, and all synthetic details are presented in the Supporting Information. All electrolytes were made in an argon-filled glovebox (MBRAUN) using lithium bis(trifluoromethanesulfonyl)imide (Li[NTf_2]) and propylene carbonate (PC) purchased from Sigma-Aldrich. The unmodified IL used in this investigation for comparison purposes is 1-butyl-3-methylimidazolium bis(trifluoromethanesulfonyl)imide ([BMIm][NTf_2]) purchased from Iolitec (used without further purification).

Ionic Conductivity and Viscosity Measurements

The ionic conductivities of [BMIm][FcNTf] in PC–[BMIm][NTf_2] mixtures were measured by AC impedance technique using a BioLogic SP-50 potentiostat controlled via EC-Lab software. The measurements were carried out in a frequency range of 1 MHz to 1 Hz around an open-circuit potential with AC amplitude of 10 mV RMS and at room temperature. The cell was calibrated daily using a standard 0.117 mol dm^{-3} KCl (15 mS cm^{-1}) aqueous solution at 25 °C. The solution resistance (R_s) was measured from the intercept of the curve of the Nyquist plot on the real impedance axis, and the specific conductivity (σ) was calculated from K (cell constant) divided by R_s. The viscosity of the [BMIm][FcNTf] and [BMIm][NTf_2] mixtures was measured on a Cambridge Applied Systems viscometer (model VL-4100) using pistons with range 200–1000 cP at 25 °C.

Electrochemical Analysis

The cyclic voltammetry experiments were done using a standard three-electrode heart-shaped cell, consisting of a Pt disk working electrode, a Pt wire counter electrode, and a lithium metal QRE with a BioLogic SP-50 potentiostat controlled via EC-lab software. The specific surface

area of the Pt working electrode was determined to be 0.022 cm^2 (geometric area = 0.020 cm^2) using the CV response of a potassium ferricyanide aqueous solution (1 M KCl). All electrochemical data were obtained in an argon-filled glovebox (H_2O, O_2 < 0.1 ppm), and before each experiment the working electrode was polished with alumina, rinsed, sonicated, and dried. All potentials are reported vs the Li/Li^+ redox couple potential reference. The diffusion coefficients were obtained from the CV measurements by plotting the gradient of peak current (I_p) against the square root of the scan rate with the Randles–Sevcik equation (eq 1)

$$I_p = 0.4463nFAC\left(\frac{nF}{RT}\right)^{1/2} v^{1/2}D^{1/2} \qquad (1)$$

where n is the number of electrons; F is the Faraday constant; A is the electrode area; C is the concentration; R is the gas constant; T is the temperature; υ is the scan rate; and D is the diffusion coefficient. The scan rates used were 50–500 mV s^{-1} to calculate the diffusion coefficient. CV responses at high scan rates (750 and 1000 mV s^{-1}), especially at high RIL concentration, can be distorted because of ohmic resistance.

PFG-STE NMR Spectroscopy Analysis

Pulsed-field gradient stimulated echo (PFG-STE) NMR has been used to investigate the self-diffusion coefficients (D_s) of all electrolyte species in a PC–IL mixture. Stimulated-echo acquisition is based on 90°–t_1–90°–t_2–90°–t_1–echo (longitudinal t_1 and transverse t_2 relaxation times), and this pulse sequence relies on the detection of the STE signal appearing at $t_1$relaxation. Monitoring of the self-diffusion of ions was accomplished by applying the magnetic field gradient during the dephasing and rephasing periods and the self-diffusion then calculated. Measurements were performed at room temperature on a Bruker AV500 NMR spectrometer. The measurement of the self-diffusion coefficients was made by selecting an appropriate peak on the NMR spectra for each constituent: ^1H at 4.64 or 4.31 ppm for PC, 8.26, 7.15, 7.10, or 0.62 ppm for $[BMIm]^+$ and 4.38, 4.09, or 4.06 ppm for $[FcNTf]^-$, ^{19}F at −80.05 and −79.52 ppm for $[NTf_2]^-$ and $[FcNTf]^-$, and ^7Li at −0.88 ppm for Li^+. The self-diffusion coefficients were calculated by fitting the NMR signal intensity with Topspin software using the Stejskal–Tanner equation[46] (eq 2)

$$Ln(S/S_0) = -\gamma^2 g^2 D_s \delta^2(\Delta - \delta/3) \qquad (2)$$

where *S* is the spin–echo signal intensity; δ is the duration of the field gradient with magnitude *g*; γ is the gyromagnetic ratio; and Δ is the diffusion time. As expected for free diffusion, NMR signal intensity attenuation against the square of magnitude of the field gradient was well described by a straight line (see **Figure S5.2**). The parameters used for the time diffusion were Δ: 0.4–1 (^{1}H), 0.45–1 (^{19}F) and 1–2 (^{7}Li) s, and for the duration of field gradient: δ: 2–6 (^{1}H), 3–5 (^{19}F), and 4.5–6 (^{7}Li) ms. The magnitude of the field gradient was optimized to obtain the highest attenuation between 8 (^{7}Li) and 16 steps up (^{1}H and^{19}F), and the gradient strength varied from around 20 to 480 mT m^{-1}. The assignments of chemical shifts of each electrolyte species were done from a preliminary NMR analysis.

LIB Coin Cell Analysis

For the positive electrode, a slurry was prepared by mixing $LiTi_2(PO_4)_3$ (preparation and X-ray diffraction pattern in Supporting Information) with carbon black and polyvinylidene fluoride (PVDF) in *N*-methyl-2-pyrrolidone (NMP) solution, with, respectively, 85:10:05 wt %. The slurry was mixed for a few hours to homogenize and then deposit on carbon-coated aluminum foil using the doctor blade method. The coating was dried at 70 °C under vacuum overnight. The dried electrodes were cut in disk shape of 2.5 ± 0.5 mg/cm^2 loading and assembled in coin cells (2032) in argon atmosphere glovebox (H_2O < 1 ppm, O_2 < 1 ppm). Lithium metal was used as an anode (as counter and reference electrode); Celgard 2400 was used as a separator; Li[NTf_2] was diluted in ethylene carbonate (EC); and diethyl carbonate (DEC) (EC-DEC 1:2 vol %) solvents were used at liquid electrolyte. [BMIm][FcNTf] or Li[FcNTf] was added in the liquid electrolyte (unless otherwise stated). Electrochemical tests were performed at 30 °C on a VMP electrochemical station (Bio-Logic), using cutoff voltages of 2.0 and 4.0 V vs Li/Li$^+$ at 0.1 C rate for galvanostatic cycling.

5.2.4. Results and Discussion

Electrochemical and Transport Properties of [BMIm][FcNTf] Using CV Analysis

This present investigation was done to evaluate the electrochemical and transport properties of the electroactive ionic liquid [BMIm][FcNTf] in solvent-in-salt conditions to provide a better understanding of this type of electrolyte. One advantage of the use of RILs as redox shuttles is their

high miscibility in carbonate solvents, providing high concentration in redox centers. To evaluate the solvating effect of an IL on the properties of the $[FcNTf]^-$ anion, we prepared several solutions by adding different concentrations of the nonelectroactive ionic liquid [BMIm][NTf_2]. The concentration of Li[NTf_2] salt in the electrolyte was also varied to study the Li[FcNTf] coordination complex, while maintaining [BMIm][FcNTf] concentration at 0.3 mol dm^{-3}. **Figure 5.2** shows the reversible oxidation CVs of these solutions to demonstrate the impact of IL addition (**Figure 5.2A**) and evaluate the effect of Li[NTf_2] concentrations (**Figure 5.2B**) on the currents and equilibrium potential of the Fc unit on [BMIm][FcNTf]. **Table 5.1** summarizes the electrochemical properties of these measurements. The midpoint potentials (E') of the $[FcNTf]^-$ anion were evaluated for [BMIm][FcNTf] solution in PC–RIL–IL mixtures containing lithium salt, showing that the E' values are around 3.45 V vs Li/Li^+ and are not affected by the concentration of [BMIm][NTf_2] or Li[NTf_2] (**Table 5.1**). Therefore, the major effect of E' comes from the NTf moiety which shifts the potential of ferrocenyl to +0.24 V (vs ferrocene measured under the same conditions). On the basis of this E', the [BMIm][FcNTf] could be considered as a candidate for the protection of cathode material with a potential of at most 3.2 V vs Li/Li^+ since the redox shuttle requires a potential of 300 mV above that of the cathode material to prevent self-discharge.[34]

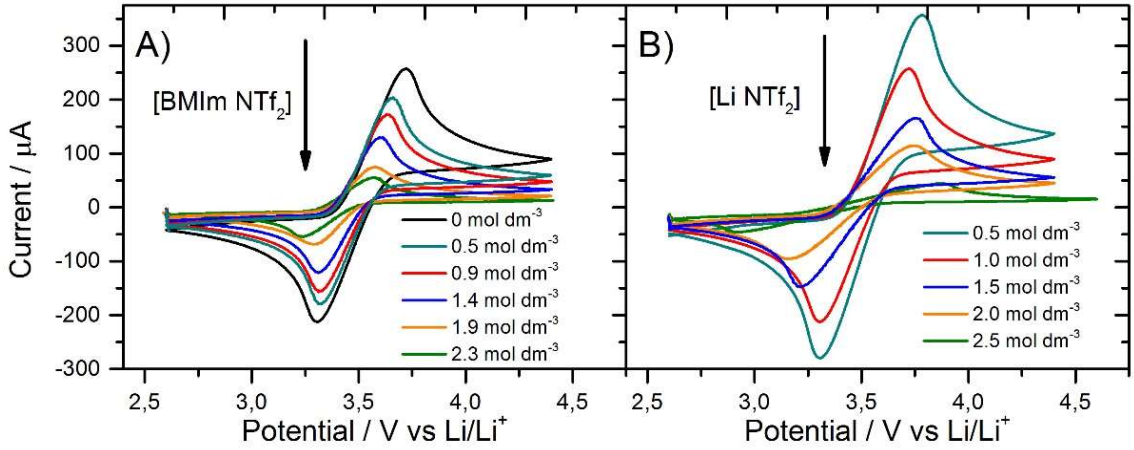

Figure 5.2. A) CVs of 0.3 mol dm^{-3} of [BMIm] [FcNTf] with 1.0 mol dm^{-3} Li [NTf_2] using various concentrations of [BMIm] [NTf_2]. B) CVs of 0.3 M of [BMIm] [FcNTf] in pure PC with various concentrations of Li [NTf_2]. All CVs was recorded at 100 mV s^{-1}.

Table 5.1. Midpoint Potentials and Diffusion Coefficients for Reduction Form of 0.3 mol dm^{-3} [BMIm][FcNTf] in Various Concentrations of [BMIm][NTf_2] and Li[NTf_2] as Supporting Electrolyte[a]

[BMIm NTf_2] mol dm^{-3}	[Li NTf_2] / mol dm^{-3}	E' / V	ΔE_p / V	D_R / X10^{-8} cm^2 s^{-1}
2.3	1.0	3.40	0.33	0.9
1.9	1.0	3.44	0.29	1.7
1.4	1.0	3.46	0.28	5.2
0.9	1.0	3.47	0.32	8.5
0.5	1.0	3.49	0.33	9.8
0	1.0	3.51	0.41	15.5
0	1.5	3.49	0.53	6.7
0	2.0	3.46	0.58	1.7

[a]The scan rates used were 50–500 mV s^{-1} to determinate diffusion rates. All potential data were obtained from CV recorded at 100 mV s^{-1}, and all potentials are given vs Li/Li^+.

The CV shape for the 0.3 mol dm^{-3} RIL solution is clearly distorted, and the peak-to-peak potential separations (ΔE_p) are higher than expected for a purely diffusional regime with a low solution resistance. The large peak splitting is therefore attributed to the iR_s increasing with the RIL concentration due to the high viscosity of the [BMIm][FcNTf] ionic liquid. A solely kinetic effect is not likely because of the relatively high heterogeneous rate transfer constant of $[FcNTf]^-$ in the acetonitrile system (k_0 = 0.27 cm s^{-1}).[45] The gradual increase in unmodified [BMIm][NTf_2] decreases the viscosity while maintaining a high salt concentration (15 cP at 55 °C[47]) since this IL is much less viscous than its $[FcNTf]^-$ counterpart (1140 cP at 56 °C[45]). **Figure S5.3** in the Supporting Information shows the exponential viscosity increase as the molar fraction of [BMIm][FcNTf] increases in the mixture. The Li^+ salt concentration in common liquid electrolytes is typically less than 1.2 mol dm^{-3} and usually limited in a range of 1–2 mol dm^{-3} which is a trade-off among salt solubility, viscosity, and ionic conductivity.[19] Similar to what is obtained from addition of IL, adding Li^+ salt at concentrations above 1.5 mol dm^{-3} rapidly increases electrolyte viscosity, as observed in **Figure 5.2B**. The distortion at high RIL or Li^+ salt concentrations affected the midpoint potential measurement due to differences in charges on the oxidized and reduced species and their interactions with the other ions in the mixture.

The effect of [BMIm][FcNTf] concentration on peak current was evaluated to describe the electrolyte system to be used as a redox shuttle in LIBs and to evaluate the mass transport, which is an important parameter in the redox shuttle mechanism. The diffusion coefficients were calculated from the Randles–Sevcik equation with the I_p vs $v^{1/2}$ curves presented in the Supporting Information (**Figure S5.4A** and **S4B**). The linear fit of Randles–Sevcik relationship using solution containing a high concentration level of electroactive species (0.3 mol dm^{-3}) gives a mass transport constant which is the summation of pure physical diffusion and migration of electroactive species according to Wagner theory and Nernst–Einstein prediction. The migration parameter is not neglected because of the electroactive species and because the supporting electrolyte is almost at the same concentration level, and for ease of explanation, the diffusion coefficient will be the discussed alias for the mass transport constant. The slope of the linear fit of Randles–Sevcik plots gradually decreases at high scan rates which explains the use of the scan rate range of 50–500 mV s^{-1} to calculate the diffusion coefficient. The diffusion coefficients of the $[FcNTf]^-$ anion (reduced form) are given in **Table 5.1** and presented in **Figure 5.3** as a function of [BMIm][NTf_2] or Li[NTf_2] concentration. The mass transport of electroactive species decreases with the increase in IL and Li[NTf_2] as both increase the viscosity of the mixture. The diffusion coefficients of [BMIm][FcNTf] solution were 0.9, 15.5, and 1.7×10^{-8} cm^2 s^{-1}, for 0.3 mol dm^{-3} [BMIm][FcNTf] in IL with 1.0 mol dm^{-3} of Li[NTf_2], in PC with 1.0 mol dm^{-3} of Li[NTf_2], and in PC with 2.0 mol dm^{-3} of Li[NTf_2], respectively. **Figure 5.3** shows a higher impact on the diffusion of the $[FcNTf]^-$ anion for lithium salt addition than IL. This can be explained by the multiple associations of $[FcNTf]^-$/$[NTf_2]^-$ anions with the lithium ion which result in a strong interaction to give a solvated complex. Higher $[FcNTf]^-$:Li^+ or $[NTf_2]^-$:Li^+ ratios generate larger complexes which favor higher viscosities. As expected from the Stokes–Einstein relation (eq 3), an ion cluster or solvated complex ($Li[NTf_2]_x[FcNTf]_y$) is formed with a much larger size than a free $[FcNTf]^-$ anion and affects the diffusion coefficient in this electrolyte.[44]

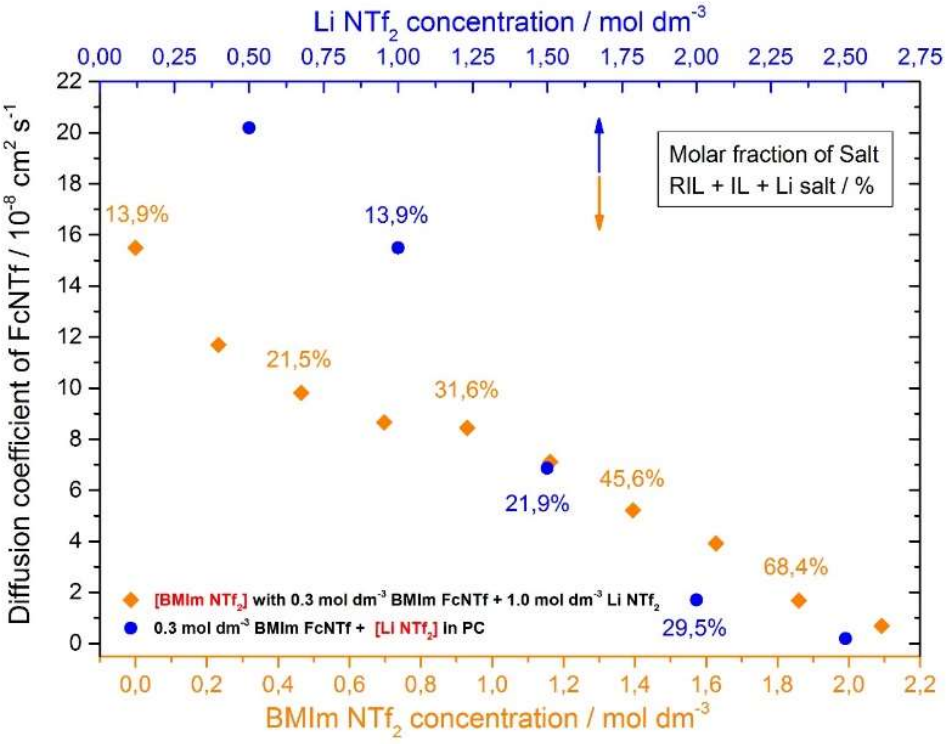

Figure 5.3. Diffusion coefficients from CV analysis as a function of various concentrations of [BMIm] [NTf_2] in PC with 0.3 mol dm^{-3} of [BMIm] [FcNTf] and 1.0 mol dm^{-3} of Li [NTf_2] (orange) and various concentrations of Li [NTf_2] in pure PC with 0.3 mol dm^{-3} [BMIm] [FcNTf] (blue).

Self-Diffusion of Li^+ and $[FcNTf]^-$ Using PFG-STE NMR

A key property that must be taken into account when developing LIB electrolytes is the transport of Li^+. Electrolytes made from pure IL or containing high proportions of IL usually suffer from low t_{Li+} due to the presence of large amounts of other cations and association of Li^+ with some anions to form large complexes. Hence, we studied solutions of a fixed concentration of [BMIm][FcNTf] (0.3 mol dm^{-3}) with various contents of PC, [BMIm][NTf_2], and Li[NTf_2] to evaluate the behavior in the "salt in solvent" and "solvent in salt" conditions. The PC to [BMIm][NTf_2] was varied since the addition of a neutral solvent in the electrolyte contributes to improving to the mass transport of ions. Pure ILs are commonly 1 or 2 orders of magnitude more viscous than typical solvent (e.g., 2.5 cP for PC and 50 cP for [BMIm][NTf_2] at 25 °C).[47] The self-diffusion coefficients for each species within the electrolyte were obtained with PFG-STE NMR spectroscopy experiments using ^1H, ^{19}F, and ^7Li nuclei. The measured values are an average

of different states in solution such as isolated species, ion-pair aggregation, and solvated species. **Figure 5.4A** shows the self-diffusion coefficients as a function of electrolyte composition. A pronounced reduction of ion mobility for mixtures of [BMIm][FcNTf] (RIL) and [BMIm][NTf_2] (IL) is observed as a function of molar fraction of the RIL in [BMIm][NTf_2] because the neat RIL exhibits a low conductivity and high viscosity (see **Figure S5.3**). The self-diffusion coefficients of $[NTf_2]^-$ and $[FcNTf]^-$ differ by a factor of 1.5, which is related to the small $[NTf_2]^-$ anion, compared to the anion bearing a large ferrocenyl unit. The self-diffusion coefficients of the ions in electrolyte as a function of the concentration of IL (**Figure 5.4B**) and lithium salt (**Figure 5.4C**) follow in the order $[FcNTf]^- < Li^+ < [NTf_2]^- < [BMIm]^+$ which can be expected from the Stokes–Einstein relation (eq 3)

$$D = \frac{kT}{6\pi\eta r} \qquad (3)$$

where D ($m^2\ s^{-1}$) is the self-diffusion coefficient; k ($J\ K^{-1}$) is Boltzmann's constant; T (K) is the absolute temperature; r (m) is the solvated radius; and η (Pa s^{-1}) is the dynamic viscosity. Generally, the self-diffusion coefficients of the cations are slightly higher than those of the anions which explain the higher diffusion of $[BMIm]^+$. In polar solvents, coordination of the Li^+ cation with solvent is often seen in the literature which increases the solvation shell of Li^+, explaining why the smaller ion (Li^+) has a lower diffusion coefficient. The addition of IL and Li[NTf_2] increases the viscosity and results in a significant decrease of self-diffusion of all ions.

The donor number is essential to understand the solvation shell and gives a good indication on the solvation of Li^+ cation. The Gutmann donor numbers, which are used as a measure of the strength of solvent following the Lewis basicity, are 15.1 and 10.2 kcal mol^{-1} for PC and [BMIm][NTf_2], respectively.[48] Carbonate solvents present a relatively high electron-donating ability to form ion clustering (Li–PC) in solution which decreases the interaction between Li^+ and $[NTf_2]^-$and explains the high solubility of lithium salt in carbonate solvent and their use in LIB electrolyte.[49] In PC–[BMIm] and [NTf_2]–Li[NTf_2] blends, the Li^+ cation is preferably solvated by PC, but at high concentrations of the $[NTf_2]^-$ anion, the interactions between Li^+ and $[NTf_2]^-$anion become significant. The strong association between PC and Li^+ contributes to its coordination with $[NTf_2]^-$ and [FcNTf], resulting in a better diffusion coefficient by a smaller solvation shell. Kameda et al. reported a demonstration on solvation shell of lithium with PC to

obtain $[Li(PC)_4]^+$ [50] and suggested that a concentrated lithium salt in PC solution can be viewed as a solvate IL because the lithium ion PC-solvated interacts less with the anion.[19, 25, 51] Angell et al. proposed this novel class of ILs in which neutral ligands were coordinating solvent, strongly coordinated with the ion center. The electrostatic interactions between the cation and anion are significantly reduced in these ionic liquids (ex. $Ca(H_2O)_4(NO_3)_2$).[52] Watanabe et al. demonstrated a robust chelate complex of glyme(G_4)–lithium $[NTf_2]$ with a high Li^+ transference number (t_{Li^+}: 0.52), but in this case, the monodentate-based mixture as $[Li(PC)_4][NTf_2]$ acts as a poor solvate IL or concentrated solutions because of the weak complex stability.[53] We summarize this section by proposing a hypothesis where a mixed coordination with PC, $[NTf_2]^-$, and [FcNTf] provides $[Li[PC]_x[NTf_2]_y[FcNTf]_z]$ in different electrolyte composition.[54] Also to be noted, a Li[FcNTf] precipitate is never observed below 1.5 mol $dm^{-3}$of $Li[NTf_2]$ in neat PC due to a strong efficient ion clustering (Li-PC). However, at 2.0–2.5 mol dm^{-3} of $Li[NTf_2]$ in PC with 0.3 mol dm^{-3} of [BMIm][FcNTf], a precipitate of Li[FcNTf] after one month is observed. A similar observation for mixtures with a high amount of $[BMIm][NTf_2]$ (over than 1.8 mol dm^{-3} of IL) was noted. Consequently, the trend of self-diffusion of PC indicates strong interactions with the ions and follows the viscosity of electrolyte (D vs $1/\eta$; see **Figure 5.4B** and **4C**).

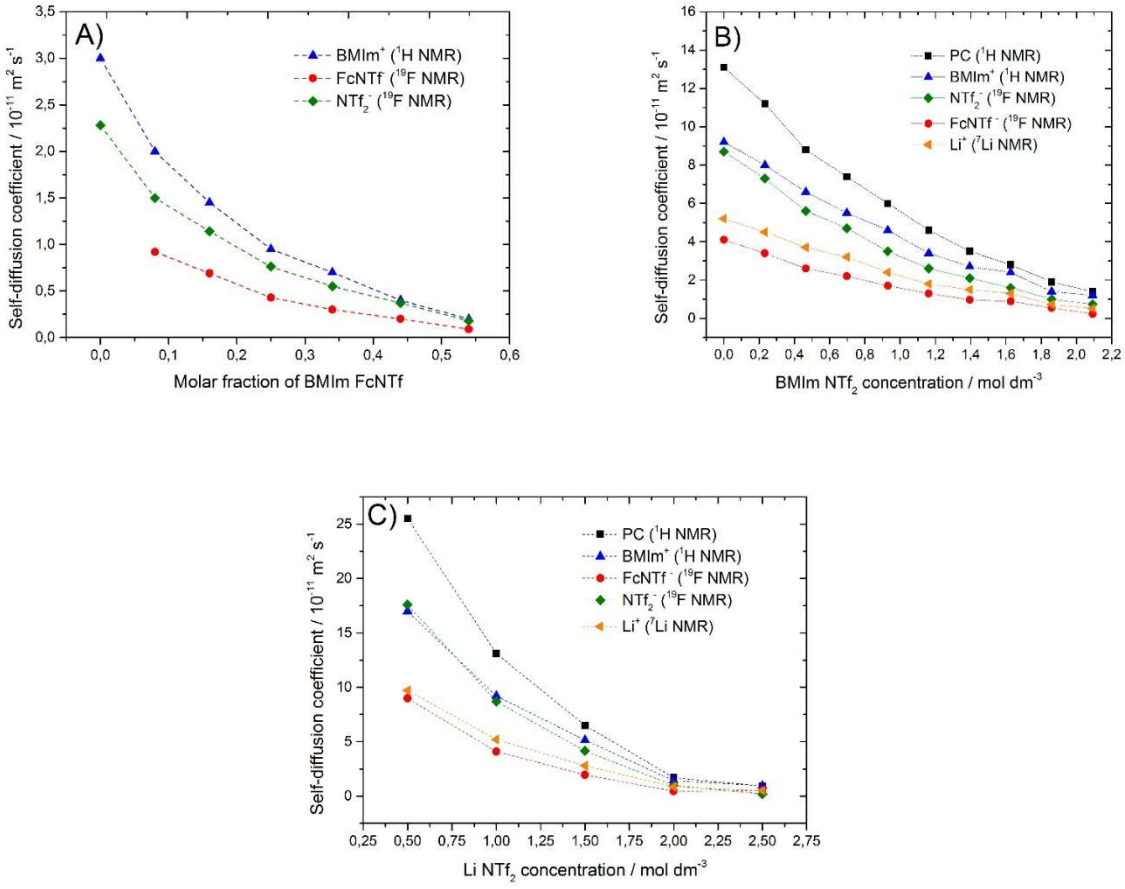

Figure 5.4. Self-diffusion coefficients as a function of A) molar fraction of [BMIm] [FcNTf] in neat [BMIm] [NTf_2], B) various concentrations of [BMIm] [NTf_2] in PC with 0.3 mol dm^{-3} of [BMIm] [FcNTf] and 1.0 mol dm^{-3} of Li [NTf_2] and C) various concentrations of Li [NTf_2] in pure PC with 0.3 mol dm^{-3} [BMIm] [FcNTf].

Transference Numbers and NMR Conductivity Properties of Li^+ and $[FcNTf]^-$

The power capability of LIB is a considerable factor for which the properties of the electrolyte play an important role. While the transference number of Li^+ must be as high (closer to unity) as possible, it is usually found closer to 0.4–0.5 in typical electrolytes and even below 0.1 in pure IL. The apparent transference numbers (t_i) of ions were obtained from the self-diffusion coefficients of all ions present in electrolyte, according to eq 4

$$t_i = \frac{x_i D_i}{\sum_i x_i D_i} \quad (4)$$

where x_i and D_i ($m^2\ s^{-1}$) are the molar fraction of ion and self-diffusion coefficient of an ion, respectively. Apparent transference numbers (t_i) for Li^+, $[NTf_2]^-$, $[BMIm]^+$, and $[FcNTf]^-$ using PC–IL mixtures and various $Li[NTf_2]$ concentrations are presented in **Figure 5.5A** and **5B**, respectively. As anticipated, the Li^+ and $[NTf_2]^-$ transference numbers are reduced when PC is gradually replaced with IL in the PC–IL mixtures. The t_{Li+} reaches 0.10 in IL concentrated solution which is an expected value for a mixture of an imidazolium IL with lithium salts (**Figure 5.5A**).[38] Consequently, [BMIm][FcNTf] showed a similar effect on t_{Li}^+ as the unmodified $[BMIm][NTf_2]$ which is an important finding since $[FcNTf]^-$ was expected to be more deleterious to the conductivity than $[NTf_2]^-$. The positive transference number is obtained by the addition of cation transference numbers ($t_+ = t_{Li}^+ + t_{[BMIm]}^+$), and the same reasoning was applied for t_- ($t_- = t_{[NTf2]}^- + t_{[FcNTf]}^-$). **Figure 5.5A** shows that the anions are the main charge carriers (t_- (0.55) > t_+ (0.45)) for solutions with a low content in IL (0.5 mol dm^{-3} $[BMIm][NTf_2]$ + 0.3 mol dm^{-3} [BMIm][FcNTf]), but this is inverted at higher concentration in $[BMIm][NTf_2]$ where cations are the main charge carrier (t_- (0.45) < t_+ (0.55)) and at high concentration of $[BMIm]^+$ cations are the main positive charge carriers. This can be explained by a large solvation shell for Li^+ cation in PC that decreases their mobility, as discussed above. Moreover, when several anions are available in solution to form an ion cluster as mentioned previously (high fraction of IL), the ion cluster decreases the mobility of an anion of $[NTf_2]^-$ and $[FcNTf]^-$ which, in turn, decreases t_-. The anionic ($[NTf_2]^-$ and $[FcNTf]^-$) transference number does not change significantly with the gradual increase in IL concentration. The investigation on electrolytes using different $Li[NTf_2]$ concentrations in neat PC with 0.3 mol dm^{-3} [BMIm][FcNTf] (**Figure 5.5B**) shows a comparable trend. However, as the concentration of the Li^+ cation is increased, Li^+ becomes the dominant charge carrier for positive charges. The $[BMIm]^+$ and $[FcNTf]^-$ transference numbers are reduced with addition of $Li[NTf_2]$, while it is the opposite for Li^+. The Li^+ transference number increased from 0.23 to 0.43 for solutions containing 0.5–2.5 mol dm^{-3} of $Li[NTf_2]$, respectively. The results show t_- (0.55) > t_+ (0.45) for solutions with a low concentration in Li^+ salt and t_-(0.45) < t_+ (0.55) with a high concentration in Li^+ salt.

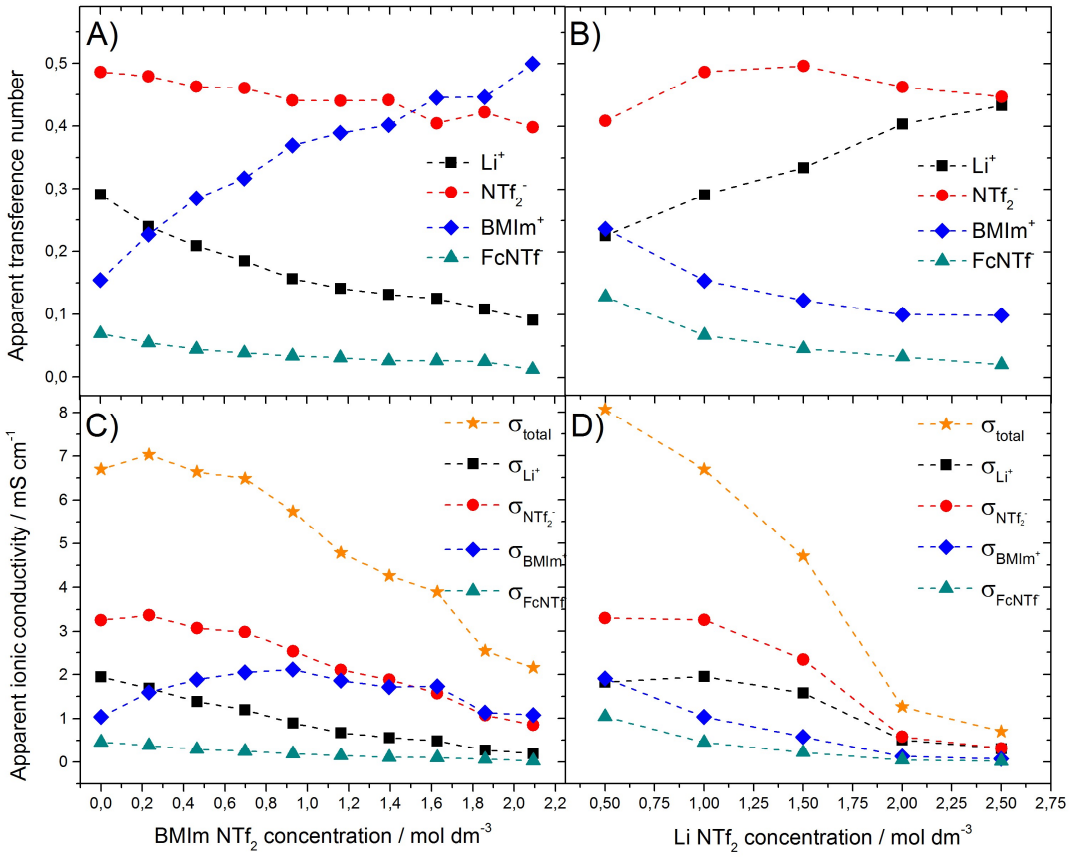

Figure 5.5. Apparent transference number of Li^+, $[NTf_2]^-$, $[BMIm]^+$ and $[FcNTf]^-$ for A) various concentrations of [BMIm] $[NTf_2]$ with 0.3 mol dm^{-3} of [BMIm] [FcNTf] and 1.0 mol dm^{-3} of Li $[NTf_2]$ and B) various concentrations of Li $[NTf_2]$ in pure PC with 0.3 mol dm^{-3} [BMIm] [FcNTf]. NMR total ionic conductivities and apparent fractional ionic conductivities of Li^+, $[NTf_2]^-$, $[BMIm]^+$ and $[FcNTf]^-$ for C) various concentrations of [BMIm] $[NTf_2]$ with 0.3 mol dm^{-3} of [BMIm] [FcNTf] and 1.0 mol dm^{-3} of Li $[NTf_2]$ and D) various concentrations of Li $[NTf_2]$ in pure PC with 0.3 mol dm^{-3} [BMIm] [FcNTf].

NMR ionic conductivity assumes that all ions contribute to the conductivity and does not consider ion pairing and aggregation states. A comparison of the NMR and impedance conductivity, therefore, can provide an evaluation of the ionicity of the mixtures. The contribution of the Li^+ to the ionic conductivity is crucial, and the fractional ionic conductivity was calculated by multiplying the apparent transference number of the ion with NMR total ionic conductivity. The NMR ionic conductivity of electrolytes depends on the diffusion coefficient given by the Nernst–Einstein relation (eq 5), as follows

$$\sigma_{NMR} = \frac{N_A e^2}{kT} \sum_i c_i D_i \quad (5)$$

where σ_{NMR} (S m^{-1}) is ionic conductivity given by NMR; e (C) is the elementary charge; k (J K^{-1}) is the Boltzmann constant; T (K) is the absolute temperature; N_A (mol^{-1}) is Avogadro's number;c (mol m^{-3}) is the ion concentration; and D (m^2 s^{-1}) is the self-diffusion coefficient of the ion. NMR ionic conductivity (σ_{NMR}) and apparent fractional conductivity (σ_i) for Li^+, $[NTf_2]^-$, $[BMIm]^+$, and [FcNTf] are presented in **Figure 5.5C** and **5D** as a function of IL and lithium salt concentration, respectively. **Figure 5.5C** and **5D** show the impact of addition of [BMIm][FcNTf] on Li^+ conductivity for 0.3 mol dm^{-3} [BMIm][FcNTf] with 1.0 mol dm^{-3} $Li[NTf_2]$ in PC. The NMR ionic conductivity and fractional Li^+ conductivity are diminished by the addition of RIL from 8.05 to 6.70 mS $cm^{-1}$and 3.22 to 1.95 mS cm^{-1}, respectively. Such a decrease is attributed to a global increase in viscosity due to the use of a viscous RIL, but the pronounced decrease for conductivity associated with Li^+ is explained by the contribution of the $[BMIm]^+$ cation added from the RIL. The issue of RIL addition in the electrolyte composition results from the higher transference number and conductivity of the imidazolium cation which is faster than the Li^+ cation. Many authors reported a low value of t_{Li^+} using IL.[38] Regardless of the conditions used, the transference number of the $[FcNTf]^-$ anion is significantly smaller than that of $[NTf_2]^-$ due to its larger size, showing the low contribution to ionic conductivity of the redox anion. According to the results of **Figure 5.5C** and **5D**, the NMR and fractional ionic conductivity decrease drastically with high concentrations of IL and lithium salt due to the formation of solvated species $[Li[PC]_x[NTf_2]_y[FcNTf]_z]$ as proposed. Despite a high Li^+ transference number for a high concentration in Li^+ salt (2.0–2.5 mol dm^{-3}), the fractional Li^+ conductivities are analogous to the value obtained upon of high amount of IL in the electrolyte.

Ion Paring and Aggregation

The ionicity of the electrolyte was evaluated as a function of IL content to study ion pairing and aggregation in the presence of [BMIm][FcNTf]. Ionicity was determined as the ratio of the ionic conductivity measured by AC impedance spectroscopy (σ_{AC}) over NMR conductivity (σ_{NMR}) evaluated by PFE-STE. **Figure 5.6** shows that both σ_{AC} and σ_{NMR} follow the same tendency to decrease with the addition of [BMIm][NTf_2] in PC. The decrease was less pronounced for the ionic conductivity measured by AC impedance. At high IL concentrations, typical ionic conductivities obtained for neat IL containing Li[NTf_2] are reached. The σ_{AC} for different Li[NTf_2] concentrations were 3.99, 4.25, and 2.52 mS cm^{-1} by adding 0.5, 1.0, and 1.5 mol dm^{-3} of Li[NTf_2], respectively. The range of ionicity was ca. 60% between 0 and 1.6 mol dm^{-3} of the IL [BMIm][NTf_2], showing significant ion pairing. While these results in this concentration range do not seem to be affected by the composition, the values obtained are similar to those reported in a study by Balducci and co-workers.[55] [BMIm][NTf_2] and [BMIm][FcNTf] have a similar impact on the ionicity which is comparable to electrolyte without RIL, and the ionicity depends on the cation–anion couple chosen and solvent added. An increase of lithium salt addition to IL usually reduces the ionicity because of the high charge density of lithium, and the Coulombic interaction was favored and increases ion pairing. Above the 1.6 mol dm^{-3} of the IL [BMIm][NTf_2], the ionicity abruptly jumps to 75%, showing a marked change in ion interactions between the different “salt-in-solvent” and “solvent-in-salt” conditions.

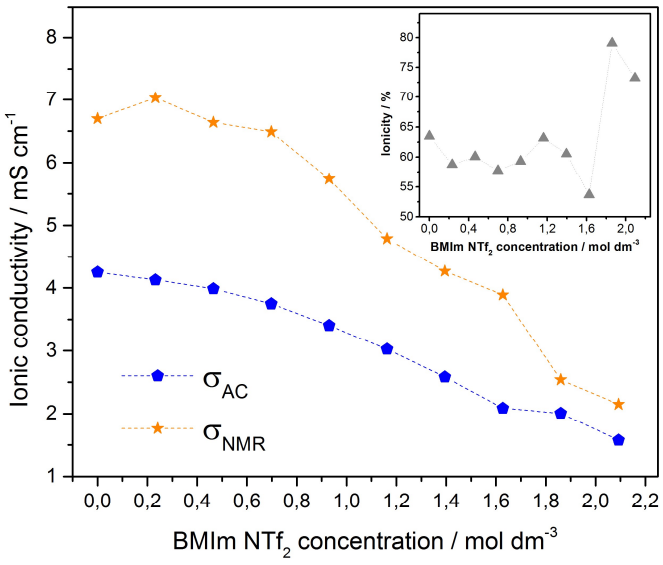

Figure 5.6. NMR and AC ionic conductivities using various concentrations of [BMIm] [NTf_2] with 0.3 mol $dm^{-3}$of [BMIm] [FcNTf] and 1.0 mol dm^{-3} of Li [NTf_2]. Ionicity is given by σ_{AC}/σ_{NMR}. Ionic conductivities were measured at room temperature.

Electrolyte Properties Using Li[FcNTf] Electroactive Lithium Salt

The results presented so far suggest that the cation of the ionic liquid is in large part responsible for the low t_{Li}^+ in the electrolyte. To confirm this effect of ionic liquids, the same $[FcNTf]^-$ anion was synthesized with a Li^+ in lieu of the $[BMIm]^+$ cation. The resulting compound, Li[FcNTf], was dissolved in the electrolyte at various conditions to achieve the in solvent-in-salt and salt-in-solvent conditions. The solubility of Li[FcNTf] in PC, limited to ca. 0.3 mol dm^{-3}, is lower than conventional Li^+ salts. In comparison, the ionic liquid made from this anion, [BMIm][FcNTf], is miscible with PC over the whole range of concentrations. **Table 5.2** summarizes all electrochemical and transport properties of ions in different electrolytes, including the results of the electroactive Li^+ salt (Li[FcNTf]). For each electrolyte, the lithium salt and redox $[FcNTf]^-$concentrations were maintained at 1.0 and 0.3 mol dm^{-3}, respectively. The diffusion and self-diffusion coefficients of $[FcNTf]^-$ obtained by CV and NMR are very similar for each method and each electrolyte composition. The electrochemical analysis of Li[FcNTf] electrolyte is presented in **Figure S5.5** in the Supporting Information, and the electrochemical

behavior of $[FcNTf]^-$ was similar in each electrolyte (see **Figure S5.6**). The NMR analysis shows a decrease of self-diffusion of all ions between a nonelectroactive (Electrolyte 1) and electroactive (Electrolytes 2 and 3) electrolyte but a slight increase of self-diffusion coefficients for electrolyte using electroactive Li^+salt (Electrolyte 3). In particular, the self-diffusion coefficients of lithium were 5.2 and 5.8 × $10^{-7}$$cm^2$ s^{-1} for Electrolytes 2 and 3, respectively. This decrease represents a difference of 33% with the nonelectroactive electrolyte, and this measurement indicates an ion paring between Li^+ and $[FcNTf]^-$ which slows down the mobility of the Li^+ cation regardless of the countercation of $[FcNTf]^-$. Normally, the solvated Li^+ is slower than the $[NTf_2]^-$ anion, and the impact of interaction between anion–cation ($Li[NTf_2]$) is less significant than the use of a large electroactive anion as $[FcNTf]^-$. The transference number of ions was also shown in **Table 5.2**. For electrolyte without IL (Electrolytes 1 and 3), t_{Li^+} is around 0.4 as expected for lithium salt in carbonate solvent, and there is a smaller value of t_{Li^+} for electrolyte with RIL (Electrolyte 2) which amounts to 0.29. The NMR conductivity follows the order Electrolyte 1 < Electrolyte 2 < Electrolyte 3, which can be expected by the slow mobility of $[FcNTf]^-$ and the fast mobility of $[BMIm]^+$. However, the fractional Li^+ conductivity follows this order, Electrolyte 1 < Electrolyte 3 < Electrolyte 2, which is explained by the contribution of $[BMIm]^+$. Also, the total salt concentration was absolutely different in each electrolyte (Electrolytes 1 and 3: 1.0 mol dm^{-3} of salt and Electrolyte 2: 1.3 mol dm^{-3} of salt). Consequently, the NMR and AC ionic conductivity are higher for Electrolyte 2 than Electrolyte 3 which results in an extra ion concentration, and obviously, the electrolyte without $[FcNTf]^-$ (Electrolyte 1) presents a higher AC ionic conductivity (5.16 cm^2 s^{-1}). The iconicity suggests a better dissociation of Li[FcNTf] in comparison with $Li[NTf_2]$. The ionicity is 0.64, 0.63, and 0.75 for the electrolyte made without electroactive [FcNTf], RIL electrolyte, and electroactive Li^+ salt electrolyte, respectively.

Table 5.2. All electrolyte parameters using CV, NMR and AC impedance (Electrolyte 1: 1.0 mol dm^{-3} of Li [NTf_2] in PC; Electrolyte 2: 0.3 mol dm^{-3} of [BMIm] [FcNTf] and 1.0 mol dm^{-3} of Li [NTf_2] in PC; Electrolyte 3: 0.3 mol dm^{-3} of Li [FcNTf] and 0.7 mol dm^{-3} of Li [NTf_2] in PC).

Parameters	Electrolyte 1	Electrolyte 2	Electrolyte 3
Salt concentrations / mol dm^{-3}	[Li NTf_2] = 1.0	[BMIm FcNTf] = 0.3 [Li NTf_2] = 1.0	[Li FcNTf] = 0.3 [Li NTf_2] = 0.7
D_{FcNTf-} via CV / x10^{-7} cm^2 s^{-1}	-	1.6	1.1
D_{FcNTf-} via NMR / x10^{-7} cm^2 s^{-1}	-	4.1	4.0
D_{NTf2-} via NMR / x10^{-7} cm^2 s^{-1}	12.9	8.7	9.4
D_{Li+} via NMR / x10^{-7} cm^2 s^{-1}	8.6	5.2	5.8
D_{BMIm+} via NMR / x10^{-7} cm^2 s^{-1}	-	9.2	-
D_{PC} via NMR / x10^{-7} cm^2 s^{-1}	18.7	13.1	14.0
t_{FcNTf-}	-	0.07	0.09
t_{NTf2-}	0.60	0.49	0.48
t_{Li+}	0.40	0.29	0.43
t_{BMIm+}	-	0.15	-
σ_{NMR} / mS cm^{-1}	8.05	6.70	5.09
σ_{FcNTf-} / mS cm^{-1}	-	0.47	0.45
σ_{NTf2-} / mS cm^{-1}	4.83	3.28	2.46
σ_{Li+} / mS cm^{-1}	3.22	1.95	2.17
σ_{BMIm+} / mS cm^{-1}	-	1.01	-
σ_{AC} / mS cm^{-1}	5.16	4.25	3.80
Ionicity	0.64	0.63	0.75

Coin Cell Testing and Battery Performance

In order to investigate the properties of these electroactive species as redox shuttles, half-cell battery characteristics were examined using the Nasicon-type titanium phosphate ($LiTi_2(PO_4)_3$; LTP)[56] as the positive electrode material. The charge–discharge curves recorded at the fifth cycle for a Li/LTP cell are presented in **Figure 5.7** to compare the cell behavior as a function of the presence or absence in a redox shuttle. The charge–discharge cycles obtained at a 0.1 C rate show the normal charging plateau at 2.5 V vs Li/Li^+. Following this full charge, an extra amount of one full charge was forced in the system to study the overcharge. When the Li/LTP coin cell electrolyte did not contain any redox shuttle the cell voltage raised rapidly until it reached the 4 V safety cutoff. However, if the electrolyte contained 0.3 mol dm^{-3} of R–S (either [BMIm][FcNTf] or Li[FcNTf]) a second plateau at a higher voltage appeared in the profiles at 3.5 V vs Li/Li^+ which is a result of the redox shuttle being oxidized and effectively preventing the overoxidation of the LTP electrode. The specific capacities calculated from the discharge curves at 0.1 C rate were 122, 126, and 124 mAh g^{-1} for the Li/LTP cell containing no redox shuttle, 0.3 mol dm^{-3} of [BMIm][FcNTf], and 0.3 mol dm^{-3} of Li[FcNTf], respectively (**Table 5.3**). The theoretical capacity for LTP is usually 138 mAh g^{-1}, but practical values are usually found at 121 mAh g^{-1}.[57]These very similar values demonstrate that the ferrocene-modified ionic liquid can be used to prevent the overoxidation of LTP and that it did not affect the normal cell operation when present at 0.3 mol dm^{-3}. In **Figure 5.7B** are compared the fifth and 50th charge–discharge cycles obtained at a 0.1 C rate with the electrolyte containing the Li[FcNTf] redox shuttle. As shown, there are only very little capacity losses after 50 cycles, and this shuttle was able to efficiently prevent LTP overoxidation even at this higher rate. While the overcharge protection of LIB cells by redox shuttles based on ionic liquids remains to be investigated in more detail, this study indicates that electroactive species based on the modification of the bistriflamides are interesting candidates as additives in an advanced electrolyte for the cathode protection in LIBs.

Table 5.3. The electrochemical characterisation of Li/LTP cell at 0.1 C rate for the 5th cycle in different electrolytes (Electrolyte A: 1.0 mol dm^{-3} of Li [NTf_2] in EC-DEC 1:2 v/v; Electrolyte B: 0.3 mol dm^{-3} of [BMIm] [FcNTf] and 1.0 mol dm^{-3} of Li [NTf_2] in EC-DEC 1:2 v/v; Electrolyte C: 0.3 mol dm^{-3} of Li [FcNTf] and 1.0 mol dm^{-3} of Li [NTf_2] in EC-DEC 1:2 v/v).

Parameters	**Electrolyte A**	**Electrolyte B**	**Electrolyte C**
Salt concentrations / mol dm^{-3}	[Li NTf_2] = 1.0	[BMIm FcNTf] = 0.3 [Li NTf_2] = 1.0	[Li FcNTf] = 0.3 [Li NTf_2] = 1.0
Charge capacity / mAh g^{-1}	124	124	128
Discharge capacity / mAh g^{-1}	122	126	124
Coulombic efficiency / %	98	102	97

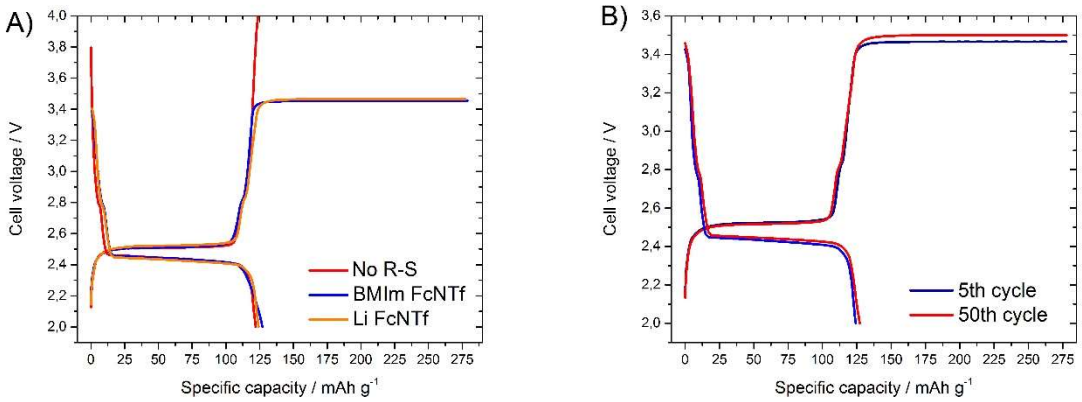

Figure 5.7. A) Capacity profile of Li/LTP cell at 0.1 C rate and 10 h. overcharge for the 5th cycle containing different electrolytes (Electrolyte A (Red line): 1.0 mol dm^{-3} of Li [NTf_2] in EC-DEC 1:2 v/v; Electrolyte B (Blue line): 0.3 mol dm^{-3} of [BMIm] [FcNTf] and 1.0 mol dm^{-3} of Li [NTf_2] in EC-DEC 1:2 v/v; Electrolyte C (Orange line): 0.3 mol dm^{-3} of Li [FcNTf] and 1.0 mol dm^{-3} of Li [NTf_2] in EC-DEC 1:2 v/v). B) Capacity profile for the 5th (Blue line) and 50th (Red line) cycle containing Electrolyte C.

5.2.5. Conclusions

This report highlights the electrochemical and transport properties of an electroactive anion (ferrocenylsulfonyl(trifluoromethylsulfonyl)imide; $[FcNTf]^-$) and Li^+ in a mixtures of PC, IL, RIL, and lithium salt. The main goal was to demonstrate the impact of [BMIm][FcNTf], with a focus on the role of the electroactive anion $[FcNTf]^-$ on Li^+ properties within this electrolyte which can be used in LIBs to prevent the overoxidation of a cathode by the redox shuttle principle. The midpoint potential of the $[FcNTf]^-$ anions was 3.51 V vs Li/Li^+, showing that [BMIm][FcNTf] is an appropriate candidate for overcharge protection of cathode material with a potential of 3.2–3.3 V vs Li/Li^+. ILs and lithium salt did not affect the midpoint potential. This study showed the importance of concentration of $Li[NTf_2]$ and RILs for LIB applications because of their strong impact on ion mobility. The substitution of ILs by PC in a PC–IL mixture improves the mobility of the ions. The Li^+ mobility was affected by the presence of ions in aggregated states such as ion pairing, solvated species, and solvate ILs in a concentrated solution. $[FcNTf]^-$ anion shows a low mobility, and its contribution to the ionic conductivity contribution was not significant. [BMIm][FcNTf] presents an equivalent impact on t_{Li^+} and σ_{Li^+} than $[BMIm][NTf_2]$, showing that the addition of Fc on the anion did not promote or prevent the formation of the complexes with Li^+. Redox shuttle using redox anions presents a great potential according with this report via the insignificant impact on t_+ and t_{Li^+} and gives the opportunity to not use unnecessary cations. The next steps will consist of an evaluation of the compatibility in LIB cells and comparing the performance of LIB cells with and without a redox shuttle based on $[FcNTf]^-$ anions.

5.2.6. Associated Content

Supporting Information

The Supporting Information is available free of charge on the ACS Publications website at DOI:10.1021/acs.jpcc.5b11911. Synthetic procedure of lithium ferrocenylsulfonyl(trifluoromethylsulfonyl) imide, summary of self-diffusion analysis, details for electrochemical analysis, and details for LTP preparation and XRD (PDF)

5.2.7. Acknowledgments

The authors acknowledge the financial support from Fonds de recherche du Québec en nature et technologies (FQRNT) under their program for the reduction of greenhouse gases and the Natural Sciences and Engineering Research Council of Canada (NSERC) for Discovery grant (D.R.). The authors also acknowledge Cédric Malveau and region centre of NMR spectroscopy from the Department of chemistry of the Université de Montréal.

5.2.8. References

[1] S. Theivaprakasam, D.R. MacFarlane, S. Mitra, Electrochemical studies of N-methyl N-propyl pyrrolidinium bis(trifluoromethanesulfonyl) imide ionic liquid mixtures with conventional electrolytes in LiFePO4/Li cells, Electrochim. Acta, 180 (2015) 737-745.
[2] S. Fang, L. Qu, D. Luo, S. Shen, L. Yang, S.-i. Hirano, Novel mixtures of ether-functionalized ionic liquids and non-flammable methylperfluorobutylether as safe electrolytes for lithium metal batteries, RSC Adv., 5 (2015) 33897-33904.
[3] A. Hofmann, M. Schulz, S. Indris, R. Heinzmann, T. Hanemann, Mixtures of ionic liquid and sulfolane as electrolytes for Li-ion batteries, Electrochim. Acta, 147 (2014) 704-711.
[4] L. Lombardo, S. Brutti, M.A. Navarra, S. Panero, P. Reale, Mixtures of ionic liquid – Alkylcarbonates as electrolytes for safe lithium-ion batteries, J. Power Sources, 227 (2013) 8-14.
[5] D.R. MacFarlane, N. Tachikawa, M. Forsyth, J.M. Pringle, P.C. Howlett, G.D. Elliott, J.H. Davis, M. Watanabe, P. Simon, C.A. Angell, Energy applications of ionic liquids, Energy Environ. Sci., 7 (2014) 232-250.
[6] B. Garcia, S. Lavallée, G. Perron, C. Michot, M. Armand, Room temperature molten salts as lithium battery electrolyte, Electrochim. Acta, 49 (2004) 4583-4588.
[7] H. Matsumoto, H. Sakaebe, K. Tatsumi, M. Kikuta, E. Ishiko, M. Kono, Fast cycling of Li/LiCoO2 cell with low-viscosity ionic liquids based on bis(fluorosulfonyl)imide [FSI]−, J. Power Sources, 160 (2006) 1308-1313.
[8] A. Balducci, U. Bardi, S. Caporali, M. Mastragostino, F. Soavi, Ionic liquids for hybrid supercapacitors, Electrochem. Comm., 6 (2004) 566-570.
[9] A. Balducci, W.A. Henderson, M. Mastragostino, S. Passerini, P. Simon, F. Soavi, Cycling stability of a hybrid activated carbon//poly(3-methylthiophene) supercapacitor with N-butyl-N-methylpyrrolidinium bis(trifluoromethanesulfonyl)imide ionic liquid as electrolyte, Electrochim. Acta, 50 (2005) 2233-2237.
[10] A. Balducci, F. Soavi, M. Mastragostino, The use of ionic liquids as solvent-free green electrolytes for hybrid supercapacitors, Appl. Phys. A, 82 (2006) 627-632.
[11] J. Sun, L.R. Jordan, M. Forsyth, D.R. MacFarlane, Acid–Organic base swollen polymer membranes, Electrochim. Acta, 46 (2001) 1703-1708.
[12] A.P. Sunda, Ammonium-based protic ionic liquid doped Nafion membranes as anhydrous fuel cell electrolytes, J. Mater. Chem. A, 3 (2015) 12905-12912.
[13] Y. He, T.P. Lodge, Thermoreversible ion gels with tunable melting temperatures from triblock and pentablock copolymers, Macromolecules, 41 (2008) 167-174.

[14] M.D. Green, D. Wang, S.T. Hemp, J.-H. Choi, K.I. Winey, J.R. Heflin, T.E. Long, Synthesis of imidazolium ABA triblock copolymers for electromechanical transducers, Polymer, 53 (2012) 3677-3686.
[15] S. Imaizumi, Y. Ohtsuki, T. Yasuda, H. Kokubo, M. Watanabe, Printable polymer actuators from ionic liquid, soluble polyimide, and ubiquitous carbon materials, ACS Appl. Mater. Interfaces, 5 (2013) 6307-6315.
[16] Y. Bai, Y. Cao, J. Zhang, M. Wang, R. Li, P. Wang, S.M. Zakeeruddin, M. Gratzel, High-performance dye-sensitized solar cells based on solvent-free electrolytes produced from eutectic melts, Nat. Mater., 7 (2008) 626-630.
[17] J.M. Pringle, V. Armel, The influence of ionic liquid and plastic crystal electrolytes on the photovoltaic characteristics of dye-sensitised solar cells, Int. Rev. Phys. Chem., 30 (2011) 371-407.
[18] T. Migita, N. Tachikawa, Y. Katayama, T. Miura, Thermoelectromotive force of some redox couples in an amide-type room-temperature ionic liquid, Electrochem., 77 (2009) 639-641.
[19] S. Liumin, H. Yong-Sheng, L. Hong, A. Michel, C. Liquan, A new class of Solvent-in-Salt electrolyte for high-energy rechargeable metallic lithium batteries, Nat. Commun., 4 (2013) 1481-1481.
[20] P.M. Bayley, G.H. Lane, N.M. Rocher, B.R. Clare, A.S. Best, D.R. MacFarlane, M. Forsyth, Transport properties of ionic liquid electrolytes with organic diluents, Phys. Chem. Chem. Phys., 11 (2009) 7202-7208.
[21] A. Guerfi, M. Dontigny, P. Charest, M. Petitclerc, M. Lagacé, A. Vijh, K. Zaghib, Improved electrolytes for Li-ion batteries: Mixtures of ionic liquid and organic electrolyte with enhanced safety and electrochemical performance, J. Power Sources, 195 (2010) 845-852.
[22] R.-S. Kühnel, M. Lübke, M. Winter, S. Passerini, A. Balducci, Suppression of aluminum current collector corrosion in ionic liquid containing electrolytes, J. Power Sources, 214 (2012) 178-184.
[23] T. Evans, J. Olson, V. Bhat, S.-H. Lee, Effect of organic solvent addition to PYR13FSI + LiFSI electrolytes on aluminum oxidation and rate performance of Li(Ni1/3Mn1/3Co1/3)O2 cathodes, J. Power Sources, 265 (2014) 132-139.
[24] A. Hofmann, L. Merklein, M. Schulz, T. Hanemann, Anodic aluminum dissolution of LiTFSA containing electrolytes for Li-ion-batteries, Electrochim. Acta, 116 (2014) 388-395.
[25] T. Mandai, K. Yoshida, K. Ueno, K. Dokko, M. Watanabe, Criteria for solvate ionic liquids, Phys. Chem. Chem. Phys., 16 (2014) 8761-8772.
[26] R.S. Kühnel, N. Böckenfeld, S. Passerini, M. Winter, A. Balducci, Mixtures of ionic liquid and organic carbonate as electrolyte with improved safety and performance for rechargeable lithium batteries, Electrochim. Acta, 56 (2011) 4092-4099.
[27] S. Menne, R.S. Kühnel, A. Balducci, The influence of the electrochemical and thermal stability of mixtures of ionic liquid and organic carbonate on the performance of high power lithium-ion batteries, Electrochim. Acta, 90 (2013) 641-648.
[28] G.H. Lane, A.S. Best, D.R. MacFarlane, M. Forsyth, A.F. Hollenkamp, On the role of cyclic unsaturated additives on the behaviour of lithium metal electrodes in ionic liquid electrolytes, Electrochim. Acta, 55 (2010) 2210-2215.
[29] H. Ota, K. Shima, M. Ue, J.-i. Yamaki, Effect of vinylene carbonate as additive to electrolyte for lithium metal anode, Electrochim. Acta, 49 (2004) 565-572.
[30] Z. Wang, Y. Cai, Z. Wang, S. Chen, X. Lu, S. Zhang, Vinyl-functionalized imidazolium ionic liquids as new electrolyte additives for high-voltage Li-ion batteries, J. Solid-State Electrochem., 17 (2013) 2839-2848.

[31] X.-W. Gao, C.-Q. Feng, S.-L. Chou, J.-Z. Wang, J.-Z. Sun, M. Forsyth, D.R. MacFarlane, H.-K. Liu, LiNi0.5Mn1.5O4 spinel cathode using room temperature ionic liquid as electrolyte, Electrochim. Acta, 101 (2013) 151-157.
[32] N. Wongittharom, T.-C. Lee, I.M. Hung, S.-W. Lee, Y.-C. Wang, J.-K. Chang, Ionic liquid electrolytes for high-voltage rechargeable Li/LiNi0.5Mn1.5O4 cells, J. Mater. Chem. A, 2 (2014) 3613-3620.
[33] M. Armand, J.M. Tarascon, Building better batteries, Nature, 451 (2008) 652-657.
[34] Z. Chen, Y. Qin, K. Amine, Redox shuttles for safer lithium-ion batteries, Electrochim. Acta, 54 (2009) 5605-5613.
[35] K. Xu, Nonaqueous liquid electrolytes for lithium-based rechargeable batteries, Chem. Rev., 104 (2004) 4303-4418.
[36] H. Sakaebe, H. Matsumoto, N-ethyl-N-propylpiperidinium bis(trifluoromethanesulfonyl)imide (PP13–TFSI) – novel electrolyte base for Li battery, Electrochem. Comm., 5 (2003) 594-598.
[37] S. Seki, Y. Kobayashi, H. Miyashiro, Y. Ohno, A. Usami, Y. Mita, N. Kihira, M. Watanabe, N. Terada, Lithium secondary batteries using modified-imidazolium room-temperature ionic liquid, J. Phys. Chem. B, 110 (2006) 10228-10230.
[38] T. Frömling, M. Kunze, M. Schönhoff, J. Sundermeyer, B. Roling, Enhanced lithium transference numbers in ionic liquid electrolytes, J. Phys. Chem. B, 112 (2008) 12985-12990.
[39] A. Fernicola, F. Croce, B. Scrosati, T. Watanabe, H. Ohno, LiTFSI-BEPyTFSI as an improved ionic liquid electrolyte for rechargeable lithium batteries, J. Power Sources, 174 (2007) 342-348.
[40] J.C. Forgie, S. El Khakani, D.D. MacNeil, D. Rochefort, Electrochemical characterisation of a lithium-ion battery electrolyte based on mixtures of carbonates with a ferrocene-functionalised imidazolium electroactive ionic liquid, Phys. Chem. Chem. Phys., 15 (2013) 7713-7721.
[41] B. Gélinas, J.C. Forgie, D. Rochefort, Conductivity and electrochemistry of ferrocenyl-imidazolium redox ionic liquids with different alkyl chain lengths, J. Electrochem. Soc., 161 (2014) H161-H165.
[42] J.C. Forgie, S. El Khakani, D.D. MacNeil, D. Rochefort, Electrochemical characterization of a lithium-ion battery electrolyte based on mixtures of carbonates with a ferrocene-functionalised imidazolium electroactive ionic liquid, Phys. Chem. Chem. Phys., 15 (2013) 7713-7721.
[43] S.E. Khakani, J.C. Forgie, D.D. MacNeil, D. Rochefort, Redox shuttles for lithium-ion batteries at concentrations up to 1 M using an electroactive ionic liquid based on 2,5-di-tert-butyl-1,4-dimethoxybenzene, J. Electrochem. Soc., 162 (2015) A1432-A1438.
[44] A. Andriola, K. Singh, J. Lewis, L. Yu, Conductivity, viscosity, and dissolution enthalpy of LiNTF2 in ionic liquid BMINTF2, J. Phys. Chem. B, 114 (2010) 11709-11714.
[45] B. Gélinas, D. Rochefort, Synthesis and characterization of an electroactive ionic liquid based on the ferrocenylsulfonyl(trifluoromethylsulfonyl)imide anion, Electrochim. Acta, 162 (2015) 36-44.
[46] E.O. Stejskal, J.E. Tanner, Spin Diffusion Measurements: Spin echoes in the presence of a time-dependent field gradient, J. Chem. Phys., 42 (1965) 288-292.
[47] H. Tokuda, S. Tsuzuki, M.A.B.H. Susan, K. Hayamizu, M. Watanabe, How ionic are room-temperature ionic liquids? An indicator of the physicochemical properties, J. Phys. Chem. B, 110 (2006) 19593-19600.
[48] M. Schmeisser, P. Illner, R. Puchta, A. Zahl, R. van Eldik, Gutmann donor and acceptor numbers for ionic liquids, Chem. Eur. J., 18 (2012) 10969-10982.

[49] M. Herstedt, M. Smirnov, P. Johansson, M. Chami, J. Grondin, L. Servant, J.C. Lassègues, Spectroscopic characterization of the conformational states of the bis(trifluoromethanesulfonyl)imide anion (TFSI−), J. Raman Spectrosc., 36 (2005) 762-770.
[50] Y. Kameda, Y. Umebayashi, M. Takeuchi, M.A. Wahab, S. Fukuda, S.-i. Ishiguro, M. Sasaki, Y. Amo, T. Usuki, Solvation structure of Li+ in concentrated LiPF6−propylene carbonate solutions, J. Phys. Chem. B, 111 (2007) 6104-6109.
[51] C. Zhang, K. Ueno, A. Yamazaki, K. Yoshida, H. Moon, T. Mandai, Y. Umebayashi, K. Dokko, M. Watanabe, Chelate effects in glyme/lithium bis(trifluoromethanesulfonyl)amide solvate ionic liquids. I. Stability of solvate cations and correlation with electrolyte properties, J. Phys. Chem. B, 118 (2014) 5144-5153.
[52] C.A. Angell, A new class of molten salt mixtures the hydrated dipositive ion as an independent cation species, J. Electrochem. Soc., 112 (1965) 1224-1227.
[53] K. Ueno, K. Yoshida, M. Tsuchiya, N. Tachikawa, K. Dokko, M. Watanabe, Glyme–lithium salt equimolar molten mixtures: Concentrated solutions or solvate ionic liquids?, J. Phys. Chem. B, 116 (2012) 11323-11331.
[54] L.J. Hardwick, M. Holzapfel, A. Wokaun, P. Novák, Raman study of lithium coordination in EMI-TFSI additive systems as lithium-ion battery ionic liquid electrolytes, J. Raman Spectrosc., 38 (2007) 110-112.
[55] R.-S. Kühnel, A. Balducci, Lithium ion transport and solvation in N-butyl-N-methylpyrrolidinium bis(trifluoromethanesulfonyl)imide–propylene carbonate mixtures, J. Phys. Chem. C, 118 (2014) 5742-5748.
[56] B. Lang, B. Ziebarth, C. Elsässer, Lithium ion conduction in LiTi2(PO4)3 and related compounds based on the NASICON structure: A first-principles study, Chem. Mater., 27 (2015) 5040-5048.
[57] V. Aravindan, J. Gnanaraj, Y.-S. Lee, S. Madhavi, Insertion-type electrodes for nonaqueous Li-ion capacitors, Chem. Rev., 114 (2014) 11619-11635.

5.3. Suppporting Information

Electrochemical and Transport Properties of Ions in Mixtures of Electroactive Ionic Liquid and Propylene Carbonate with a Lithium Salt for Lithium-ion Batteries

*Bruno Gélinas, Myriann Natali, Thomas Bibienne, Lily Li, Michaël Dollé and Dominic Rochefort**

Département de chimie, Université de Montréal, CP6128 Succ. Centre-Ville, Montréal, Québec, Canada H3C 3J7

*Corresponding author: Tel: +1-514-343-6733, Fax: +1-514-343-7586, email: dominic.rochefort@umontreal.ca

List of Contents:

5.3.1. Synthetic procedure of Lithium Ferrocenylsulfonyl (trifluoromethylsulfonyl)imide (Li [FcNTf]) in two step procedure.

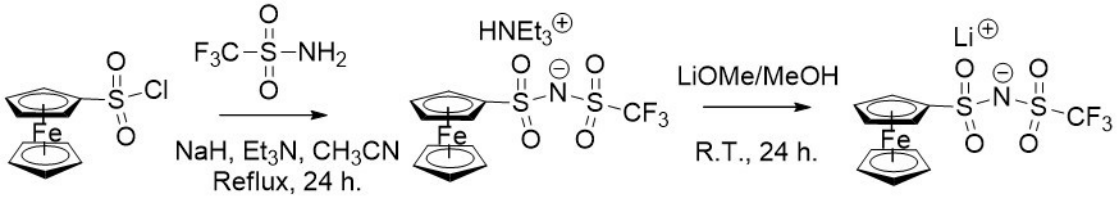

Figure S5.1. Synthetic pathway of Lithium Ferrocenylsulfonyl (trifluoromethylsulfonyl)imide (Li [FcNTf])

Sodium hydride (1 eq., 60% dispersion in oil) was placed in a round-bottom flask under argon atmosphere and placed in ice bath. Trifluoromethanesulfonamide (1 eq.) was dissolved in acetonitrile and was cautiously added dropwise to sodium hydride. The solution was stirred during 10 minutes at 0 °C. A slow addition of ferrocenylsulfonyl chloride (1 eq.) was then made and trimethylamine (1.15 eq.) was also added. The resulting solution was stirred and heated at reflux temperature for 24 hours. The brown solution was filtered and the precipitate was washed with acetone to achieve a white precipitate. Removal of the solvent under reduced pressure produced a brown oil and the oil was washed with diethyl ether to remove the unreacted ferrocenylsulfonyl chloride. Dichloromethane was used to dissolve the oil, the organic phase was washed with 1.0 M HCl aqueous solution and dried over $MgSO_4$. The triethylammonium ferrocenylsulfonyl(trifluoromethylsulfonyl)imide ([Et_3HN] [FcNTf]) was dried overnight under reduce pressure at room temperature and enough pure to be directly used in the next procedure. [Et_3HN] [FcNTf] was dissolved in methanol and lithium methoxide (2 eq.) was added. The mixture was stirred during 24 h. at room temperature and the solvent was then removed under vacuum. The lithium salt was extracted with diethyl ether and the solution was filtered over filter agent Celite. The solvent was removed under vacuum, Li [FcNTf] was triturated by methyl tert-butyl ether to remove coordinated diethyl ether and the brown-yellow salt was dried overnight under reduce pressure at 80 °C. ^{1}H NMR (DMSO-d_6, 300 MHz): δ (ppm) = 4.53 (t, 2H), 4.28 (s, 7H). ^{19}F NMR (DMSO-d_6, 282 MHz): δ (ppm) = -79.06. ^{13}C NMR (DMSO-d_6, 125 MHz): δ (ppm) = 122.74; 118.43; 94.57; 70.42; 69.18; 68.59. (ESI) m/z: [M^{*-}](calcd for $C_{11}H_9F_3FeNO_4S_2^-$) : 395.928 Found: 395.926.

5.3.2. Summary of self-diffusion analysis

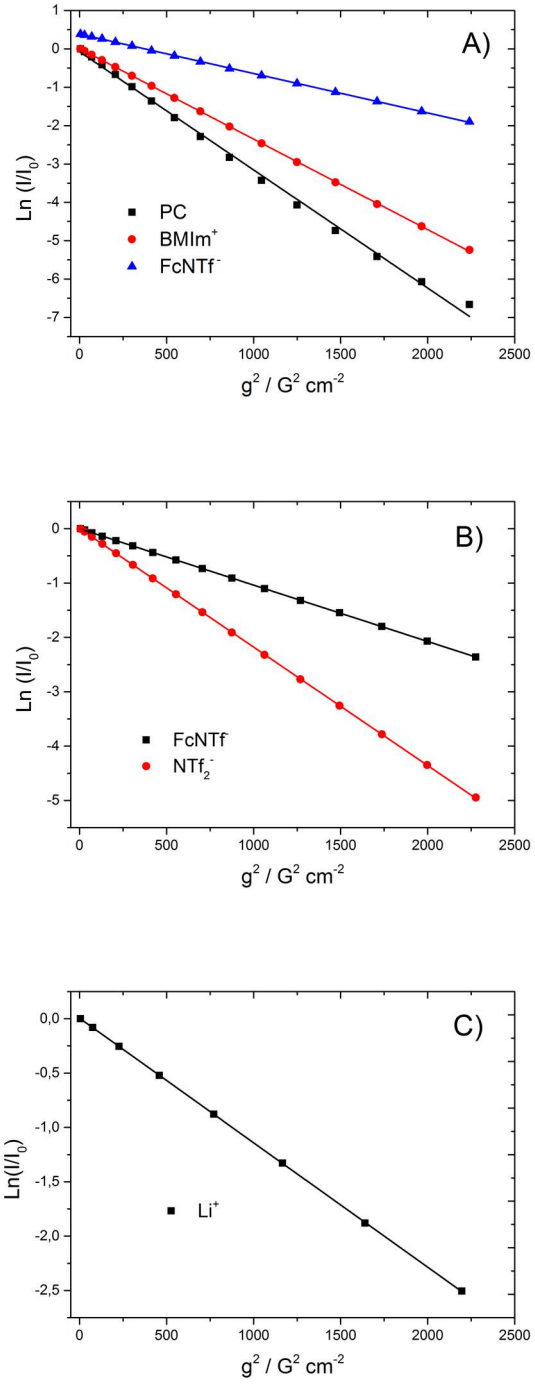

Figure S5.2. Stejskal-Tanner plots ($Ln(I/I_0)$ vs g^2) of 0.3 M of [BMIm] [FcNTf] with 1.0 M $LiNTf_2$ in pure PC using A) ^{1}H, B) ^{19}F and C) ^{7}Li NMR.

5.3.3. Viscosity measurements

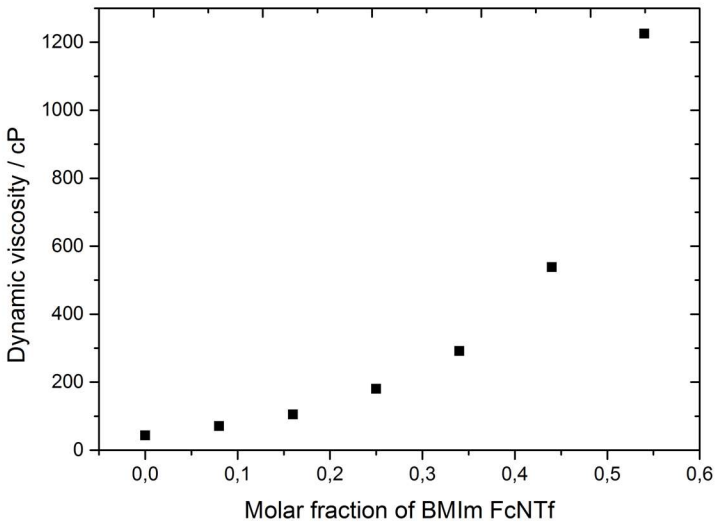

Figure S5.3. Dynamic viscosity as a function of molar fraction of [BMIm] [FcNTf] in Neat IL

5.3.4. Electrochemical analysis and additional figures

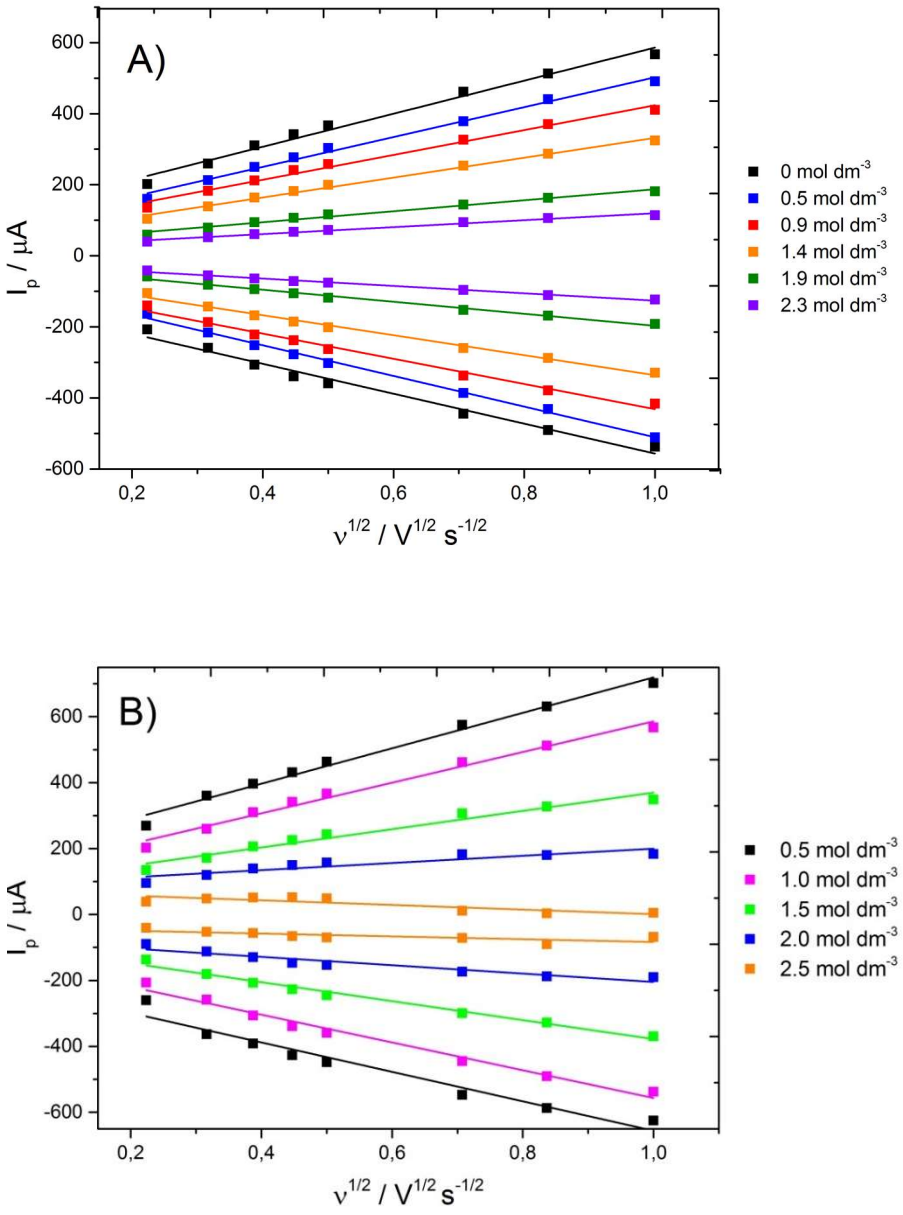

Figure S5.4. A) Randles-Sevcik plots (I_p vs $v^{1/2}$) of 0.3 M of [BMIm] [FcNTf] with 1.0 mol dm^{-3} Li [NTf_2] in PC using various concentrations of [BMIm] [NTf_2]. B) Randles-Sevcik plots (I_p vs $v^{1/2}$) of 0.3 mol dm^{-3} of [BMIm] [FcNTf] in pure PC with various concentrations of Li [NTf_2]. The scan rates used were 50 to 1000 mV s^{-1}.

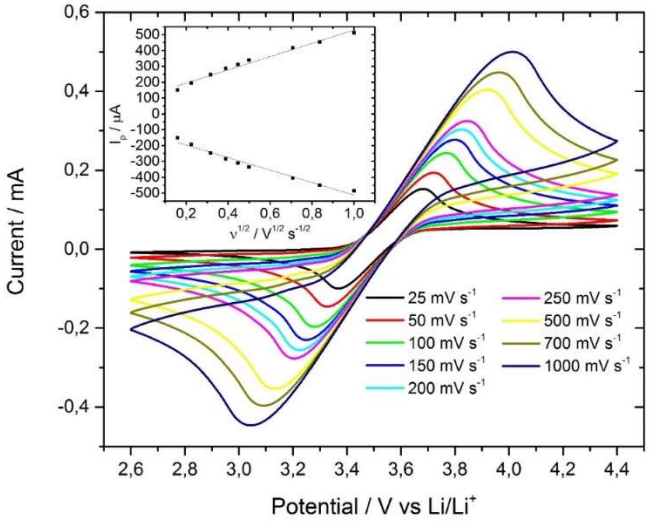

Figure S5.5. CVs and Randles-Sevcik plots (I_p vs $v^{1/2}$) 0.3 mol $dm^{-3}$of Li [FcNTf] with 0.7 mol dm^{-3} of Li [NTf_2] in PC. The scan rates used were 25 to 1000 mV s^{-1}.

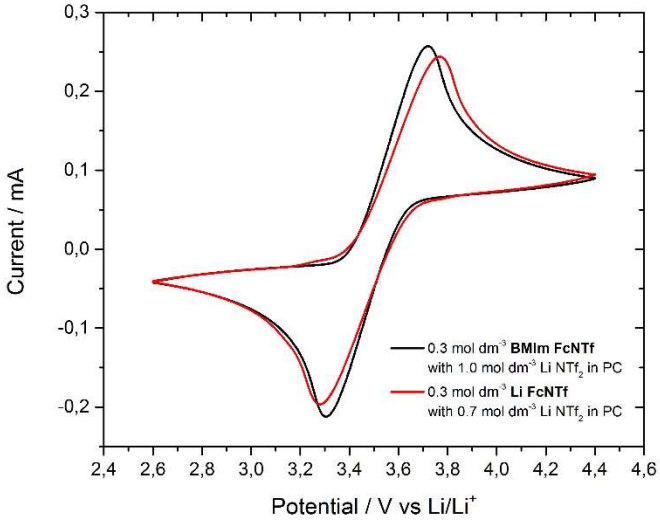

Figure S5.6. CVs of 0.3 mol $dm^{-3}$of [BMIm] [FcNTf] with 1.0 mol dm^{-3} of Li [NTf_2] in PC (Electrolyte 2; black line) and 0.3 mol $dm^{-3}$of Li [FcNTf] with 0.7 mol dm^{-3} of Li [NTf_2] in PC (Electrolyte 3; red line) at 100 mV s^{-1}.

5.3.5. $LiTi_2(PO_4)_3$ preparation and X-Ray diffraction

Synthesis of $LiTi_2(PO_4)_3$ (LTP). Li_2CO_3, $NH_4H_2PO_4$ (MAP) and TiO_2 were used as precursors, stirred in 50 mL of water for 2 hours. Then, the liquid media was completely evaporated using hot plate. Then, the remained powder was calcined at 900 °C for 12 hours. Finally, a size reduction was performed using a continuous-flow agitator wet mill (Netszch Microcer) to obtain submicron-sized particles. The milling process includes preparing a 4 wt. % of LTP in isopropyl alcohol (IPA). This mixture was then passed through the mill containing yttria-stabilized zirconia beads with size of 0.5 mm. Besides, 11 wt. % of β-lactose (Acros Organics) was added as the source of carbon. The milling process was carried out for 2h30 at a speed of 2100 RPM. Then, the slurry was collected from the mill and dried on a hot plate until evaporation of IPA. Finally, the dry powder was heated up at 700 °C for 2 hours in a N_2 atmosphere.

X-Ray diffraction (XRD) of LTP. XRD patterns were recorded on a Philips X-ray spectrometer, using Cu Ka radiation (l = 1.5406 Å). XRD measurements were collected in steps of 0.02° in 2θ range of 10-80°. The unit cell parameters were determined using pattern matching with the program Powder Cell.The X-Ray diffraction of LTP is presented in **Figure S5.7**. The diffraction pattern may crystallizes in the R-3C rhombohedral space group with a = 8.48 Å and c = 20.84 Å, as indexed on **Figure S5.7**. One can notice that the Al sample holder is observed (38°, indexed by a star).

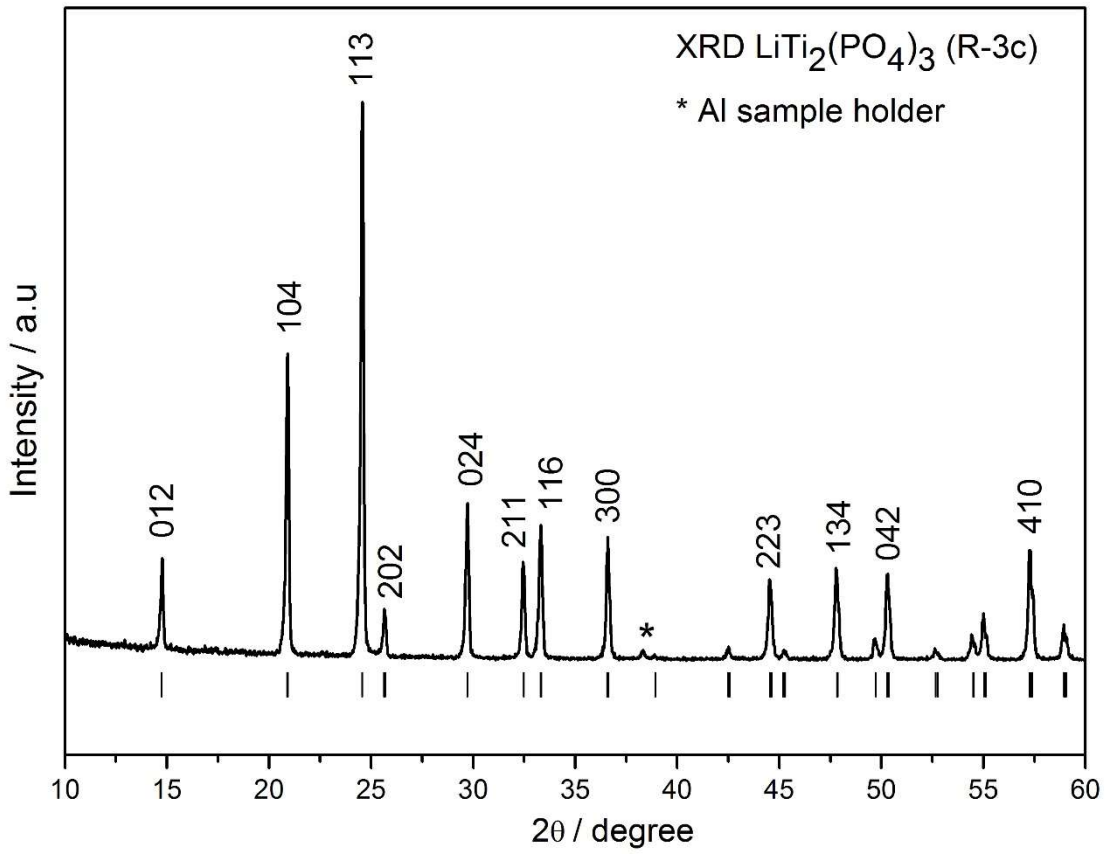

Figure S5.7. X-Ray diffraction (XRD) of $LiTi_2(PO_4)_3$ (LTP), with R-3c space group indexation. The star (*) refers to the Al sample holder.

Chapitre 6 : Liquide ionique électroactif utilisant un anion redox basé sur le ferrocène pour contrer les surtensions

6.1. Avant-propos et mise en contexte

Ce chapitre a été rédigé sous forme d'un article qui a été soumis à *Journal of Power Sources*. Cette étude a permis d'approfondir la compréhension des liquides ioniques électroactifs qui est basé sur un anion di(sulfonyl)imide et le ferrocenyle. Ayant démontré préalablement l'impact de l'additif électroactif sur le nombre de transport du lithium, cette étude démontre l'habilité de cette espèce électroactive de jouer le rôle de navette redox. Il s'agit aussi d'une preuve de concept que pour la première fois, une navette redox peut participer au stockage d'énergie et d'améliorer la stabilité thermique de l'électrolyte. En résumé, un électrolyte redox est caractérisé et ensuite, employé dans une pile au lithium.

6.2. Bifunctional ionic liquids to improve Lithium-ion battery electrolytes

Bruno Gélinas,[a] Thomas Bibienne,[a] Mickaël Dollé[a] and Dominic Rochefort [a]

[a]Département de Chimie, Université de Montréal, Montréal, Québec H3C 3J7, Canada

J. Power Sources

6.2.1. Abstract

Used in their pure, undiluted form, ionic liquids usually result in Li-ion battery electrolytes with inadequate performance due low Li^+ transport numbers (t_{Li+}). Alternatively, they can be used as additives dissolved in conventional solvents such as carbonates to maintain a high t_{Li+} while providing the electrolyte with additional properties such as resistance to combustion, current collector passivation and decreased Li dendritic growth. Such properties are inherent to the ionic liquid and therefore ionic liquids are often used "off-the-shelf" to obtain the desired functional electrolyte. Here we demonstrate that ionic liquids modified with ferrocene as the electroactive moiety can be used as an additive in Li-ion battery electrolyte to prevent the positive from over-oxidation via the redox shuttle mechanisms and provide flame resistance at the same time. These bifunctional ionic liquids can be dissolved in conventional carbonate solvent mixtures over a wide range of concentrations. We show that at 1 M, a very high concentration for a redox shuttle, the electrolyte is non-flammable and prevents a $LiTi_2(PO_4)_3$ positive electrode from over-oxidation over a period of 45 days of continuous overcharge. Based on this principle, it is expected that novel bifunctional ionic liquids can be designed for development of other types of additives and contribute to developing safer battery electrolytes.

Keywords: Redox ionic liquids, electroactive lithium salt, redox shuttle, Li-ion battery.

Graphical abstract

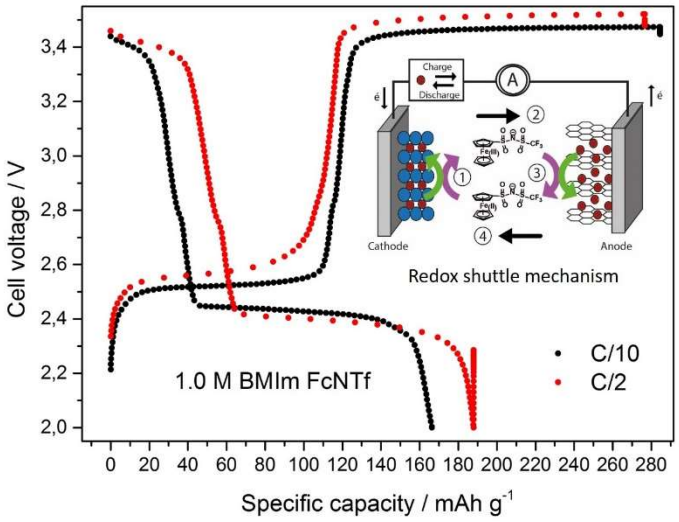

6.2.2. Introduction

Since the introduction of lithium-ion batteries (LIBs) on the market by Sony in 1991, LIBs have been the most employed energy storage in portable electronic devices such as cellular and portable computers due to their high energy density and good cycle life.[1] Transportation applications such as hybrid, plug-in hybrid and pure battery electric vehicles, demand an increased size/number of lithium-ion cells, higher energies and power rating.[2-4] Meeting these demands also requires the development of advanced safety features to protect the battery and users against situations such as overcharge and thermal abuse. Overcharge abuse is a potentially serious issue for battery packs containing hundreds or thousands individual cells the charge of which for different reasons could be imbalanced. Upon charging the pack, in such cases, the low-capacity cells will reach their full state before the high-capacity cells, resulting in an over-oxidation of the positive electrode in the former ones.[5, 6] For high voltage materials such as oxides, over-oxidation can generate reactive species via material degradation, cause electrolyte breakdown and oxygen evolution which can result in an explosion.[6] In moderate voltage, more stable, materials such as metal phosphates over-oxidation is potentially less hazardous but result nevertheless in an irreversible degradation of electrode material,

shortening battery life. Preventing over-oxidation is essential for the long-term, safe battery operation and can be achieved through the use of a redox shuttle (R-S, **Figure 6.2**), an electroactive molecule added to the electrolyte which will shuttle the excess charge from the positive to the negative electrodes. Several R-S have been investigated such as the halides media,[7-9] ferrocene derivatives,[10, 11] 2,2,6,6-tetramethylpiperinyloxide derivatives,[12] phenothiazine derivatives,[13] thiantrene,[14] 2-(pentafluorophenyl)-tetrafluoro-1,3,2-benzodioxaborole,[15] lithium borate cluster salt,[16] and 2,5-di-tert-butyl-1,4-dimethoxybenzene (DDB)[17] to name only a few.

In addition to overcharge protection, advanced electrolytes should also present flame-retarding properties. This can be achieved using ionic liquids (ILs) with structure such as pyrrolidinium and imidazolium cations with bis(trifluoromethylsulfonyl)imide anion.[18, 19]. While the use of ILs in pure, undiluted form could be limiting battery performance due to their high viscosity, low ionic conductivity and lithium ion transference numbers ($t_{Li}+$), mixtures of ILs and carbonates can be used to overcome these limitations. Electrolytes containing high IL concentrations, solvent-in-salt systems, have shown high $t_{Li}+$,[20] non-flammability,[19] inhibition of lithium dendrites and aluminum corrosion,[21-23] and an overall improvement of cycling and thermal stability.[19, 24-28] Such examples highlight the advantages of conventional ILs, which are related to the inherent properties of the nature of ionic liquids. Modifying the structure of ionic liquids components can provide additional properties to the electrolyte.

The functionalization of ionic liquids with a redox group is a highly potent strategy to increase the concentration in redox centers in an electrolyte and thereby address the low solubility issue of many redox shuttles. Using this strategy, we showed that a tenfold increase in DDB redox shuttle concentration (from 0.1 to 1 M) in EC/DEC mixtures, is possible.[29] Higher R-S concentrations is desirable to provide a better protection at high charging rates where concentration gradients at low concentrations can limit shuttle efficiency.[30] Other redox ionic liquids have been reported to study self-exchange as ionic liquids based on iodide and 5-mercapto-1-methyltetrazole for dye-sensitized solar cell[31] and increase the energy density of supercapacitors.[32, 33] In this research, we aim at demonstrating that electroactive ionic liquids can be used as bifunctional additives in

lithium-ion batteries. The electroactive moiety on the IL, here ferrocene, should fulfill the redox shuttle task and the imidazolium / (trifluoromethylsulfonyl)imide structures should provide flame resistance.[19, 34-36]

In order to gain an understanding of the importance of the ionic liquid's structure on the shuttle and electrolyte properties, three systems have been studied. Of these three, two are ionic liquids where the ferrocenyl moiety was linked either on the cation (1-(ferrocenylmethyl)-3-methylimidazolium bis(trifluoromethylsulfonyl)imide, [FcEMIm][NTf_2]) or the anion (1-butyl-3-methylimidazolium ferrocenylsulfonyl (trifluoromethylsulfonyl)imide ([BMIm][FcNTf]). Their structures are provided in **Figure 6.1**. The third species is the lithium salt of the redox anion, Li[FcNTf]. We begin by describing the properties of electrolytes containing [FcEMIm][NTf_2], [BMIm][FcNTf] or Li[FcNTf] such as the viscosity, ionic conductivity and flammability. Next the diffusion coefficient of the redox shuttle, measured by the accurate double potential step chronoamperometry (DPSC) techniques, will be studied at various concentrations to evaluate transport properties. Finally, the compatibility and applicability of the redox ILs will be demonstrated using Li/$LiTi_2(PO_4)_3$ (LTP) coins cell to show the overcharge protection provided by the shuttle mechanisms.

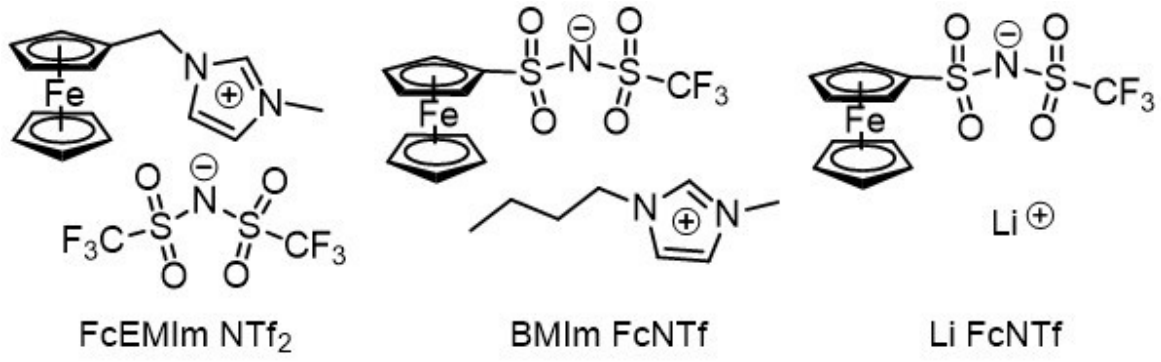

Figure 6.1. Chemical structure of 1-(ferrocenylmethyl)-3-methylmidazolilium bis(trifluoromethylsulfonyl)imide ([FcEMIm][NTf_2]) and 1-butyl-3-methylimidazolium ferrocenylsulfonyl (trifluoromethylsulfonyl)imide ([BMIm][FcNTf]) and lithium ferrocenylsulfonyl (trifluoromethylsulfonyl)imide (Li[FcNTf]).

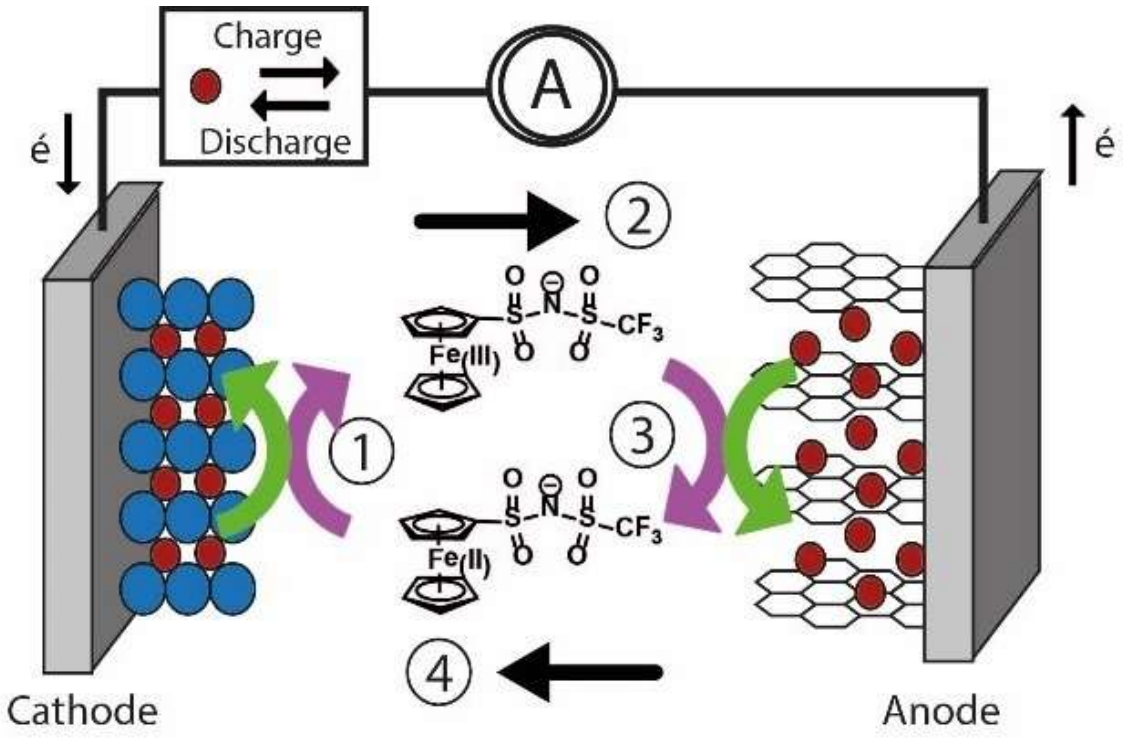

Figure 6.2. Schematic illustration of the redox shuttle mechanism.

6.2.3. Experimental

Material, synthesis and electroactive species characterization

All reagents used were obtained from Sigma-Aldrich using the highest purity grade available, except for trifluoromethanesulfonamide which was purchased from Synquest Laboratories and for the solvents which were obtained from Fisher. These were used as received. The synthetic procedures used to obtain 1-(methylferrocenyl)-3-methylimidazolium bis(trifluoromethanesulfonyl)imide ([FcEMIm][NTf_2]), 1-butyl-3-methylimidazolium ferrocenylsulfonyl (trifluoromethylsulfonyl)imide ([BMIm][FcNTf]) and lithium ferrocenylsulfonyl (trifluoromethylsulfonyl)imide (Li[FcNTf]) were slightly modified from our previous publications.[37-39] The detailed procedures and characterization results are provided in the Supporting Information. All compounds synthesized were characterized by ^{1}H, ^{19}F and ^{13}C NMR on a Bruker AMX 300 MHz spectrometer at room temperature using DMSO-d_6 and by electrospray ionization mass spectrometry. Accurate mass values were obtained by Agilent LC-MSD TOF. Elemental

analysis of RIL and Li[FcNTf] were performed on an EAS 1108 apparatus from a Fisons Instruments SPA. The water used in the procedures was purified with a Milli-Q system to a resistivity of 18.2 MΩ·cm (25 °C).

Thermal analysis

Thermogravimetric analysis (TGA) was performed on TGA Q500 (TA Instruments) under a helium atmosphere from room temperature to 450 °C with a ramp of 10 °C·min^{-1}. The temperature decomposition was determined at a 5% weight loss. TGA was coupled with Discovery MS (TA Instruments) to follow the weight loss. Differential scanning calorimetry (DSC) was performed on DSC2910 (TA Instruments) and using universal analysis software. The measurements were done between -50 to 80 °C with a ramp of 5 °C·min^{-1} and with isothermal periods of 5 minutes between the cooling and heating.

Ionic Conductivity and Viscosity Measurements

The viscosity of the electrolytes was measured using a microviscometer (Lovis 2000 ME, Anton Paar) which is based on the rolling ball principle (Höppler principle). The standard deviations of the measured viscosity were lower than ±0.5 %. The instrument was calibrated daily using air and milli-Q water at 25°C and at atmospheric pressure. An U-tube digital density meter (DMA 5000 M, Anton Paar) was used for density measurements. Prior to all measurements, the cell and glass capillary were washed with Milli-Q water (20 mL) then acetone (20 mL) and were dried for 15 minutes with an internal air pump. The ionic conductivity of these electrolytes were carried out with a Jenway 4510 conductivity meter. Before each series of measurement, the glass conductivity microvolume probe (027815, K=0.90 at 25°C) was calibrated using a standard 0.117 mol dm^{-3} KCl (15 mS cm^{-1}) aqueous solution at 25°C. The conductivity probe and the electrolyte were placed in a tube cell and the temperature was controlled using a thermostated water jacket around the cell. The dynamic viscosity and ionic conductivity measurements were measured from 25 to 75 °C at 5 °C intervals.

Electrochemical Analysis

The cyclic voltammetry (CV) experiments were done using a standard three-electrode heart-shaped cell, consisting a Pt macrodisk working electrode, a Pt wire counter electrode and a lithium metal QRE with a BioLogic SP-50 potentiostat controlled via EC-lab software. The specific surface area of the Pt working macroelectrode was determined to be 0.022 cm^2 (geometric area = 0.020 cm^2) using the CV response of a potassium ferricyanide aqueous solution (1.0 M KCl). All CV data (diluted and concentrated solutions) were obtained in an argon-filled glove box (H_2O, O_2 < 1 ppm) and before each experiment the working electrode was polished with alumina, rinsed, sonicated and dried. All potentials are reported vs. the Li/Li^+ redox couple potential reference.

The diffusion coefficients were obtained either from CV using the macro electrode or double potential step chronoamperometry (DPSC) with a Pt microdisk electrode. CV peak current (I_p) were plotted against the square root of the scan rate with the Randles-Sevcik equation (Equation 1)

$$I_p = 0.4463nFAC\left(\frac{nF}{RT}\right)^{1/2} v^{1/2}D^{1/2} \qquad (1)$$

where n is the number of electrons, F is the Faraday constant, A is the electrode area, C is the concentration, R is the gas constant, T is the temperature, υ is the scan rate and D is the diffusion coefficient.

DPSC measurements used a Pt microdisk electrode (100 μm diameter) and the diffusion coefficients were obtained from the data analysis proposed by Compton et al.[40, 41] The microelectrode radius was determined from steady state voltammetry measurements on ferrocene (Fc) solutions at different concentrations (0.5, 1.0 and 2.0 mM) in acetonitrile containing 0.1 M tetrabutylammonium perchlorate. The microelectrode radius (54±1 μm) was calculated using Fc diffusion coefficient from the literature ($2.3x10^{-9}$ m^2 s^{-1}).[40, 41] Chronoamperometric experiments were performed inside a Faraday cage in a glovebox (Ar atmosphere with O_2 and H_2O below 1 ppm). The microelectrode was modified with a PTFE heat shrink tubing to create a cavity at its end to accommodate a small volume of the sample. A silver wire acted as pseudo-reference and counter electrode.

An equilibrium potential was maintained for 5 s where zero faradaic current was measured. Then, the step potential was applied at higher potential than midpoint potential for oxidation and a lower potential for a reduction. The current decay was measured for 5 s and the data points were recorded at every 10 ms or 10 nA. The time-dependent current response obtained on the forward step was analyzed either by the Shoup and Szabo equation using Origin software (nonlinear curve fitting function)[42, 43] for concentrated solutions (viscous) or by the Stojek equation for diluted electrolytes.

LIB Coin Cell Analysis

$LiTi_2(PO_4)_3$ (LTP) was prepared using Li_2CO_3, $NH_4H_2PO_4$ and TiO_2 as precursors which was described earlier.[39] For the positive electrode, a slurry was prepared by mixing LTP with carbon black and polyvinylidene fluoride in N-methyl-2-pyrrolidone solution, at 85:10:05 wt.%.[39] The slurry was mixed for few hours to full homogenization, and then deposited on carbon-coated aluminium foil using a doctor blade. The coating was dried at 70 °C under vacuum overnight. The dried electrodes were cut in disks of 2.5 ± 0.5 mg/cm^2 loading and assembled in coin cells (2032) in argon atmosphere glove box (H_2O and O_2 < 1 ppm). Lithium metal was used as the negative electrode, Celgard 2400 was used as a separator, and $Li[NTf_2]$ diluted in ethylene carbonate (EC) and diethyl carbonate (DEC) (EC-DEC 1:2 vol.%) mixture was used at the reference electrolyte. $[FcEMIm][NTf_2]$, [BMIm][FcNTf] or Li[FcNTf] were added in the liquid electrolyte at various concentrations. Electrochemical characterization was performed at 30 °C on a VMP electrochemical station (Bio-Logic), using cut-off voltages of 2.0 and 4.0 V vs Li/Li^+ at 0.1 C to 0.5 C rate for galvanostatic cycling.

6.2.4. Results and discussion

Thermochemical properties of RILs

Before using RILs in LIB electrolyte to provide higher thermal stability, a thermal analysis of the ionic liquids in their pure form was carried out to determine their transitions and degradation temperatures. This is particularly important to understand the effect of

adding a ferrocenyl unit to the structure of the IL. The thermochemical properties of neat [FcEMIm][NTf_2] and [BMIm][FcNTf] were determined by thermogravimetric analysis (TGA) and differential scanning calorimetry (DSC) which showed a similar melting point and decomposition temperature for both RILs. Melting and decomposition temperatures for the RILs are presented in **Table S6.1**. The thermal analysis of Li[FcNTf] was inconclusive due to the fast water uptake by the salt. The melting point temperature found for the RIL with the ferrocenyl unit on the cation, [FcEMIm][NTf_2], are 46.1 °C which are in agreement with those reported earlier by Gharib et al.[44] When the Fc is linked to the anion, the RIL shows higher melting and decomposition temperatures. The higher T_m could be a result of interactions between the Fc center on the anion and the imidazolium ring that are less likely to take place when the Fc is linked on the cation. These interactions also result in a higher viscosity of [BMIm][FcNTf] compared to [FcEMIm][NTf_2].[38, 45] RIL based on Fc present a supercooled state because no crystallization temperature is observed on DSC thermograms, which is common in ILs.

TGA curves with a heating ramp of 10 °C min^{-1} are presented in **Figure S6.2A**, the T_d is measured at a 5% weight loss and are given in **Table S6.1**. The T_d of [FcEMIm] [NTf_2] are 271°C (under He) and 297°C (under air). For [BMIm] [FcNTf], the T_d of [FcNTf] RIL is slightly higher than [FcEMIm] RIL with 298°C (under He) and 304°C (under air). The difference of T_d between the two atmospheres is not very significant but the decomposition of RIL under air presents an exothermic reaction and a contribution of oxygen in decomposition mechanism. A higher decomposition temperature is obtained for [BMIm][FcNTf] suggesting that linking Fc on the cation destabilizes the imidazolium likely from the weaker Fc-N bond. Both RIL however have significantly lower T_d than the unmodified IL (e.g. 455 °C for [EMIm][NTf_2]).[46] In order to evaluate the impact of Fc on the reactions leading to the degradation TGA-MS analysis was also carried out. **Figure S6.3** shown a MS histogram recorded during the thermal decomposition of [BMIm][FcNTf] under helium or air atmosphere. The thermal decomposition products identified over this temperature range contains fragments associated from the decomposition of both the cation and the anion. The presence of C_5H_5 and C_5H_6 indicates that ferrocenyl also decomposes. Under air, the decomposition fragments present a higher oxidation state as seen from the increased peak intensity for CO_2 and SO_4 for instance. To

evaluate the stability at lower temperatures, an isothermal TGA curve of [BMIm][FcNTf] at 150 °C for 24 h is presented in **Figure S6.2B**, The weight loss after this period of time is around 2 % and occurred essentially by the evaporation of water. The MS analysis did not show any volatile by-products. Del Sesto et al. demonstrated a beginning of decomposition at 150 °C for [BMIm][NTf_2] [47] and the long-term thermal stability of [BMIm][FcNTf] presents a good thermal stability which is comparable to an unmodified IL, suggesting that a decomposition in a battery operating under normal conditions should not occur.

Electrochemical properties and diffusion of RIL in electrolytes

The redox potential and mass transport of the electroactive species are two essential properties that define the efficiency of a redox shuttle. In order to evaluate the structural impact of the ionic liquid on these properties of the redox group in a conventional LiB electrolyte, the electrochemistry of [FcEMIm][NTf_2], [BMIm][FcNTf] and Li[FcNTf] was studied using ethylene-diethyl carbonate (EC-DEC) mixtures at a 1:2 v./v. with 1.0 M of Li[NTf_2] containing a low concentration of 10 mM of redox species. The diffusion coefficients and midpoint potential (E') for the oxidation of the ferrocenyl moiety are presented in **Table 6.1** and **Table 6.2**. CVs obtained with the diluted R-S electrolyte are shown in **Figure 6.3A** (see **Figure S6.5** for CVs at various scan rates) and the CV shapes correspond to what is expected for a reversible electrochemical reaction ($I_{pa}/I_{pc} \approx 1$ and $I_p \alpha v^{1/2}$). The redox potentials of [FcEMIm] [NTf_2], [BMIm] [FcNTf] and Li [FcNTf] are 3.42, 3.51 and 3.51 V vs. Li/Li^+.

Table 6.1. Potential parameters obtained from cyclic voltammograms at 100 mV s^{-1} of 10 mM [FcEMIm][NTf_2], [BMIm][FcNTf] and Li[FcNTf] in EC-DEC 1:2 (v/v) with 1.0 M Li[NTf_2].

Electroactive species	Midpoint Potential / V vs. Li/Li^+	ΔE_{pa-pc} / V	Onset Potential (1^{st}) / V vs. Li/Li^+
[FcEMIm][NTf_2]	3.42	0.090	3.35
[BMIm][FcNTf]	3.51	0.086	3.44
Li[FcNTf]	3.51	0.090	3.43

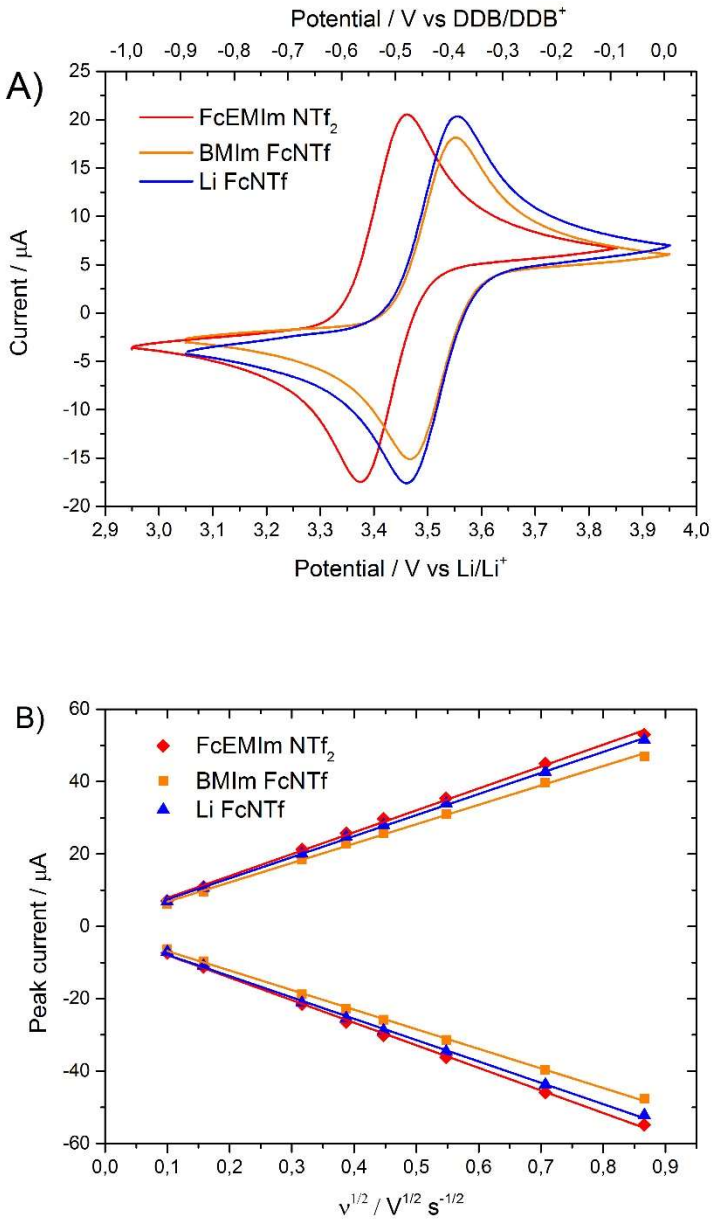

Figure 6.3. A) CVs of electroactive species of 10 mM solution of [FcEMIm][NTf_2] (red line), [BMIm][FcNTf] (orange line) and Li[FcNTf] (blue line) in EC-DEC 1:2 (v/v) with 1 M Li[NTf_2] at 100 mV s^{-1}. B) Randles-Sevcik plots of these electroactive solutions. The scan rates used were 10 to 750 mV s^{-1}.

The electrochemical response of [FcNTf] anion at higher concentrations of RIL was investigated to evaluate the impact on electrochemical parameters and the CVs are presented in **Figure 6.4**. The shape of CV using electrolyte containing 0.3 to 1.0 M of RIL is clearly distorted at 100 mV s^{-1} (**Figure 6.4B**) and the peak-to-peak potential separation is significantly higher than expected due to the iR drop associated with a decrease in ionic conductivity. This distortion is attenuated at 10 mV s^{-1} (**Figure 6.4A**) and a quasi-steady state appears after the oxidation peak especially when the lithium salt as supporting electrolyte is in low concentration (Supporting information; **Figure S6.6**). This effect is likely due to a non-negligible contribution of migration to the mass transport since it occurs only for the negatively-charged [FcNTf] at positively-poised electrodes. The lower electrolyte viscosity of electrolyte containing a low concentration of $Li[NTf_2]$ also favors establishing this quasi-steady state.

Table 6.2. Transport properties using CV and DPSC of 10 mM $[FcEMIm][NTf_2]$, [BMIm][FcNTf] and Li[FcNTf] in EC-DEC 1:2 (v/v) with 1.0 M $Li[NTf_2]$.

Electroactive species	D_R (CV) /10^{-6} cm^2 s^{-1}	I_{pc}/I_{pa} at 100 mV s^{-1}	D_R (DPSC) /10^{-6} cm^2 s^{-1}	D_O (DPSC) /10^{-6} cm^2 s^{-1}	γ D_O / D_R
$[FcEMIm][NTf_2]$	1.05	1.01	1.15±0.05	1.75±0.09	1.52
[BMIm][FcNTf]	0.82	1.02	0.75±0.03	1.01±0.05	1.35
Li[FcNTf]	0.97	1.05	0.75±0.03	0.97±0.05	1.29

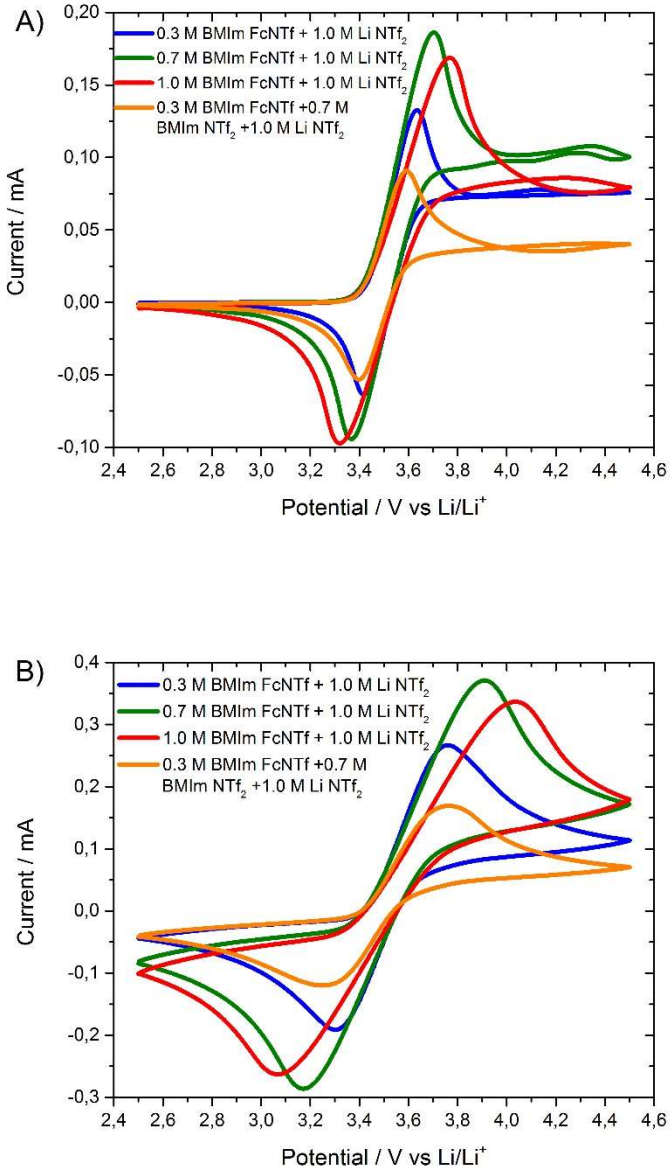

Figure 6.4. CVs of comparison between different [FcNTf] solutions (0.3, 0.7 and 1.0 M) in EC-DEC 1:2 (v/v) with 1.0 M Li[NTf_2] in presence or absence of [BMIm][NTf_2] at A) 10 mV s^{-1} and B) 100 mV s^{-1}.

The diffusion coefficient is a key factor to evaluate the efficiency of R-S protection especially if this R-S was used in LIB which undergoes high charge-discharge rate capabilities. By definition, the pure physical diffusion is a slow mass transport according to Fick law, but in this study, the charged electroactive species (e.g. RIL and Li[FcNTf]) at high concentrations can be transported by diffusion and by migration, as just shown. A redox-active anion as anodic species seems particularly well-adapted for the protection of the positive LIB cathodes. The diffusion coefficients of the reduced form in the given electrolyte containing [FcEMIm][NTf_2], [BMIm][FcNTf] and Li[FcNTf] are 1.05, 0.82, 0.97 $x10^{-6}$ cm^2 s^{-1}, respectively and the diffusion was obtained from the peak current measurements at various scan rates (Randles-Sevcik curves in **Figure 6.3B**). To determinate an accurate value for the diffusion coefficient of both reduced and oxidized forms, double potential step chronoamperometry (DPSC) was used with a microelectrode (**Figure 6.5A**). The time-dependent current responses of the forward and backward potential steps were analyzed by the Stojek equation to obtain the diffusion coefficient of both oxidized and reduced form which is an advantage on the Shoup and Szabo equation (**Figure 6.5**). The more accurate diffusion coefficients using Stojek's method are 1.15, 0.75 and 0.75 $x10^{-6}$ cm^2 s^{-1} for [FcEMIm][NTf_2], [BMIm][FcNTf] and Li[FcNTf], respectively. As expected, the [FcEMIm] cation diffuses significantly faster than [FcNTf] anion. The diffusion coefficient of [FcNTf] anion is slightly slower using LIB electrolyte (EC-DEC 1:2 v/v + 1.0 M Li[NTf_2]) than the coefficient previously reported using acetonitrile electrolyte corresponding to 1.03 $x10^{-6}$ cm^2 s^{-1} for [BMIm][FcNTf].[38] **Table 6.2** shows a larger diffusion coefficient for the oxidized form, this suggests a faster diffusion of the zwitterion [Fc^+NTf^-] and a smaller solvation sphere due to the overall neutral charge of the oxidized form.

Because of the interactions taking place between the redox ionic liquid ions, mass transport becomes more complex as the concentration increases. In order to identify the parameters affecting transport in these solutions, the electrolyte concentration in redox-electroactive was varied from 0.3 to 1.0 M and evaluated by CV with Randles-Sevcik equation and DPSC with Shoup and Szabo or Stojek method. All details of the 20 electrolyte compositions are summarized in **Table S6.2**. The fluidity of these electrolytes are calculated from viscosity given in **Table S6.3**. The impact of the type of technique used

to evaluate diffusion must be emphasized at this point. Despite the linearity of Randles-Sevcik plot ($I_p \alpha v^{1/2}$) between 25 and 500 mV s^{-1}, the diffusion coefficients measured from CV are underestimated by a factor of 5, based on the analysis of radius from the Stokes-Einstein relation ($D = k_BT/C\pi\eta r$, **Figure S6.7B**). This discrepancy can be explained by the high currents measured with the macroelectrode in concentrated electrolyte. Consequently, the high iR_s and CV distortion prohibit the evaluation the mass transport from CV despite its common use reported in the literature. This is exemplified by comparing the Stokes-Einstein plots of **Figure 6.6** (microelectrode DPSC measurements results using Shoup and Szabo fitting) and **Figure S6.7** (macroelectrode using CV). DPSC of concentrated electroactive species solution (**Figure 6.6A**) and the obtained solved radius of [FcNTf] anion for different electrolytes is plausible (**Figure 6.6C**, crystallographic radius of ferrocene r= 0.27 nm[48]). The D values and the correlation coefficient are significantly higher using DPSC (e.g. Using Electrolyte #7: 7.0 and 0.6 x 10^{-7} cm^2 s^{-1} for DPSC and CV method, respectively). According to **Figure 6.6B**, the diffusion coefficients of 0.3 M redox-active electrolyte using [FcEMIm][NTf_2], [BMIm][FcNTf] and Li[FcNTf] are 9.1, 6.6 and 8.1 x 10^{-7} cm^2 s^{-1}, respectively. These mass transports of 0.3 M redox-active electrolyte are slightly lower than pure diffusion coefficient obtained in diluted electrolyte (10 mM) which is coherent with the viscosity measurement (**Table 6.3**; 4.516 and 6.777 mPa s without and with 0.3 M of [BMIm][FcNTf]). We also evaluated the impact of [BMIm][FcNTf] concentration on the mass transport and obtained diffusion coefficient from DPSC are 6.6, 2.7 and 1.5 x 10^{-7} cm^2 s^{-1} for electrolyte containing 0.3, 0.7 and 1.0 M of [BMIm][FcNTf], respectively. Generally, the mass transport of electroactive species depends on electrolyte viscosity which explains the higher mass transport of [FcNTf] anion for electrolyte containing a low concentration of Li[NTf_2].

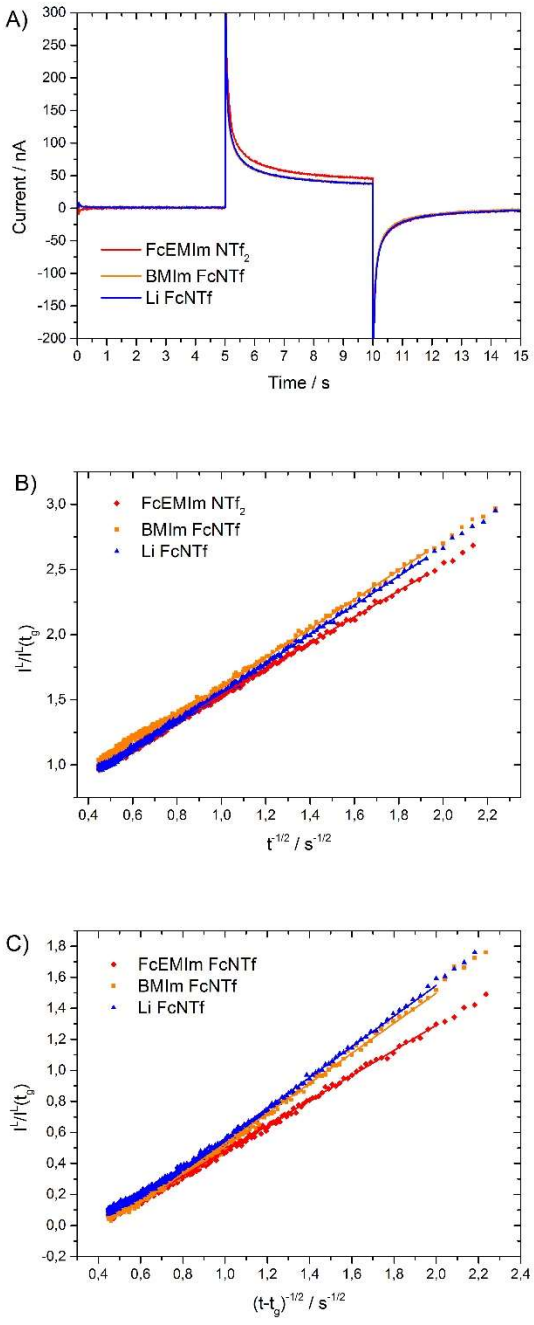

Figure 6.5. A) DPSC using a microelectrode of 10 mM [FcEMIm][NTf_2] (red line), [BMIm][FcNTf] (orange line) and Li[FcNTf] (blue line) in EC-DEC 1:2 (v/v) with 1 M Li[NTf_2]. The duration τ was used 5 s. The initial and final potentials were -0.14 V. The step potentials were 0.37 V. (Potential vs. Fc/Fc^+) Stojek plots for the B) oxidation and C) reduction of these electrolytes.

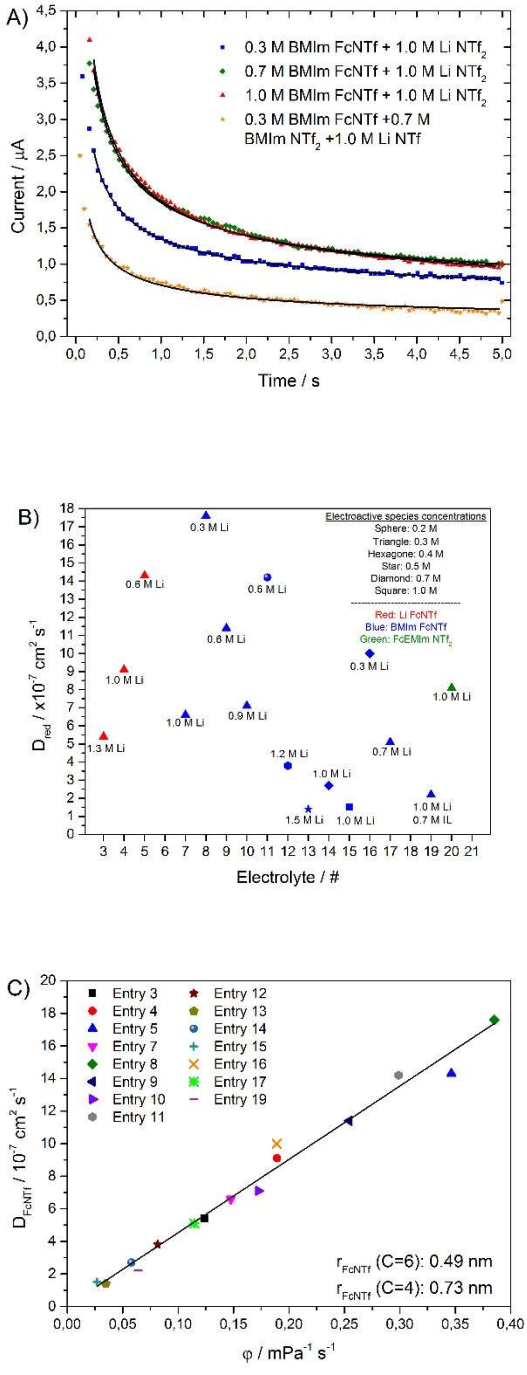

Figure 6.6. A) DPSC using a microelectrode of different [FcNTf] solutions (0.3, 0.7 and 1.0 M) in EC-DEC 1:2 (v/v) with 1.0 M Li[NTf_2] solution in presence or absence of [BMIm][NTf_2]. The duration τ was used 5 s. B) Diffusion coefficients using DPSC and C) diffusion of [FcNTf] anion dependence on the fluidity (Stokes-Einstein relation) for different electrolytes.

Conductivity and flammability of RIL electrolytes

Table 6.3 summarizes dynamic viscosity (η) and ionic conductivity (σ) measured for selected redox-active LIB electrolytes, in addition to the activation energy ($E_{a,\sigma \text{ or } \varphi}$), entropy ($\Delta S_{\sigma \text{ or } \varphi}$), enthalpy ($\Delta H_{\sigma \text{ or } \varphi}$) and results from the flammability tests. All ionic components of the electrolyte, the RILs, the electroactive salt Li[FcNTf] and the Li[NTf_2] were independently varied to study their interactions and impact on the conductivity. In addition, the unmodified (i.e. non-electroactive) ionic liquid [BMIm][NTf_2] was added in electrolytes #18 and 19 to replace a fraction of the RIL to highlight the effect of the ferrocenyl moiety on the electrolyte's properties. All data obtained on dynamic viscosity and ionic conductivity are presented in **Table S6.3** and **Table S6.4** in Supporting Information. **Figure S6.8** shows the Arrhenius and Eyring plots used to extract the E_a, ΔS and ΔH. As expected, the addition of RIL and Li[FcNTf] increases slightly the electrolyte viscosity which consequently decreases the ionic conductivity of the electrolyte, when compared to the solvent mixture (entry #1) and to an electrolyte without additives (EC-DEC 1:2 v/v with 1 M Li[NTf_2], entry #2). Consequently, the redox-active electrolytes present higher E_a, higher ΔH and lower ΔS than electrolyte with no R-S. Comparing entries #3, 7, 18 and 20 allows ranking the impact of the different structures of ionic liquid (all at 0.3 M) on the electrolyte conductivity from the highest conductivity to the lowest as follows: [BMIm][NTf_2] > [BMIm][FcNTf] ≈ [FcEMIm][NTf_2] > Li[FcNTf]. Interestingly the Li[FcNTf] provided the lowest conductivity despite the fact that Li^+ is much smaller than any of the imidazolium studied. The complexation between Li^+ and $[FcNTf]^-$ and $[NTf_2]^-$ has a stronger negative impact on the electrolyte viscosity.

The electrolyte properties depend on [BMIm][FcNTf] concentration and the viscosity (ionic conductivity) at 25°C are 6.78 (4.89), 17.27 (3.20) and 37.16 (2.10) mPa s (mS cm^{-1}) for 0.3, 0.7 and 1.0 M of [FcNTf] RIL, respectively. These results are in agreement with our previous investigations.[37, 39, 45] In context of solvent-in-salt electrolyte, we also investigated to replace RIL by IL to evaluate the impact on electrolyte properties and we can see clearly that redox-active electrolyte used unmodified IL is less viscous and more conductive.

Table 6.3. The viscosity, ionic conductivity, activation energies, entropy and enthalpy for fluidity and ionic conductivity of redox-active electrolytes (EC-DEC 1:2 (v/v) with 1.0 M Li[NTf_2]).

Redox shuttles	[RS] / M	[Li NTf_2] ([IL]) / M	σ (25°C) / mS cm^{-1}	η (25°C) / mPa s	$E_{a,\sigma}$ ($E_{a,\varphi}$) / kJ mol^{-1}	ΔH_σ (ΔH_φ) / kJ mol^{-1} K^{-1}	ΔS_σ (ΔS_φ) / J mol^{-1} K^{-1}	Flammable electrolytes
-	-	1.0	6.26	4.52	11.5 (15.9)	8.8 (13.3)	-200.0 (-213.0)	Yes
[FcEMIm][NTf_2]	0.3	1.0	4.98	7.44	13.4 (18.4)	10.7 (15.7)	-195.9 (-209.0)	Yes
Li[FcNTf]	0.3	1.0	4.06	8.08	13.2 (18.8)	10.5 (16.1)	-198.0 (-208.3)	Yes
[BMIm][FcNTf]	0.3	1.0	4.89	6.78	13.7 (18.0)	11.0 (15.3)	-194.1 (-209.5)	Yes
[BMIm][FcNTf]	0.7	1.0	3.20	17.27	18.0 (22.9)	15.3 (20.2)	-183.8 (-200.8)	Yes
[BMIm][FcNTf]	1.0	1.0	2.10	37.16	21.7 (27.8)	19.0 (25.2)	-174.8 (-190.4)	No
[BMIm][FcNTf]	0.3	1.0 (0.7)	4.76	15.63	16.7 (22.2)	14.0 (19.5)	-185.0 (-202.3)	Yes

A qualitative estimation of the ion dissociation of the redox-active electrolyte was obtained by the Walden rule ($\Lambda\eta$ = constant)[49] and the Walden plots are presented in **Figure 6.7** which correlates the molar conductivity and the fluidity at different temperatures. The ideal Walden line (e.g. 0.01 M KCl aqueous solution) which is employed as the reference curve illustrates the case where ions are fully dissociated and are not interacting with each other.[49] The Walden curves for the electrolytes containing redox ionic liquids and electroactive lithium salt are lower to this line, showing ionic association, although they fall within same region as the electrolyte with only Li[NTf_2]. Increasing temperature favors the ion pairing phenomena as seen from the larger deviation from ideality at 75 °C, in agreement with Angell and coworkers.[50] In a previous study the $\Lambda_{imp}/\Lambda_{NMR}$ ratio was used to evaluate the iconicity at 63 % for an RIL electrolyte containing

0.3 M [BMIm][FcNTf] in propylene carbonate in presence of 1.0 M Li[NTf_2], which is in agreement with the behavior reported here.[39]

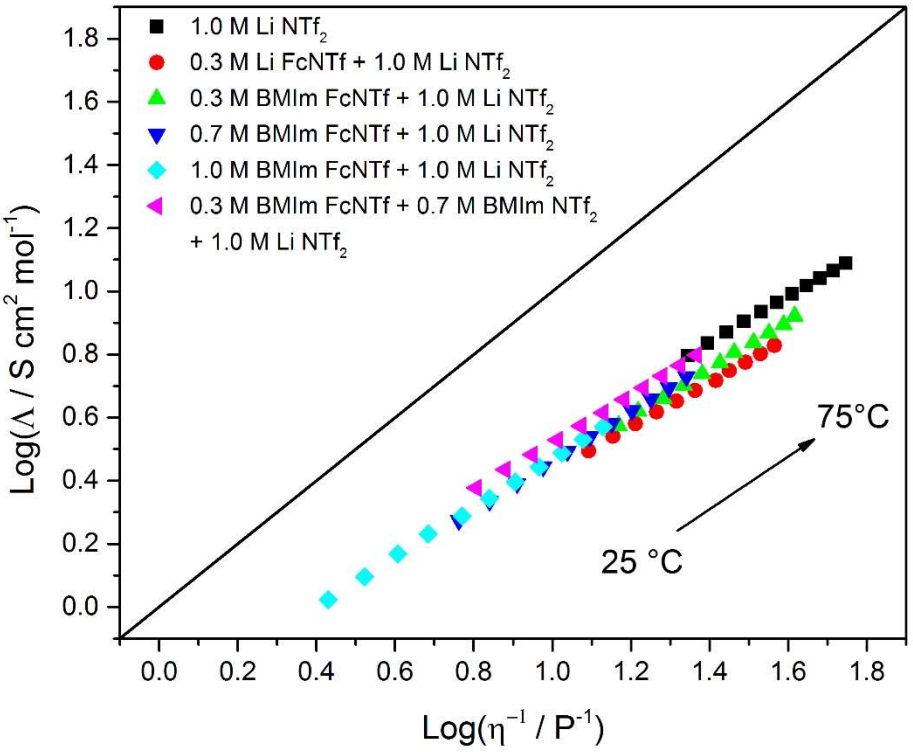

Figure 6.7. Walden plot of redox-active electrolytes based on [FcNTf] electrolyte. The straight line illustrates the ideal Walden line (0.01 M KCl aqueous solution). The molar ionic conductivity and fluidity are measured from 25 to 75 °C at 5 °C intervals.

Finally, the flammability of several RIL-based electrolytes was examined by placing a flame directly on the surface of a small volume of electrolyte for few second. After this period the flame was removed to determine if the combustion of the electrolyte was self-maintained. Photographic images taken immediately after following removal of the flame are shown in **Figure S6.9**. The only electrolyte that never showed any combustion is electrolyte #15 (1.0 M of [BMIm][FcNTf] in EC-DEC 1:2 v/v with 1.0 M Li[NTf_2], **Figure S6.9** H). However, all electrolytes containing a high ionic concentration of either RIL or IL such as 0.7 M of RIL or 1.0 M of RIL-IL rapidly extinguished within a few seconds without external intervention. This result indicates that safety of electrolyte

can be improved by employing RIL as fire-retardant additive. While conventional redox shuttles don't present this ability, the functionalization of a redox group on an ionic liquid allows having high ion concentrations to reach the solvent-in-salt conditions which are well-known to improve the thermal stability.

Protection against overcharging with redox-active ionic liquids

To demonstrate the use of bifunctional electroactive ionic liquids as redox shuttle, half-cells were investigated using the Nasicon-type titanium phosphate ($LiTi_2(PO_4)_3$; LTP)[51] as positive electrode material. A lithium metal foil was used as the negative electrode. **Figure 6.8A** and **Figure S6.9A** present the charge-overcharge-discharge cycles at a 0.1 C rate for Li/LTP cells with the electrolyte containing $[FcEMIm]^+$ or $[FcNTf]^-$ as redox shuttle. During charge, a first plateau is observed at 2.5 V vs. Li/Li^+ which corresponds to the expected voltage for LTP. A second charging step of 10 hours (= 0.1 C rate) is then applied to the cell, which represents an overcharge of 100 %. For Li/LTP cell using an electrolyte without any redox shuttle additives, the cell voltage rises rapidly until it reaches the 4 V cut-off set by the instrument (curve not shown). However in the presence of $[FcEMIm]^+$ or $[FcNTf]^-$, the redox-active electrolyte prevents reaching the cut-off voltage and the curve shows second voltage plateau corresponding to the oxidation of the shuttle (see **Figure 6.8** and **S6.9**). The shuttling plateau of $[FcEMIm]^+$ and $[FcNTf]^-$ are found at 3.4 and 3.5 V vs. Li/Li^+, respectively, in agreement with what was predicted from the CV measurements. Such flat plateau during overcharging indicates an effective activity of R-S, meaning that a fast and steady charge shuttling cycle is achieved between both electrodes. According to the midpoint potential, the electrolyte containing the [FcEMIm] cation or [FcNTf] anion would be adequate for the overcharge protection of $Li/LiTi_2(PO_4)_3$ cells. At a concentration of 0.3 M in R-S and a 0.1 C rate, the specific capacities were very similar regardless of the structure of the redox shuttle ($[FcEMIm][NTf_2]$, [BMIm][FcNTf] or Li[FcNTf]). In all cases, the discharge capacities were found to be larger than the charge capacities This extra capacity is explained by the time spent at high potential by the electrode. The overcharge current is not only used to oxidize the RIL but also lightly the LTP. In reduction, this overcharged cells display then a higher capacity. The discharge

capacities are closer the theoretical capacity of LTP of 138 mAh g^{-1}. This is also observed when the C rate is increased. Huang et al. reported also a low capacity contribution to the reduction of the oxidized R-S molecules during the discharge process.[52] The fastest C-rate where R-S is able to efficiently prevent overoxidation is 0.5 C. At 1 C and above, the overcharge is only partially controlled and the cut-off potential is reached. The R-S overcharging potential increase with C-rate and the flat plateau of [FcNTf] redox-active electrolyte suggests that this RIL has a better ability to shuttle and protect the LTP cathode than [FcEMIm] at 0.5 C.

Increasing the rate to C/2 decreased the charge capacity, as expected, but increased the discharge capacity for all cells that used $[FcNTf]^-$ as the redox shuttle, as observed in **Figure 6.8B**. The values for discharge capacity in these conditions are even higher than the LTP theoretical value. We believe the deposition of a film of the oxidized zwitterionic species [Fc(III)NTf] is responsible for this effect. In previous work, we demonstrated that the RIL based on $[FcNTf]^-$ was being electrodeposited at the surface of a carbon electrode, achieving efficient inhibition of self-discharge in redox-active electrolyte capacitors.[32] This electrodeposition process also occurs on the LTP electrode and is particularly evident when the electrolyte uses a concentration of 1.0 M of [BMIm][FcNTf], as seen in **Figure 6.8A**. The highly concentrated [FcNTf] electrolyte shows unusual high discharge capacities of 166.5 and 186.9 mAh g^{-1} at 0.1 and 0.5 C, respectively. These values cannot be explained only by the energy stored in LTP. Indeed, one can notice on **Figure 6.8A** that the discharge voltage of the 1.0 M of [BMIm][FcNTf] IL is not as steep as the lower concentrated ones. A S-shaped voltage curve is observed during the discharge process at 3.4V, close to the shuttling plateau of $[FcNTf]^-$ found at 3.5 V vs. Li/Li^+, which can be attributed to the deposition of the oxidized ferrocenium NTf anion. This extra capacity comes in addition to the 138 mAh/g expected from LTP itself. Such deposition might be beneficial by preventing electrolyte oxidation in the event of a high voltage overcharge and provide a protection for extended periods of time. To illustrate this, **Figure 6.9** shows the galvanostatic curves obtained for a long overcharge. The overcharge was controlled by the shuttling of [FcNTf] anion during at least 48 days with no sign of failure which corresponds to 115 cycles of charge-overcharge-discharge. Using the charge shuttled over this period of time and the amount of redox centers in the electrolyte, we found that on average each

$[FcNTf]^-$ is carrying out 53 redox cycles. Galvanostatic long overcharge profile at 1.0 M of [BMIm] [FcNTf] demonstrates coexistence of redox shuttle ability and electrodeposition process.

Table 6.4. Electrochemical characterisation of Li/LTP cells in different redox-active electrolytes. (IL: $[BMIm][NTf_2]$)

Redox shuttles	[RS] / M	[Li NTf_2] ([IL]) / M	RS potential at C/10 / V vs Li/Li^+	Charge specific capacity / mAh g^{-1}		Discharge specific capacity / mAh g^{-1}		Coulombic Efficiency at C/10 (C/2) / %		Fastest C-rate where RS ability works
				C/10	C/2	C/10	C/2	C/10	C/2	
[FcEMIm] [NTf_2]	0.3	1.0	3.38	129.0	128.5	135.6	136.5	105.1	106.2	C/2
Li [FcNTf]	0.3	1.0	3.48	127.4	126.0	138.5	145.3	108.7	115.3	C/2
[BMIm] [FcNTf]	0.3	1.0	3.46	130.3	124.2	132.9	140.9	102.0	113.4	C/2
[BMIm] [FcNTf]	0.7	1.0	3.48	124.1	124.6	133.4	144.5	107.5	116.0	C/2
[BMIm] [FcNTf]	1.0	1.0	3.47	125.0	118.3	166.5	186.9	133.2	158.0	C/2
[BMIm] [FcNTf]	0.3	1.0 (0.7)	3.50	129.4	-	138.0	-	106.6		C/4

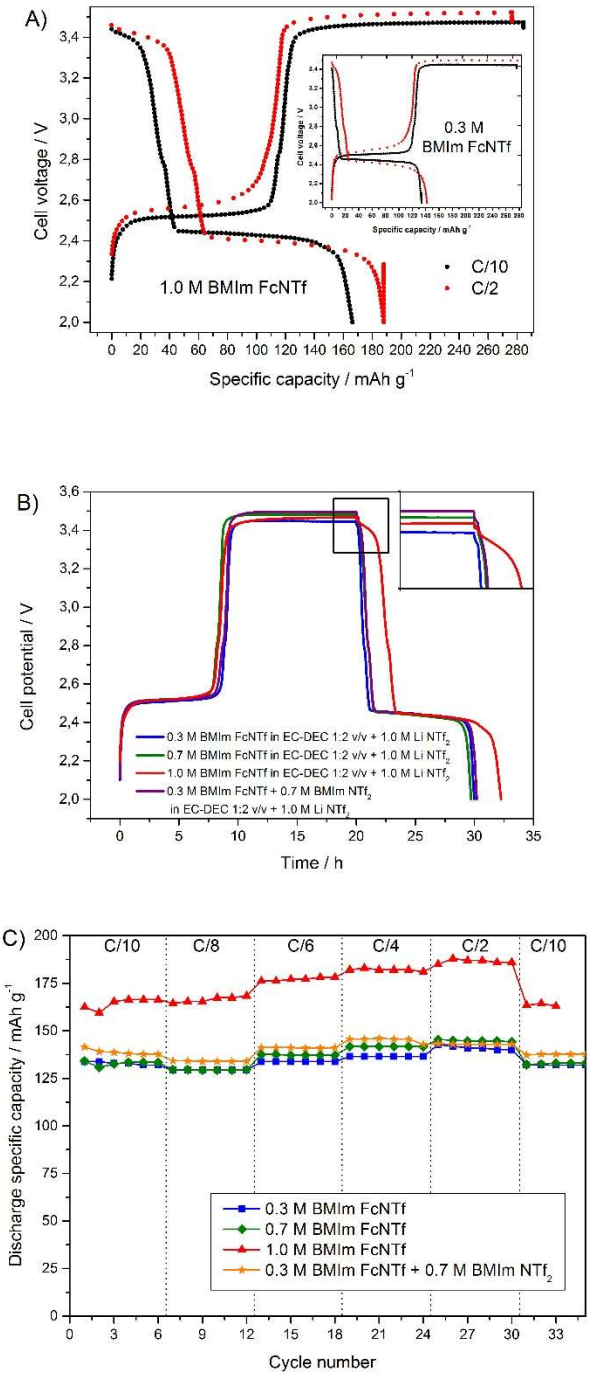

Figure 6.8. A) Galvanostatic charge-overcharge-discharge profiles of Li/LTP cell at 0.1 C rate and 10 h overcharge for different [FcNTf] solutions (0.3, 0.7 and 1.0 M) in EC-DEC 1:2 (v/v) with 1.0 M Li[NTf_2] solution in presence or absence of [BMIm][NTf_2]. B) Capacity profiles at 0.1 C and 0.5 C rates for electrolyte containing 1.0 M or 0.3 M of [BMIm][FcNTf]. C) The rate capability study for discharge using [FcNTf] anion as RS.

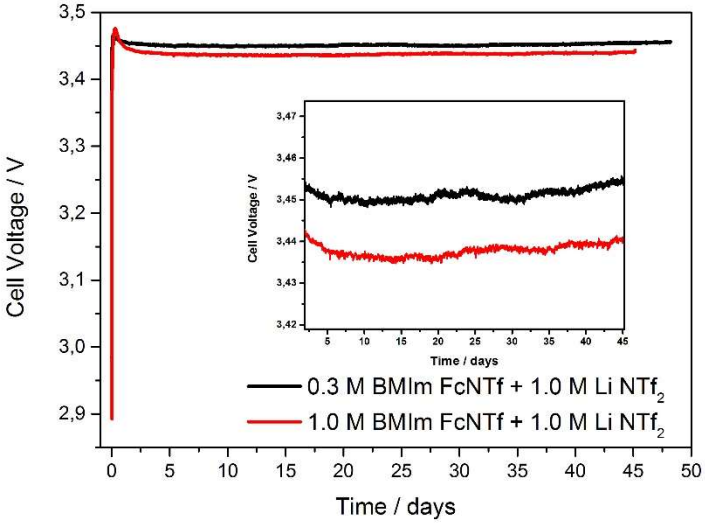

Figure 6.9. Overcharge floating profiles of Li/LTP cell at 0.1 C rate for electrolyte containing 1.0 M or 0.3 M of [BMIm][FcNTf] in EC-DEC 1:2 (v/v) with 1.0 M Li[NTf_2] solution.

6.2.5. Conclusions

We demonstrated the use of redox ionic liquids as bifunctional materials to prevent cathode overcharging and reduce the flammability of lithium-ion battery electrolytes. The electrochemical and mass transport properties of an electroactive anion based on ferrocene, (ferrocenylsulfonyl(trifluoromethylsulfonyl)imide; [FcNTf]), compared favourably to the (1-(ferrocenylmethyl)-3-methylimidazolium, [FcEMIm]) cation which is more commonly found in the literature. The oxidation potential of [FcNTf] RIL, at 3.5 V vs Li/Li^+ in the LIB electrolyte, was found to be independent of the concentration of lithium salt and is suitable for the efficient protection of cathode active materials with low to moderate voltages. Redox-active LIB electrolytes containing RIL or electroactive salt demonstrated a concentration-dependent viscosity higher than conventional electrolytes although without detrimental effect on the normal cell operation for concentrations up to 1.0 M. The redox ionic liquids significantly improved the thermal stability of the electrolyte and provided a non-flammable electrolyte when the overall salt concentration was high enough to reach the solvent-in-salt conditions. The overcharge protection using [FcNTf] was able to stand a charge-overcharge-discharge rate of up to 0.5 C for extended periods of time (45 days of continuous overcharge). This stability is linked to the ability of the [FcNTf] to deposit on the positive electrode surface and achieve an efficient passivation, preventing electrolyte oxidation at the same time. Consequently, this study demonstrates the high potential of modified ionic liquids to be designed with specific functionalities to replace additives in lithium-ion battery electrolytes. Among the several benefits imparted by the ionic liquid structure, we believe that their high miscibility with conventional solvents and carbonate mixture is particularly attracting.

6.2.6. Acknowledgments

The authors acknowledge the financial support from Fonds de recherche du Québec en nature et technologies (FQRNT) under their program for the reduction of greenhouse gases and the Natural Sciences and Engineering Research Council of Canada (NSERC) for Discovery grant (D.R.).

6.2.7. References

[1] Y. Nishi, Lithium ion secondary batteries; past 10 years and the future, J. Power Sources, 100 (2001) 101-106.
[2] J.B. Goodenough, Cathode materials: A personal perspective, J. Power Sources, 174 (2007) 996-1000.
[3] M. Armand, J.M. Tarascon, Building better batteries, Nature, 451 (2008) 652-657.
[4] J.M. Tarascon, M. Armand, Issues and challenges facing rechargeable lithium batteries, Nature, 414 (2001) 359-367.
[5] J. Chen, C. Buhrmester, J.R. Dahn, Chemical overcharge and overdischarge protection for lithium-ion batteries, Electrochem. Solid-State Lett., 8 (2005) A59-A62.
[6] Z. Chen, Y. Qin, K. Amine, Redox shuttles for safer lithium-ion batteries, Electrochim. Acta, 54 (2009) 5605-5613.
[7] W.K. Behl, D.T. Chin, Electrochemical overcharge protection of rechargeable lithium batteries. 1. Kinetics of iodide tri-iodide iodine redox reactions on platinum in LiAsF6 tetrahydrofuran solution, J. Electrochem. Soc., 135 (1988) 16-21.
[8] W.K. Behl, D.T. Chin, Electrochemical overcharge protection of rechargeable lithium batteries. 2. Effect of lithium iodide-iodine additive on the behavior of lithium electrode in LiAsF6-tetrahydrofuran solutions, J. Electrochem. Soc., 135 (1988) 21-25.
[9] W.K. Behl, Anodic oxidation of lithium bromide in tetrahydrofuran solutions, J. Electrochem. Soc., 136 (1989) 2305-2310.
[10] K.M. Abraham, D.M. Pasquariello, E.B. Willstaedt, Normal-butylferrocene for overcharge protection of secondary lithium batteries, J. Electrochem. Soc., 137 (1990) 1856-1857.
[11] M.N. Ates, C.J. Allen, S. Mukerjee, K.M. Abraham, Electronic effects of substituents on redox shuttles for overcharge protection of Li-ion batteries, J. Electrochem. Soc., 159 (2012) A1057-A1064.
[12] C. Buhrmester, L.M. Moshurchak, R.L. Wang, J.R. Dahn, The use of 2,2,6,6-tetramethylpiperinyl-oxides and derivatives for redox shuttle additives in Li-ion cells, J. Electrochem. Soc., 153 (2006) A1800-A1804.
[13] C. Buhrmester, L. Moshurchak, R.L. Wang, J.R. Dahn, Phenothiazine molecules: Possible redox shuttle additives for chemical overcharge and overdischarge protection for lithium-ion batteries, J. Electrochem. Soc., 153 (2006) A288-A294.
[14] C.-L. Lin, C.-C. Lee, K.-C. Ho, Spectroelectrochemical studies of manganese phthalocyanine thin films for applications in electrochromic devices, J. Electroanal. Chem., 524–525 (2002) 81-89.
[15] Z. Chen, K. Amine, Bifunctional electrolyte additive for lithium-ion batteries, Electrochem. Comm., 9 (2007) 703-707.
[16] Z. Chen, Y. Ren, A.N. Jansen, C.-k. Lin, W. Weng, K. Amine, New class of nonaqueous electrolytes for long-life and safe lithium-ion batteries, Nat. Commun., 4 (2013) 1513.
[17] C. Buhrmester, J. Chen, L. Moshurchak, J.W. Jiang, R.L. Wang, J.R. Dahn, Studies of aromatic redox shuttle additives for LiFePO4-based Li-ion cells, J. Electrochem. Soc., 152 (2005) A2390-A2399.
[18] C. Arbizzani, G. Gabrielli, M. Mastragostino, Thermal stability and flammability of electrolytes for lithium-ion batteries, J. Power Sources, 196 (2011) 4801-4805.

[19] A. Guerfi, M. Dontigny, P. Charest, M. Petitclerc, M. Lagacé, A. Vijh, K. Zaghib, Improved electrolytes for Li-ion batteries: Mixtures of ionic liquid and organic electrolyte with enhanced safety and electrochemical performance, J. Power Sources, 195 (2010) 845-852.
[20] P.M. Bayley, G.H. Lane, N.M. Rocher, B.R. Clare, A.S. Best, D.R. MacFarlane, M. Forsyth, Transport properties of ionic liquid electrolytes with organic diluents, Phys. Chem. Chem. Phys., 11 (2009) 7202-7208.
[21] R.-S. Kühnel, M. Lübke, M. Winter, S. Passerini, A. Balducci, Suppression of aluminum current collector corrosion in ionic liquid containing electrolytes, J. Power Sources, 214 (2012) 178-184.
[22] T. Evans, J. Olson, V. Bhat, S.-H. Lee, Effect of organic solvent addition to PYR13FSI + LiFSI electrolytes on aluminum oxidation and rate performance of Li(Ni1/3Mn1/3Co1/3)O2 cathodes, J. Power Sources, 265 (2014) 132-139.
[23] A. Hofmann, L. Merklein, M. Schulz, T. Hanemann, Anodic aluminum dissolution of LiTFSA containing electrolytes for Li-ion-batteries, Electrochim. Acta, 116 (2014) 388-395.
[24] T. Mandai, K. Yoshida, K. Ueno, K. Dokko, M. Watanabe, Criteria for solvate ionic liquids, Phys. Chem. Chem. Phys., 16 (2014) 8761-8772.
[25] S. Liumin, H. Yong-Sheng, L. Hong, A. Michel, C. Liquan, A new class of Solvent-in-Salt electrolyte for high-energy rechargeable metallic lithium batteries, Nat. Commun., 4 (2013) 1481-1481.
[26] R.S. Kühnel, N. Böckenfeld, S. Passerini, M. Winter, A. Balducci, Mixtures of ionic liquid and organic carbonate as electrolyte with improved safety and performance for rechargeable lithium batteries, Electrochim. Acta, 56 (2011) 4092-4099.
[27] S. Menne, R.S. Kühnel, A. Balducci, The influence of the electrochemical and thermal stability of mixtures of ionic liquid and organic carbonate on the performance of high power lithium-ion batteries, Electrochim. Acta, 90 (2013) 641-648.
[28] L. Lombardo, S. Brutti, M.A. Navarra, S. Panero, P. Reale, Mixtures of ionic liquid – Alkylcarbonates as electrolytes for safe lithium-ion batteries, J. Power Sources, 227 (2013) 8-14.
[29] S.E. Khakani, J.C. Forgie, D.D. MacNeil, D. Rochefort, Redox shuttles for lithium-ion batteries at concentrations up to 1 M using an electroactive ionic liquid based on 2,5-di-tert-butyl-1,4-dimethoxybenzene, J. Electrochem. Soc., 162 (2015) A1432-A1438.
[30] P.G. Balakrishnan, R. Ramesh, T. Prem Kumar, Safety mechanisms in lithium-ion batteries, J. Power Sources, 155 (2006) 401-414.
[31] H. Wu, Z. Lv, S. Hou, X. Cai, D. Wang, H. Kafafy, Y. Fu, C. Zhang, Z. Chu, D. Zou, A new ionic liquid organic redox electrolyte for high-efficiency iodine-free dye-sensitized solar cells, J. Power Sources, 221 (2013) 328-333.
[32] H.J. Xie, B. Gélinas, D. Rochefort, Redox-active electrolyte supercapacitors using electroactive ionic liquids, Electrochem. Comm., 66 (2016) 42-45.
[33] E. Mourad, L. Coustan, P. Lannelongue, D. Zigah, A. Mehdi, A. Vioux, S.A. Freunberger, F. Favier, O. Fontaine, Biredox ionic liquids with solid-like redox density in the liquid state for high-energy supercapacitors, Nat. Mater., advance online publication (2016).
[34] K. Xu, Nonaqueous liquid electrolytes for lithium-based rechargeable Batteries, Chem. Rev., 104 (2004) 4303-4418.

[35] A. Lewandowski, A. Swiderska-Mocek, Ionic liquids as electrolytes for Li-ion batteries-An overview of electrochemical studies, J. Power Sources, 194 (2009) 601-609.
[36] Y.D. Wang, K. Zaghib, A. Guerfi, F.F.C. Bazito, R.M. Torresi, J.R. Dahn, Accelerating rate calorimetry studies of the reactions between ionic liquids and charged lithium ion battery electrode materials, Electrochim. Acta, 52 (2007) 6346-6352.
[37] B. Gélinas, J.C. Forgie, D. Rochefort, Conductivity and electrochemistry of ferrocenyl-imidazolium redox ionic liquids with different alkyl chain lengths, J. Electrochem. Soc., 161 (2014) H161-H165.
[38] B. Gélinas, D. Rochefort, Synthesis and characterization of an electroactive ionic liquid based on the ferrocenylsulfonyl(trifluoromethylsulfonyl)imide anion, Electrochim. Acta, 162 (2015) 36-44.
[39] B. Gélinas, M. Natali, T. Bibienne, Q.P. Li, M. Dollé, D. Rochefort, Electrochemical and transport properties of ions in mixtures of electroactive ionic liquid and propylene carbonate with a lithium salt for lithium-ion batteries, J. Phys. Chem. C, 120 (2016) 5315-5325.
[40] L. Xiong, A.M. Fletcher, S.G. Davies, S.E. Norman, C. Hardacre, R.G. Compton, Tuning solute redox potentials by varying the anion component of room temperature ionic liquids, Chem. Comm., 48 (2012) 5784.
[41] Y. Wang, E.I. Rogers, R.G. Compton, The measurement of the diffusion coefficients of ferrocene and ferrocenium and their temperature dependence in acetonitrile using double potential step microdisk electrode chronoamperometry, J. Electroanal. Chem., 648 (2010) 15-19.
[42] R.G. Evans, O.V. Klymenko, P.D. Price, S.G. Davies, C. Hardacre, R.G. Compton, A comparative electrochemical study of diffusion in room temperature ionic liquid solvents versus acetonitrile, ChemPhysChem, 6 (2005) 526-533.
[43] E.I. Rogers, D.S. Silvester, D.L. Poole, L. Aldous, C. Hardacre, R.G. Compton, Voltammetric characterization of the ferrocene|ferrocenium and cobaltocenium|cobaltocene redox couples in RTILs, J. Phys. Chem. C, 112 (2008) 2729-2735.
[44] B. Gharib, A. Hirsch, Synthesis and characterization of new ferrocene-containing ionic liquids, Eur. J. Org. Chem., 2014 (2014) 4123-4136.
[45] J.C. Forgie, S. El Khakani, D.D. MacNeil, D. Rochefort, Electrochemical characterisation of a lithium-ion battery electrolyte based on mixtures of carbonates with a ferrocene-functionalised imidazolium electroactive ionic liquid, Phys. Chem. Chem. Phys., 15 (2013) 7713-7721.
[46] H.L. Ngo, K. LeCompte, L. Hargens, A.B. McEwen, Thermal properties of imidazolium ionic liquids, Thermochim. Acta, 357–358 (2000) 97-102.
[47] R.E. Del Sesto, T.M. McCleskey, C. Macomber, K.C. Ott, A.T. Koppisch, G.A. Baker, A.K. Burrell, Limited thermal stability of imidazolium and pyrrolidinium ionic liquids, Thermochim. Acta, 491 (2009) 118-120.
[48] J.B. Shotwell, R.A. Flowers, Electrochemical investigation of the solvolytic properties of ethylammonium nitrate (EAN) and propylammonium nitrate (PAN), Electroanalysis, 12 (2000) 223-226.
[49] W. Xu, E.I. Cooper, C.A. Angell, Ionic liquids: Ion mobilities, glass temperatures, and fragilities, J. Phys. Chem. B, 107 (2003) 6170-6178.

[50] S.-Y. Lee, K. Ueno, C.A. Angell, Lithium salt solutions in mixed sulfone and sulfone-carbonate solvents: A walden plot analysis of the maximally conductive compositions, J. Phys. Chem. C, 116 (2012) 23915-23920.
[51] B. Lang, B. Ziebarth, C. Elsässer, Lithium ion conduction in LiTi2(PO4)3 and related compounds based on the NASICON structure: A first-principles study, Chem. Mater., 27 (2015) 5040-5048.
[52] X. Huang, L. Wang, H. Liao, R. Meng, J. Li, X. He, Charge rate influence on the electrochemical performance of LiFePO4 electrode with redox shuttle additive in electrolyte, Ionics, 18 (2012) 501-505.

6.3. Supporting Information

Bifunctional ionic liquids to improve the safety of Lithium-ion battery

Bruno Gélinas[1], *Thomas Bibienne*[1], *Mickael Dollé*[1], *Dominic Rochefort*[1*]

Département de chimie, Université de Montréal, CP6128 Succ. Centre-Ville, Montréal, Québec, Canada H3C 3J7

*Corresponding author: Tel: +1-514-343-6733, Fax: +1-514-343-7586, email: dominic.rochefort@umontreal.ca

List of Contents:

6.3.1. Synthetic procedure of redox shuttle

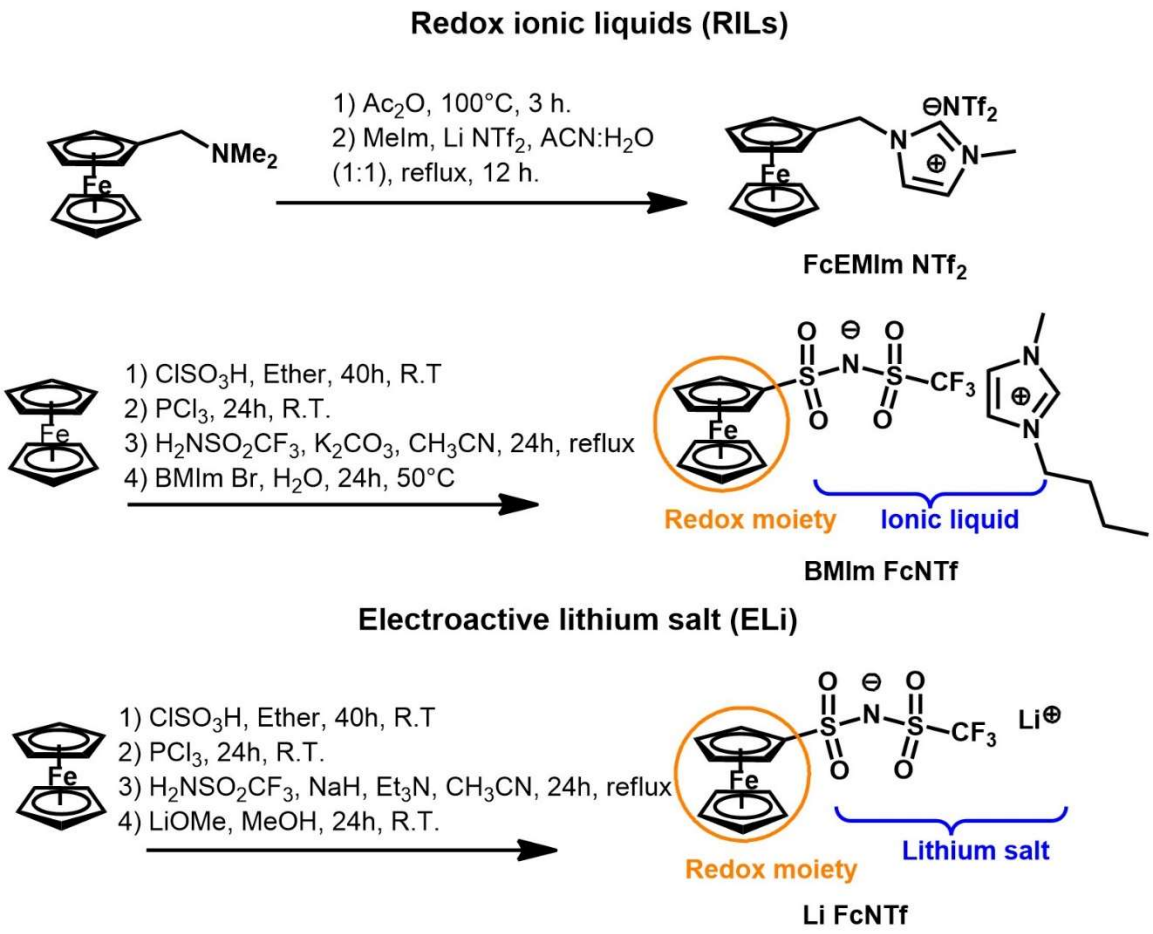

Figure S6.1. Synthetic pathway of [FcEMIm][NTf_2], [BMIm][FcNTf] and Li[FcNTf].

Preparation of ferrocenylmethylacetate. In acetic anhydride, N,N-dimethylaminomethyl) ferrocene (reactant: reagent 1:9 w/v) was dissolved and the reaction flask was transferred in an oil bath kept at 100°C. The mixture was stirred for 3 hours, the reaction was stopped with an aqueous solution of high concentration of Na_2CO_3 and the mixture was stirred in an ice bath until complete deactivation. The product was extracted using diethyl ether (3x50 mL) and the organic phase was washed with Milli-Q water (3x60 mL) and with a saturated solution of $NaHCO_3$. The organic phase was dried with magnesium sulfate, then filtered and after dried. The solvent was then removed under a vacuum, and the residue was purified by flash column chromatography using silica gel as the stationary phase and diethyl ether:hexane (1:1) as the eluent. A mixture of chloroform/Hexane was used for recrystallization to obtain an orange crystal. Yield: 82 %. ^{1}H RMN ($CDCl_3$, 300 MHz): δ (ppm) = 4.90 (s,2H), 4.29 (t,2H), 4.20 (t,2H), 4.18 (s,5H), 2.05 (s,3H). ^{13}C RMN ($CDCl_3$, 125

MHz): δ (ppm) = 170.94; 81.21; 69.67; 68.89; 68.89; 68.58; 62.89; 21.03. (ESI) m/z: [M*$^{+}$](calcd for $C_{13}H_{14}FeO_2$: 258.03377 Found: 258.03415. Elementary analysis: Calcd for $C_{13}H_{14}FeO_2$: C 60.50; H 5.47. Found: C 60.58; H 5.56.

Preparation of 1-(methylferrocenyl)-3-methylimidazolium ([FcEMIm][NTf$_2$]). In a mixture acetonitrile:Milli-Q water (1:1), ferrocenylmethylacetate (1.0 eq) was dissolved, methylimidazole (1.5 eq) and Li [NTf$_2$] (1.2 eq) was added. The resulting solution was stirred and heated at reflux temperature for 12 hours. Removal of the solvent under reduced pressure and the product was dissolved in dichloromethane. The organic phase was washed with Milli-Q water (3x100 mL). The organic phase was dried with magnesium sulfate, then filtered and after dried. [FcEMIm] [NTf$_2$] was triturated with diethyl ether and was purified by flash column chromatography using silica gel as the stationary phase and acetone as the eluent. The salts were dried overnight under reduce pressure at 65 °C to give red-brown oil or red-yellow solid. Yield: 69 %. According to a previous study, this present procedure shows an overall yield of 57% which is an improvement if compared to the 6 step procedure in literature (Overall yield: 17%).[1] ^{1}H NMR (300 MHz, DMSO-d$_6$) δ (ppm): 9.06 (s, 1H); 7.71 (t, 1H); 7.63 (t, 1H); 5.15 (s, 2H); 4.43 (t, 2H); 4.23 (m, 7H); 3.81 (s, 3H). ^{19}F NMR (DMSO-d$_6$, 282 MHz): δ (ppm) = -80.13. ^{13}C NMR (125 MHz, DMSO-d$_6$) δ (ppm): 136.34; 124.04; 122.45; 122.10; 117.82; 113.58; 81.34; 69.19; 48.78; 36.21. (ESI) m/z: [M*$^{+}$](calcd for $C_{15}H_{17}FeN_2$: 281.07412 Found: 281.07577; m/z: [M*$^{-}$](calcd for $C_2F_6NO_4S_2$: 279.91784 Found: 279.91857. Elementary analysis: Calcd for $C17H17F_6FeN_3O_4S_2$: N 7.49; C 36.38; H 3.05; S 11.43. Found: N 7.41; C 36.53; H 2.87; S 11.44.

Preparation of potassium ferrocenylsulfonyl(trifluoromethylsulfonyl)imide. Potassium ferrocenylsulfonyl(trifluoromethylsulfonyl)imide (K[FcNTf]) was synthesized according to a similar procedure given by our previous paper[2] and K[FcNTf] salt was chosen because of less hygroscopic than sodium [FcNTf] salt (Humid Na[FcNTf] is slightly soluble in dichloromethane) . Trifluoromethanesulfonamide (1 eq.) was dissolved in a flask in acetonitrile and anhydrous potassium carbonate (1.5 eq.) was added. The solution was stirred for 10 minutes at room temperature. A slow addition of ferrocenylsulfonyl chloride (1 eq.) was then made. The resulting solution was stirred and heated at reflux temperature for 24 hours. The brown solution was filtered and the precipitate was washed with acetone to achieve a white precipitate. Removal of the solvent under reduced pressure produced a brown-yellow product. Dichloromethane was used to wash the

salt, obtaining a light brown-yellow powder. The salt was dried overnight under reduce pressure at room temperature. A better purification was done using this procedure via the removal of unreacted Trifluoromethanesulfonamide. Yield: 76 %. ^{1}H NMR (DMSO-d_6, 300 MHz): δ (ppm) = 4.53 (t, 2H), 4.28 (s, 7H). ^{19}F NMR (DMSO-d_6, 282 MHz): δ (ppm) = -77.62. ^{13}C NMR (DMSO-d_6, 125 MHz): δ (ppm) = 121.90; 119.32; 94.61; 70.44; 69.19; 68.61. (ESI) m/z: [M*$^{-}$](calcd for $C_{11}H_9F_3FeNO_4S_2^-$) : 395.928 Found: 395.926.

Preparation of electroactive FcNTf ionic liquids ([BMIm][FcNTf]). Potassium ferrocenylsulfonyl (trifluoromethylsulfonyl)imide (1.0 eq) and 1-Butyl-3-methylimidazolium bromide (1.1 eq) were dissolved in acetone. The mixture was stirred at room temperature for 24 hours. Following this step, the solution was filtered and removal of the solvent under reduced pressure produced a dark-brown viscous liquid. The compound was purified by alumina (Al_2O_3) as adsorptive filtration and then, by column chromatography silica (SiO_2) gel as the stationary phase and acetone as eluent. After removing the solvent, orange product was washed dried at 65 °C overnight under vacuum and cooled down at room temperature to obtain an orange crystal. Yield: 90%. ^{1}H NMR (DMSO-d_6, 300 MHz): δ (ppm) = 9.10 (s,1H), 7.76 (t,1H), 7.69 (t,1H), 4.53 (t,2H), 4.28 (s,7H), 4.15 (t,2H), 3.84 (s,3H), 1.76 (q,2H) 1.31-1.19 (m,2H), 0.90 (t,3H). ^{19}F NMR (DMSO-d_6, 282 MHz): δ (ppm) = -79.08. ^{13}C NMR (DMSO-d_6, 125 MHz): δ (ppm) = 136.96; 124.08; 122.75; 118.44; 94.57; 70.41; 60.17; 68.60; 48.96; 36.20; 31.80; 19.19; 13.72. (ESI) m/z: [M*$^{+}$](calcd for $C_8H_{15}N_2^+$): 139.12352 found: 139.12341. [M*$^{-}$](calcd for $C_{11}H_9F_3FeNO_4S_2^-$) : 395.92745 Found: 395.92917. Calcd for $C_{19}H_{24}F_3FeN_3O_4S_2$: N 7.85; C 42.62; H 4.52; S 11.98. Found: N 7.90; C 42.69; H 4.52; S 11.96.

Preparation of electroactive lithium salt (Li[FcNTf]). Li[FcNTf] was synthesized according to our previous publication.[3] ^{1}H NMR (DMSO-d_6, 300 MHz): δ (ppm) = 4.53 (t, 2H), 4.28 (s, 7H). ^{19}F NMR (DMSO-d_6, 282 MHz): δ (ppm) = -79.06. ^{13}C NMR (DMSO-d_6, 125 MHz): δ (ppm) = 122.74; 118.43; 94.57; 70.42; 69.18; 68.59. (ESI) m/z: [M*$^{-}$](calcd for $C_{11}H_9F_3FeNO_4S_2^-$) : 395.928 Found: 395.926.

6.3.2. Thermal analysis

Table S6.1. Thermochemical properties of neat [FcEMIm][NTf_2] and [BMIm][FcNTf].

RILs	T_m / °C	T_d (T_d under air) / °C
FcEMIm NTf_2 (Ref. [4],[5])	46.3	241
FcEMIm NTf_2 (This report)	46.1	271 (268)
BMIm FcNTf (This report)	55.1	297 (304)

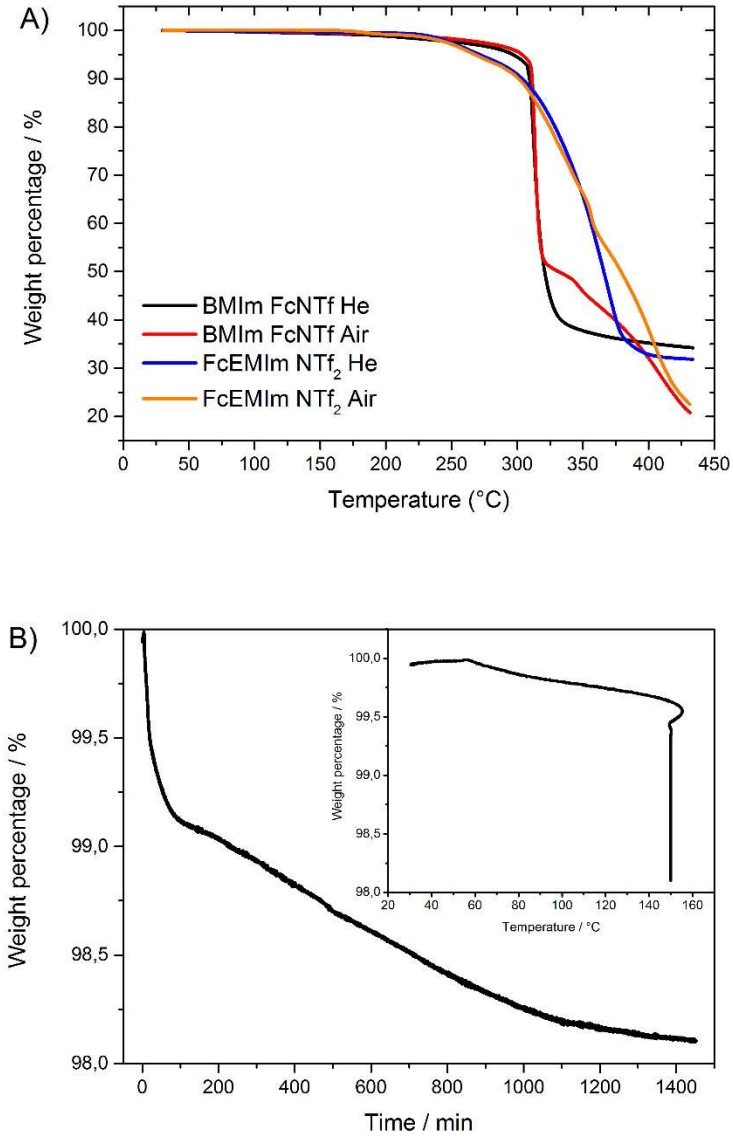

Figure S6.2. A) TGA of neat [BMIm][FcNTf] and [FcEMIm][NTf_2] with a ramp of 10°C per minute under air or helium atmosphere (short-term). B) TGA of neat [BMIm][FcNTf] at 150°C for 24 h (long-term).

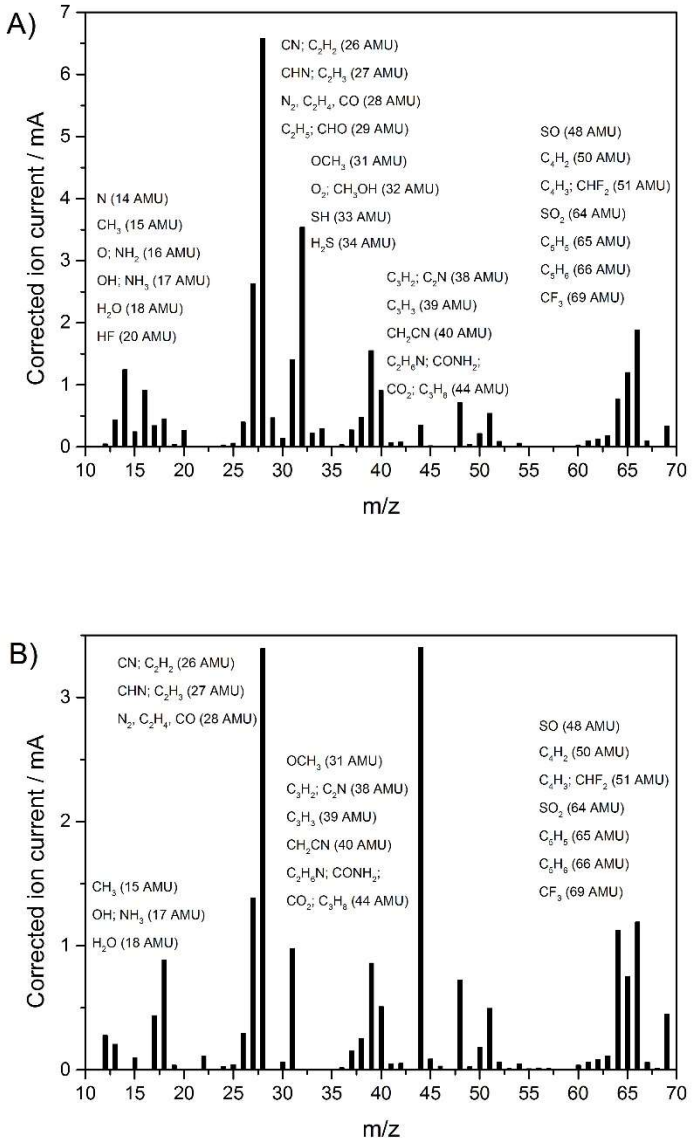

Figure S6.3. TGA-MS of neat [BMIm] [FcNTf] under A) helium and B) air atmosphere. The MS histograms were recorded during the main thermal decomposition period of the redox ionic liquid. Peaks were assigned to parents or fragments of expected decomposition products and spectra are shown in the region 10–70 m/z.

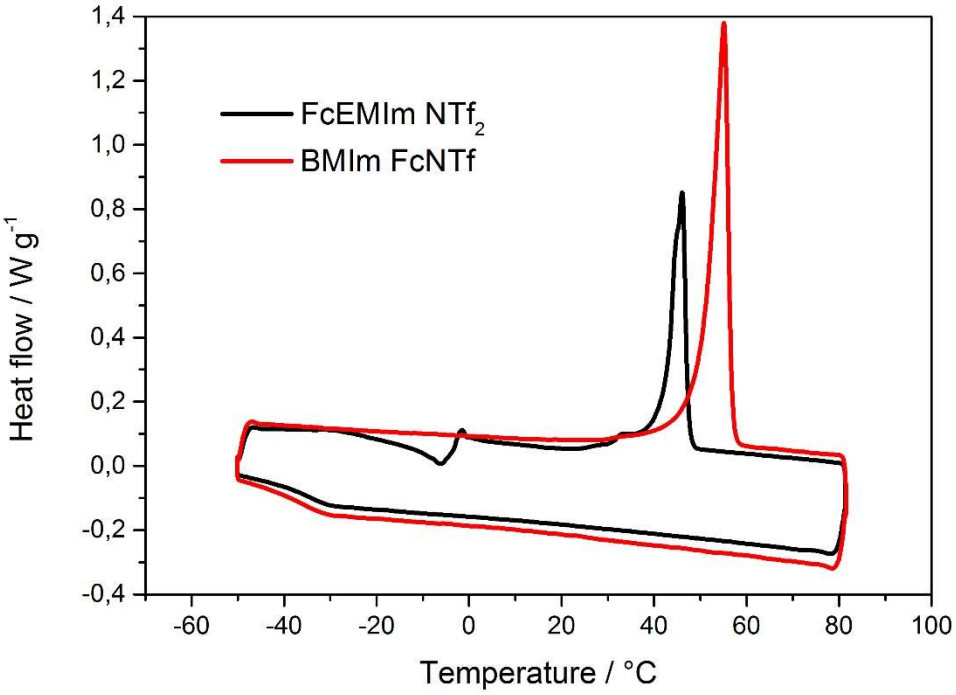

Figure S6.4. DSC thermogram of neat [FcEMIm] [NTf_2] and [BMIm] [FcNTf]. The measurements were done between -50 to 80°C with a ramp of 5 °C per minute and with isothermal of 5 minutes between the cooling and heating. (exo, down)

6.3.3. Extra CVs and electrochemical analysis

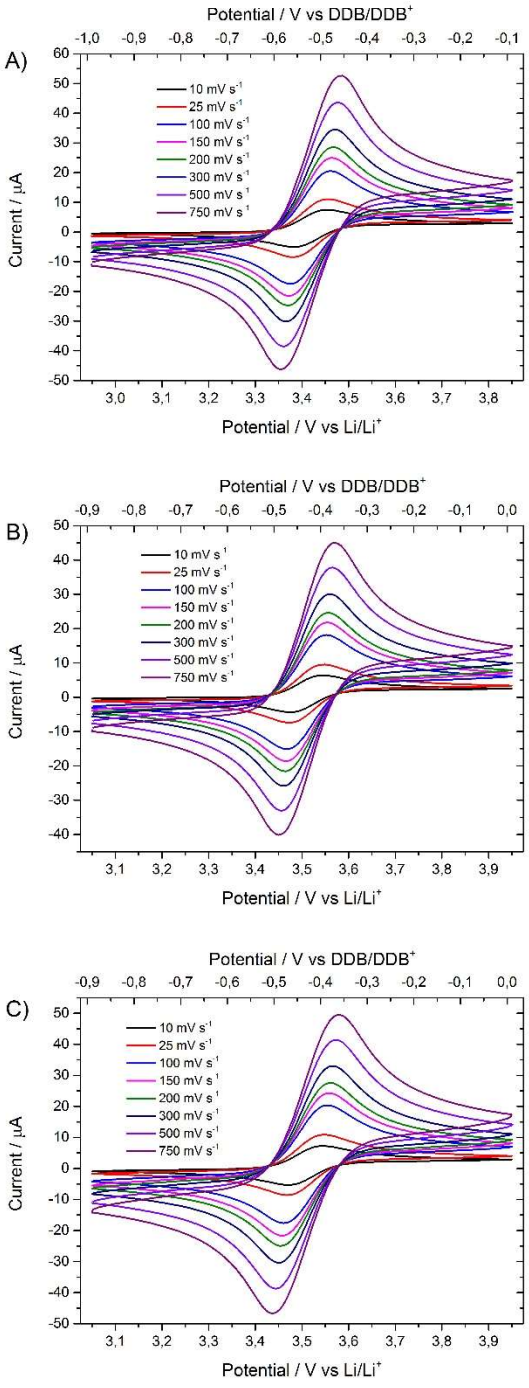

Figure S6.5. CVs of 10 mM solution of A) [FcEMIm] [NTf_2] B) [BMIm] [FcNTf] and C) Li [FcNTf] in EC-DEC 1:2 (v/v) with 1 M Li [NTf_2] at various scan rates. The scan rates used were 10 to 750 mV s^{-1}.

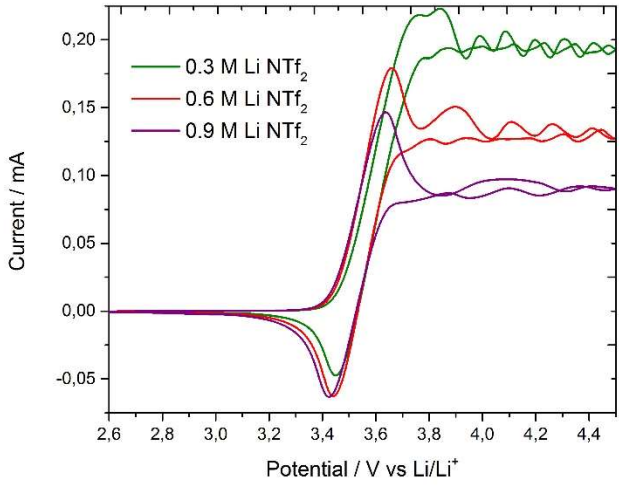

Figure S6.6. CVs of comparison between different 0.3 M [BMIm] [FcNTf] solutions in EC-DEC 1:2 (v/v) with (0.3, 0.6 and 0.9 M) Li [NTf_2] at 10 mV s^{-1}. ([BMIm] [FcNTf]:Li [NTf_2] 1:1; 1:2 and 1:3).

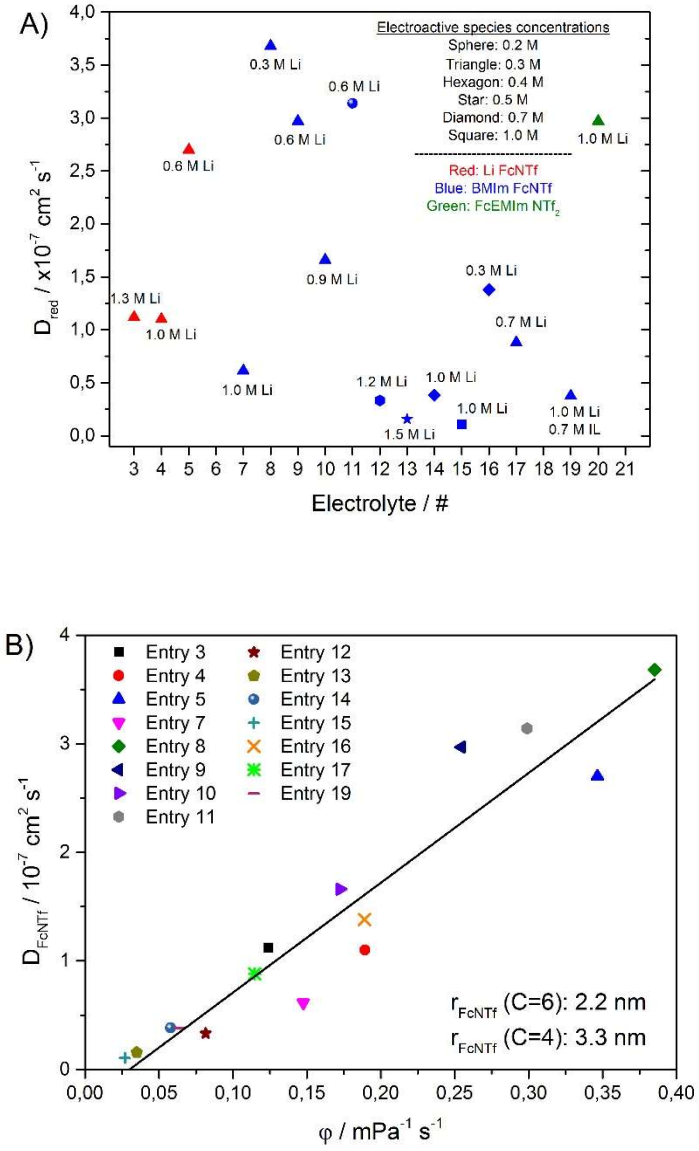

Figure S6.7. A) Diffusion coefficients using CV and Randles-Sevcik equation and C) diffusion of [FcNTf] anion dependence on the fluidity (Stokes-Einstein relation) for different electrolytes.

6.3.4. Complete viscosity/ionic conductivity study and flammability test

Table S6.2. Advanced electrolytes using EC-DEC 1:2 (v/v) as solvents were characterized in the complete study.

Entry #	[Li FcNTf] / M	[BMIm FcNTf] / M	[FcEMIm NTf_2] / M	[BMIm NTf_2] / M	[Li NTf_2] / M
1	-	-	-	-	-
2	-	-	-	-	1.0
3	0.3	-	-	-	1.0
4	0.3	-	-	-	0.7
5	0.3	-	-	-	0.3
6	-	0.3	-	-	-
7	-	0.3	-	-	1.0
8	-	0.3	-	-	0.3
9	-	0.3	-	-	0.6
10	-	0.3	-	-	0.9
11	-	0.2	-	-	0.6
12	-	0.4	-	-	1.2
13	-	0.5	-	-	1.5
14	-	0.7	-	-	1.0
15	-	1.0	-	-	1.0
16	-	0.7	-	-	0.3
17	-	0.7	-	-	0.7
18	-	-	-	0.3	1.0
19	-	0.3	-	0.7	1.0
20	-	-	0.3	-	1.0

Table S6.3. All viscosities (η), activation energies of fluidity (φ = 1/η) ($E_{a,\varphi}$), entropy (ΔS_{φ}) and enthalpy (ΔH_{φ}) of [FcNTf] solutions in EC-DEC 1:2 (v/v) with or without Li [NTf_2] are summarized.

Entry #	η at 25°C / mPa s	η at 75°C / mPa s	$E_{a,\varphi}$ / kJ mol^{-1}	ΔH_{φ} / kJ mol^{-1} K^{-1}	ΔS_{φ} / J mol^{-1} K^{-1}
1	1.231	0.690	9.79	7.1	-222.9
2	4.516	1.793	15.9	13.3	-213.0
3	8.076	2.720	18.8	16.1	-208.3
4	5.284	2.016	16.7	14.0	-211.9
5	2.886	1.299	13.9	11.2	-216.3
6	1.910	0.919	12.6	9.9	-217.1
7	6.777	2.416	18.0	15.3	-209.5
8	2.596	1.164	13.8	11.2	-215.5
9	3.929	1.588	15.6	12.9	-213.0
10	5.800	2.120	17.3	14.6	-210.5
11	3.345	1.416	14.8	12.2	-214.3
12	12.26	3.605	21.1	18.4	-203.9
13	28.66	6.081	26.9	24.3	-191.3
14	17.27	4.559	22.9	20.2	-200.8
15	37.16	7.420	27.8	25.2	-190.4
16	5.288	1.959	17.1	14.4	-210.5
17	8.719	2.832	19.4	16.7	-207.0
18	5.529	2.098	16.6	14.0	-212.3
19	15.63	4.303	22.2	19.5	-202.3
20	7.439	2.554	18.4	15.7	-209.0

Table S6.4. All ionic conductivities (σ), activation energies of ionic conductivity ($E_{a,\sigma}$), entropy (ΔS_σ) and enthalpy (ΔH_σ) of [FcNTf] solution in EC-DEC 1:2 (v/v) with or without Li [NTf_2] are summarized.

Entry #	σ at 25°C / mS cm^{-1}	σ at 75°C / mS cm^{-1}	$E_{a,\sigma}$ / kJ mol^{-1}	ΔH_σ / kJ mol^{-1} K^{-1}	ΔS_σ / J mol^{-1} K^{-1}
1	-	-	-	-	-
2	6.26	12.27	11.5	8.8	-200.0
3	4.06	8.76	13.2	10.5	-198.0
4	4.26	8.66	12.2	9.5	-201.1
5	3.81	6.98	10.5	7.9	-207.5
6	2.98	5.92	11.7	9.0	-205.5
7	4.89	10.87	13.7	11.0	-194.1
8	4.57	9.08	11.8	9.1	-201.8
9	5.26	10.83	12.4	9.7	-198.5
10	4.89	10.78	13.5	10.8	-195.4
11	5.57	10.91	11.6	8.9	-200.8
12	4.12	9.98	15.3	12.6	-190.8
13	2.55	7.63	18.7	16.0	-183.2
14	3.20	9.13	18.0	15.3	-183.8
15	2.10	7.44	21.7	19.0	-174.8
16	4.08	9.63	14.8	12.1	-192.6
17	3.85	9.84	16.0	13.4	-188.8
18	6.64	14.06	12.9	10.2	-195.0
19	4.76	12.56	16.7	14.0	-185.0
20	4.98	10.84	13.4	10.7	-195.9

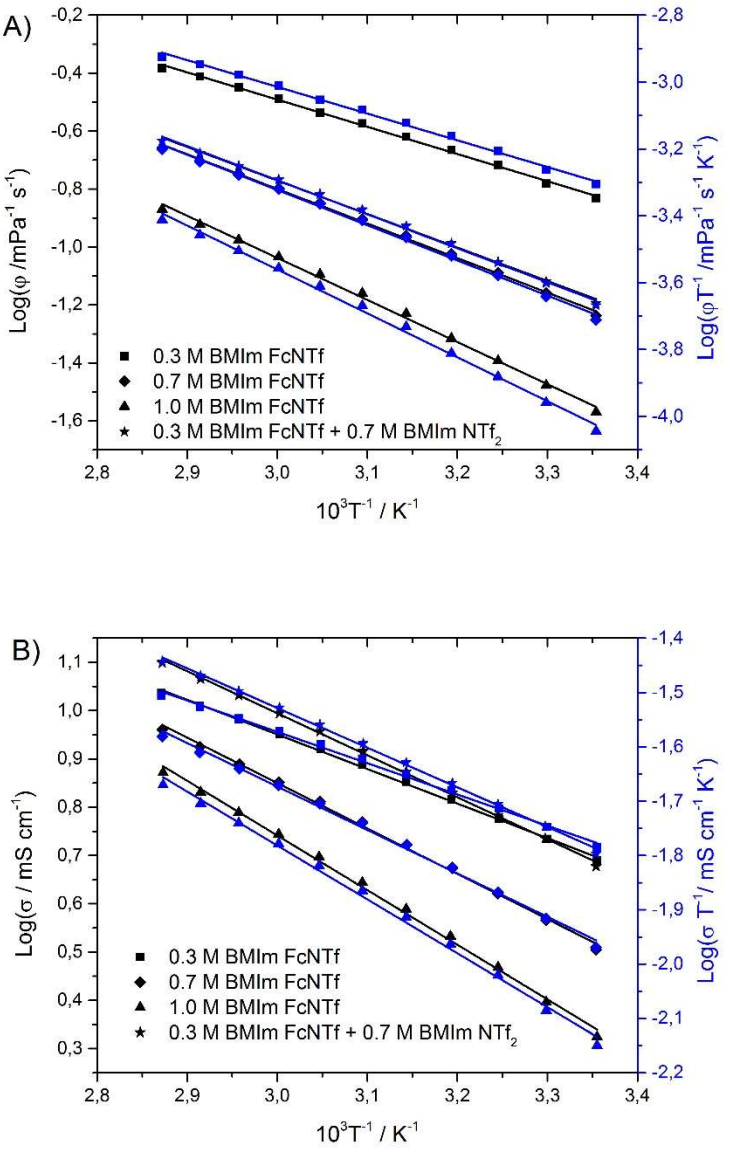

Figure S6.8. Arrhenius plots (black line) and Eyring plots (blue line) of A) fluidity and B) ionic conductivity for different [FcNTf] solutions (0.3, 0.7 and 1.0 M) in EC-DEC 1:2 (v/v) with 1.0 M Li [NTf_2] solution in presence or absence of [BMIm] [NTf_2]. Measurements were done at 5°C intervals between 25 and 75°C.

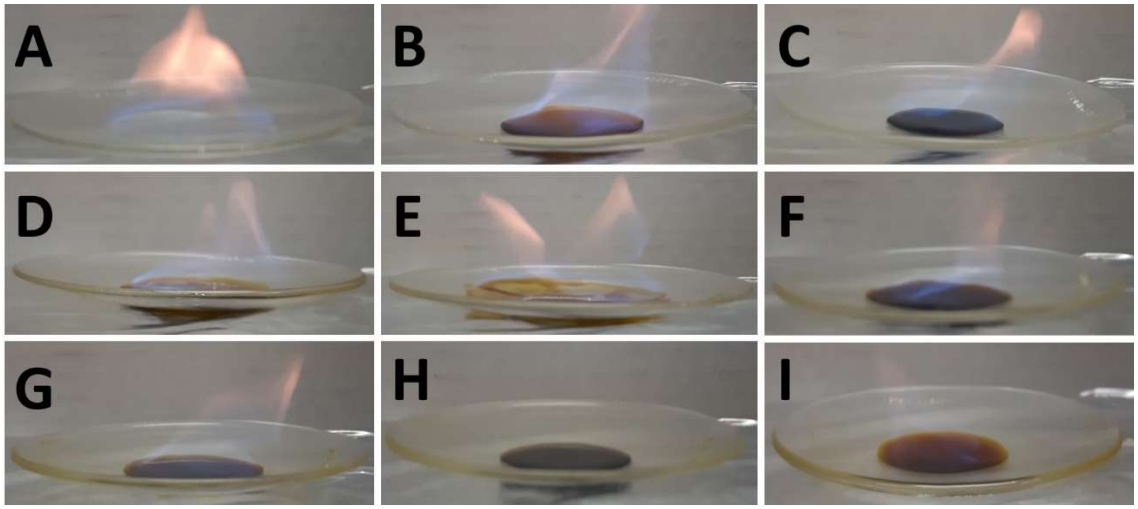

Figure S6.9. The flammability test for different electrolytes A) Entry 2, B) Entry 20, C) Entry 3, D) Entry 7, E) Entry 8, F) Entry 14, G) Entry 16, H) Entry 15 (Inflammable, 1.0 M [BMIm] [FcNTf] + 1.0 M Li [NTf_2]), I) Entry 19.

6.3.5. Extra Galvanostatic charge-overcharge-discharge curves and rate capability study

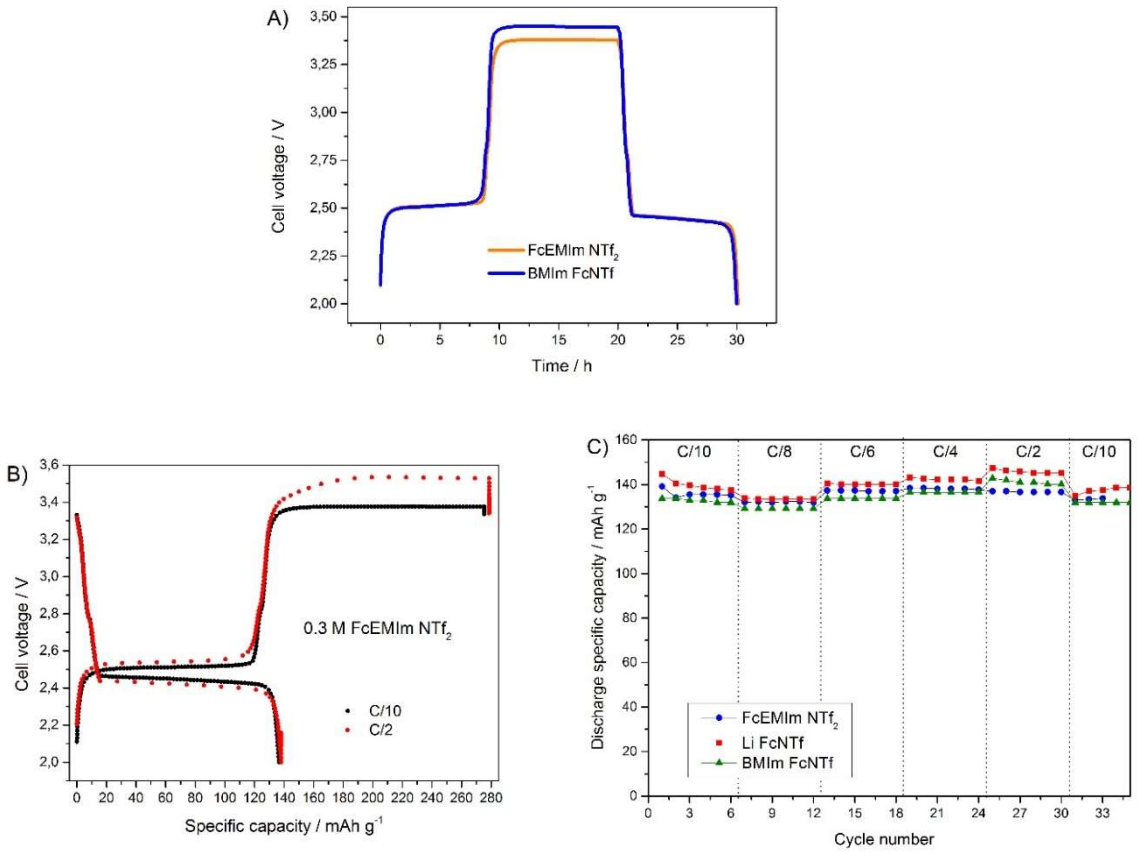

Figure S6.10. A) Galvanostatic charge-overcharge-discharge profiles of Li/LTP cell at 0.1 C rate and 10 h overcharge for different 0.3 M solutions of FcEMIm NTf_2, Li FcNTf or BMIm FcNTf in EC-DEC 1:2 (v/v) with 1.0 M Li [NTf_2] B) Capacity profiles at 0.1 C and 0.5 C rates for electrolyte containing 0.3 M of [FcEMIm] [NTf_2] in EC-DEC 1:2 (v/v) with 1.0 M Li [NTf_2]. The rate capability study for discharge using RIL or Li[FcNTf] as RS.

6.3.6. References

[1] J.C. Forgie, S. El Khakani, D.D. MacNeil, D. Rochefort, Electrochemical characterisation of a lithium-ion battery electrolyte based on mixtures of carbonates with a ferrocene-functionalised imidazolium electroactive ionic liquid, Phys. Chem. Chem. Phys., 15 (2013) 7713-7721.
[2] B. Gélinas, D. Rochefort, Synthesis and characterization of an electroactive ionic liquid based on the ferrocenylsulfonyl(trifluoromethylsulfonyl)imide anion, Electrochim. Acta, 162 (2015) 36-44.
[3] B. Gélinas, M. Natali, T. Bibienne, Q.P. Li, M. Dollé, D. Rochefort, Electrochemical and transport properties of ions in mixtures of electroactive ionic liquid and propylene carbonate with a lithium salt for lithium-ion batteries, J. Phys. Chem. C, 120 (2016) 5315-5325.
[4] A.W. Taylor, P. Licence, X-ray photoelectron spectroscopy of ferrocenyl- and ferrocenium-based ionic liquids, ChemPhysChem, 13 (2012) 1917-1926.
[5] B. Gharib, A. Hirsch, Synthesis and characterization of new ferrocene-containing ionic liquids, Eur. J. Org. Chem., 2014 (2014) 4123-4136.

Chapitre 7 : Liquide ionique électroactif basé sur la modification du centre redox diméthoxybenzène comme navette redox

7.1. Avant-propos et mise en contexte

Ce chapitre a été rédigé sous forme d'un article qui a été soumis à *Journal of Power Sources*. Selon la littérature, le 2,5-di-tert-butyl-1,4-diméthoxybenzène est la navette redox la plus efficace par le biais de sa stabilité électrochimique, mais la solubilité de cette espèce électroactive est faible dans les solvants de carbonate et selon le potentiel d'oxydation, cette navette redox peut seulement protéger des batteries-3,5V. Par conséquent, l'utilisation de la plateforme des liquides ioniques est exploitée pour augmenter la solubilité en centre redox et la modification de la structure est évaluée pour étudier la stabilité électrochimique. La caractérisation de l'électrolyte électroactif et de la pile au lithium contenant cet électrolyte a été rapportée dans cet article.

6.3. Electroactive ionic liquids based on 2,5-ditert-butyl-1,4-dimethoxybenzene and triflimide anion as redox shuttle for LFP/LTO lithium-ion batteries

Bruno Gélinas,[a] Thomas Bibienne,[a] Mickaël Dollé[a] and Dominic Rochefort [a]

[a]Département de Chimie, Université de Montréal, Montréal, Québec H3C 3J7, Canada

J. Power Sources

7.2.1. Abstract

In order to increase the solubility and oxidation potential of redox shuttles, electroactive ionic liquids (RILs) based on the modification of 1,4-dimethoxybenzene with triflimide anions were synthesized. We developed two synthetic routes to obtain these RILs in which the triflimide was either linked on the benzene ring or as a ether on 2,5-ditert-butyl-1,4-dimethoxybenzene (DDB). These RILs all have melting points below 100 °C, but above room temperature. The structural impact of electroactive anion was evaluated in this study by determining the redox potential and electrochemical stability. The electrochemical properties of these RILs were investigated by cyclic voltammetry and the diffusion coefficients were measured by double potential step chronoamperometry. The viscosity and ionic conductivity measurements of redox-active electrolyte were obtained at different temperatures and the RIL additives are shown to have a low impact on these electrolyte properties at concentrations up to 0.3 M. The charge-overcharge-discharge cycles of Li/ $LiFePO_4$ half-cells and $Li_4Ti_5O_{12}$/$LiFePO_4$ full cells with a 100% overcharge are presented using redox-active electrolyte (0.3 M concentration level) at 0.1 C rate. This study highlights the potential of electroactive ionic liquids as highly soluble and stable functional additives in Li-ion battery electrolytes.

Keywords: Lithium-ion battery, redox shuttle, sacrificing additive, redox ionic liquid and redox-active electrolyte

7.2.2. Introduction

Lithium-ion batteries (LIBs) are promising candidates to meet the high power and high energy density storage requirements of electric vehicles. Safety issues arise from the use of high voltage materials due to their high reactivity but also with materials with moderate voltage subjected to high current densities used for fast charging. Parasitic reactions involving electrode material and electrolyte decomposition occur when the voltage of the positive electrode goes beyond the oxidation potential of the active material. Such overoxidation of the cathode can initiate cascading thermal runaways and, eventually, cell explosion.[1] Redox shuttle are overcharge protection additive that are used to transport the excess charge from the positive electrode to the negative, thereby protecting the LIB by limiting the cathode voltage potential to the oxidation potential of the R-S.[2] The electroactive species used as redox shuttle needs to be stable in both oxidation states, able to diffuse rapidly, establish fast heterogeneous electron transfer and be readily soluble. The oxidation potential of the R-S must be adapted to the cathode material (i.e. 300-400 mV above that of the cathode) to ensure inaction during normal LIB operation to avoid self-discharge. Several electroactive compounds have been proposed as redox shuttles. Iodide media (3.0 V)[3, 4], bromide (3.5 V)[5], ferrocene derivatives (3.0-3.6 V)[6, 7], 2,2,6,6-tetramethylpiperinyloxide derivatives (TEMPO, 3.5-3.6 V)[8], phenothiazine derivatives (3.5-3.8 V)[9], thiantrene (4.0-4.4 V)[10], 2-(pentafluorophenyl)-tetrafluoro-1,3,2-benzodioxaborole (4.4 V)[11], lithium borate cluster salt, $Li_2B_{12}H_{12-x}F_x$ (x = 9 and 12, 4.5-4.6 V)[12] and 2,5-di-tertbutyl-1,4-dimethoxybenzene (DDB, 3.9 V)[13] are only a few examples. The latter, DDB, clearly stands out of the pack due to its high stability. It has been used to provide over 300 cycles of 100% overcharge per cycle with $LiFePO_4$ as the cathode and many researchers investigate the very high stability of DDB [14-16]. The electrochemical stability of DDB electroactive center can be explained by the presence of methoxy groups in positions 1 and 4 which prevent decomposition via intramolecular hydrogen bond. In addition, the methoxy groups are not affected by the first oxidation which is not the case for all alkoxy substituents. Finally, the dimerization proton elimination and polymerization reactions are not possible due to steric effect of t-butyl groups in positions 2 and 5 which protect the hydrogen at positions 3 and 6.

The major challenges faced in the development of efficient R-S are the design of electrochemically stable centers with adjustable oxidation potential to cover several types of cathode materials and the improvement of the R-S solubility. High energy materials require R-S with high potential, but high power batteries need to have high concentrations of R-S to avoid concentration polarisation. The oxidation potential can be tuned by modifying the substituents on the DDB electroactive center. Some examples of R-S obtained from the modification of DDB are 1,4-di-t-butyl-2,5-bis(2,2,2-trifluoroethoxy)benzene (4.25 V vs Li/Li^+; 170 cycles)[17], 1,4-bis(trimethylsilyl)-2,5-dimethoxybenzene (4.1 V vs Li/Li^+; 81 cycles)[18] and tetraethyl-2,5-di-tertbutyl-1,4-phenylene diphosphate (4.8 V vs Li/Li^+; 10 cycles).[19] The limited solubility of DDB in conventional carbonate LiB electrolytes (0.08 M) can be improved by adding toluene to the solvent mixture (0.2 M, [20]) or by introducing oligo ether groups instead of methoxy group (0.4 M, [21]). We presented a novel approach to improve the solubility of DDB by its covalent attachment on an imidazolium cation which was then combined with a suitable anion to form an ionic liquid. Using this approach, we were able to increase DDB concentration above 1 M in a EC/DEC mixture without the help of a solubilizing agent due to the high miscibility of ionic liquids in the solvent.[22, 23] In the present report, we extend this approach to not only increase the solubility of DDB but to modulate its oxidation potential. In our imidazolium-modification approach, the redox and ionic liquid centers were separated via a spacer of 3 carbons which prevented extensive induced electronic effect. Here, we used a different approach where the DDB center is modified with an triflimide anion, the structure of which is often encountered in ionic liquids. By linking the triflimide moiety directly on the aromatic ring of DDB, we should be able to increase the oxidation potential while maintaining the high solubility properties. We present the synthesis pathways developed to achieve such DDB-triflimides with different structures. These redox anions, once combined with the 1-butyl-3-methylimidazolium cation, form redox ionic liquids (RILs) with melting points below 100°C. The electrochemical and transport properties were determined for each RIL using cyclic voltammetry (CV) and double potential step chronoamperometry (DPSC) in carbonate electrolyte. The effect of the RIL additive on the electrolyte viscosity and ionic conductivity was studied at different temperatures. Half-cells and full cells using Li/

$LiFePO_4$ (LFP) or $Li_4Ti_5O_{12}$ (LTO)/LFP were then studied with the DDB-triflimide redox ionic liquids electrolytes to evaluate the efficiency of these redox shuttles in relevant conditions.

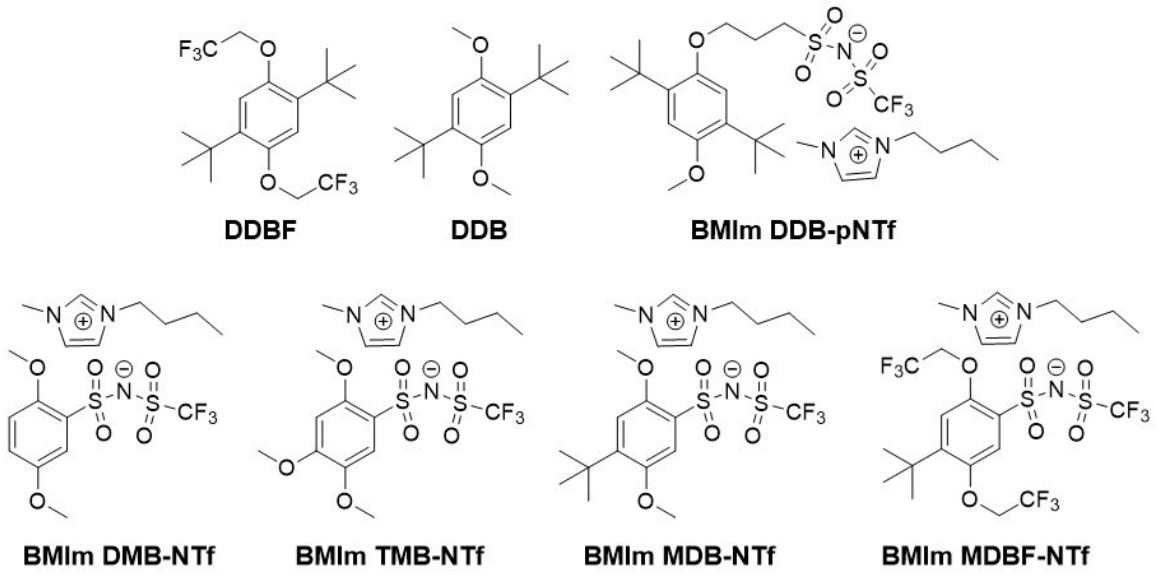

Figure 7.1. Chemical structure of electroactive ionic liquids based on 2,5-ditert-butyl-1,4-dimethoxybenzene (DDB) and triflimide anion.

7.2.3. Experimental

Materials and electroactive species characterization

All reagents used were obtained from Sigma-Aldrich (unless stated otherwise) except for trifluoromethanesulfonamide which was purchased from Synquest Laboratories. All solvents were obtained from Fisher. The precursors used in this study are 2-tert-butylhydroquinone, 2,5-ditert-butylhydroquinone, 2,5-ditert-butyl-4-methoxyphenol, 1,2,4-trimethoxybenzene and 2,5-dimethoxybenzene sulfonyl chloride. The details of each synthesis and of the product characterization given in Supporting Information. All synthesized compounds were characterized by ^{1}H, ^{19}F and ^{13}C NMR on a Bruker AMX 300 MHz spectrometer at room temperature using DMSO-d_6 and NMR spectra are reported in Supporting Information (**Figure S7.1 to S7.49**). Accurate mass values were obtained by Agilent LC-MSD TOF and the electrospray ionization was used. Elemental analysis of

organic electroactive species was performed on the EAS 1108 apparatus from Fisons Instruments SPA. The water used in the procedures was purified with a Milli-Q system to a resistivity of 18.2 MΩ·cm (25 °C). The synthesis details are described in Supporting Information.

Thermal analysis

Thermogravimetric analysis (TGA) was performed on TGA Q500 (TA Instruments) under a helium atmosphere from room temperature to 450 °C with a ramp of 10 °C·min^{-1}. The temperature decomposition was determined at a 5% weight loss. TGA was coupled with Discovery MS (TA Instruments) to follow the weight loss. Differential scanning calorimetry (DSC) was performed on DSC2910 (TA Instruments) and using universal analysis software. The measurements were done between -50 to 80 °C with a ramp of 5 °C·min^{-1} and with isothermal periods of 5 minutes between the cooling and heating.

Ionic Conductivity and Viscosity Measurements

The viscosity of the electrolytes was measured using a microviscometer (Lovis 2000 ME, Anton Paar) which is based on the rolling ball principle (Höppler principle). The standard deviations of the measured viscosity were lower than ±0.5 %. The instrument was calibrated daily using air and milli-Q water at 25°C and at atmospheric pressure. An U-tube digital density meter (DMA 5000 M, Anton Paar) was used for density measurements. Prior to all measurements, the cell and glass capillary were washed with Milli-Q water (20 mL) then acetone (20 mL) and were dried for 15 minutes with an internal air pump. The ionic conductivity of these electrolytes were carried out with a Jenway 4510 conductivity meter. Before each series of measurement, the glass conductivity microvolume probe (027815, K=0.90 at 25°C) was calibrated using a standard 0.117 mol dm^{-3} KCl (15 mS cm^{-1}) aqueous solution at 25°C. The conductivity probe and the electrolyte were placed in a tube cell and the temperature was controlled using a thermostated water jacket around the cell. The dynamic viscosity and ionic conductivity measurements were measured from 25 to 75 °C at 5 °C intervals.

Electrochemical Analysis

The cyclic voltammetry (CV) experiments were done using a standard three-electrode heart-shaped cell, consisting a Pt macrodisk working electrode, a Pt wire counter electrode and a lithium metal QRE with a BioLogic SP-50 potentiostat controlled via EC-lab software. The specific surface area of the Pt working macroelectrode was determined to be 0.022 cm^2 (geometric area = 0.020 cm^2) using the CV response of a potassium ferricyanide aqueous solution (1.0 M KCl). All CV data (diluted and concentrated solutions) were obtained in an argon-filled glove box (H_2O, O_2 < 1 ppm) and before each experiment the working electrode was polished with alumina, rinsed, sonicated and dried. All potentials are reported vs. the Li/Li^+ redox couple potential reference.

The diffusion coefficients were obtained either from CV using the macro electrode or double potential step chronoamperometry (DPSC) with a Pt microdisk electrode. CV peak current (I_p) were plotted against the square root of the scan rate with the Randles-Sevcik equation (Equation 1)

$$I_p = 0.4463nFAC\left(\frac{nF}{RT}\right)^{1/2} v^{1/2}D^{1/2} \qquad (1)$$

where n is the number of electrons, F is the Faraday constant, A is the electrode area, C is the concentration, R is the gas constant, T is the temperature, υ is the scan rate and D is the diffusion coefficient.

DPSC measurements used a Pt microdisk electrode (100 μm diameter) and the diffusion coefficients were obtained from the data analysis proposed by Compton et al.[24, 25] The microelectrode radius was determined from steady state voltammetry measurements on ferrocene (Fc) solutions at different concentrations (0.5, 1.0 and 2.0 mM) in acetonitrile containing 0.1 M tetrabutylammonium perchlorate. The microelectrode radius (54±1 μm) was calculated using Fc diffusion coefficient from the literature ($2.3x10^{-9}$ m^2 s^{-1}).[24, 25] Chronoamperometric experiments were performed inside a Faraday cage in a glovebox (Ar atmosphere with O_2 and H_2O below 1 ppm). The microelectrode was modified with a PTFE heat shrink tubing to create a cavity at its end to accommodate a small volume of the sample. A silver wire acted as pseudo-reference and counter electrode.

An equilibrium potential was maintained for 5 s where zero faradaic current was measured. The initial and final potentials were 0.46 V (DDB and [BMIm] [DDB-pNTf]), 0.66 V ([BMIm] [MDB-NTf] and DDBF) and 1.06 V ([BMIm] [MDBF-NTf]). The step potentials were 0.96 V (DDB and [BMIm] [DDB-pNTf]), 1.36 V ([BMIm] [MDB-NTf] and DDBF) and 1.46 V ([BMIm] [MDBF-NTf]). All applied potentials are expressed versus Fc/Fc^+ couple. The current decay was measured for 5 s and the data points were recorded at every 10 ms or 10 nA. The time-dependent current response obtained was analyzed by the Stojek equation for 10 mM electrolytes.

LIB Coin Cell Analysis

For the positive and negative composite electrode, the slurry consists of mixing 83 wt. % of C-$LiFePO_4$ (LFP, $LiFePO_4$ was synthesized according to a melt synthesis process given in a previous study[26]) or $Li_4Ti_5O_{12}$ (LTO, T2 Clariant, Johnson-Matthey), 9 wt. % of carbon black Timcal C65, and 8 wt. % of polyvinylidene difluoride (PVDF) (Sigma-Aldrich) in n-methyl pyrrolidone (NMP) solvent (anhydrous, 99.5%, Sigma-Aldrich) to form a slurry. The slurry was mixed for a few hours to homogenize, and then deposited on carbon-coated aluminum foil using the doctor blade method. The coating was dried at 70 °C under vacuum overnight. The dried electrodes of LFP were cut in 14 mm disks of 2.2 ± 0.3 mg/cm^2 loading and assembled in coin cells (2032) in argon atmosphere glove box (H_2O < 1 ppm, O_2 < 1 ppm). For the batteries LFP/LTO, the latter electrodes were cut in a 16 mm disks of 2.5 ± 0.2 mg/cm^2 loading to make sure that the LTO will be able to host the whole lithium amount from the LFP. A lithium foil was used as the anode for half-cell measurements. Celgard 2400 was used as a separator, and Li [NTf_2] diluted in ethylene carbonate (EC) and diethyl carbonate (DEC) (EC-DEC 1:2 vol.%) solvents were used as liquid electrolytes. The redox ionic liquids [BMIm] [DDB-pNTf], [BMIm] [MDB-NTf] and [BMIm] [MDBF-NTf] were added in the liquid electrolyte (unless otherwise stated). Electrochemical testing these cells was done at 30 °C on a VMP electrochemical station (Bio-Logic) with a 0.1 C rate using cut-off voltages of 2.5 V and 4.5 V for Li/LFP half-cells and 1.0 V and 3.5 V for LTO/LFP full cells.

7.2.4. Results and discussion

Synthetic pathway and thermochemical properties of 1,4-dimethoxybeenzene redox ionic liquids based on triflimide anion

The redox shuttle 2,5-ditert-butyl-1,4-dimethoxybenzene (DDB) is the most stable organic electroactive species reported in literature and, as such, DDB was employed as a reference in this report. 1,4-dimethoxybenzene and its neutral derivatives were synthesized by an O-alkylation of hydroquinone (Williamson ether synthesis; etherification) under basic conditions and methyl iodide and 2,2,2-trifluoroethyl perfluorobutylsulfonate were used as alkylating agent (See Scheme 1 and Supporting Information). Tetrabutylammonium bromide was used as a phase transfer catalyst when necessary. According to Scheme 2, (2,5-ditert-butyl-4-methoxyphenoxy)propylsulfonyl chloride was obtained by an O-alkylation of 2,5-ditert-butyl-4-methoxyphenol by a ring-opening of 1,3-propanesultone as sulfoalkylating agent which is followed by a treatment of sulfonate with thionyl chloride as chlorinating reagent. Scheme 3 describes the aromatic sulfonation by chlorosulfonic acid and the arylsulfonic acid was treated by thionyl chloride to produce an arylsulfonyl chloride. The chlorosulfonation is regioselective via the ortho/para-directing activating substituents such as the tert-butyl group at position 5 and the alkoxy group at position 1 and 4 (trimethoxybenzene, methoxy group also at position 5) and the alkoxy group (1,4) are antagonistic substituents. The motivation of the chlorosulfonation pathway is to provide a large anionic moiety to protect the hydrogen at position 3 and to increases the redox potential. Then, the asymmetric triflimide anion was synthesized by S-N coupling between the sulfonyl chloride precursor and trifluoromethanesulfonamide under basic conditions. The sodium triflimide and imidazolium bromide salts are subjected to a metathesis reaction to form a redox ionic liquid.

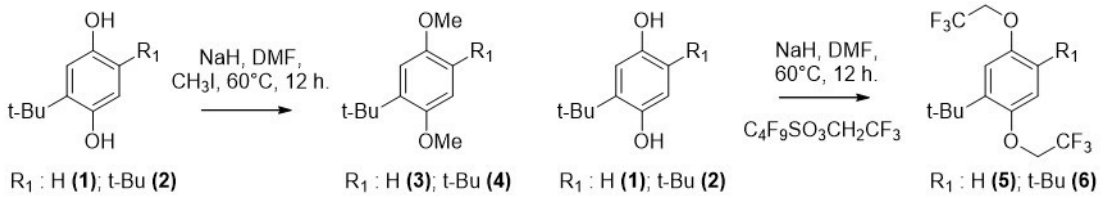

Scheme 7.1. Synthetic pathway of electroactive species based on 1,4-dimethoxybenzene and 1,4-bis(2,2,2-trifluoroethoxy)benzene.

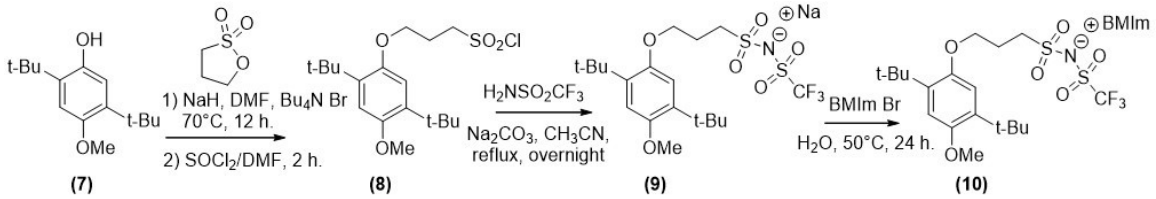

Scheme 7.2. Synthetic pathway of redox ionic liquid based on triflimide and DDB via O-alkylation synthesis route.

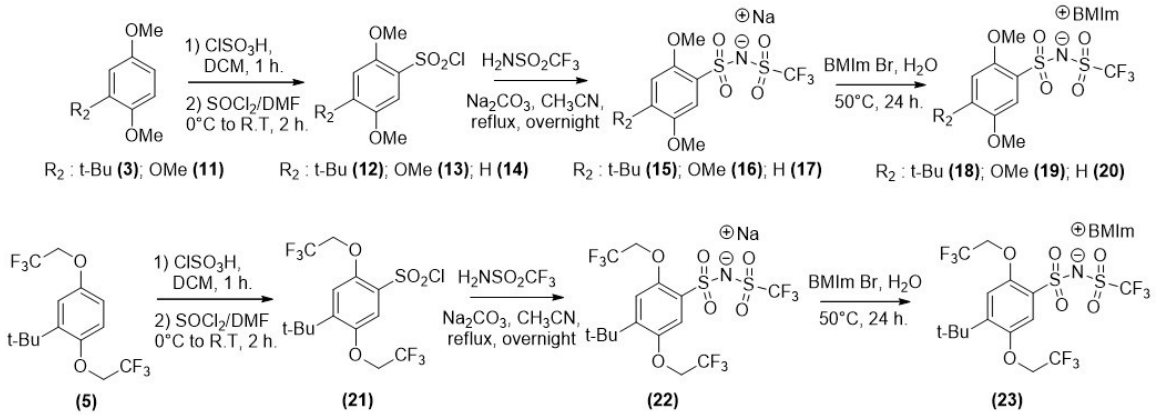

Scheme 7.3. Synthetic pathway of redox ionic liquid based on triflimide and 1,4-dimethoxybenzene via chlorosulfonation synthesis route**.**

Table 7.1 reports all thermochemical properties of RIL based on DDB such as decomposition temperatures (T_d) and melting points (T_m). The thermogravimetric analysis (TGA) curves and differential scanning calorimetry (DSC) thermograms are reported in Supporting Information (**Figure S7.50** and **S7.51**). The thermal stability of pure RILs was measured at a 5% weight loss using TGA thermograms with a heating ramp of 10 °C min^{-1} under either helium or air atmosphere. This family of triflimide RIL has a thermal decomposition temperature in temperature ranges from 343 to 362 °C and the atmosphere has no significant impact on T_d. According to DSC thermograms, the melting points of these RILs were all below 100 °C and slightly above the ambient temperature. The structural impact affects only slightly the melting temperature. No crystallization temperature (T_c) on DSC thermogram is observed because of highly viscous supercooled state commonly observed for ionic liquids and, once melted, several days are needed to reach a solid phase. In a previous work, we reported on the thermal properties of RIL where the DDB moiety was linked to an imidazolium (T_m of 94.4 °C, T_c of 51.3 °C and T_d of 320 °C).[22] In comparison, the [BMIm] [DDB-pNTf] proposed here has a much lower melting point (52.9 °C) but a higher decomposition temperature (351 °C), showing the advantage of redox IL based on triflimide for redox shuttles.

Table 7.1. Thermochemical properties of neat organic RILs based on DDB and triflimide anion.

RILs	**T_m / °C**	**T_d (T_d under air) / °C**
BMIm DDB-pNTf	52.9	351 (331)
BMIm DMB-NTf	66.8	362
BMIm TMB-NTf	49.8	343
BMIm MDB-NTf	67.8	362 (357)
BMIm MDBF-NTf	73.6	347 (364)

Electrochemical and transport properties of electrolyte containing diluted redox ionic liquids

Achieving a balance between a high redox potential and electrochemical stability constitutes a real challenge for the development of redox shuttle (R-S) for high voltage cathodes. Herein, redox shuttle additives are based on redox ionic liquids (RILs) where the electroactive moiety 1,4-dimethoxybenzene (electrochemically stable) is bound to highly electronegative groups to increase its oxidation potential. The electrochemistry of 2-tert-butyl-1,4-dimethoxybenzene (MDB) and 2,5-ditert-butyl-1,4-dimethoxybenzene 4 (DDB). was studied using ethylene-diethyl carbonate (EC-DEC) 1:2 vol./vol. with 1.0 M of Li [NTf_2] as the electrolyte, with 10 mM of electroactive species to evaluate the electrochemical response. CVs obtained for these electrolyte are shown in **Figure 7.4A** and CVs of DDB and DDBF are presented in Supporting Information (**Figure S7.52**). Only a few known radical cations based on 1,4 dimethoxybenzene formed by one-electron oxidation are stable in polar organic electrolytes and the benzene ring substituted by bulky group at position 2,5 improves the reversibility. The required steric protection suppresses the oxidative coupling and bimolecular decomposition pathways, such as radical addition in the benzene ring (i.e. oxidized form react with reduced form, EC mechanism).[27] The use of tert-butyl groups is the most effective strategy which is established by Dahn and al.,[13] resulting in up to 300 cycles of charge-overcharge-discharge. CV of MDB (mono substituted by tert-butyl groups) shows an extra peak at 4.25 vs. Li/Li^+ which is explained by an oxidative coupling. However, the non-polar and symmetrical DDB is poorly soluble in the polar solvents that are used as electrolytes. Our strategy to increase the solubility is to add these stable redox centers on the structure of an ionic liquid which are miscible with a broad range of solvents. **Table 7.2** listed all mid-point potential versus Li/Li^+ and DDB/DDB^+ couples of neutral and RIL electroactive species. The first approach to design new RILs is to modify the DDB redox center by an O-alkylation while keeping the bulky tert-butyl group on the benzene ring. The CV of this RIL, [BMIm] [DDB-pNTf], is presented in **Figure 7.2B**. The redox potential of [BMIm] [DDB-pNTf] is not affected by the modification, resulting to 3.96 V and 0.02 V versus Li/Li^+ and DDB/DDB^+, respectively. The second pathway to obtain

a RIL is the chlorosulfonation route in which the modification is made on the benzene ring. The triflimide anion group has a strong electron withdrawing effect and its large size acts also as steric protection to prevent dimerization of the radical cation. This RIL, [BMIm] [MDB-NTf], has a benzene ring substituted by triflimide anion group at position 2 and a tert-butyl group at position 5. The redox potential of [BMIm] [MDB-NTf] is higher than [BMIm] [DDB-pNTf] with 4.28 V vs Li/Li^+. The electrochemistry of [BMIm] [MDB-NTf] is reversible (**Figure 7.2B** and **Figure 7.3A**) for 10 mM electrolyte and the bulky tert-butyl group at position 5 is essential to obtain the reversible oxidation of benzene ring. If either a methoxy group ([BMIm] [TB-NTf]) or and hydrogen ([BMIm] [TB-NTf]) are used in position 5, dimerization of the aromatic radical cation occurs, leading to the formation of an electroactive dimer with a lower potential which promotes self-discharge of the cell. Dahn and coworker presented a DDB derivative through the modification of methoxy groups and the more-electron-withdrawing 2,2,2-trifluoroethoxy groups increase the redox potential at 4.26 V vs Li/Li^+ (DDBF).[17] To push the potential even further, we evaluated the combination two electron withdrawing groups, the triflimide and 2,2,2-trifluoroethoxy. As expected, this RIL, [BMIm] [MDBF-NTf] shows a high midpoint potential of 4.59 V vs Li/Li^+, however, this high-potential electroactive species displays a low electrochemical stability (See **Figure 7.3B**). The CV shapes of [BMIm] [DDB-pNTf] and [BMIm] [MDB-NTf] using diluted electrolyte correspond to an expected CV for a reversible electrochemical reaction at various scan rates which is presented in **Figure 7.4** (In Supporting Information for DDB and DDBF).

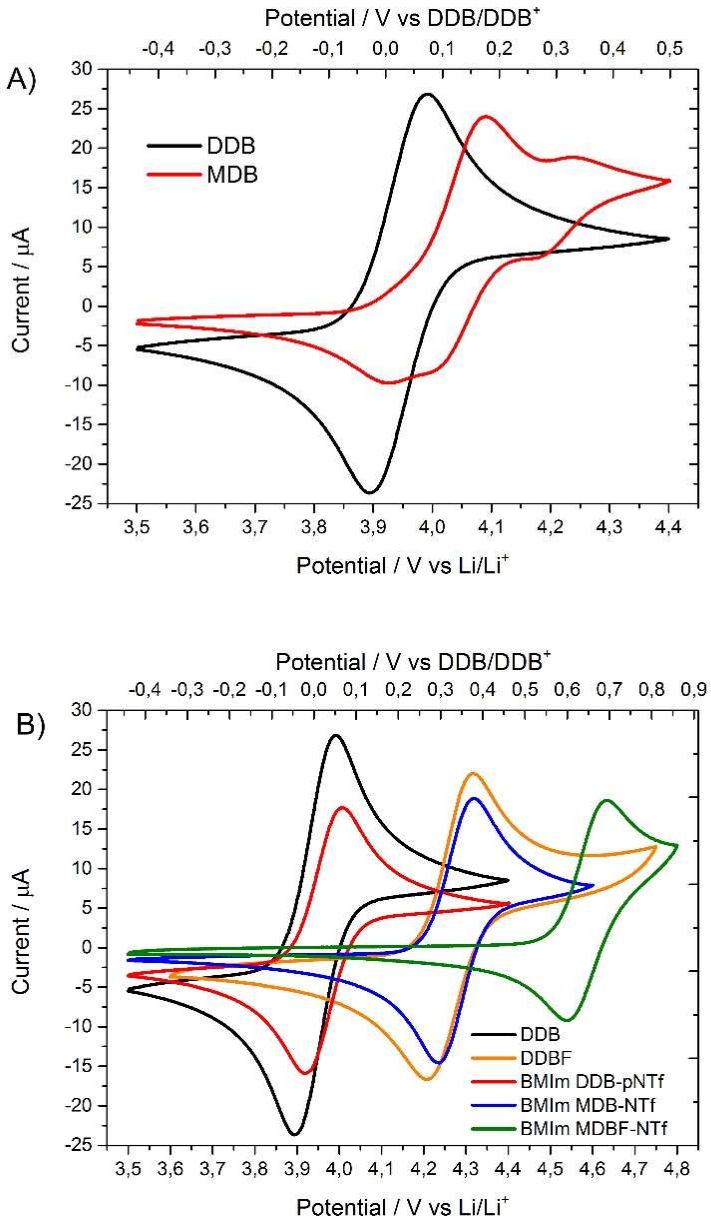

Figure 7.2. A) CVs of 10 mM DDB (black line) and MDB (red line) and B) CVs of organic redox species of 10 mM DDB (black line), DDBF (orange line), [BMIm] [DDB-pNTf] (red line), [BMIm] [MDB-NTf] (blue line) and [BMIm] [MDBF-NTf] (green line) in EC-DEC 1:2 (v/v) with 1.0 M Li [NTf_2] at 100 mV s^{-1}.

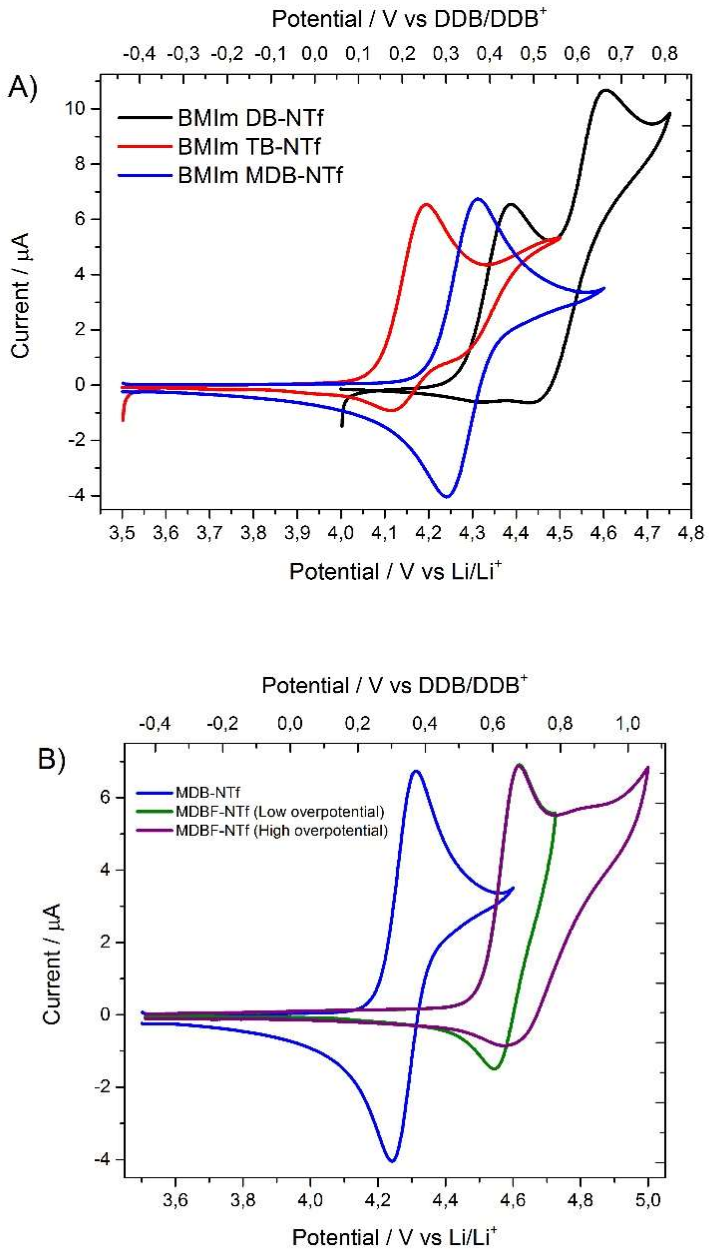

Figure 7.3. CVs of redox ionic liquids via chlorosulfonation of A) 10 mM [BMIm] [DB-NTf] (black line), [BMIm] [TB-NTf] (red line) and [BMIm] [MDB-NTf] (blue line) in EC-DEC 1:2 (v/v) with 1.0 M Li [NTf_2] at 100 mV s^{-1}. B) CVs of 10 mM [BMIm] [MDB-NTf] (blue line) and [BMIm] [MDBF-NTf] (green and purple line) to analysis irreversible electrochemical side reaction in EC-DEC 1:2 (v/v) with 1.0 M Li [NTf_2] at 10 mV s^{-1}.

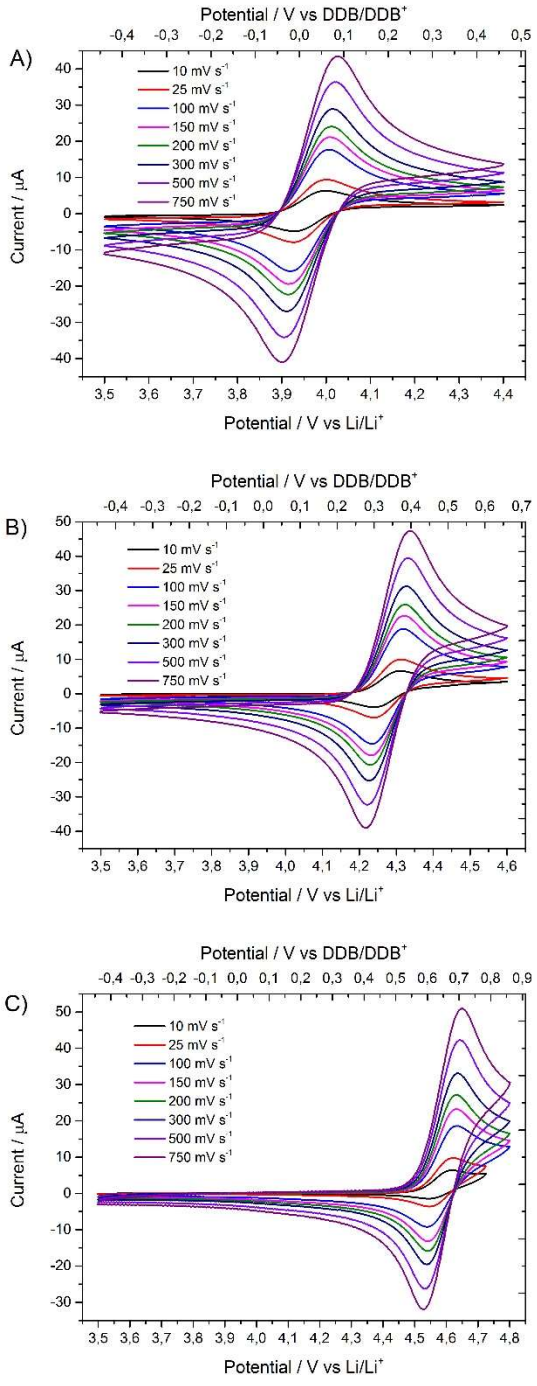

Figure 7.4. CVs of redox ionic liquid using 10 mM solutions of A) [BMIm] [DDB-pNTf], B) [BMIm] [MDB-NTf] and C) [BMIm] [MDBF-NTf] in EC-DEC 1:2 (v/v) with 1.0 M Li [NTf_2] at various scan rates. The scan rates used were 10 to 750 mV s^{-1}.

Table 7.2. Potential parameters obtained from cyclic voltammograms at 100 mV s^{-1} of 10 mM DDB, DDBF, [BMIm] [DDB-pNTf], [BMIm] [MDB-NTf] and [BMIm] [MDBF-NTf] in EC-DEC 1:2 (v/v) with 1.0 M Li [NTf_2].

Electroactive species	Mid-point Potential / V vs. Li/Li^+	Mid-point Potential / V vs. DDB/DDB^+	ΔE_{pa-pc} / V
DDB	3.94	0	0.097
DDBF	4.26	0.32	0.105
BMIm DDB-pNTf	3.96	0.02	0.082
BMIm MDB-NTf	4.28	0.34	0.083
BMIm MDBF-NTf	4.59	0.65	0.093

The transport properties using CV (macroelectrode) and double potential step chronoamperometry (DPSC, microelectrode) for electrolyte containing electroactive species are reported in **Table 7.3**. The diffusion coefficients of the reduced form in the LIB electrolyte containing 10 mM of [BMIm] [DDB-pNTf] and [BMIm] [MDB-NTf] are 0.83 and 0.88 $x10^{-6}$ cm^2 s^{-1}, respectively and the diffusion coefficient was calculated from the peak current measurements at different scan rates (Randles-Sevcik plots in **Figure 7.5**). To obtain an accurate diffusion coefficient of both reduced and oxidized forms in organic electrolyte, DPSC was employed and the time-dependent current responses of the forward and backward potential steps are shown in **Figure 7.6**. DPSC curves were analyzed by the Stojek equation to calculate the diffusion coefficient of both oxidized (radical cation for DDB and DDBF; radical/zwitterion for RILs) and reduced form (**Figure 7.7**). The diffusion coefficients measured with the microelectrode (r =50 μm) are 0.48 and 0.47 $x10^{-6}$ cm^2 s^{-1} for [BMIm] [DDB-pNTf] and [BMIm] [MDB-NTf], respectively. The chemical structure of triflimide redox anion have a low impact on mass transport following the electrochemical measurements and as expected, the redox anion diffuses more slowly than the neutral electroactive species. The trend of diffusion coefficient is in agreement with the molecular size and, generally, the anions have a large solvation shell.

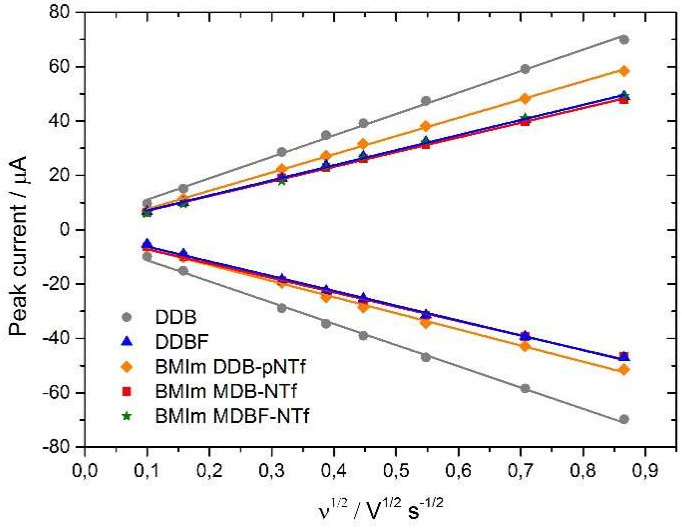

Figure 7.5. Randles-Sevcik plots of organic redox species of 10 mM DDB (gray line), DDBF (orange line), [BMIm] [DDB-pNTf] (red line), [BMIm] [MDB-NTf] (blue line) and [BMIm] [MDBF-NTf] (green line) in EC-DEC 1:2 (v/v) with 1.0 M Li [NTf_2]. The scan rates used were 10 to 750 mV s^{-1}.

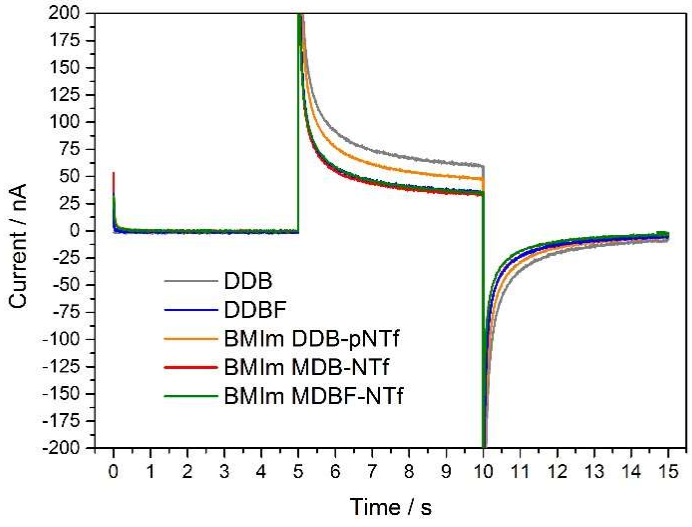

Figure 7.6. DPSC using a microelectrode of 10 mM DDB (gray line), DDBF (orange line), [BMIm] [DDB-pNTf] (red line), [BMIm] [MDB-NTf] (blue line) and [BMIm] [MDBF-NTf] in EC-DEC 1:2 (v/v) with 1.0 M Li [NTf_2].

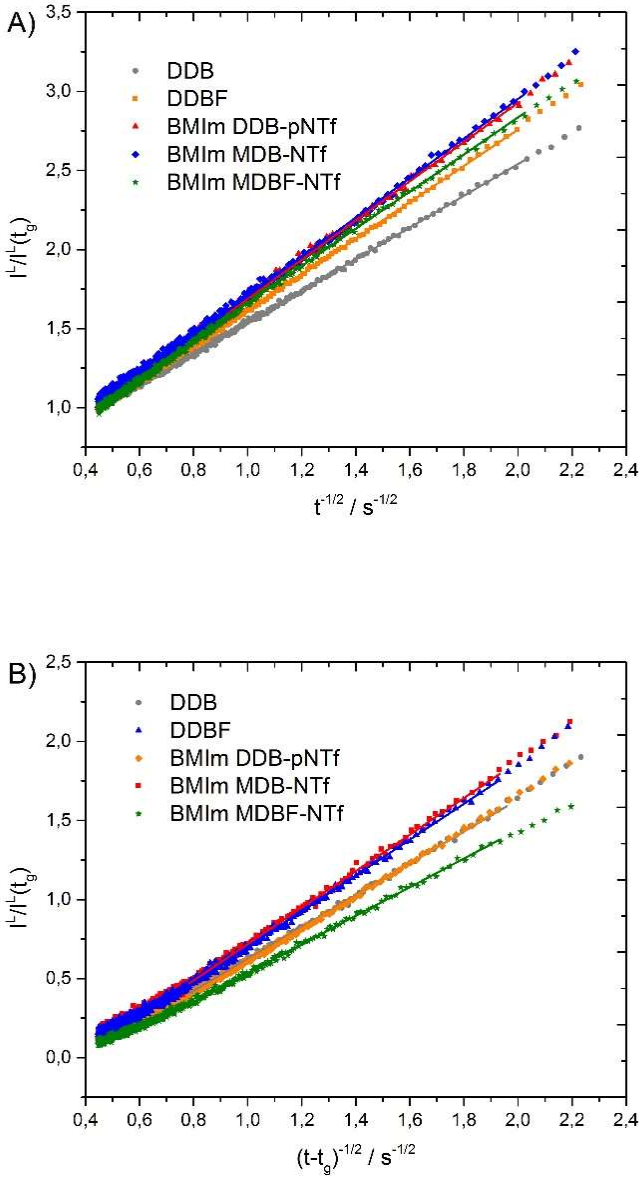

Figure 7.7. Stojek plots for the oxidation A) and reduction B) of 10 mM DDB (gray line), DDBF (orange line), [BMIm] [DDB-pNTf] (red line), [BMIm] [MDB-NTf] (blue line) and [BMIm] [MDBF-NTf] (green line) in EC-DEC 1:2 (v/v) with 1.0 M Li [NTf_2].

Table 7.3. Transport properties using CV and DPSC of 10 mM DDB, DDBF, [BMIm] [DDB-pNTf] and [BMIm] [MDB-NTf] in EC-DEC 1:2 (v/v) with 1.0 M Li [NTf_2].

Electroactive species	D_R (CV) /10^{-6} cm^2 s^{-1}	I_{pc}/I_{pa} at 100 mV s^{-1}	D_R (DPSC) /10^{-6} cm^2 s^{-1}	D_O (DPSC) /10^{-6} cm^2 s^{-1}	γ D_O / D_R
DDB	1.78	1.01	1.14±0.04	1.13±0.04	0.99
DDBF	1.29	0.88	0.68±0.03	0.85±0.04	1.25
BMIm DDB-pNTf	0.83	0.99	0.48±0.02	0.56±0.03	1.17
BMIm MDB-NTf	0.88	0.97	0.47±0.02	0.57±0.03	1.21

Viscosity and ionic conductivity of redox-active electrolyte

In this section, we evaluate the impact of RIL additive on the electrolyte properties such as the viscosity, ionic conductivity and ionicity. The lithium mobility, a key parameter to maintain an efficient charge/discharge mechanism in LIB, is strongly dependent on electrolyte properties. While the R-S molecule is inactive during normal charge and discharge, its effect on the electrolyte viscosity must be assessed to determine the maximal concentration to be used to avoid detrimental impact on cell performance. This is particularly important for RIL shuttles as they are fully miscibile in carbonate solvents. In contrast, the solubility of DDB in typical carbonate mixtures is around 0.08 M.[28] **Table 7.4** and **7.5** summarize dynamic viscosity (η) and ionic conductivity (σ) of redox-active electrolytes at 25 and 75 °C and also include the activation energy ($E_{a,\sigma \text{ or } \varphi}$), entropy ($\Delta S_{\sigma \text{ or } \varphi}$), enthalpy ($\Delta H_{\sigma \text{ or } \varphi}$). **Figure S7.53** and **Figure S7.54** present the Arrhenius and Eyring plots used to obtain the E_a and ΔS and ΔH, respectively, for the ionic conductivity and fluidity. A reference electrolyte of 1.0 M Li [NTf_2] in EC-DEC 1:2 was found to have an ionic conductivity of 6.26 mS cm^{-1} and a viscosity of 4.516 mPa s at 25 °C. The addition of 0.3 M of RIL additives shows a similar impact on viscosity and ionic conductivity. The viscosity (ionic conductivity) measurements at 25°C using electrolyte containing 0.3 M RIL additive are 9.186 (3.84), 7.439 (4.37) and 8.563 (4.16) mPa s (mS cm^{-1}) for [BMIm] [DDB-pNTf], [BMIm] [MDB-NTf] and [BMIm] [MDBF-NTf], respectively. Although the concentration in ion increases with the addition of RIL, the ionic conductivity decreases as

expected due to an increase in the viscosity. These redox anions have a lower mobility because of the large chemical structure. The redox-active electrolyte shows higher E_a, higher ΔH and lower ΔS than an electrolyte containing no additive. We can estimate the ion dissociation of the redox-active electrolyte from the Walden rule ($\Lambda\eta$ = constant)[29] and the Walden plots which correlates the molar ionic conductivity and the fluidity are reported in **Figure 7.8**. The Walden curves of redox-active electrolytes containing RILs are slightly further from the ideal line in comparison with the reference electrolyte and the iconicity, or the ion dissociation, is similar between the electrolytes containing the different RIL additives.

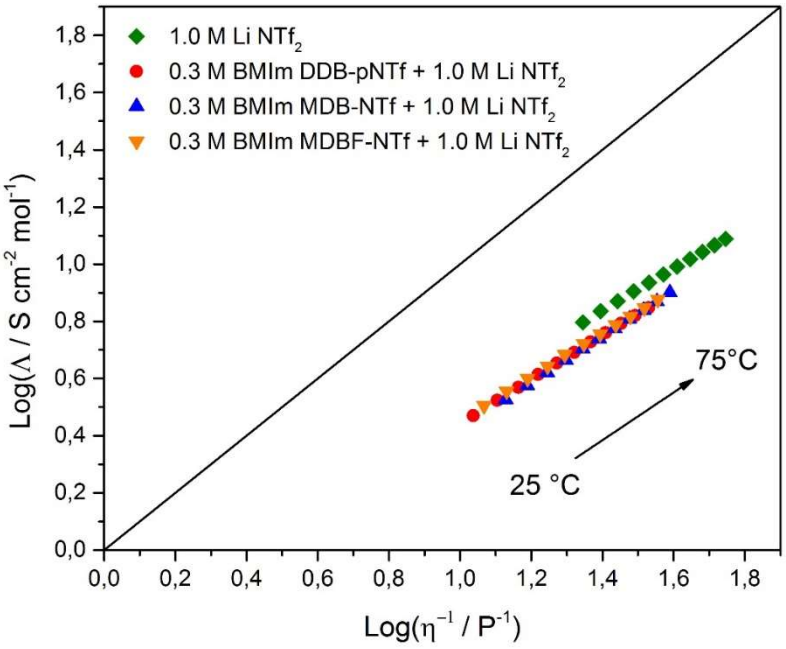

Figure 7.8. Walden plot of redox ionic liquids electrolytes based on DDB center modification. The straight line illustrates the ideal Walden line (0.01 M KCl aqueous solution). The molar ionic conductivity and fluidity are measured from 25 to 75 °C at 5 °C intervals.

Table 7.4. All viscosities (η), activation energies of fluidity (φ = 1/η) ($E_{a,\varphi}$), entropy (ΔS_φ) and enthalpy (ΔH_φ) of 0.3 M RIL electrolyte in EC-DEC 1:2 (v/v) with 1.0 M Li [NTf_2].

RILs	η at 25°C / mPa s	η at 75°C / mPa s	$E_{a,\varphi}$ / kJ mol^{-1}	ΔH_φ / kJ mol^{-1} K^{-1}	ΔS_φ / J mol^{-1} K^{-1}
-	4.516	1.793	15.9	13.3	-213.0
BMIm DDB-pNTf	9.186	2.951	19.4	16.7	-207.1
BMIm MDB-NTf	7.439	2.574	18.2	15.5	-209.5
BMIm MDBF-NTf	8.563	2.780	19.4	16.7	-206.8

Table 7.5. All ionic conductivities (σ), activation energies of ionic conductivity ($E_{a,\sigma}$), entropy (ΔS_σ) and enthalpy (ΔH_σ) of 0.3 M RIL electrolyte in EC-DEC 1:2 (v/v) with 1.0 M Li [NTf_2].

RILs	σ at 25°C / mS cm^{-1}	σ at 75°C / mS cm^{-1}	$E_{a,\sigma}$ / kJ mol^{-1}	ΔH_σ / kJ mol^{-1} K^{-1}	ΔS_σ / J mol^{-1} K^{-1}
-	6.26	12.27	11.5	8.8	-200.0
BMIm DDB-pNTf	3.84	9.16	14.9	12.2	-192.6
BMIm MDB-NTf	4.37	10.34	14.7	12.1	-192.2
BMIm MDBF-NTf	4.16	9.77	14.6	11.9	-193.0

Electrochemistry of lithium-ion cell with redox-active electrolytes

To evaluate the overcharge protection of the RIL additives based on dimethoxybenzene, coin cells containing redox-active electrolyte were fully charged at a 0.1 C rate, then overcharged by a 100 % overcharge step (one extra full charge) and, subsequently, the cells were also discharged at a 0.1 C rate. In a first step, Li/LFP half-cells were studied. Control cells without the overcharging step showed a charging plateau at 3.45 V vs. Li/Li^+ and discharge plateau at 3.40 V vs. Li/Li^+. Figure 9A presents the galvanostatic profile of a Li/LFP cell containing 0.3 M of [BMIm] [DDB-pNTf] and 1.0 M of Li [NTf_2] in EC-DEC 1:2 v/v and Figure 9B shows the capacity profile at different cycles of charge-overcharge-discharge. The flat overcharge plateau assigned to the

oxidation of the [DDB-pNTf] redox anion at 3.96 V takes 1 or 2 cycles to stabilize and reach the potential expected from CV results shown above. Redox-active electrolyte containing [BMIm] [DDB-pNTf] can protect the Li/$LiFePO_4$ cell during at least 70 cycles of charge-overcharge-discharge without any losses in performance, which corresponds to 720 hours of overcharge. During this overcharge time, it can be estimated that each [DDB-pNTf] redox anion is oxidized 67 times (100% overcharge at 0.1 C is 0.525 mAh; oxidized R-S charge is 2.026 C for the electrolyte volume of 70 μL and RIL concentration of 0.3 M). This demonstrates the true shuttling effect between the two electrodes. [BMIm] [DDB-pNTf] additive does not have a significant impact on both discharge and charge capacities. The specific discharge and charge capacity obtained for half-cell using RIL electrolyte were 166 mAh g^{-1} and 163 mAh g^{-1}, respectively, being close to the Theoretical capacity of $LiFePO_4$ - 170 mAh g^{-1} Then, the experimental coulombic efficiency is however slightly higher than 100% which may be attributed to the reduction of the oxidized electroactive species during the discharge.[30] A flat plateau recorded for both charge and discharge indicates a good LIB performance and a flat overcharging plateau demonstrates an effective R-S additive.

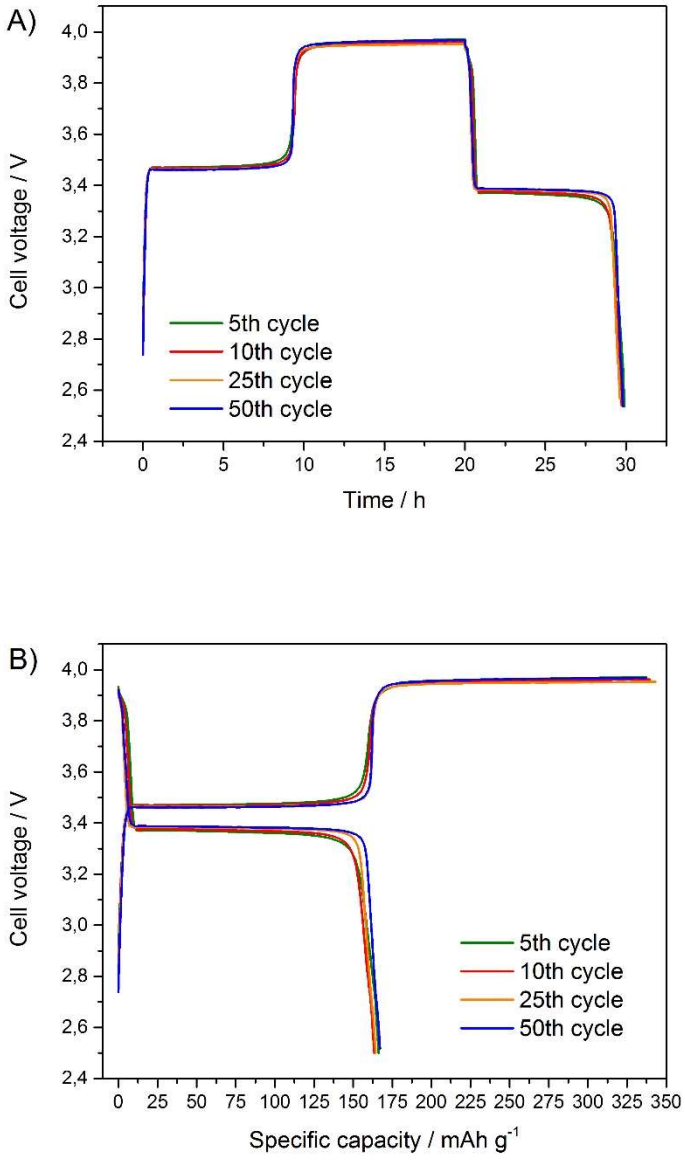

Figure 7.9. A) Galvanostatic charge-overcharge-discharge profiles and B) capacity profile of Li/LFP half-cell at 0.1 C rate and 10 h. overcharge containing 0.3 M of [BMIm] [DDB-pNTf] and 1.0 M of Li [NTf_2] in EC-DEC 1:2 v/v.

We also evaluated RILs as R-S in full lithium-ion cells using LTO as anode material. The cathode protection against overcharging is observed in **Figure 7.10A**. The various chemical structures of redox anion provide different redox potentials (see CV section). From **Figure 7.10A** that, even though the plateau of the RIL are almost flat and at a constant voltage, a slight overcharge can be observed at the beginning of the plateau. **Figure 7.10B** shows the capacity profile of LTO/LFP cells using the redox-active electrolyte with different RILs. To provide a better comparison between the cells, the curves have been normalized for the discharge capacity. The behavior of the cells employing [BMIm] [DDB-NTf] and [BMIm] [MDB-NTf] as redox shuttles is similar to that of the control cell without any shuttle. The voltage of each overcharging plateau is defined by the potential of the RIL. The [BMIm] [MDBF-NTf] has a different behavior with a much larger charging capacity, exceeding that of the LTO/LFP cell. This extra charge is associated with a self-discharge mechanism that occurs with the presence of a redox molecule with a too low potential vs. that of the cathode material. Knowing that 5 cycles of normal charging (i.e. without going into overcharge regime) were applied to the cells before recording the curves of **Figure 7.10** and that the [BMIm] [MDBF-NTf] is unstable, we hypothesize that degradation occurred over the 5 normal charging cycles, generating species with lower potential in the electrolytes.

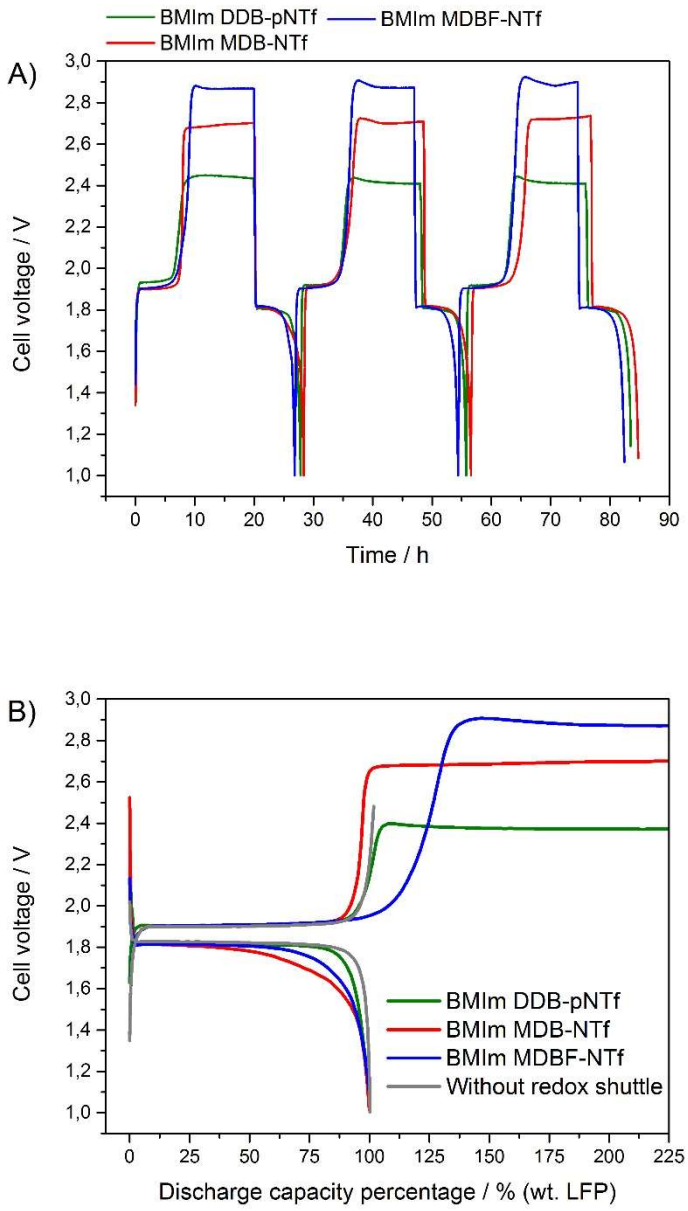

Figure 7.10. A) Galvanostatic charge-overcharge-discharge profiles and B) capacity profile of LTO/LFP cell at 0.1 C rate and 10 h. overcharge containing 0.3 M of RIL such as [BMIm] [DDB-pNTf], [BMIm] [MDB-NTf] and [BMIm] [MDBF-NTf] with 1.0 M of Li [NTf_2] in EC-DEC 1:2 v/v.

The [BMIm] [MDB-NTf] RIL using triflimide anion as steric group on benzene ring is limited to 8 cycles of charge-overcharge-discharge. To understand the low electrochemical stability of this type of RIL, CV was performed using concentrated redox-active electrolyte at 0.3 M of RIL. **Figure 7.11A** shows the oxidation shape of CV using electrolyte containing 0.3 M of [BMIm] [DDB-pNTf] which is clearly distorted and the peak-to-peak potential separation is really higher than expected for a pure diffusional regime. [BMIm] [DDB-pNTf] is electrochemically stable and reversible but iR drop increases with RIL addition and the amplitude of the current (0.1 to 0.25 mA, **Figure 7.11A**), resulting in a larger peak-to-peak potential separation according to Ohm's law. Huang and coworker observed the decomposition of oxidized derivative of dimethoxybenzene on lithium metal[31] and for this reason, the CV of [BMIm] [MDB-NTf] was done using Ag silver wire as reference electrode to avoid this artefact (**Figure 7.11B**). In this CV, we can observe the appearance of peak at lower potential than the midpoint potential of [MDB-NTf] which is not present on the curves recorded with 10 mM of the ionic liquid. This result explains the poor cycle life of [BMIm] [MDB-NTf] in LTO/LFP cell. To identify the new electroactive species formed during the EC mechanism, we electrolyzed (1.6 V vs. Ag) the electrolyte for 12 hours and analyzed the resulting solution using mass spectroscopy. Huang et al. showed that the yield of the dimer formation increases significantly in concentrated electrolyte and they demonstrated that ring-to-ring bridging occurs for unprotected dimethoxybenzene derivatives.[32] In our case, we found a species at a m/z ratio of 566 which corresponds to oxidative coupling following by the elimination of methoxy and triflimide groups. [MDB-NTf] redox anion is vulnerable to ring-to-ring addition of the radical zwitterion to the reduced form at 0.3 M concentration. The triflimide substitution is therefore insufficient to provide the steric protection against the radical addition reactions in high-concentration regime. The dimer and intramolecular reorganization reactions are irreversible and the electroactive species formed from the ring-to-ring addition is not reversible according to **Figure 7.11B**.

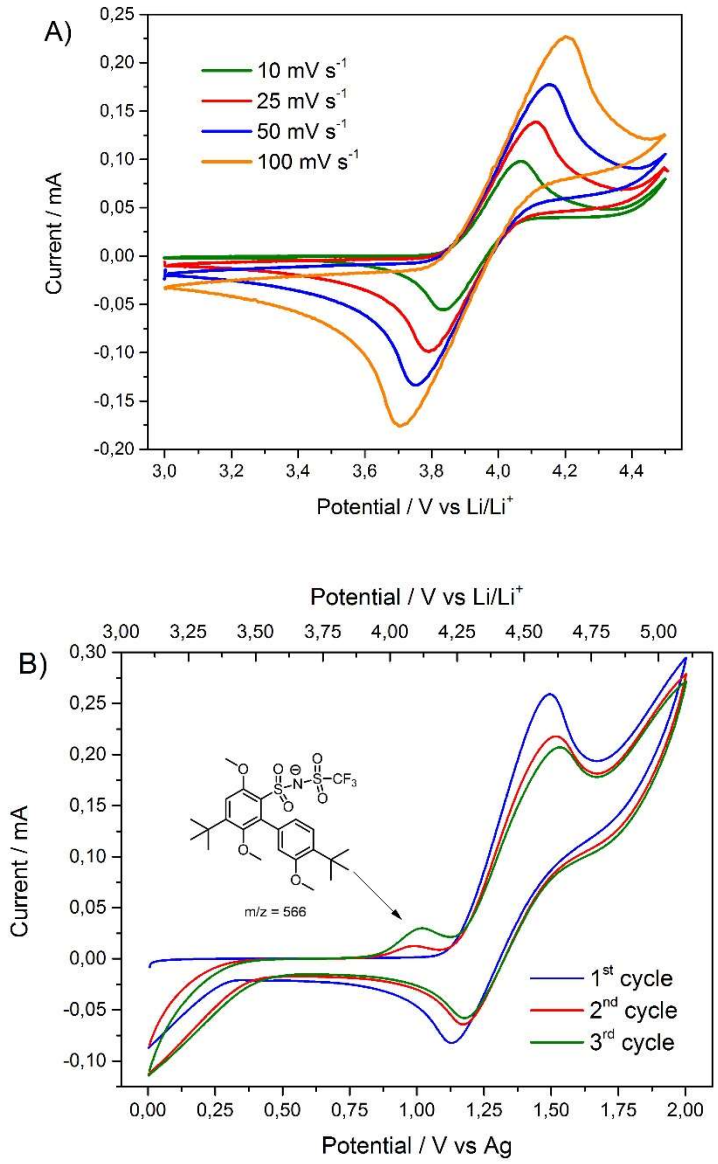

Figure 7.11. A) CVs of 0.3 M of [BMIm] [DDB-pNTf] in EC-DEC 1:2 (v/v) with 1.0 M Li [NTf_2] at different scan rates and B) CVs of 0.3 M of [BMIm] [MDB-NTf] in EC-DEC 1:2 (v/v) with 1.0 M Li [NTf_2] at 100 mV s^{-1}.

7.2.5. Conclusions

The major challenges faced in the development of efficient R-S are the design of electrochemically stable centers with adjustable oxidation potential to cover several types of cathode materials and the improvement of the R-S solubility. In this report, we presented an approach that consists in linking efficient redox shuttles (2,5-ditert-butyl-1,4-dimethoxybenzene, DDB, in this case) to a triflimide anion, which structure is commonly used in ionic liquids. By linking the triflimide moiety directly on the aromatic ring of DDB, we were able to increase the oxidation potential due to the electron withdrawing effect of the triflimide, while maintaining the high solubility properties. We showed that this effect is position-dependent. The dimethoxybenzene RIL employing t-Butyl groups as steric protection against ring-to-ring addition presents the same oxidation potential in comparison with 2,5-ditert-butyl-1,4-dimethoxybenzene. Triflimide anion bound directly on the aromatic ring was evaluated as a mean to achieve steric hindrance and prevent dimerization. The oxidative coupling was however observed at high concentrations. Electrolytes containing 0.3 M of RIL showed a higher viscosity and lower ionic conductivity than unmodified electrolytes but the charge and discharge capacities of lithium-ion cells were not significantly affected by the lower transport. Using electrolytes modified with 0.3 M of [BMIm] [DDB-pNTf] we were able to achieve an overcharge protection in lithium and lithium-ion cells and we demonstrated the redox shuttle ability of [DDB-pNTf] redox anion. This study highlights the high potential of functionalised ionic liquids to design novel additives for lithium-ion battery electrolytes.

7.2.6. Acknowledgments

The authors acknowledge the financial support from Fonds de recherche du Québec en nature et technologies (FQRNT) under their program for the reduction of greenhouse gases and the Natural Sciences and Engineering Research Council of Canada (NSERC) for Discovery grant (D.R.).

7.2.7. References

[1] Z. Chen, Y. Qin, K. Amine, Redox shuttles for safer lithium-ion batteries, Electrochim. Acta, 54 (2009) 5605-5613.

[2] J.R. Dahn, J. Jiang, L.M. Moshurchak, M.D. Fleischauer, C. Buhrmester, L.J. Krause, High-rate overcharge protection of LiFePO4-based Li-ion cells using the redox shuttle additive 2,5-ditertbutyl-1,4-dimethoxybenzene, J. Electrochem. Soc., 152 (2005) A1283-A1289.
[3] W.K. Behl, D.T. Chin, Electrochemical overcharge protection of rechargeable lithium batteries. 1. Kinetics of iodide tri-iodide iodine redox reactions on platinum in LiAsF6 tetrahydrofuran solution, J. Electrochem. Soc., 135 (1988) 16-21.
[4] W.K. Behl, D.T. Chin, Electrochemical overcharge protection of rechargeable lithium batteries. 2. Effect of lithium iodide-iodine additive on the behavior of lithium electrode in LiAsF6-tetrahydrofuran solutions, J. Electrochem. Soc., 135 (1988) 21-25.
[5] W.K. Behl, Anodic oxidation of lithium bromide in tetrahydrofuran solutions, J. Electrochem. Soc., 136 (1989) 2305-2310.
[6] K.M. Abraham, D.M. Pasquariello, E.B. Willstaedt, Normal-butylferrocene for overcharge protection of secondary lithium batteries, J. Electrochem. Soc., 137 (1990) 1856-1857.
[7] M.N. Ates, C.J. Allen, S. Mukerjee, K.M. Abraham, Electronic effects of substituents on redox shuttles for overcharge protection of Li-ion batteries, J. Electrochem. Soc., 159 (2012) A1057-A1064.
[8] C. Buhrmester, L.M. Moshurchak, R.L. Wang, J.R. Dahn, The use of 2,2,6,6-tetramethylpiperinyl-oxides and derivatives for redox shuttle additives in Li-ion cells, J. Electrochem. Soc., 153 (2006) A1800-A1804.
[9] C. Buhrmester, L. Moshurchak, R.L. Wang, J.R. Dahn, Phenothiazine molecules: Possible redox shuttle additives for chemical overcharge and overdischarge protection for lithium-ion batteries, J. Electrochem. Soc., 153 (2006) A288-A294.
[10] C.-L. Lin, C.-C. Lee, K.-C. Ho, Spectroelectrochemical studies of manganese phthalocyanine thin films for applications in electrochromic devices, J. Electroanal. Chem., 524–525 (2002) 81-89.
[11] Z. Chen, K. Amine, Bifunctional electrolyte additive for lithium-ion batteries, Electrochem. Comm., 9 (2007) 703-707.
[12] Z. Chen, Y. Ren, A.N. Jansen, C.-k. Lin, W. Weng, K. Amine, New class of nonaqueous electrolytes for long-life and safe lithium-ion batteries, Nat. Commun., 4 (2013) 1513.
[13] C. Buhrmester, J. Chen, L. Moshurchak, J.W. Jiang, R.L. Wang, J.R. Dahn, Studies of aromatic redox shuttle additives for LiFePO4-based Li-ion cells, J. Electrochem. Soc., 152 (2005) A2390-A2399.
[14] T. Li, L. Xing, W. Li, B. Peng, M. Xu, F. Gu, S. Hu, Theoretic Calculation for Understanding the Oxidation Process of 1,4-Dimethoxybenzene-Based Compounds as Redox Shuttles for Overcharge Protection of Lithium Ion Batteries, J. Phys. Chem. A, 115 (2011) 4988-4994.
[15] Z. Zhang, L. Zhang, J.A. Schlueter, P.C. Redfern, L. Curtiss, K. Amine, Understanding the redox shuttle stability of 3,5-di-tert-butyl-1,2-dimethoxybenzene for overcharge protection of lithium-ion batteries, J. Power Sources, 195 (2010) 4957-4962.
[16] J.-H. Chen, L.-M. He, R.L. Wang, The stability of redox shuttles for overcharge protection in lithium-ion cells: Studied by a computational model and molecular orbital analysis, J. Electrochem. Soc., 160 (2013) A155-A159.

[17] L.M. Moshurchak, W.M. Lamanna, M. Bulinski, R.L. Wang, R.R. Garsuch, J. Jiang, D. Magnuson, M. Triemert, J.R. Dahn, High-potential redox shuttle for use in lithium-ion batteries, J. Electrochem. Soc., 156 (2009) A309-A312.
[18] J. Huang, I.A. Shkrob, P. Wang, L. Cheng, B. Pan, M. He, C. Liao, Z. Zhang, L.A. Curtiss, L. Zhang, 1,4-Bis(trimethylsilyl)-2,5-dimethoxybenzene: a novel redox shuttle additive for overcharge protection in lithium-ion batteries that doubles as a mechanistic chemical probe, J. Mater. Chem. A, 3 (2015) 7332-7337.
[19] L. Zhang, Z. Zhang, H. Wu, K. Amine, Novel redox shuttle additive for high-voltage cathode materials, Energy Environ. Sci., 4 (2011) 2858-2862.
[20] J. Chen, C. Buhrmester, J.R. Dahn, Chemical overcharge and overdischarge protection for lithium-ion batteries, Electrochem. Solid-State Lett., 8 (2005) A59-A62.
[21] L. Zhang, Z. Zhang, P.C. Redfern, L.A. Curtiss, K. Amine, Molecular engineering towards safer lithium-ion batteries: a highly stable and compatible redox shuttle for overcharge protection, Energy Environ. Sci., 5 (2012) 8204-8207.
[22] J.C. Forgie, D. Rochefort, Electroactive imidazolium salts based on 1,4-dimethoxybenzene redox groups: synthesis and electrochemical characterisation, RSC Adv., 3 (2013) 12035-12038.
[23] S.E. Khakani, J.C. Forgie, D.D. MacNeil, D. Rochefort, Redox shuttles for lithium-ion batteries at concentrations up to 1 M using an electroactive ionic liquid based on 2,5-di-tert-butyl-1,4-dimethoxybenzene, J. Electrochem. Soc., 162 (2015) A1432-A1438.
[24] L. Xiong, A.M. Fletcher, S.G. Davies, S.E. Norman, C. Hardacre, R.G. Compton, Tuning solute redox potentials by varying the anion component of room temperature ionic liquids, Chem. Comm., 48 (2012) 5784.
[25] Y. Wang, E.I. Rogers, R.G. Compton, The measurement of the diffusion coefficients of ferrocene and ferrocenium and their temperature dependence in acetonitrile using double potential step microdisk electrode chronoamperometry, J. Electroanal. Chem., 648 (2010) 15-19.
[26] M. Talebi-Esfandarani, S. Rousselot, M. Gauthier, P. Sauriol, G. Liang, M. Dollé, LiFePO4 synthesized via melt synthesis using low-cost iron precursors, J. Solid-State Electrochem., 20 (2016) 1821-1829.
[27] Z. Chen, Q. Wang, K. Amine, Understanding the stability of aromatic redox shuttles for overcharge protection of lithium-ion cells, J. Electrochem. Soc., 153 (2006) A2215-A2219.
[28] J. Chen, C. Buhrmester, J.R. Dahn, Chemical overcharge and overdischarge protection for lithium-ion batteries, Electrochem. Solid-State Lett., 8 (2005) A59-A62.
[29] W. Xu, E.I. Cooper, C.A. Angell, Ionic liquids: Ion mobilities, glass temperatures, and fragilities, J. Phys. Chem. B, 107 (2003) 6170-6178.
[30] X. Huang, L. Wang, H. Liao, R. Meng, J. Li, X. He, Charge rate influence on the electrochemical performance of LiFePO4 electrode with redox shuttle additive in electrolyte, Ionics, 18 (2012) 501-505.
[31] J. Huang, N. Azimi, L. Cheng, I.A. Shkrob, Z. Xue, J. Zhang, N.L. Dietz Rago, L.A. Curtiss, K. Amine, Z. Zhang, L. Zhang, An organophosphine oxide redox shuttle additive that delivers long-term overcharge protection for 4 V lithium-ion batteries, J. Mater. Chem. A, 3 (2015) 10710-10714.
[32] J. Huang, B. Pan, W. Duan, X. Wei, R.S. Assary, L. Su, F.R. Brushett, L. Cheng, C. Liao, M.S. Ferrandon, W. Wang, Z. Zhang, A.K. Burrell, L.A. Curtiss, I.A. Shkrob, J.S.

Moore, L. Zhang, The lightest organic radical cation for charge storage in redox flow batteries, Sci. Rep., 6 (2016) 32102.

7.3. Supporting Information

Electroactive ionic liquid based on 2,5-ditert-butyl-1,4-dimethoxybenzene and triflimide anion as anodic redox shuttle in lithium-ion battery

Bruno Gélinas[1], *Thomas Bibienne*[1], *Mickael Dollé*[1], *Dominic Rochefort*[1*]

Département de chimie, Université de Montréal, CP6128 Succ. Centre-Ville, Montréal, Québec, Canada H3C 3J7

*Corresponding author: Tel: +1-514-343-6733, Fax: +1-514-343-7586, email: dominic.rochefort@umontreal.ca

List of Contents:

- Synthesis characterization such as MS, NMR and elemental analysis
- NMR spectra
- Thermal analysis
- Extra CVs of DDB and DDBF
- Arrhenius/Eyring plots of ionic conductivity/fluidity

7.3.1. General procedure for the preparation of 1,4-dimethoxybenzene (3,4) and 1,4-bis(2,2,2-trifluoroethoxy)benzene (5,6)

2-tert-butyl-1,4-dimethoxybenzene 3, 2,5-ditert-butyl-1,4-dimethoxybenzene 4, 2-tert-butyl-1,4-bis(2,2,2-trifluoroethoxy)benzene 5 and 2,5-tert-butyl-1,4-bis(2,2,2-trifluoroethoxy)benzene 6 was synthesized from 2-tert-butylhydroquinone 1 and 2,5-ditert-butylhydroquinone 2, respectively in a manner according to a literature procedure (From ref [1] and [2]). In a dry round-bottom flask equipped with a condenser placed in iced bath, the hydroquinone 1 or 2 (1 equiv.) and NaH (2.2 equiv., 60% dispersion in oil) were dissolved in dry DMF under argon atmosphere. For the synthesis of 4 and 6, tetra-n-butylammonium bromide (0.2 equiv.) was also added. After 15 minutes, the evolution of H_2 had ceased, methyl iodide (4 equiv.) or 2,2,2-Trifluoroethyl perfluorobutylsulfonate (2.15 equiv.) was added dropwise. The reaction mixture was stirred at 60 °C for 12 hours and then was added to brine solution placed in an ice bath. The resulting mixture was extracted with diethyl ether (3x150 ml) and the combined organic layers were washed with 10% sol. NaOH (3x150 ml), water (3x150 ml), brine (3x150 ml) and dried over $MgSO_4$. The solvent was removed under reduced pressure and the compounds were purified by column chromatography using silica gel as the stationary phase and pentane–diethyl ether (20:1) as eluents. Products 4 and 6 were recrystallized in hexane.

7.3.2. Preparation of (2,5-ditert-butyl-4-methoxyphenoxy)propylsulfonyl chloride (8)

In a dry round-bottom flask equipped with a condenser placed in iced bath, the 2,5-ditert-butyl-4-methoxyphenol 7 (1 equiv.), NaH (1.2 equiv., 60% dispersion in oil) and tetra-n-butylammonium bromide (0.2 equiv.) were dissolved in dry DMF under argon atmosphere. After 30 minutes, the evolution of H_2 had ceased, 1,3-propanesultone (1 equiv.) was added dropwise to the yellow solution. The reaction mixture was stirred at 80 °C for 12 hours. Thionylchloride was added at 0°C and the mixture was stirred at room temperature for 2 hours. The reaction solution was added to brine solution placed in an ice bath and the compound was collected by filtration. The powder was dissolved in diethyl ether and the organic layers were washed with water (3x150 ml), 10% sol. LiCl (3x150 ml), brine (3x150 ml) and dried over $MgSO_4$. The solvent was then removed under a vacuum, and the residue was purified by flash column chromatography using silica gel as the stationary phase and hexane-ethyl acetate (9:1) as the eluent.

7.3.3. General procedure for the preparation of 2,5-dimethoxyphenylsulfonyl chloride and 1,4-bis(2,2,2-trifluoroethoxy)phenylsulfonyl chloride (12, 13 and 21)

In a dry 3-necked round-bottom flask equipped with calcium chloride guard tube under argon atmosphere placed in an ice bath, chlorosulfonic acid (1.15 equiv.) was cautiously added to a solution of 1,4 dimethoxybenzene (3 and 5) or 1,4,5 trimethoxybenzene (11) in anhydrous dichloromethane under high stirring over 15 minutes. After stirring the yellow solution for 1 hour at 0°C, the solvent was removed under reduced pressure and a mixture DMF and thionyl chloride (2:1) were added. The mixture was stirred for 1 hour at 0°C and 1 hour at room-temperature under argon atmosphere. The reaction solution was added to brine solution placed in an ice bath and the compound was collected by filtration. The powder was dissolved in dichloromethane and the organic layers were washed with 5% sol. Na_2CO_3 (3x150 ml), water (3x150 ml), brine (3x150 ml) and dried over $MgSO_4$. The solvent was then removed under a vacuum, and the residue was purified by flash column chromatography using silica gel as the stationary phase and dichloromethane as the eluent.

7.3.4. General procedure for the preparation of sodium electroactive triflimide salt (11-13, 18 and 22)

In a flask, trifluoromethanesulfonamide was dissolved in acetonitrile and anhydrous sodium carbonate was added. The solution was stirred for 10 minutes at room temperature. Then slow addition of 1,4-dimethoxybenzene sulfonyl chloride (8, 12-14 and 21) was made. The resulting solution was stirred and heated at reflux temperature for 24 hours. The solution was filtered and the precipitate was washed with acetone to have a white precipitate. Removal of the solvent under reduced pressure gave yellow oil. The product (9 and 15-17) was washed several times with dichloromethane, diethyl ether and the product (22) was washed with a mixture between pentane and ether. The salts were dried overnight under reduce pressure at 80°C.

7.3.5. General procedure for the preparation of electroactive triflimide ionic liquids (14-16, 19 and 23)

In a minimum volume of milli-Q water, sodium electroactive triflimide salt (15-17) was dissolved and sodium electroactive triflimide salt (9 and 22) was dissolved in a mixture water:acetone (3:1) v/v. 1.1 equivalent of 1-butyl-3-methylimidazolium bromide was added slowly dropwise. The combined solution was heated to 50°C for 24 hours, the solution was concentrated for products (10

and 23) and the electroactive ionic liquids were extracted with dichloromethane. The light yellow solution was washed thrice with milli-Q water. The organic phase was dried with magnesium sulfate, then filtered and after dried.

7.3.6. Synthesis characterization such as MS, NMR and elemental analysis

2-tert-butyl-1,4-dimethoxybenzene **3** (MDB). Yellow oil; 97 % yield. ^{1}H RMN (DMSO-d_6, 300 MHz): δ (ppm) = 6.87 (d,1H), 6.77-6.70 (m,2H), 3.73 (s,3H), 3.68 (s,3H), 1.31 (s,9H). ^{13}C RMN (DMSO-d_6, 125 MHz): δ (ppm) = 153.34, 152.76, 139.07, 113.96, 113.19, 110.53, 56.02, 55.54, 34.84, 29.91. [M+H*$^{+}$](calcd for $C_{12}H_{18}O_2$): 194.13013 found: 194.12941.

2,5-ditert-butyl-1,4-dimethoxybenzene **4** (DDB). White crystal; 84 % yield. ^{1}H RMN (DMSO-d_6, 300 MHz): δ (ppm) = 6.79 (s,2H), 3.75 (s,6H), 1.31 (s,18H). ^{13}C RMN (DMSO-d_6, 125 MHz): δ (ppm) = 151.94, 135.93, 111.86, 56.23, 34.65, 30.07. (ESI) m/z: [M*$^{+}$](calcd for $C_{16}H_{26}O_2$): 250.19273 found: 250.19240. Elementary analysis: Calcd for $C_{16}H_{26}O_2$: C 76.75, H 10.47. Found: C 77.01, H 10.40.

2-tert-butyl-1,4-bis(2,2,2-trifluoroethoxy)benzene **5** (MDBF). Yellow oil; 94 % yield. ^{1}H RMN (DMSO-d_6, 300 MHz): δ (ppm) = 7.01-6.98 (m,1H), 6.93-6.89 (m,2H), 4.74-4.63 (dq,4H), 1.32 (s,9H). ^{19}F RMN (DMSO-d_6, 282 MHz): δ (ppm) = -74.12 (t,3F), -73.83 (t,3F). ^{13}C RMN (DMSO-d_6, 125 MHz): δ (ppm) = 151.89, 150.98, 139.52, 130.13, 130.06, 126.44, 126.37, 122.76, 122.69, 119.08, 118.99, 115.24, 113.87, 112.33, 34.94, 29.74. [M+*$^{+}$](calcd for $C_{14}H_{16}F_6O_2$): 330.10490 found: 330.10608.

2,5-tert-butyl-1,4-bis(2,2,2-trifluoroethoxy)benzene **6** (DDBF). White crystal; 49 % yield. ^{1}H RMN (DMSO-d_6, 300 MHz): δ (ppm) = 6.83 (s,2H), 4.74 (q,4H), 1.33 (s,18H). ^{19}F RMN (DMSO-d_6, 282 MHz): δ (ppm) = -73.67 (t,6F). ^{13}C RMN (DMSO-d_6, 125 MHz): δ (ppm) = 149.94, 136.29, 112.60, 65.48, 34.74, 29.91. (ESI) m/z: [M*$^{+}$](calcd for $C_{18}H_{24}F_6O_2$): 386.1680 found: 386.1678. Elementary analysis: Calcd for $C_{16}H_{26}O_2$: C 55.95, H 6.26. Found: C 56.18, H 6.39.

3-(2,5-ditert-butyl-4-methoxyphenoxy)propane-1-sulfonyl chloride **8** (DDB-pSO_2Cl). This compound (white powder) prepared in two steps (51% overall yield). ^{1}H RMN ($CDCl_3$, 300 MHz): δ (ppm) = 6.86 (s,1H), 6.80 (s,1H), 4.17 (t,2H), 3.99-3.94 (m,2H), 3.83 (s,3H), 2.62-2.53 (m,2H), 1.39 (s,9H), 1.37 (s,9H). ^{13}C RMN ($CDCl_3$, 125 MHz): δ (ppm) = 152.47, 150.22, 136.52, 136.16,

111.96, 111.78, 65.32, 62.88, 55.82, 35.62, 30.04, 29.72, 25.21. Elementary analysis: Calcd for $C_{18}H_{29}ClO_4S$: C 57.35, H 7.75, S 8.51. Found: C 57.67, H 7.99, S 8.70.

Sodium 3-(2,5-ditert-butyl-4-methoxyphenoxy)propylsulfonyl) (trifluoromethylsulfonyl) imide **9** (Na DDB-pNTf). White powder; 94 % Yield. ^{1}H RMN (DMSO-d_6, 300 MHz): δ (ppm) = 6.79 (s,1H), 6.77 (s,1H), 4.04 (t,2H), 3.75 (s,3H), 3.20-3.14 (m,2H), 2.19-2.10 (m,2H), 1.32 (s,9H), 1.30 (s,9H). ^{19}F RMN (DMSO-d_6, 282 MHz): δ (ppm) = -78.97 (s,3F). ^{13}C RMN (DMSO-d_6, 125 MHz): δ (ppm) = 151.87, 150.91, 135.86, 135.73, 122.74, 118.44, 111.98, 66.83, 53.23, 52.40, 34.68, 34.64, 30.14, 30.07, 24.91. (ESI) m/z: [M*$^-$](calcd for $C_{19}H_{29}F_3NO_6S_2^-$) : 488.13939 Found: 488.13966.

1-butyl-3-methylimidazolium 3-(2,5-ditert-butyl-4-methoxyphenoxy)propylsulfonyl (trifluoromethylsulfonyl) imide **10** (BMIm DDB-pNTf). Yellow liquid; 73 % Yield. ^{1}H RMN (DMSO-d_6, 300 MHz): δ (ppm) = 9.09 (s,1H), 7.76 (s,1H), 7.69 (s,1H), 6.80 (s,1H), 6.77 (s,1H), 4.15 (t,2H), 4.04 (t,2H), 3.84 (s,3H), 3.75 (s,3H), 3.21-3.16 (m,2H), 2.20-2.11 (m,2H), 1.76 (q,2H), 1.33-1.20 (m,20H), 0.90 (t,3H). ^{19}F RMN (DMSO-d_6, 282 MHz): δ (ppm) = -79.00 (s,3F). ^{13}C RMN (DMSO-d_6, 125 MHz): δ (ppm) = 151.87, 150.92, 136.95, 135.86, 135.72, 127.04, 124.07, 122.72, 118.44, 111.97, 66.84, 56.22, 52.40, 48.95, 36.19, 34.67, 34.64, 31.81, 30.14, 30.06, 24.92, 19.22, 13.70. (ESI) m/z: [M*$^+$](calcd for $C_8H_{15}N_2^+$): 139.12297 found: 139.12328. [M*$^-$](calcd for $C_{19}H_{29}F_3NO_6S_2^-$) : 488.13939 Found: 488.14132. Elementary analysis: Calcd for $C_{27}H_{44}F_3N_3O_6S_2$: N 6.69, C 51.66, H 7.06, S 10.22. Found: N 6.61, C 51.61, H 7.04, S 10.26.

4-tert-butyl-2,5-dimethoxyphenylsulfonyl chloride **12** (MDB-SO_2Cl). Yellow powder; 81 % yield. ^{1}H RMN ($CDCl_3$, 300 MHz): δ (ppm) = 7.37 (s,1H), 7.08 (s,1H), 4.03 (s,3H), 3.88 (s,3H) 1.41 (s,9H). ^{13}C RMN ($CDCl_3$, 125 MHz): δ (ppm) = 151.64, 151.11, 149.09, 128.95, 112.72, 111.35, 56.88, 55.87, 36.03, 29.16. Elementary analysis: Calcd for $C_{12}H_{17}ClO_4S$: C 49.23; H 5.85; S 10.95. Found: C 49.36; H 5.93; S 11.25.

2,4,5-trimethoxyphenylsulfonyl chloride **13** (TMB-SO_2Cl). Yellow powder; 65 % Yield. ^{1}H RMN ($CDCl_3$, 300 MHz): δ (ppm) = 7.31 (s,1H), 6.52 (s,1H), 3.97 (s,3H), 3.93 (s,3H) 3.82 (s,3H). ^{13}C RMN ($CDCl_3$, 125 MHz): δ (ppm) = 156.41, 153.69, 142.25, 122.61, 111.62, 97.21, 57.10, 56.66, 56.51. Elementary analysis: Calcd for $C_9H_{11}ClO_5S$: C 40.53, H 4.16, S 12.02. Found: C 40.56, H 4.18, S 12.05.

Sodium 4-tert-butyl-2,5-dimethoxyphenylsulfonyl (trifluoromethylsulfonyl) imide **15** (Na MDB-NTf). White powder; 96 % yield. ^{1}H RMN (DMSO-d_6, 300 MHz): δ (ppm) = 7.31 (s,1H), 6.91 (s,1H), 3.78 (s,3H), 3.76 (s,3H) 1.34 (s,9H). ^{19}F RMN (DMSO-d_6, 282 MHz): δ (ppm) = -79.31 (s,3F). ^{13}C RMN (DMSO-d_6, 125 MHz): δ (ppm) = 151.18, 150.36, 142.66, 131.21, 122.68, 118.38, 113.02, 112.79, 56.91, 56.31, 35.36, 29.77. (ESI) m/z: [M*$^-$](calcd for $C_{13}H_{17}F_3NO_6S_2^-$) : 404.04549 Found: 404.0469.

Sodium 2,4,5-trimethoxyphenylsulfonyl (trifluoromethylsulfonyl) imide **16** (Na TMB-NTf). White powder; 88 % yield. ^{1}H RMN (DMSO-d_6, 300 MHz): δ (ppm) = 7.26 (s,1H), 6.72 (s,1H), 3.84 (s,3H), 3.80 (s,3H), 3.69 (s,3H). ^{19}F RMN (DMSO-d_6, 282 MHz): δ (ppm) = -77.81 (s,3F). ^{13}C RMN (DMSO-d_6, 125 MHz): δ (ppm) = 152.23, 151.63, 140.79, 123.80, 117.91, 113.06, 98.68, 56.57, 56.19, 55.85. (ESI) m/z: [M*$^-$](calcd for $C_{10}H_{11}F_3NO_7S_2^-$) : 377.99345 Found: 377.99427.

Sodium 2,5-dimethoxyphenylsulfonyl (trifluoromethylsulfonyl) imide **17** (Na DMB-NTf). White powder; 81 % yield. ^{1}H RMN (DMSO-d_6, 300 MHz): δ (ppm) = 7.28 (s,1H), 7.04 (s,2H), 3.75 (s,3H), 3.71. ^{19}F RMN (DMSO-d_6, 282 MHz): δ (ppm) = -77.89 (s,3F). ^{13}C RMN (DMSO-d_6, 125 MHz): δ (ppm) = 151.68, 150.52, 133.17, 122.16, 117.86, 117.59, 114.46, 114.10, 56.33, 55.55. (ESI) m/z: [M*$^-$](calcd for $C_9H_9F_3NO_6S_2^-$): 347.98289 Found: 347.98289.

1-butyl-3-methylimidazolium 4-tert-butyl-2,5-dimethoxyphenylsulfonyl (trifluoromethylsulfonyl) imide **18** (BMIm MDB-NTf). Yellow liquid or white crystal; 49 % yield. ^{1}H RMN (DMSO-d_6, 300 MHz): δ (ppm) = 9.09 (s,1H), 7.76 (t,1H), 7.69 (t,1H), 7.32 (s,1H), 6.91 (s,1H), 4.15 (t,2H), 3.85 (s,3H), 3.78 (s,3H), 3.76 (s,3H), 1.76 (q, 2H), 1.35 (s,9H), 1.32-1.19 (m,2H), 0.89 (t,3H). ^{19}F RMN (DMSO-d_6, 282 MHz): δ (ppm) = -79.31 (s,3F). ^{13}C RMN (DMSO-d_6, 125 MHz): δ (ppm) = 151.12, 150.37, 142.67, 136.95, 131.23, 124.07, 122.72, 118.39, 113.03, 112.80, 56.89, 56.30, 48.94, 36.17, 35.36, 31.81, 29.76, 19.21, 13.69. (ESI) m/z: [M*$^-$](calcd for $C_{13}H_{17}F_3NO_6S_2^-$) : 404.04549 Found: 404.04674 et [M*$^+$](calcd for $C_8H_{15}N_2^+$) : 139.12297 Found: 139.12338. Elementary analysis: Calcd for $C_{21}H_{32}F_3N_3O_6S_2$: N 7.73, C 46.40, H 5.93, S 11.80. Found: N 7.68 C 46.31, H 6.09, S 11.87.

1-butyl-3-methylimidazolium 2,4,5-trimethoxyphenylsulfonyl (trifluoromethylsulfonyl) imide **19** (BMIm TMB-NTf). Yellow liquid or white crystal; 66 % yield.^{1}H RMN (DMSO-d_6, 300 MHz): δ (ppm) = 9.09 (s,1H), 7.75 (t,1H), 7.69 (t,1H), 7.26 (s,1H), 6.72 (s,1H), 4.15 (t,2H), 3.84 (s,6H),

3.79 (s,3H), 3.68 (s,3H), 1.75 (q, 2H), 1.31-0.92 (m,2H), 0.89 (t,3H). ^{19}F RMN (DMSO-d_6, 282 MHz): δ (ppm) = -77.81 (s,3F). ^{13}C RMN (DMSO-d_6, 125 MHz): δ (ppm) = 152.24, 151.63, 140.79, 136.44, 123.80, 123.57, 122.23, 117.91, 113.07, 98.67, 56.55, 56.18, 55.85, 48.44, 35.69, 31.30, 18.72, 13.20. (ESI) m/z: [M*$^-$](calcd for $C_{10}H_{11}F_3NO_7S_2^-$) : 377.99345 Found: 377.99452 et [M*$^+$](calcd for $C_8H_{15}N_2^+$) : 139.12297 Found: 139.12352. Elementary analysis: Calcd for $C_{18}H_{26}F_3N_3O_7S_2$: N 8.12, C 41.77, H 5.06, S 12.39. Found: N 8.03, C 41.59, H 5.13, S 12.40.

1-butyl-3-methylimidazolium 2,5-dimethoxyphenylsulfonyl (trifluoromethylsulfonyl) imide **20** (BMIm DMB-NTf). White crystal; 60 % yield. ^{1}H RMN (DMSO-d_6, 300 MHz): δ (ppm) = 9.08 (s,1H), 7.75 (s,1H), 7.68 (s,1H), 7.04 (s,1H), 4.15 (t,2H), 3.84 (s,3H). 3.73 (d,6H), 1.75 (q,2H), 1.25 (m,2H), 0.88 (t,3H). ^{19}F RMN (DMSO-d_6, 282 MHz): δ (ppm) = -77.91 (s,3F). ^{13}C RMN (DMSO-d_6, 125 MHz): δ (ppm) = 151.70, 150.52, 136.43, 133.14, 123.55, 122.20, 117.56, 114.50, 114.10, 56.30, 55.54, 48.45, 35.65, 31.30, 18.70, 13.16. (ESI) m/z: [M*$^+$](calcd for $C_8H_{15}N_2^+$): 139.12297 found: 139.12318. [M*$^-$](calcd for $C_9H_9F_3NO_6S_2^-$) : 347.98289 Found: 347.98395. Elementary analysis: Calcd for $C_{17}H_{24}F_3N_3O_6S_2$: N 8.62, C 41.88, H 4.96, S 13.15. Found: N 8.56, C 41.84, H 4.96, S 13.16.

4-tert-butyl-2,5-bis(2,2,2-trifluoroethoxy)phenylsulfonyl chloride **21** (MDBF-SO_2Cl). Yellow powder; 71 % yield. ^{1}H RMN ($CDCl_3$, 300 MHz): δ (ppm) = 7.32 (s,1H), 7.15 (s,1H), 4.55 (q,2H), 4.43 (q,2H) 1.43 (s,9H). ^{19}F RMN ($CDCl_3$, 282 MHz): δ (ppm) = -74.72 (t,3F), -74.94 (t,3F). ^{13}C RMN ($CDCl_3$, 125 MHz): δ (ppm) = 150.40, 149.63, 149.44, 131.07, 124.76, 124.59, 116.03, 111.72, 68.16, 67.67, 66.15, 65.67, 36.08, 29.08.

Sodium 4-tert-butyl-2,5-bis(2,2,2-trifluoroethoxy)phenylsulfonyl (trifluoromethylsulfonyl) imide **22** (Na MDBF-NTf). White powder; 68 % yield. ^{1}H RMN (DMSO-d_6, 300 MHz): δ (ppm) = 7.32 (s,1H), 7.05 (s,1H), 4.77-4.66 (dq,4H), 1.35 (s,9H). ^{19}F RMN (DMSO-d_6, 282 MHz) δ (ppm) = -73.66 (t,3F), -73.78 (t,3F), -79.39 (s,3F). ^{13}C RMN (DMSO-d_6, 125 MHz): δ (ppm) = 150.13, 148.81, 143.02, 133.54, 117.25, 113.31, 68.12, 67.67, 65.65, 65.19, 35.33, 29.59. (ESI) m/z: [M*$^-$](calcd for $C_{15}H_{15}F_9NO_6S_2^-$): 540.02026 Found: 540.02152.

1-butyl-3-methylimidazolium 4-tert-butyl-2,5-bis(2,2,2-trifluoroethoxy)phenylsulfonyl (trifluoromethylsulfonyl) imide **23** (BMIm MDBF-NTf). Yellow oil or white crystal; 93 % yield. ^{1}H RMN (DMSO-d_6, 300 MHz): δ (ppm) = 9.09 (s,1H), 7.76 (t,1H), 7.69 (t,1H), 7.33 (s,1H), 7.06

(s,1H), 4.77-4.66 (dq,4H), 4.15 (t,2H), 3.84 (s,3H), 1.81-1.71 (m,2H) 1.35 (s,9H), 1.31-1.19 (m,2H), 0.89 (t,3H). ^{19}F RMN (DMSO-d_6, 282 MHz) δ (ppm) = -73.69 (t,3F), -73.81 (t,3F), -79.42 (s,3F). ^{13}C RMN (DMSO-d_6, 125 MHz): δ (ppm) = 150.13, 148.82, 143.05, 136.94, 133.51, 126.87, 126.23, 126.14, 124.07, 122.72, 122.58, 118.28, 117.24, 113.33, 68.12, 67.67, 65.66, 65.21, 48.95, 36.18, 35.33, 31.81, 29.58, 13.21, 13.69. (ESI) m/z: [M*$^+$](calcd for $C_8H_{15}N_2^+$): 139.12297 found: 139.12349. (ESI) m/z: [M*$^-$](calcd for $C_{15}H_{15}F_9NO_6S_2^-$): 540.02026 Found: 540.02215. Elementary analysis: Calcd for $C_{23}H_{30}F_9N_3O_6S_2$: N 6.18, C 40.65, H 4.45, S 9.44. Found: N 6.16, C 40.72, H 4.54, S 9.36.

7.3.7. NMR spectra

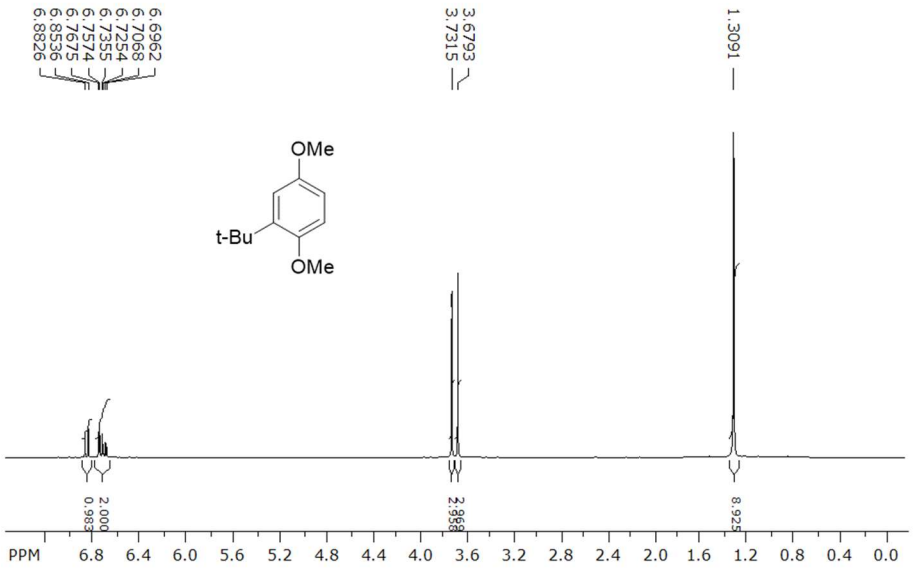

Figure S7.1. ^{1}H RMN (DMSO-d_6, 300 MHz): δ (ppm) = 6.87 (d,1H), 6.77-6.70 (m,2H), 3.73 (s,3H), 3.68 (s,3H), 1.31 (s,9H). (MDB)

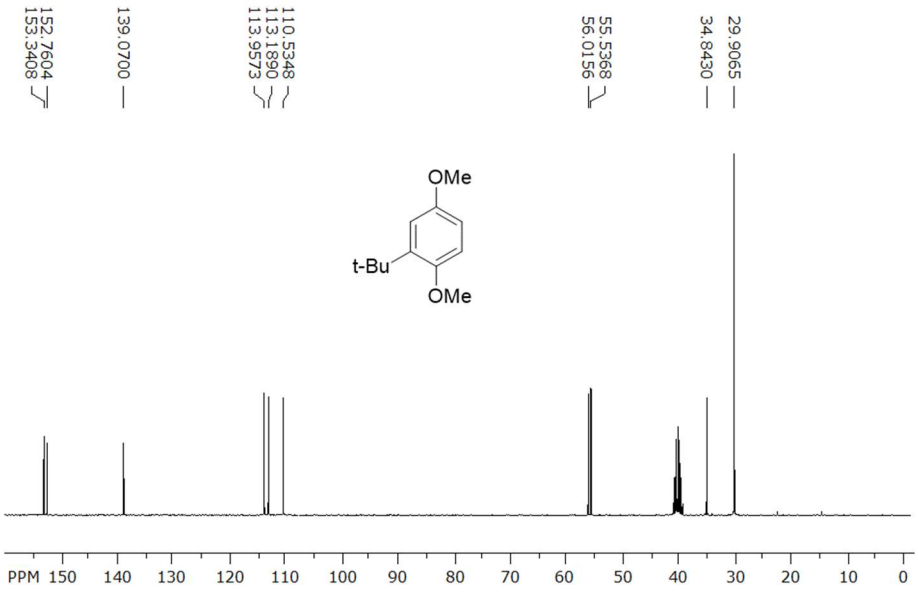

Figure S7.2. ^{13}C RMN (DMSO-d_6, 125 MHz): δ (ppm) = 153.34, 152.76, 139.07, 113.96, 113.19, 110.53, 56.02, 55.54, 34.84, 29.91. (MDB)

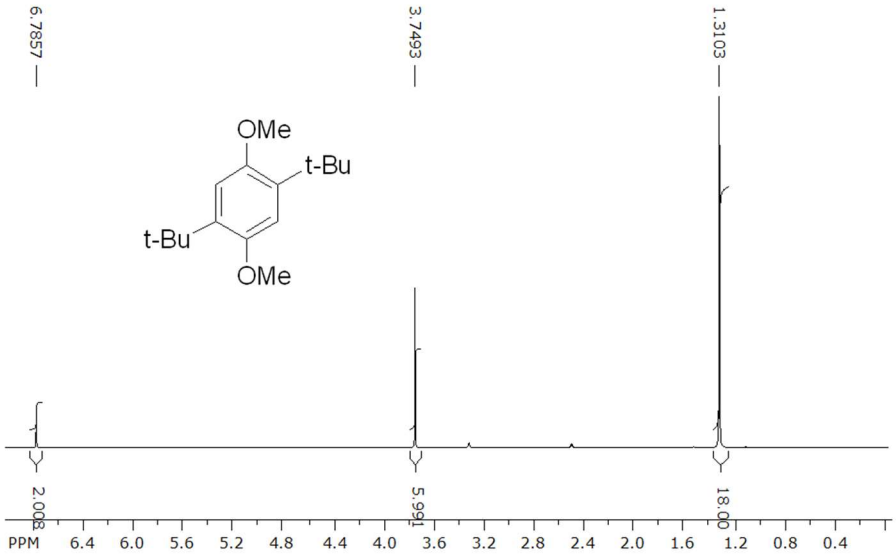

Figure S7.3. ^{1}H RMN (DMSO-d$_6$, 300 MHz): δ (ppm) = 6.79 (s,2H), 3.75 (s,6H), 1.31 (s,18H). (DDB)

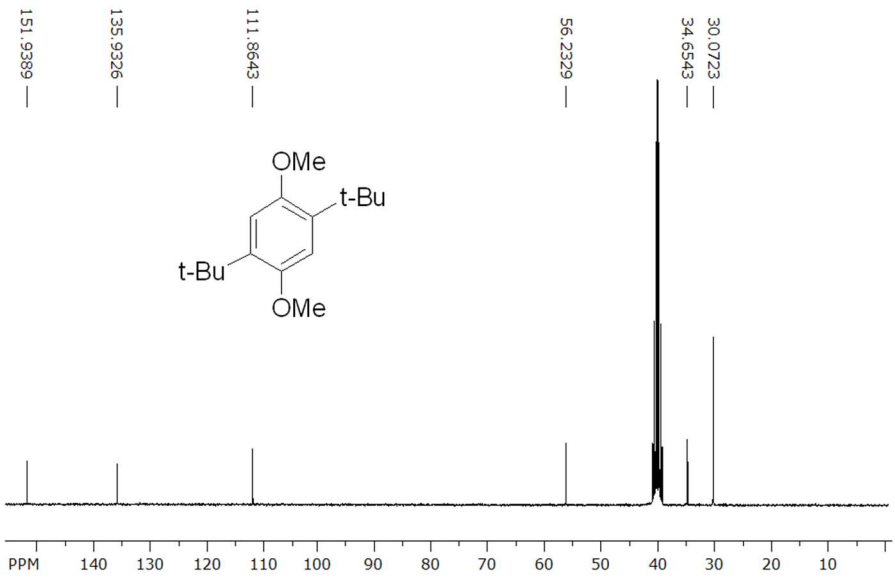

Figure S7.4. ^{13}C RMN (DMSO-d$_6$, 125 MHz): δ (ppm) = 151.94, 135.93, 111.86, 56.23, 34.65, 30.07. (DDB)

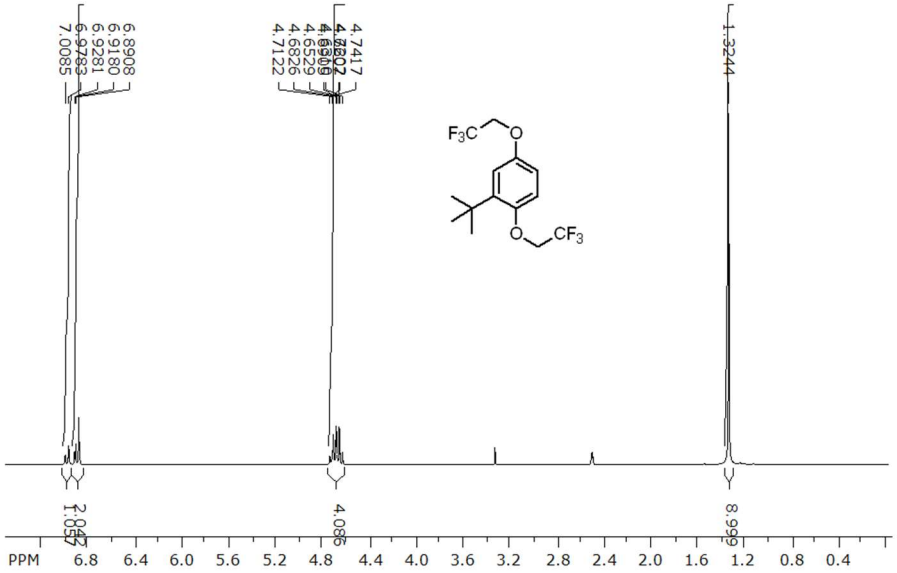

Figure S7.5. ^{1}H RMN (DMSO-d$_6$, 300 MHz): δ (ppm) = 7.01-6.98 (m,1H), 6.93-6.89 (m,2H), 4.74-4.63 (dq,4H), 1.32 (s,9H). (MDBF)

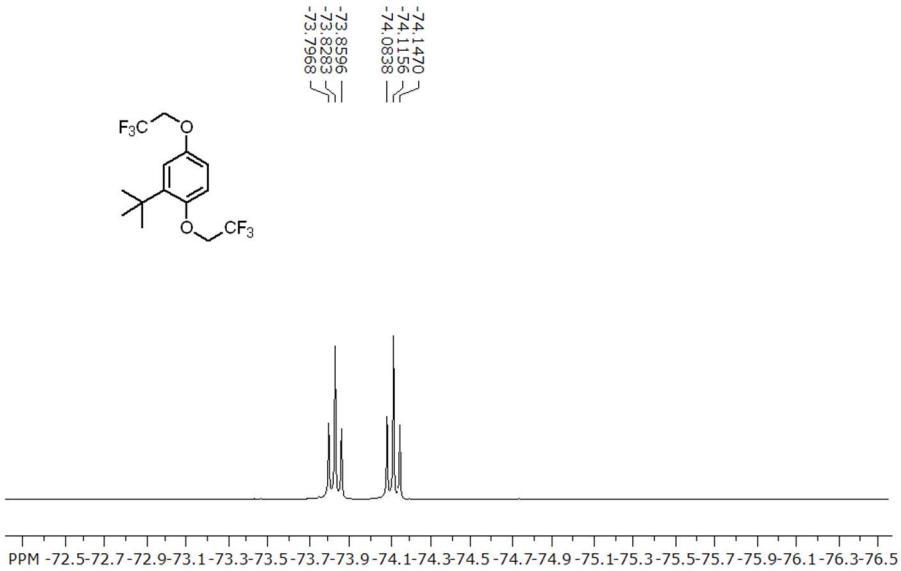

Figure S7.6. ^{19}F RMN (DMSO-d$_6$, 282 MHz): δ (ppm) = -74.12 (t,3F), -73.83 (t,3F). (MDBF)

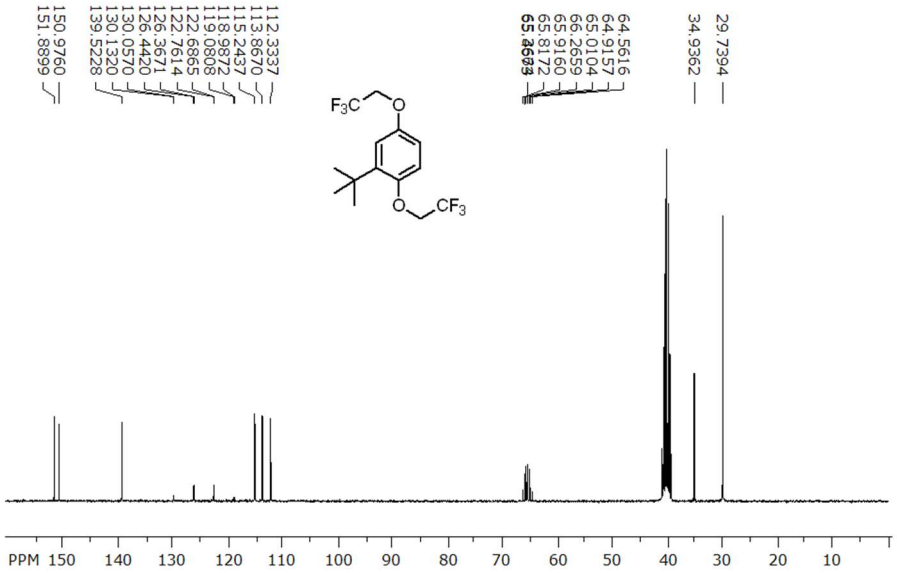

Figure S7.7. ^{13}C RMN (DMSO-d$_6$, 125 MHz): δ (ppm) = 151.89, 150.98, 139.52, 130.13, 130.06, 126.44, 126.37, 122.76, 122.69, 119.08, 118.99, 115.24, 113.87, 112.33, 34.94, 29.74. (MDBF)

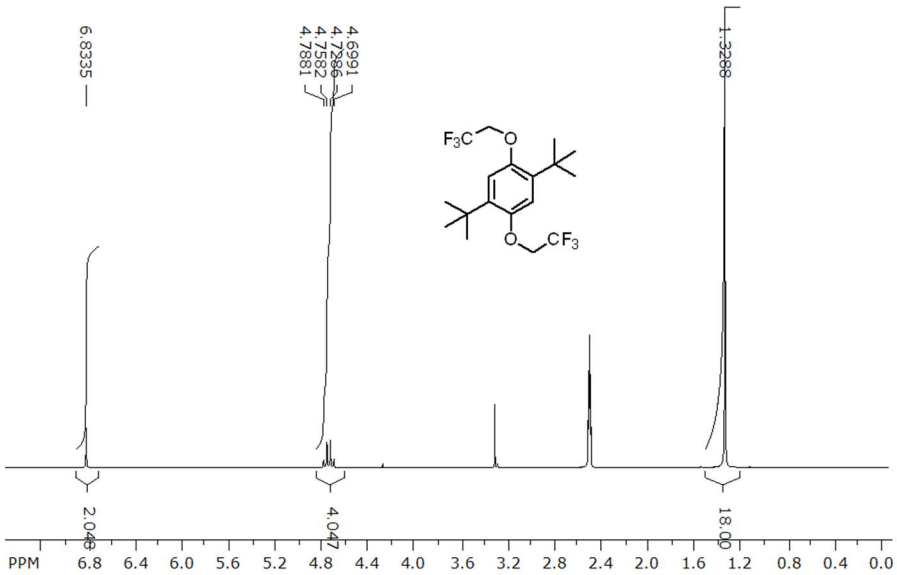

Figure S7.8. ^{1}H RMN (DMSO-d$_6$, 300 MHz): δ (ppm) = 6.83 (s,2H), 4.74 (q,4H), 1.33 (s,18H). (DDBF)

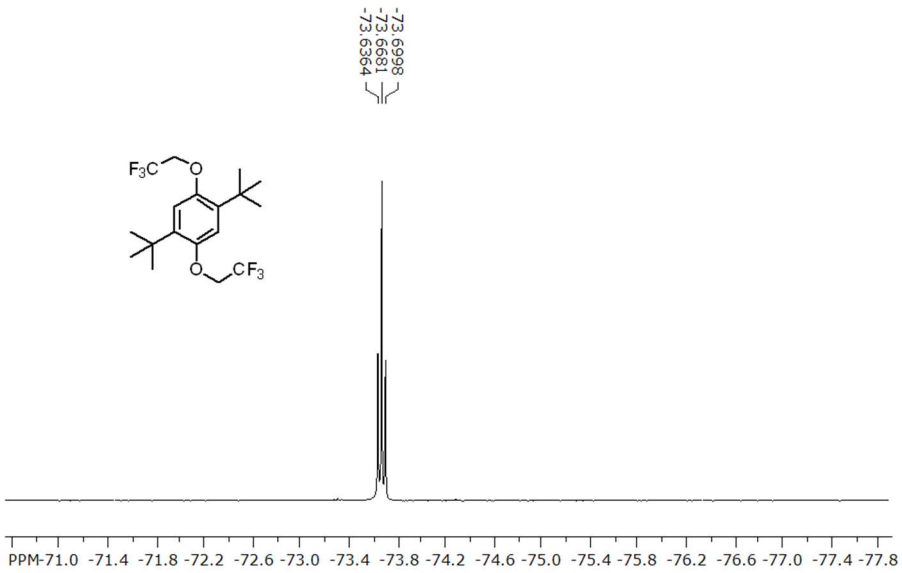

Figure S7.9. ^{19}F RMN (DMSO-d_6, 282 MHz): δ (ppm) = -73.67 (t,6F). (MDBF)

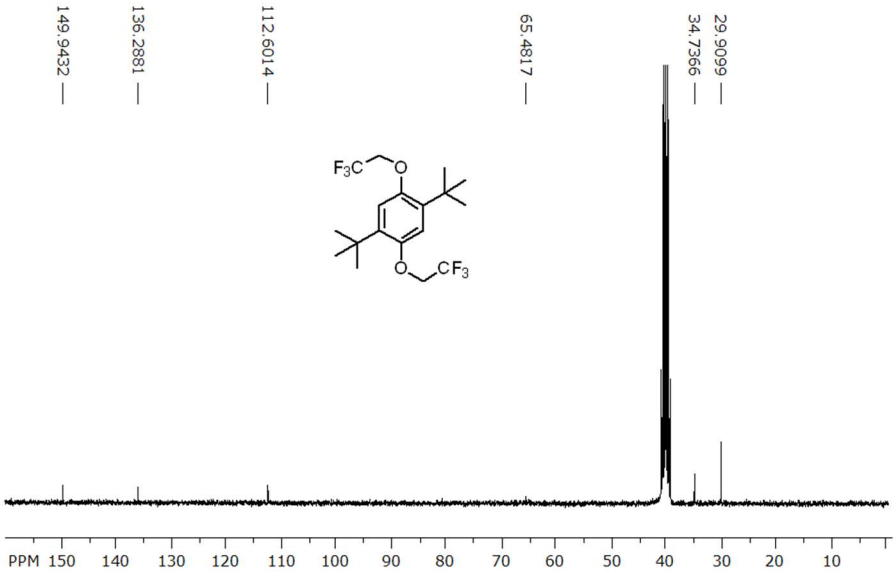

Figure S7.10. ^{13}C RMN (DMSO-d_6, 125 MHz): δ (ppm) = 149.94, 136.29, 112.60, 65.48, 34.74, 29.91. (DDBF)

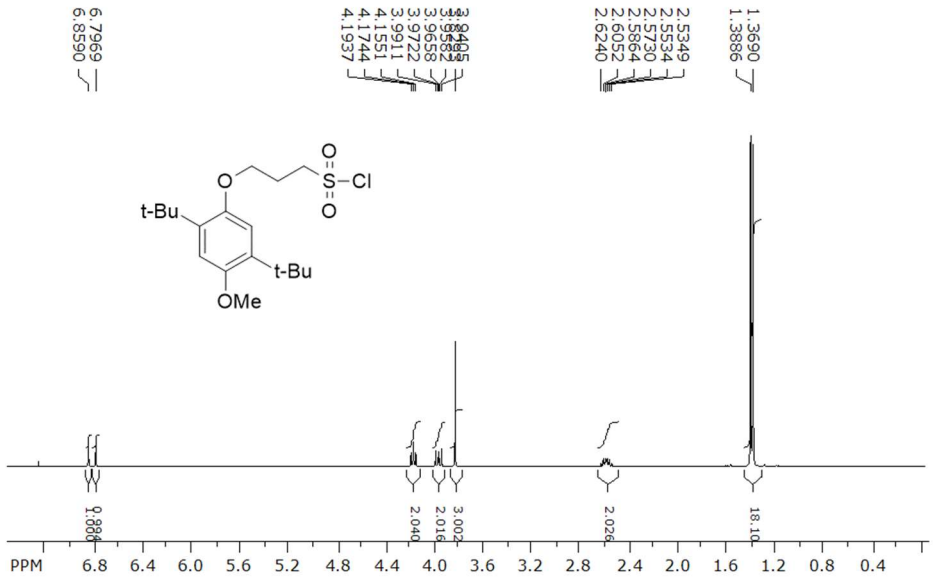

Figure S7.11. ^{1}H RMN ($CDCl_3$, 300 MHz): δ (ppm) = 6.86 (s,1H), 6.80 (s,1H), 4.17 (t,2H), 3.99-3.94 (m,2H), 3.83 (s,3H), 2.62-2.54 (m,2H), 1.39 (s,9H), 1.37 (s,9H). (DDB-pSO_2Cl)

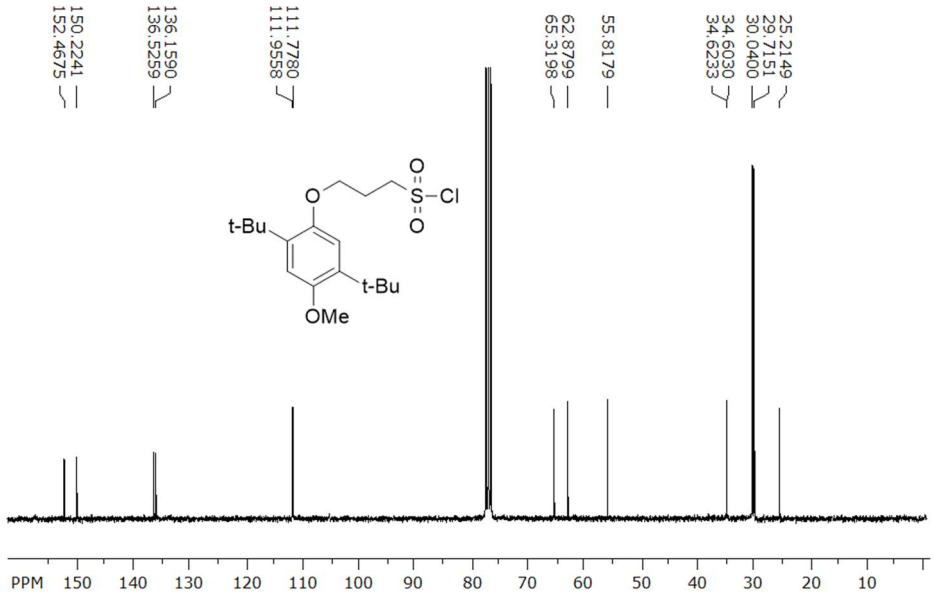

Figure S7.12. ^{13}C RMN ($CDCl_3$, 125 MHz): δ (ppm) = 152.47, 150.22, 136.53, 136.16, 111.96, 111.78, 65.32, 62.88, 55.82, 35.62, 30.04, 29.72, 25.21. (DDB-pSO_2Cl)

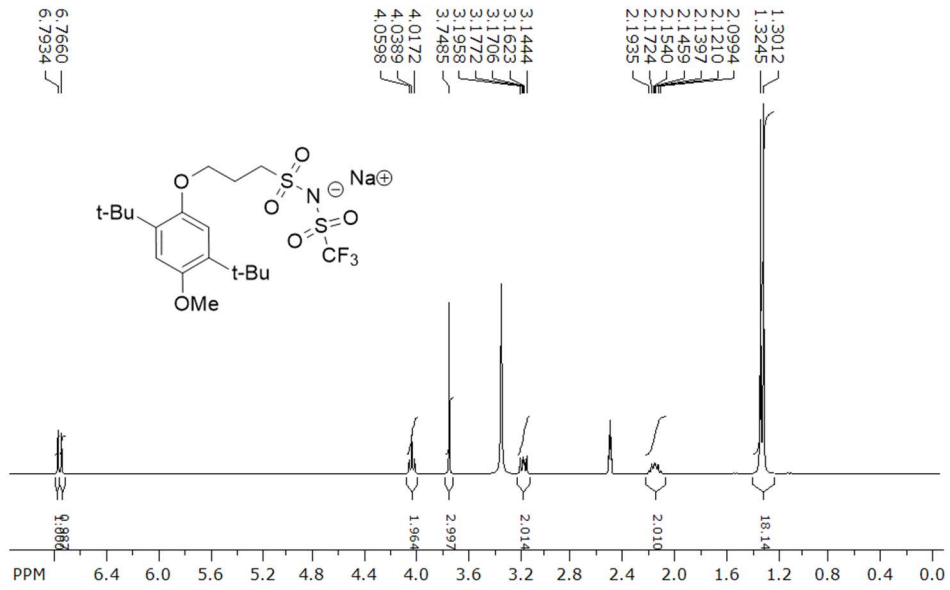

Figure S7.13. ^{1}H RMN (DMSO-d_6, 300 MHz): δ (ppm) = 6.79 (s,1H), 6.77 (s,1H), 4.04 (t,2H), 3.75 (s,3H), 3.20-3.14 (m,2H), 2.19-2.10 (m,2H), 1.32 (s,9H), 1.30 (s,9H). (Na DDB-pNTf)

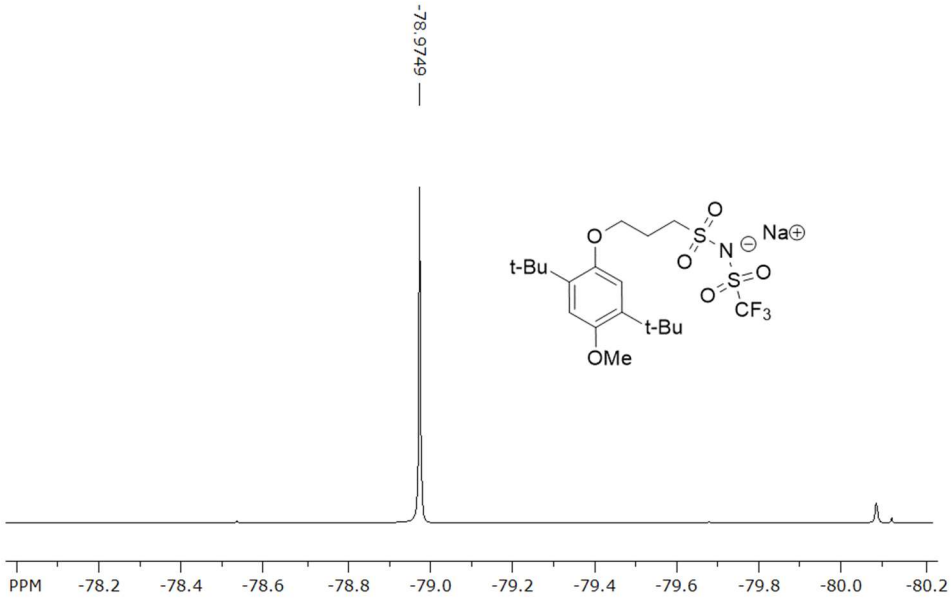

Figure S7.14. ^{19}F RMN (DMSO-d_6, 282 MHz): δ (ppm) = -78.97 (s,3F). (Na DDB-pNTf)

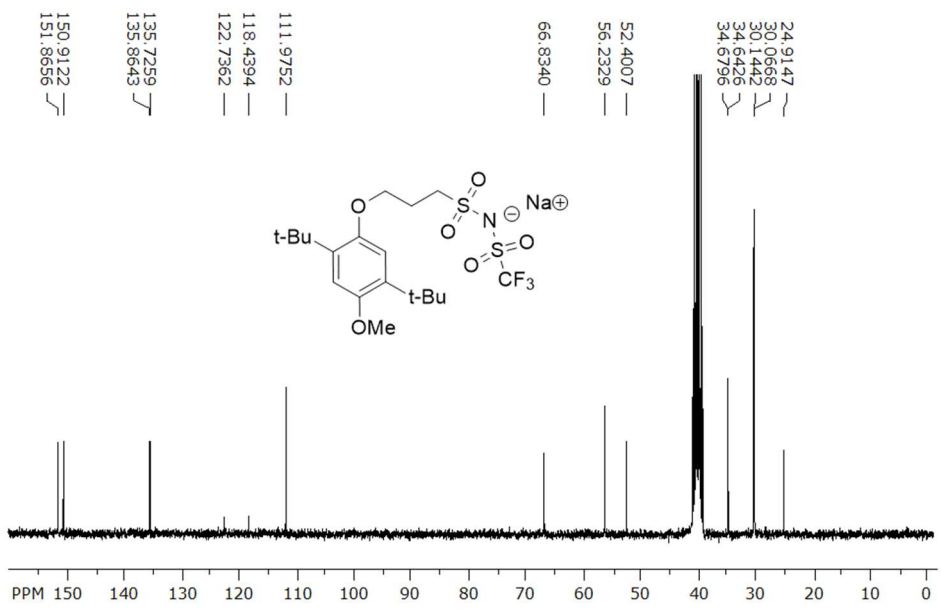

Figure S7.15. ^{13}C RMN (DMSO-d$_6$, 125 MHz): δ (ppm) = 151.87, 150.91, 135.86, 135.73, 122.74, 118.44, 111.98, 66.83, 53.23, 52.40, 34.68, 34.64, 30.14, 30.07, 24.91. (Na DDB-pNTf)

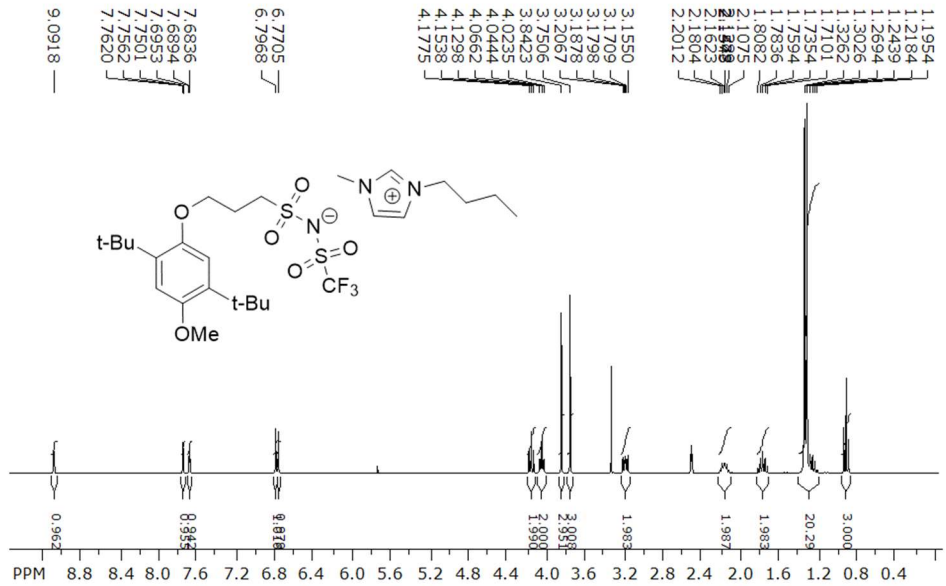

Figure S7.16. ^{1}H RMN (DMSO-d$_6$, 300 MHz): δ (ppm) = 9.09 (s,1H), 7.76 (s,1H), 7.69 (s,1H), 6.80 (s,1H), 6.77 (s,1H), 4.15 (t,2H), 4.04 (t,2H), 3.84 (s,3H), 3.75 (s,3H), 3.21-3.16 (m,2H), 2.20-2.11 (m,2H), 1.76 (q,2H), 1.33-1.20 (m,20H), 0.90 (t,3H). (BMIm DDB-pNTf)

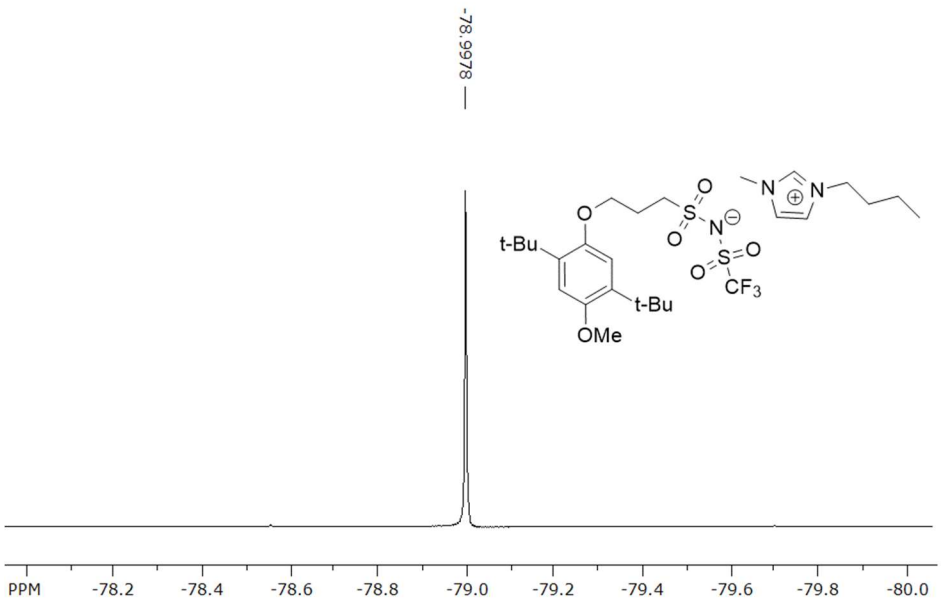

Figure S7.17. ^{19}F RMN (DMSO-d_6, 282 MHz): δ (ppm) = -79.00 (s,3F). (BMIm DDB-pNTf)

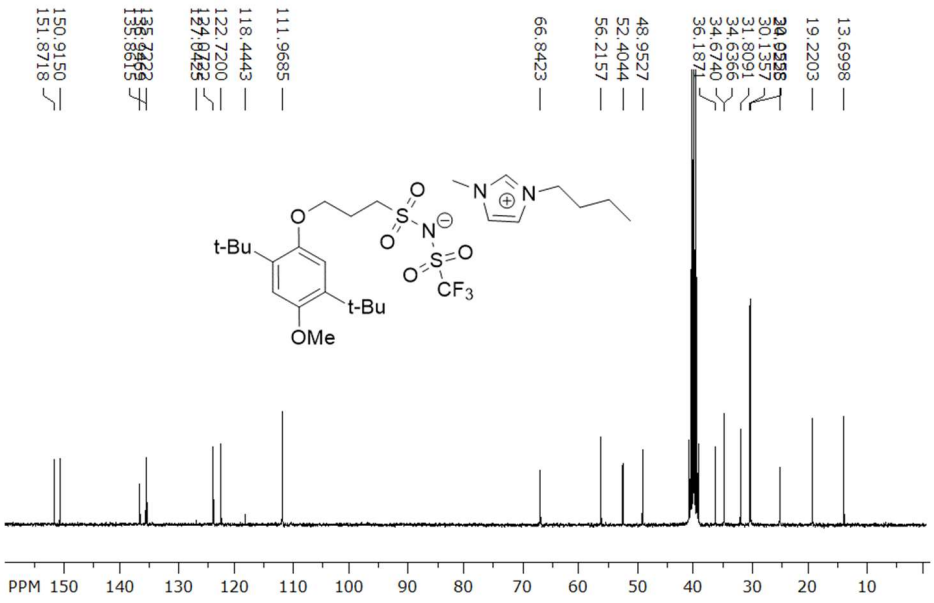

Figure S7.18. ^{13}C RMN (DMSO-d_6, 125 MHz): δ (ppm) = 151.87, 150.92, 136.95, 135.86, 135.72, 127.04, 124.07, 122.72, 118.44, 111.97, 66.84, 56.22, 52.40, 48.95, 36.19, 34.67, 34.64, 31.81, 30.14, 30.06, 24.92, 19.22, 13.70. (BMIm DDB-pNTf)

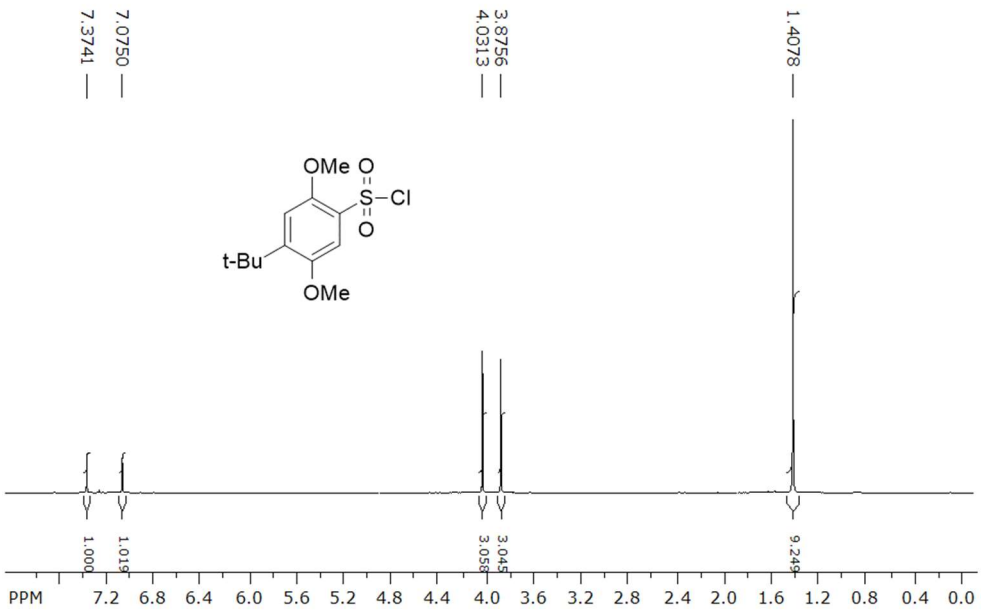

Figure S7.19. ^{1}H RMN ($CDCl_3$, 300 MHz): δ (ppm) = 7.37 (s,1H), 7.08 (s,1H), 4.03 (s,3H), 3.88 (s,3H) 1.41 (s,9H). (MDB-SO_2Cl)

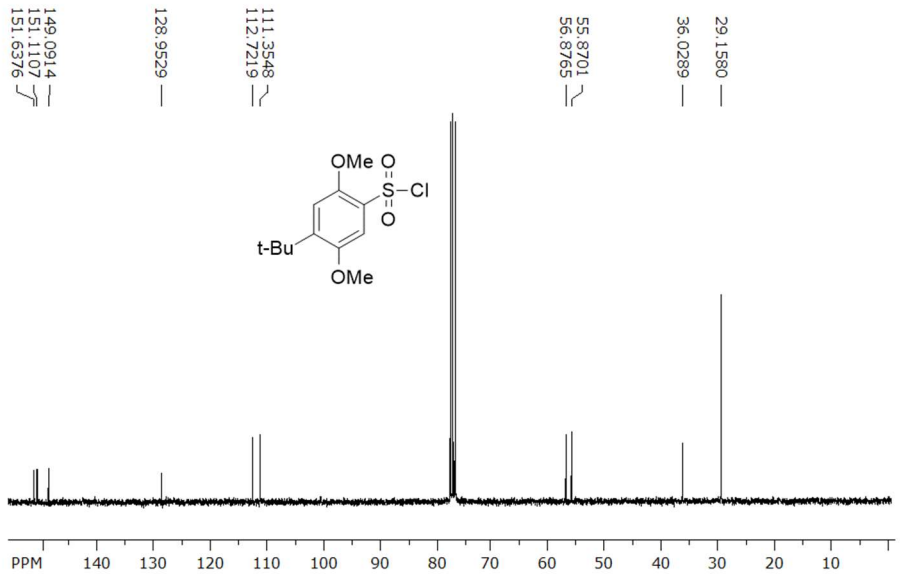

Figure S7.20. ^{13}C RMN ($CDCl_3$, 125 MHz): δ (ppm) = 151.64, 151.11, 149.09, 128.95, 112.72, 111.35, 56.88, 55.87, 36.03, 29.16. (MDB-SO_2Cl)

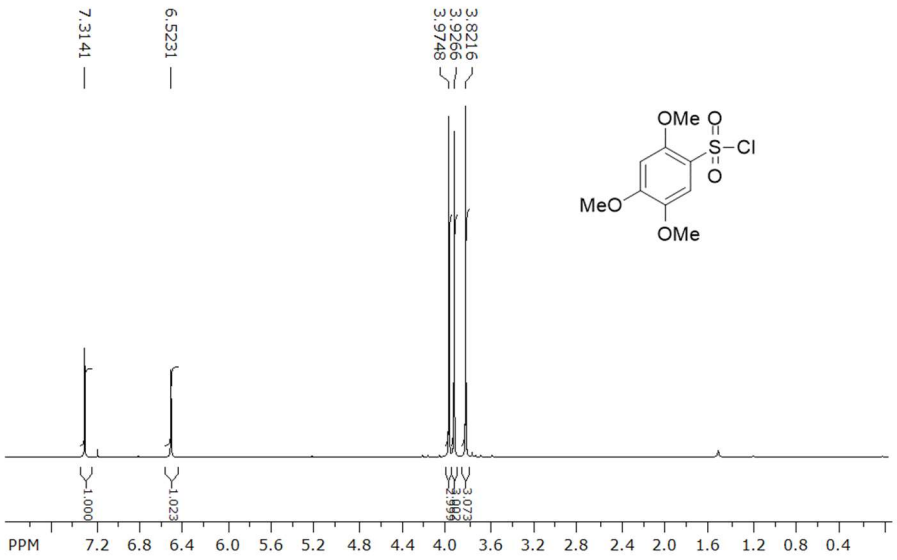

Figure S7.21. ^{1}H RMN ($CDCl_3$, 300 MHz): δ (ppm) = 7.31 (s,1H), 6.52 (s,1H), 3.97 (s,3H), 3.93 (s,3H) 3.82 (s,3H). (TDB-SO_2Cl)

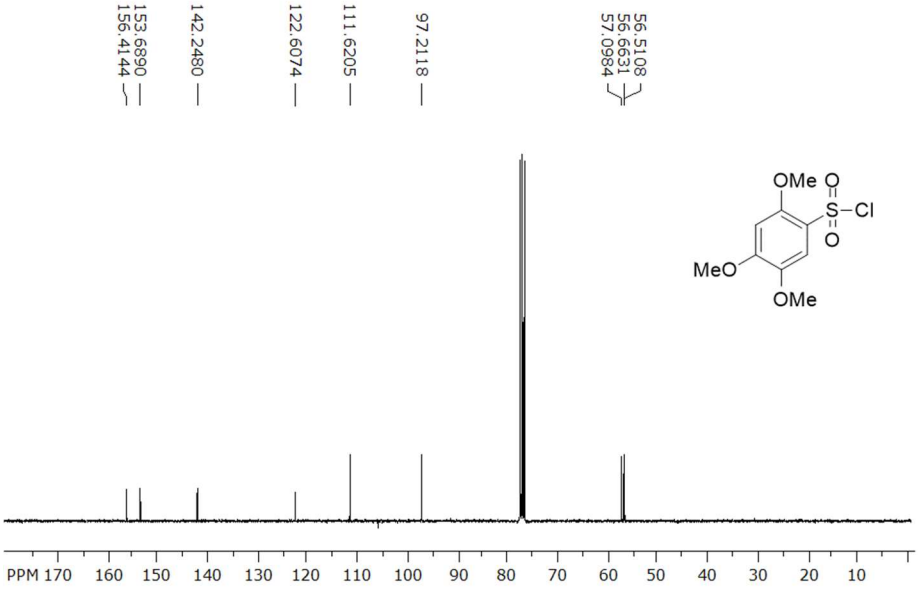

Figure S7.22. ^{13}C RMN ($CDCl_3$, 125 MHz): δ (ppm) = 156.41, 153.69, 142.25, 122.61, 111.62, 97.21, 57.10, 56.66, 56.51. (TDB-SO_2Cl)

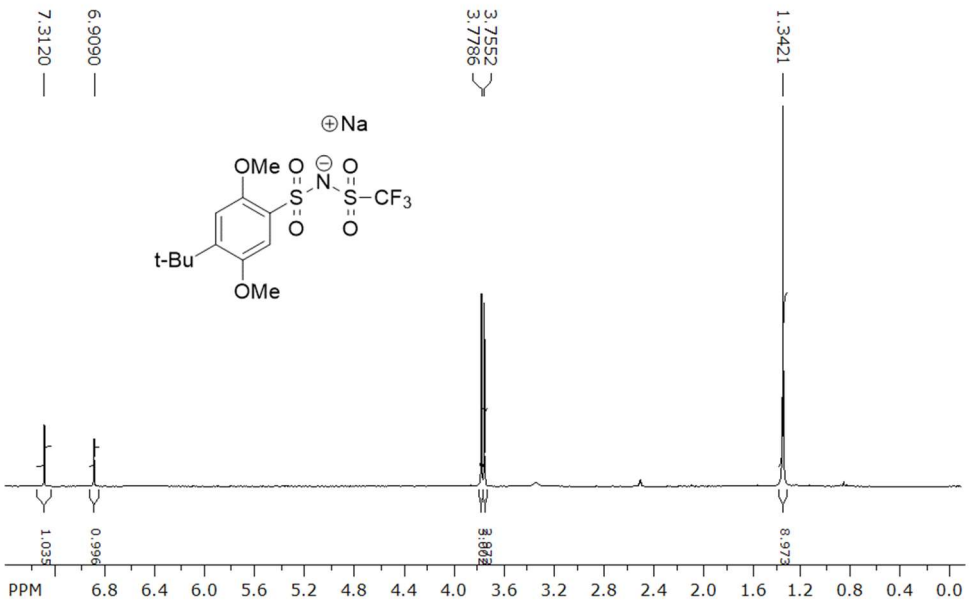

Figure S7.23. ^{1}H RMN (DMSO-d_6, 300 MHz): δ (ppm) = 7.31 (s,1H), 6.91 (s,1H), 3.78 (s,3H), 3.76 (s,3H) 1.34 (s,9H). (Na MDB-NTf)

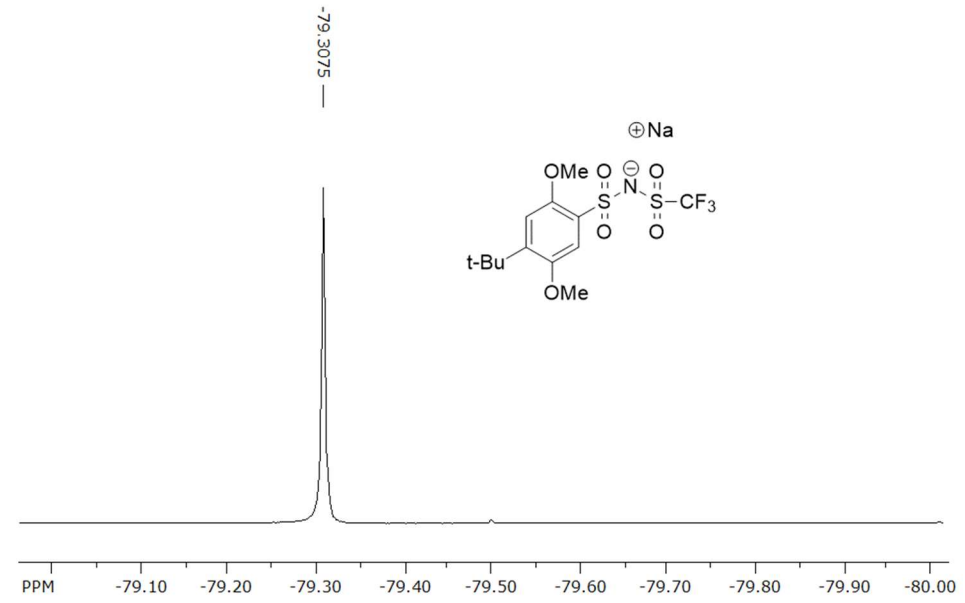

Figure S7.24. ^{19}F RMN (DMSO-d_6, 282 MHz): δ (ppm) = -79.31 (s,3F). (Na MDB-NTf)

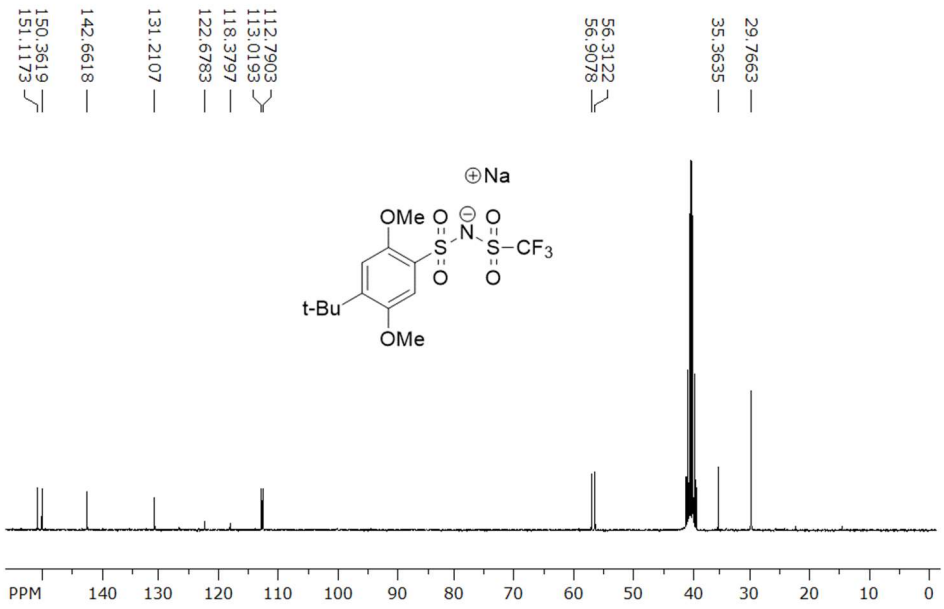

Figure S7.25. ^{13}C RMN (DMSO-d_6, 125 MHz): δ (ppm) = 151.12, 150.36, 142.66, 131.21, 122.68, 118.38, 113.02, 112.79, 56.91, 56.31, 35.36, 29.77. (Na MDB-NTf)

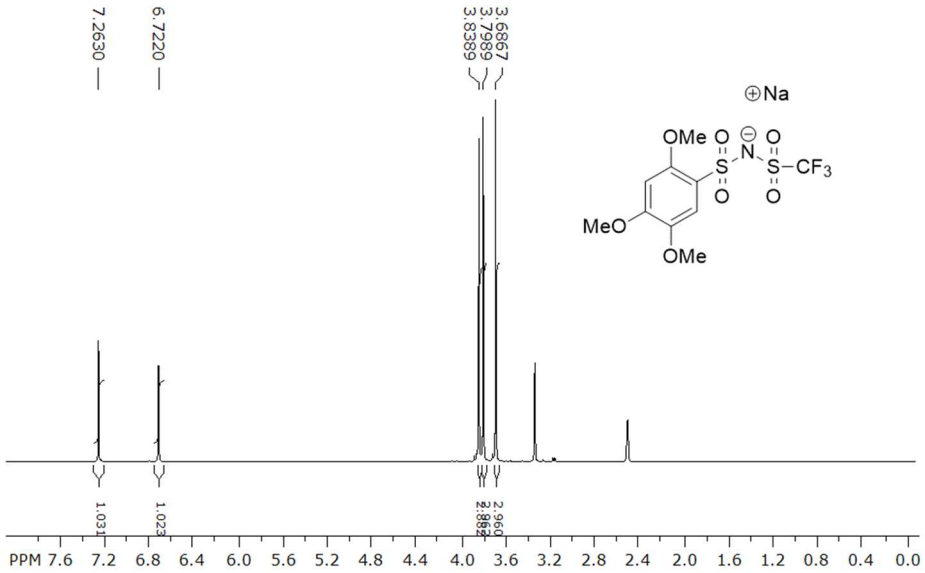

Figure S7.26. ^{1}H RMN (DMSO-d_6, 300 MHz): δ (ppm) = 7.26 (s,1H), 6.72 (s,1H), 3.84 (s,3H), 3.80 (s,3H), 3.69 (s,3H). (Na TMB-NTf)

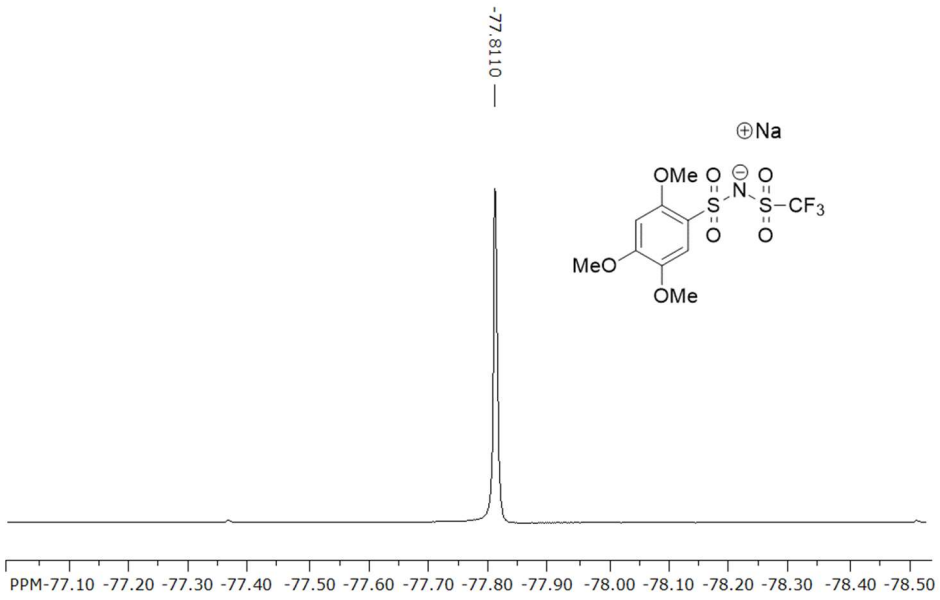

Figure S7.27. ^{19}F RMN (DMSO-d_6, 282 MHz): δ (ppm) = -77.81 (s,3F). (Na TMB-NTf)

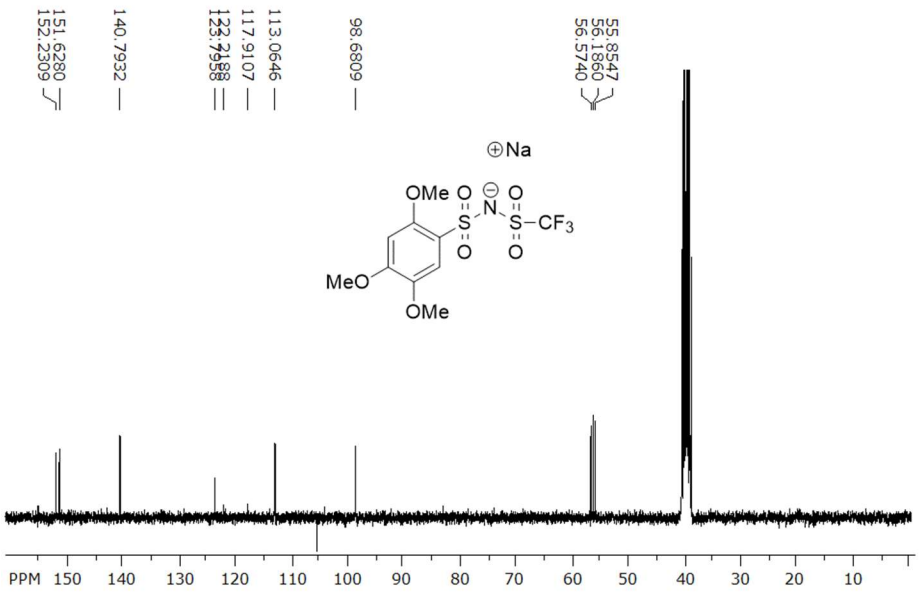

Figure S7.28. ^{13}C RMN (DMSO-d_6, 125 MHz): δ (ppm) = 152.23, 151.63, 140.79, 123.80, 117.91, 113.06, 98.68, 56.57, 56.19, 55.85. (Na TMB-NTf)

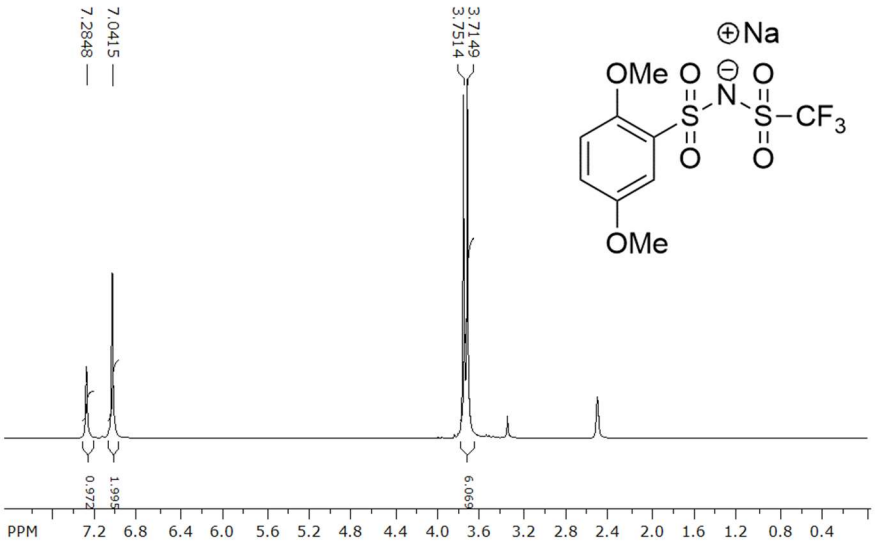

Figure S7.29. ^{1}H RMN (DMSO-d_6, 300 MHz): δ (ppm) = 7.28 (s,1H), 7.04 (s,2H), 3.75 (s,3H), 3.71. (Na DMB-NTf)

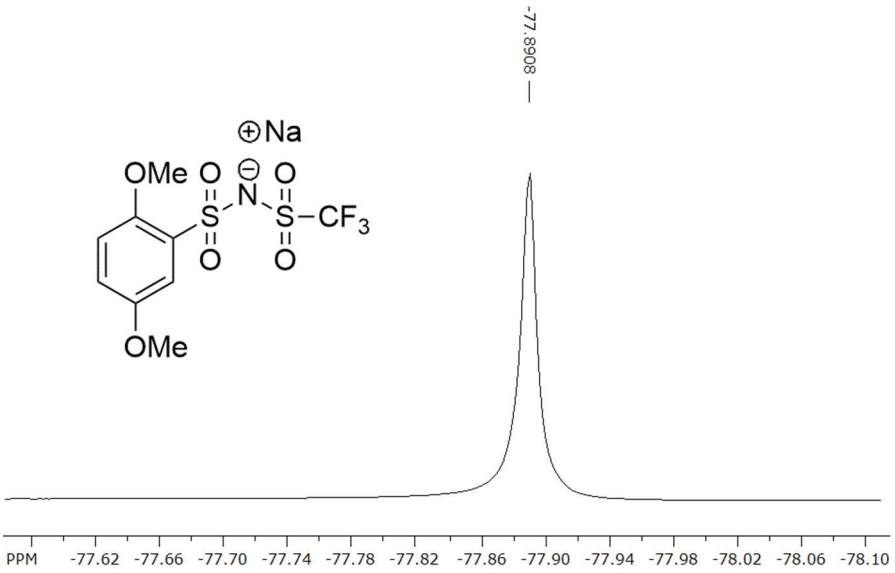

Figure S7.30. ^{19}F RMN (DMSO-d_6, 282 MHz): δ (ppm) = -77.89 (s,3F). (Na DMB-NTf)

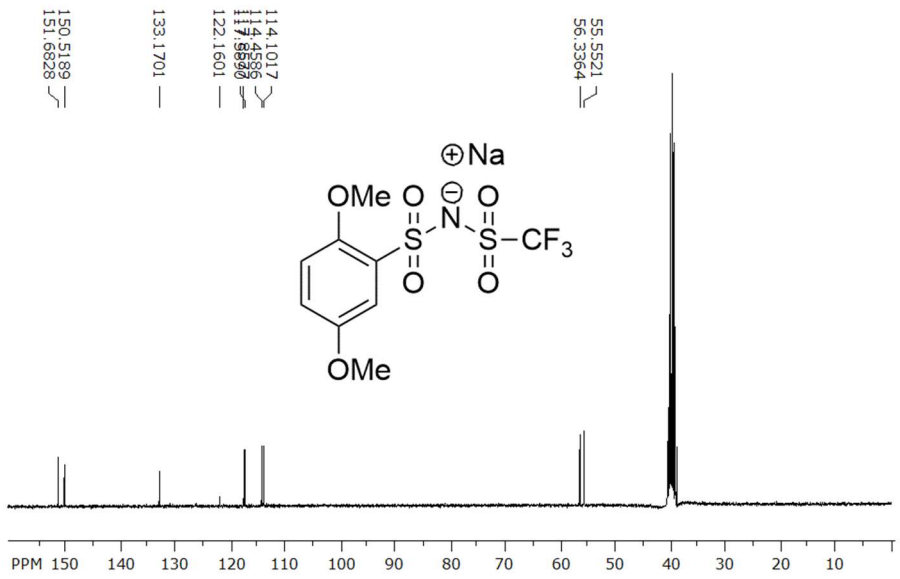

Figure S7.31. ^{13}C RMN (DMSO-d$_6$, 125 MHz): δ (ppm) = 151.68, 150.52, 133.17, 122.16, 117.86, 117.59, 114.46, 114.10, 56.34, 55.55. (Na DMB-NTf)

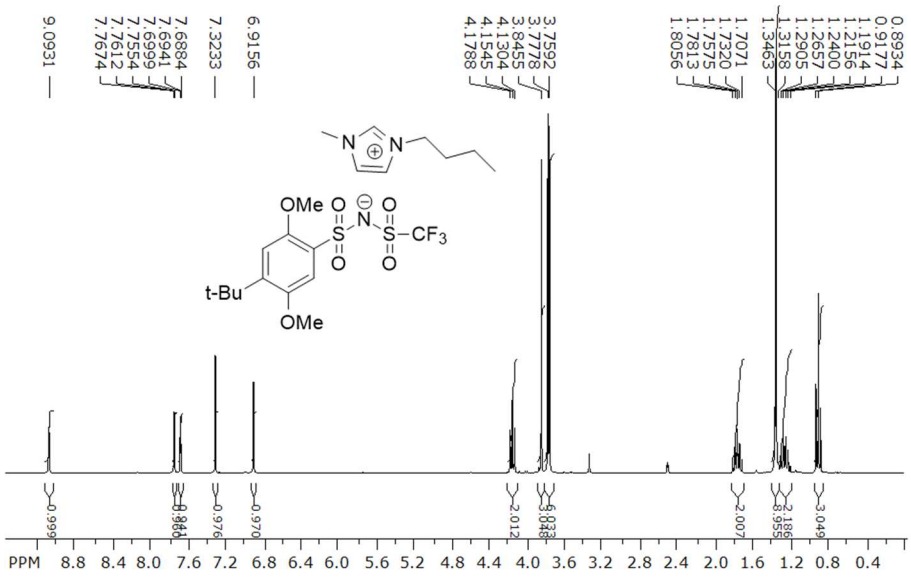

Figure S7.32. ^{1}H RMN (DMSO-d$_6$, 300 MHz): δ (ppm) = 9.09 (s,1H), 7.76 (t,1H), 7.69 (t,1H), 7.32 (s,1H), 6.92 (s,1H), 4.15 (t,2H), 3.85 (s,3H), 3.78 (s,3H), 3.76 (s,3H), 1.76 (q, 2H), 1.35 (s,9H), 1.32-1.19 (m,2H), 0.89 (t,3H). (BMIm MDB-NTf)

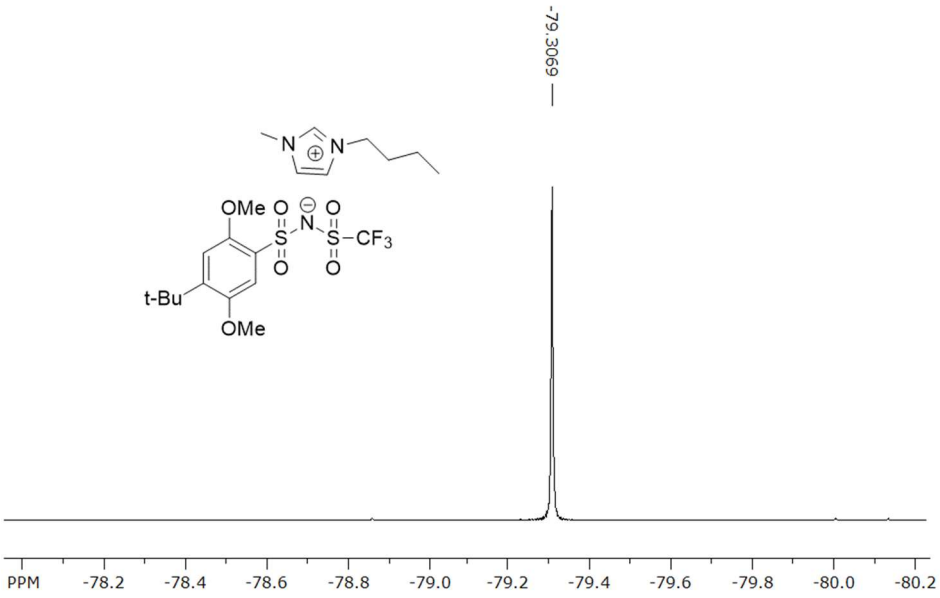

Figure S7.33. ^{19}F RMN (DMSO-d_6, 282 MHz): δ (ppm) = -79.31 (s,3F). (BMIm MDB-NTf)

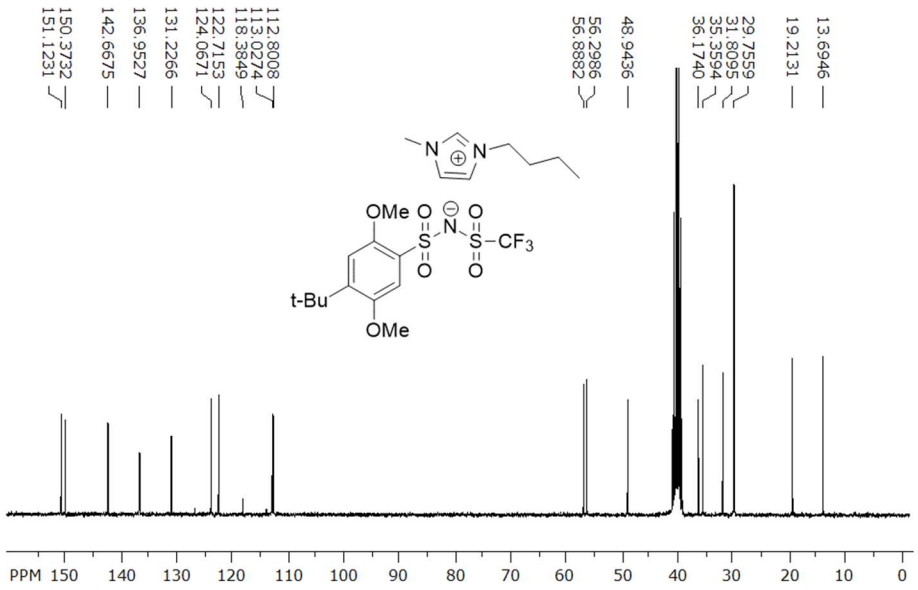

Figure S7.34. ^{13}C RMN (DMSO-d_6, 125 MHz): δ (ppm) = 151.12, 150.37, 142.67, 136.95, 131.23, 124.07, 122.72, 118.39, 113.03, 112.80, 56.89, 56.30, 48.94, 36.17, 35.36, 31.81, 29.76, 19.21, 13.69. (BMIm MDB-NTf)

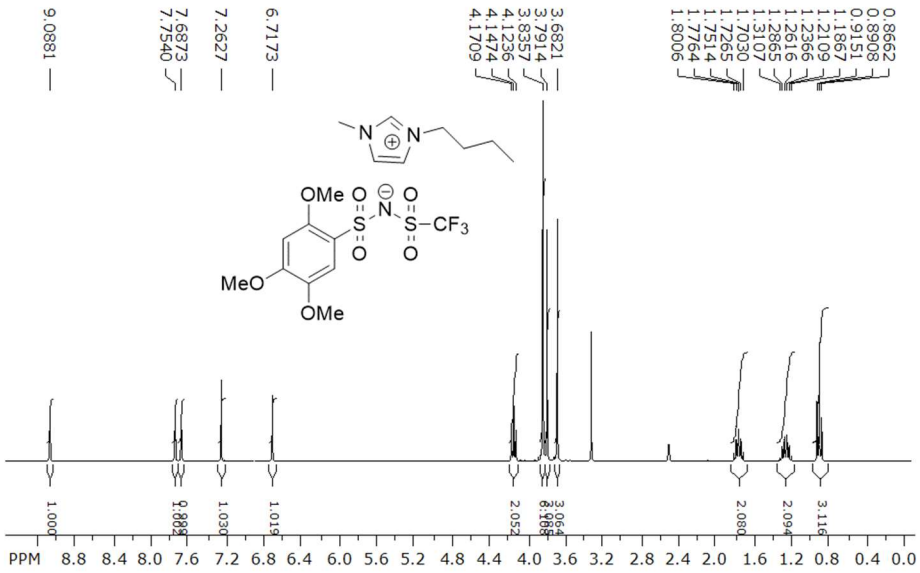

Figure S7.35. ^{1}H RMN (DMSO-d_6, 300 MHz): δ (ppm) = 9.09 (s,1H), 7.75 (t,1H), 7.69 (t,1H), 7.26 (s,1H), 6.72 (s,1H), 4.15 (t,2H), 3.84 (s,6H), 3.79 (s,3H), 3.68 (s,3H), 1.75 (q, 2H), 1.31-0.92 (m,2H), 0.89 (t,3H). (BMIm TMB-NTf)

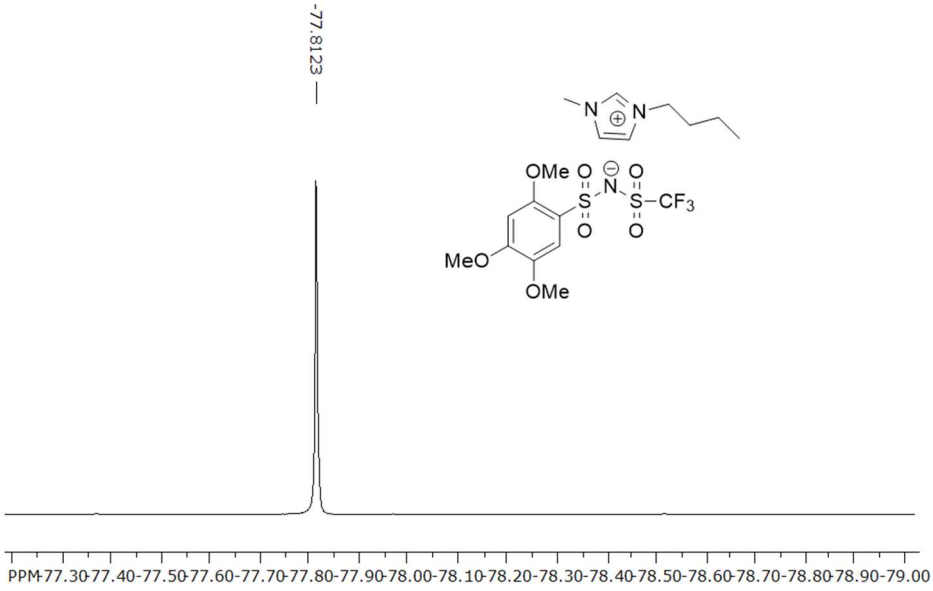

Figure S7.36. ^{19}F RMN (DMSO-d_6, 282 MHz): δ (ppm) = -77.81 (s,3F). (BMIm TMB-NTf)

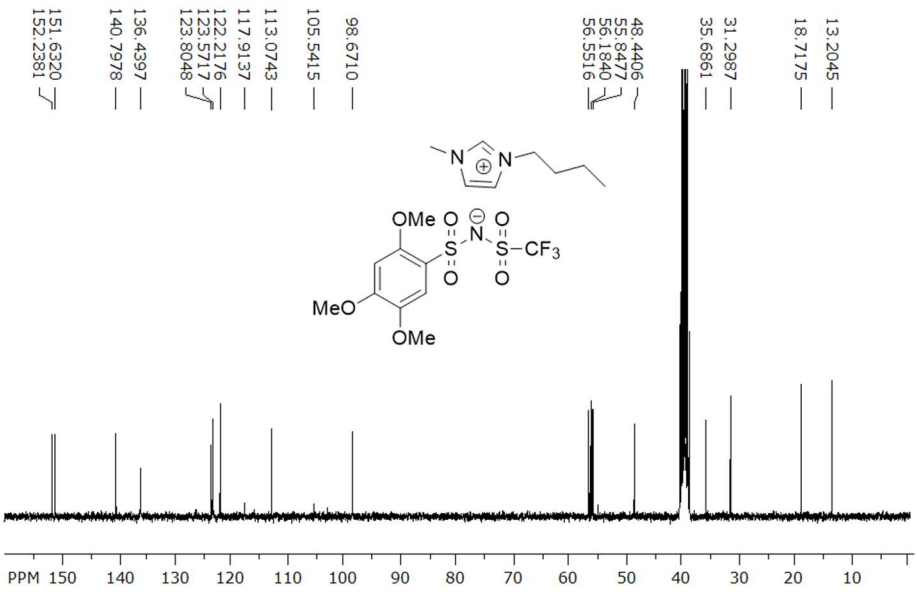

Figure S7.37. ^{13}C RMN (DMSO-d_6, 125 MHz): δ (ppm) = 152.24, 151.63, 140.79, 136.44, 123.80, 123.57, 122.22, 117.91, 113.07, 98.67, 56.55, 56.18, 55.85, 48.44, 35.69, 31.30, 18.72, 13.20. (BMIm TMB-NTf)

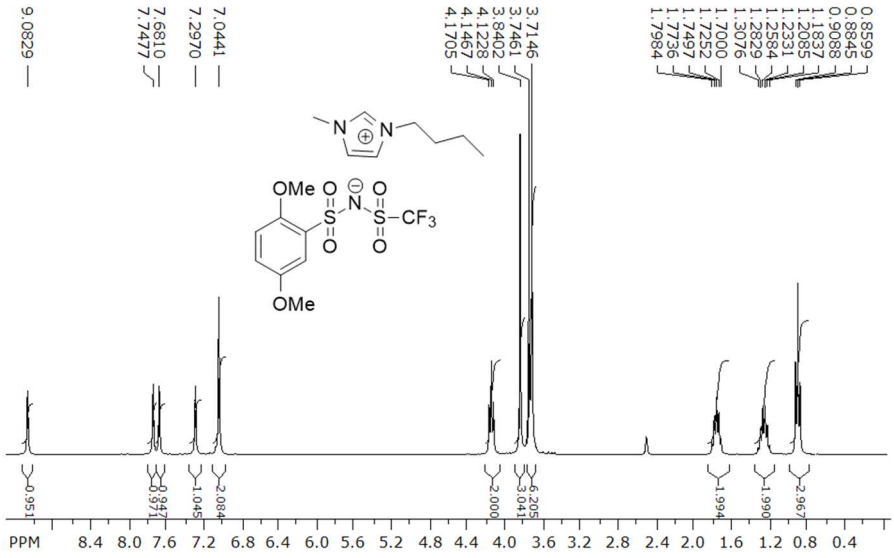

Figure S7.38. ^{1}H RMN (DMSO-d_6, 300 MHz): δ (ppm) = 9.08 (s,1H), 7.75 (s,1H), 7.68 (s,1H), 7.04 (s,1H), 4.15 (t,2H), 3.84 (s,3H). 3.73 (d,6H), 1.75 (q,2H), 1.25 (m,2H), 0.88 (t,3H). (BMIm DMB-NTf)

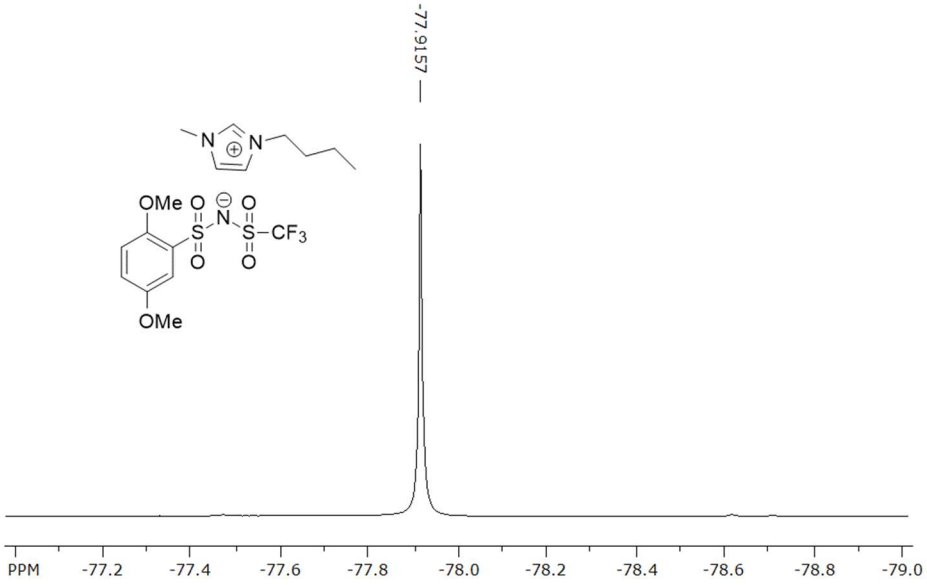

Figure S7.39. ^{19}F RMN (DMSO-d_6, 282 MHz): δ (ppm) = -77.92 (s,3F). (BMIm DMB-NTf)

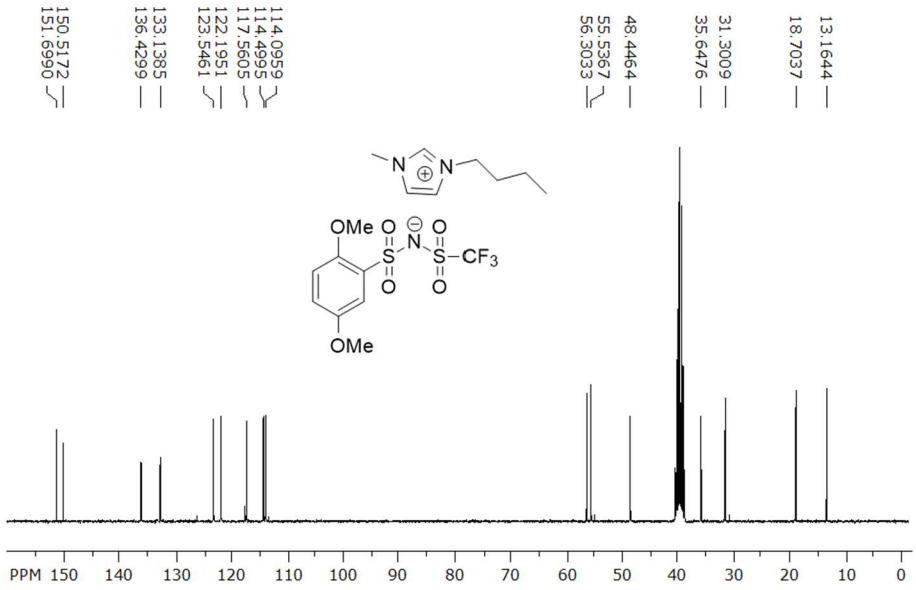

Figure S7.40. ^{13}C RMN (DMSO-d_6, 125 MHz): δ (ppm) = 151.70, 150.52, 136.43, 133.14, 123.55, 122.20, 117.56, 114.50, 114.10, 56.30, 55.54, 48.45, 35.65, 31.30, 18.70, 13.16. (BMIm DMB-NTf)

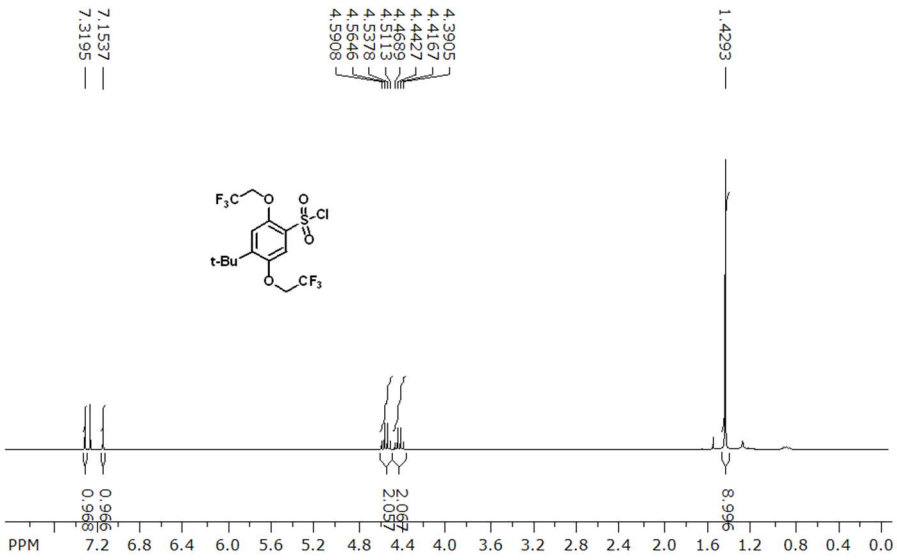

Figure S7.41. ^{1}H RMN ($CDCl_3$, 300 MHz): δ (ppm) = 7.32 (s,1H), 7.15 (s,1H), 4.55 (q,2H), 4.43 (q,2H) 1.43 (s,9H). (MDBF-SO_2Cl)

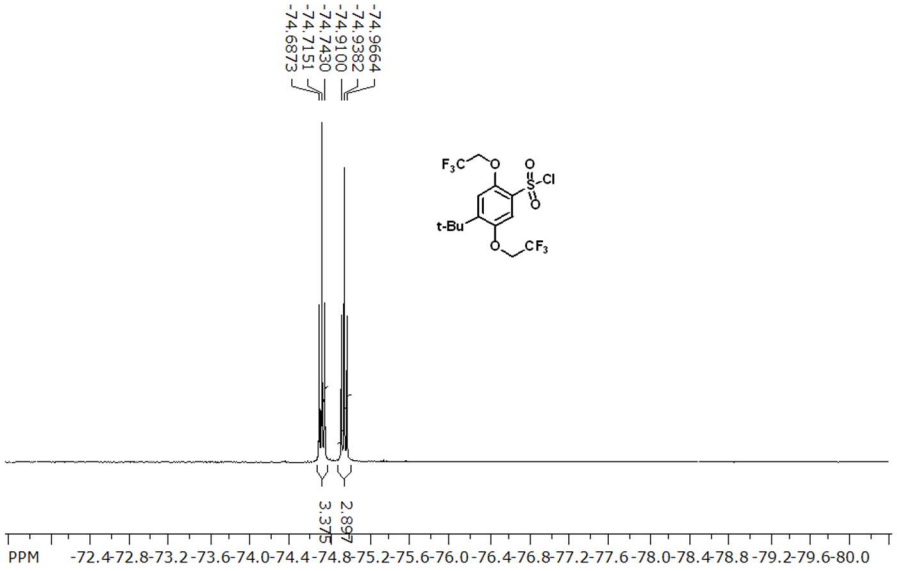

Figure S7.42. ^{19}F RMN ($CDCl_3$, 282 MHz): δ (ppm) = -74.72 (t,3F), -74.94 (t,3F). (MDBF-SO_2Cl)

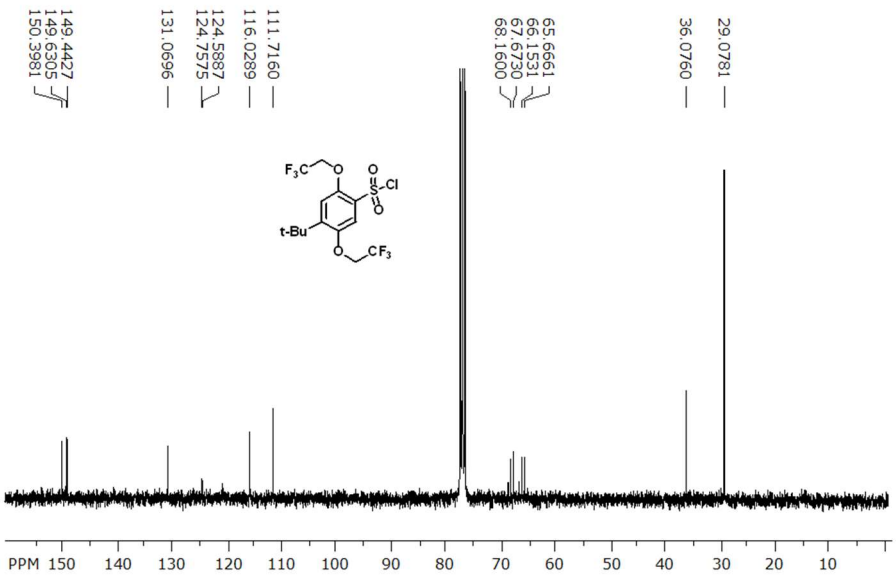

Figure S7.43. ^{13}C RMN ($CDCl_3$, 125 MHz): δ (ppm) = 150.40, 149.63, 149.44, 131.07, 124.76, 124.59, 116.03, 111.72, 68.16, 67.67, 66.15, 65.67, 36.08, 29.08. (MDBF-SO_2Cl

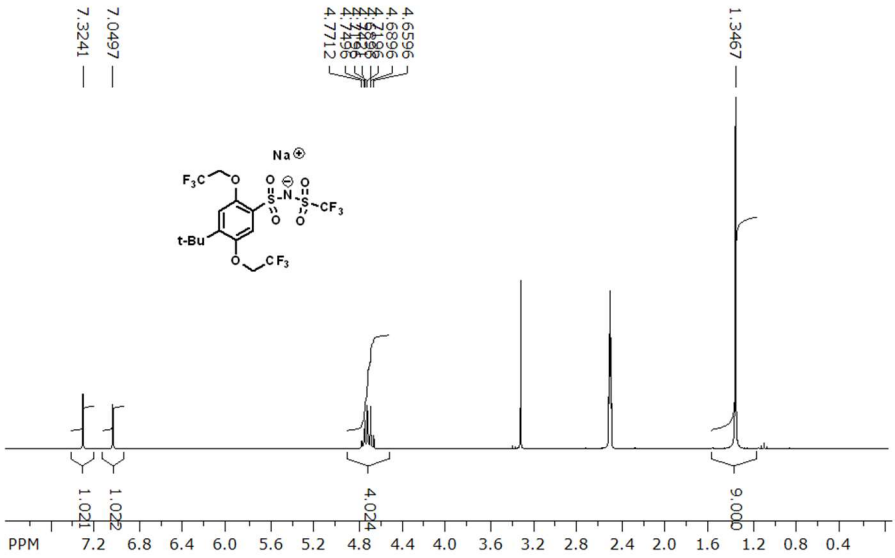

Figure S7.44. ^{1}H RMN (DMSO-d_6, 300 MHz): δ (ppm) = 7.32 (s,1H), 7.05 (s,1H), 4.77-4.66 (dq,4H), 1.35 (s,9H). (Na MDBF-NTf)

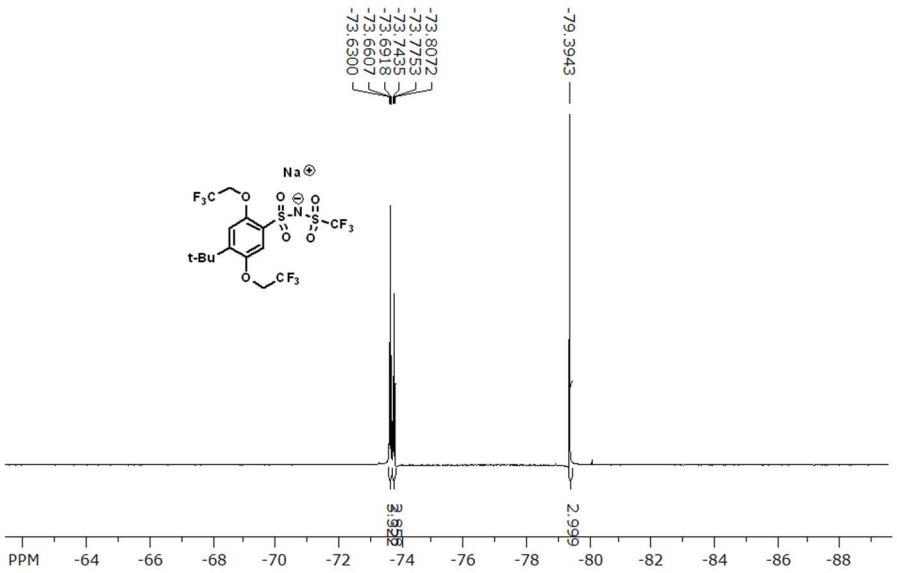

Figure S7.45. ^{19}F RMN (DMSO-d_6, 282 MHz) δ (ppm) = -73.66 (t,3F), -73.78 (t,3F), -79.39 (s,3F). (Na MDBF-NTf)

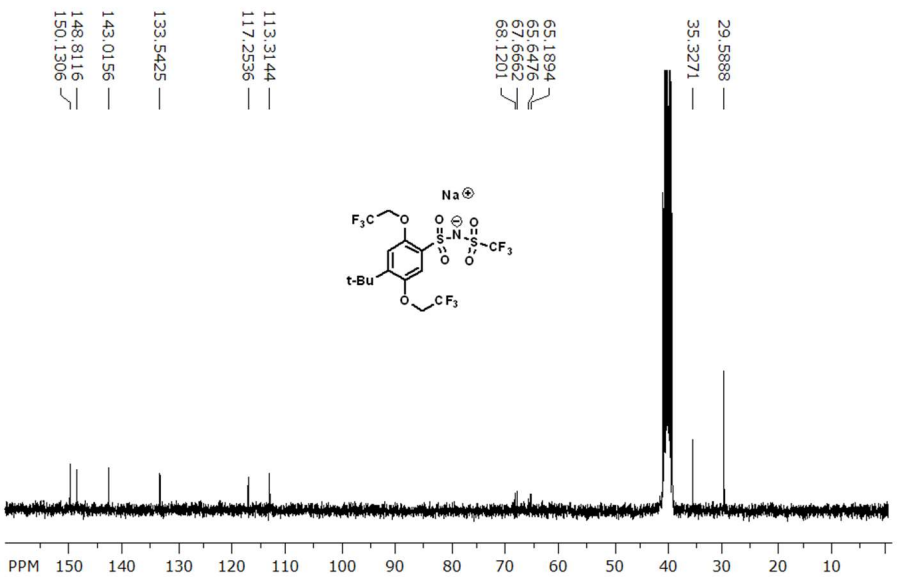

Figure S7.46. ^{13}C RMN (DMSO-d_6, 125 MHz): δ (ppm) = 150.13, 148.81, 143.02, 133.54, 117.25, 113.31, 68.12, 67.67, 65.65, 65.19, 35.33, 29.59. (Na MDBF-NTf)

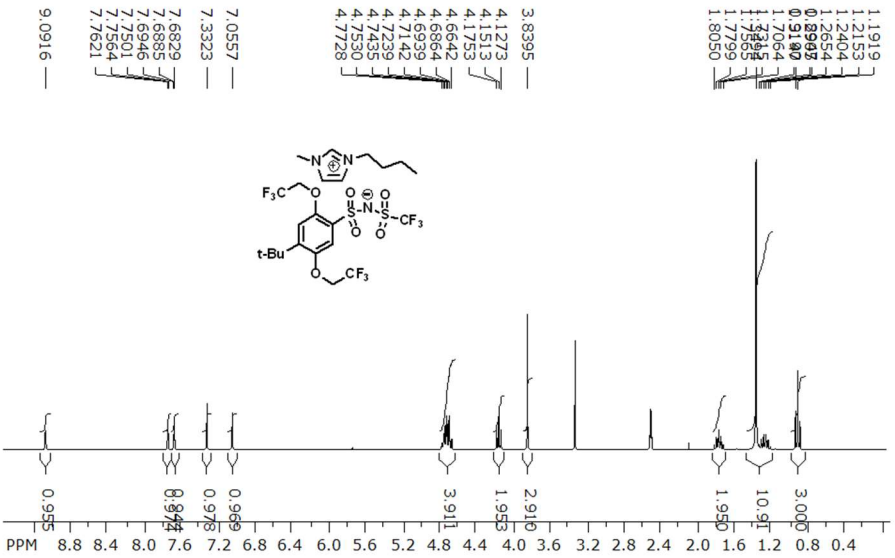

Figure S7.47. ^{1}H RMN (DMSO-d_6, 300 MHz): δ (ppm) = 9.09 (s,1H), 7.76 (t,1H), 7.69 (t,1H), 7.33 (s,1H), 7.06 (s,1H), 4.77-4.66 (dq,4H), 4.15 (t,2H), 3.84 (s,3H), 1.81-1.71 (m,2H) 1.35 (s,9H), 1.31-1.19 (m,2H), 0.89 (t,3H). (BMIm MDBF-NTf)

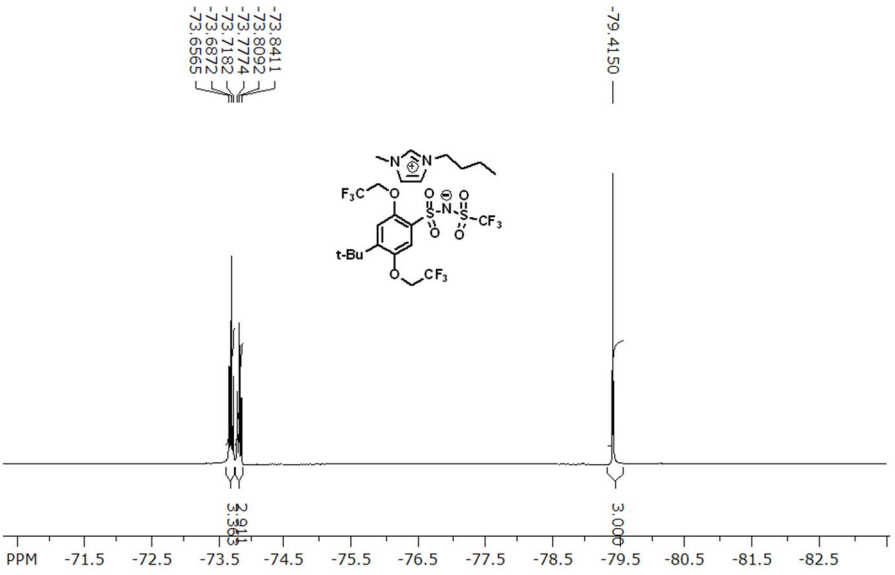

Figure S7.48. ^{19}F RMN (DMSO-d_6, 282 MHz) δ (ppm) = -73.69 (t,3F), -73.81 (t,3F), -79.42 (s,3F). (BMIm MDBF-NTf)

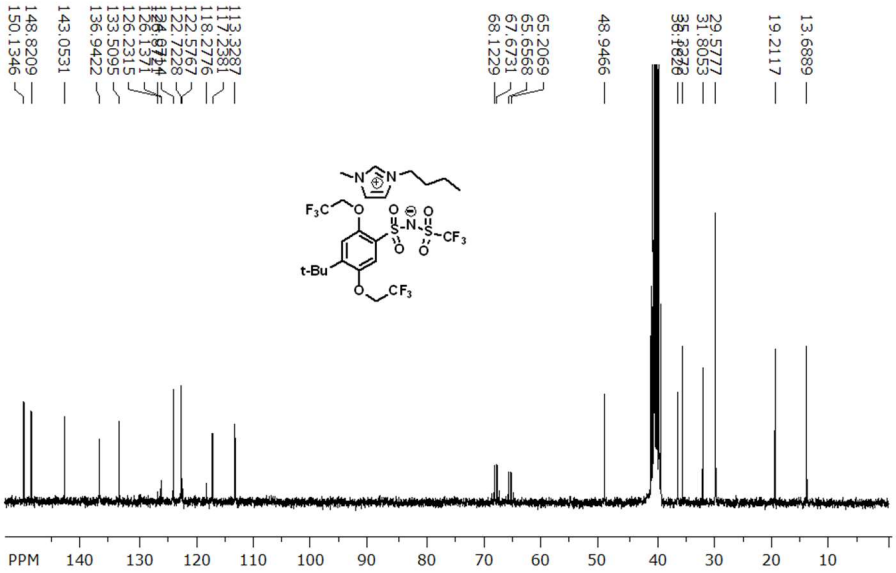

Figure S7.49. ^{13}C RMN (DMSO-d_6, 125 MHz): δ (ppm) = 150.13, 148.82, 143.05, 136.94, 133.51, 126.87, 126.23, 126.14, 124.07, 122.72, 122.58, 118.28, 117.24, 113.33, 68.12, 67.67, 65.66, 65.21, 48.95, 36.18, 35.33, 31.81, 29.58, 13.21, 13.69. (BMIm MDBF-NTf)

7.3.8. Thermal analysis

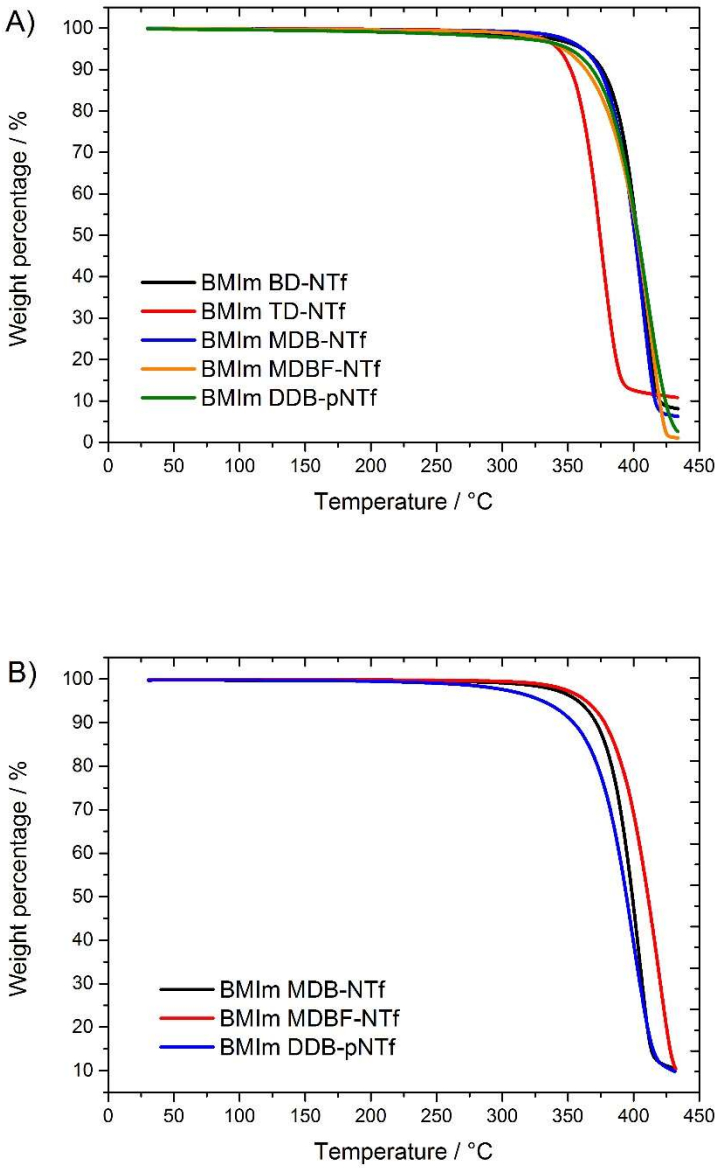

Figure S7.50. TGA thermograms of organic RILs based on DDB and triflimide anion with a ramp of 10°C per minute under A) helium or B) air atmosphere.

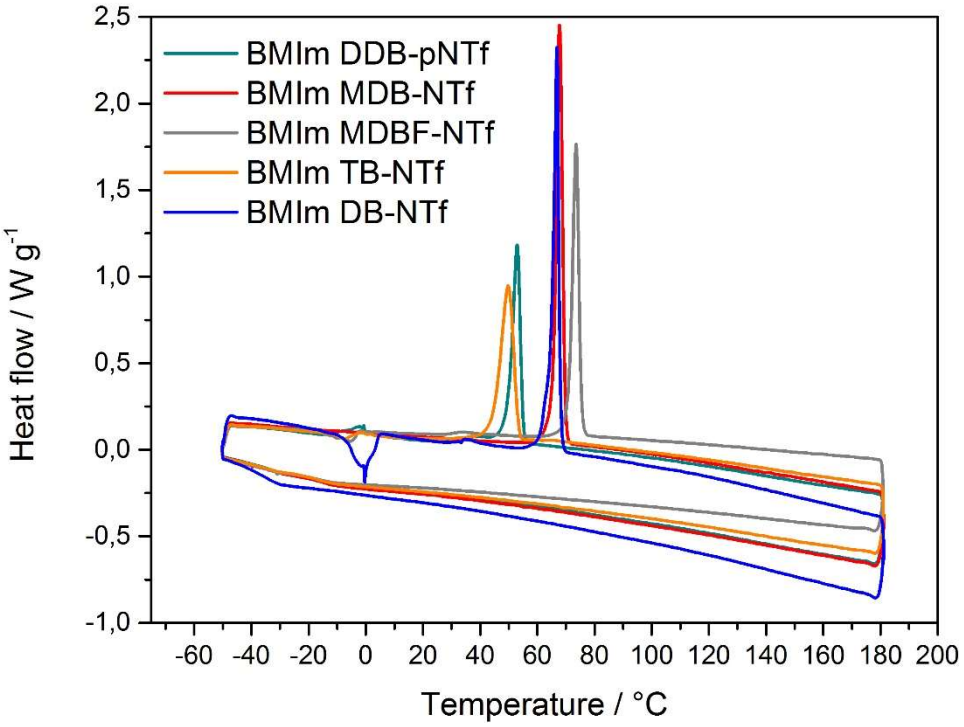

Figure S7.51. DSC thermograms of organic RILs based on DDB and triflimide anion. The measurements were done with a ramp of 5 °C per minute and with isothermal of 5 minutes between the cooling and heating. (exo, down)

7.3.9. Extra CVs of DDB and DDBF

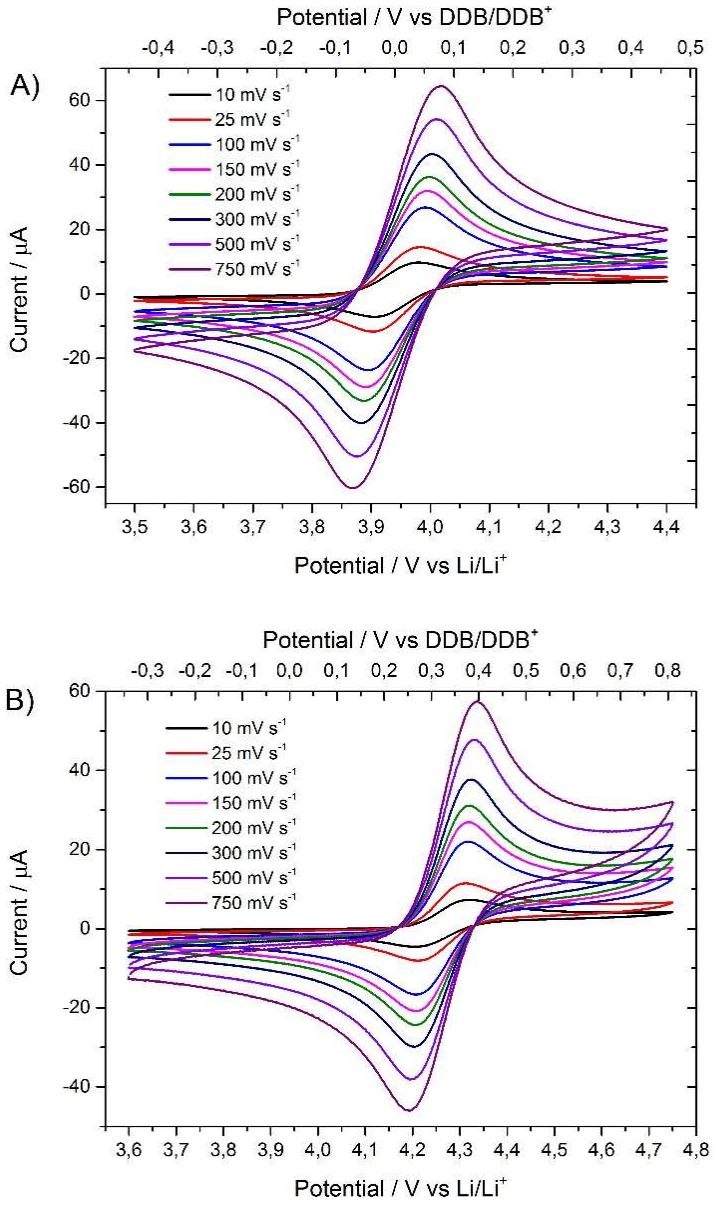

Figure S7.52. CVs of 10 mM solutions of A) DDB and B) DDBF in EC-DEC 1:2 (v/v) with 1.0 M Li [NTf_2] at various scan rates. The scan rates used were 10 to 750 mV s^{-1}.

7.3.10. Arrhenius/Eyring plots of ionic conductivity/fluidity

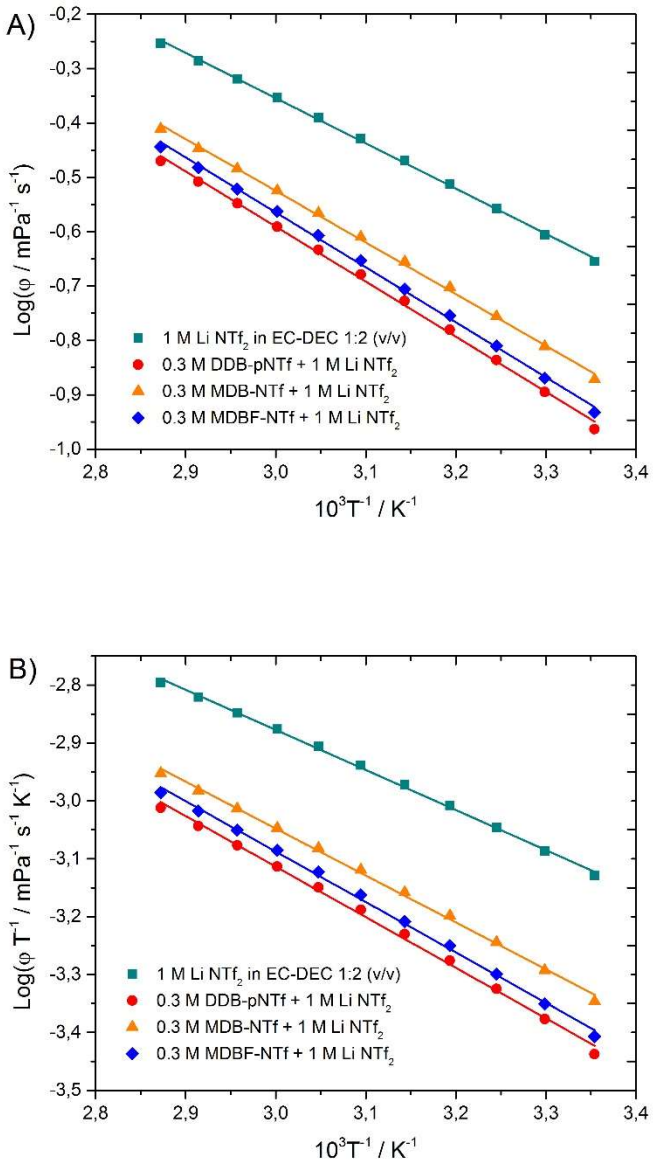

Figure S7.53. Arrhenius plots A) and Eyring plots B) for fluidity using 0.3 M solution of [BMIm] [DDB-pNTf], [BMIm] [MDB-NTf] and [BMIm] [MDBF-NTf] in EC-DEC 1:2 (v/v) with 1.0 M Li [NTf_2]. Measurements were done at 5°C intervals between 25 and 75°C.

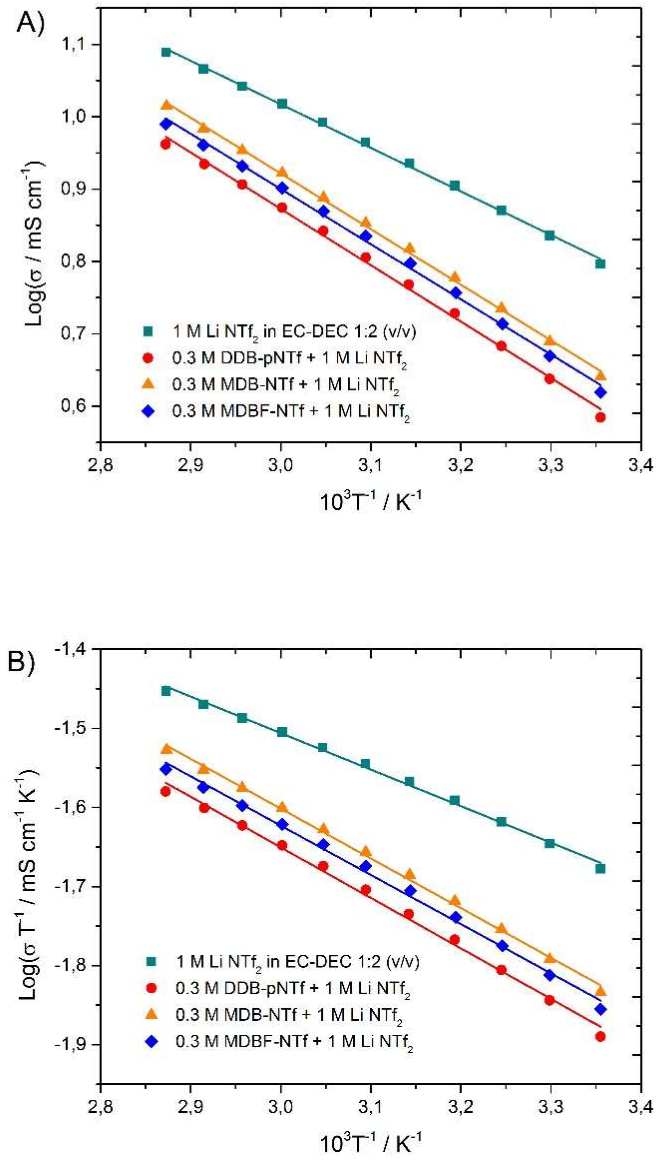

Figure S7.54. Arrhenius plots A) and Eyring plots B) for ionic conductivity using 0.3 M solution of [BMIm] [DDB-pNTf], [BMIm] [MDB-NTf] and [BMIm] [MDBF-NTf] in EC-DEC 1:2 (v/v) with 1.0 M Li [NTf_2]. Measurements were done at 5°C intervals between 25 and 75°C.

7.3.11. Reference

[1] J. Huang, I.A. Shkrob, P. Wang, L. Cheng, B. Pan, M. He, C. Liao, Z. Zhang, L.A. Curtiss, L. Zhang, 1,4-Bis(trimethylsilyl)-2,5-dimethoxybenzene: a novel redox shuttle additive for overcharge protection in lithium-ion batteries that doubles as a mechanistic chemical probe, J. Mater. Chem. A, 3 (2015) 7332-7337.
[2] A.V. Zaytsev, R.J. Anderson, A. Bedernjak, P.W. Groundwater, Y. Huang, J.D. Perry, S. Orenga, C. Roger-Dalbert, A. James, Synthesis and testing of chromogenic phenoxazinone substrates for [small beta]-alanyl aminopeptidase, Org. Biomol. Chem., 6 (2008) 682-692.

Chapitre 8 : Dispositif électrochromique utilisant un anion redox à base de ferrocène et le viologène

8.1. Avant-propos et mise en contexte

Ce chapitre a été rédigé sous forme d'un article qui a été soumis à *ACS Applied Materials Interfaces*. Cet article est une preuve de concept qui présente l'emploi d'un liquide ionique électroactif oxydant en présence du viologène, une espèce réductrice, dans l'objectif de fabriquer un dispositif électrochromique. La propriété intéressante de ce dispositif est qu'il ne nécessite aucune énergie pour revenir à transparent et ce comportement est intéressant pour quelques applications. Quand il y a un potentiel appliqué, il y a une réaction électrochimique à chaque interface verre conducteur|électrolyte et quand il n'a aucune différence de potentiel, les espèces électroactives produites sont impliquées dans une réaction d'oxydoréduction au cœur de l'électrolyte. L'électrolyte et les dispositifs électrochromiques sont caractérisés et présentés dans l'article suivant.

8.2. Air-stable, self-bleaching electrochromic device based on viologen and ferrocene-containing triflimide redox ionic liquids

*Bruno Gélinas, Dyuman Das, Dominic Rochefort**

[1]Département de chimie, Université de Montréal, CP6128 Succ. Centre-Ville, Montréal, Québec, Canada H3C 3J7

ACS Appl. Mater. Interfaces, 9 (2017) 28726-28736.

DOI: 10.1021/acsami.7b04427. Publication Date (Web): July 21, 2017.

8.2.1. Table of contents graphic:

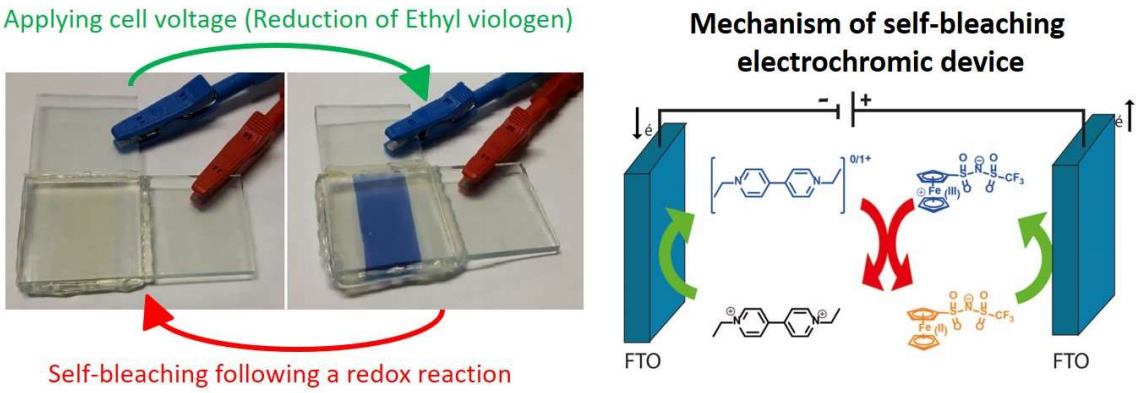

8.2.2. Abstract

We demonstrate an electrochromic device with self-bleaching ability that uses ethyl viologen- ($[EV]^{2+}$) and ferrocene-based redox ionic liquids ($[FcNTf]^{-}$) as the electroactive species. These electroactive compounds are insensitive to atmospheric O_2 and H_2O in both their oxidized and reduced states once dissolved in a typical ionic liquid electrolyte ($[BMIm][NTf_2]$), allowing for the device to be assembled outside a glovebox without any encapsulation. This device could generate a deep blue color by the application of a 2.0 V

potential between two fluorine-doped tin oxide (FTO) substrates to oxidize the ferrocenyl centers to $[FcNTf]^0$ while reducing viologen to $[EV]^{+\bullet}$. Self-bleaching occurs at OCP as $[EV]^{+\bullet}$ and $[FcNTf]^0$ undergo homogeneous electron transfer in the electrolyte. The mass transport of ethyl viologen and ferrocenylsulfonyl(trifluoromethylsulfonyl)imide ($[FcNTf]^-$) anion was evaluated by double potential step chronoamperometry to study the impact of the diffusion coefficient on the self-bleaching mechanism. The electrochromic device demonstrated here shows a contrast ΔT (610 nm) around 40% at 2.0 V as colored cell voltage, a switching time in the order of few seconds for coloration and bleaching, coloration efficiency of 105.4 to 146.2 $cm^2\ C^{-1}$ at 610 nm, and very high stability (94.8% ΔT after 1000 cycles) despite the presence of O_2 and H_2O in the electrolyte.

Keywords: Electrochromic materials and devices, redox ionic liquids, viologen, diffusion coefficient.

8.2.3. Introduction

Electrochromic materials (ECMs) possess the ability to change their optical properties, such as absorbance and transmittance, under the influence of an external electrical stimulus. Electrochromic devices (ECDs) employing ECMs can find applications in smart windows, antiglare mirrors, optical displays, and sensors. ECDs stand out from other color-switching devices by the simplicity of their construction, which consists of the integration of the electrolyte containing the ECMs between two transparent conducting electrodes such as indium tin oxide (In_2O_3/SnO_2, ITO) or fluorine-doped tin oxide (SnO_2/F, FTO) coated glass slides. These constituents can be applied in ECDs via three configurations. The optical battery-like configuration where the immobilized anodic and cathodic active layers are separated by a thin-film electrolyte, the solution-phase configuration in which the ECMs are dissolved in the liquid or polymeric electrolyte and the hybrid structures, which consists of a combination between layer(s) and electroactive solution.[1] ECDs using a battery-like configuration show an open circuit memory because the electrochromic species are bound on the substrate surface. This means that they will maintain their coloration at open circuit potential (OCP) and require the application of a potential to revert to the original state. Solution-phase ECDs, however, will revert to their initial colored state without the help of an external stimulus at a rate that depends on the

mass transport of electroactive species. This report deals with the latter. Normally, the solution-phase ECDs are faster optical switching devices than the optical-battery ECDs.

Many electrochromic materials for optical switching devices have been investigated in these various configurations. Metal oxide–metal complexes (e.g., oxides of W, Ni, Ir, V, Ti, Co, and Mo[1-7] and Prussian blue),[8-10] metallo-supramolecular polymers,[11-13] conductive organic polymers,[14-16] dimethyl terephthalate,[17] metal phthalocyanine,[18] and free and polymeric viologen[19, 20] have been shown to possess the required spectroelectrochemical properties for a use as ECM. The well-known ethyl viologen dication (1,1′-diethyl-4,4′-dipyridinium, [EV], **Figure 8.1**) presents three redox states (dication, radical cation, and neutral viologen) and was selected here as the cathodic species. [EV] is colorless in its oxidized state, but the reduced state of viologen (radical [EV]) shows an intense blue color because of intramolecular optical charge transfer between the charged nitrogen (+1) and zero-valence nitrogen, in which the delocalization provides a good electrochemical stability.[21-24] The molar extinction coefficient of radical methyl viologen is 13 900 M^{-1} cm^{-1} at 607 nm in acetonitrile.[25] The colors of radical cations are dependent on the type of substituents in the nitrogen position. For example, 1,1′-bis(4-cyanophenyl)-4,4′-bipyridinium gives a green color,[26] while alkyl side-chain substituents promote a deep blue color. While [EV] could be used on its own to generate a high-enough contrast due to its high ε, the use of an anodic species is generally required to define a maximum voltage at the positive electrode and to prevent unwanted electrochemical decomposition of the electrolyte.[21, 27] In addition, self-bleaching at OCP can only occur in the presence of an anodic species. Moon et al. presented a low-voltage ECD (<1 V), employing methyl viologen and ferrocene as the cathodic and anodic species, respectively.[28] However, this ECD using gel polymer electrolyte showed a moderate cycling stability as their device showed a limited relative transmittance (ΔT) of 60% after operating for 24 h.[28] Ferrocene have been added to the electrolyte as redox shuttle with which to obtain shorter response time for the switching device using viologen polymeric in optical-battery-type ECD.[29] In the hybrid ECD configuration, viologen adsorbed on oxide titanium with electrolyte containing ferrocene as the redox shuttle and anodic species have been demonstrated.[30] Ionic liquids (ILs) could be used advantageously in such devices to improve the electrochemical stability of the electrolyte

and decrease the volatility of the solvent, which would result in a device with enhanced stability. However, doing so would result in a solubility issue of the electroactive species, which are generally much less soluble in ILs. For example, Compton and co-workers determined that the solubility of ferrocene (Fc) in 1-butyl-3-methylimidazolium bis(trifluoromethylsulfonyl)imide ([BMIm] [NTf_2]) at ambient temperature is 77 mM, showing poor solubility in this medium.[31] Charged species are often more soluble in ILs than their neutral form. Yang et al. showed that Fc^+ is more soluble than Fc.[32] Dimethylferrocene was proposed by Moon et al. to improve anodic species concentration in IL gel electrolyte,[33] but the level of solubility and rate of dissolution of neutral Fc derivatives in ionic liquid is highly sensitive to the residual water content. The motivation is the development of a simple assembly of ECD and the exposure of components to air and moisture.

In this report, we propose the use of redox ionic liquids to solve this issue and to increase the stability of ECD. The ionic liquid [BMIm] [NTf_2] was selected as the electrolyte, to which we added ethylviologen as the [NTf_2] salt (**Figure 8.1**, [EV]) and ferrocenylsulfonyl(trifluoromethylsulfonyl)imide anion (**Figure 8.1**, [FcNTf]) as the cathodic and anodic electroactive species, respectively. To identify the most-suitable ionic liquid for a use in ECD, different redox ionic liquids (RILs) based on [FcNTf] with different counter cations such as 1-butyl-3-methylimidazolium [BMIm], trimethylbutylammonium [Me_3BuN], butylpyridinium [BPyr], and 1-butyl-1-methylpiperidinium [MBPip] were prepared. We will begin by discussing on the transport and electrochemical properties of redox ionic liquids based on the [FcNTf] anion as a function of the cation structure (see **Figure 8.1**) to establish structure–property relationships. Diffusion coefficients at different temperatures were measured by double-potential-step chronoamperometry (DPSC) using a microelectrode. Spectroelectrochemical analysis and EDC performance using [EV] and [FcNTf] are then reported and the [FcNTf] concentration impact on the electrochromic ability of viologen evaluated. The performance of the all-ionic liquid ECD during electrochromic transitions is then assessed.

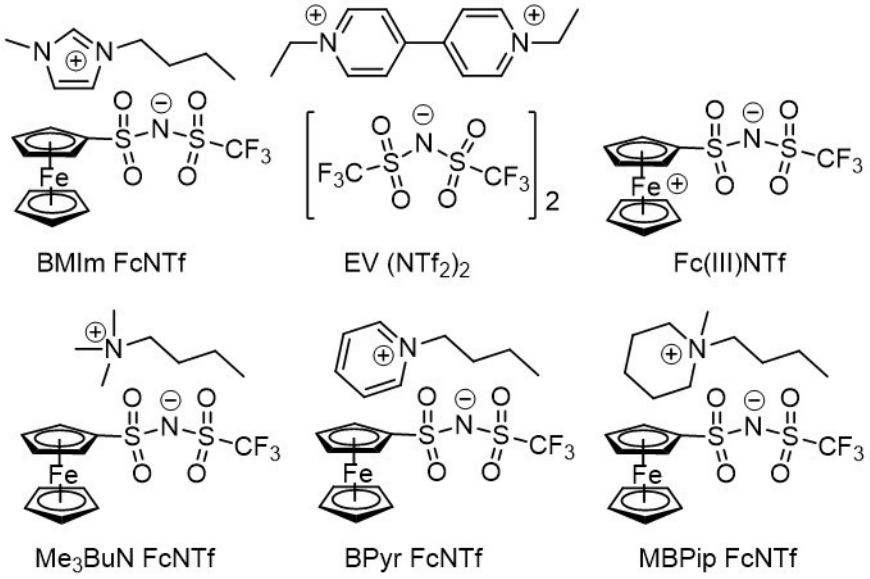

Figure 8.1. Chemical structure of redox ionic liquids based on ferrocenylsulfonyl(trifluoromethylsulfonyl)imide [FcNTf] with different counter cations : 1-butyl-3-methylimidazolium [BMIm], Trimethylbutylammonium [Me_3BuN], Butylpyridinium [BPyr] and 1-Butyl-1-methylpiperidinium [MBPip]. Ferrocenium sulfonyl(trifluoromethylsulfonyl)imide [Fc(III)NTf] and ethylviologen di[bis(trifluoromethylsulfonyl)imide] ([EV] [$(NTf_2)_2$]) are also shown.

8.2.4. Experimental

Material and electroactive species characterization

The detailed procedures followed for the synthesis of [FcNTf] and its ionic liquids are available in the Supporting Information. The reagents ferrocene, chlorosulfonic acid, phosphorus trichloride, anhydrous potassium carbonate, 1-butyl-3-methylimidazolium bromide, 1-bromobutane, bromobutane, trimethylamine solution, lithium bis(trifluoromethylsulfonyl)imide, and 4,4′-dipyridyl, which were obtained from Sigma-Aldrich (highest purity grade available, unless stated otherwise). Trifluoromethanesulfonamide was purchased from Synquest Laboratories, and solvents were obtained from Fisher. All ILs such as 1-butylpyridinium bromide, 1-butyl-1-methylpiperidinium bromide, 1-butyl-3-methylimidazolium bis(trifluoromethylsulfonyl)imide, butyltrimethylammonium

bis(trifluoromethylsulfonyl)imide, 1-butylpyridinium bis(trifluoromethylsulfonyl)imide, and 1-butyl-1-methylpiperidinium bis(trifluoromethylsulfonyl)imide were purchased from Iolitec. These were used as received. All compounds synthesized were characterized by ^{1}H, ^{19}F, and ^{13}C NMR on a Bruker AMX 300 MHz spectrometer at room temperature using DMSO-d_6 and by direct injection electrospray ionization mass spectrometry. Accurate mass values were obtained by Agilent liquid chromatograph/ mass selective detector time-of-flight (LC/MSD TOF) instrument. Elemental analysis of all RILs was performed on the EAS 1108 apparatus from Fisons Instruments SPA. The water used in the procedures was purified with a Milli-Q system to a resistivity of 18.2 MΩ·cm (25 °C). The synthetic details are described in the Supporting Information. BMIm FcNTf and Fc(III)NTf were also investigated by XPS (**Table S8.1–S8.3** and **Figure S8.1–S8.4**). Electrochemical grade tetrabutylammonium perchlorate (TBAP; Sigma-Aldrich) was used as supporting electrolyte to measure the microelectrode radius. The water content of all commercial ILs (Iolitec) was found around 150 ppm using Karl Fischer method, which is a typical value,[34] and ILs were stored in glovebox.

Thermal analysis

Thermogravimetric analysis (TGA) was performed on TGA Q500, TA Instruments, and the measurements were done under a helium atmosphere from room temperature to 450 °C with a ramp of 10 °C per min. The decomposition temperature was determined at a 5% weight loss. TGA was coupled with Discovery MS (TA Instruments) to follow the weight loss. Differential scanning calorimetry (DSC) was accomplished via a DSC2910 device (TA Instruments) and universal analysis software. The measurements were done with a ramp of 5 °C per minute and with an isothermal of 5 min between the cooling and heating.

Electrochemical Analysis

The cyclic voltammetry (CV) experiments were done using a standard three-electrode heart-shaped cell with a Pt macrodisk working electrode, a Pt wire counter electrode, and a Pt wire pseudoreference on a BioLogic SP-50 potentiostat controlled via EC-lab software. The specific surface area of the Pt working macroelectrode was determined to be 0.022 cm^2 (geometric area of 0.020 cm^2) using the CV response of a potassium ferricyanide aqueous solution (1 M KCl). The working electrode was polished with alumina, rinsed, sonicated, and dried before each experiment. The solutions were degassed with a flow of argon for 15 min prior to measurements, which was maintained over the surface of the solution during measurements. All potentials are reported to the midpoint potential of the ferrocene and ferrocenium (Fc/Fc^+) redox couple, which was recorded in the same media. CV was also carried out on FTO-coated glass slide working electrodes to evaluate the effect of substrate on the electrochemical response prior to building the ECDs. To do so, the substrate was placed at the bottom of a specifically designed PTFE cell.

The diffusion coefficients were measured using a Pt microdisk electrode (100 μm diameter) using double potential step chronoamperometry (DPSC) with the data analysis proposed by Compton et al.[35, 36] The microelectrode radius was determined from steady-state voltammetry measurements on ferrocene solutions at different concentrations (0.5, 1.0, and 2.0 mM) in acetonitrile containing 0.1 M tetrabutylammonium perchlorate. The microelectrode radius (54 ± 1 μm) was calculated using Fc diffusion coefficient reported in the literature (2.3×10^{-9} m^2 s^{-1}).[35, 36] Chronoamperometric experiments were performed inside thermostated box, which also acted as a Faraday cage. The microelectrode was modified with a PTFE heat-shrink tubing to create a cavity at the end of electrode into which a small volume of the sample was placed. The microelectrodes was placed in a T-cell with a Ag wire pseudoreference and counter electrode under an argon atmosphere. An equilibrium potential was maintained for 5 s, at which point the zero faradaic current was measured. Next, the step potential was applied at higher potential than midpoint potential for an oxidation and a lower potential for a reduction. The current decay was measured for 5 s, and the data points were recorded at every 10 ms or 10 nA. The time-

dependent current response obtained on the forward step was analyzed by the Shoup and Szabo eq (eq 1) using Origin software (nonlinear curve fitting function):

$$i = 4nFDCr\, f(\tau) \quad (1)$$

$$where\ \ f(\tau) = 0.7854 + 0.8862\left(\frac{Dt}{r^2}\right)^{-\frac{1}{2}} + 0.2146\exp\left(-0.7823\left(\frac{Dt}{r^2}\right)^{-\frac{1}{2}}\right)$$

where n is the number of electrons, F is the Faraday constant, C is the electroactive species concentration, r is the microelectrode radius, and D is the diffusion coefficient. Such DPSCs were recorded at room temperature and from 35 to 75 °C at 10 °C intervals.[31, 37]

Fabrication of the electrochromic device

Fluorine-doped tin oxide (FTO, R_{sh} = 7 Ω/sq) coated glasses were cut into 2.5 × 5.0 cm^2 surfaces and used as the conducting substrates. Prior to mounting, the substrates were ultrasonically cleaned by acetone for 15 min and were dried. The two FTO-coated slides were separated by two fine stripes of a 30 μm thick thermoplastic sealant (Surlyn-30, Dyesol) to create a cavity for the electrolyte, and the assembly was hot-pressed. The cell was filled by the electrochromic electrolyte composed of a solution of [Cat][FcNTf] and [EV][NTf_2] at various concentrations in an ionic liquid. The ECDs were finally sealed with hot-melt adhesive. The entire procedure was carried out in ambient air.

Spectroelectrochemical analysis

Spectroelectrochemical measurements were done using a BioLogic SP-50 potentiostat coupled with an Ocean Optic spectrometer. The UV–vis spectra of the electrochromic species were recorded using a Pt mesh working electrode and two Pt wires as the counter and pseudoreference electrodes. Quartz spectroelectrochemical cells with an optical path length of 1 mm were used. Measurements on the ECD were done using a square wave potential step method to determine the response times. In this double potential

step experiment, the potential was set at an initial value of 0 V versus OCP for 30 s and then stepped to 2.0 V for another 30 s. Transmittance change (ΔT) was recorded at 610 nm, and switching times were taken when 95% of the transmittance plateau was reached.

8.2.5. Results and discussion

Thermal characterization of [FcNTf] redox ionic liquids and viologen electroactive salt

The thermochemical properties of [EV] [$(NTf_2)_2$] and of the redox ionic liquids (RIL) based on the [FcNTf] anion were studied as a function of the different cation structure listed in **Figure 8.1**. **Table 8.1** reports all of the thermochemical properties of different electroactive species in this study, and the TGA/DSC thermograms are presented in **Figure S8.5** and **S8.6**. [EV] [$(NTf_2)_2$] was thermally stable up to its decomposition temperature (T_d) of 380 °C measured at a 5% weight loss (see the DSC thermogram in **Figure S8.6A**). DSC shows the T_m of the [EV] [$(NTf_2)_2$] used here at 136 °C. Luis et al. reported a melting point (T_m) for the methyl viologen [MV] [$(NTf_2)_2$] at 130 °C,[24] showing a low impact of the substituent chain length. We also observed the crystallization of [EV] salt happening at 98 °C (see the DSC thermogram in **Figure S8.6A**), which is 38 °C lower than the T_m, and this temperature interval between the melting and crystallization suggest a supercooled state commonly observed for ILs. For the [FcNTf] RIL family, we reported T_d close to each other from 294 to 322 °C regardless on the nature of the cation used to form the ionic liquid. This is explained by the fact that the decomposition these RIL is initiated by the breaking of the S–C bond linking cyclopentadienyl to the trifluoromethylsulfonylimide moiety, which is common to all of our RILs. This claim is further supported by the finding that decomposition temperature of the isolated oxidized form of the anion, [Fc(III)NTf], is lower than [FcNTf]. Sulfur dioxide is released during degradation (TGA-MS) as expected from the known decomposition pathway of triflimide anion.[38] DSC shows that the T_m of the electroactive species based on [FcNTf] anion is strongly affected by the cation structure. [BMIm] [FcNTf], [BPyr] [FcNTf], [Me_3BuN] [FcNTf], and [BMPip] [FcNTf] melt at 55.1, 63.7, 99.5, and 116.1 °C, respectively. The T_m trend of these [FcNTf] electroactive species follows the trend of unmodified and common IL but with a higher T_m due to additional interactions with the ferrocene centers. The zwitterionic

[Fc(III)NTf] redox species presents no melting point transition below the T_d. This is very different from the T_m of ferrocenium [NTf_2] (here, the ferrocenium is the cation, and it is not bound to the triflimide) of 131.5 °C reported by Mochida and Inagaki.[39] Strictly speaking, only [BMIm] [FcNTf], [BPyr] [FcNTf], and [BMPip] [FcNTf] can be considered as redox ionic liquids according to the melting temperature below 100 °C criterion. The other species will be referred to as electroactive salts.

Table 8.1. Thermochemical properties of neat [FcNTf] and [EV] RIL.

RILs	**T_m (T_c) / °C**	**T_d / °C**
BMIm FcNTf	55.1	297
BPyr FcNTf	63.7	303
BMPip FcNTf	99.5	322
Me_3BuN FcNTf	116.1	294
Fc(III)NTf	-	216
EV $(NTf_2)_2$	135.8 (98.0)	380

Electrochemical and transport properties [FcNTf] and [EV] in IL

The response times for the color generation and self-bleaching of solution-phase ECDs are strongly correlated to the electrochemical and mass-transport properties of the electrochromic species dissolved in the electrolyte. Such properties are still unknown for the electroactive ionic liquids and salts described here and must be defined. The cyclic voltammograms of **Figure 8.2** shows the midpoint potentials of the [EV] dication at −0.79 V (first exchanged electron) and −1.21 V versus Fc/Fc^+ (second exchanged electron), while that of [FcNTf] anion was found at 0.27 V versus Fc/Fc^+. These redox potentials ($E^{0\prime}$) are presented in **Table 8.2**, and the difference between the $E^{0\prime}$ of the anodic and cathodic species is 1.06 V. The CVs of [Fc(II)NTf] and [Fc(III)NTf] at different scan rates are presented in the Supporting Information, and the linearity of the Randles–Sevcik plot ($I_p \alpha v^{1/2}$) between 10 and 500 mV s^{-1} confirm the reversible electrochemistry of [FcNTf](**Figure S8.7**).[40] FTO transparent electrode was compared to Pt, and the CVs

employing different working electrodes show that FTO has good catalytic properties for both the [FcNTf] anion and the viologen (**Figure S8.8**).

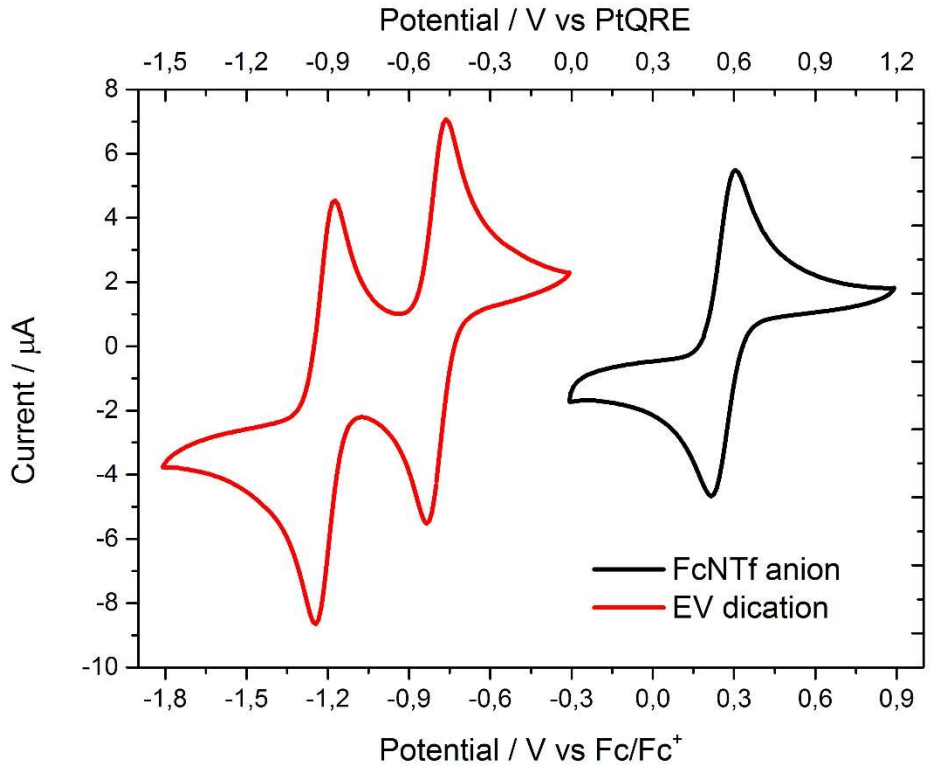

Figure 8.2. CVs of 10 mM solution of [EV] dication and [FcNTf] anion in [BMIm] [NTf_2] performed using Pt disk working electrodes at 100 mV s^{-1}.

Table 8.2. Potential parameters obtained from CV at 100 mV s^{-1} of 10 mM solution of [EV] dication and [FcNTf] anion in [BMIm] [NTf_2].

Electroactive ions	Midpoint Potential (1) / V vs. Fc/Fc^+	ΔE_{pa-pc} / V	Midpoint Potential (2) / V vs. Fc/Fc^+	ΔE_{pa-pc} / V	ΔE of midpoint potential (EV^+/ EV^{2+} and $FcNTf^-$ /$FcNTf^0$) / V
FcNTf	0.261	0.08	-	-	1.06
EV	-0.798	0.07	-1.211	0.08	

The diffusion coefficients of electroactive species in the [BMIm] [NTf_2] electrolyte were obtained from DPSC using a disk microelectrode (**Table 8.3**). The time-dependent current responses of the forward potential steps using Shoup and Szabo fitting (eq 1) are presented in **Figure 8.3A**, and coefficients of 1.65, 1.01, and 2.12 × 10^{-7} cm^2 s^{-1} were found for [BMIm] [FcNTf], [Fc(III)NTf], and [EV] [[NTf_2)$_2$], respectively (at 10 mM in [BMIm] [NTf_2]).

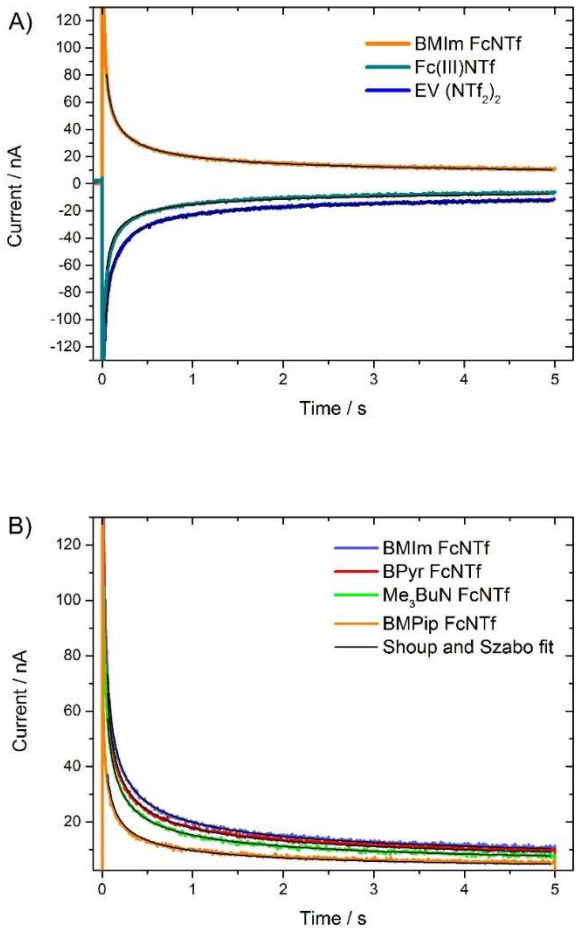

Figure 8.3. DPSC using a microelectrode of 10 mM solution of A) [BMIm] [FcNTf], [Fc(III)NTf] and [EV] $[NTf_2]_2$ in [BMIm] $[NTf_2]$ and B) [BMIm] [FcNTf], [BPyr] [FcNTf], $[Me_3BuN]$ [FcNTf] and [BMPip] [FcNTf] in corresponding common IL ([BMIm], [BPyr], $[Me_3BuN]$ or [BMPip] $[NTf_2]$) at room temperature using Shoup and Szabo fit.

The diffusion coefficient of [FcNTf] anion in IL medium is 1 order of magnitude lower than in acetonitrile (1.03×10^{-6} cm^2 s^{-1}).[40] Compton et al. reported the diffusion coefficient for ferrocene in [BMIm] $[NTf_2]$ using the same method, and the diffusion coefficient of Fc was 3.77×10^{-7} cm^2 s^{-1}, which is significantly higher than the [FcNTf] diffusion, due to the larger radius of the latter. We investigated the [FcNTf] diffusion in other $[NTf_2]$ ILs media using [BPyr] $[Me_3BuN]$ and [BMPip] as the cations. In accordance with Stokes–Einstein relation (eq 2), the [FcNTf] diffusion is significantly affected by the

IL viscosity. The time-dependent current responses in different IL media were presented in **Figure 8.3B**.

$$D = \frac{k_B T}{c\pi\eta r} \qquad (2)$$

where D (m^2 s^{-1}) is the self-diffusion coefficient, k (J K^{-1}) is Boltzmann's constant, T (K) is the absolute temperature, r (m) is the solvated radius, c is a constant that depends on the model used (see below), and η (Pa s^{-1}) is the dynamic viscosity.

In **Figure S8.9** and **S8.10**, we show the DPSC curves at different temperatures for all electroactive species and studied ILs in this work to obtain the enthalpy, entropy, and activation energy resulting from the Arrhenius and Eyring equations. The Arrhenius plot (Figures **8.4A** and **S8.10A**) was used to calculate the activation energy, and the Eyring eq (Figures **8.4B** and **S8.10B**) was employed for the enthalpy and entropy of diffusion. As can be seen, it is observed that the more-viscous ILs have correspondingly larger activation energies, entropy, and enthalpy. The activation energy of [BMIm] [FcNTf] in [BMIm] [NTf_2] for the diffusion coefficient is comparable to the literature for Fc in the same IL medium with a value of 30.2 kJ mol^{-1}.[31] The Stokes–Einstein relation predicts the solvated radius of diffusing electroactive species using a linear relationship between diffusion coefficient multiplied by the temperature and the reciprocal of viscosity corresponding to the temperature (all dynamic viscosity and temperature measurements of common ILs are reported in the literature[41-44] and confirmed at 25 °C with our measurements). The Stokes–Einstein plots are presented in **Figures 8.4C** and **S8.10C**, and the solvated radius of electroactive species are given in **Table 8.3** using c = 6 or 4 (n is a factor based on Stokes law with c = 6 for a perfect stick model or c = 4 for a perfect slip model). The obtained solvated radius of [FcNTf] anion in IL medium is plausible for c = 6 (crystallographic radius of ferrocene: r = 2.7 Å),[45] and we can observe the impact of cation size on the measured solvated radius of [FcNTf] anion. All solvated radii for [FcNTf] are very similar except in the case of [Me_3BuN] ionic liquid, which is the smaller cation. The solvated radius of electroactive species in the [BMIm] [NTf_2] electrolyte containing [BMIm] [FcNTf], [Fc(III)NTf], and [EV] [[NTf_2)$_2$] are 3.2, 3.4, and 1.6 Å (c = 6), respectively. Taking into account all of these parameters, we selected [BMIm] [NTf_2]

as the ionic liquid to provide a faster diffusion of the electroactive species in the ECD electrolyte.

Table 8.3. Transport properties using DPSC of 10 mM RIL such as [BMIm] [FcNTf], [BPyr] [FcNTf], [Me_3BuN] [FcNTf], [MBPip] [FcNTf] and [Fc(III)NTf] in corresponding common IL ([Fc(III)NTf] and [EV] $[NTf_2]_2$ in [BMIm] $[NTf_2]$). Diffusion coefficients were calculated from Shoup and Szabo fit.

Electroactive Species	D $/10^{-7}$ cm^2 s^{-1}	$E_{a,D}$ / kJ mol^{-1}	ΔH_D / kJ mol^{-1} K^{-1}	ΔS_D / J mol^{-1} K^{-1}	Solvated radius c=6 / Å	Solvated radius c=4 / Å	$[NTf_2]$ IL viscosity / cP
EV $(NTf_2)_2$	2.12	28.4	28.4	-353.4	1.6	2.4	51.6
BMIm FcNTf	1.65	24.9	22.2	-376.1	3.2	4.9	51.6
Fc(III)NTf	1.01	29.9	29.9	-355.7	3.4	5.1	51.6
BPyr FcNTf	1.36	26.7	24.0	-366.4	3.5	5.2	61.5
Me_3BuN FcNTf	1.02	30.9	28.2	-352.1	2.7	4.0	105.2
MBPip FcNTf	0.43	34.9	32.2	-353.9	3.4	5.0	180.2

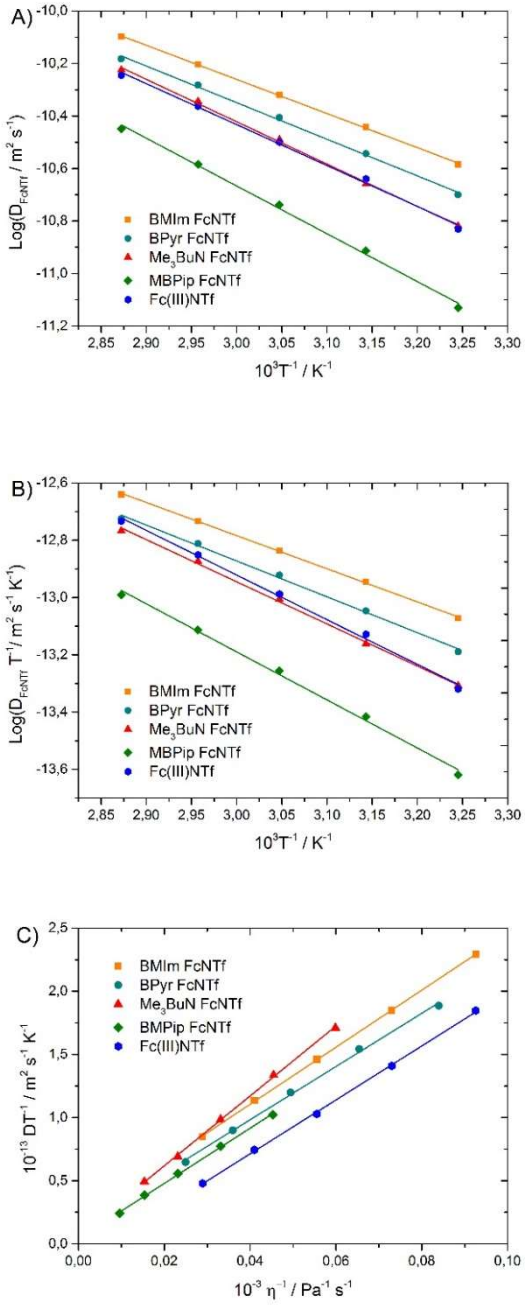

Figure 8.4. A) Arrhenius plots, B) Eyring plots and C) Stokes-Einstein plots for 10 mM RIL such as [BMIm] [FcNTf] (orange line), [BPyr] [FcNTf] (cyan line), [Me_3BuN] [FcNTf] (red line), [MBPip] [FcNTf] (green line) and [Fc(III)NTf] (blue line) in corresponding common IL ([Fc(III)NTf] in [BMIm] [NTf_2]). Measurements were done at 10°C intervals between 35 and 75°C.

Spectroelectrochemical properties of [FcNTf] and [EV]

Electrochromic devices (ECDs) based on [FcNTf]/[EV]/IL will be described in detail in this section. The electrochromic characterization was done using a UV–vis coupled to a potentiostat to measure the absorbance of each half-cell containing the anodic or cathodic species at various potentials. **Figure 8.5A** shows the absorption peak of the viologen radical in the [BMIm] [NTf_2] ionic liquid appearing at 608 nm at potential below −1.5 V versus PtQRE when the cation radical is generated. This is in agreement with the CV presented in **Figure 8.2**. The absorption spectra of [FcNTf] in its oxidized and reduced forms are presented in **Figure 8.5C**, showing the maximum absorbance peaks for [Fc(II)NTf] and [Fc(III)NTf] at 426 and 608 nm, respectively. The molar extinction coefficient of [FcNTf] RIL are 108.0 and 177.5 M cm^{-1} for the reduced and oxidized electroactive species in [BMIm] [NTf_2]. Vorotyntsev and co-worker reported similar result for Fc in [BMIm] [NTf_2] with a molar extinction coefficient of 94 M^{-1} cm^{-1} at 440 nm,[46] showing that the ferrocene center on [FcNTf] behaves similarly as free ferrocene. [FcNTf], once oxidized, however, appears to be more stable than free ferrocene. In the presence of dissolved oxygen in polar solvents, a fast decomposition of ferrocenium cations occurs to generate Fe(III) and Fe_2O_3.[47, 48] However, Brennecke et al. demonstrated a very low oxygen solubility in [BMIm] [NTf_2] in comparison to other gas and presented a high Henry's constant for [BMIm] [NTf_2] containing O_2(1730 bar at 25 °C).[49] Nevertheless, Perissi et al. observed a decrease of peak current with the time using IL electrolyte containing the Fc/Fc^+ couple, and they suggest that it is related to the oxidation by the dissolved oxygen react with Fc^+.[50] We observed that the ferrocenium-containing zwitterionic redox species is, however, stable in IL, as shown by comparing the UV–vis spectra recorded for a fresh solution and one aged for 1 month under air. This could be explained by the different charge distribution on the FcNTf, which makes nucleophilic attack less-efficient. The transition occurring at ca. 600 nm is much stronger for viologen than for [Fc(III)NTf], the molar extinction coefficient differing by 2 orders of magnitude. Because the absorption peaks overlap, a pure blue color is expected to be generated by the ECD, and for this reason, researchers investigated ECD based on ferrocenium, Prussian blue, and viologen.[19, 29, 51]

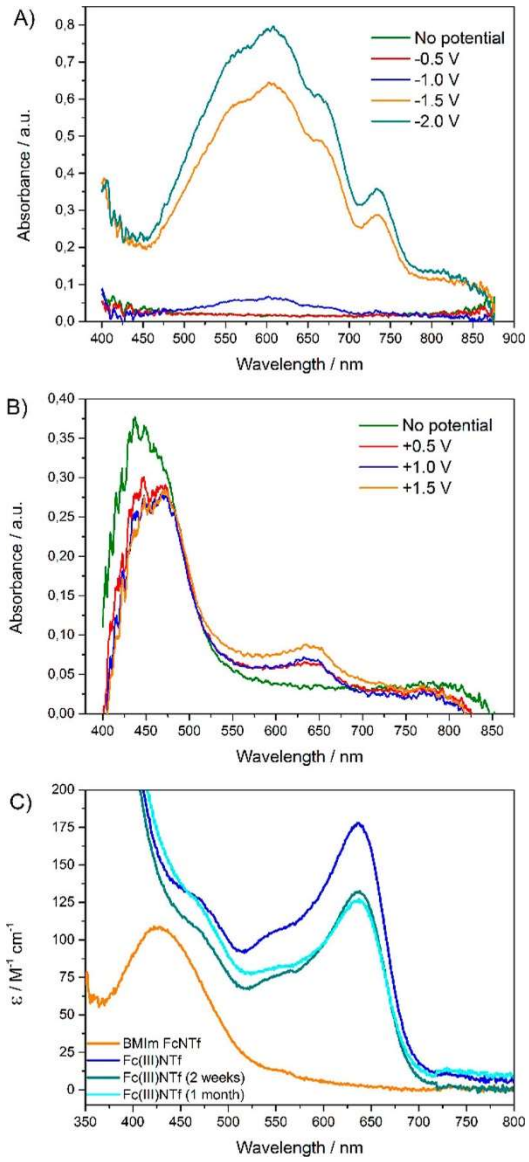

Figure 8.5. UV-vis spectra of 50 mM solution containing A) [EV] [$(NTf_2)_2$] and B) [BMIm] [FcNTf] in [BMIm] [NTf_2] at different potential versus pseudo-reference Pt wire. C) UV-Vis spectra of 1 mM [BMIm] [FcNTf] (orange line) and [Fc(III)NTf] (blue line) in [BMIm] [NTf_2] and at different times following the solution preparation. Quartz spectroelectrochemical cells with an optical path of 1 mm were used.

Electrochromic cell characterization

As the final step of this work, an ECD was assembled using an electrolyte containing 50 mM of [EV] [$(NTf_2)_2$] and 50 mM of [BMIm] [FcNTf] RIL in the [BMIm] [NTf_2] ionic liquid. While [BMIm] [FcNTf] is fully miscible with [BMIm] [NTf_2], [EV] [$(NTf_2)_2$] is soluble at 50 mM at the most. Upon application of an electric potential to ECD, the colorless [EV] is reduced as the negative electrode to a blue-colored radical cation, while the yellow [FcNTf] anion is oxidized to a blue [Fc(III)NTf] zwitterion at the positive electrode. The initial (E = 0 V) and final (E = +2.0 V) stages of the ECD are seen in panels A and B of **Figure 8.6**, respectively. When the colored ECD is left at the open-circuit potential, both $[EV]^{+\bullet}$ and [Fc(III)NTf] undergo homogeneous electron transfer to revert back to their initial state, causing the ECD to return to its original color. This self-bleaching mechanism is presented in **Figure 8.6C** (red arrows).

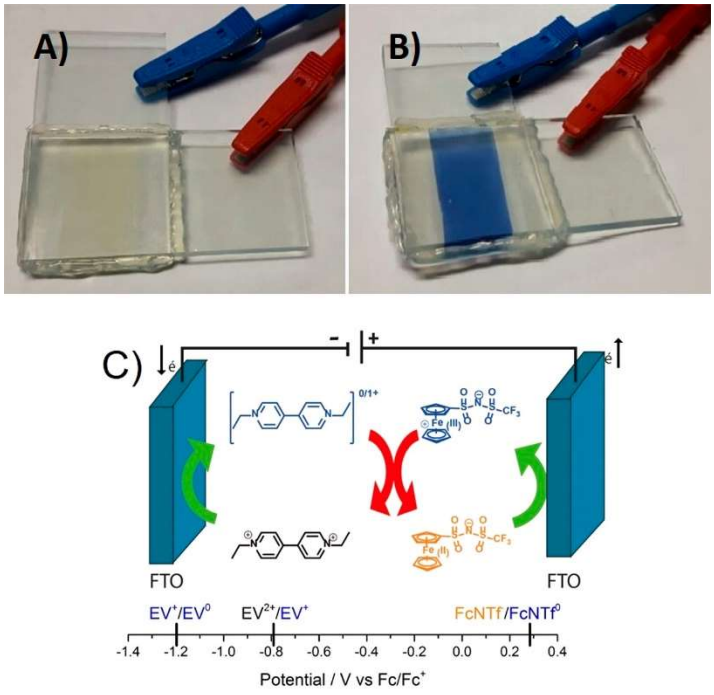

Figure 8.6. Images of [FcNTf]/[EV]/IL ECD (50 mM/50 mM) in the (A) bleached state (left; 0 V) and (B) colored state (right; 2 V). (C) ECD mechanism of [FcNTf] and [EV], in which the heterogeneous reactions (green) are nonspontaneous and the homogeneous reaction (red) is spontaneous. The potentials reported are from Figure 8.2 and were determined on a Pt disk.

The absorption spectra of the device in its bleached and colored states are shown in **Figure 8.7A**. The spectra of the colored cell show an absorption peak in the visible region centered at 605 nm, similar to what was observed in the half-cell, while no apparent peaks are found in the spectrum of the bleached ECD (at OCP). The absorbance difference (ΔA) between the bleached and colored state at 605 nm with an applied potential of 2 V is around 0.40 absorbance units. To determine the appropriate switching potentials of [FcNTf]/[EV]/IL ECD, the cell voltage was applied, starting at the open circuit potential (OCP), 0.00 V, and extending to 2 V. The optimum switching potentials of the ECDs were established as 0 V for the bleached state and 2.0 V for the colored state, representing a compromise between enhancing the colored intensity and avoiding over-oxidation and reduction of the electroactive species and electrolyte. We used 30 μm thick thermoplastic sealant to separate the two FTO-coated slides, which is the space for IL electrolyte. ECD based on gel-polymer electrolyte presented electrolyte between the two electrodes that was usually of a greater thickness, and this explains the lower absorbance for this type of ECD. Also, we have a fast self-bleaching occurring from the homogeneous reaction between [Fc(III)NTf] and $[EV]^{+\bullet}$, and this prevents the accumulation of $[EV]^{+\bullet}$. **Figure 8.7B** displays the time-dependent current response obtained by the ECD and shows clearly a deviation of Cottrell equation at long-time regime, resulting from the homogeneous redox reaction between both electroactive species in the bulk of the electrolyte.

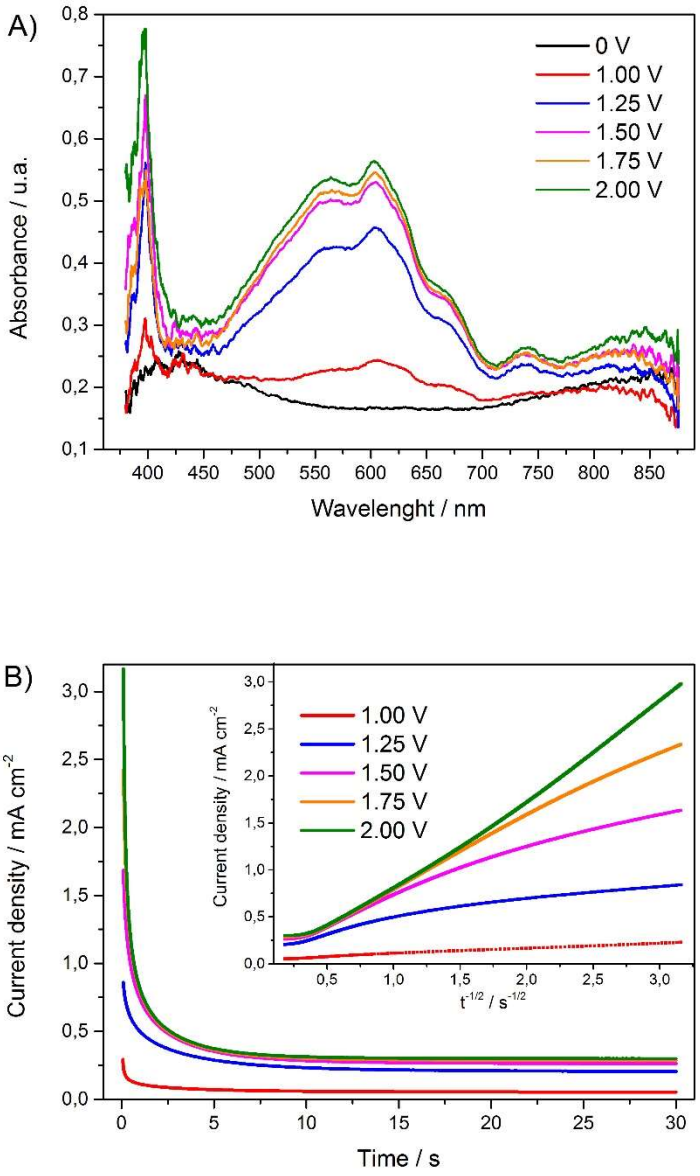

Figure 8.7. A) UV-Vis spectra of [FcNTf]/[EV]/IL ECD (50 mM:50 mM) and B) transient profiles of the ECD current density at various cell potentials from 1 to 2 V.

Table 8.4 lists the switching time, contrast, optical density and coloration efficiency of the all ionic liquid ECD. **Figure 8.8** shows the evolution of the current density along with the corresponding transmittance at 610 nm for the ECD for successive voltage switching between 0 and +2.0 V. The coloration voltage was chosen using spectroelectrochemical data in previous section to obtain the max contrast and to show the

high electrochemical stability of this electroactive electrolyte. The transmittance difference between the colored and bleached states is given by ΔT. The ΔT of a freshly assembled ECD and one that underwent 1000 cycles are 38.8 and 36.8%, showing a very high stability of the electrochromic species because [EV] and [FcNTf] are highly electrochemical reversible in the presence of oxygen and water. The switching time required to reach 95% of the maximal ΔT value is 9.5 s for coloration (t_c, E = +2.0 V) and 5.5 s for bleaching (t_b, E = 0 V). **Figure 8.9** compares the bleaching profile of a device in its colored state during self-bleaching (OCP) and forced bleaching (E = 0 V). Both modes will reach the same uncolored intensity, but self-bleaching requires more time for the species to diffuse and react homogeneously.

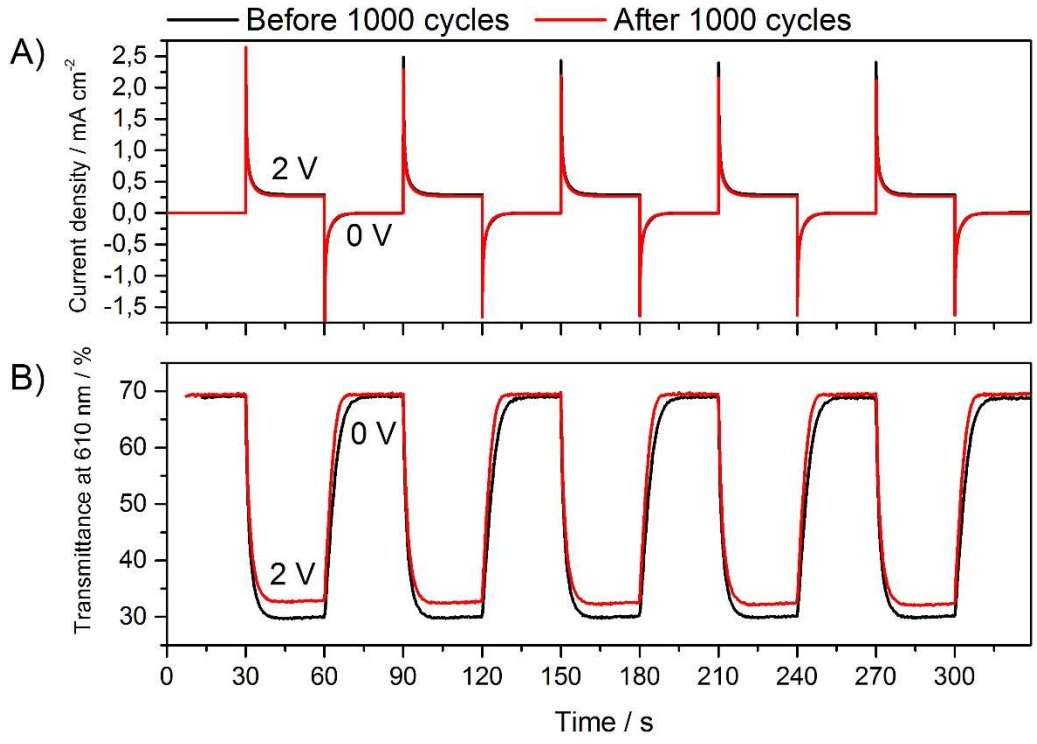

Figure 8.8. A) The profile of the current density and B) variation of transmittance at 610 nm for [FcNTf]/[EV]/IL ECD (50 mM:50 mM) with an applied asymmetric square wave between 0 and 2 V during 30 s for each potential step. The black and red lines show profiles corresponding to before and after 1000 cycle, respectively.

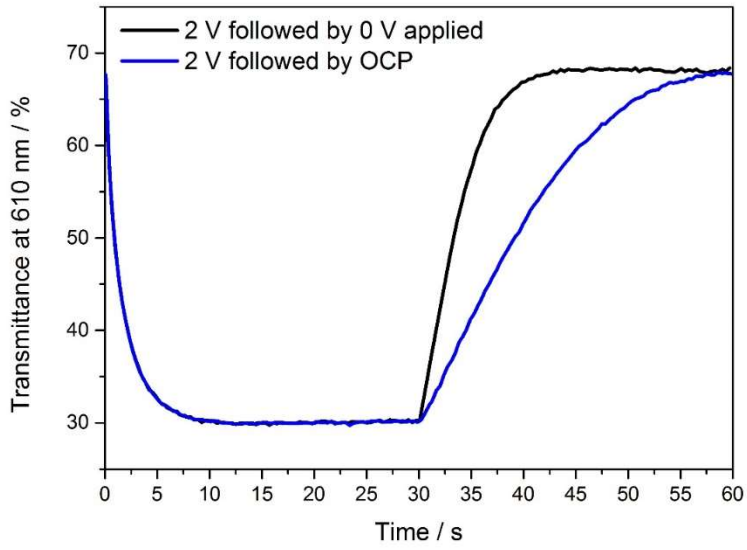

Figure 8.9. The profile of the variation of transmittance at 610 nm for [FcNTf]/[EV]/IL ECD (50 mM:50 mM) with a 2 V step potential following by 0 V vs OCP (black line) or no applied potential (blue line) during 30 s for each step.

To evaluate the impact of the [FcNTf] anion concentration, ECDs with electrolyte containing 25, 50, and 100 mM of [BMIm] [FcNTf] with 50 mM viologen were investigated. **Figure 8.10A** shows the transmittance profile (610 nm) with an applied asymmetric square wave using IL-phase electrolyte containing different the three different concentration ratios. The contrast (ΔT) is significantly affected by [FcNTf] concentration as values of 25.8, 38.8, and 48.0% were obtained for ECD (25:50), ECD (50:50), and ECD (100:50), respectively. While the contrast is an important parameter to define ECD performance, the coloration efficiency (CE) provides a better comparison of performance between different ECDs. Eq 3 is used to calculate the CE:

$$CE = \frac{\Delta OD}{\Delta Q_c} \ \ where \ \ \Delta OD = \log\left(\frac{T_b}{T_c}\right) \qquad (3)$$

where T_b and T_c are the light transmittance of the bleached and colored states at a certain wavelength (here, 610 nm). ΔQ_c is the transferred charge that is measured by chronoamperometry. The CE depends on optical density (ΔOD) obtained by transmittance

of bleached and colored state of ECD, and **Figure 8.10B** shows ΔOD against the ΔQ_c. The CEs for this type of liquid-phase ECD using ethyl viologen as electrochromic material are 146.2, 113.7, and 105.4 $cm^2\ C^{-1}$ for ECD (25:50), ECD (50:50), and ECD (100:50), respectively. Hence, the CE is slightly affected by [EV]/[FcNTf] ratio via the self-bleaching mechanism, while the contrast increase with [FcNTf] concentration. If we compare our value with those of the other viologen system, Diamond et al. reported an ECM using ionogel containing phosphonium–viologen as EC, which shows 10.7 $cm^2\ C^{-1}$ for CE;[52] Ho et al. demonstrated the use of poly(ionic liquids) containing viologen and ferrocene as an EC polyelectrolyte, which exhibits 38.6 $cm^2\ C^{-1}$,[53] and Fitzmaurice et al. showed ECD employing a viologen-modified TiO_2, which gives 270 $cm^2\ C^{-1}$.[54] Recently, Murakami et al. presented redox-active ionic liquids in which ferrocene and viologen are linked together. They reported 70 $cm^2\ C^{-1}$ for CE, but their ECD need a high switching time (>30 s).[55] Recently, other anodic electroactive species were be evaluated in ECD as dimethylferrocene (DMFc)[33] and *N*,*N*,*N*′,*N*′-tetramethyl-*p*-phenylenediamine (TMPD).[56] Hexyl viologen–DMFc EDC based on IL gel presents a CE of 78 $cm^2\ C^{-1}$ and a colored time of 11 s to reach 90%.[33] To compare [FcNTf] to TMPD, the hexyl viologen–TMPD ECD exhibits a contrast of 60.1% at 615 nm with a coloration efficiency value of 120.8 $cm^2\ C^{-1}$, but the performance decreases significantly after 2000 cycles.[56] Finally, these result suggest that the [FcNTf]/[EV]/IL electrolytes are attractive candidates for ECD.

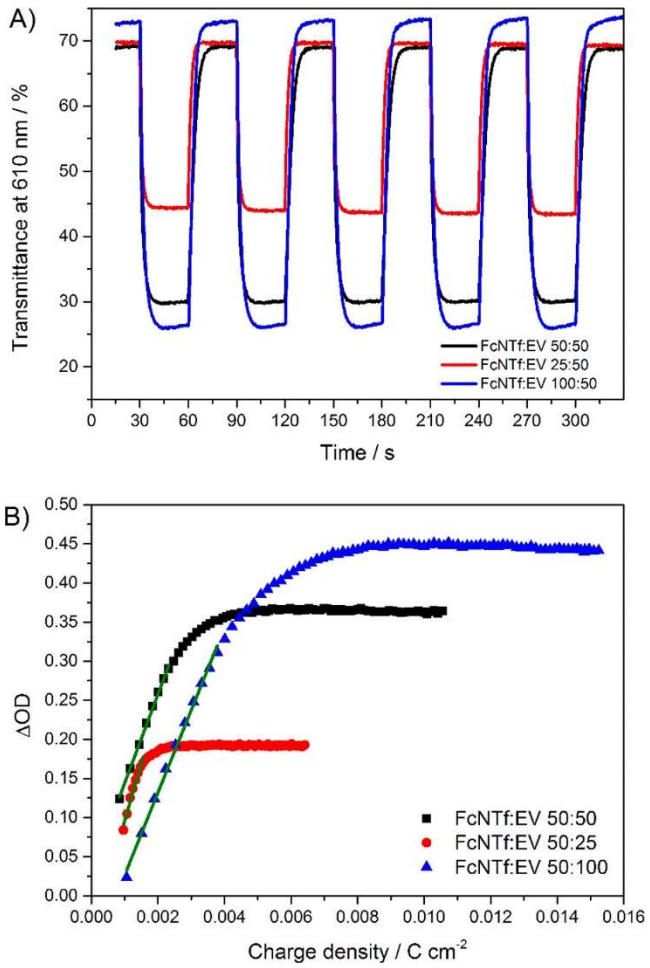

Figure 8.10. (A) Profile of the variation of transmittance at 610 nm with an applied asymmetric square wave between 0 and 2 V during 30 s for each potential step employing [FcNTf]/[EV]/IL ECD with different [FcNTf] concentrations. (B) Dependence of optical density difference on the charge density of [FcNTf]/[EV]/IL ECD.

Table 8.4. Performance of [FcNTf]/[EV]/IL ECD with an applied asymmetric square wave between 0 and 2.0 V during 30 s for each potential step where the bleaching and coloring times are defined as the time required to reach 95% ΔT at 610 nm

ECDs	t_b / s	t_c / s	ΔT / %	ΔT_{1000} / %	ΔOD (610 nm)	CE (610 nm) / $cm^2\ C^{-1}$
FcNTf/EV/IL (50 mM:50 mM)	5.5	9.5	38.8	36.8 (94.8 % ΔT)	0.36	113.7
FcNTf/EV/IL (25 mM:50 mM)	3.8	4.7	25.8	-	0.20	146.2
FcNTf/EV/IL (100 mM:50 mM)	9.5	9.7	48.0	-	0.44	105.5

8.2.6. Conclusions

This study highlights the electrochemical and transport properties of a family of ferrocene-containing triflimide redox ionic liquids and ethyl viologen in ionic liquid electrolyte. The objective was to demonstrate the impact of [FcNTf] anion on the electrochromic performance of IL-phase ECD and the compatibility of this redox species with the electrochromic ethyl viologen. Redox ionic liquids are the subject of an increased interest mainly because they allow very high concentrations of redox centers and increase their stability. In this paper we showed how these features can be beneficial to build a simple yet efficient electrochromic device. The midpoint potential of the [Fc(II)NTf]/[Fc(III)NTf] and [EV(II)/EV(I)] couples of 0.261 and −0.798 V versus Fc/Fc^+ differs by about 1.06 V, which is sufficiently high to promote a rapid homogeneous charge transfer for efficient self-bleaching. We demonstrated that the slower [FcNTf] diffusion in the IL electrolyte could be counterbalanced by its higher solubility, which arises from its IL-inspired structure. Increasing the concentration of the [FcNTf] in the ionic liquid provided the ECD with a larger contrast, and the intensity of the switching color was only controlled by the mass transport and charge transfer of viologen at a given cell voltage. The [FcNTf]/[EV]/IL ECD (100 mM/50 mM) reported in this study shows a contrast about 48% at 610 nm, switching time in the order of seconds, with an optical

density of 0.44 and coloration efficiency of 105.4 cm^2 C^{-1}. The electrochromic device was constructed in an open atmosphere simply by trapping a thin layer of electrolyte between two FTO electrodes. Further improvement of such devices will require increasing the solubility of electrochromatic viologen in ionic liquid and developing a flexible ECD based on the proposed [FcNTf] redox shuttle.

8.2.7. Acknowledgments

The authors acknowledge the financial support from Fonds de recherche du Québec en nature et technologies (FQRNT) under their program for the reduction of greenhouse gases and the Natural Sciences and Engineering Research Council of Canada (NSERC) for Discovery grant (D.R.). The authors also acknowledge Prof. William Skene of University of Montréal for equipment loan.

8.2.8. References

[1] R.D. Rauh, Electrochromic windows: an overview, Electrochim. Acta, 44 (1999) 3165-3176.
[2] J.S.E.M. Svensson, C.G. Granqvist, Electrochromic tungsten oxide films for energy efficient windows, Sol. Energy Mat., 11 (1984) 29-34.
[3] C.G. Granqvist, Electrochromic tungsten oxide films: Review of progress 1993–1998, Sol. Energy Mater. Sol. Cells, 60 (2000) 201-262.
[4] L. Liang, J. Zhang, Y. Zhou, J. Xie, X. Zhang, M. Guan, B. Pan, Y. Xie, High-performance flexible electrochromic device based on facile semiconductor-to-metal transition realized by WO(3)·2H(2)O ultrathin nanosheets, Sci. Rep., 3 (2013) 1936.
[5] A. Guerfi, L.H. Dao, Electrochromic molybdenum oxide thin films prepared by electrodeposition, J. Electrochem. Soc., 136 (1989) 2435-2436.
[6] G.A. Niklasson, C.G. Granqvist, Electrochromics for smart windows: thin films of tungsten oxide and nickel oxide, and devices based on these, J. Mater. Chem., 17 (2007) 127-156.
[7] I. Bouessay, A. Rougier, P. Poizot, J. Moscovici, A. Michalowicz, J.M. Tarascon, Electrochromic degradation in nickel oxide thin film: A self-discharge and dissolution phenomenon, Electrochim. Acta, 50 (2005) 3737-3745.
[8] K. Itaya, K. Shibayama, H. Akahoshi, S. Toshima, Prussian-blue-modified electrodes: An application for a stable electrochromic display device, J. Appl. Phys., 53 (1982) 804-805.
[9] E.A.R. Duek, M.-A. De Paoli, M. Mastragostino, An electrochromic device based on polyaniline and prussian blue, Adv. Mat., 4 (1992) 287-291.
[10] M. Deepa, A. Awadhia, S. Bhandari, Electrochemistry of poly(3,4-ethylenedioxythiophene)-polyaniline/Prussian blue electrochromic devices containing an ionic liquid based gel electrolyte film, Phys. Chem. Chem. Phys., 11 (2009) 5674-5685.

[11] F.S. Han, M. Higuchi, D.G. Kurth, Metallo-supramolecular polymers based on functionalized bis-terpyridines as novel electrochromic materials, Adv. Mat., 19 (2007) 3928-3931.
[12] C.-W. Hu, T. Sato, J. Zhang, S. Moriyama, M. Higuchi, Three-dimensional Fe(II)-based metallo-supramolecular polymers with electrochromic properties of quick switching, large contrast, and high coloration efficiency, ACS Appl. Mater. Interfaces, 6 (2014) 9118-9125.
[13] M. Higuchi, Y. Akasaka, T. Ikeda, A. Hayashi, D.G. Kurth, Electrochromic solid-state devices using organic-metallic hybrid polymers, J. Inorg. Organomet. Polym. Mater., 19 (2009) 74-78.
[14] P.M. Beaujuge, J.R. Reynolds, Color control in π-conjugated organic polymers for use in electrochromic devices, Chem. Rev., 110 (2010) 268-320.
[15] F. Carpi, D. De Rossi, Colours from electroactive polymers: Electrochromic, electroluminescent and laser devices based on organic materials, Opt. Laser Technol., 38 (2006) 292-305.
[16] G. Sonmez, H. Meng, F. Wudl, Organic polymeric electrochromic devices: Polychromism with very high coloration efficiency, Chem. Mater., 16 (2004) 574-580.
[17] Y. Watanabe, K. Imaizumi, K. Nakamura, N. Kobayashi, Effect of counter electrode reaction on coloration properties of phthalate-based electrochromic cell, Sol. Energy Mater. Sol. Cells, 99 (2012) 88-94.
[18] C.-L. Lin, C.-C. Lee, K.-C. Ho, Spectroelectrochemical studies of manganese phthalocyanine thin films for applications in electrochromic devices, J. Electroanal. Chem., 524–525 (2002) 81-89.
[19] T.-H. Kuo, C.-Y. Hsu, K.-M. Lee, K.-C. Ho, All-solid-state electrochromic device based on poly(butyl viologen), Prussian blue, and succinonitrile, Sol. Energy Mater. Sol. Cells, 93 (2009) 1755-1760.
[20] J. Palenzuela, A. Viñuales, I. Odriozola, G. Cabañero, H.J. Grande, V. Ruiz, Flexible viologen electrochromic devices with low operational voltages using reduced graphene oxide electrodes, ACS Appl. Mater. Interfaces, 6 (2014) 14562-14567.
[21] E. Hwang, S. Seo, S. Bak, H. Lee, M. Min, H. Lee, An electrolyte-free flexible electrochromic device using electrostatically strong graphene quantum dot–viologen nanocomposites, Adv. Mat., 26 (2014) 5129-5136.
[22] C.L. Bird, A.T. Kuhn, Electrochemistry of the viologens, Chem. Soc. Rev., 10 (1981) 49-82.
[23] R.J. Mortimer, T.S. Varley, Novel color-reinforcing electrochromic device based on surface-confined ruthenium purple and solution-phase methyl viologen, Chem. Mater., 23 (2011) 4077-4082.
[24] N. Jordão, L. Cabrita, F. Pina, L.C. Branco, Novel bipyridinium ionic liquids as liquid electrochromic devices, chem. Eur. J., 20 (2014) 3982-3988.
[25] T. Watanabe, K. Honda, Measurement of the extinction coefficient of the methyl viologen cation radical and the efficiency of its formation by semiconductor photocatalysis, J. Phys. Chem., 86 (1982) 2617-2619.
[26] R.G. Compton, A.M. Waller, P.M.S. Monk, D.R. Rosseinsky, Electron paramagnetic resonance spectroscopy of electrodeposited species from solutions of 1,1[prime or minute]-bis-(p-cyanophenyl)-4,4[prime or minute]-bipyridilium (cyanophenyl paraquat, CPQ), J. Chem. Soc., Faraday Trans., 86 (1990) 2583-2586.

[27] G. Chidichimo, M. De Benedittis, J. Lanzo, B.C. De Simone, D. Imbardelli, B. Gabriele, L. Veltri, G. Salerno, Solid thermoplastic laminable electrochromic film, Chem. Mater., 19 (2007) 353-358.
[28] H.C. Moon, T.P. Lodge, C.D. Frisbie, Solution processable, electrochromic ion gels for sub-1 V, flexible displays on plastic, Chem. Mater., 27 (2015) 1420-1425.
[29] H.-C. Lu, S.-Y. Kao, T.-H. Chang, C.-W. Kung, K.-C. Ho, An electrochromic device based on Prussian blue, self-immobilized vinyl benzyl viologen, and ferrocene, Sol. Energy Mater. Sol. Cells, 147 (2016) 75-84.
[30] R. Cinnsealach, G. Boschloo, S. Nagaraja Rao, D. Fitzmaurice, Coloured electrochromic windows based on nanostructured TiO2 films modified by adsorbed redox chromophores, Sol. Energy Mater. Sol. Cells, 57 (1999) 107-125.
[31] E.I. Rogers, D.S. Silvester, D.L. Poole, L. Aldous, C. Hardacre, R.G. Compton, Voltammetric characterization of the ferrocene|ferrocenium and cobaltocenium|cobaltocene redox couples in RTILs, J. Phys. Chem. C, 112 (2008) 2729-2735.
[32] Y. Yang, L. Yu, Theoretical investigations of ferrocene/ferrocenium solvation in imidazolium-based room-temperature ionic liquids, Phys. Chem. Chem. Phys., 15 (2013) 2669-2683.
[33] H.C. Moon, C.-H. Kim, T.P. Lodge, C.D. Frisbie, Multicolored, low-power, flexible electrochromic devices based on ion gels, ACS Appl. Mater. Interfaces, 8 (2016) 6252-6260.
[34] A.M. O'Mahony, D.S. Silvester, L. Aldous, C. Hardacre, R.G. Compton, Effect of water on the electrochemical window and potential limits of room-temperature ionic liquids, J. Chem. Eng. Data, 53 (2008) 2884-2891.
[35] L. Xiong, A.M. Fletcher, S.G. Davies, S.E. Norman, C. Hardacre, R.G. Compton, Tuning solute redox potentials by varying the anion component of room temperature ionic liquids, Chem. Comm., 48 (2012) 5784.
[36] Y. Wang, E.I. Rogers, R.G. Compton, The measurement of the diffusion coefficients of ferrocene and ferrocenium and their temperature dependence in acetonitrile using double potential step microdisk electrode chronoamperometry, J. Electroanal. Chem., 648 (2010) 15-19.
[37] R.G. Evans, O.V. Klymenko, P.D. Price, S.G. Davies, C. Hardacre, R.G. Compton, A comparative electrochemical study of diffusion in room temperature ionic liquid solvents versus acetonitrile, ChemPhysChem, 6 (2005) 526-533.
[38] M.C. Kroon, W. Buijs, C.J. Peters, G.-J. Witkamp, Quantum chemical aided prediction of the thermal decomposition mechanisms and temperatures of ionic liquids, Thermochim. Acta, 465 (2007) 40-47.
[39] T. Inagaki, T. Mochida, Metallocenium ionic liquids, Chem. Lett., 39 (2010) 572-573.
[40] B. Gélinas, D. Rochefort, Synthesis and characterization of an electroactive ionic liquid based on the ferrocenylsulfonyl(trifluoromethylsulfonyl)imide anion, Electrochim. Acta, 162 (2015) 36-44.
[41] J. Salgado, T. Regueira, L. Lugo, J. Vijande, J. Fernández, J. García, Density and viscosity of three (2,2,2-trifluoroethanol + 1-butyl-3-methylimidazolium) ionic liquid binary systems, J. Chem. Thermodyn., 70 (2014) 101-110.
[42] F.S. Oliveira, M.G. Freire, P.J. Carvalho, J.A.P. Coutinho, J.N.C. Lopes, L.P.N. Rebelo, I.M. Marrucho, Structural and positional isomerism influence in the physical

properties of pyridinium NTf2-based ionic liquids: Pure and water-saturated mixtures, J. Chem. Eng. Data, 55 (2010) 4514-4520.
[43] A. Bhattacharjee, A. Luís, J.H. Santos, J.A. Lopes-da-Silva, M.G. Freire, P.J. Carvalho, J.A.P. Coutinho, Thermophysical properties of sulfonium- and ammonium-based ionic liquids, Fluid Phase Equilib., 381 (2014) 36-45.
[44] A. Bhattacharjee, P.J. Carvalho, J.A.P. Coutinho, The effect of the cation aromaticity upon the thermophysical properties of piperidinium- and pyridinium-based ionic liquids, Fluid Phase Equilib., 375 (2014) 80-88.
[45] J.B. Shotwell, R.A. Flowers, Electrochemical investigation of the solvolytic properties of ethylammonium nitrate (EAN) and propylammonium nitrate (PAN), Electroanalysis, 12 (2000) 223-226.
[46] M.A. Vorotyntsev, V.A. Zinovyeva, D.V. Konev, M. Picquet, L. Gaillon, C. Rizzi, Electrochemical and spectral properties of ferrocene (Fc) in ionic liquid: 1-Butyl-3-methylimidazolium triflimide, [BMIM][NTf2]. concentration effects, J. Phys. Chem. B, 113 (2009) 1085-1099.
[47] A. Singh, D.R. Chowdhury, A. Paul, A kinetic study of ferrocenium cation decomposition utilizing an integrated electrochemical methodology composed of cyclic voltammetry and amperometry, Analyst, 139 (2014) 5747-5754.
[48] J.P. Hurvois, C. Moinet, Reactivity of ferrocenium cations with molecular oxygen in polar organic solvents: Decomposition, redox reactions and stabilization, J. Organomet. Chem., 690 (2005) 1829-1839.
[49] J.L. Anthony, J.L. Anderson, E.J. Maginn, J.F. Brennecke, Anion effects on gas solubility in ionic liquids, J. Phys. Chem. B, 109 (2005) 6366-6374.
[50] I. Perissi, U. Bardi, S. Caporali, A. Fossati, A. Lavacchi, Ionic liquids as diathermic fluids for solar trough collectors' technology: A corrosion study, Sol. Energy Mater. Sol. Cells, 92 (2008) 510-517.
[51] C.-F. Lin, C.-Y. Hsu, H.-C. Lo, C.-L. Lin, L.-C. Chen, K.-C. Ho, A complementary electrochromic system based on a Prussian blue thin film and a heptyl viologen solution, Sol. Energy Mater. Sol. Cells, 95 (2011) 3074-3080.
[52] A. Kavanagh, K.J. Fraser, R. Byrne, D. Diamond, An electrochromic ionic liquid: Design, characterization, and performance in a solid-state platform, ACS Appl. Mater. Interfaces, 5 (2013) 55-62.
[53] H.-C. Lu, S.-Y. Kao, H.-F. Yu, T.-H. Chang, C.-W. Kung, K.-C. Ho, Achieving low-energy driven viologens-based electrochromic devices utilizing polymeric ionic liquids, ACS Appl. Mater. Interfaces, 8 (2016) 30351-30361.
[54] D. Cummins, G. Boschloo, M. Ryan, D. Corr, S.N. Rao, D. Fitzmaurice, Ultrafast electrochromic windows based on redox-chromophore modified nanostructured semiconducting and conducting films, J. Phys. Chem. B, 104 (2000) 11449-11459.
[55] H. Tahara, R. Baba, K. Iwanaga, T. Sagara, H. Murakami, Electrochromism of a bipolar reversible redox-active ferrocene-viologen linked ionic liquid, Chem. Comm., 53 (2017) 2455-2458.
[56] T.-H. Chang, C.-W. Hu, S.-Y. Kao, C.-W. Kung, H.-W. Chen, K.-C. Ho, An all-organic solid-state electrochromic device containing poly(vinylidene fluoride-co-hexafluoropropylene), succinonitrile, and ionic liquid, Sol. Energy Mater. Sol. Cells, 143 (2015) 606-612.

8.3. Supporting information

Air-stable, self-bleaching electrochromic device based on viologen and ferrocene-containing triflimide redox ionic liquids

Bruno Gélinas[1], *Dyuman Das*[1], *Dominic Rochefort*[1*]

[1]Département de chimie, Université de Montréal, CP6128 Succ. Centre-Ville, Montréal, Québec, Canada H3C 3J7

*Corresponding author: Tel: +1-514-343-6733, Fax: +1-514-343-7586, email: dominic.rochefort@umontreal.ca

List of Contents:

8.3.1. Synthesis of FcNTf redox ionic liquids and viologen

Preparation of potassium ferrocenylsulfonyl(trifluoromethylsulfonyl)imide.

Potassium ferrocenylsulfonyl(trifluoromethylsulfonyl)imide (K [FcNTf]) was synthesized according to a similar procedure given by our previous paper[1] and K [FcNTf] salt was chosen because of less hygroscopic than sodium [FcNTf] salt (Humid Na [FcNTf] is slightly soluble in dichloromethane) . Trifluoromethanesulfonamide (1 eq.) was dissolved in a flask in acetonitrile and anhydrous potassium carbonate (1.5 eq.) was added. The solution was stirred for 10 minutes at room temperature. A slow addition of ferrocenylsulfonyl chloride (1 eq.) was then made. The resulting solution was stirred and heated at reflux temperature for 24 hours. The brown solution was filtered and the precipitate was washed with acetone to achieve a white precipitate. Removal of the solvent under reduced pressure produced a brown-yellow product. Dichloromethane was used to wash the salt, obtaining a light brown-yellow powder. The salt was dried overnight under reduce pressure at room temperature. A better purification was done using this procedure via the removal of unreacted Trifluoromethanesulfonamide. Yield: 76 %. ^{1}H NMR (DMSO-d_6, 300 MHz): δ (ppm) = 4.53 (t, 2H), 4.28 (s, 7H). ^{19}F NMR (DMSO-d_6, 282 MHz): δ (ppm) = -77.62. ^{13}C NMR (DMSO-d_6, 125 MHz): δ (ppm) = 121.90; 119.32; 94.61; 70.44; 69.19; 68.61. (ESI) m/z: [M*$^{-}$](calcd for $C_{11}H_9F_3FeNO_4S_2^-$) : 395.928 Found: 395.926.

General procedure for the preparation of electroactive FcNTf ionic liquids. Potassium ferrocenylsulfonyl(trifluoromethylsulfonyl)imide and the appropriate cation (1-Butyl-3-methylimidazolium, Trimethylbutylammonium, Butylpyridinium and 1-Butyl-1-methylpyrrolidinium) with bromide as counter anion were dissolved in acetone. The mixture was stirred at room temperature for 24 hours. Following this, the solution was filtered and removal of the solvent under reduced pressure produced a dark-brown viscous liquid. The compound was purified by alumina (Al_2O_3) as adsorptive filtration and then, by column chromatography silica (SiO_2) gel as the stationary phase and acetone as eluent. After removing the solvent, orange product was washed dried at 65 °C overnight under vacuum and cooled down at room temperature to obtain an orange crystal.

Preparation of trimethylbutylammonium bromide ([Me$_3$BuN] Br). Trimethylbutylammonium bromide was prepared by reacting trimethylamine in excess with 1-bromobutane in ethanol at 50

°C for 24 h. After removing the solvent, white solid was washed with ether and dried at 65 °C overnight under vacuum. Yield: 91 %. ^{1}H NMR (DMSO-d_6, 300 MHz): δ (ppm) = 3.34-3.29 (m,2H), 3.07 (s,9H), 1.70-1.59 (m,2H), 1.35-1.23 (m,2H) 0.92 (t,3H). ^{13}C NMR (DMSO-d_6, 125 MHz): δ (ppm) = 65.50, 65.47, 65.43, 52.60, 53.55, 52.49, 24.48, 19.62, 13.96. [M*$^{+}$](calcd for $C_7H_{18}N^{+}$): 116.14338 found: 116.14328. Elemental analysis: Calcd for $C_7H_{18}BrN$: N 7.14; C 42.87; H 9.25. Found: N 7.07; C 42.64; H 9.67.

1-Butyl-3-methylimidazolium ferrocenylsulfonyl(trifluoromethylsulfonyl)imide ([BMIm] [FcNTf]). Yield: 90%. ^{1}H NMR (DMSO-d_6, 300 MHz): δ (ppm) = 9.10 (s,1H), 7.76 (t,1H), 7.69 (t,1H), 4.53 (t,2H), 4.28 (s,7H), 4.15 (t,2H), 3.84 (s,3H), 1.76 (q,2H) 1.31-1.19 (m,2H), 0.90 (t,3H). ^{19}F NMR (DMSO-d_6, 282 MHz): δ (ppm) = -79.08. ^{13}C NMR (DMSO-d_6, 125 MHz): δ (ppm) = 136.96; 124.08; 122.75; 118.44; 94.57; 70.41; 60.17; 68.60; 48.96; 36.20; 31.80; 19.19; 13.72. (ESI) m/z: [M*$^{+}$](calcd for $C_8H_{15}N_2^{+}$): 139.12352 found: 139.12341. [M*$^{-}$](calcd for $C_{11}H_9F_3FeNO_4S_2^{-}$) : 395.92745 Found: 395.92917. Calcd for $C_{19}H_{24}F_3FeN_3O_4S_2$: N 7.85; C 42.62; H 4.52; S 11.98. Found: N 7.90; C 42.69; H 4.52; S 11.96.

Trimethylbutylammonium ferrocenylsulfonyl(trifluoromethylsulfonyl)imide ([Me$_3$BuN] [FcNTf]). Yield: 71%. ^{1}H NMR (DMSO-d_6, 300 MHz): δ (ppm) = 4.53 (s,2H), 4.28 (s,7H), 3.25 (t,2H), 3.02 (s,9H), 1.65 (q,2H), 1.36-1.23 (m,2H), 0.93 (t,3H). ^{19}F NMR (DMSO-d_6, 282 MHz): δ (ppm) = -79.07. ^{13}C NMR (DMSO-d_6, 125 MHz): δ (ppm) = 122.73, 118.43, 94.55, 70.42, 69.18, 68.59, 65.62, 65.59, 65.55, 52.66, 52.61, 52.56, 24.48, 19.63, 13.94. (ESI) m/z: [M*$^{+}$](calcd for $C_7H_{18}N^{+}$): 116.14392 found: 116.14401. [M*$^{-}$](calcd for $C_{11}H_9F_3FeNO_4S_2^{-}$) : 395.92745 Found: 395.92883. Calcd for $C_{18}H_{27}F_3FeN_2O_4S_2$: N 5.47; C 42.19; H 5.31; S 12.52. Found: N 5.42; C 42.16; H 5.39; S 12.56.

Butylpyridinium ferrocenylsulfonyl(trifluoromethylsulfonyl)imide ([BPy] [FcNTf]). Yield: 83%. ^{1}H NMR (DMSO-d_6, 300 MHz): δ (ppm) = 9.08 (s,2H), 8.60 (dd,1H), 8.16 (tt,2H), 4.59 (t,2H), 4.53 (t,2H), 4.27 (t,7H), 1.89 (q,2H), 1.35-1.22 (m,2H) 0.91 (t,3H). ^{19}F NMR (DMSO-d_6, 282 MHz): δ (ppm) = -79.07. ^{13}C NMR (DMSO-d_6, 125 MHz): δ (ppm) = 145.93, 145.21, 128.57, 122.74, 94.58, 70.41, 69.17, 68.57, 61.03, 33.10, 19.22, 13.76. (ESI) m/z: [M*$^{+}$](calcd for $C_9H_{14}N^{+}$): 136.11262 found: 136.11242. [M*$^{-}$](calcd for $C_{11}H_9F_3FeNO_4S_2^{-}$) : 395.92745 Found: 395.92898. Calcd for $C_{20}H_{23}F_3FeN_2O_4S_2$: N 5.26; C 45.12; H 4.35; S 12.05. Found: N 5.22; C 45.24; H 4.39; S 12.05.

1-Butyl-1-methylpyrrolidinium ferrocenylsulfonyl(trifluoromethylsulfonyl)imide ([MBPip][FcNTf]). Yield: 69%. ^{1}H NMR (DMSO-d_6, 300 MHz): δ (ppm) = 4.53 (t,2H), 4.28 (s,7H), 3.28 (q,6H), 2.97 (s,3H), 1.77-1.44 (m,8H), 1.37-1.25 (m,2H), 0.93 (s,3H). ^{19}F NMR (DMSO-d_6, 282 MHz): δ (ppm) = -77.63. ^{13}C NMR (DMSO-d_6, 125 MHz): δ (ppm) = 136.97; 124.09; 122.74; 121.89; 119.32; 94.58; 70.44; 60.21; 68.60; 48.99; 36.25; 31.82; 19.23; 13.71. (ESI) m/z: [M*$^{+}$](calcd for $C_{10}H_{22}N^{+}$): 156.17522 found: 156.17504. [M*$^{-}$](calcd for $C_{11}H_9F_3FeNO_4S_2^{-}$) : 395.92745 Found: 395.92881. Calcd for $C_{21}H_{31}F_3FeN_2O_4S_2$: N 5.07; C 45.66; H 5.66; S 11.61. Found: N 5.22; C 44.61; H 5.54; S 11.91.

Preparation of ferrocenium sulfonyl(trifluoromethylsulfonyl)imide (Fc(III)NTf). Potassium ferrocenylsulfonyl (trifluoromethylsulfonyl) imide (1 eq.) and iron(III) chloride hexahydrate (3 eq) were dissolved in Milli-Q water at 0 °C. A blue precipitate was instantly formed and the mixture was stirred for 30 minutes at 0 °C. The mixture was filtered and the blue precipitate was washed with cold Milli-Q water and diethyl ether. The salt was dried overnight under reduce pressure at room temperature. Yield: 75 %. Elementary analysis: Calcd for $C_{11}H_9F_3FeNO_4S_2$: N 3.54, C 33.35, H 2.29, S 16.19. Found: N 3.45 C 33.42, H 2.24, S 16.20.

Preparation of Ethylviogen di[bis(trifluoromethylsulfonyl)imide] ([EV] [$(NTf_2)_2$]. 4,4'-dipyridyl (1 eq.) and bromoethane (10 eq.) were dissolved in acetonitrile at room temperature and the resulting solution was refluxed for 24 hours. A precipitate was formed and the mixture was cooled at room temperature. The mixture was filtered and the yellow precipitate was washed with acetone and diethyl ether. The dication salt was dried overnight under reduce pressure at room temperature. Ethylviogen dibromide (1 eq.) and lithium bis(trifluoromethylsulfonyl)imide (2.3 eq.) were dissolved in Milli-Q water at room temperature and the mixture was stirred for 24 hours. A white precipitate was formed and was filtered. The precipitate was washed with Milli-Q water and the [NTf_2] salt was dried overnight under reduce pressure at 65°C. Yield: 79% (1st step); 96% (2nd step). ^{1}H NMR (DMSO-d_6, 300 MHz): δ (ppm) = 9.38 (d,4H), 8.77 (d,4H), 4.72 (q,4H), 1.60 (t,6H). ^{19}F NMR (DMSO-d_6, 282 MHz): δ (ppm) = -80.13. ^{13}C NMR (DMSO-d_6, 125 MHz): δ (ppm) = 149.05; 146.07; 127.00; 122.06; 117.78; 57.06; 16.74. Calcd for $C_{18}H_{18}F_{12}N_4O_8S_4$: N 7.23; C 27.91; H 2.34; S 16.56. Found: N 7.25; C 27.93; H 2.19; S 17.02.

8.3.2. XPS analysis of BMIm Fc(II)NTf and Fc(III)NTf

Table S8.1. Conditions of XPS experiment.

Instrument		**VG ESCALAB 3 MKII**
Source		Al Kα
Power		300 W (15kV, 20mA)
Pressure in the analysis chamber		3.0 x 10^{-9} Torr
Area		2 mm x 3 mm
Photoelectron emission angle		90 degres
Depth		< 10 nm
Detection limit		~ 0.1 % atomic percentage
Survey spectrum	Interval between points	1.0 eV
	Pass energy	100 eV
High-resolution spectrum	Interval between points	0.05 eV
	Pass energy	20 eV
Background substraction		Shirley
Sensitivity factor		Wagner
Corrected binding energy with C1s		285.0 eV

Table S8.2. Identification and quantification of elements following the survey.

Atom/orbital	**BE**	**At. %**	
		BMIm Fc(II)NTf	**Fc(III)NTf**
Si2p	101.8	0.7	---
S2p	168.4	5.5	6.7
C1s	285.0	51.9	47.8
N1s	400.6	8.9	4.5
O1s	531.8	15.1	21.8
F1s	688.1	14.7	14.2
Fe2p	707.8	3.3	5.1

Table S8.3. Identification of chemical bonds following the high-resolution spectrum.

Atom/orbital	BE	Identification	At. %	
			BMIm	**Fc(III)NTf**
S2p3/2	168.1	S (Sulfonyl)	4.8	6.6
C1s	285.0	C-C et C=C	38.2	41.7
	286.6	C-C*-N and C=C*-N	10.7	
	287.4	N-C=N	3.6	
	292.2	CF_3		3.2
	292.6		3.4	
N1s	398.5	N-	2.8	3.5
	399.8	C-N		0.6
	401.6	N+	5.5	
O1s	530.2	Fe-O		1.9
	531.8	O (Sulfonyl), SiO_2		20.9
	532.0		15.6	
F1s	684.3	F-metal	0.9	
	688.1	CF_3	11.1	14.7
Fe2p3/2	707.9	Fe (II) (Ferrocene)	3.4	1.6
	709.5	Fe (III) (Ferrocene)		2.6
	711.2	Fe (III) (Oxide)		1.8
	716.0	Fe (III) (Shake up)		0.9

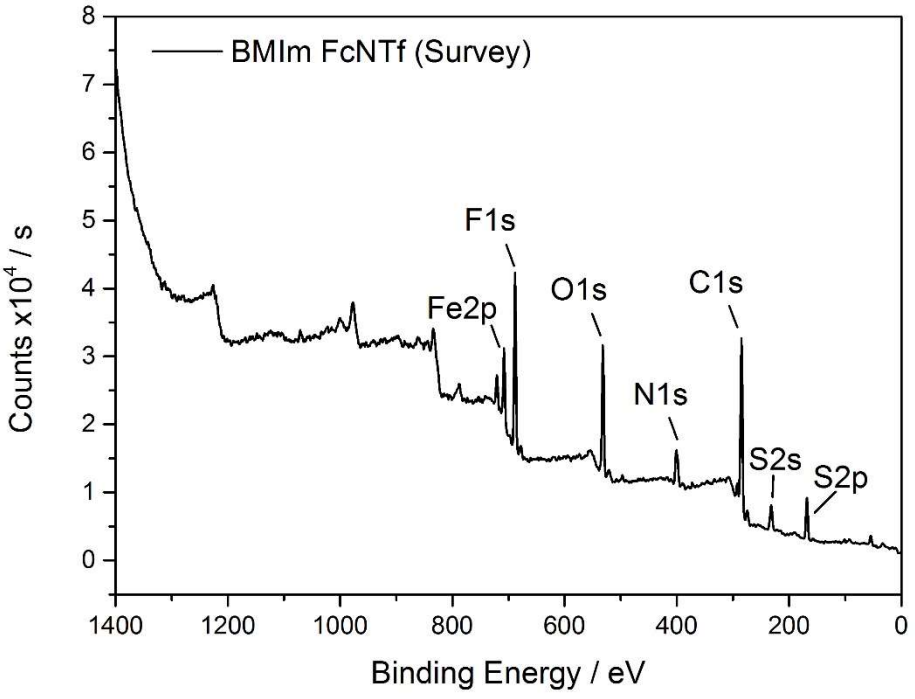

Figure S8.1. XPS survey spectra measured on BMIm Fc(II)NTf.

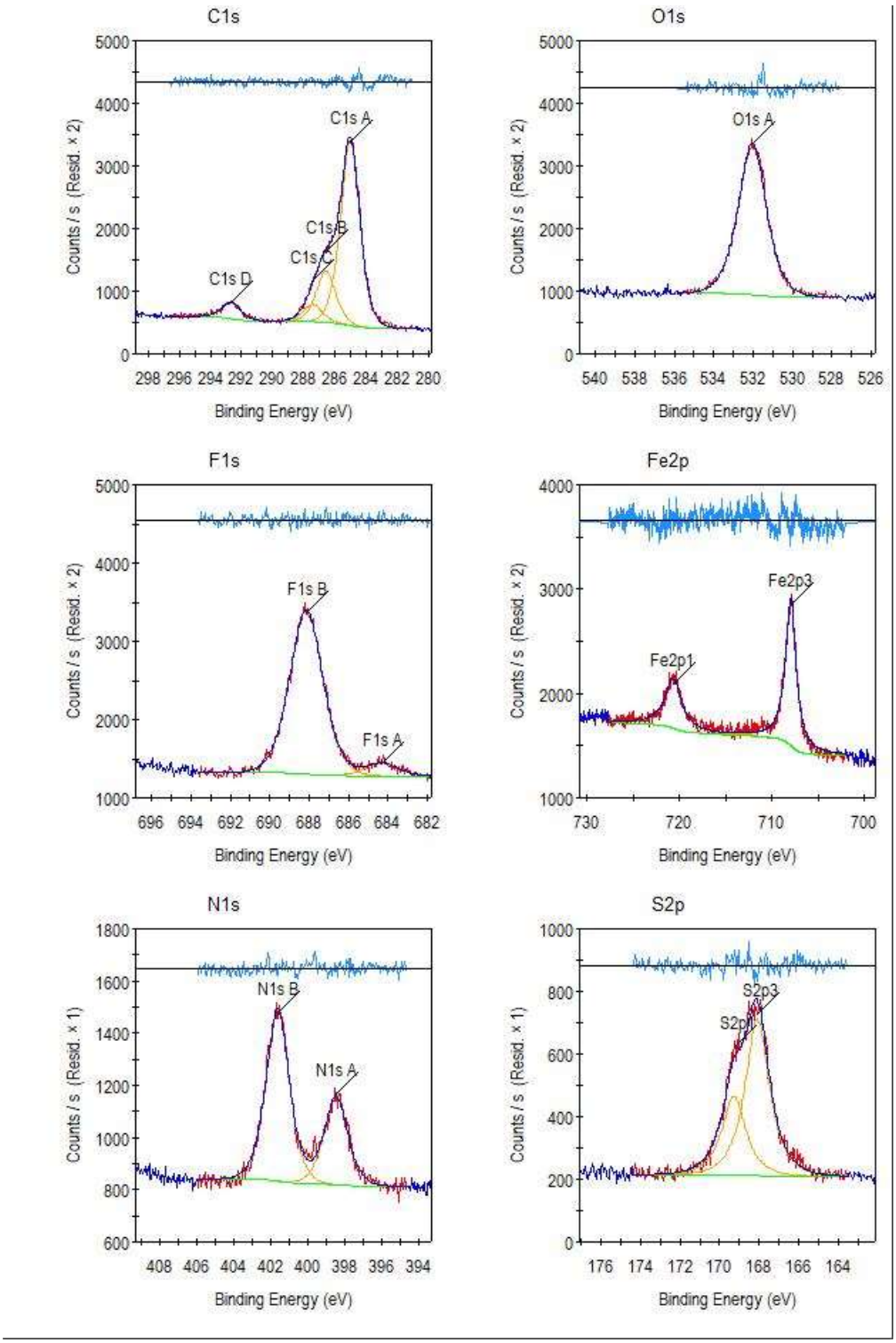

Figure S8.2. XPS high-resolution spectra measured on BMIm Fc(II)NTf.

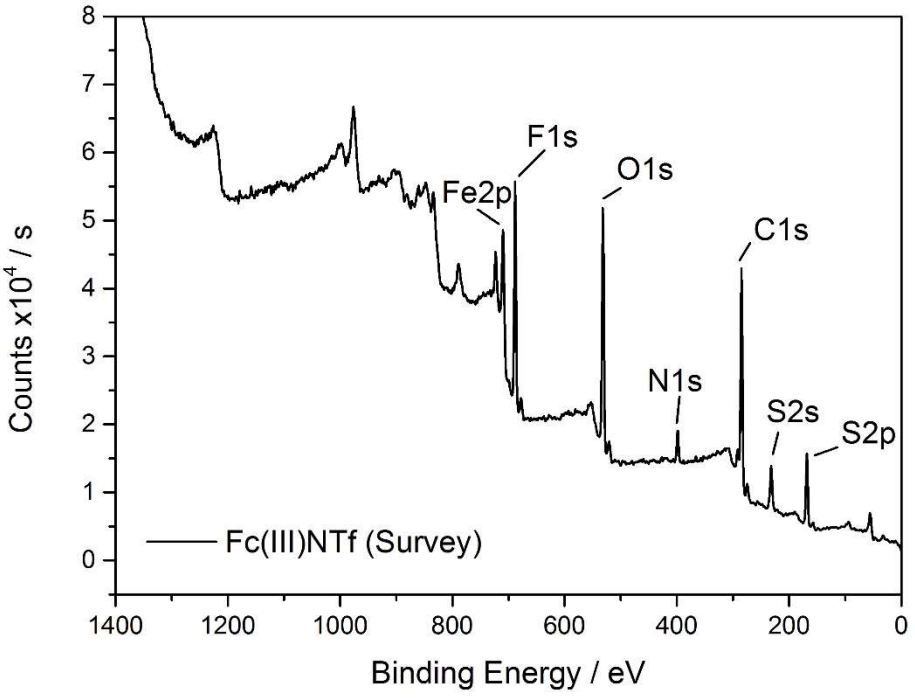

Figure S8.3. XPS survey spectra measured on Fc(III)NTf.

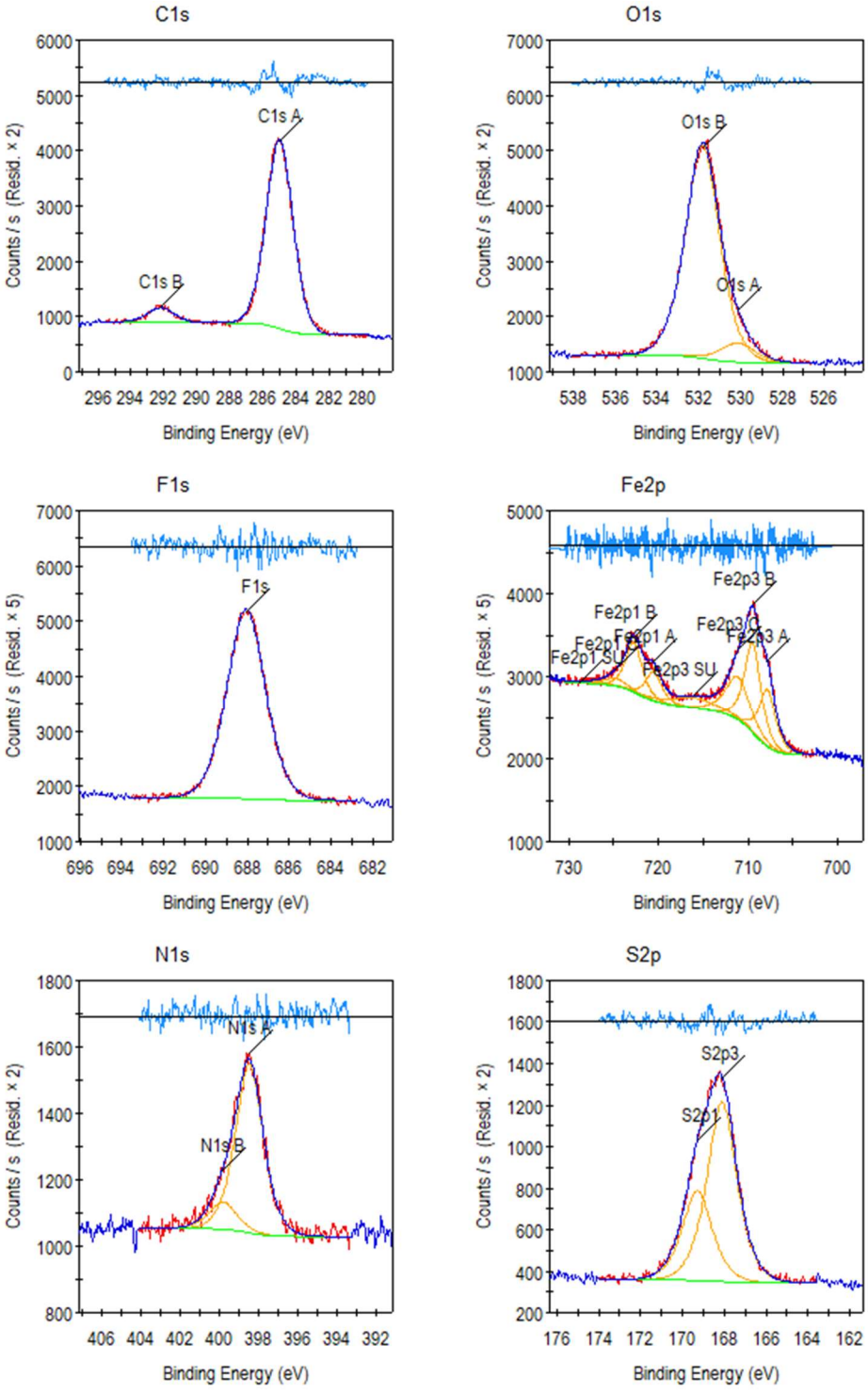

Figure S8.4. XPS high-resolution spectra measured on Fc(III)NTf.

8.3.3. Thermal analysis

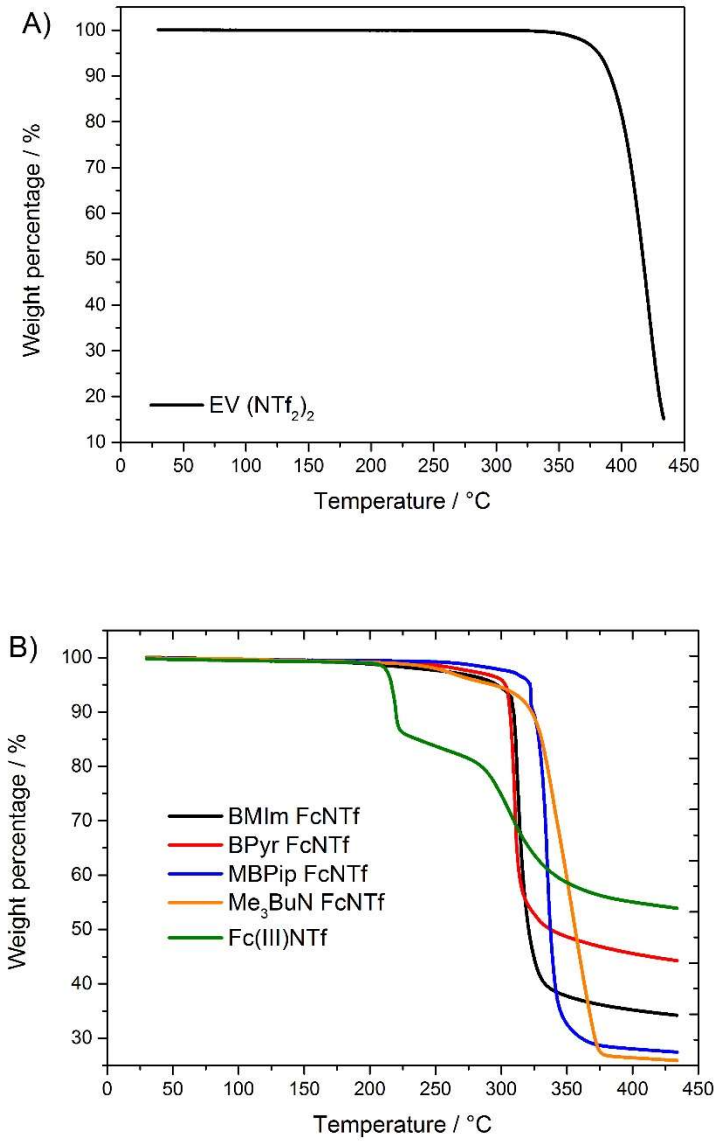

Figure S8.5. A) TGA thermogram of [EV] [$(NTf_2)_2$] and B) TGA thermograms of neat [BMIm] [FcNTf], [BPyr] [FcNTf], [MBPip] [FcNTf], [Me_3BuN] [FcNTf] and [Fc(III)NTf] with a ramp of 10°C per minute under helium atmosphere.

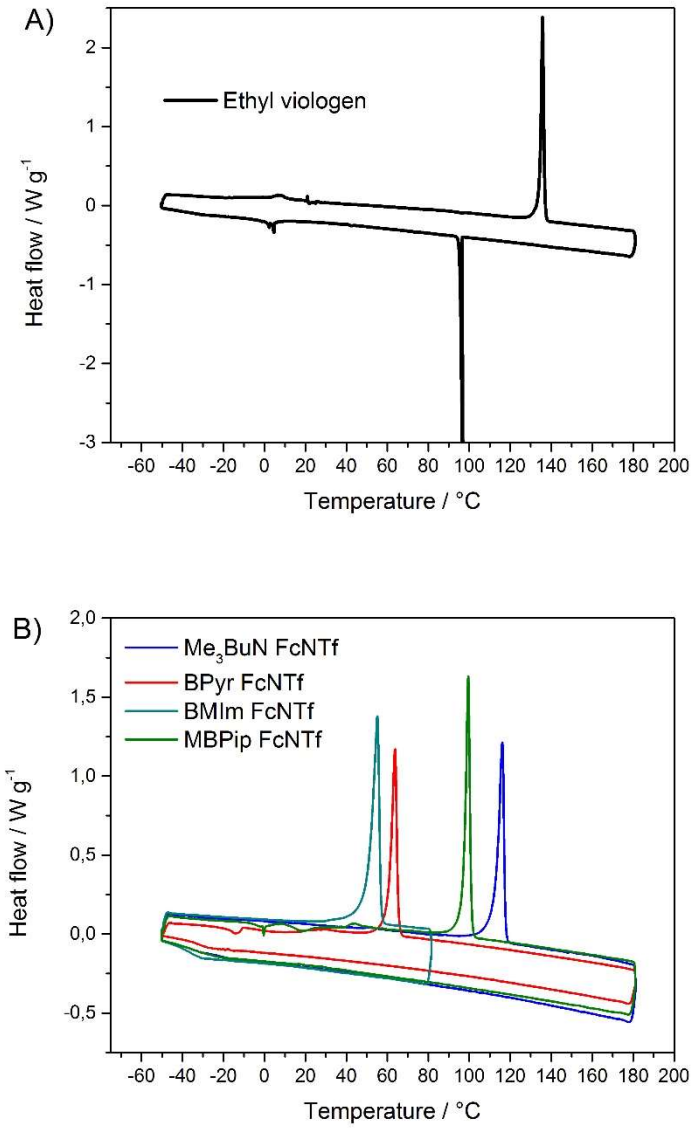

Figure S8.6. A) DSC thermogram of [EV] [$(NTf_2)_2$] and B) DSC thermograms of redox species based on [FcNTf] anion such as [Me_3BuN] [FcNTf], [BPyr] [FcNTf], [BMIm] [FcNTf] and [MBPip] [FcNTf]. The measurements were done with a ramp of 5 °C per minute and with isothermal of 5 minutes between the cooling and heating. (exo, down)

8.3.4. Extra cyclic voltammetry and chronoamperometry

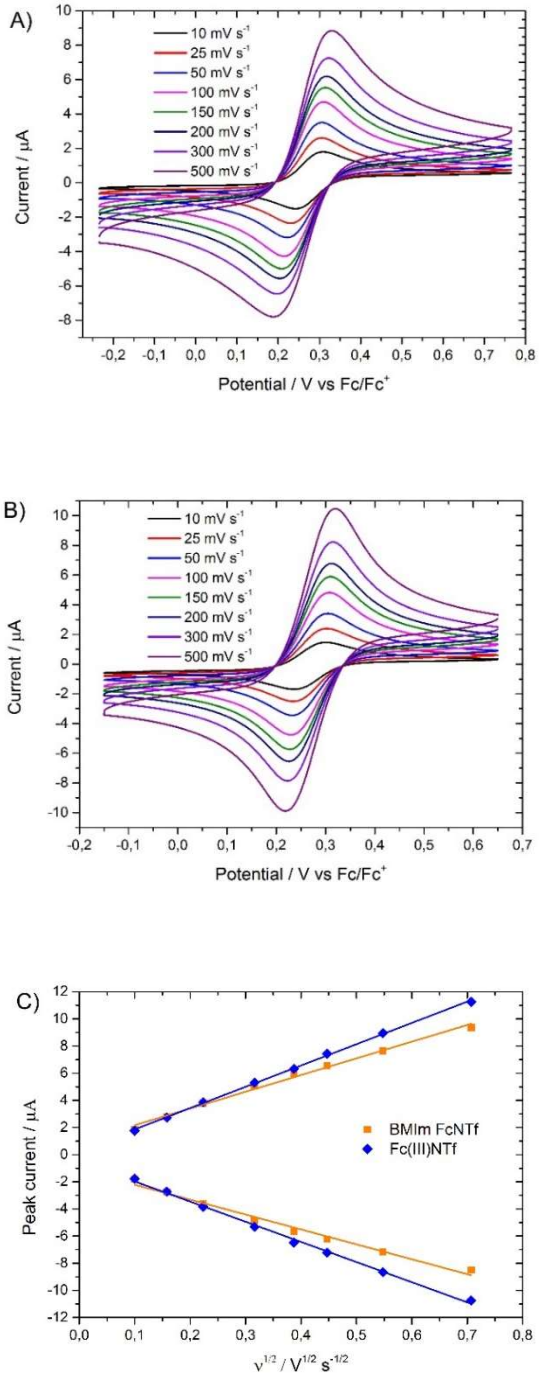

Figure S8.7. CVs of 10 mM solution of A) [BMIm] [FcNTf] and B) [Fc(III)NTf] in [BMIm] [NTf_2] at various scan rates. C) Randles-Sevcik plot and the scan rates used were 10 to 500 mV s^{-1}.

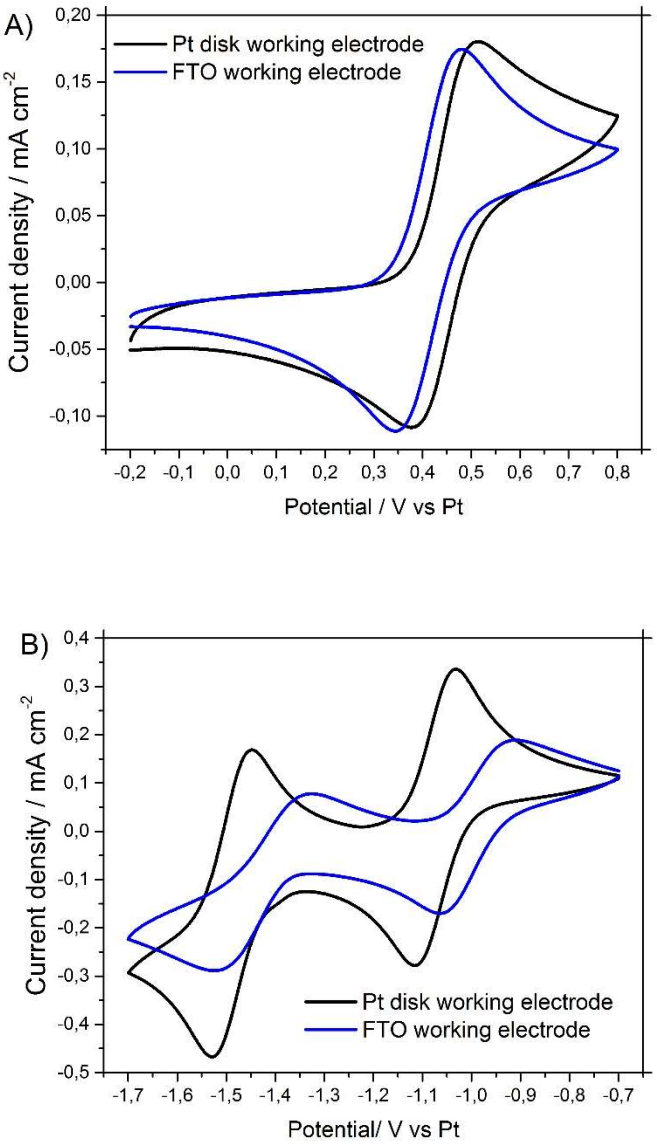

Figure S8.8. CVs of 10 mM solution of A) [FcNTf] anion and B) [EV] dication in [BMIm] [NTf_2] performed at 100 mV s^{-1} using Pt disk and FTO working electrodes.

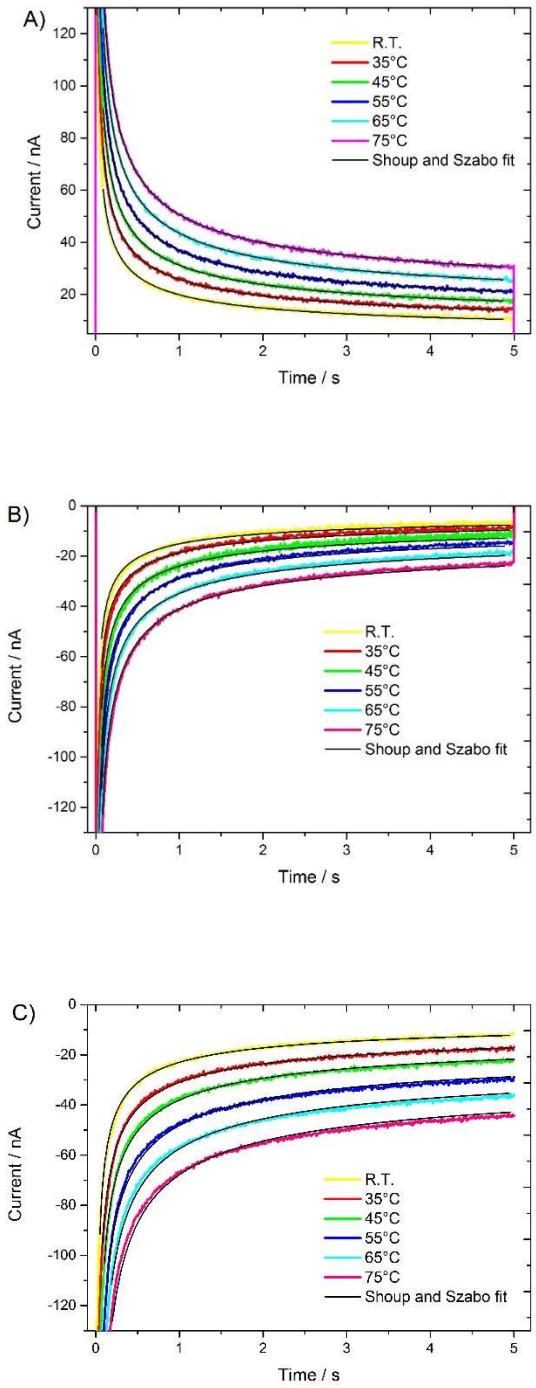

Figure S8.9. DPSC using a microelectrode of 10 mM solution of A) [BMIm] [FcNTf], B) [Fc(III)NTf] and [EV] $[NTf_2]_2$ in [BMIm] $[NTf_2]$ at different temperatures using Shoup and Szabo fit.

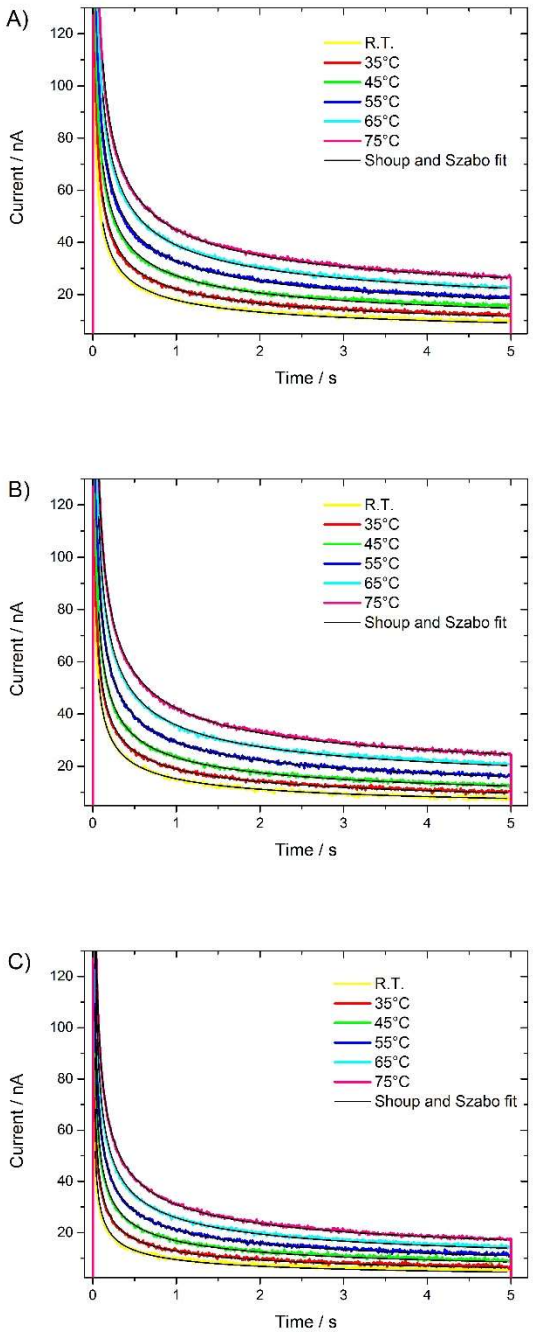

Figure S8.10. DPSC using a microelectrode of 10 mM solution of A) [BPyr] [FcNTf], B) [Me_3BuN] [FcNTf], C) [BMPip] [FcNTf] in corresponding common IL ([BMIm], [BPyr], [Me_3BuN] or [BMPip] [NTf_2]) at different temperatures using Shoup and Szabo fit.

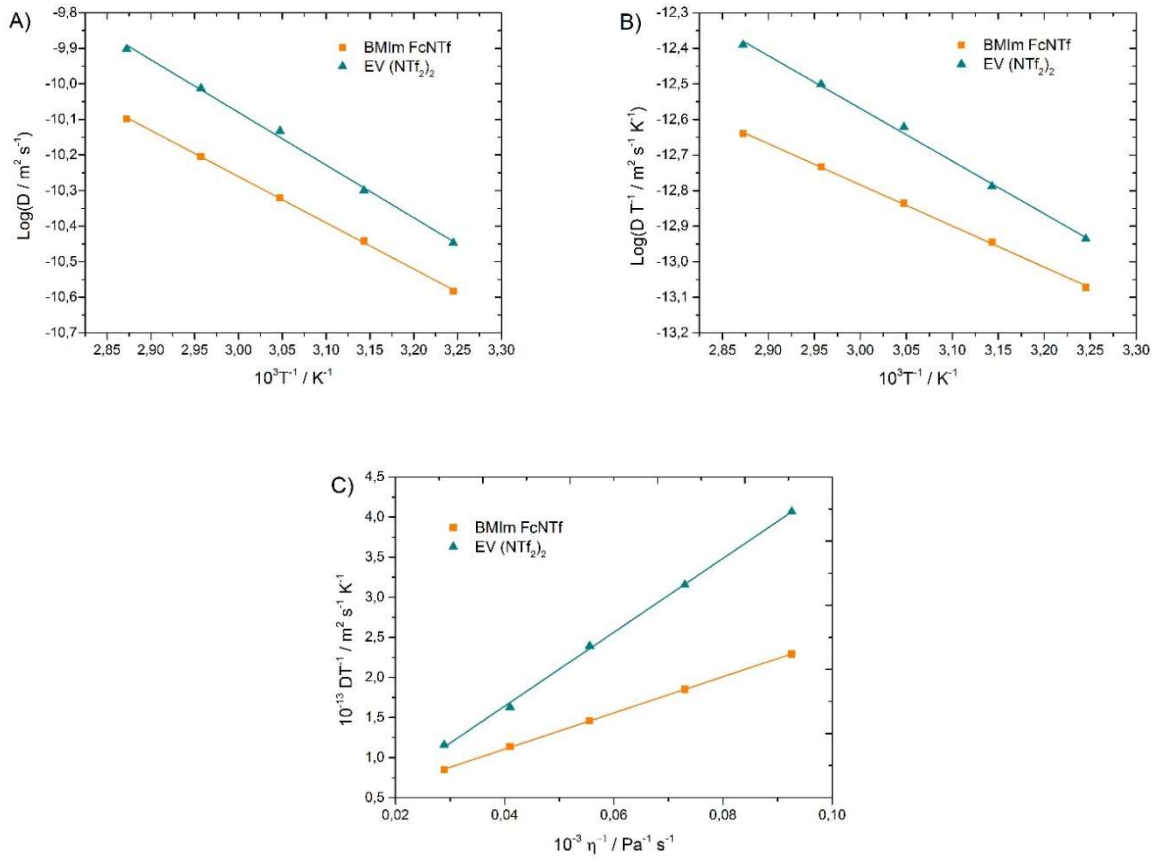

Figure S8.11. A) Arrhenius plots, B) Eyring plots and C) Stokes-Einstein plots for 10 mM of [BMIm] [FcNTf] (orange line) and [EV] [$(NTf_2)_2$] (cyan line) in [BMIm] [NTf_2]. Measurements were done at 10°C intervals between 35 and 75°C.

8.3.5. References

[1] B. Gélinas, D. Rochefort, Synthesis and characterization of an electroactive ionic liquid based on the ferrocenylsulfonyl(trifluoromethylsulfonyl)imide anion, Electrochim. Acta, 162 (2015) 36-44.

Chapitre 9 : Conclusions et perspectives

9.1. Avant-propos

En résumé, cette thèse recueille une introduction aux liquides ioniques électroactifs et à la sécurité des piles à ion lithium, un sommaire de la méthodologie et six articles scientifiques ayant un impact dans le domaine de l'électrochimie et du stockage d'énergie. Ces travaux ont permis d'améliorer la compréhension des électrolytes concentrés en espèce électroactive, l'électrochimie des anions électroactifs et des navettes redox dans des piles au lithium. En général, cette thèse est constituée de deux approches scientifiques dont une approche fondamentale où la structure chimique des liquides ioniques électroactifs a été étudiée et la seconde approche est davantage appliquée où une pile au lithium contenant un électrolyte redox-actif est caractérisée. Il y a plusieurs avenues afin d'améliorer la sécurité des piles au lithium et l'objectif de la thèse était d'améliorer la compréhension des liquides ioniques électroactifs afin qu'un jour peut-être les liquides ioniques redox pourront contrôler les surtensions des piles commerciales qui ont subi un viellisement prématuré. Le choix d'utiliser ce type d'électrolyte s'explique afin d'avoir un électrolyte thermiquement stable qui est à prescrire, car les surtensions génèrent de la chaleur par la production de réactions exothermiques. Les liquides ioniques électroactifs présentent les propriétés pour répondre à cette problématique par le biais de leur ininflammibilité, leur miscibilité dans les solvants polaires et leur fonction électroactive pouvant jouer le rôle de navette redox comme une composante additive dans un électrolyte.

9.2. Résumé et conclusions générales

La démarche scientifique de cette thèse est constituée en premier lieu, d'une étape de synthèse de nouveaux liquides ioniques électroactifs dont l'anion a été fonctionnalisé pour la plupart, dans un deuxième temps, la caractérisation des propriétés électrochimiques et physicochimiques des électrolytes électroactifs a été réalisée et en dernier lieu, l'assemblage d'une pile bouton utilisant les électrolytes développés dans cette thèse. Au démarrage de ce projet de thèse, la compréhension de l'électrochimie d'espèces électroactive à haute concentration était peu

présent dans la littérature et encore aujourd'hui, il n'y a que quelques études à ce sujet dont les investigations menées durant cette thèse. Comme première étude, nous sommes intéressés aux modifications structurelles d'un imidazolium greffé à un méthylferrocenyl et nous avons fait varier la chaine latérale d'un méthyle à un dodécanyle. L'impact structurel est atténué avec la dilution du liquide ionique électroactif dans un électrolyte typique pour les piles au lithium et cette étude est très complémentaire aux travaux de Royce W. Murray qui a caractérisé l'électrochimie de ce type de matériaux à l'état pur et à différentes températures.

Sachant que l'impact structurel est significatif seulement à l'état pur et moins en solution, à ce moment, les ions électroactifs étaient pratiquement issus exclusivement de la modification de l'imidazolium. Nous avons décidé de développer des anions électroactifs pour enrichir la littérature qui présentait seulement l'iodure de 1-butyl-3-méthylimidazolium. La stratégie optée pour la synthèse est le couplage entre un chlorure sulfonyl et un sulfonyl amine qui est suivi d'une réaction de métathèse d'ion. La partie électroactive choisie dans un premier temps a été le ferrocenyl, car la littérature traitant de l'électrochimie du ferrocène est riche et le ferrocène est très abordable économiquement parlant. De plus, il a été ainsi possible de comparer l'électrochimie de l'anion électroactif avec le ferrocène et le liquide ionique électroactif où le cation a été modifié aussi avec le ferrocène afin d'établir les bases des relations structure-propriétés pour cette nouvelle famille de liquides ioniques. Il a été observé une augmentation du point de fusion, de la viscosité et d'une diminution de la conductivité ionique en comparaison avec les liquides ioniques communs. À partir de ces résultats, ce type de liquides ioniques seront considérés comme additif et ils ne présentent aucunement les propriétés requises pour être utilisées comme solvant.

Par la suite, cet additif a été employé comme une composante d'un électrolyte électroactif destiné à améliorer la sécurité des piles à ion lithium. Le nombre de transport et la conductivité ionique attribuée aux ions lithium ont été évalués, car ces propriétés sont des paramètres clés qui ont un impact sur les performances d'une pile à ion lithium. L'ajout de cet additif a un léger impact sur la viscosité et la conductivité ionique de l'électrolyte basé sur un mélange d'un sel de lithium, d'un liquide ionique électroactif et d'un solvant de carbonate. Cet électrolyte électroactif à très haute concentration a montré un caractère ininflammable face à une flamme. Il y a été démontré que ce liquide ionique électroactif est bien une navette redox, car un anion redox est oxydé à plusieurs reprises lors du contrôle d'une surtension. Il y a trois propriétés essentielles à connaitre

pour le développement de navettes redox telles que le potentiel d'équilibre, la stabilité électrochimique et le transport de masse de l'espèce électroactive. Par conséquent, le coefficient de diffusion de l'anion électroactif a été évalué et la fonctionnalisation d'un anion donne des espèces électroactives qui diffusent légèrement plus lentement, mais la polarisation positive de la l'électrode de haut potentiel peut favoriser la migration de l'anion redox. Finalement, le potentiel d'équilibre pour l'anion redox basé sur le ferrocène est trop bas pour des applications avec les matériaux d'électrode positive à haut voltage ou de voltage modéré comme le $LiFePO_4$. De plus, une propriété inattendue qui dépend de la structure rigide de l'anion est l'électrodéposition de cet anion à haute concentration. Ce comportement a été exploité pour réduire l'autodécharge dans les supercapaciteurs utilisant des électrolytes électroactifs et un premier exemple de navette redox électroactif qui peut contribuer au stockage d'énergie.

Les chercheurs dans le domaine du développement de navettes redox travaillent activement pour augmenter le potentiel dans l'objectif de protéger des matériaux d'électrode positive de plus haut potentiel et qui sont du même coup plus dangereux. Le 2,5-ditert-butyl-1,4-dimethoxybenzene présente la navette la plus stable électrochimique, mais la solubilité de cette espèce électroactive est faible et le potentiel est relativement bas. La contribution de cette thèse est sans aucun doute l'amélioration de la solubilité en utilisant la plateforme des liquides ioniques. Nous avons aussi étudié la modification du centre électroactif du dimethoxybenzène et le constat de cette étude est qu'il n'est pas une mince tâche d'obtenir une espèce électroactive à très haut potentiel. La stabilité électrochimique diminue, car les espèces électroactives produites lors de l'oxydation sont davantage réactives.

Dans un tout autre ordre d'idée, nous avons évalué l'utilisation de l'anion redox à base de ferrocène précédemment discuté comme navette redox dans les piles à ion lithium dans un autre type de dispositif électrochimique. Ce liquide ionique électroactif a été utilisé comme une espèce électroactive anodique et en présence du viologène étant une espèce électroactive cathodique et électrochromique qu'ils sont dissous dans un liquide ionique commun pour former un électrolyte. L'objectif est d'exploiter la différence de potentiel entre ces sels électroactifs pour fabriquer un dispositif électrochromique qui revient transparent quand aucun potentiel n'est appliqué. Plusieurs liquides ioniques électroactifs basés sur l'anion électroactif utilisant différents contre-cations. Les

performances du dispositif électrochromique sont limitées par la concentration du viologène dans le liquide ionique.

9.3. Travaux futurs

Les avancées scientifiques présentées dans cette thèse permettront d'augmenter l'intérêt des chercheurs d'utiliser les liquides ioniques électroactifs dans différentes applications et de continuer d'explorer l'électrochimie concentrée où des phénomènes électrochimiques peuvent se produire seulement à certaines concentrations. Les prochains travaux à partir de cette thèse sont l'étude de la décomposition à long terme et la stabilité des liquides ioniques électroactifs inactifs avant leur utilisation comme navette redox après des centaines de cycles de charge et décharge normaux. Évidemment, le développement de liquides ioniques électroactifs dont le potentiel d'oxydation se retrouve au-delà de 4 V est toujours un objectif à atteindre afin d'en élargir la portée d'application. L'utilisation de fonctions électroactives de faible masse molaire dans l'objectif d'obtenir des liquides ioniques électroactifs qui sont dans leur phase liquide à la température ambiante et avec cette propriété, ce liquide ionique fonctionnalisé pourrait jouer le rôle de solvant. Dans le but d'approfondir notre compréhension au sujet de la formation du film zwitterionique à la base de ferrocenium avec un anion triflimide, des analyses de surfaces ont déjà débuté à l'écriture de cette thèse. L'amélioration de la compréhension du diméthoxybenzene comme centre électroactif est essentielle pour désigner de nouvelles structures chimiques et ce centre électroactif est le plus prometteur pour répondre au besoin d'un haut potentiel et d'une bonne stabilité électrochimique.

Les résultats de cette thèse laissent présager qu'il serait possible d'employer nos électrolytes électroactifs dans des systèmes hybrides comme les supercapaciteurs à ion lithium qui pourraient combiner mes travaux avec l'étude de Han Jin Xie qui a caractérisé les supercapaciteurs utilisant un électrolyte concentré en liquide ionique électroactif (l'étude se retrouve à l'Annexe 2). Toujours dans le domaine du stockage d'énergie, les batteries à flux (en anglais, redox flow batteries) utilisent des électrolytes concentrés d'espèces électroactives très oxydantes et réducteurs pourraient bénéficier de ce type de liquides ioniques rédox. D'après les potentiels oxydants des liquides ioniques électroactifs développés selon l'objectif de la thèse, les liquides ioniques électroactifs joueront comme rôle de catholyte qui est la matière active de l'électrolyte à l'électrode positive. Les hautes concentrations en centres rédox et la large plage de stabilité électrochimique

des liquides ioniques rédox pourraient être particulièrement avantageux pour augmenter la densité énergétique de ces batteries à flux. Ces mêmes liquides ioniques électroactifs peuvent être utilisés comme médiateur dans une batterie lithium-air et une cellule photovoltaïque à colorant.

Il demeure bien entendu beaucoup de travail à accomplir pour atteindre une compréhension profonde des propriétés des liquides ioniques rédox. Cette thèse a démontré qu'il est possible de faire le design et la synthèse d'une grande panoplie de liquides ioniques rédox et qu'ils peuvent trouver une application dans différents systèmes électrochimiques. Il est souvent remarqué que le nombre de structures de liquides ioniques est théoriquement « infiniment » grand et que l'apparition de nouveaux systèmes n'est limitée que par l'imagination des chercheurs oeuvrant dans le domaine et par les voies de synthèse afin de les obtenir. Cette thèse en a fait une bonne démonstration et a proposé de nouvelles voies de synthèse qui pourront être reprises par la communauté et contribuer à matérialiser les futures structures imaginées par les chercheurs dans le domaine des liquides ioniques.

Annexe 1: L'effet de la chaîne latérale d'un liquide ionique utilisant un anion électroactif

A1.1. Avant-propos et mise en contexte

Cette annexe a été rédigée sous forme d'un article qui a été soumis à *Electrochimica Acta*. Cette recherche est une continuité du **Chapitre 4** et l'objectif de cette investigation est d'établir le cation d'imidazolium approprié en évaluant les propriétés physicochimiques et électrochimiques de ces liquides ioniques électroactifs. L'impact de la modification de la chaîne latérale des liquides ioniques non-électroactifs à base d'imidazolium a bien été établi par le Prof. Watanabe et par conséquent, c'est dans la même veine d'idée que cette publication contribue en présentant une étude similaire avec les liquides ioniques utilisant un anion électroactif. L'impact de la modification structurelle a été démontré à l'état pur et en solution. Évidemment, la modification de liquides ioniques électroactifs peut être comparée aux cations d'imidazolium fonctionnalisé avec un groupement ferrocenylméthyle et cette investigation est présentée dans le **Chapitre 1**.

Les liquides ioniques redox basés sur l'anion FcNTf électrodépose à haute concentration ce qui est mentionné antérieurement et cet article montre une étude plus approfondie pour éventuellement utiliser cette propriété dans les supercapaciteurs. L'électrodéposition est un stratagème pour réduire l'autodécharge et il sera le principal sujet dans l'**Annexe 2**.

A1.2. Article: Electrochemical and physicochemical properties of redox ionic liquids using electroactive anions: influence of alkylimidazolium chain length

Han Jin Xie[a], Bruno Gélinas[a] and Dominic Rochefort[a],

[a]Département de Chimie, Université de Montréal, Montréal, Québec H3C 3J7, Canada

Electrochimica Acta 200 (2016) 283–289

Article history: Received 18 November 2015 Received in revised form 5 February 2016 Accepted 12 March 2016 Available online 22 March 2016, http://dx.doi.org/10.1016/j.electacta.2016.03.075

A1.2.1. Highlights

- NTf_2 anion commonly used in ionic liquids is modified with ferrocene.
- Combining Fc-modified NTf anion with alkylimidazolium provides redox ionic liquids.
- Longer alkyl chains increase viscosity and decrease conductivity.
- Electrochemistry in pure phases shows transport by diffusion and migration.
- A film is formed upon oxidation of the Fc-anion, which is removed by reduction.

A1.2.2. Abstract

Ferrocenylsulfonyl(trifluoromethylsulfonyl)imide [FcNTf] is reported as a redox anionic species used to obtain an electroactive ionic liquid with a typical alkylimidazolium cation. Here, several of these redox ionic liquids (RILs) were prepared by combining FcNTf with alkylimidazolium cations in order to understand the influence of symmetry and alkyl chain length on the RIL system. The physicochemical and electrochemical properties are characterized for $[C_xC_yIm][FcNTf]$, where x and y were varied between 1 and 8, both in the pure, undiluted state and in solutions of acetonitrile. In pure form, the ionic conductivity of $[C_xC_yIm][FcNTf]$ was found to range between 0.22 and 0.42 mS cm^{-1} at 60 °C, and the alkyl chain length was found to have a similar effect on viscosity as in conventional imidazolium-NTf_2 ionic liquids. While an increase in

alkyl chain length increases viscosity and decreases mass transport, it was found to have no effect on the redox potential of the ferrocene center. The cyclic voltammetry of $[C_xC_yIm][FcNTf]$ solutions diluted in acetonitrile exhibited behavior which depends on concentration and on the presence of a supporting electrolyte. At concentrations above 50 wt.% and in the absence of any supporting electrolyte, the electroactive anion was found to deposit as a dense film on the electrode upon oxidation. This behavior is linked to formation of Fc^+NTf^- zwitterions, which accumulates in the double-layer and precipitates on the electrode surface. This study also investigates the electrochemical properties of film deposition.

Keywords: Redox ionic liquids; ionic conductivity; ferrocenyl; imidazolium; cyclic voltammetry.

A1.2.3. Introduction

Ionic liquids (ILs) are composed entirely of ions and present a melting point below 100 °C [1, 2]. Their potential application in the field of electrochemistry is very attractive due to the potential – depending on the selected ion – to obtain liquid phases with a low vapour pressure, good thermal and chemical stability, good ionic conductivity, and a large electrochemical window of stability. Ionic liquids become increasingly appealing when considering the numerous possibilities for structure modification and ion combinations. The incorporation of functional groups on the cation or anion structure can be used in order to accomplish specific tasks for a specific application [3-5]. The use of redox-active ionic liquids (RILs) is increasingly prevalent in the literature for fundamental studies on electron transfer in concentrated phases as well as for application in energy storage devices. Redox ionic liquids may be considered intrinsically electroactive with the presence of redox-active counter-ions. Examples of RILs include iodide-based ([I]) [6-8], metal complexes based on ([Ru],[Co],[Fe]) [9, 10] and metallocenium [11] or viologen ($[C_4VC_7]$) [12]—based counter ions. Additionally, ILs may be made electroactive by grafting a redox functional group on a common cation or anion structure. Functional groups such as ferrocenyl (Fc) [13-21], 2,5-di-tert-butyl-1,4-dimethoxybenzene (DDB) [22], 2,2,6,6-Tetramethylpiperidin-1-yl)oxyl (TEMPO) [23, 24], and metal complexes [25, 26] have been reported in the literature. Redox ionic liquids could replace traditional redox systems which are used in several electrochemical applications to transfer electrons in homogeneous or heterogeneous reactions. Related to energy storage and conversion RIL can increase the specific energy in

pseudocapacitors [6, 27], achieve internal electron transfer in dye-sensitized solar cells [8, 23] and act as redox shuttles in lithium-ion batteries to prevent cathode over-oxidation [15, 28].

Designing redox-active ILs with improved properties is required to achieve an application in this area, but insufficient fundamental understanding of the relationship between various structure properties is currently impeding progress. While most examples of RILs were obtained through modification of the cation, our group reported on the first example of anion modification with ferrocene in order to generate an electroactive ionic liquid. A ferrocenylsulfonyl(trifluoromethylsulfonyl)imide anion (FcNTf) [14] was combined with 1-butyl-3-methylimidazolium, and the resulting RIL's physicochemical and electrochemical properties were discussed in a previous paper. Since only one cation was used in the aforementioned study, the effect of its structure on the ionic liquid's properties was not established. Systematic studies of the effect of structural modifications of the cation in conventional ionic liquids have been previously reported, for example by Watanabe [29, 30]. In this study, we wish to determine the role of the imidazolium alkyl's chain length on the transport and electrochemical properties of electroactive ionic liquids employing a redox anion.

To do so, seven different RILs were prepared based on the ferrocenylsulfonyl(trifluoromethylsulfonyl)imide anion (FcNTf) and imidazolium cation (C_xC_yIm). Their structures are presented in **Figure A1.1**. The effect of alkyl chain length and symmetry on the imidazolium was investigated for all cation structures, and viscosity, conductivity and redox properties were measured for the RIL, in pure form as well as in acetonitrile solutions. These properties were compared with conventional, unmodified IL systems found in the literature. Results of cyclic voltammetry experiments on the RIL at high concentrations are discussed to provide additional data on the electrochemistry of these redox liquid phases.

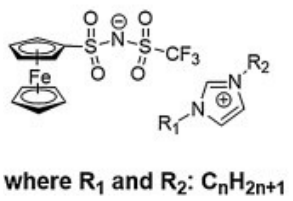

Asymmetric			Symmetric		
Abbreviations	R_1	R_2	Abbreviations	R_1	R_2
C_1C_2Im	CH_3	C_2H_5	C_1C_1Im	CH_3	CH_3
C_1C_4Im	CH_3	C_4H_9	C_2C_2Im	C_2H_5	C_2H_5
C_1C_8Im	CH_3	C_8H_{17}	C_4C_4Im	C_4H_9	C_4H_9
			C_8C_8Im	C_8H_{17}	C_8H_{17}

Figure A1.1. General structure of $[C_xC_xIM][FcNTf]$ with cation structure variations and abbreviations.

A1.2.4. Experimental

Materials

All reagents and precursor chemicals were obtained from Sigma-Aldrich unless otherwise stated, and all solvents were obtained from Fisher. The trifuoromethanesulfonamide was ordered from Synquest Laboratories. All products were used as received.

Synthesis of RILs

Synthesis of the redox anion ferrocenylsulfonyl(trifluoromethylsulfonyl)imide (FcNTf) was performed in accordance with a method published earlier [14]. All alkylimidazolium cations were prepared following established procedures, and detailed synthetic steps for the imidazolium cations $[C_1C_2Im]$, $[C_4C_4Im]$, $[C_2C_2Im]$ and $[C_1C_8Im]$ are provided in **Figure A1.S1**(B) [31]. In short, a solution of the corresponding alkylimidazole and alkylhalides was mixed in an acetonitrile solution. The resulting reaction product was washed with ethyl ether and the final product dried under vacuum at 75 °C before characterization (yield: 98%). For the synthesis of $[C_1C_1Im]$ and $[C_8C_8Im]$, a different procedure (**Figure A1.S1**(C)) was used due to a low reaction yield of pathway B and some difficulty in eliminating impurities from the final product. In this case, sodium imidazolate was added to a 10 ml of THF solution. Two molar equivalents of alkyl halide (1-iodomethane, bromooctane) were then added to the mixture. The mixture was maintained under reflux for four hours. The resulting substance was washed with THF, followed by dichloromethane and diethyl ether (yields: 67% and 99%). The final steps in RIL synthesis consisted of a recombination reaction of cation and redox anion from the metathesis reaction with Na FcNTf

dissolved in water, carried out in an ultrasonic bath for two hours (**Figure A1.S1**(D)). This step was followed by intensive washing with water to eliminate the sodium halide salt. The RILs were dried overnight under vacuum and stored in the glove box for further analysis. Following this drying step, the resulting water concentration in undiluted RIL was found at 144 ppm for $[C_1C_2Im][FcNTf]$ and 170 ppm for the $[C_1C_4Im][FcNTf]$. These values are similar to those reported for vacuum-dried unmodified ionic liquids [32].

Characterization

All synthesized compounds were characterized by ^{1}H, ^{13}C and ^{19}F NMR on a Bruker ADVANCE 300 MHz spectrometer at room temperature and by mass spectrometry (MS) on an Agilent ESI-LC-MSD TOF. Elemental analysis was performed on an EAS 1108 apparatus from Fisons Instruments SPA. Detailed results of this characterization are provided in the supporting information. The presence of water in IL was determined through coulometric Karl Fisher titration (Mettler Toledo Coulometric KI Titrator). The determination of w_{H2O} was performed three times for each sample. The density measurement was made through a very simple method with an electronic balance (Mettler Toledo XS105 Dual Range) and a 1 ml syringe. The viscosity values were obtained by a viscometer from Cambridge Applied Systems between 50 °C and 80 °C, at temperature intervals of 4 °C. Thermal properties were obtained by DSC analysis on a TA Q2000. Two heating cycles were done on each RIL with a scan rate of 1 °C min^{-1} at temperatures ranging −70 °C to 100 °C. The ionic conductivity was measured by AC impedance using a Parstat 2273 potentiostat from Princeton Applied Research, with a flow conductivity Orion (018012) cell composed of two platinized Pt electrodes that were calibrated daily with a standard solution of 0.117 M KCl (0.015 S cm^{-1} at 25 °C). The measurement was carried out from 1 MHz to 1 Hz at 25 °C- 80 °C, at temperature intervals of 4 °C. A BioLogic SP-50 potentiostat was used for cyclic voltammetry (CV) and AC impedance measurements, using a three-electrode setup composed of a silver wire quasi-reference electrode, a Pt wire counter electrode, and a platinum disk working electrode with a surface area of 0.0194 cm^2. All RILs were diluted in acetonitrile solution with 1 M TBAP and the total volume of solution in the cell for each experiment was about 1.5 mL. All potentials are reported to the mid-point potential of the ferrocene/ferrocenium (Fc/Fc^+) redox couple which was determined separately in the given electrolyte.

A1.2.4. Results and discussion

Physicochemical properties of RILs based on FcNTf

The thermal properties of the RILs obtained by DSC analysis (see curves in **Figure A1.S2**) are summarized in **Table A1.1**. An endothermic peak ascribed to the melting point (T_m) is observed for all RILs, but only upon the first heating cycle. No exothermic peaks corresponding to crystallization temperature (T_{cr}) are seen at a 1 °C min^{-1} rate due to slow crystallization kinetics, which is a common behavior of ionic liquids. Such slow kinetics are caused by the asymmetric structure of the FcNTf anion moiety and the high viscosity of RILs. All FcNTf-based RILs are solids at room temperature; however, they are frequently found in a super-cooled state for several days at ambient conditions prior to crystallization [14], thus permitting cyclic voltammetry experiments on the pure phase. For all cooling cycles, a glassy transition temperature (T_g) of similar value is observed, despite different cooling cycles. Common ILs generally tend to form a glass state rather than a crystalline state upon cooling. This is due to low energy gain in crystal formation rather than a loss of entropy [33-35], which often leads to observation of a T_g instead of a T_{cr}. In **Table A1.1**, a decreasing T_m is observed along with an increasing alkyl side chain length on imidazolium, due to larger cation size and increased interactions between the chains. Furthermore, linear alkyl substituents on the cation may also generate multiple rotation degrees of freedom, which also contribute to a lower T_m value [36]. The variance in T_m along with alkyl side chain for RILs follows a tendency similar to the one observed with common redox ILs [29]. No clear trend may be established as a function of chain length symmetry on the cation structure. The presence of a symmetrical structure generally provides more efficient ion–ion packing − and thus a higher crystalline order − and increases T_m. For the systems studied, symmetry has a limited influence over columbic attraction, which appears to be the dominant force. In comparison with conventional unmodified ionic liquids, the physicochemical properties of RILs showed an increase of T_m and T_g, likely due to additional π-π intermolecular interactions between ferrocene units between the FcNTf anions. The DSC analysis of [C_1C_8Im][FcNTf] and [C_8C_8Im] [FcNTf] showed no T_m and T_g due to their super cooled state within the temperature range measured. Density values are also listed in **Table A1.1** for all RILs except [C_1C_1Im][FcNTf] which is in a solid form at room

temperature. A decrease in density with an increased cation size and decreased symmetry are observed [37, 38]. This tendency is typical for common imidazolium-based ILs and results from less densely-packed ions [39-41].

Table A1.1. Physicochemical properties of [CxCyIm][FcNTf] and its corresponding common IL. The values in italic are from other sources (see footnote).

RILs [FcNTf]	T_m /°C	T_g /°C	Density /g cm^{-3} (20 °C)	ILs [NTf_2]	T_m /°C	T_g /°C	Density /g cm^{-3} (20 °C)
C_1C_1Im	89.2	-23.47	-	C_1C_1Im[b]	*26*	-	*1.57*
C_1C_2Im	64.7	-32.54	1.53	C_1C_2Im[b]	*-18*	*-87*	*1.53*
C_2C_2Im	58.1	-34.57	1.42	C_2C_2Im[c,d]	*-11*	-	*1.47*
C_1C_4Im	55.2	-36.20	1.51	C_1C_4Im[b]	*-3*	*-87*	*1.44*
C_4C_4Im	51.0	-38.64	1.35	C_4C_4Im	-	-	-
C_1C_8Im	-	-	1.39	C_1C_8Im[b]	-	*-80*	*1.33*
C_8C_8Im	-	-	1.28	C_8C_8Im	-	-	-

[b]Watanabe *et al.* [29], [c]Andrzej *et al.* [48], [d]Gardas *et al.* [49].

Ionic conductivity of undiluted RILs

Next, the ionic conductivity and electrochemical response of the pure redox ionic liquid phases were studied to provide a better understanding of the cation's impact on RIL properties. The ionic conductivity of pure RILs, as measured by impedance spectroscopy, is shown in **Figure A1.2** as a function of temperature. As a comparison between conventional and modified ionic liquids, the ionic conductivity of RIL [C_1C_2Im][FcNTf] and [C_1C_2Im][NTf_2] is 0.136 mS cm^{-1} and 13.78 mS cm^{-1}, respectively, at 40 °C [29]. The decrease in ionic conductivity of the ferrocenyl-modified IL is due to the presence of a larger anion, which significantly lowers ion mobility. With different cation sizes, higher ionic conductivity is observed with shorter cation alkyl chains due a decreased number of van der Waals interactions between side chains. This tendency is similar to

that of conventional ILs reported in the literature [29, 42, 43]. The ionic conductivity's dependency on temperature does not follow the typical linear Arrhenius law seen with diluted solutions, and a slight curvature is observed at lower temperatures. Most ionic liquids do exhibit such fragile behavior, which is not attributable specifically to the structure of the FcNTf anion [44]. Therefore, the ionic conductivity curve in **Figure A1.2** has been fitted with an empirical Vogel-Fulcher-Tamman model (VFT) shown in Eq. (1):

$$\sigma = \sigma_0 exp^{\left(\frac{-B}{T-T_0}\right)} \qquad (1)$$

where σ is ionic conductivity, σ_0 is the infinite ionic conductivity, T is the absolute temperature, and B and T_0 are fitting parameters, with the B parameter in this model related to the activation energy for ionic conductivity. The values obtained are 684 K, 1199 K, 915 K, and 1159 K for $[C_1C_2Im][FcNTf]$, $[C_2C_2Im][FcNTf]$, $[C_1C_4Im][FcNTf]$, $[C_4C_4Im][FcNTf]$, respectively. An increase in the value of the B parameter with increased alkyl chain length is observed for our RILs (**Table A1.2**). Watanabe et al. published a systematic study of the physicochemical properties of several imidazolium-NTf_2 ionic liquids with different alkyl chain lengths [29]. They found B parameter values from the VFT fitting ranging between 604 and 625 K for ILs with short chains ($[C_1C_1Im][NTf_2]$ to $[C_1C_4Im][NTf_2]$) as well as increasing values for chains with more than four carbon atoms. They also demonstrated that conductivity, diffusivity and viscosity had the same structural dependency. The $[C_1C_1Im]^+$ and $[C_1C_2Im]^+$ cations provided ILs with the same properties, and a decrease in conductivity and diffusivity (along with increased viscosity) was observed with alkyl chains having more than four carbon atoms. This tendency appears to apply also to ionic liquids modified with ferrocene. **Figure A1.3** shows a comparison of the conductivity of three families of ionic liquids with different alkyl chains: the unmodified $[C_1C_YIm][NTf_2]$, the redox ionic liquids $[FcEC_YIm][NTf_2]$ where the cation bears the ferrocene, and $[C_1C_YIm][FcNTf]$ with the redox anion. All three ionic liquids show a very similar decrease in conductivity with a single alkyl chain length increase.

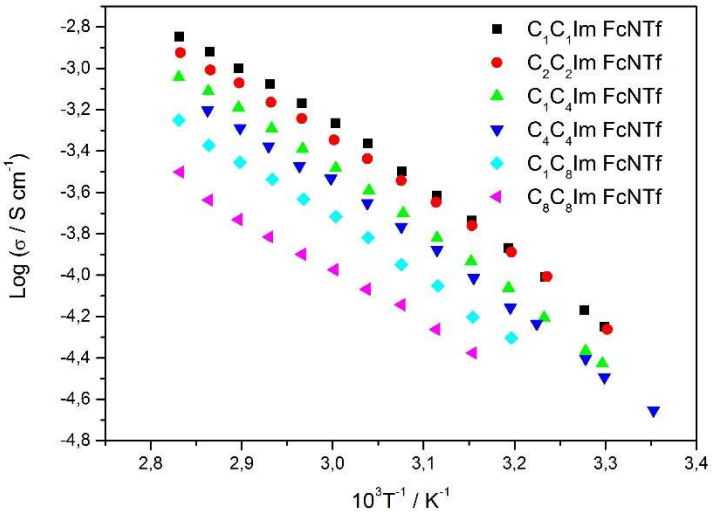

Figure A1.2. Temperature dependence tendencies for ionic conductivity in pure [C_xC_xIm][FcNTf].

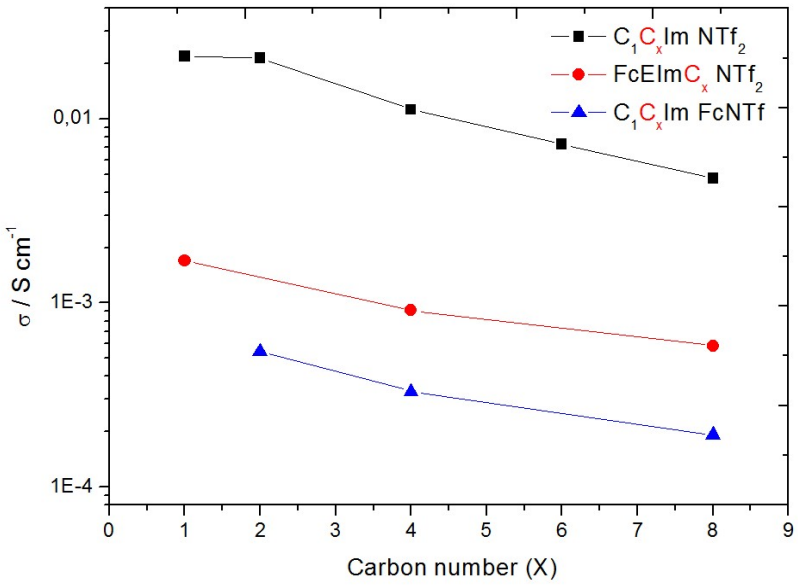

Figure A1.3. Ionic conductivity tendencies based on variations in alkyl side chain length for pure [C_xC_xIm][FcNTf] and [FcEImC_x][NTf_2] [17] RILs and corresponding uncommon ILs [47] at 60°C.

Table A1.2. VFT fitting parameters of $[C_xC_xIm][FcNTf]$ in their undiluted state. The parameters for the RILs with C_8 chains are not listed because of unreliable fitting.

RILs	B/K	T_0/K	σ_0/ S m^{-1}
C_1C_2Im FcNTf	684	223,69	0,28
C_2C_2Im FcNTf	1199	184,59	1,46
C_1C_4Im FcNTf	915	207,66	0,49
C_4C_4Im FcNTf	1159	189,46	0,88

Diffusion in diluted solutions

The diffusion of RILs diluted in acetonitrile has been characterized at 0.3 M and 1 mM in the presence of 1 M TBAP as supporting electrolyte, in order to assess the role of cation size in transport. This would suggest that the strong interaction between RIL ions would be maintained even at low concentrations. The CVs obtained at various scan rates for $[C_1C_2Im][FcNTf]$ at both concentrations are presented in **Figure A1.4**. The curves show a reversible electrochemical system with a mid-point potential shifted to values higher than that of ferrocene, due to the electron-withdrawing effect of the $-(SO_2)N(SO_2)CF_3$ group in FcNTf. A large peak splitting ($\Delta E_{p,a-p,c}$) is observed for all scan rates at a concentration of 0.3 M (**Figure A1.4**(A)), which is caused by solution resistance. The diffusion coefficients were calculated using the Randles-Sevcik equation [45]:

$$\boldsymbol{i_p = 0.4463\, n\, FAC \left(\frac{nF}{RT}\right)^{1/2} v^{1/2} D^{1/2}} \qquad (2)$$

where i_p is the peak current (A), n the equivalent number of electrons exchanged during the reaction, A the surface area of the electrode (cm^2), C the concentration (mol/cm^3), D the diffusion coefficient (cm^2/s), T the temperature (K), ν the potential scan rate (V/s), and F and R the Faraday (C/mol) and ideal gas (J/mol·K) constants, respectively.

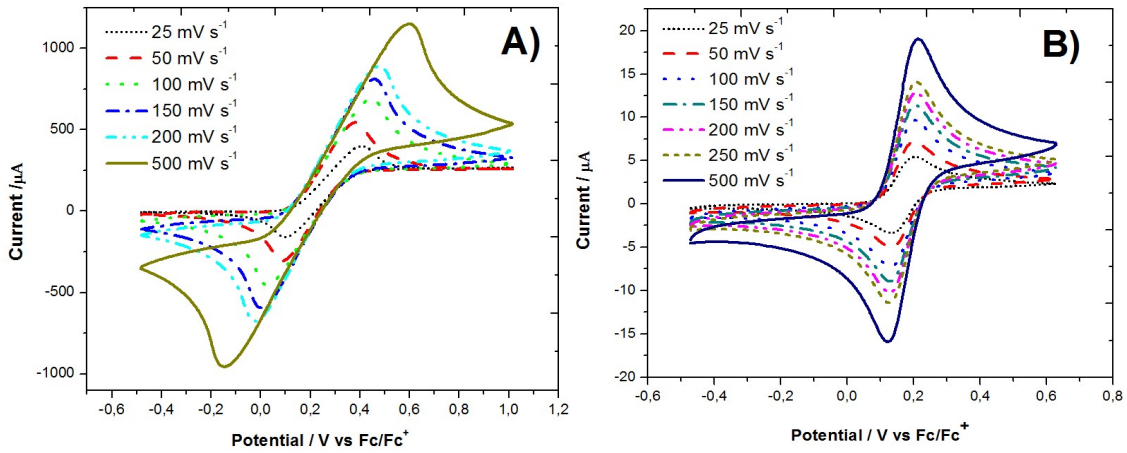

Figure A1.4. Cyclic voltammograms of A) 0.3 M $[C_1C_2IM][FcNTf]$ and B) 1 mM $[C_1C_2IM][FcNTf]$ in acetonitrile with 1 M TBAP at different scan rates (25 to 500 mV s^{-1} range).

The CV curves and Randles-Sevcik plots obtained for all solutions of RILs are shown in **Figure A1.S3** to **S6** and the diffusion coefficient values are listed in **Table A1.3**. At high concentration (0.3 M), an effect on chain length is noted in the $[C_8C_8Im][FcNTf]$ and $[C_1C_8Im][FcNTf]$ ionic liquids. The impact of cation structure on anion transport properties indicates a partial association between cation and anion in the 0.3 M solution. However, the ion association and impact of viscosity become less significant for the 1 mM solution, where all diffusion coefficient values are located within the same range. This is likely caused by maximum solvation of both species as the concentration of ionic liquid is lower in solution. Therefore, in diluted solutions the cation size has little impact on the transport properties of the anionic electroactive species. In comparison with ferrocene, the [FcNTf] anions diffuse less rapidly because of a significantly larger radius. Our previous work showed that the diffusion coefficient of [FcNTf] ($D_{FcNTf} = 1.03 \times 10^{-5}$ cm^2 s^{-1}) was only half the value for ferrocene ($D_{Fc} = 1.99 \times 10^{-5}$ cm^2 s^{-1}) in diluted solutions (1 mM in CH_3CN with 0.1 M TBAP) [14]. The electrochemical parameters of RIL are listed in **Table A1.4** for 0.3 M and 1 mM solutions. As the redox active-group is linked to anion structure, no obvious cation influence can be reported for the 1 mM solutions. All mid-point potential (E') values, as well as $\Delta E_{pa\text{-}pc}$ and oxidation and reduction limits, fall within the same range of values. The $\Delta E_{pa\text{-}pc}$ values obtained at 0.3 M are significantly larger than those in the 1 mM solutions due to higher solution viscosity. The mid-point potentials (E') for the 0.3 M solutions are also found to be slightly higher than those obtained in the 1 mM solutions and some effect of the cation on the E' is noted. This is a result of a difference between

the diffusion coefficients of the oxidized (neutral) and reduced (anionic) species which distorts the CV at high concentrations of RIL. This effect was explained in a previous publication [14].

Table A1.3. Diffusion coefficients of 0.3 M and 1 mM $[C_xC_xIm][FcNTf]$ in acetonitrile with 1M TBAP.

RILs	0.3 M in acetonitrile $D_{red}/cm^2\ s^{-1}$	1 mM in acetonitrile $D_{red}/cm^2\ s^{-1}$
C_1C_1Im FcNTf	$5.11x10^{-7}$	$1.70x10^{-5}$
C_1C_2Im FcNTf	$5.28\ x10^{-7}$	$1.87\ x10^{-5}$
C_2C_2Im FcNTf	$5.85\ x10^{-7}$	$1.78\ x10^{-5}$
C_1C_4Im FcNTf	$5.65\ x10^{-7}$	$1.52\ x10^{-5}$
C_4C_4Im FcNTf	$5.18\ x10^{-7}$	$1.57\ x10^{-5}$
C_1C_8Im FcNTf	$4.46\ x10^{-7}$	$1.51\ x10^{-5}$
C_8C_8Im FcNTf	$2.77\ x10^{-7}$	$1.73\ x10^{-5}$

Table A1.4. Electrochemical parameters for 0.3 M and 1 mM $[C_xC_xIM][FcNTf]$ in acetonitrile with 1 M TBAP at a scan rate of 100 mV s^{-1}. Oxidation and reduction limit at 0.3 M.

RILs	0.3 M		1 mM		Oxidation limit /V	Reduction limit /V
	E'/V	$\Delta E_{pa\text{-}pc}$ /V	E'/V	$\Delta E_{pa\text{-}pc}$ /V		
C_1C_1Im FcNTf	0.23	0.40	0.21	$6.8\ x\ 10^{-2}$	2.1	-1.2
C_1C_2Im FcNTf	0.24	0.42	0.21	$7.1\ x\ 10^{-2}$	2.1	-1.3
C_2C_2Im FcNTf	0.27	0.45	0.21	$7.4\ x\ 10^{-2}$	2.1	-1.2
C_1C_4Im FcNTf	0.23	0.40	0.21	$6.9\ x\ 10^{-2}$	2.1	-1.2
C_4C_4Im FcNTf	0.25	0.43	0.21	$7.3\ x\ 10^{-2}$	2.0	-1.3
C_1C_8Im FcNTf	0.29	0.44	0.21	$7.2\ x\ 10^{-2}$	2.1	-1.2
C_8C_8Im FcNTf	0.23	0.41	0.20	$6.9\ x\ 10^{-2}$	2.1	-1.3

Electrochemistry

Due to its low viscosity in the pure state, the $[C_1C_2Im][FcNTf]$ RIL was selected for all remaining studies on the electrochemical behavior of the redox anion. While the $[C_1C_1Im][FcNTf]$ RIL may provide slightly lower viscosity, its 90 °C melting point complicates the measurement process. **Figure A1.5**(A) shows the cyclic voltammograms for pure $[C_1C_2Im][FcNTf]$ at different temperatures between 50 °C and 80 °C. As discussed above, once melted, these RILs remain in a super cooled liquid state for a substantial period of time, allowing CV experiments to be made below T_m. The CV curves in **Figure A1.5**(A) indicate that the transport properties are improved at higher temperatures, as the liquid becomes less viscous. A noticeable feature of these curves is the different shapes of the oxidation and reduction peaks. The maximum peak current is significantly higher during the oxidation process than during reduction. This difference may be an effect of a migrational contribution to mass transport which increases the flux of FcNTf anion to the positively-poised electrode, since it is the sole anionic species found in the ionic liquid. This is further evidenced by looking at the effect of scan rate on current (**Figure A1.5**(B)). The current increases with scan rate; however, this increase does not show the linear dependency with $\nu^{1/2}$ expected for a purely diffusional regime (see inset of **Figure A1.5**(B)). The oxidation current also decays rapidly in a manner that cannot be explained by diffusion of the electroactive species. We recently reported on this behavior, which was also observed in a $[C_1C_4Im][FcNTf]$ RIL solution at high concentration and in the absence of a supporting electrolyte [14]. We demonstrated that a blue film was deposited on the electrode surface as a result of the oxidation of $Fc°NTf^-$ to the zwitterion Fc^+NTf^-. The shape of the curves in **Figure A1.5** show that formation of this film, which passivates the electrode, is therefore also obtained in the pure RIL and for different cations, confirming that it is related to the electroactive anion's structure. The absorbance spectrum of the film deposited on ITO obtained after sweeping the potential above 2 V vs. Ag/Ag^+(Supporting Information, Figure S-7) shows a peak at 640 nm which is indicative of ferrocenium [46] and supports the hypothesis of the presence of Fc^+NTf^-. This process is reversible in the sense that a reduction peak is observed during the backwards potential sweep and no residual film can be noticed visually after the reduction occurred. However, there is a considerable difference in voltammetric charge between the oxidation and the reduction processes which could be ascribe to

dissolution of the film or to incomplete reduction. The whole deposition process is still under investigation.

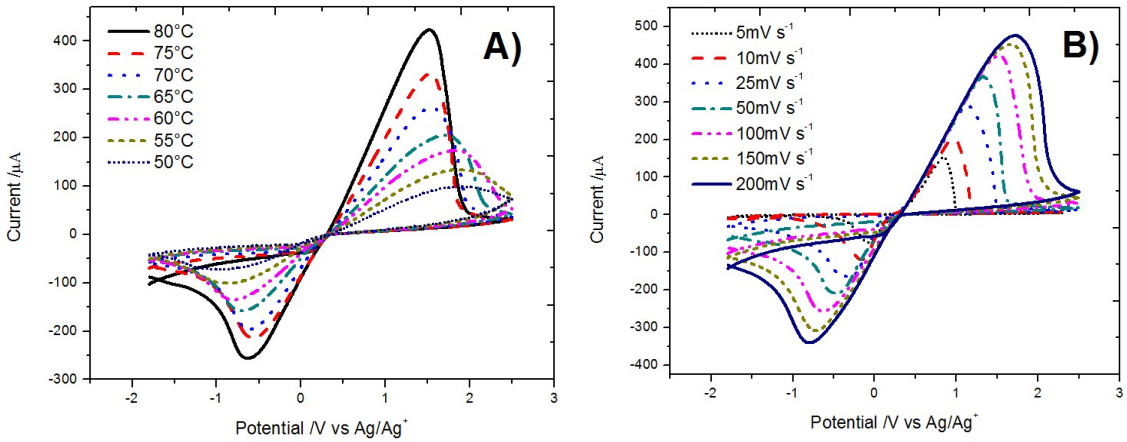

Figure A1.5. Cyclic voltammograms of A) pure $[C_1C_2Im][FcNTf]$ at different temperatures (50-80°C range) at scan rates of 100 mV s^{-1} B) pure $[C_1C_2Im][FcNTf]$ at different scan rates (5-200 mV s^{-1} range) at 80°C.

Further details on the deposition process were obtained from the CV curves recorded at different concentrations of the $[C_1C_2Im][FcNTf]$ RIL in acetonitrile with no supporting electrolyte (**Figure A1.6**(A)). Although they were severely distorted because of the high resistance of the solution (no TBAP), the curves for the 10 and 50 wt.%, show processes that may be ascribed to mixed diffusion and migration transport. The oxidation current is maintained upon inversion of the potential sweep in the range of 1.5 to 0.4 V, showing that the electrode is not passivated upon oxidation of the FcNTf anion. At 60 and 70 wt.%, the curve shows the same pattern as for pure RIL, in which the oxidation current drops rapidly to 0 after the peak value, thus indicating passivation of the electrode due to film formation. This film is dense and thick enough to prevent any further oxidation, even of the solvent, as no other oxidation processes are observed up to 5 V (**Figure A1.6**(B)). In all cases, this process is reversible and reduction of the $Fc^{+}NTf^{-}$ species back to soluble $Fc°NTf^{-}$ is observed during the reverse sweep. While the exact process leading to film formation under such specific conditions is not fully solved at the moment, it may be hypothesized that at high concentrations, the combination of high viscosity and strong interactions between the FcNTf anions (possible π-π interactions between Fc) allows high enough amounts of the oxidized

$Fc^{+}NTf^{-}$ zwitterion to exist near the electrode to enable deposition of this species into a film.

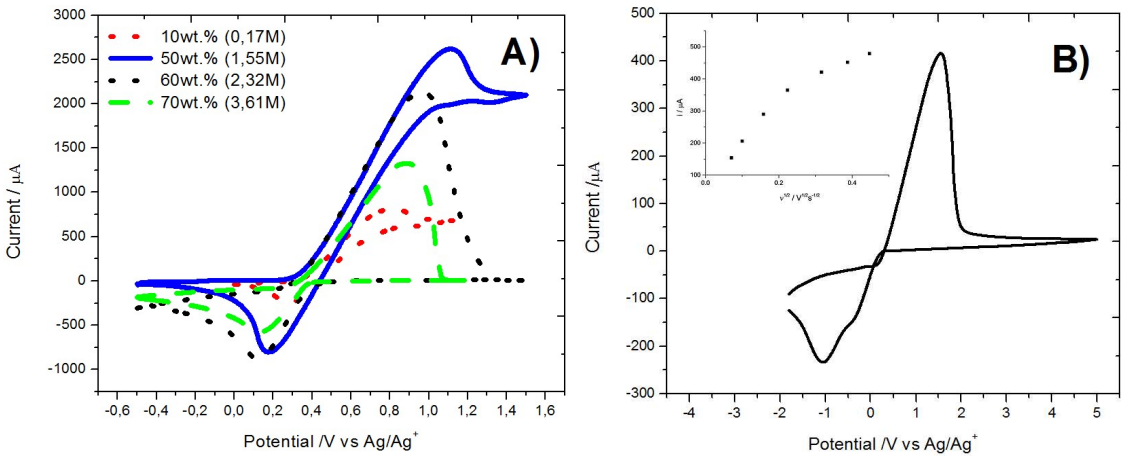

Figure A1.6. Cyclic voltammograms of A) different concentrations of $[C_xC_xIm]$ [FcNTf] in acetonitrile (10-70 wt.% range) without supporting electrolytes at scan rates of 100 mV s^{-1} B) oxidation scan of pure $[C_1C_2IM]$[FcNTf] to 5 V.

A1.2.5. Conclusions

The properties of ionic liquids using alkylimidazolium cations and the redox anion ferrocenylsulfonyl(trifluoromethylsulfonyl)imide (FcNTf) are reported herein, in an effort to understand their structure-property relationships. In particular, this study focuses on the effect of alkylimidazolium chain length and symmetry on the ionic liquid's physicochemical and electrochemical properties. Variations in cation structure have negligible impact when the RIL is diluted in acetonitrile, due to the dissociation of cation and anions in solution. At high concentrations of RILs and in pure phases, shorter alkyl chains provide lower viscosity and higher ionic conductivity and diffusion coefficients. However, reducing the chain length increased the melting point due to higher lattice free energy, as is the case in unmodified ionic liquids. In pure phases but also in highly concentrated solutions (>50 wt.%) and in the absence of supporting electrolytes, a film is deposed at the electrode surface upon oxidation of the FcNTf anion to the neutral species $[Fc^{+}NTf^{-}]$. This deposition is believed to result from the accumulation of the zwitterion at the electrode surface; such accumulation is made possible by high viscosity and strong existing interactions between the FcNTf anions. The potential applications of this type of electroactive ionic liquids in redox-active electrolyte supercapacitors are currently being

investigated, as film formation prevents diffusion of the oxidized species to the negative electrode, thus suppressing device self-discharge [50].

A1.2.6. Acknowledgments

The authors acknowledge the financial support of the Natural Sciences and Engineering Research Council of Canada (NSERC), under their Discovery Grant Program.

A1.2.7. Appendix A. Supplementary data

Supplementary data associated with this article can be found, in the online version, at http://dx.doi.org/10.1016/j. electacta.2016.03.075.

A1.2.8. References

[1] K.E. Johnson, What's an ionic liquid, Interface, Electrochem. Soc. Interface, (spring 2007) 38-41.
[2] K.R. Seddon, Ionic liquids for clean technology, J. Chem. Technol. Biotechnol., 68 (1997) 351-356.
[3] J.J. H. Davis, Task-specific ionic liquids, Chem. Lett., 33 (2004) 1072-1077.
[4] R. Giernoth, Task-specific ionic liquids, Angew. Chem. Int. Ed., 49 (2010) 2834-2839.
[5] A.C. Cole, J.L. Jensen, I. Ntai, K.L.T. Tran, K.J. Weaver, D.C. Forbes, J.H. Davis, Novel brønsted acidic ionic liquids and their use as dual solvent-catalysts, J. Am. Chem. Soc., 124 (2002) 5962-5963.
[6] T. Tooming, T. Thomberg, L. Siinor, K. Tõnurist, A. Jänes, E. Lust, A type high capacitance supercapacitor based on mixed room temperature ionic liquids containing specifically adsorbed iodide anions, J. Electrochem. Soc., 161 (2014) A222-A227.
[7] V.K. Thorsmølle, G. Rothenberger, D. Topgaard, J.C. Brauer, D.-B. Kuang, S.M. Zakeeruddin, B. Lindman, M. Grätzel, J.-E. Moser, Extraordinarily efficient conduction in a redox-active ionic liquid, ChemPhysChem, 12 (2011) 145-149.
[8] M. Bidikoudi, L.F. Zubeir, P. Falaras, Low viscosity highly conductive ionic liquid blends for redox active electrolytes in efficient dye-sensitized solar cells, J. Mater. Chem. A, 2 (2014) 15326-15336.
[9] A. Komurasaki, Y. Funasako, T. Mochida, Colorless organometallic ionic liquids from cationic ruthenium sandwich complexes: Thermal properties, liquid properties, and crystal structures of [Ru(η5-C5H5)(η6-C6H5R)][X] (X = N(SO2CF3)2, N(SO2F)2, PF6), Dalton Trans., 44 (2015) 7595-7605.
[10] A.M. Leone, S.C. Weatherly, M.E. Williams, H.H. Thorp, R.W. Murray, An ionic liquid form of DNA: Redox-active molten salts of nucleic acids, J. Am. Chem. Soc., 123 (2001) 218-222.
[11] T. Inagaki, T. Mochida, Metallocenium ionic liquids, Chem. Lett., 39 (2010) 572-573.
[12] N. Bodappa, P. Broekmann, Y.-C. Fu, J. Furrer, Y. Furue, T. Sagara, H. Siegenthaler, H. Tahara, S. Vesztergom, K. Zick, T. Wandlowski, Temperature-dependent transport properties of a redox-active ionic liquid with a viologen group, J. Phys. Chem. C, 119 (2015) 1067-1077.

[13] R. Balasubramanian, W. Wang, R.W. Murray, Redox ionic liquid phases: Ferrocenated imidazoliums, J. Am. Chem. Soc., 128 (2006) 9994-9995.
[14] B. Gélinas, D. Rochefort, Synthesis and characterization of an electroactive ionic liquid based on the ferrocenylsulfonyl(trifluoromethylsulfonyl)imide anion, Electrochim. Acta, 162 (2015) 36-44.
[15] J.C. Forgie, S. El Khakani, D.D. MacNeil, D. Rochefort, Electrochemical characterisation of a lithium-ion battery electrolyte based on mixtures of carbonates with a ferrocene-functionalised imidazolium electroactive ionic liquid, Phys. Chem. Chem. Phys., 15 (2013) 7713-7721.
[16] P. Kubler, J. Sundermeyer, Ferrocenyl-phosphonium ionic liquids—synthesis, characterisation and electrochemistry, Dalton Trans., 43 (2014) 3750-3766.
[17] B. Gélinas, J.C. Forgie, D. Rochefort, Conductivity and electrochemistry of ferrocenyl-imidazolium redox ionic liquids with different alkyl chain lengths, J. Electrochem. Soc., 161 (2014) H161-H165.
[18] J.E.F. Weaver, D. Breadner, F. Deng, B. Ramjee, P.J. Ragogna, R.W. Murray, Electrochemistry of ferrocene-functionalized phosphonium ionic liquids, J. Phys. Chem. C, 115 (2011) 19379-19385.
[19] T. Mochida, Y. Miura, F. Shimizu, Assembled structures and cation-anion interactions in crystals of alkylimidazolium and alkyltriazolium iodides with ferrocenyl substituents, Cryst. Growth Des., 11 (2011) 262-268.
[20] O. Fontaine, C. Lagrost, J. Ghilane, P. Martin, G. Trippé, C. Fave, J.C. Lacroix, P. Hapiot, H.N. Randriamahazaka, Mass transport and heterogeneous electron transfer of a ferrocene derivative in a room-temperature ionic liquid, J. Electroanal. Chem., 632 (2009) 88-96.
[21] V.O. Nyamori, M. Gumede, M.D. Bala, Synthesis, characterisation and properties of ferrocenylalkylimidazolium salts, J. Organomet. Chem., 695 (2010) 1126-1132.
[22] J.C. Forgie, D. Rochefort, Electroactive imidazolium salts based on 1,4-dimethoxybenzene redox groups: Synthesis and electrochemical characterisation, RSC Adv., 3 (2013) 12035-12038.
[23] X. Chen, D. Xu, L. Qiu, S. Li, W. Zhang, F. Yan, Imidazolium functionalized tempo/iodide hybrid redox couple for highly efficient dye-sensitized solar cells, J. Mater. Chem. A, 1 (2013) 8759-8765.
[24] C.-T. Li, C.-P. Lee, C.-T. Lee, S.-R. Li, S.-S. Sun, K.-C. Ho, Iodide-free ionic liquid with dual redox couples for dye-sensitized solar cells with high open-circuit voltage, ChemSusChem, 8 (2015) 1244-1253.
[25] N. Audic, H. Clavier, M. Mauduit, J.-C. Guillemin, An ionic liquid-supported ruthenium carbene complex: A robust and recyclable catalyst for ring-closing olefin metathesis in ionic liquids, J. Am. Chem. Soc., 125 (2003) 9248-9249.
[26] Q. Yao, M. Sheets, An ionic liquid-tagged second generation hoveyda–grubbs ruthenium carbene complex as highly reactive and recyclable catalyst for ring-closing metathesis of di-, tri- and tetrasubstituted dienes, J. Organomet. Chem., 690 (2005) 3577-3584.
[27] G. Sun, K. Li, C. Sun, Electrochemical performance of electrochemical capacitors using cu(ii)-containing ionic liquid as the electrolyte, Microporous and Mesoporous Mater., 128 (2010) 56-61.
[28] S.E. Khakani, J.C. Forgie, D.D. MacNeil, D. Rochefort, Redox shuttles for lithium-ion batteries at concentrations up to 1 m using an electroactive ionic liquid based on 2,5-di-tert-butyl-1,4-dimethoxybenzene, J. Electrochem. Soc., 162 (2015) A1432-A1438.
[29] H. Tokuda, K. Hayamizu, K. Ishii, M.A.B.H. Susan, M. Watanabe, Physicochemical properties and structures of room temperature ionic liquids. 2. Variation of alkyl chain length in imidazolium cation, J. Phys. Chem. B, 109 (2005) 6103-6110.

[30] H. Tokuda, K. Ishii, M.A.B.H. Susan, S. Tsuzuki, K. Hayamizu, M. Watanabe, Physicochemical properties and structures of room-temperature ionic liquids. 3. Variation of cationic structures, J. Phys. Chem. B, 110 (2006) 2833-2839.
[31] M.S. Gruzdev, L.M. Ramenskaya, U.V. Chervonova, R.S. Kumeev, Preparation of 1-butyl-3-methylimidazolium salts and study of their phase behavior and intramolecular intractions, Russ. J. Gen. Chem., 79 (2009) 1720-1727.
[32] A.M. O'Mahony, D.S. Silvester, L. Aldous, C. Hardacre, R.G. Compton, Effect of water on the electrochemical window and potential limits of room-temperature ionic liquids, J. Chem. Eng. Data, 53 (2008) 2884-2891.
[33] L.C. Branco, J.N. Rosa, J.J. Moura Ramos, C.A.M. Afonso, Preparation and characterization of new room temperature ionic liquids, Chem. Eur. J., 8 (2002) 3671-3677.
[34] Z. Hu, C.J. Margulis, Room-temperature ionic liquids: Slow dynamics, viscosity, and the red edge effect, Acc. Chem. Res., 40 (2007) 1097-1105.
[35] A.S. Larsen, J.D. Holbrey, F.S. Tham, C.A. Reed, Designing ionic liquids: Imidazolium melts with inert carborane anions, J. Am. Chem. Soc., 122 (2000) 7264-7272.
[36] H.L. Ngo, K. LeCompte, L. Hargens, A.B. McEwen, Thermal properties of imidazolium ionic liquids, Thermochim. Acta, 357–358 (2000) 97-102.
[37] Y. Hu, X. Peng, Effect of the Structures of Ionic Liquids on Their Physical Chemical Properties, in: S. Zhang, J. Wang, X. Lu, Q. Zhou (Eds.) Structures and Interactions of Ionic Liquids, vol. 151, Springer Berlin Heidelberg, 2014, pp. 141-174.
[38] K.N. Marsh, J.A. Boxall, R. Lichtenthaler, Room temperature ionic liquids and their mixtures—a review, Fluid Phase Equilib., 219 (2004) 93-98.
[39] H. Seemann, R. Winter, C.A. Royer, Volume, expansivity and isothermal compressibility changes associated with temperature and pressure unfolding of staphylococcal nuclease1, J. Mol. Biol., 307 (2001) 1091-1102.
[40] R. Gomes de Azevedo, J.M.S.S. Esperança, V. Najdanovic-Visak, Z.P. Visak, H.J.R. Guedes, M. Nunes da Ponte, L.P.N. Rebelo, Thermophysical and thermodynamic properties of 1-butyl-3-methylimidazolium tetrafluoroborate and 1-butyl-3-methylimidazolium hexafluorophosphate over an extended pressure range, J. Chem. Eng. Data, 50 (2005) 997-1008.
[41] R. Gomes de Azevedo, J.M.S.S. Esperança, J. Szydlowski, Z.P. Visak, P.F. Pires, H.J.R. Guedes, L.P.N. Rebelo, Thermophysical and thermodynamic properties of ionic liquids over an extended pressure range: [BMIm][NTf2] and [HMIm][NTf2], J. Chem. Thermodyn., 37 (2005) 888-899.
[42] J.A. Widegren, E.M. Saurer, K.N. Marsh, J.W. Magee, Electrolytic conductivity of four imidazolium-based room-temperature ionic liquids and the effect of a water impurity, J. Chem. Thermodyn., 37 (2005) 569-575.
[43] A. Stoppa, O. Zech, W. Kunz, R. Buchner, The conductivity of imidazolium-based ionic liquids from (−35 to 195) °C. A. Variation of cation's alkyl chain, J. Chem. Eng. Data, 55 (2010) 1768-1773.
[44] W. Xu, E.I. Cooper, C.A. Angell, Ionic liquids: Ion mobilities, glass temperatures, and fragilities, J. Phys. Chem. B, 107 (2003) 6170-6178.
[45] A.J. Bard, L.R. Faulkner, Electrochemical Methods Fundamentals and Applications, Second ed., John Wiley & Sons, Inc., 2001.
[46] A.W. Taylor, P. Licence, X-ray photoelectron spectroscopy of ferrocenyl- and ferrocenium-based ionic liquids, Chemphyschem, 13 (2012) 1917-1926.

[47] H. Tokuda, S. Tsuzuki, M.A.B.H. Susan, K. Hayamizu, M. Watanabe, How ionic are room-temperature ionic liquids? An indicator of the physicochemical properties, J. Phys. Chem. B, 110 (2006) 19593-19600.
[48] U. Domańska, A. Rękawek, A. Marciniak, Solubility of 1-alkyl-3-ethylimidazolium-based ionic liquids in water and 1-octanol, J. Chem. Eng. Data, 53 (2008) 1126-1132.
[49] L.I.N. Tomé, P.J. Carvalho, M.G. Freire, I.M. Marrucho, I.M.A. Fonseca, A.G.M. Ferreira, J.A.P. Coutinho, R.L. Gardas, Measurements and correlation of high-pressure densities of imidazolium-based ionic liquids, J. Chem. Eng. Data, 53 (2008) 1914-1921.
[50] H.J. Xie, B. Gélinas, D. Rochefort, Redox-active electrolyte supercapacitors using electroactive ionic liquids, Electrochem. Comm., 66 (2016) 42-45.

A1.3. Supporting Information

Electrochemical and physicochemical properties of redox ionic liquids using electroactive anions: influence of alkylimidazolium chain length

Han Jin Xie, Bruno Gélinas, and Dominic Rochefort[*]

Département de chimie, Université de Montréal, CP6128 Succ. Centre-Ville, Montréal, Québec, Canada H3C 3J7

*Corresponding author: Tel: +1-514-343-6733, Fax: +1-514-343-7586, email: dominic.rochefort@umontreal.ca

List of Contents:

A1.3.1. Synthesis of redox ionic liquids and imidazolium cation

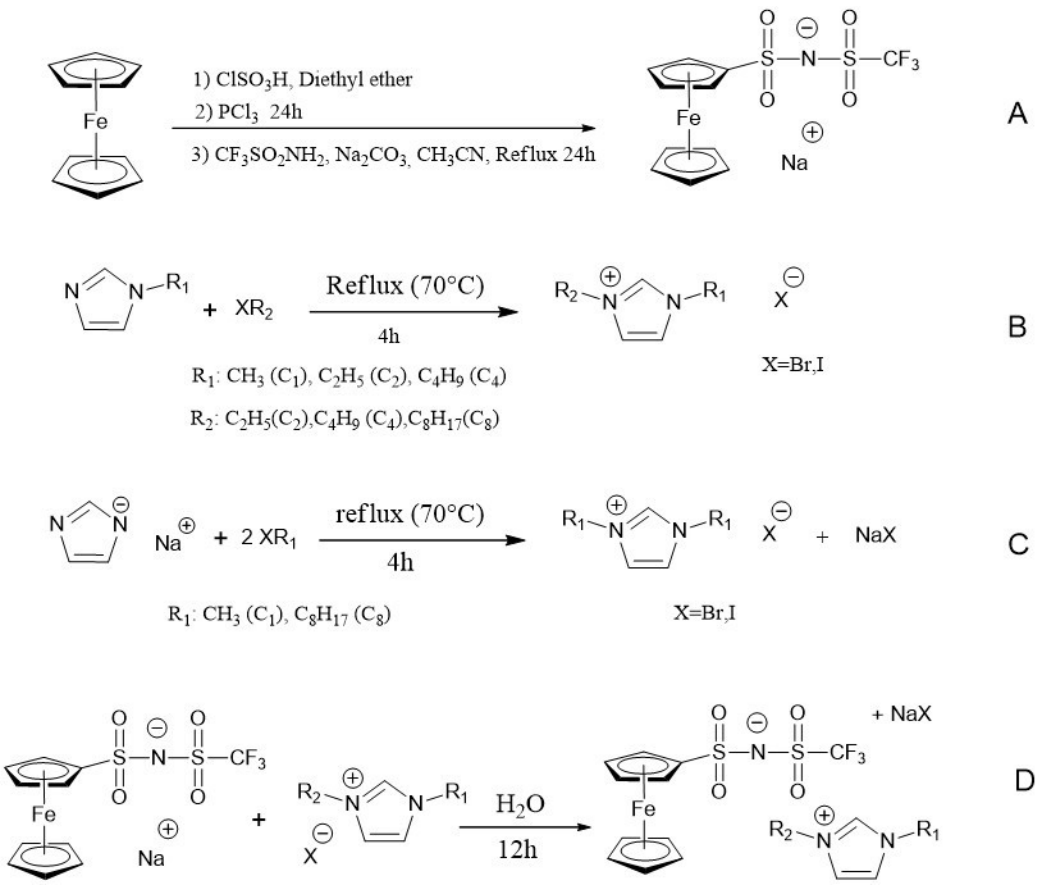

Figure A1.S1. Synthetic steps of ferrocenyl sulfonyl(trifluoromethanesulfonyl)imide imidazolium based redox ionic liquids (RILs).

The synthesis of redox ionic liquids follows the general process described by Gelinas[14]. The synthesis of cation C_1C_2IM, C_4C_4IM, C_2C_2IM, C_1C_8IM (**Figure A1.S1**) was achieved by preparing a solution of alkylimidazole and alkyl halides in acetonitrile. The resulting reaction product was washed with diethyl ether and the final product was dried under vacuum at 75 °C before characterization. For the synthesis of C_1C_1IM and C_8C_8IM FcNTf a different procedure has been used due to a low reaction yield and difficulties to eliminate impurities from final product. Instead, imidazole sodium derivative was added to a 10 ml of THF solution. Two molar equivalents of alkyl halide (1-iodomethane, bromooctane) were then added to the mixture which was maintained under reflux for 4 hours. The resulting substance was washed by THF, then by

dichloromethane and diethyl ether. The final steps of ionic liquids synthesis consist of a recombination reaction of cation and anion in water achieved over 2 hours in an ultrasonic bath. This step was followed by intensive washing with water in order to eliminate as much as possible the unwanted salts present in solution.

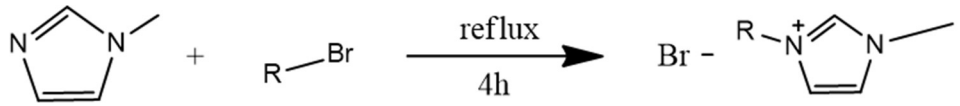

R= C_2H_5 (C_2), C_8H_{17}(C_8)

1-Methylimidazole was dissolved in 10 ml of acetonitrile, then a molar equivalent of alkyl bromide (bromoethane, bromooctane) was added. The resulting mixture was stirred for 4 hours at 70 °C. Then, the solvent was evaporated with a rotary evaporator and a yellow liquid was obtained. The resulting solution was washed several time with diethyl ether in order to remove unreacted species. The final product was dried under vacuum overnight.

1-Ethyl-3-methylimidazolium bromide [C_1C_2Im][Br]: Yield 99%.^{1}H NMR (DMSO-d_6, 300 MHz): δ (ppm) = 1.37 (t,3H), 3.84 (s,3H) , 4.19 (m,2H), 7.76 (s,1H) , 7.86 (s,1H), 9.36 (s,1H). ^{13}C NMR (DMSO-d_6, 125 MHz): δ (ppm) = 15.57; 36.20; 44.61; 122.45; 124.06; 136.72. (ESI) m/z: [M*$^+$](calcd for $C_6H_{11}N_2$): 111.09167 Found: 111.09199. Elemental analysis: Calcd for $C_6H_{11}BrN_2$: N 14.66; C 37.72; H 5.80; Found: N 14.44; C 37.25; H 5.98.

1-octyl-3-methylimidazolium bromide [C_1C_8Im][Br]: Yield 99%. ^{1}H NMR (DMSO-d_6, 300 MHz): δ (ppm) = 0.83 (t,3H), 1.22 (m,10H), 1.76 (m,2H), 3.85 (s,3H), 4.16 (t,2H), 7.75 (s,1H), 7.81 (s,1H), 9.26 (s,1H). ^{13}C NMR (DMSO-d_6, 125 MHz): δ (ppm) = 13.88; 22.00; 25.4; 25.29; 28.43; 29.36; 31.10; 35.72; 48.67; 122.21; 123.52; 136.47. (ESI) m/z: [M*$^+$](calcd for $C_{12}H_{23}N_2$): 195.18558 Found: 195.18597. Calcd for $C_{12}H_{23}BrN_2$: N10.11; C 51.84; H 9.78; Found: N 10.16; C 51.92; H 8.61.

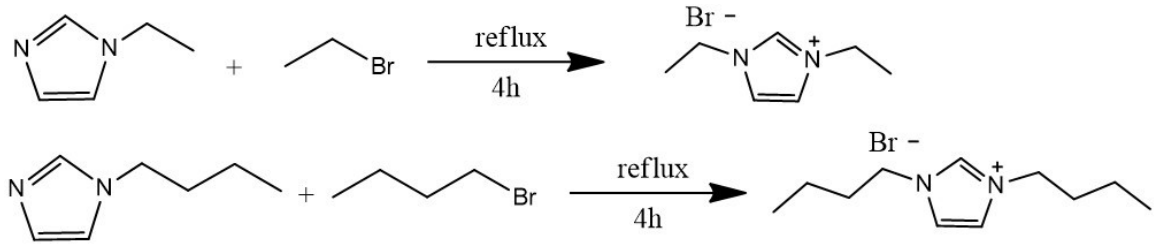

1-Ethylimidazole and 1-Butylimidazole were dissolved in 10 ml of acetonitrile, then a molar equivalent of alkyl bromide (bromoethane, 1-bromobutane) was added. The resulting mixture was stirred for 4 hours at 70 °C and the solvent evaporated to give a yellow liquid. The resulting solution was washed several time with diethyl ether and the final product was dried under vacuum overnight.

1,3-diethylimidazolium bromide [C_2C_2Im][Br]: Yield 97%. ^{1}H NMR (DMSO-d_6, 300 MHz): δ (ppm) = 1.40 (t,6H), 4.21 (m,4H), 7.87 (s,2H), 9.44 (s,1H).^{13}C NMR (DMSO-d_6, 125 MHz): δ (ppm) = 15.06; 44.09; 122.03; 135.45; (ESI) m/z: [M*$^+$](calcd for $C_7H_{13}N_2$):125.10732 Found:125.10721. Calcd for $C_7H_{13}BrN_2$: N 13.66; C 40.99; H 6.39. Found: N 13.55; C 40.48; H 6.49.

1,3-dibutylimidazolium bromide [C_4C_4Im][Br]: Yield 99%.^{1}H NMR (DMSO-d_6, 300 MHz): δ (ppm)= 0.84 (t,6H), 1.20 (m,4H), 1.74 (m,4H), 4.18 (t,4H), 7.88 (d,2H), 9.49 (s,1H). ^{13}C NMR (DMSO-d_6, 125 MHz): δ (ppm) = 13.25; 18.61; 31.36; 48.53; 122.39; 135.98. (ESI) m/z: [M*$^+$](calcd for $C_{11}H_{21}N_2$): 181.16993 Found: 181.16975 Calcd for $C_{11}H_{21}BrN_2$: N 10.72; C 50.58; H 8.10; Found: N 10.54; C 50.01; H 8.27.

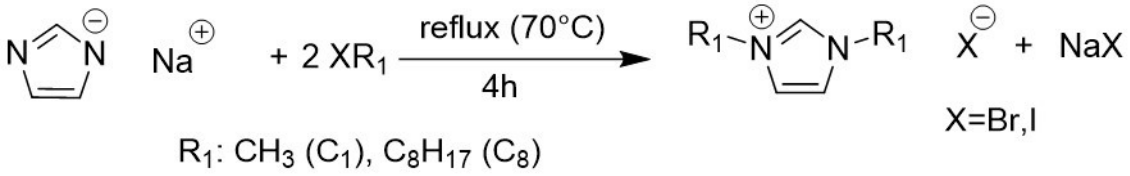

Imidazole sodium derivative was added to 10 ml of THF. Two molar equivalents of alkyl halide (1-iodomethane, bromooctane) were then added to the mixture which was maintained under reflux for 4 hours. The resulting substance was washed with THF, then dichloromethane and diethyl ether. The final product was dried under vacuum overnight.

1,3-methylimidazolium bromide [C_1C_1Im][Br]: Yield 67%. ^{1}H NMR (DMSO-d_6, 300 MHz): δ (ppm) = 3.84 (s,6H), 7.68 (d,2H), 9.04 (s,1H). ^{13}C NMR (DMSO-d_6, 125 MHz): δ (ppm) = 136.96; 123.44; 35.65; 30.52. (ESI) m/z: [M*$^+$] (calcd for $C_5H_9N_2$): 97.07602 Found: 97.07642. Calcd for $C_5H_9IN_2$: N 12.50; C 26.80; H 4.05; Found: N 12.28; C 26.67; H 4.29.

1,3-dioctylimidazolium bromide [C_8C_8Im][Br]: Yield 99%. ^{1}H NMR (DMSO-d_6, 300 MHz): δ (ppm) = 0.83 (m,6H), 1.22 (m,20H), 1.78 (m,4H), 4.17 (t,4H), 7.84 (s,2H), 9.35 (s,1H).

[M*$^{+}$](calcd for $C_5H_9N_2$): 395.928 Found: 395.92765. ^{13}C NMR (DMSO-d_6, 125 MHz): δ (ppm) = 13.86, 21.99, 25.41, 28.25, 28.52, 31.10, 48.75, 122.44, 135.95. Calcd for $C_{19}H_{37}BrN_2$: N 7.50; C 61.11; H 9.99; Found: N 7.58; C 60.48; H 9.99.

5 g of ferrocenylsulfonyl (trifluoromethanesulfonyl)imide was dissolved in 3 mL of water and then a molar equivalent of alkylimidazolium iodine was added to the solution. The resulting solution was refluxed for 3 hours at 50 °C while stirring. The black liquid was diluted in dichloromethane and washed 3 times with water. The final organic phase was dried with magnesium sulfate. The filtrate was concentrated on a rotary evaporator, resulting a dark viscous liquid. All ionic liquids were dried with under vacuum overnight and stored in a glove box for further use.

1,3-Dimethylimidazolium Ferrocenylsulfonyl(trifluoromethanesulfonyl)imide [C_1C_1Im] [FcNTf]: Yield 46%. ^{1}H NMR (DMSO-d_6, 300 MHz): δ (ppm) = 3.82 (s,6H), 4.27 (m,7H), 4.52 (t,2H), 7.6586 (d,2H), 9.00 (s,1H). ^{19}F NMR (DMSO-d_6, 282 MHz): δ (ppm) = -77.65. ^{13}C NMR (DMSO-d_6, 125 MHz): δ (ppm) = 35.61; 68.08; 68.68; 69.91; 94.05; 117.92; 122.23; 123.39; 136.98. (ESI) m/z: [M*$^{-}$](calcd for $C_{11}H_9F_3FeNO_4S_2^{-}$) : 395.92879 Found: 395.928. (ESI) m/z: [M*$^{+}$](calcd for $C_5H_9N_2^{+}$) : 97.07642 Found: 97.07602. Calcd for $C_{17}H_{20}F_3FeN_3O_4S_2$: N 8.52; C 38.96; H 3.68; S 13.00. Found: N 8.28; C 39.53; H 3.60; S 12.34.

1-Ethyl-3-methylimidazolium ferrocenylsulfonyl(trifluoromethanesulfonyl)imide [C_1C_2Im][FcNTf]: Yield 83%. ^{1}H NMR (DMSO-d_6, 300 MHz): δ (ppm) = 1.38 (t,3H), 3.81 (s,3H), 4.15 (q,2H), 4.26 (s,7H), 4.51 (t,2H), 7.66 (s,1H), 7.74 (s,1H) 9.07 (s,1H). ^{19}F NMR (DMSO-d_6, 282 MHz): δ (ppm) = -77.63. ^{13}C NMR (DMSO-d_6, 125 MHz): δ (ppm) = 15.57; 36.20; 44.61; 68.60; 69.20; 70.44; 94.60; 119.29; 121.91; 122.45; 124.06; 136.72. (ESI) m/z: [M*$^{-}$](calcd for $C_{11}H_9F_3FeNO_4S_2^{-}$) : 395.92877 Found: 395.928. (ESI) m/z: [M*$^{+}$](calcd for $C_6H_{11}N_2^{+}$) : 111.09199 Found: 111.09167. Calcd for $C_{19}H_{24}F_3FeN_3O_4S_2$: N 8.12; C 39.46; H 5.84; S 12.39. Found: N 8.22; C 40.04; H 3.93; S 113.02.

1-Octyl-3-methylimidazolium ferrocenylsulfonyl(trifluoromethanesulfonyl)imide [C_1C_8Im][FcNTf]: Yield 86%. ^{1}H NMR (DMSO-d_6, 300 MHz): δ (ppm) = 0.84 (t,3H), 1.24 (m,10H), 1.74 (m,2H), 3.81 (s,3H), 4.11 (t,2H), 4.25(m,7H), 4.51(m,2H), 7.66(s,1H), 7.73(s,1H), 9.06(s,1H). ^{19}F NMR (DMSO-d_6, 282 MHz): δ (ppm) = -77.65. ^{13}C NMR (DMSO-d_6, 125 MHz): δ (ppm) =13.88; 21.99; 25.43; 28.27; 28.41; 29.32; 31.10; 35.70; 48.72; 68.08; 68.67; 69.90; 94.06;

117.92; 122.21; 123.56; 136.43. (ESI) m/z: [M*-](calcd for $C_{11}H_9F_3FeNO_4S_2^-$) : 393.93239 Found: 393.93267. (ESI) m/z: [M*+] (calcd for $C_{12}H_{23}N_2^+$): 195.18597 Found: 195.18558. Calcd for $C_{23}H_{32}F_3FeN_3O_4S_2$: N 7.10; C 46.70; H 5.45; S 10.84. Found: N 7.09; C 46.33; H 5.45; S 10.94.

1,3-Diethylimidazolium ferrocenylsulfonyl(trifluoromethanesulfonyl)imide [C_2C_2Im] [FcNTf]: Yield 68%. ^{1}H NMR (DMSO-d_6, 300 MHz): δ (ppm) = 1.48 (t,6H), 4.24 (q,4H), 4.34 (m,7H), 4.60 (s,2H), 7.85 (s,2H), 9.23 (s,1H). ^{19}F NMR (DMSO-d_6, 282 MHz): δ (ppm) = -77.64.^{13}C NMR (DMSO-d_6, 125 MHz): δ (ppm) = 14.97; 44.14; 68.08; 68.68; 69.91; 94.05; 117.93; 122.05; 135.34 (ESI) m/z: [M*-](calcd for $C_{11}H_9F_3FeNO_4S_2^-$) : 395.92874 Found:395.928. (ESI) m/z: [M*+](calcd for $C_7H_{13}N_2^+$): 125.10721 Found: 125.10732. Calcd for $C_{18}H_{22}F_3FeN_3O_4S_2$: N 8.06; C 41.47; H 4.25; S 12.30 Found: N 7.90; C 41.30; H 4.34; S 12.24.

1,3-Dibutylimidazolium ferrocenylsulfonyl(trifluoromethanesulfonyl)imide [C_4C_4Im] [FcNTf]: Yield 90%. ^{1}H NMR (DMSO-d_6, 500 MHz): δ (ppm) = 0.90 (t,6H), 1.25 (m, 4H), 1.78 (m, 4H), 4.16 (t,4H), 4.29 (s,6H), 4.54 (t,2H), 7.79 (s,2H), 9.18 (s,1H). ^{19}F NMR (DMSO-d_6, 282 MHz): δ (ppm) = -77.67. ^{13}C NMR (DMSO-d_6, 125 MHz): δ (ppm) = 13.73; 19.25; 31.74; 49.05; 68.59; 69.19; 70.43; 94.58; 119.31; 121.90; 122.93; 136.39.(ESI) m/z: [M*+](calcd for $C_{11}H_{21}N_2$): 181.16993 found: 181.16998. [M*-](calcd for $C_{11}H_9F_3FeNO_4S_2^-$) : 395.92801 Found: 395.92936. Calcd for $C_{22}H_{30}F_3FeN_3O_4S_2$: N 7.28; C 45.76; H 5.24; S 11.11. Found: N 7.39; C 45.35; H 5.34; S 11.13.

1,3-Dioctylimidazolium ferrocenylsulfonyl(trifluoromethanesulfonyl)imide [C_8C_8Im] [FcNTf]: Yield 68%. ^{1}H NMR (DMSO-d_6, 500 MHz): δ (ppm) = 0.84 (t,6H), 1.23 (m,20H), 1.77(m,4H), 4.14 (t,4H), 4.27 (s,6H), 4.52 (t,2H), 7.78 (s,2H), 9.19 (s,1H). ^{19}F NMR (DMSO-d_6, 282 MHz): δ (ppm) = -77. 66.^{13}C NMR (DMSO-d_6, 125 MHz): δ (ppm) = 13.87; 22.00; 25.41; 28.23; 28.43; 29.19; 48.80; 68.08; 68.65; 69.90; 94.07; 122.23; 122.43; 135.88. (ESI) m/z: [M*+](calcd for $C_{19}H_{37}N_2$): 293.29555 found: 293.29513. [M*-](calcd for $C_{11}H_9F_3FeNO_4S_2^-$) : 395.92765 Found: 395.928. Calcd for $C_{23}H_{32}F_3FeN_3O_4S_2$: N 6.09; C 52.25; H 6.72; S 9.30. Found: N 6.64; C 53.01; H 7.03; S 9.79.

A1.3.2. Thermal analysis

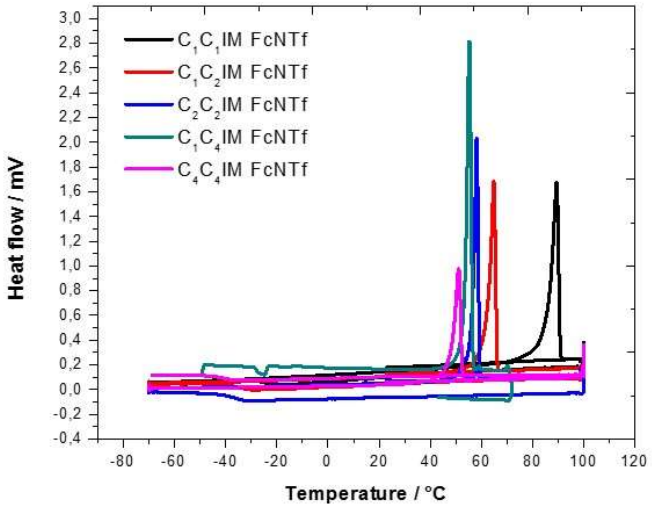

Figure A1.S2. DSC curves of C_xC_xIm FcNTf. The measurements were done between -70°C and 100°C for 3 cycles with heating rate of 1 °C per minute.

A1.3.3. Electrochemical analysis

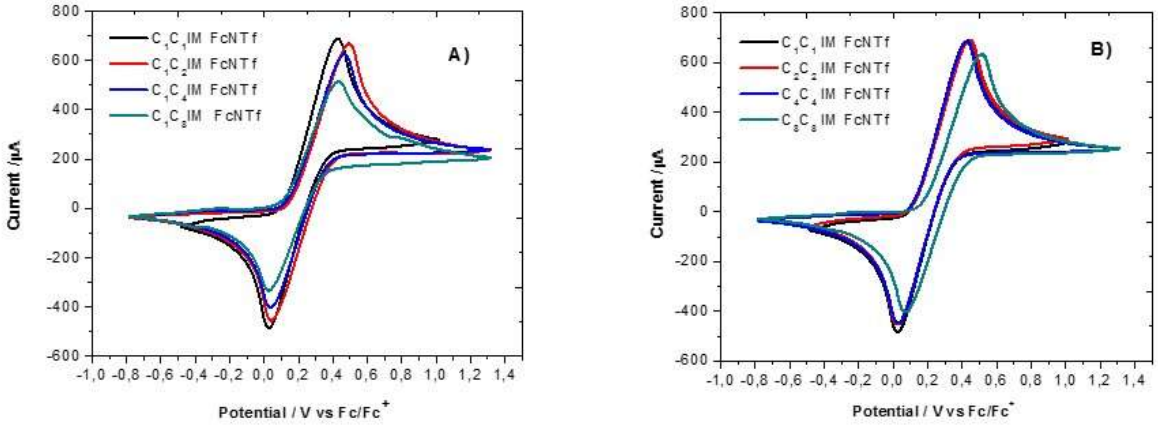

Figure A1.S3. CVs of 0.3 M of A) chain variation and B) symmetry variation of C_xC_xIM FcNTf based redox ionic liquid in acetonitrile with 1 M TBAP. The scan rate is 100 mV s^{-1}.

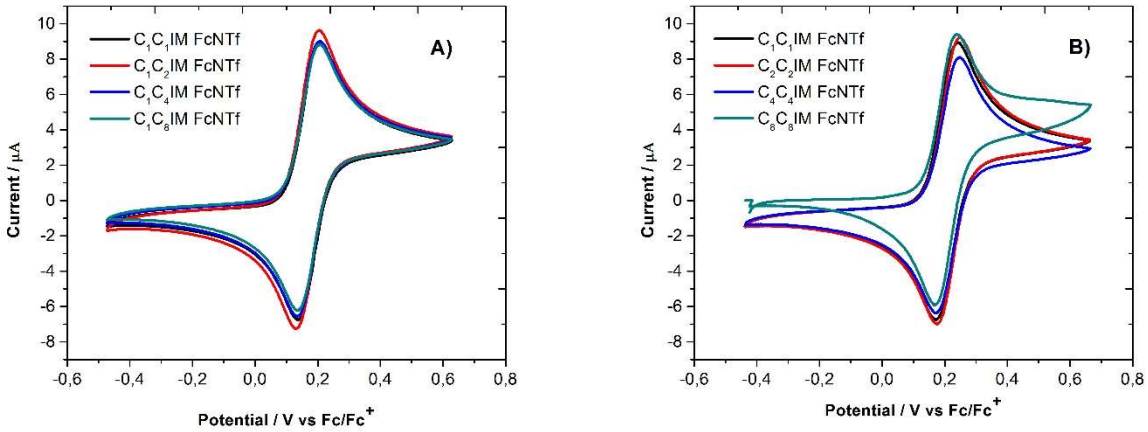

Figure A1.S4. CVs of 1 mM of A) chain variation and B) symmetry variation of C_xC_xIM FcNTf based redox ionic liquid in acetonitrile with 1 M TBAP. The scan rate is 100 mV s^{-1}.

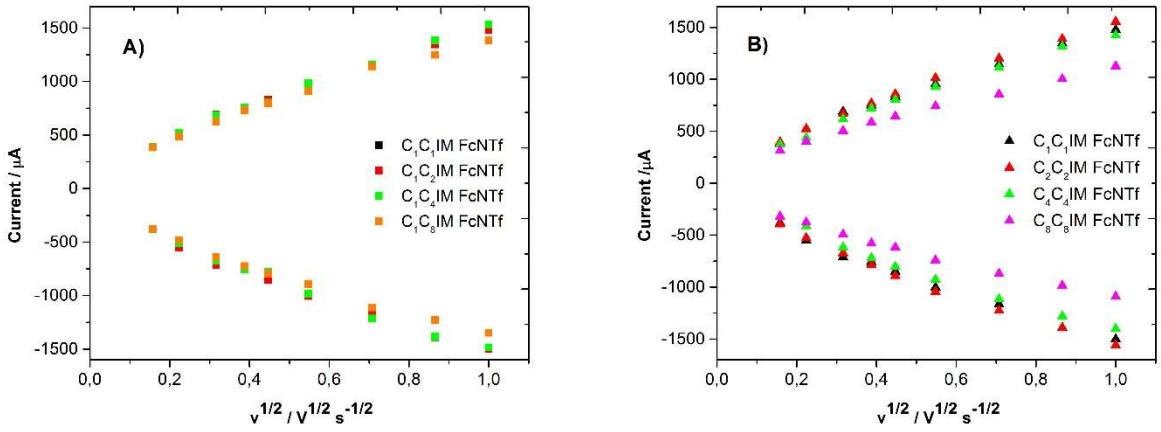

Figure A1.S5. Randles Sevcik plots of I_p vs $\nu^{1/2}$ from 25-500 mV s^{-1} for 0.3M C_xC_xIM FcNTf based redox ionic liquid in acetonitrile with 1 M TBAP. Curve A) chain variation and B) symmetric variation of alkyl chain.

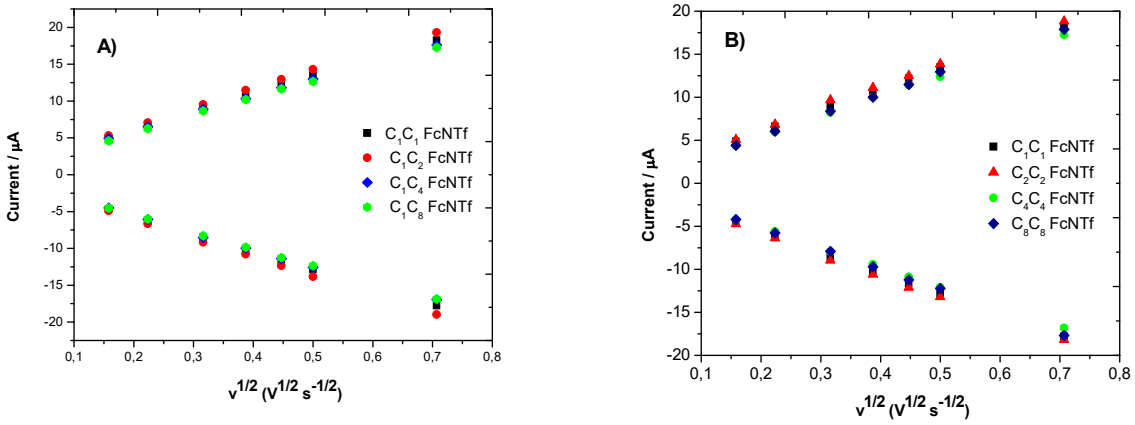

Figure A1.S6. Randles Sevcik plot of I_p vs $V^{1/2}$ from 25-500 mV s^{-1} for 1mM C_xC_xIM FcNTf based redox ionic liquid in acetonitrile with 1 M TBAP. Curve A) chain variation and B) symmetric variation of alkyl chain.

A1.3.4. UV-Vis spectrum

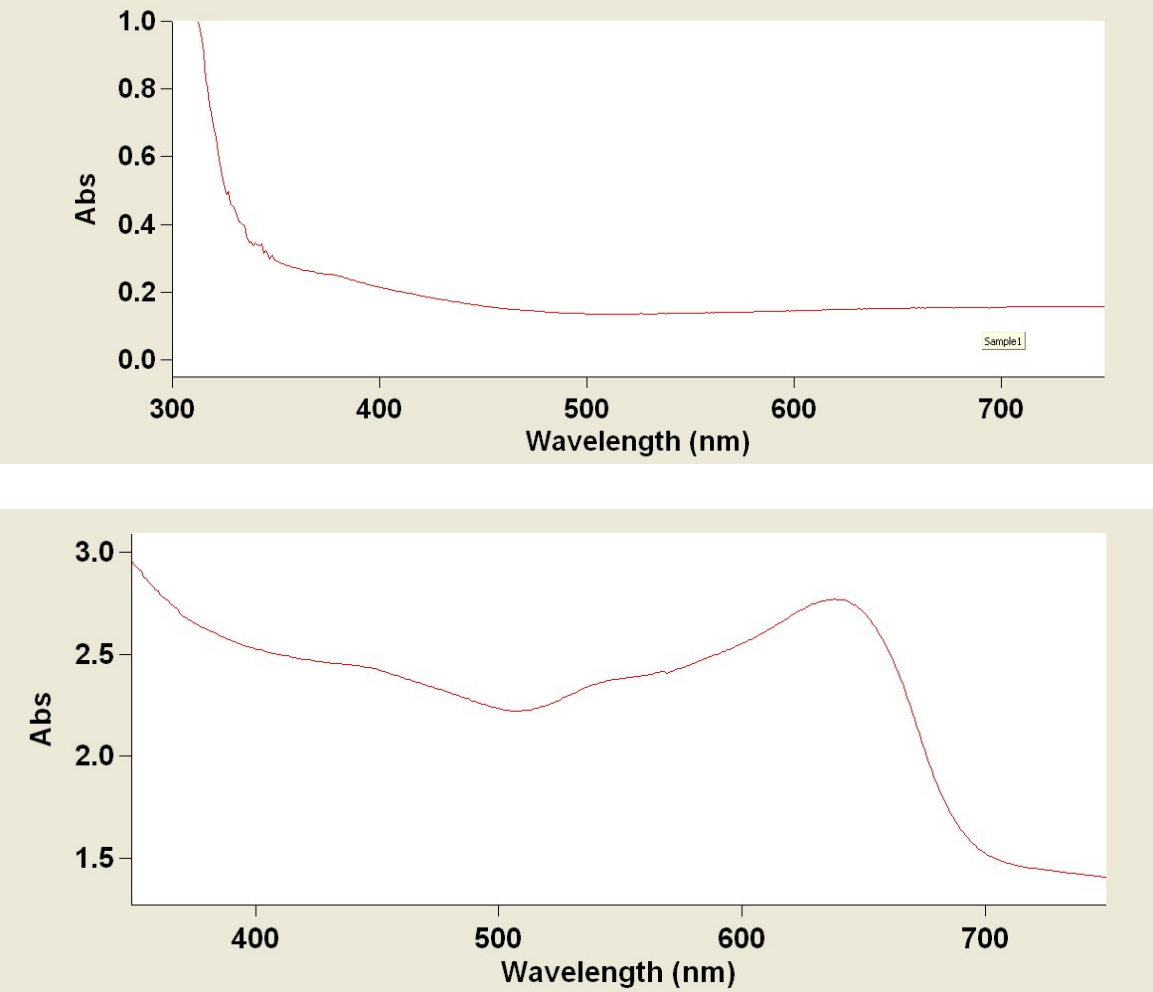

Figure A1.S7. Absorbance spectra recorded for the bare ITO susbstrate (upper panel) and for the film of [$Fc^{+}NTf^{-}$] deposited on the substrate (lower panel). The peak at 640 nm corresponds to the absorbance by the ferrocenium uni

Annexe 2 : Liquide ionique électroactif pour les supercapaciteurs

A2.1. Avant-propos et mise en contexte

Cette annexe a été rédigée sous forme d'un article qui a été soumis à *Electrochemistry Communication.* Comme il est possible de le constater dans les chapitres précédents (**Chapitre 4** et **Annexe 1**), le BMIm FcNTf électrodépose à haute concentration quand il s'agit de l'unique sel dans le système. Cette propriété répond à une problématique au niveau des supercapaciteurs utilisant un électrolyte électroactif, car l'électrodéposition est une méthode efficace pour réduite l'autodécharge via le mécanisme de navette rédox. La contribution de cette communication est la présentation d'un nouveau système qui démontre l'augmentation de la capacitance en comparant à un électrolyte non-électroactif et la diminution de l'autodécharge.

A2.2. Article: Redox-active electrolyte supercapacitors using electroactive ionic liquids

Han Jin Xie,[a] Bruno Gélinas[a] and Dominic Rochefort[a]

[a]Département de Chimie, Université de Montréal, Montréal, Québec H3C 3J7, Canada

Electrochemistry Communications 66 (2016) 42–45

Article history: Received 20 January 2016, Revised 23 February 2016, Accepted 24 February 2016, Available online 4 March 2016. http://dx.doi.org/10.1016/j.elecom.2016.02.019,1388-2481/

A2.2.1. Highlights

- Electroactive ionic liquids are proposed as electrolyte for supercapacitors.
- Specific energy of carbon electrodes is increased from faradaic reactions.
- Deposition of the species oxidized during charging prevents self-discharge.

A2.2.2. Abstract

Here we present redox ionic liquid supercapacitors (RILSCs) which use electrolytes made from ionic liquids modified with an electroactive function to increase the energy density of activated carbon electrodes via faradaic reactions. More specifically, two different ionic liquids were made by modifying either the imidazolium cation or the bis(trifluoromethanesulfonyl)imide anion with ferrocene in order to determine the importance of the electroactive ion's polarity. The functionalization of an ionic liquid with ferrocene led to high concentrations of redox moieties in the electrolyte (2.4 M) and a large maximum operating voltage (2.5 V). An energy density of up to 13.2 Wh per kg (both electrodes) was obtained which represents an 83% increase vs. the unmodified ionic liquid. When the ionic liquid's anion is modified with ferrocene, the self-discharge at the positive electrode is fully suppressed due to the deposition of a film on the electrode. The results presented herein demonstrate that electroactive ionic liquids constitute a promising alternative to conventional solute in solvent electrolytes found in energy storage devices, and are particularly well-suited for redox-active electrolyte supercapacitors.

Keywords: Redox-active electrolyte capacitor; Energy storage; Supercapacitors; Ferrocene; Ionic liquids

A2.2.3. Introduction

. Redox-active electrolyte supercapacitors (RESCs) are obtained by dissolving electroactive species in the electrolyte as a mean to increase the energy density of carbon-based capacitors.[1-4] Some of the most common redox centers previously used to modify carbon electrodes were also investigated as redox additives in RESCs. The oxidation of hydroquinone (at 0.38 M concentration in H_2SO_4 electrolyte) into benzoquinone attained 901 F g^{-1} at low current density (2.65 mA cm^{-2}) during the charging step of a KOH-activated carbon capacitor, while the same electrode provided 320 F g^{-1} in the absence of hydroquinone.[2] Similar enhancements in capacitance were obtained by adding KI at 0.08 M in H_2SO_4 electrolyte (increase from 472 to 912 F g^{-1} at 2 mA cm^{-2}).[5] Other redox additives with activated carbon electrodes reported in recent years include $VOSO_4$, ***p***-phenylenediamine, acetylferrocene, and methylene blue.[4, 6, 7] RESCs are often based on aqueous electrolytes due to a higher solubility of redox molecules in water than in organic solvents. For the same reason, ionic liquids have not been extensively studied as electrolyte in RESCs despite the fact that they could present the advantage of an increased maximum operating voltage. For example, Sun et al. reported on the reduction of Cu^{2+} dissolved in 1-ethyl-3-methylimidazolium tetrafluoroborate ($EMImBF_4$) ionic liquid at porous carbon electrodes, providing a cell voltage of 2.0 V.[8] So far, a compromise must be done between fast transport and high solubility of the redox molecule (obtained in aqueous electrolytes) and a high cell voltage (obtained with organic solvents and ionic liquids).

Clearly, RESCs may benefit from the development of electroactive electrolytes specifically formulated for this purpose, and which should ***i***) allow high concentrations in redox species, ***ii***) present a high maximum voltage, and ***iii***) include a self-discharge suppression mechanism. This work demonstrates that electroactive ionic liquids, in which a redox moiety is covalently linked to one of the ions,[9-11] may be used to meet these challenges. No study on redox ionic liquid supercapacitors (RILSCs) has ever been reported in the past, and the importance of the ionic liquid structure on charge storage and self-discharge requires investigation. Therefore, two redox ionic liquids (RILs) obtained by modifying either the cation or the anion with ferrocene, are studied here as redox-active electrolytes for carbon-based RILSCs. The RIL with the Fc attached on the cation was use to demonstrate self-discharge in RILSCs. Electrolytes based on these ionic liquids were

applied in carbon-based supercapacitor cells to establish how the polarity of the electroactive ion impacts energy storage and self-discharge processes in RILSCs.

A2.2.4. Experimental Section

The synthesis and characterization of both electroactive ionic liquids are detailed in previous studies.[12, 13] The unmodified ionic liquid 1-ethyl-3-methylimidazolium bis(trifluoromethanesulfonyl)imide, [EMIm][NTf_2] was purchased from Iolitec and used without further purification. The water content of all ILs was found between 144 and 170 ppm after vacuum drying, which are typical values.[14] The electrodes were prepared by mixing activated carbon (Black Pearl 2000, Cabot),[15] acetylene black (Alfa Aesar), graphite (Alfa Aesar) and PTFE (1 μm particles, Sigma-Aldrich) in a mortar, at a ratio of 80:7.5:7.5:5 based on weight. The mixture was then pressed into a film, from which 15 mm-diameter disks were cut. These electrodes were assembled in Swagelok cells in a glovebox, with four stacked paper disks soaked with the electrolyte used as separators. For the three-electrode setup, a Pt wire (quasi-reference electrode) was inserted between the paper disks to prevent contact with the electrodes. Cyclic voltammograms and galvanostatic charge/discharge measurements were made with a VMP3 potentiostat from BioLogic.

A2.2.5. Results and Discussion

Two imidazolium redox ionic liquids (RILs), each with one ion modified with ferrocene, were selected to provide faradaic reactions and increase the specific energy (W_g, Wh kg^{-1}) of carbon-based supercapacitors. The structures of their reduced form are presented in **Figure A2.1**. The redox ionic liquid 1-(methylferrocenyl)-3-ethylimidazolium bis(trifluoromethanesulfonyl)imide, [FcEIm][NTf_2], presents a ferrocene on the cation which forms a dication upon oxidation and remains in the liquid phase. The details of the synthesis and characterization of the electrochemical properties of [FcEIm][NTf_2] were previously published.[12] The second RIL was obtained by modifying ferrocene with an anionic function, the structure of which is inspired by the NTf_2 anion (**Figure A2.1**). In 1-ethyl-3-methylimidazolium ferrocenylsulfonyl-(trifluoromethylsulfonyl)-imide, [EMIm][FcNTf], the anion is the electroactive species and has been shown to deposit on electrodes when oxidized to the zwitterion $[Fc^+ NTf^-]^0$.[13]

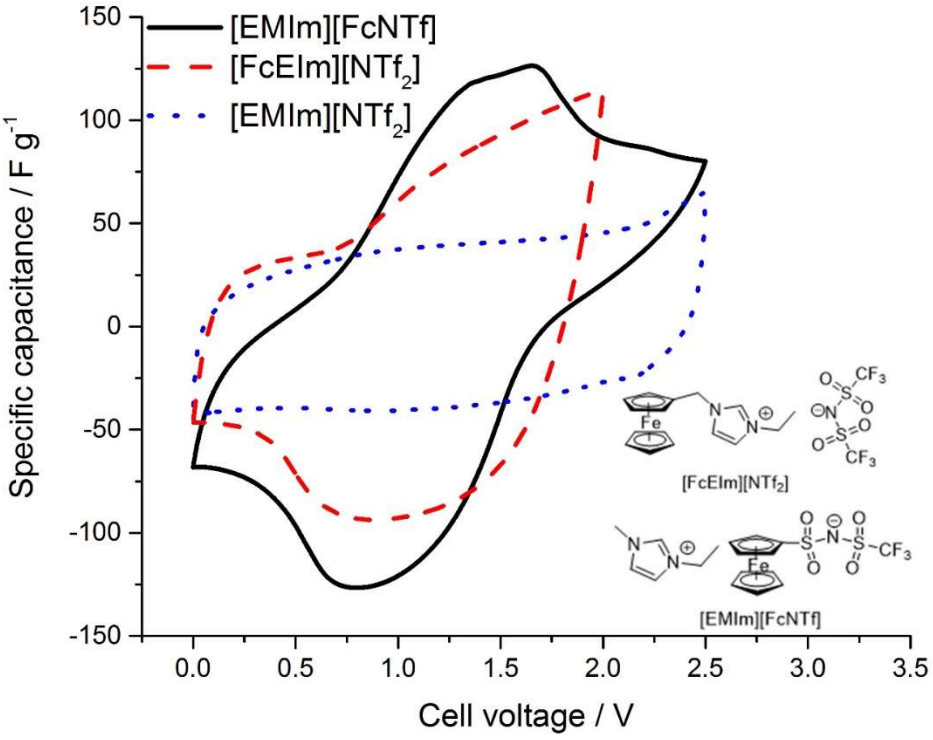

Figure A2.1. Cyclic voltammograms recorded with two-electrode cells with 80 wt.% of the ionic liquid in acetonitrile. Each carbon electrode weighed 3.5 mg and contained 80 wt.% of activated carbon. The curves were obtained at a scan rate of 10 mV s^{-1} at a temperature of 25°C.

Figure A2.1 shows the cyclic voltammetric curves obtained with three different solutions composed of 80 wt.% of ionic liquid in acetonitrile. The oxidation and reduction of the ferrocenyl moiety in [FcEIm][NTf_2] and [EMIm][FcNTf] appear clearly on the CV, while the unmodified [EMIm][NTf_2] yielded a featureless, rectangular curve typical of double-layer charging. The use of RILs-CH_3CN mixtures results in higher cell reproducibility, due to the former's high melting points (> 55 °C) and high viscosity (> 1000 cP at 60 °C). Mixtures with RIL concentration between 10 and 80 wt.% in CH_3CN were evaluated and while the 40 wt.% provided the highest specific energy (compromise between concentration and viscosity) the 80 wt.% will be studied in details hereon due to its ability to prevent self-discharge (discussed later) which was not observed in more diluted mixtures. These 80 wt.% mixtures in acetonitrile have a concentration of 2.4 M in ferrocene centers, a figure three times higher than the ferrocene concentration in acetonitrile at saturation.[16]

Galvanostatic charge–discharge (GCD) experiments were carried out to evaluate the energy density of the devices employing the two different electroactive ionic liquids (**Figure A2.2**). The redox processes observed in **Figure A2.1** with both [FcEIm][NTf_2] and [EMIm][FcNTf] RILs are also evidenced in the curvature of the GCD profiles in **Figure A2.2A**. The gravimetric specific energy (W_g) for discharge was calculated from the integration of area under the curve (see **Table A2.1**), according to Eq. 1, rather than by evaluating the capacitance which tends to overestimate charge storage involving faradaic processes [17]:

$$W_g = \frac{I}{w} \int_{t=0}^{t=t} U(t)dt$$

where I is the current (A), w is the total weight of both electrodes (kg), and $U(t)$ is the non-linear function of the voltage over time (V s).

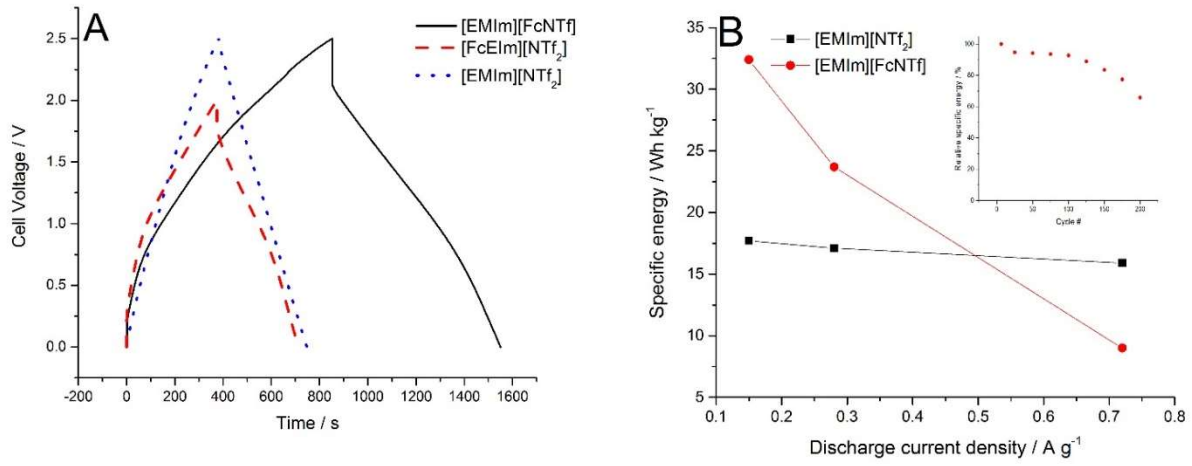

Figure A2.2. A: GCD profiles of supercapacitors with different ionic liquids (i = 1 mA). B: Effect of discharge rate on the W_g for the RILSC ([EMIm][FcNTf]) and EDLC ([EMIm][NTf_2]). Inset of B shows the W_g losses over the first 200 cycles.

Table A2.1. Specific energy values (during discharge) at different maximum voltages and iR drop obtained for the devices (charge and discharge currents of 2 mA).

	Electrolyte (in CH_3CN)				
	1 M TBAP	80 wt.% [EMIm][NTf_2]	80 wt.% [FcEIm][NTf_2]	80 wt.% [EMIm][FcNTf]	40 wt.% [EMIm][FcNTf]
Specific energy, 2.0 V / Wh kg^{-1}	6.4	7.2	9.0	13.2	21.6
Specific energy, 2.5 V / Wh kg^{-1}	n/a	17.1	n/a	23.7	n/a
iR drop / mV	35	45	426	513	250

The gravimetric specific energy values, based on total weight of both electrodes for the RILSCs presented here, are presented in **Table A2.1**. The values obtained with the [EMIm][FcNTf] redox ionic liquid represent a significant increase from equivalent double-layer devices using either the unmodified ionic liquid [EMIm][NTf_2] or the conventional electrolyte 1 M TBAP in CH_3CN. No significant gain in energy was obtained with the RIL [FcEIm][NTf_2] because of a less efficient oxidation of the Fc-based cation and of self-discharge (see below). To better understand the reactions involved at each electrode during GCD, the charge–discharge profiles obtained with [EMIm][FcNTf] RIL in a three-electrode Swagelok setup with a Pt wire quasi-reference inserted in the separator are presented in **Figure A2.3**. The profiles in **Figure A2.3A** show a double-layer charge storage mechanism at the negative electrode and more complex behavior at the positive electrode. **Figure A2.3B** presents the charging mechanism at the positive electrode. The first region shows a linear potential increase which is attributed to the $[FcNTf]^-$ anions populating the double-layer (capacitive charging). As the charge accumulates, the potential increases to a value where the ferrocenyl unit on $[FcNTf]^-$ becomes oxidized to $[Fc^+ NTf^-]^0$, resulting in a potential plateau which is typical when faradaic processes dominate. This plateau corresponds to the rise in current in the CV presented in **Figure A2.1**, and maintains the same potential up to 2 V (full cell voltage), a higher maximum voltage (by a factor of 2) compared to most of the RESCs based on aqueous electrolytes.[4] Upon discharging the device, the reverse processes occur, according to the profile in **Figure A2.3A**. This deposition/dissolution process occurs at the positive electrode every cycle and is part of the storage and self-discharge suppression mechanisms described below.

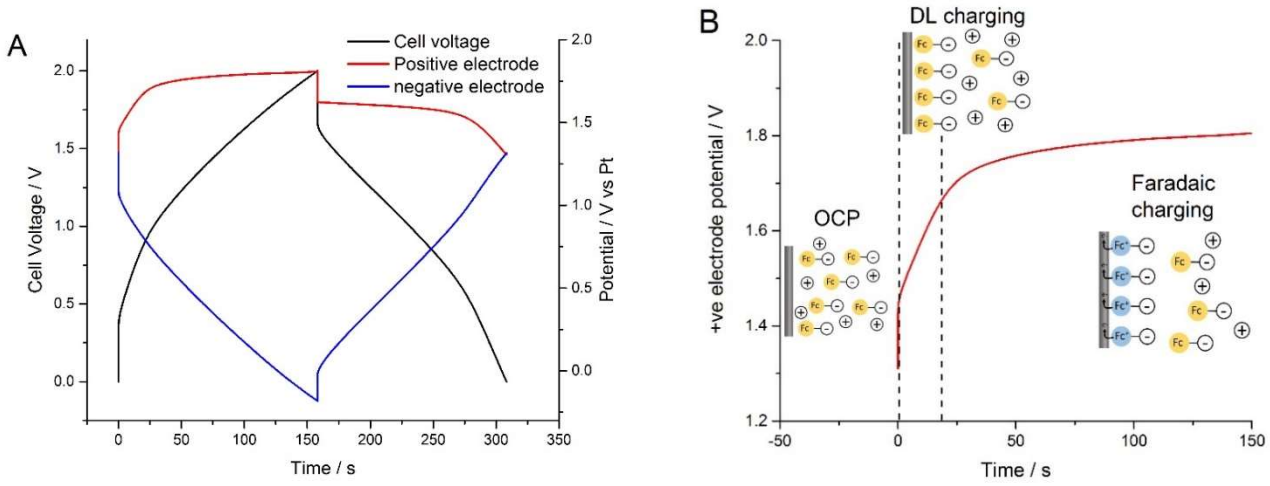

Figure A2.3. A: Galvanostatic charge–discharge profiles for the RILSC with 80 wt.% of [EMIm][FcNTf] in acetonitrile at 25 °C and a 2 mA current. B: The charging potential profile of the positive electrode showing the processes during charge.

Self-discharge (SDC) represents a major issue with RESCs.[18] In conventional EDLCs, SDC occurs mainly through diffusion of the ions away from the double-layer where they accumulated during charge storage. In RESCs, SDC is more rapid because a shuttle discharge mechanism (reduction oxidized species at the negative electrode) adds up to the diffusion-based SDC.[18] Such charge-shuttling issues may be addressed by the use of ion-selective membranes to retain redox species in one compartment, but at the cost of an increased internal resistance, which lowers the device's overall power output. The deposition of insoluble species may also prevent SDC through charge-shuttling.[19] This shuttling effect is clearly seen in **Figure A2.4A** with the device based on the cationic RIL [FcEIm][NTf_2] (blue dotted line), which discharged at OCP at a faster rate than the EDLC device based on the [EMIm][NTf_2] ionic liquid electrolyte (red dash curve). The inset in **Figure A2.4A** shows the linear dependency of voltage with $t^{1/2}$ for SDC for the [EMIm][NTf_2] device, demonstrating the diffusion-based self-discharge mechanism in EDLC. A very similar SDC is noted with the RILSC based on the anionic ferrocenyl ([FcNTf]$^-$) species, suggesting a diffusion-based discharge while the charging mechanism involves faradaic reactions. To clarify this behavior, the SDC was then studied more closely, using a reference electrode in the cell. The profiles of individual electrodes shown in **Figure A2.4B** demonstrate that voltage loss

over time results exclusively from the negative electrode, where charge storage occurs in the double-layer. After a sharp initial decrease due to ohmic drop, the potential of the positive electrode remained constant for three hours. After 20 h of OCP, the potential of the positive electrode was still 1.3 V (not shown). This slow discharge is explained by the formation of a film at the positive electrode upon oxidation of $[FcNTf]^-$ to $[Fc^+ NTf^-]^0$. This behavior was reported earlier and was found to occur in highly concentrated solutions of RIL based on $[FcNTf]^-$ and in the absence of any other salt. [13] The zwitterionic oxidized species $[Fc^+ NTf^-]^0$ of neutral charge has a limited solubility in the electrolyte and precipitates out on the electrode surface, resulting in a stable passivation layer and thereby efficiently suppressing self-discharge of the RILSC. This suppression does not occur in RILSC using the cationic ferrocenyl species $[FcEIm][NTf_2]$ which remain in the electrolyte as a dication upon oxidation.

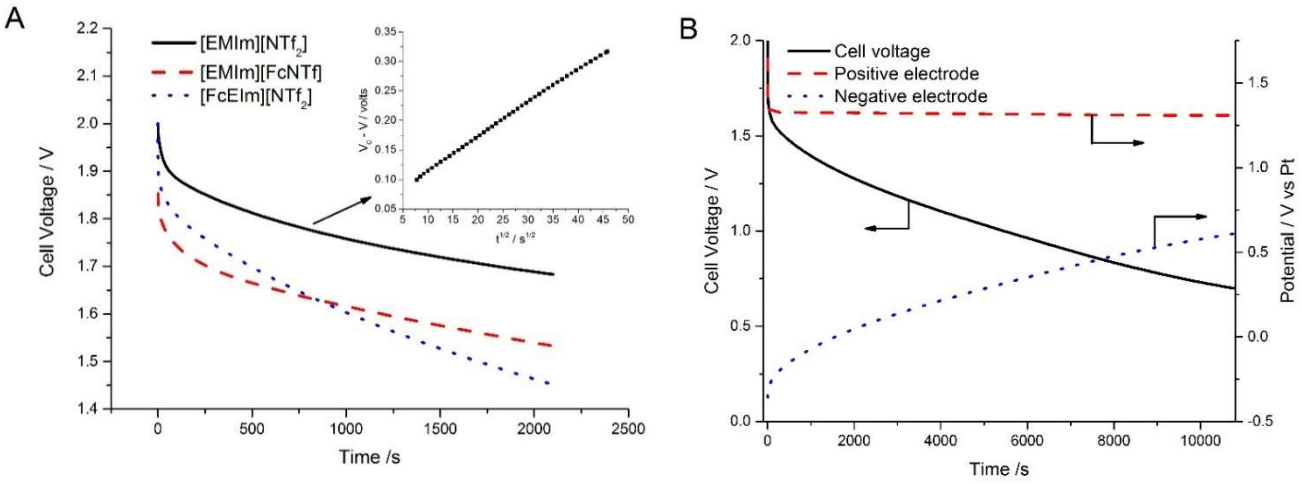

Figure A2.4. A: Self-discharge curves recorded at OCP for the three ionic liquids, showing a pronounced voltage decrease for $[FcEIm][NTf_2]$. Inset of A: Linear fitting of voltage with $t^{1/2}$ for double-layer capacitor with $[EMIm][NTf_2]$. B: Discharge profiles of individual electrodes for RILSC using [EMIm][FcNTf]. All conditions are as in **Figure A2.3**. (For interpretation of the references to color in this figure, the reader is referred to the web version of this article.)

A2.2.6. Conclusions

This study provided another example on the potential design of ionic liquids which outperform traditional solvents in fulfilling specific tasks. The redox ionic liquids provided higher specific energy by adding a faradaic component to the charge storage mechanism of activated carbon electrodes. The redox moieties were linked directly to the structure of the ionic liquid's ions, allowing concentrations up to 2.4 M in ferrocenyl units in acetonitrile which increased the specific energy of the device by 83% (vs. unmodified ionic liquid). While redox ionic liquid electrolyte capacitors with Fc attached to the cation provided an important self-discharge rate, the Fc-anion [FcNTf] enabled the complete suppression of self-discharge at the positive electrode. While the rate dependency of the specific energy and stability could be improved, these findings suggest that electroactive ionic liquids are particularly well-suited for use in redox-active electrolyte supercapacitors.

A2.2.7. Acknowledgments

The authors acknowledge the financial support of the Natural Sciences and Engineering Research Council of Canada (NSERC), under their Discovery Grants Program (#RGPIN/05743-2014).

A2.2.8. References

[1] E. Frackowiak, K. Fic, M. Meller, G. Lota, Electrochemistry serving people and nature: High-energy ecocapacitors based on redox-active electrolytes, ChemSuschem, 5 (2012) 1181-1185.
[2] S. Roldan, C. Blanco, M. Granda, R. Menendez, R. Santamaria, Towards a further generation of high-energy carbon-based capacitors by using redox-active electrolytes, Angew. Chem. Int. Ed., 50 (2011) 1699-1701.
[3] E. Frackowiak, M. Meller, J. Menzel, D. Gastol, K. Fic, Redox-active electrolyte for supercapacitor application, Faraday Discuss., 172 (2014) 179-198.
[4] S.T. Senthilkumar, R.K. Selvan, J.S. Melo, Redox additive/active electrolytes: a novel approach to enhance the performance of supercapacitors, J. Mater. Chem. A, 1 (2013) 12386-12394.
[5] S.T. Senthilkumar, R.K. Selvan, Y.S. Lee, J.S. Melo, Electric double layer capacitor and its improved specific capacitance using redox additive electrolyte, J. Mater. Chem. A, 1 (2013) 1086-1095.
[6] M. Tachibana, T. Ohishi, Y. Tsukada, A. Kitajima, H. Yamagishi, M. Murakami, Supercapacitor using an electrolyte charge storage system, Electrochemistry (Tokyo, Jpn.), 79 (2011) 882-886.
[7] S. Roldan, M. Granda, R. Menendez, R. Santamaria, C. Blanco, Supercapacitor modified with methylene blue as redox active electrolyte, Electrochim. Acta, 83 (2012) 241-246.

[8] G. Sun, K. Li, C. Sun, Electrochemical performance of electrochemical capacitors using Cu(II)-containing ionic liquid as the electrolyte, Microporous Mesoporous Mater., 128 (2010) 56-61.
[9] O. Fontaine, C. Lagrost, J. Ghilane, P. Martin, G. Trippé, C. Fave, J.C. Lacroix, P. Hapiot, H.N. Randriamahazaka, Mass transport and heterogeneous electron transfer of a ferrocene derivative in a room-temperature ionic liquid, J. Electroanal. Chem., 632 (2009) 88-96.
[10] Y. Miura, F. Shimizu, T. Mochida, Preparation, properties, and crystal structures of organometallic ionic liquids comprising 1-ferrocenyl-3-alkylimidazolium-based salts of bis(trifluoromethanesulfonyl)amide and hexafluorophosphate, Inorg. Chem., 49 (2010) 10032-10040.
[11] R. Balasubramanian, W. Wang, R.W. Murray, Redox ionic liquid phases: Ferrocenated imidazoliums, J. Am. Chem. Soc., 128 (2006) 9994-9995.
[12] B. Gelinas, J.C. Forgie, D. Rochefort, Conductivity and electrochemistry of ferrocenyl-imidazolium redox ionic liquids with different alkyl chain lengths, J. Electrochem. Soc., 161 (2014) H161-H165.
[13] B. Gélinas, D. Rochefort, Synthesis and characterization of an electroactive ionic liquid based on the ferrocenylsulfonyl(trifluoromethylsulfonyl)imide anion, Electrochim. Acta, 162 (2015) 36-44.
[14] A.M. O'Mahony, D.S. Silvester, L. Aldous, C. Hardacre, R.G. Compton, Effect of water on the electrochemical window and potential limits of room-temperature ionic liquids, J. Chem. Eng. Data, 53 (2008) 2884-2891.
[15] A. Gambou-Bosca, D. Belanger, Chemical mapping and electrochemical performance of manganese dioxide/activated carbon based composite electrode for asymmetric electrochemical capacitor, J. Electrochem. Soc., 162 (2015) A5115-A5123.
[16] J.-L. Brisset, Solubilities of various nitroanilines in water-pyridine, water-acetonitrile, and water-ethylene glycol solvents, J. Chem. Eng. Data, 30 (1985) 381-383.
[17] B. Akinwolemiwa, C. Peng, G.Z. Chen, Redox electrolytes in supercapacitors, J. Electrochem. Soc., 162 (2015) A5054-A5059.
[18] L.B. Chen, H. Bai, Z.F. Huang, L. Li, Mechanism investigation and suppression of self-discharge in active electrolyte enhanced supercapacitors, Energy Environ. Sci., 7 (2014) 1750-1759.
[19] L.-Q. Mai, A. Minhas-Khan, X. Tian, K.M. Hercule, Y.-L. Zhao, X. Lin, X. Xu, Synergistic interaction between redox-active electrolyte and binder-free functionalized carbon for ultrahigh supercapacitor performance, Nat. Commun., 4 (2013).